

Ocean Dynamics and the Carbon Cycle

Principles and Mechanisms

Richard G. Williams
Michael J. Follows

CAMBRIDGE

CAMBRIDGE

more information – www.cambridge.org/9780521843690

This page intentionally left blank

Ocean Dynamics and the Carbon Cycle: Principles and Mechanisms

The oceans play a crucial role in the climate system by redistributing heat and carbon across the planet through a complex interplay of physical, chemical and biological processes. This textbook for advanced undergraduate and graduate students presents a modern, multidisciplinary approach – essential for a complete understanding of ocean circulation and how it drives and controls marine biogeochemistry and biological productivity at a global scale.

Background chapters on ocean physics, chemistry and biology provide students from a variety of disciplines with a solid platform of knowledge to then examine the range of large-scale physical and dynamic phenomena that control the ocean carbon cycle and its interaction with the atmosphere. Throughout the text, observational data are integrated with basic physical theory to address cutting-edge research questions in ocean biogeochemistry.

- Simple theoretical models, data plots and schematic illustrations are used to summarise key results and connect the physical theory to real observations.
- Advanced mathematics is provided in boxes and the appendix where it can be drawn on as needed to put theory into practice.
- Numerous worked examples and homework exercises encourage students to develop first-hand experience and skills with real data and research problems.
- Further reading lists at the end of each chapter and a comprehensive glossary provide students and instructors with a complete learning package.

Ric Williams obtained a Ph.D. in Physical Oceanography from University of East Anglia in 1987. He worked as a researcher at Imperial College and as a research Fellow at the Massachusetts Institute of Technology before taking up a Lectureship at the University of Liverpool in 1993. In 2004, he was promoted to a Professor with a Chair in Ocean Dynamics and Biogeochemistry, and he is now Director of a Research Centre in Marine Sciences and Climate Change in Liverpool. Professor Williams' research focusses on understanding how the ocean circulates and its role in the climate system and he teaches undergraduate courses in 'Climate, Atmospheres and Oceans' and 'Ocean Dynamics'.

Mick Follows obtained a Ph.D. in Atmospheric Sciences from the University of East Anglia in 1991. After a year as a Royal Society Post-Doctoral Fellow at the Max Planck Institute for Chemistry in Mainz, Germany, he moved to the Massachusetts Institute of Technology where he is now a Senior Research Scientist in the Program for Atmospheres, Oceans and Climate. His research is focussed on understanding the interplay of physical, chemical and biological processes which determines the distributions and fluxes of elements in the ocean, and the relationship between marine ecosystems and their environment.

Cover illustrations (front and back): snapshots of surface current speed and the abundance of phytoplankton from a global ocean model (see linked website for animated views). Bright whites indicate fast speed revealing coherent streams linked to the ocean currents. The intensity of green represents the abundance of modelled phytoplankton, revealing the strong influence of the current structure. Model integrations and image processing by Oliver Jahn with Chris Hill, Stephanie Dutkiewicz and Mick Follows.

Ocean Dynamics and the Carbon Cycle

Principles and Mechanisms

Richard G. Williams

University of Liverpool

Michael J. Follows

Massachusetts Institute of Technology



CAMBRIDGE
UNIVERSITY PRESS

CAMBRIDGE UNIVERSITY PRESS
Cambridge, New York, Melbourne, Madrid, Cape Town,
Singapore, São Paulo, Delhi, Tokyo, Mexico City

Cambridge University Press
The Edinburgh Building, Cambridge CB2 8RU, UK

Published in the United States of America by Cambridge University Press, New York

www.cambridge.org
Information on this title: www.cambridge.org/9780521843690

© Richard G. Williams and Michael J. Follows 2011

This publication is in copyright. Subject to statutory exception
and to the provisions of relevant collective licensing agreements,
no reproduction of any part may take place without the written
permission of Cambridge University Press.

First published 2011

Printed in the United Kingdom at the University Press, Cambridge

A catalogue record for this publication is available from the British Library

Library of Congress Cataloguing in Publication data

Williams, Richard G., 1960-

Ocean dynamics and the carbon cycle : principles and mechanisms /

Richard G. Williams, Michael J. Follows.

p. cm.

Includes index.

ISBN 978-0-521-84369-0 (hardback)

1. Chemical oceanography. 2. Carbon cycle (Biogeochemistry)

I. Follows, Michael J. II. Title.

GC117.C37W55 2011

551.46'6 - dc22 2011010800

ISBN 978-0-521-84369-0 Hardback

Additional resources for this publication at www.cambridge.org/williamsandfollows

Cambridge University Press has no responsibility for the persistence or
accuracy of URLs for external or third-party internet websites referred to
in this publication, and does not guarantee that any content on such
websites is, or will remain, accurate or appropriate.

Contents

Preface	page	ix
Acknowledgements		xi
Illustration credit		xii

Part I	Introduction	1
---------------	---------------------	---

I	Why is the ocean important?	3
1.1	What is special about water?	3
1.2	How does the ocean store and transfer heat?	5
1.3	What is the role of the ocean in the global carbon cycle?	7
1.4	How have climate and life evolved on the planet?	10
1.5	Summary and outlook	15
1.6	Recommended reading	16

2	An introductory view of the ocean	17
----------	--	----

2.1	Ocean circulation	17
2.2	Atmospheric circulation	26
2.3	Life and nutrient cycles in the ocean	30
2.4	The carbon cycle in the ocean	34
2.5	Summary	38
2.6	Questions	38
2.7	Recommended reading	40

Part II	Fundamentals	41
----------------	---------------------	----

3	Transport fundamentals	43
3.1	How do tracers spread?	43
3.2	Tracer conservation and transport	49
3.3	What is the effect of a time-varying, eddy circulation?	55
3.4	Summary	62
3.5	Questions	63
3.6	Recommended reading	65

4	Physics fundamentals	66
----------	-----------------------------	----

4.1	Which forces are important for the ocean circulation?	66
4.2	How is the surface circulation determined?	68
4.3	How is the interior circulation determined?	76
4.4	Global-scale patterns of atmospheric forcing	80
4.5	Summary	89
4.6	Questions	90
4.7	Recommended reading	92

5 Biological fundamentals	93
5.1 Photosynthesis and respiration	93
5.2 What are marine microbes made of?	94
5.3 How is phytoplankton growth affected by the environment?	98
5.4 Phytoplankton community structure	106
5.5 Primary production and the fate of organic matter	110
5.6 Consequences for ocean biogeochemistry	115
5.7 Summary	121
5.8 Questions	122
5.9 Recommended reading	124
 6 Carbonate chemistry fundamentals	 125
6.1 Solubility of carbon dioxide	125
6.2 What are the reactions of the carbonate system in seawater?	128
6.3 What controls DIC in the surface ocean?	131
6.4 Coupling of DIC and alkalinity cycles with depth	139
6.5 How are changes in pCO ₂ related to changes in DIC?	142
6.6 Air-sea exchange of carbon dioxide	145
6.7 Summary	152
6.8 Questions	154
6.9 Recommended reading	155
 Part III Physical Phenomena and their Biogeochemical Signals	 157
 7 Seasonality of the upper ocean	 159
7.1 Seasonality in the physics	159
7.2 Seasonality in phytoplankton	164
7.3 Seasonality in the carbon cycle	172
7.4 Seasonality in the shelf and coastal seas	175
7.5 Summary	179
7.6 Questions	180
7.7 Recommended reading	182
 8 Ocean gyres and intense currents	 183
8.1 What are ocean gyres?	183
8.2 What are western boundary currents?	189
8.3 A theoretical view of ocean gyres and boundary currents	191
8.4 How is the Southern Ocean different to the rest of the globe?	203
8.5 Summary	206
8.6 Questions	208
8.7 Recommended reading	210

9 Ocean eddies	211
9.1 How does eddy variability alter over the globe?	211
9.2 A theoretical view of ocean eddy variability	215
9.3 Eddy fluxes of tracers	222
9.4 Summary	233
9.5 Questions	233
9.6 Recommended reading	235
10 Ventilation	236
10.1 How does ventilation vary over the globe?	236
10.2 A mechanistic view of ventilation	243
10.3 Summary	257
10.4 Questions	258
10.5 Recommended reading	259
11 Cycling and transport of nutrients and carbon	260
11.1 How are basin-scale contrasts in biological productivity maintained?	260
11.2 How is biological productivity sustained in ocean deserts?	267
11.3 What sets the nutrient distributions in the ocean interior?	276
11.4 Quantifying the ocean's carbon reservoirs	280
11.5 Summary	287
11.6 Questions	287
11.7 Recommended reading	288
12 The deep ocean and overturning	290
12.1 Why is the deep ocean important?	290
12.2 How does dense water form, mix and spread?	300
12.3 How does the deep ocean circulate?	311
12.4 How is dense water returned to the surface?	316
12.5 Summary	324
12.6 Questions	324
12.7 Recommended reading	326
Part IV Synthesis	327
13 Integral frameworks	329
13.1 Variations in the ocean–atmosphere carbon cycle	329
13.2 What is the fate of fossil-fuel carbon dioxide?	331
13.3 Glacial–interglacial changes in atmospheric CO ₂	338
13.4 Water-mass formation and transformation	344
13.5 Summary	350
13.6 Questions	351
13.7 Recommended reading	352

14 Overview and further challenges	354
14.1 Interconnections between the physics, chemistry and biology	354
14.2 Research approaches	356
14.3 Challenges	357
 <i>Appendix</i>	
A.1 Mathematical definitions	360
A.2 Derivation of the momentum equations	362
A.3 Solving the carbonate chemistry system	368
<i>Symbols and definitions</i>	
Biological and chemical symbols	370
Physical symbols	371
Mathematical definitions	374
<i>Glossary</i>	
Biological glossary	375
Chemical glossary	376
Physical glossary	377
<i>Answers</i>	381
<i>References</i>	388
<i>Index</i>	400

The colour plates are situated between pages 20 and 21.

Preface

We are all aware of how climate is continually changing on the Earth, but what is the role of the ocean in the climate system? To address this challenge, one needs to understand how the ocean circulates, how life flourishes in this environment and how carbon is stored and redistributed in the ocean. Understanding these issues requires an interdisciplinary approach, including fundamental knowledge and skills in physics, chemistry and biology.

This book is designed to provide a starting guide for any student or researcher enquiring as to how the ocean operates on the planet, bringing together the fundamentals needed to understand how the ocean behaves and a discussion of large-scale phenomena. The main themes addressed in the book are:

- How does the ocean circulate? Which are the principal physical phenomena in the ocean and how are they formed?
- How is the ocean ecosystem shaped by biological, physical and chemical processes?
- How is the ocean carbon cycle controlled and how is carbon dioxide exchanged between the atmosphere and ocean?

Our approach is to focus on the fundamental processes and mechanisms using observational data whenever possible to motivate our discussion. To make the material accessible, we have selected the appropriate theory that we feel is most relevant for interpreting the observational signals, rather than provide a more comprehensive theoretical review.

The book is divided into four parts. Part I provides an overall introduction: [Chapter 1](#) starts with a broad-ranging context as to why the ocean is important for the planet, and [Chapter 2](#) a descriptive and preliminary view of the themes addressed in more detail in the book – how the ocean circulates, where phytoplankton grow in the ocean and how carbon is cycled on the planet.

Part II applies basic undergraduate physics, chemistry and biology to address the underlying fundamental principles at work in the ocean:

the transport concepts of advection, diffusion and eddy transfer; the physical concepts of large-scale flow and atmospheric forcing; the basic biological principles of cell growth and production of organic matter; and the chemical concepts of mass balance, energetics and charge balance regulating the carbon cycle.

Part III addresses a range of physical phenomena and their effects on the biogeochemistry and cycling of carbon, including the following themes: how seasonality varies; why there are gyres and boundary currents; how ocean eddies form and their large-scale effect; how surface waters are transferred to the ocean interior; how the interplay of physical and biological processes affect the carbon cycle; and how the deep ocean overturns.

Part IV provides two integrated frameworks to understand, firstly, how carbon is cycled and partitioned between the atmosphere and ocean, and secondly, how water masses are formed over the globe. Finally, we provide concluding remarks about the way forward.

Colour plates are used to provide a mini atlas, conveying how physical and biogeochemical properties vary throughout the ocean, complementing the black and white figures used throughout the book.

The book is designed for two different audiences: Honours or graduate students wishing to gain an understanding of how the ocean behaves, with a firm emphasis on observational signals, as well as researchers in a particular discipline who wish to acquire a broader, more interdisciplinary view of the ocean. Students are recommended to read through Part I to gain a preliminary view, then work through the Fundamental chapters in Part II, before embarking on the more advanced material in Part III. More experienced researchers are recommended to work through the Fundamental chapters outside their own expertise in Part II, then examine the more detailed description of physical phenomena and their impacts on the carbon cycle in Part III, and the integrated frameworks in Part IV.

Understanding these topics can often be challenging at times and the language and level of mathematics off-putting. Consequently, we have designed this book to be as accessible as possible for an interdisciplinary audience. The scientific questions are discussed through a combination of data-based diagnostics, schematic illustrations and, in some cases, theoretical balances requiring an understanding of calculus, where a more quantitative understanding can be gained by working through the equations governing rates of change

or identifying equilibrium states. More formal material is included in boxes and the appendix detailing derivations and mathematical tools, as well as in targeted questions to work through at the end of the chapters. Hopefully, readers can find the appropriate level to suit themselves.

Finally, we have presented our own perspective in addressing these questions and, in some cases, there is no clear consensus and readers need to be aware that many of the research topics are ongoing and merit further investigation.

Acknowledgements

We are grateful to the many researchers cited in the text who have generously allowed their carefully collected data to be reproduced here, as well as those researchers who have compiled ocean and atmospheric datasets, and developed visualisation tools; without their help we could not have written this book. Many people deserve thanks, but special mention goes to Kay Lancaster for meticulous work in fine editing and drawing the figures, Susan Lozier and her research group for hospitality and detailed feedback during a sabbatical at Duke University, and David Marshall for insightful discussions and encouragement. In developing the material for the book, we are grateful for thoughtful discussions with Arnaud Czaja, Stephanie Dutkiewicz, Phil Goodwin, John Green, Chris Hughes, Taka Ito, John

Marshall, Jonathan Sharples, Darryn Waugh and Chris Wilson. For detailed feedback on draft chapters and assistance with figures, we also thank Gualtiero Badin, Simon Evans, Raf Ferrari, David Ferreira, Steve Groom for supplying the satellite images, Anna Hickman, John Huthnance, Oliver Jahn and Chris Hill for providing the cover images, Susan Leadbetter, Claire Mahaffey, Anne-Willem Omta, Andreas Oschlies, Vassil Roussenov, Geoff Vallis, Ben Ward, Martin White, Sam Williams, George Wolff and Carl Wunsch, as well as other friends, colleagues and students at Liverpool University, the Proudman Oceanography Laboratory and Massachusetts Institute of Technology. Finally, we especially thank our families for their encouragement, humour and support.

Illustration credits

The publishers listed below are gratefully acknowledged for giving their permission to reproduce original figures, and to use redrawn figures based on illustrations in journals and books for which they hold the copyright. The original authors of the figures are cited in the figure captions, and we are grateful to them also for the use of their figures. Publication details are given in the captions/References list. Every effort has been made to obtain permission to use copyrighted materials, and apologies are made for any errors or omissions.

American Geophysical Union: all original figures are © American Geophysical Union in the year as stated in caption/references, and reproduced/modified by permission.

Figures: 2.8, 5.17, 7.11, 8.19, 9.4, 11.3a, 11.4, 11.6, 11.15, 12.9, 12.22, 13.2.

American Meteorological Society: all original figures are © American Meteorological Society

in the year as stated in caption/references, and reprinted/modified with permission.

Figures: 1.3, 2.13, 3.3, 3.18, 8.9, 8.18, 9.2, 9.3, 9.5, 9.9, 9.10, 9.11, 9.12, 9.14, 9.17, 9.18, 10.9, 10.10, 10.11, 10.14, 10.15, 10.16, 10.18, 12.4, 12.7, 12.11a, 12.15, 13.11

Elsevier journals: all original figures are copyrighted in the year as stated in caption/references, and reprinted/modified with permission from Elsevier.

Figures: 2.15, 3.5, 3.7, 3.17, 5.8, 5.14, 6.18, 7.9, 7.16, 7.21, 8.10, 11.12, 12.10, 12.11b, 12.12, 12.14, 12.21.

Nature/Nature Geoscience journals: all original figures are copyrighted in the year as stated in caption/references, and reprinted/modified by permission from Macmillan Publishers.

Figures: 1.2b, 3.8, 3.19, 11.14, 12.13, 12.16, 12.17, 12.18.

Part I

Introduction

Chapter I

Why is the ocean important?

The ocean is vast, covering more than two thirds of the Earth's surface (Fig. 1.1). This reservoir of liquid water has helped determine the Earth's climate, storing and transporting heat, making the atmosphere warm and moist, and enabling life to flourish in the sea and on land. In turn, the emergence of life has altered the composition of the atmosphere, increasing the amount of oxygen and ozone, which shields harmful radiation from the Earth's surface.

The anthropogenic release of carbon dioxide is currently perturbing the climate system. The ocean is taking up typically a third of the extra carbon dioxide emitted to the atmosphere, as well as storing and redistributing much of the extra heat supplied to the climate system. To understand this ocean uptake and warming, one needs to understand how the ocean circulates, redistributing heat and carbon, how gases are transferred across the air-sea interface, how carbon dioxide reacts in seawater and the relationship between living plants and carbon.

Our aim in this book is to consider the dynamics of the ocean and effect on the carbon cycle, presenting relevant observations, and discussing the fundamental principles and mechanisms at work. In this chapter, we provide a broad context for the book, addressing how the ocean and the carbon cycle have been important in the climate system throughout Earth's history.

1.1 | What is special about water?

Many important characteristics of the ocean originate from the special properties of water (Table 1.1). A water molecule consists of two hydrogen atoms joined to an oxygen atom: the hydrogen atoms lying on one side of the molecule and the oxygen atom on the other, which leads to a positive charge on the hydrogen side and a negative charge on the oxygen side. At low temperatures, this charge contrast leads to water molecules preferentially orientating themselves in an ordered structure, such that the positive side of a water molecule is opposite the negative side of another water molecule; these inter-molecular bonds are referred to as hydrogen bonds. Extra energy is needed to disrupt this ordered structure in order to make water molecules vibrate more and increase their temperature, as well as to change their phase from ice to a liquid and then to a vapour. Hence, water has a high heat capacity and, combined with its large volume, makes the ocean the largest heat store in the climate system.

Water is a good solvent and dissolves many compounds relatively easily, so that the ocean contains all the natural elements in dissolved form, including dissolved salts making seawater characteristically salty, as well as dissolved gases, oxygen and carbon dioxide, and dissolved nutrients that support life. Water strongly absorbs



Figure I.1 The ocean covers the majority of the Earth's surface, as emphasised by this visible satellite picture of the Pacific sector of the globe for 6 March 2008 at 2100 UTC. The ocean absorbs much of the incident sunlight and has low reflectance (dark), while there is higher reflectance from land (grey) showing the west coast of America and cloud (white). From GOES West along 135°W; courtesy of NERC Satellite Receiving Station, University of Dundee.

Table I.1 Properties of water and their implications for the ocean.

Property	Definition	How water compares with other substances	Implications for the ocean and climate system
Specific heat capacity	Heat required to raise temperature of a unit mass by 1 K.	Highest for all liquids and solids (except NH ₃).	Limits temperature range over the Earth.
Latent heat of evaporation	Heat required to evaporate a unit mass.	Highest.	Phase changes are important for the storage and release of heat.
Solvent power	Ability to dissolve substances.	Highest.	Ocean has a high storage of dissolved elements, including nutrients.
Surface tension	Attraction of liquid surface to itself.	Highest.	Bubbles and drops form, which enhance the air-sea transfer of water and gases.
Conduction of heat	Transfer of heat between molecules.	Highest of all liquids.	Heat easily transferred, although turbulence usually dominates.
Molecular viscosity	Resistance to flow.	Less than most liquids.	Ocean easily circulates over the Earth.

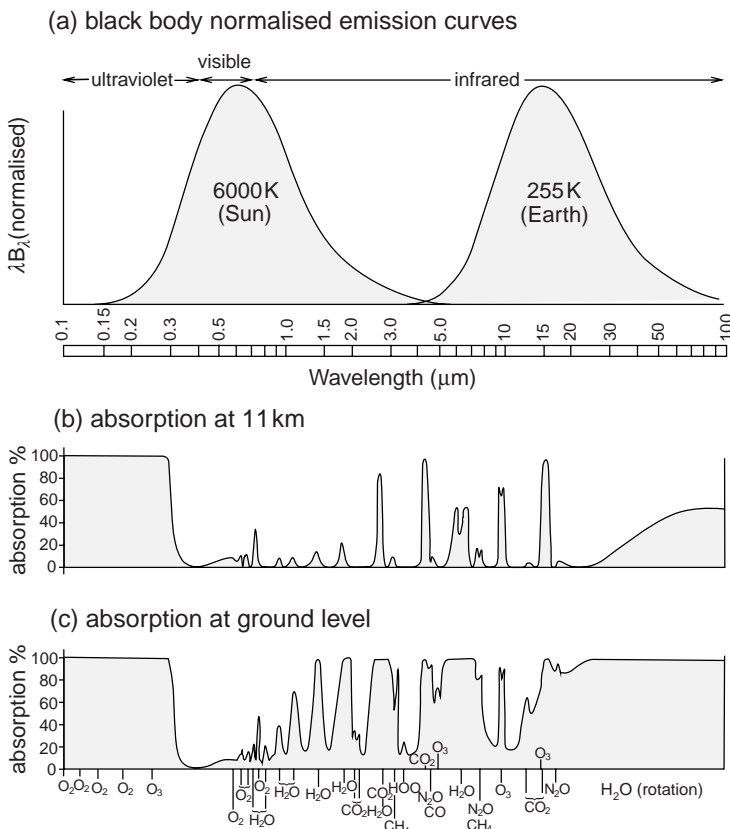


Figure 1.2 (a) Normalised curves for the emission of radiation versus wavelength ($\mu\text{m} = 10^{-6} \text{ m}$) from the Sun with a temperature of 6000 K and the Earth with a temperature of 255 K assuming blackbody emission spectra, which span the ultraviolet, visible (0.4 to 0.7 μm) and infrared wavelengths. The radiation from the Sun and Earth is referred to as solar and long wave, respectively; (b) percentage absorption of radiation at a height of 11 km versus wavelength; and (c) at the ground. The absorption of radiation depends on the chemical composition of the atmosphere: oxygen and ozone molecules in the ultraviolet band; oxygen, ozone and water vapour, carbon dioxide, methane and nitrous oxide for the infrared band.

Redrawn from Goody and Yung (1989).

electromagnetic radiation and sunlight only penetrates a few tens of metres in the ocean, leading to the surface ocean being sunlit and warm, while the vast bulk of the ocean is dark and cold. Water has a low viscosity and moves more freely than many liquids, so that the ocean easily circulates and redistributes heat, carbon and other properties over the globe.

1.2 How does the ocean store and transfer heat?

The ocean affects the properties of the overlying atmosphere, modifying the radiation balance, as well as the storage and transport of heat.

1.2.1 How does atmospheric composition affect radiative heating?

The chemical composition of the atmosphere determines the radiative heating of the Earth, as

the molecular structure of each gas affects which wavelengths of radiation are absorbed and emitted (Fig. 1.2):

- Oxygen accounts for about one fifth of the gas molecules in the atmosphere and is formed by biological activity in the oceans and on land. Ultraviolet radiation from the Sun splits oxygen molecules forming ozone, a molecule of three oxygen atoms. Ozone effectively absorbs much of the incoming ultraviolet radiation high in the atmosphere, acting as a ‘sunscreen’ for the living creatures at the surface of the Earth.
- Water vapour is an important minor constituent of the atmosphere, supplied by evaporation from the ocean and land surface, and returned in the form of rain and snow when the atmosphere becomes saturated. Water vapour primarily absorbs infrared radiation emitted from the Earth, as well as some infrared radiation emitted from the Sun. The atmosphere absorbs and emits infrared radiation both out to space and back down to the surface, which then warms

the Earth's surface; this process is referred to as the 'greenhouse effect'.

- Carbon dioxide and other minor atmospheric constituents including methane and nitrous oxide absorb strongly in the infrared, and so collectively contribute to the greenhouse effect.

At first sight, radiative heating of the planet might appear only to depend on the atmosphere. However, the ocean plays an important modulating role. Firstly, the ocean has a low albedo compared with most land surfaces and ice, so absorbs a large proportion of the incident sunlight. Secondly, the ocean affects the properties of the overlying atmosphere by releasing moisture and affecting the concentration of trace gases. For example, a warmer ocean leads to more water vapour and carbon dioxide being held in the atmosphere, which increases the atmospheric absorption and emission of infrared radiation. In turn, this increase in radiative heating warms the ocean, which further increases the amount of water vapour and carbon dioxide in the atmosphere. This feedback process plays an important role in the climate system, since the ocean store of carbon dwarfs that of the atmosphere; typically more than fifty times as much carbon is stored in the ocean as in the atmosphere. Hence, small fractional changes in the ocean store of carbon can drive much larger changes in atmospheric carbon dioxide, which then alters the radiative heating.

1.2.2 How does the ocean storage of heat affect the planet?

The oceans provide a stabilising effect on the Earth since the presence of water limits temperature changes over the globe. Energy supplied to water molecules is used to break hydrogen bonds, as well as increase the temperature of the molecules.

The ocean store of heat far exceeds that of the atmosphere or the surface land due to two factors. Firstly, the ocean storage of heat is much larger than that of the atmosphere due to the greater density of water and the greater heat capacity per unit mass (Table 1.1); the upper 2.5 m of ocean holds as much heat as the entire overlying atmosphere. Secondly, the ocean holds more heat than the surface land (defined by the upper few metres

of soil) because heat is transferred more effectively in a convecting fluid than within a solid. Seasonal temperature changes extend to depths of several hundreds of metres in the upper ocean, but only penetrate a few metres in soil. Thus, seasonal heat storage is spread over a larger mass in the ocean than in the surface land. Hence, seasonal temperature changes are much smaller in the air over the surface ocean than the land surface, defining the contrasting marine and continental climates over the Earth.

1.2.3 How does the ocean affect the redistribution of heat?

Rather than only acting as a local reservoir of heat, the ocean assists the atmosphere in redistributing heat over the globe. To understand this process, one needs to consider how the Earth is heated. The Earth is warmed by the incident radiation from the Sun, with about 70% of sunlight absorbed by the ocean, land and the atmosphere, and the remainder reflected back to space. In return, thermal energy is emitted back to space as infrared radiation from the atmosphere, ocean and land. Averaged over the globe and over several years, the net incoming solar radiation (incident sunlight minus reflected sunlight) balances the amount of outgoing infrared radiation at the top of the Earth's atmosphere.

However, this overall balance does not apply locally. There is a greater intensity of sunlight in the tropics than at the poles due to the angle between the incident sunlight and the Earth's surface. Outgoing infrared radiation instead only weakly decreases with latitude due to relatively small changes in absolute temperature in the upper atmosphere. Consequently, there is a net radiative heating over the tropics and cooling over the poles (Fig. 1.3a). In response to this latitudinal contrast, the atmosphere and ocean together transfer heat poleward (Fig. 1.3b), reaching 5 PW at mid latitudes ($1 \text{ PW} \equiv 10^{15} \text{ watt}$; $1 \text{ watt} \equiv \text{joule s}^{-1}$). This heat transfer prevents the tropics becoming even warmer and the poles even cooler. Indeed, if there was *not* this heat transfer, the latitudinal temperature contrast would increase across the globe, probably becoming twice as large as in the present day, until a local radiative heat balance was reached.

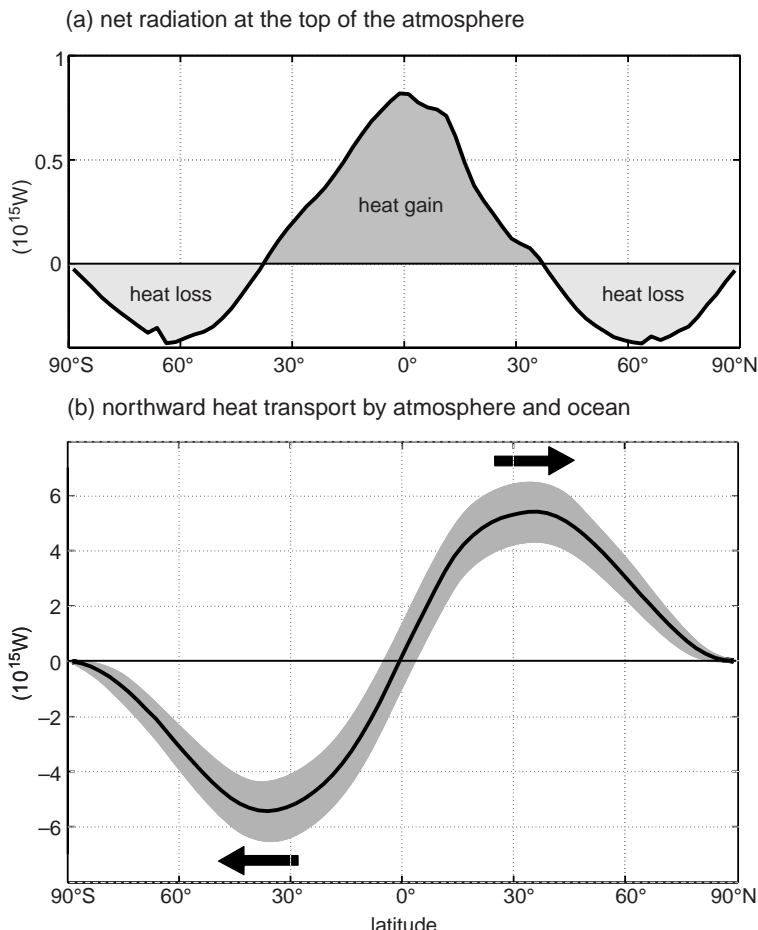


Figure I.3 (a) The net radiation at the top of the atmosphere averaged over latitude bands ($PW \equiv 10^{15}$ watts) revealing heat gain in the tropics (dark grey) and loss over the mid and high latitudes (light grey). (b) The implied northward transfer of heat (PW) with shading denoting the error range and arrow denoting the direction. Data from the Earth Radiation Budget Experiment from 1987–1989; redrawn from Wunsch (2005).

We next consider how the ocean affects the climate system through the carbon cycle.

1.3 What is the role of the ocean in the global carbon cycle?

The amount of carbon dioxide residing in the atmosphere is important in affecting the Earth's radiative heating. However, this atmospheric store of carbon is dwarfed by the amount of carbon stored in the land and the oceans (Table 1.2). The carbon reservoir in terrestrial plants and soil is also several times larger than that in the atmosphere. Since all of these reservoirs are connected, minor changes in the ocean or geological reserves of carbon can lead to large changes in atmospheric carbon dioxide.

Table 1.2 Carbon budget for the Earth in the pre-industrial era (Sarmiento and Gruber, 2002; Tyrell and Wright, 2001).

Reservoir	Mass of carbon (10^{15} g = Pg)
Atmosphere	600
Ocean	38 000
Vegetation/soils	2 000
Fossil fuels	3 700
Rocks (organic)	14 000 000
Rocks (as calcium carbonate)	60 000 000

1.3.1 How does the ocean store carbon? Carbon dioxide is soluble and reacts with seawater to form bicarbonate and carbonate ions; the sum of the bicarbonate and carbonate ions, and dissolved carbon dioxide is collectively referred to

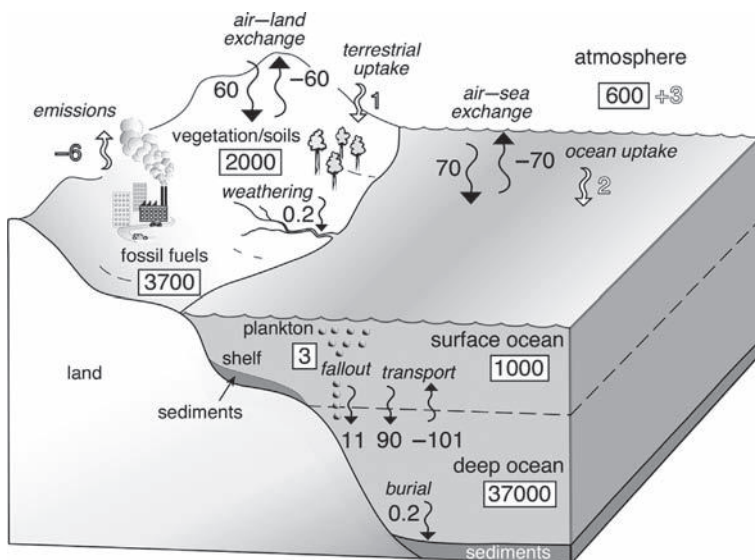


Figure 1.4 Estimated reservoir sizes (Pg C, boxed numbers) and annual fluxes (Pg C yr⁻¹, associated with arrows) for the global carbon cycle in the immediate pre-industrial era. The emissions from fossil fuels are driving fluxes of anthropogenic carbon dioxide (white arrows). Estimates are for the 1990s taken from Sarmiento and Gruber (2002), where a more detailed evaluation can be found. Drawn by K. Lancaster.

as dissolved inorganic carbon. Due to the particular chemistry of seawater and the influence of dissolved salts, more than 99% of the dissolved inorganic carbon is in the form of bicarbonate and carbonate ions, enhancing the ocean capacity as a carbon reservoir by more than 100-fold to about 38 000 Pg C. Most of the ocean's storage of carbon is due to this chemical reactivity. This store of carbon is not restricted to the surface ocean. Instead, most of the carbon is held in the deep ocean through its greater volume and higher concentrations of dissolved inorganic carbon (Fig. 1.4). The increase in dissolved inorganic carbon concentration in the deep ocean is primarily due to carbon being more soluble in cold waters and the physical transport of cold, carbon-rich waters from the surface to the deep ocean. Biological transfer of organic carbon also leads to an increase in dissolved inorganic carbon in the deep ocean, accounting for perhaps 10% of its increase with depth.

1.3.2 How is carbon exchanged between the atmosphere and ocean?

There are large seasonal exchanges of carbon dioxide between the atmosphere, ocean and terrestrial biosphere, leading to the atmospheric reservoir of carbon being replaced every few years. The spring and summer expansion of the terrestrial biosphere is imprinted on atmospheric CO₂: low-

est CO₂ during the autumn and highest CO₂ during spring, with the strongest seasonality in the northern hemisphere due to the greater extent of land masses (Fig. 1.5). The exchange between the atmosphere and ocean is communicated through the surface mixed layer of the ocean, which is on the order of 100 m thick, and holds a comparable amount of carbon as stored in the atmosphere. Over the globe, ocean circulation transfers about 100 Pg C between this surface layer and the deep ocean each year, taking several hundred years for the carbon in the deep ocean to be replaced and flushed through, since its reservoir is so large, reaching 37 000 Pg C.

The available fossil-fuel reservoir is large relative to the atmospheric store of carbon dioxide (Table 1.2). The release of fossil-fuel carbon has increased the atmospheric concentration over the past century (Fig. 1.4); only about half of anthropogenic emissions have remained in the atmosphere since the pre-industrial era, with the remainder going into the terrestrial biosphere and oceans in roughly equal proportions. However, the fluxes of anthropogenic carbon into the terrestrial biosphere and ocean are relatively small compared with the natural, seasonal exchanges; only one to two per cent of the seasonal fluxes (Fig. 1.4, white arrows). Thus, it is difficult to quantify accurately the fate of anthropogenic carbon dioxide in the global system.

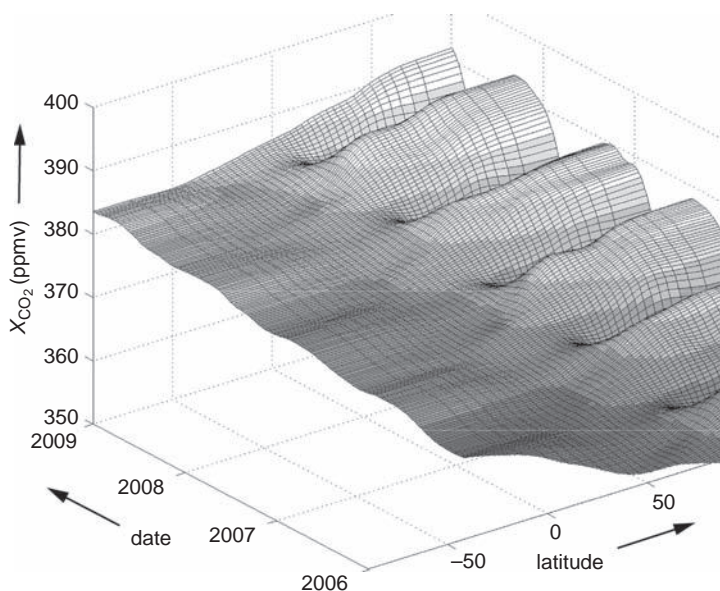


Figure 1.5 Near-surface mixing ratio of atmospheric carbon dioxide X_{CO_2} (ppmv) as a function of latitude and time, for years 2006–2008 inclusive, interpolated from observations by the GLOBALVIEW-CO₂ network of monitoring stations (GLOBALVIEW-CO₂, 2009). Note date increases to the left.

1.3.3 How do marine ecosystems cycle carbon?

The Sun's rays not only provide the ultimate source of heat to the Earth, they also provide the fundamental energy source for photosynthesis: the energy from photons in visible wavelengths are utilised to create organic molecules from water, carbon dioxide and other nutrients. The organic molecules form the machinery enabling life to function and provide a store of energy which can be accessed by respiration, ultimately sustaining most of life on land and in the oceans.

The most abundant photosynthesising organisms in the sea are the phytoplankton, tiny unicellular organisms ranging between 1 and 100 microns in size, often forming chains or colonies constituting many cells, and extremely diverse in both form and function, as depicted in the microscope images in Fig. 1.6.

Due to the efficient absorption of electromagnetic radiation by seawater, phytoplankton are only able to grow in the upper, sunlit layer of the ocean, typically above the upper 100 m or so. The organic matter created by phytoplankton and their detritus is respired by other organisms, including submicron size bacteria and archaea (both single-celled micro-organisms without a

nucleus). Larger organisms, including zooplankton graze upon living phytoplankton and are, in turn, eaten by fish. Phytoplankton cells and faecal pellets from the larger organisms sink into the deeper, dark waters where, even though photosynthesis cannot occur, there is a rich and diverse ecosystem. The surface ocean ecosystem produces about 11 Pg C of sinking organic particles each year, but maintains a biomass of only 3 Pg C at any time, reflecting a rapid cycle of production and loss.

Almost all of the sinking organic matter is respired back to dissolved inorganic form before reaching the sea floor. In this way, dissolved inorganic carbon is biologically transferred to organic carbon in the surface, sunlit ocean, the organic carbon sinks, and then is respired and returned to dissolved inorganic carbon at depth (Fig. 1.4). This biologically mediated transfer of carbon enhances the deep ocean's store of dissolved inorganic carbon by about 10%.

1.3.4 How does ocean circulation affect the ecosystem?

Phytoplankton use chlorophyll *a*, a pigment which absorbs sunlight at red and blue wavelengths while scattering green wavelengths. Remotely sensed images of the Gulf Stream reveal a ribbon

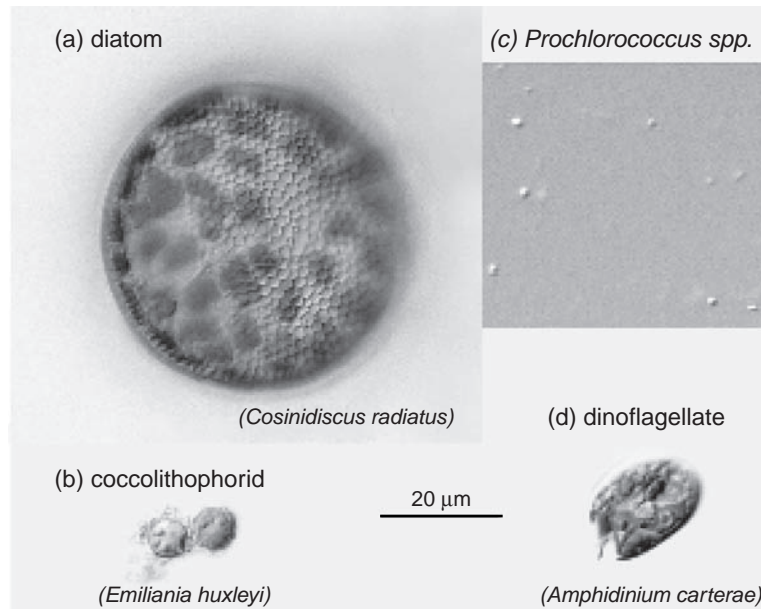


Figure 1.6 Light microscope images of representatives of several ‘functional groups’ of phytoplankton at the same magnification scale (horizontal line represents $20 \mu\text{m} = 20 \times 10^{-6} \text{ m}$). The phytoplankton population is extremely diverse in terms of function and genetic make-up, as well as spanning many orders of magnitude in cell volume. Cell size places some important restrictions on their ability to acquire resources and their interaction with predators. (a) Diatoms form silica-based cell structures (here seen as a beautiful honeycomb pattern in *Coscinidiscus radiatus*, which may provide an energy saving relative to a cellulose structure. (b) Coccolithophorids, like *Emiliania huxleyi* form calcium carbonate mineral structures, providing defence against grazing. (c) *Prochlorococcus* are the smallest photosynthesising cells on the planet. Their small size makes them highly suited to nutrient starved situations. (d) Dinoflagellates combine both photosynthesis and predation as energy sources. In coastal waters, some dinoflagellates, such as *Amphidinium carterae*, produce toxins, possibly as a defence strategy, which lead to harmful algal blooms and can affect shell fisheries. Images M. Follows with help from R. Andersen.

of warm water running along the western boundary of the North Atlantic, separating from the North Carolina coast and extending into the open ocean (Fig. 1.7a, light shading). As is common in the ocean, there are higher chlorophyll concentrations in the cooler waters to the north of the Gulf Stream (Fig. 1.7b, light shading) than in the warmer waters within the current or to the south.

Biochemical reactions proceed faster at warmer temperatures, so more biomass might be expected in warmer waters. However, the opposite situation occurs, reflecting how photosynthesis is more strongly controlled by the availability of nutrients than by temperature. The organic molecules of living organisms require elements, including nitrogen, phosphorus, silica and other trace metals, in addition to carbon, hydrogen and oxygen. These nutrients are often in scarce supply

in the surface ocean and, thus, their availability controls the production of new organic matter. In the open ocean, nutrients are primarily supplied to surface waters by the physical circulation transferring nutrient-enriched deep waters to the surface. In turn, the consumption and sinking of organic matter, as well as the sinking of cold waters, returns nutrients back to the deep waters.

1.4 | How have climate and life evolved on the planet?

Stepping back in time, the ocean has played a central role in the evolution of the planet by assisting in the burial of carbon in sedimentary rocks and providing the habitat for the first living creatures.

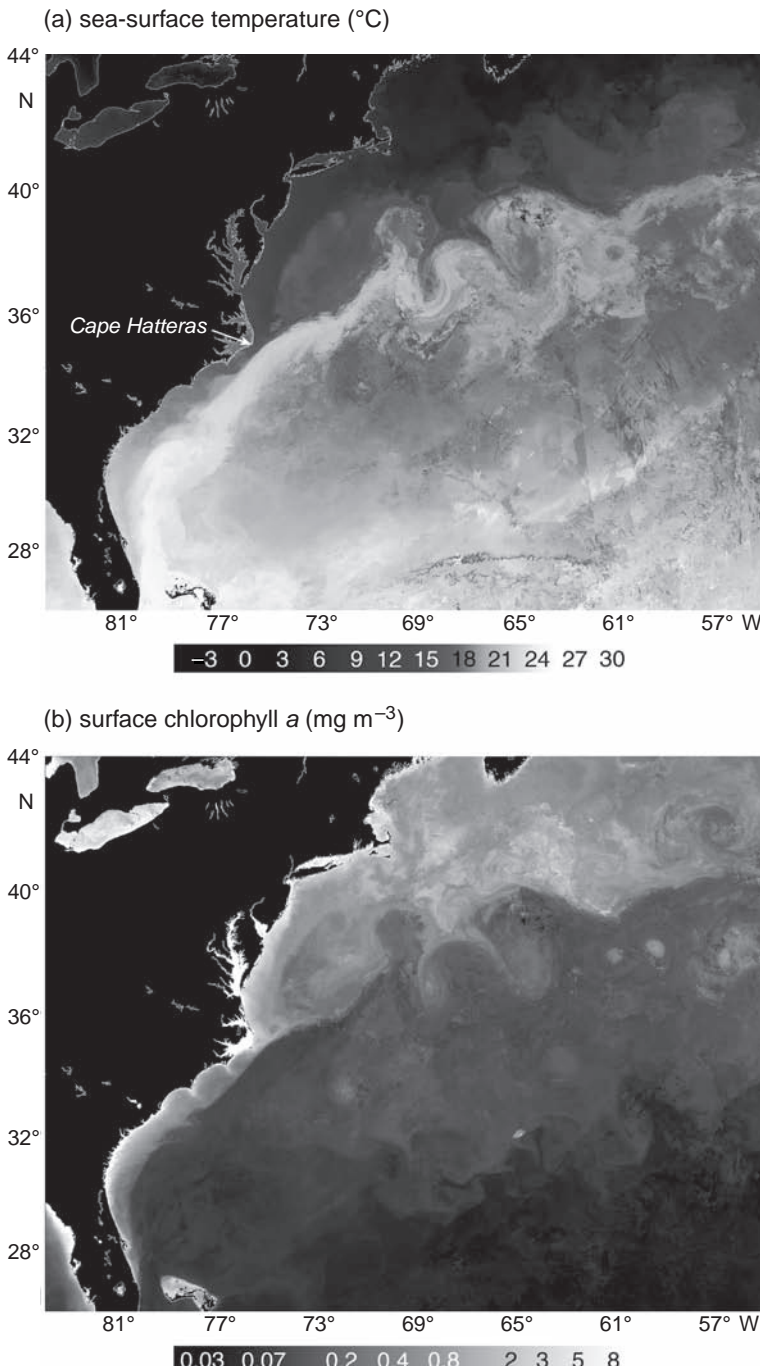


Figure I.7 The path of the Gulf Stream in remotely sensed images of (a) sea-surface temperature ($^{\circ}\text{C}$, warm is light, cold is dark) and (b) surface chlorophyll *a* (mg m^{-3} , light shading is high concentration, dark is low concentration) from 13 to 21 May 2006 over the North Atlantic. The core of the Gulf Stream is apparent as the plume of warmest waters, leaving the coast at Cape Hatteras, and spreading into the interior. The colder waters on the northern flank of the Gulf Stream are more productive, as there are more inorganic nutrients to sustain the growth of phytoplankton, than in the warmer waters. The image is derived from NASA Moderate-Resolution Imaging Spectroradiometer (MODIS) and formed by a composite of cloud-free data with any remaining missing data replaced from a monthly composite; processing and images supplied by Rhys Elsworth and Steve Groom, Plymouth Marine Laboratory.

1.4.1 How has atmospheric carbon dioxide decreased over geological timescales?

The presence of water and oceans facilitated a dramatic reduction in the abundance of carbon dioxide in the early atmosphere. At present, the

Earth's atmosphere consists mainly of nitrogen and oxygen, with only a trace of carbon dioxide of about 0.04% by volume. However, over 4000 Ma ago, Earth's atmosphere had a much higher proportion of carbon dioxide probably more similar to the present day atmospheres of Venus and Mars

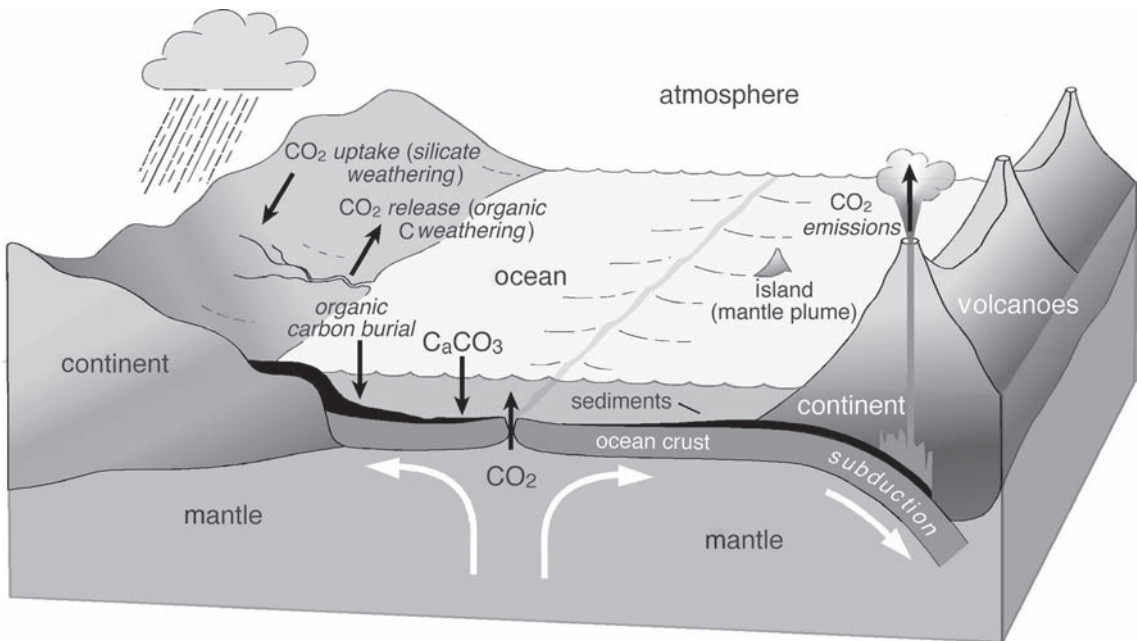


Figure 1.8 Schematic figure of the long-term carbon system involving the exchange of carbon between the atmosphere, ocean and terrestrial systems on geological timescales. Carbon is transferred from the atmosphere to ocean sediments via chemical weathering, where acidic rain reacts with silica rocks, forming calcium and carbonate ions washed out to sea, which precipitate and form calcium carbonate sediments: $\text{CO}_2 + \text{CaSiO}_3 \rightarrow \text{CaCO}_3 + \text{SiO}_2$. Subduction of ocean crust below continents leads to eventual melting, releasing carbon dioxide contained within any organic carbon or calcium carbonate in the sediments through volcanic emissions, hydrothermal vents or mantle plumes. For a detailed discussion of the chemical and geological processes, see Berner (1999); drawn by K. Lancaster.

made up mainly of carbon dioxide. How did this dramatic change in the Earth's atmosphere come about?

The high concentrations of carbon dioxide in the atmosphere are thought to have decreased due to chemical weathering of rocks facilitated by liquid water (Fig. 1.8). Carbon dioxide dissolves in rain, forming a weak carbonic acid that reacts with silicate rocks to release calcium and bicarbonate ions. These ions are carried by rivers out to sea, where calcium carbonate is formed and deposited on the sea floor to become chalk and limestone. Over time weathering of silicate rocks has led to the bulk of Earth's carbon being transferred from the atmosphere and ocean into calcium carbonate rocks (Table 1.2).

Since the rise of life on the Earth, the formation of calcium carbonate in the oceans has been almost entirely mediated by living organisms. Certain plankton, such as coccolithophorids depicted in Fig. 1.6b, use calcium carbonate to form struc-

tural and defensive hard shell components. When these organisms die or are eaten, the calcium carbonate material sinks through the water column, carrying some organic carbon. Depending upon the chemistry of the deep waters, some of the sinking calcium carbonate and associated organic carbon may then be deposited and buried on the sea floor.

The drawdown of atmospheric carbon dioxide into sediments has not been entirely unchecked, since carbon dioxide is returned to the atmosphere through geological activity (Fig. 1.8). Heating in the Earth's core drives convection currents in the mantle and the slow movement of the continents, which open and close ocean basins on timescales of several hundred million years; continents move at speeds comparable to the rate at which your fingernails grow. The denser ocean floor material is pushed beneath the continents, melting the ocean crust and releasing any organic carbon and calcium carbonate into

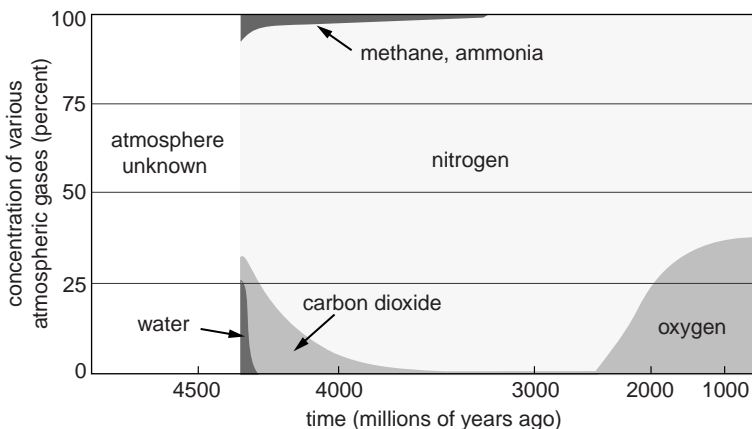


Figure 1.9 Estimates for the composition of different gases (%) in the Earth's atmosphere over geological age (1000 Ma). Redrawn from Allegre and Schneider (2005). Image by Ian Warpole, reproduced with permission.

the magma. Carbon dioxide degasses from the magma to the atmosphere and ocean through a variety of pathways, including volcanoes on colliding plate boundaries and subduction zones, above mantle plumes beneath continents and oceans, as well as from deep-sea hydrothermal vents. Hence, carbon is exchanged between the ocean-atmosphere and solid Earth on timescales ranging from years linked to volcanic emissions to hundreds of million years linked to the movement of continents.

1.4.2 How did oxygen first emerge?

Life first emerged in the oceans. Oxygen was formed as a by-product of photosynthesis, first released from cyanobacteria, and later from algae and plants in the oceans, where they were protected from harmful ultraviolet radiation. The first signs of a significant elevation of atmospheric oxygen occurred 2.4 billion years ago when concentrations are thought to have increased from less than 10^{-5} to 10^{-2} or 10^{-1} of the present-day values (Kasting, 2001; Holland, 2006) (Fig. 1.9). This chemical signature of life makes our planet distinct from its nearest neighbours, Venus and Mars.

Oxygen is consumed during respiration, the reverse process of photosynthesis, in which organic matter is oxidised to recover the energy stored within. Almost all non-photosynthesising organisms make their living by respiring organic matter. Integrated over the globe, the total production of oxygen by photosynthesis is very nearly balanced by respiration. If the production and loss terms balanced exactly, oxygen would never

have accumulated in the atmosphere. However, the balance is broken when sinking organic matter is buried in sediments of the deep oceans, away from oxygen and then protected from respiration (Falkowski and Isozaki, 2008). Though only a tiny fraction of the total production of organic carbon in the surface ocean is eventually buried (Fig. 1.8), this burial led to an imbalance and a long-term accumulation of oxygen in the atmosphere.

The emergence of oxygen has enabled more complex life forms to evolve on the planet. The presence of molecular oxygen has also led to the formation of the 'ozone layer' in the upper atmosphere, which absorbs harmful ultraviolet radiation from the Sun. After the shielding of the Earth's surface from this harmful radiation, life has moved from the oceans and successfully colonised the land. Hence, the ocean has facilitated the emergence of life, providing a supportive environment for photosynthesis and assisting the rise of atmospheric oxygen through the burial of organic carbon in sediments.

1.4.3 How has atmospheric carbon dioxide varied with glacial-interglacial cycles?

Ice-core records reveal dramatic changes in atmospheric carbon dioxide, varying between 180 and 300 ppmv in regular cycles over more than 400 000 years prior to the industrial era, as depicted in Fig. 1.10a. During cold glacial periods with expanded ice cover, atmospheric temperatures were as much as 8°C cooler than the present day (Fig. 1.10b) and were associated with relatively

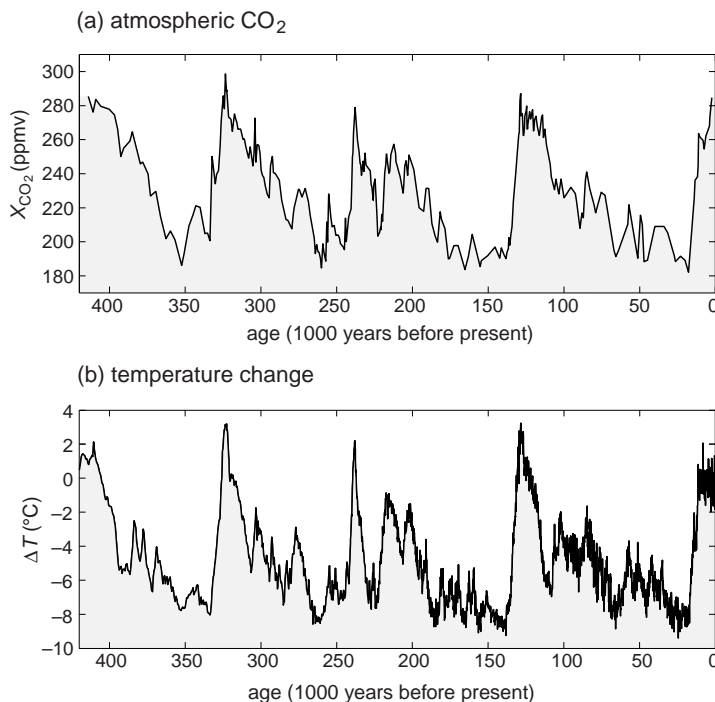


Figure 1.10 Reconstructions of (a) atmospheric carbon dioxide mixing ratio X_{CO_2} in parts per million by volume (ppmv) and (b) temperature change ($^{\circ}\text{C}$) from the Vostok ice core in Antarctica over the last 400 000 years. The data are taken from trapped gas bubbles taken from depths ranging from 148 m to 3304 m in the ice, with corresponding gas ages of 2342 to 417 160 years before the present. The ice record reveals four glacials with low carbon dioxide mixing ratios and temperatures, interspersed with warmer interglacials; the plot does not include the recent anthropogenic rise in carbon dioxide. The temperature change is inferred from the deuterium concentration in bubbles in the ice core, and the accuracy of the CO_2 measurements is 2–3 ppmv. Further details, see Petit *et al.* (1999) and (2001), and Barnola *et al.* (1991).

low concentrations of atmospheric carbon dioxide. These cold glacial periods were interspersed by shorter, warmer interglacial periods, with reduced ice cover and relatively high concentrations in atmospheric carbon dioxide. The onset of these glaciations appear to be driven by temperature changes with lagged changes in carbon dioxide, while de-glaciations appear to have temperature and carbon dioxide varying in phase (or with the carbon dioxide lagging by less than 1000 years).

The mechanisms underpinning these dramatic variations in atmospheric carbon dioxide are not fully understood, but almost certainly involve exchanges in carbon between the atmosphere and the terrestrial or ocean reservoirs. The rapid increases between glacial and interglacial periods are too swift to be explained by interactions with the sediments, although they may be significant over the full 100 000 year cycle. It is also difficult to envisage how the terrestrial ecosystem might have stored more carbon during the cold glacials, since then there was a massive expansion of ice sheets over land. Hence, the glacial-interglacial cycles probably involve carbon exchanges between the atmosphere and ocean, particularly as the car-

bon stored in the deep ocean is refreshed on a timescale of a thousand years: enhanced ocean uptake of carbon dioxide during the cold glacials and reduced ocean uptake during the warmer interglacials. A range of mechanisms by which the ocean might take up more carbon during the glacials have been proposed, involving climate-driven changes in ocean temperature, circulation, biology and chemistry; however, no single mechanism by itself convincingly explains the amplitude of the recorded changes.

1.4.4 How is atmospheric carbon dioxide changing today?

The amount of carbon dioxide in the atmosphere is now higher than at any time over the past 400 000 years and is set to continue increasing, as seen by comparing Figs. 1.11a and 1.10a. The rise of atmospheric carbon dioxide since the pre-industrial era is largely due to the recovery and burning of fossil fuels, which are stores of organic carbon that were buried many million years ago, as well as affected by deforestation and cement production; this increase in carbon dioxide since the pre-industrial era is referred to as anthropogenic carbon dioxide.

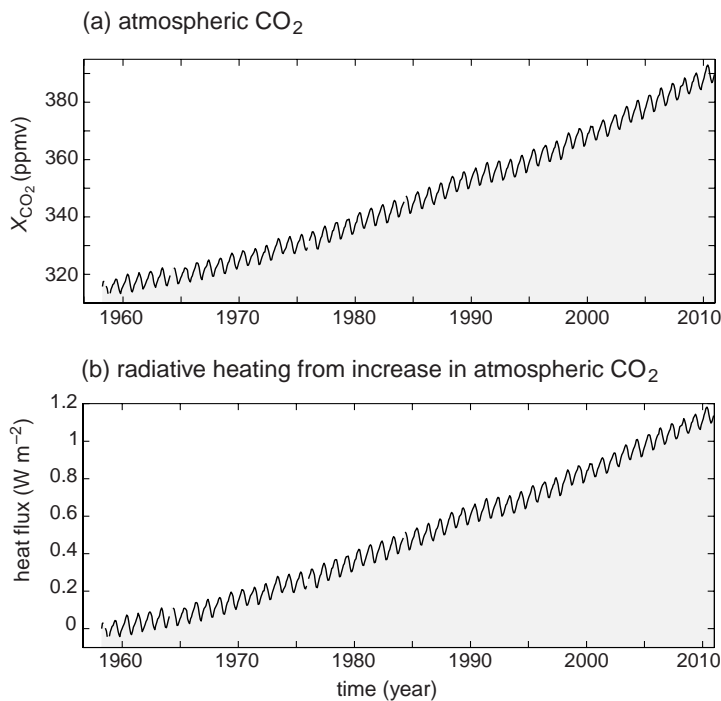


Figure 1.11 Time series of (a) the atmospheric mixing ratio of carbon dioxide (X_{CO_2} , ppmv) derived from air samples collected at Mauna Loa Observatory, Hawaii and (b) implied extra radiative heating ($\Delta\mathcal{H}$, $W m^{-2}$) from atmospheric CO₂. The time series reveals the rise in atmospheric CO₂ from 315 ppmv in 1958 to 390 ppmv in 2010, which is off the scale with the changes seen over the 400 000 years prior to the industrial era (previous highest was 299 ppmv for 323 485 years ago; Fig. 1.10); the mixing ratio is defined as the number of molecules of carbon dioxide divided by the number of molecules of dry air multiplied by one million (ppmv). This CO₂ time series was started by C. D. Keeling of Scripps. Data available from NOAA/ESRL. In (b), the change in radiative heating is estimated from $\Delta\mathcal{H}(t) = \alpha_r \ln(X_{CO_2}(t)/X_{CO_2}(t_0))$ as X_{CO_2} increases in concentration from time t_0 to t , and $\alpha_r = 5.4 W m^{-2}$.

Over the last fifty years, the increase in atmospheric carbon dioxide, along with anthropogenic emissions of other greenhouse gases, is estimated to have increased the downward flux of heat at the Earth's surface by about $1 W m^{-2}$ due to increased absorption and emission of infrared radiation by the atmosphere (Fig. 1.11b). Presently, the oceans absorb about a third of the extra carbon dioxide released by humans to the atmosphere, ameliorating the potential warming. However, ocean uptake of carbon dioxide is likely to diminish as the oceans warm and become more acidic; both of these changes appear to be underway and are expected to increase in the future.

Due to the rise in atmospheric carbon dioxide (Fig. 1.11) and other greenhouse gases, there is, understandably, widespread concern about global warming (IPCC, 2007). Indeed, there are multiple signals that warming is taking place; a rise in atmospheric temperatures over the last century, a progressive retreat of glaciers over much of the globe, a general warming of the upper ocean and a corresponding rise in sea level.

While greenhouse warming is almost certainly happening on a global scale, the regional picture,

where natural variability can be significant, is rather more complicated. In the same way that weather fluctuates from day to day, the climate system also naturally fluctuates on inter-annual, decadal and longer timescales, which can often locally mask the background response to anthropogenic forcing.

1.5 | Summary and outlook

The Earth is unique in the Solar System through the presence of the ocean, a readily available source of liquid water. Many features of the ocean result from the special properties of water: the high heat storage, the solubility of carbon dioxide and other gases, and the ability of the fluid to move easily. The ocean provides the dominant heat store of the climate system and limits the temperature changes over the Earth. Sunlight is absorbed in the surface ocean, so that the sea surface is relatively warm, while the ocean interior is cold and dark.

Life first flourished in the ocean. The evolution of photosynthesis drove dramatic changes

in the atmosphere, producing oxygen and ozone, which in turn protected the land and sea surface from harmful ultraviolet rays emitted from the Sun. In the present day, phytoplankton flourish in the surface, sunlit ocean whenever there are sufficient concentrations of essential nutrients. While organisms consume these nutrients, producing organic particles that sink into the deep ocean, circulation and mixing resupplies the nutrients to the surface, sustaining the growth of phytoplankton.

Carbon is continually cycled between the atmosphere, ocean and the land. During Earth's early history, the presence of water enabled the initial drawdown of carbon dioxide from the atmosphere into the sediments through weathering of silicate rocks. The ocean cycling of carbon has contributed to the glacial and interglacial variations in atmospheric carbon dioxide, while the ocean is absorbing up to a third of the carbon dioxide being presently emitted to the atmosphere by humans.

Moving on from this broad context, we next consider for the present day a descriptive view of how the ocean and atmosphere circulate, where phytoplankton grow and how carbon is cycled in the ocean.

1.6 | Recommended reading

For informed short articles as to how the Earth has evolved and the cycling of carbon, see: C. J. Allegre and S. H. Schneider (2005). The evolution of Earth. *Sci. Am.* (Spec. Ed.), 4–13; and J. L. Sarmiento and N. Gruber (2002). Sinks for anthropogenic carbon. *Phys. Today* (August), 30–36.

For a readable view of how the Earth formed and contrasting its evolution with Mars and Venus, see J. Kasting (2010). *How to Find a Habitable Planet*. Princeton, NJ: Princeton University Press, 360pp.

For a comprehensive summary of the climate system and climate change, see IPCC (2007). *Climate Change 2007: The Physical Science Basis*. Contribution of Working Group I to the Fourth Assessment Report of the Intergovernmental Panel on Climate Change. Cambridge: Cambridge University Press, 996pp.

For a substantial review of the state of the ocean, see G. Siedler, J. Church and J. Gould (2001). *Ocean Circulation and Climate: Observing and Modelling the Global Ocean*. San Diego, CA: Academic Press, 693pp.

For an accessible introductory view of global warming, see D. Archer (2007). *Global Warming: Understanding the Forecast*. Malden: Blackwell Publishing, 208pp.

Chapter 2

An introductory view of the ocean

Many aspects of the ocean are challenging to understand, including how the ocean stores and redistributes heat over the globe, how life has colonised the ocean and how carbon is cycled between the ocean, atmosphere and land. To answer these questions, we need to adopt a holistic view to understand the relevant physical, chemical and biological processes, and how they are connected to each other. For example, a western boundary current, like the Gulf Stream, has a range of signatures: a rapid transfer of heat, nutrients and carbon along the current, enhanced contrasts in physical, chemical and biological properties across the current, and increased exchanges of heat, moisture and dissolved gases with the overlying atmosphere.

A difficulty in understanding the ocean, as compared to the atmosphere, is the problem of taking observations due to the ocean being a more inaccessible and hostile environment. To counter that difficulty, a range of different techniques have been developed to unravel how the ocean circulates, drawing on a combination of ship-based measurements, remote sensing from space and freely drifting floats spreading throughout the ocean.

In this chapter, we provide an introductory view of the large-scale ocean circulation, and basic property distributions (Plates 2 to 7), as well as briefly introduce the atmospheric circulation, and then discuss how life flourishes in the ocean and, finally, how carbon is cycled in the ocean. This material provides a starting point for the rest of the book.

2.1 | Ocean circulation

Water has a very low viscosity compared with most other liquids and moves easily whenever there is forcing, rather than moving sluggishly like it does in a soggy marsh. The ocean circulates due to a combination of mechanical and density forcing:

- Air moving over the surface water provides a frictional drag, depending on the difference in the speed of both fluids. Since the atmosphere moves so much faster than the ocean, there is a transfer of momentum into the ocean, ultimately driving most of the currents in the upper ocean.
- Variations in the gravitational acceleration across the Earth from the Moon lead to bulges of water forming around the Earth, orientated towards and away from the Moon. As the Earth rotates about its own axis, these bulges appear as a regular rise and fall of sea level at the coast, occurring typically once or twice a lunar day (24 hours 50 minutes). There are similar, albeit weaker, tidal oscillations formed by the gravitational forcing from the Sun. While tides are most pronounced near the coast, they occur throughout the water column and can lead to enhanced mixing when the tidal flows interact with rough topography.
- Surface density is altered through the exchange of heat and fresh water with the atmosphere; increasing with surface cooling or evaporation.

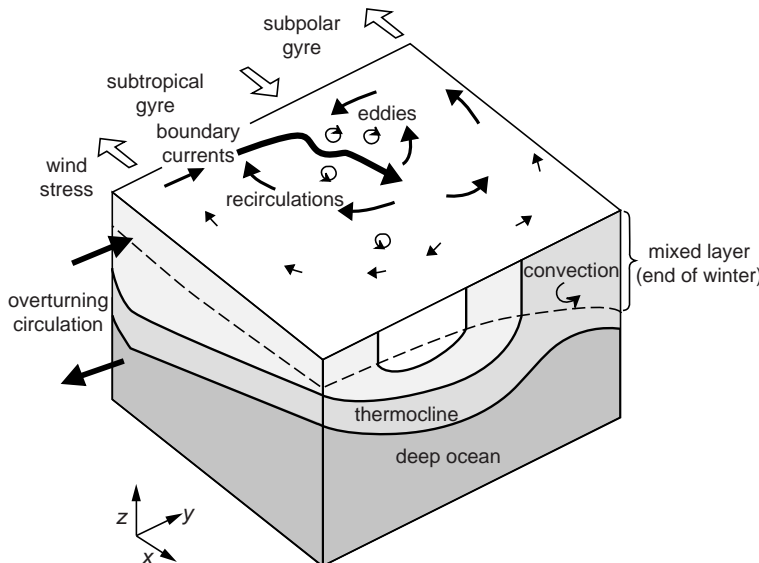


Figure 2.1 A schematic view of the circulation within an ocean basin, including recirculating gyres and overturning. Surface winds induce the gyres containing western boundary currents, interior flows and eddies. The horizontal circulation is connected with sloping temperature and density surfaces (full line) in the interior. In the vertical, there is a surface mixed layer (dashed line) where convection occurs, together with a thermocline, where there are strong vertical temperature gradients, and deep waters with more uniform properties.

In polar regions, density also increases through cooling by any overlying ice or by the atmosphere over gaps in the ice, as well by the addition of salt released when ice freezes. Whenever surface waters become denser than deeper waters, convection occurs and the fluid vertically overturns. Density contrasts lead to horizontal pressure gradients, which then accelerate the flow. Dense waters formed at high latitudes can sink to great depths and spread horizontally over the ocean, replaced at the surface by lighter waters, which then generate an overturning circulation.

With the exception of the tidal oscillations, the ocean moves relatively slowly, so that water takes many days to cross a basin, leading to currents being strongly constrained by the Earth's rotation; this rotational constraint leads to ocean flows persisting, rather than being quickly dissipated (as instead occurs for water sloshing from side to side in a bath).

The pattern of ocean circulation is also affected by topography, since deep flows move around any physical barriers and follow the pattern of channels and gaps in the topography. Surface currents are also sometimes influenced by the underlying topography, since currents often prefer to move around a submerged bump, rather than move directly over the bump.

The combination of forcing, rotation and topography leads to an intriguing range of physical phenomena, as illustrated in Fig. 2.1: there are strong boundary currents alongside some land boundaries, but not others; basin-scale circulations confined within continental barriers; overturning circulations, including deep boundary currents; and vibrant, time-varying eddies occurring throughout the ocean.

Next we consider observational views of the surface circulation and their connection to the underlying temperature and density distributions.

2.1.1 How does the surface flow vary?

Beneath a thin surface boundary layer, ocean currents follow the dynamic height of the sea surface in the same manner that air moves along pressure contours, as depicted on a weather chart; the dynamic height is the displacement of any pressure surface from a reference surface, called the geoid. A glance at a global map of dynamic height, as shown in Fig. 2.2, reveals several dominant, large-scale regimes:

- The ocean circulates on a horizontal scale of several thousand kilometres between the continents; these basin-scale circulations are called gyres (Fig. 2.3a). These gyre circulations rotate in a clockwise manner in the subtropics of

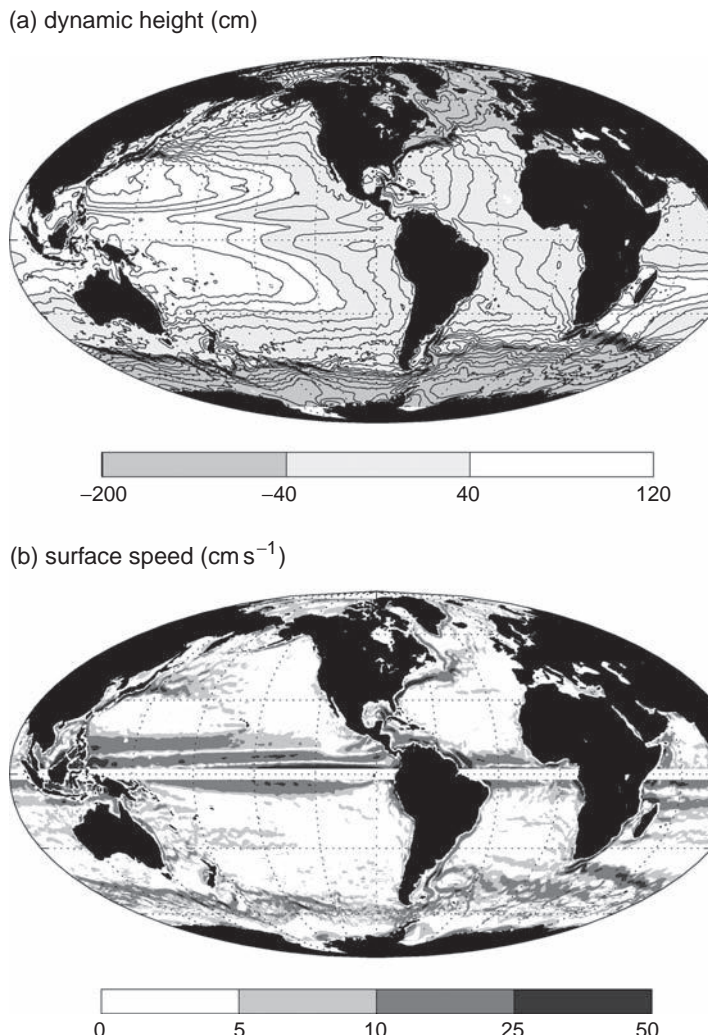


Figure 2.2 Different regimes for the near-surface circulation (excluding a frictional contribution from the wind) revealed in (a) mean dynamic height (contours with an interval of 10 cm and increased to 20 cm over the Southern Ocean) and (b) surface speed (cm s^{-1}) diagnosed from the gradient in mean dynamic height (assuming geostrophic balance with values excluded within 2° of the equator where this balance does not apply; see later Section 4.2.1). The dynamic height is the displacement of a pressure surface from a reference surface, called the geoid. Below a thin surface boundary layer, the surface flow is directed approximately along contours of dynamic height. There are large-scale recirculations within basins, referred to as gyres, including intense western, boundary currents, over much of the globe. In the Southern Ocean, the surface flow is directed broadly eastward and circumnavigates the globe, and is referred to as the Antarctic Circumpolar Current. The dynamic height was taken from a combined dataset integrating information from surface drifters in the ocean, remotely sensed measurements of sea-surface height from altimetry, surface winds and measurements of the geoid from the GRACE gravity mission (Niiler et al., 2003; Maximenko and Niiler, 2005).

the northern hemisphere and anticlockwise in the subtropics of the southern hemisphere. The gyre circulations rotate in the opposite sense at higher latitudes. This change in rotation of the gyres reflects the pattern of the overlying winds. The rotation of the flow is defined as cyclonic whenever the rotation is in the same sense as the rotation of the Earth, anticlockwise in the northern hemisphere and clockwise in the southern hemisphere.

- Accompanying these gyre circulations are vigorous and narrow boundary currents along the western sides of the ocean basins, such as the Gulf Stream in the North Atlantic, the Brazil Current in the South Atlantic, and the Kuroshio in the North Pacific (Fig. 2.2b).

- In the tropics, there is an equatorial current system consisting of reversing, zonal flows with high speeds. Over the tropics, currents are forced by the prevailing westward winds: on either side of the equator, there are two westward flowing equatorial currents, together with a narrow eastward return flow in an equatorial counter current located between them; note that the speed is not mapped within 2° of the equator in Fig. 2.2b.
- Within the southern hemisphere, there are gaps between Antarctica and the northern land masses, allowing an uninterrupted flow to circumnavigate the globe roughly along latitude circles (Fig. 2.3b). This eastward current, the Antarctic Circumpolar Current, extends from

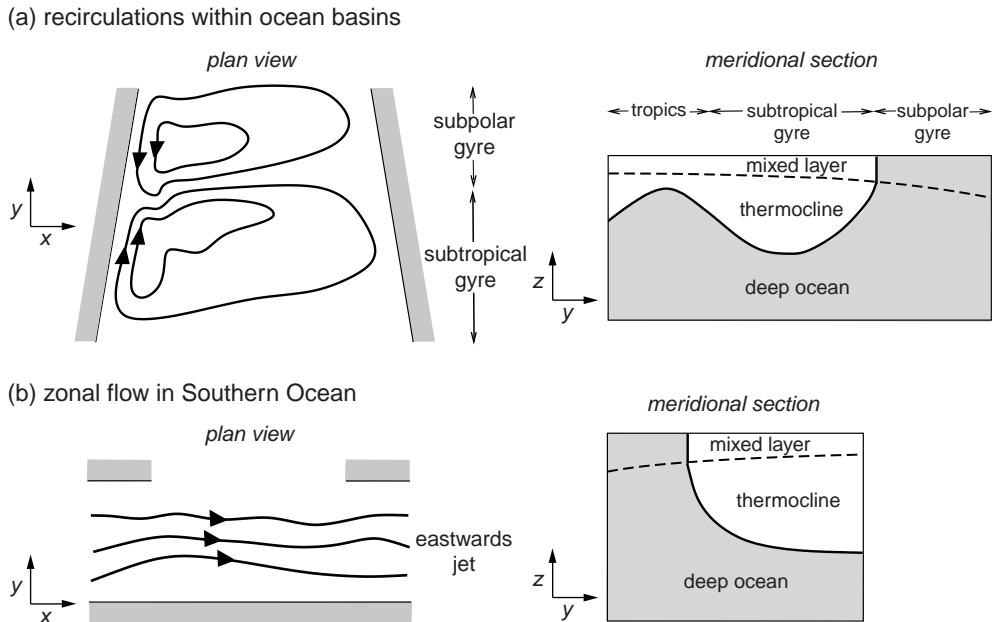


Figure 2.3 A schematic figure depicting (a) recirculating flows within ocean basins in the northern hemisphere and (b) near zonal flows within the Southern Ocean for a plan view (left panel) and a meridional section (right panel), including the base of the mixed layer (dashed line). In (a), the circulations are associated with a thin thermocline in the tropics and a thicker thermocline in the subtropical gyre, and a thin or seasonal thermocline over the subpolar gyre. In (b), an eastward wind-driven current in the Southern Ocean is associated with cold water outcropping on the poleward side of the current. On the equatorial side of the Southern Ocean, the near-zonal flows can interact with the gyre circulations in the Atlantic, Indian and Pacific basins.

the surface to the sea floor and is made up of a series of narrow jets (regions of fast-moving flow). The Antarctic Circumpolar Current is analogous to the fast moving Jet Stream in the upper atmosphere.

In addition to this network of persistent currents covering the globe, there are also intense time-varying circulations on smaller scales of several tens to a hundred kilometres, referred to as mesoscale eddies; although much smaller in size, these ocean eddies are analogous to atmospheric weather systems. Ocean eddies are preferentially formed along intense western boundary currents, such as the Gulf Stream, and within the jets making up the Antarctic Circumpolar Current.

2.1.2 How does the ocean vary in the vertical?

The ocean has a characteristic vertical structure (Fig. 2.4a) consisting of a surface mixed layer, overlying a stratified upper ocean and a weakly stratified, deep ocean:

- The surface layer is well mixed with nearly homogeneous properties in the vertical. This mixed layer varies in thickness from typically 30 m to 500 m, as depicted in Fig. 2.4b-e. The surface layer is in direct contact with the atmosphere or, in polar regions, with overlying ice. The mixing in this layer is driven by turbulence generated by the wind blowing over the sea surface and by convection from the sinking of dense waters formed by surface cooling or evaporation to the atmosphere, or by brine release from underneath ice.
- In the upper ocean, there is usually a strong vertical temperature gradient, referred to as the thermocline, which is typically accompanied by similar vertical gradients in salinity and density, such as seen extending from 500 m to 1500 m in Fig. 2.4. This strong stratification inhibits vertical mixing below the surface mixed layer. The thermocline can be separated into an upper, seasonal thermocline and a deeper, permanent or main thermocline. The seasonal thermocline strengthens from the

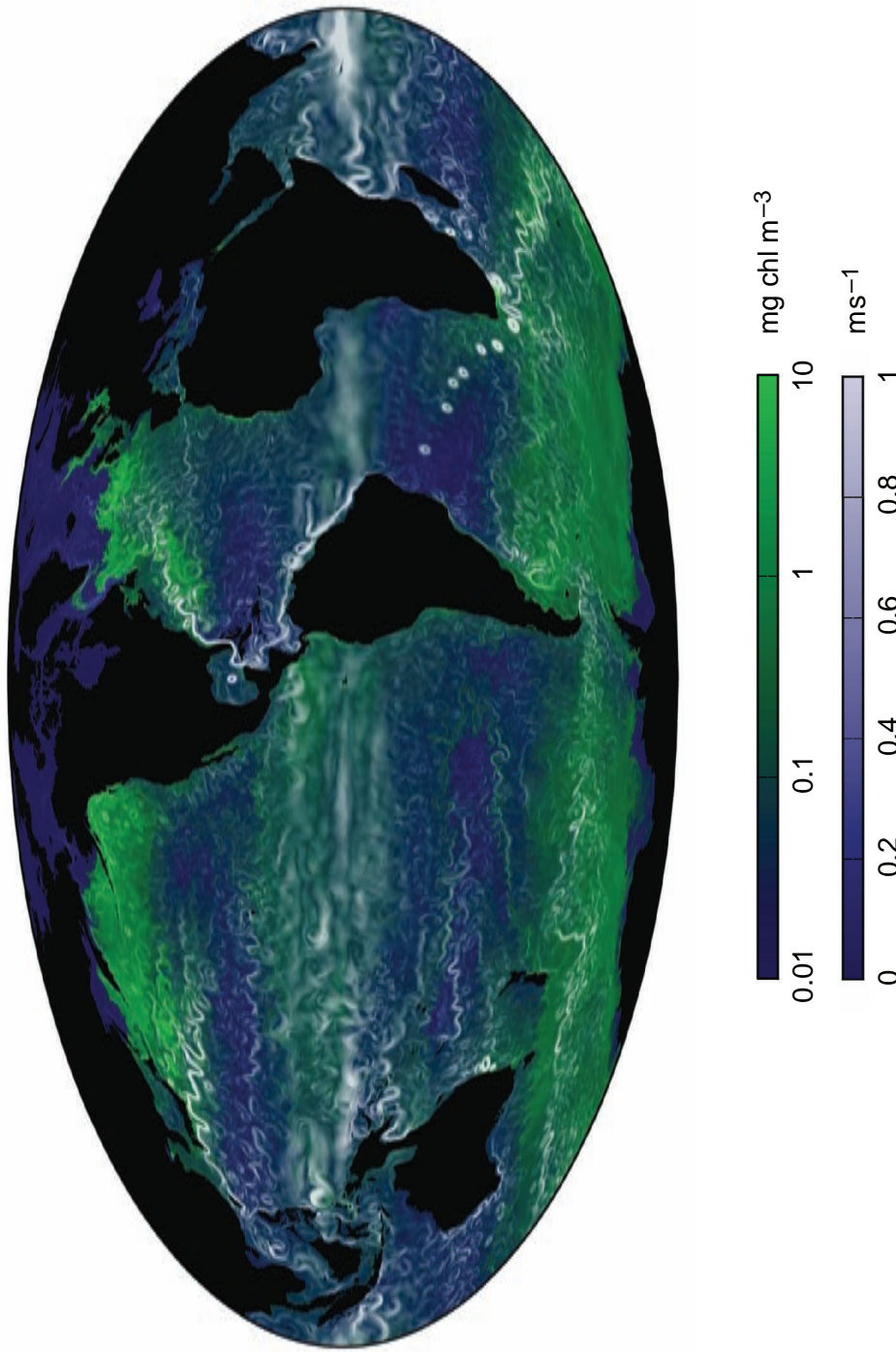


Plate I. Snapshot of simulated surface chlorophyll on a day in April (mg chl a m^{-3} , blue to green for low to high concentrations) and surface speed (m s^{-1} , blue to white for low to high speed) from an integration of the MIT gcm ocean model, configured with 18 km horizontal resolution to explicitly capture geostrophic eddies (physical configuration – Menemenlis et al., 2005; ecological model – Follows et al., 2007). Figure courtesy of Oliver Jahn. Linked animations at www.cambridge.org/williamsandfollows.

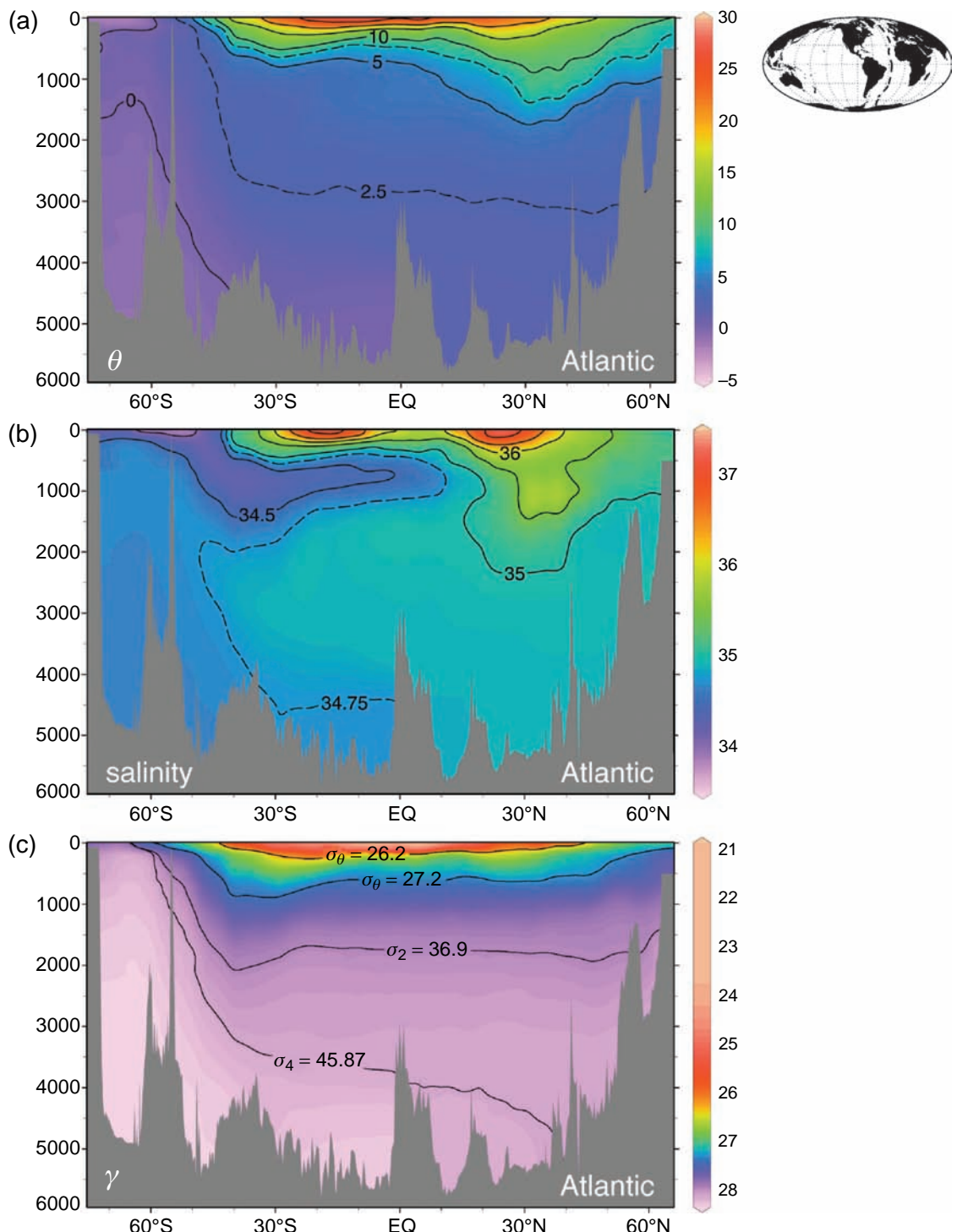


Plate 2. Physical tracers for the Atlantic along 20°W (dashed line along map insert): observed meridional sections of (a) potential temperature, θ (°C), (b) salinity, S (g kg⁻¹) and (c) neutral density, γ (kg m⁻³) versus depth (m), together with selected potential density surfaces (contours); see Sections 2.1, 8.1 and 12.1.

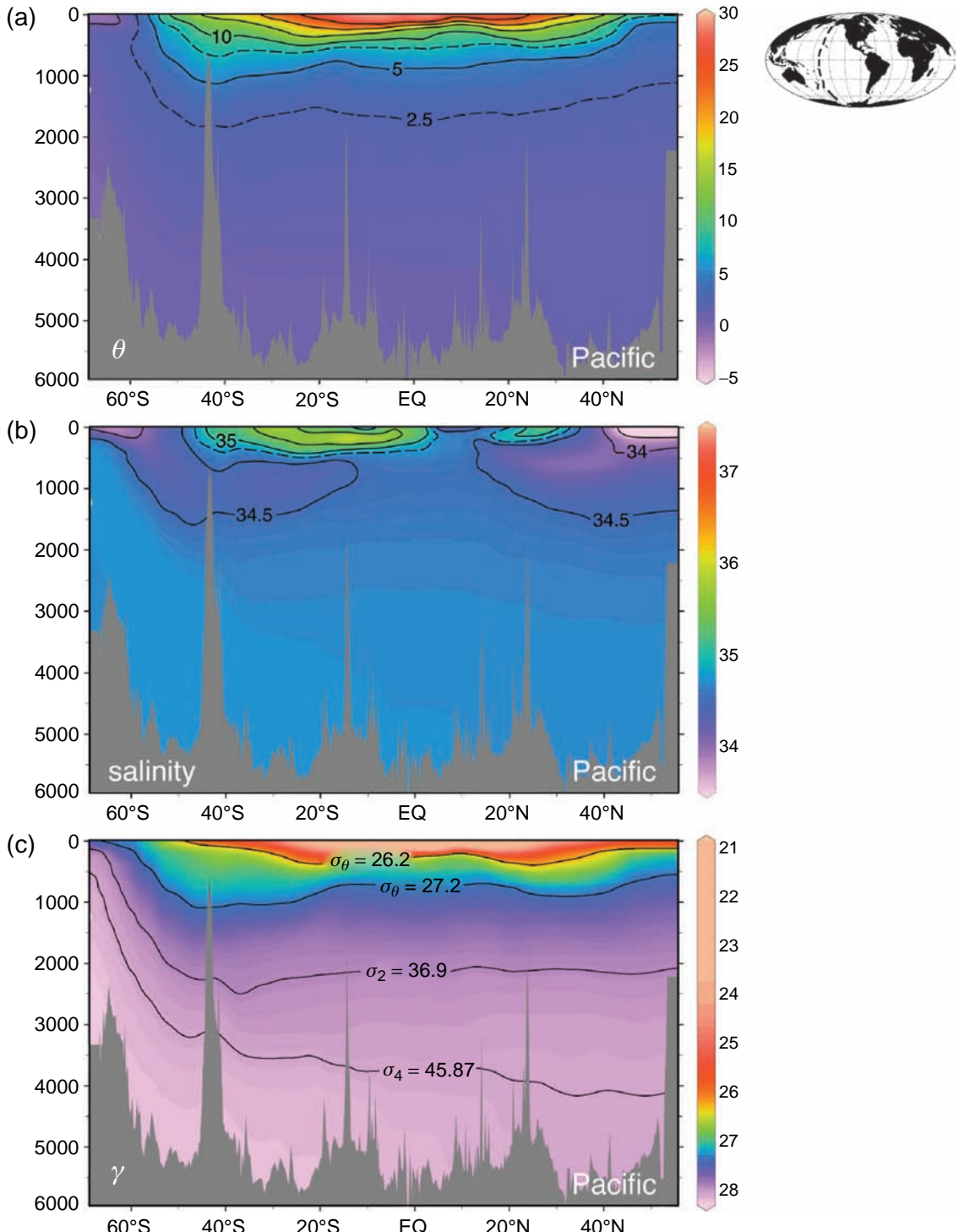


Plate 3. Physical tracers for the Pacific along 170°W (dashed line along map insert): (a) potential temperature, θ ($^{\circ}\text{C}$), (b) salinity, S (g kg^{-1}) and (c) neutral density, γ (kg m^{-3}) versus depth (m), together with selected potential density surfaces (contours); see Sections 2.1, 8.1 and 12.1.

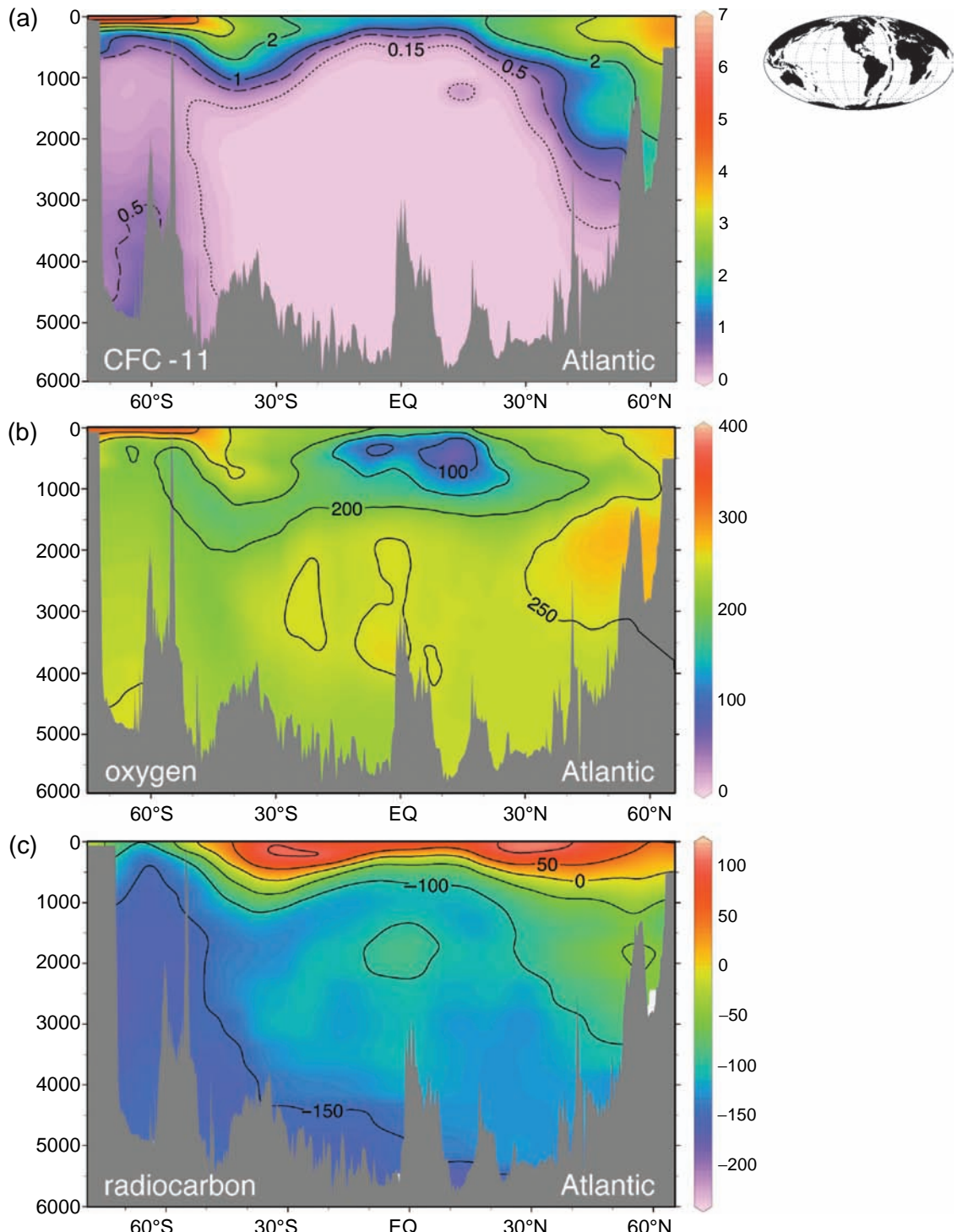


Plate 4. Ventilation tracers for the Atlantic along 20°W: observed meridional sections of (a) CFC-11 (trichlorofluoromethane, CCl_3F ; $10^{-12} \text{ mol kg}^{-1}$), (b) dissolved oxygen, O_2 (ml l^{-1}), and (c) radiocarbon, $\Delta^{14}\text{C}$ (‰) versus depth (m); see Sections 10.1 and 12.1.

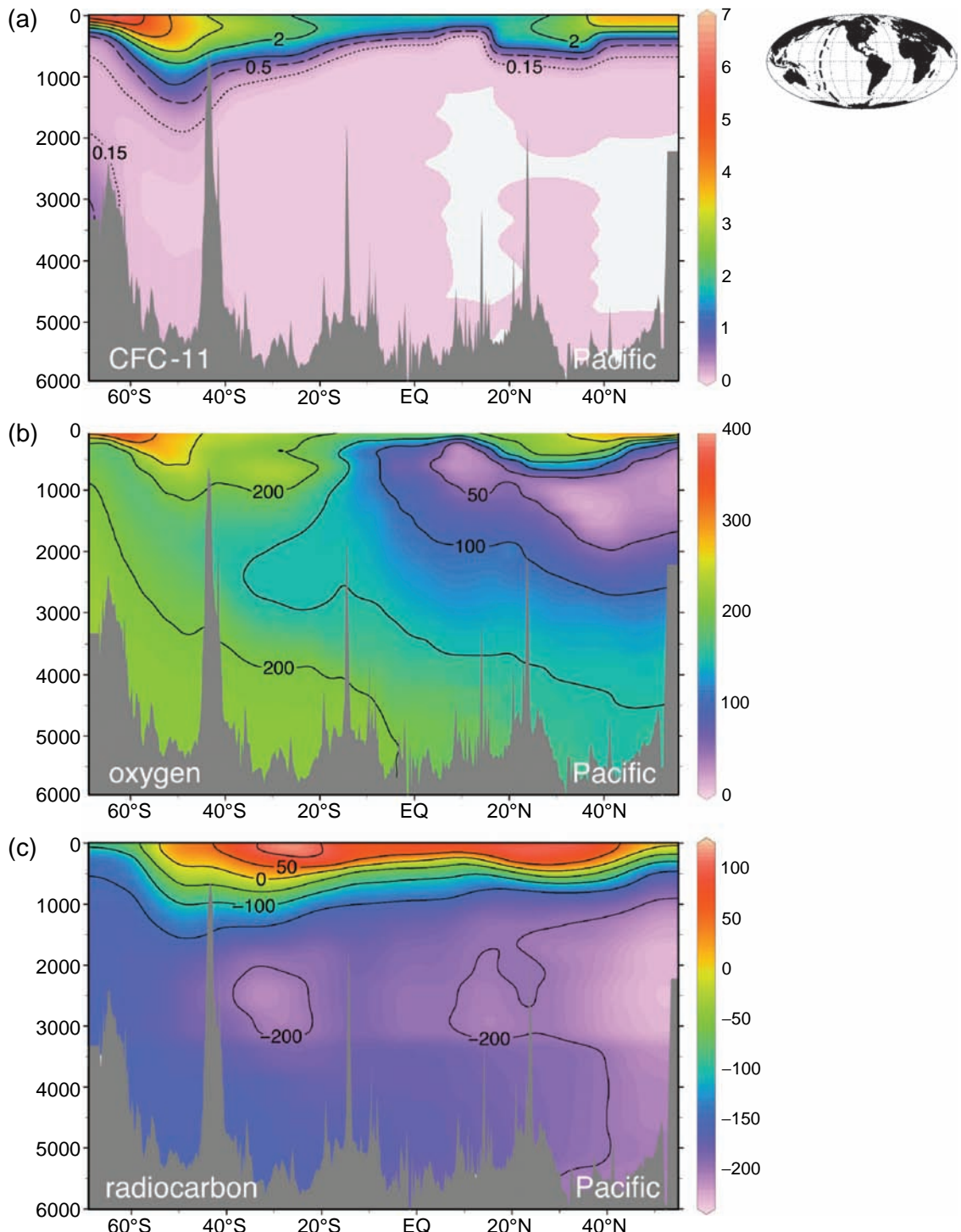


Plate 5. Ventilation tracers for the Pacific along 170°W : observed meridional sections of (a) CFC-11 (trichlorofluoromethane, CCl_3F ; $10^{-12} \text{ mol kg}^{-1}$, white is no detectable concentration), (b) dissolved oxygen, $\text{O}_2 (\text{ml l}^{-1})$, and (c) radiocarbon, $\Delta^{14}\text{C} (\text{\textperthousand})$ versus depth (m); see Sections 10.1 and 12.1.

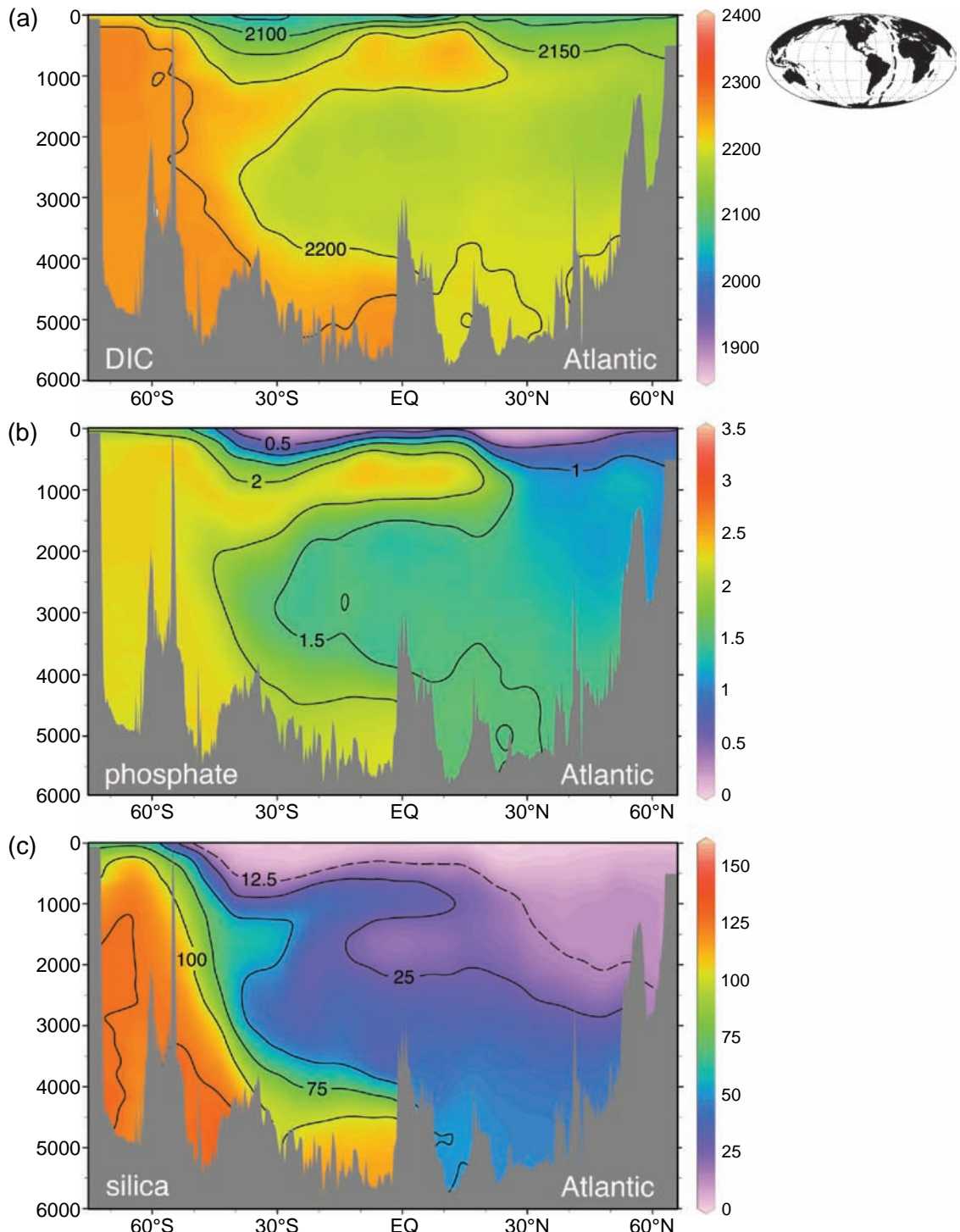


Plate 6. Biogeochemical properties for the Atlantic along 20°W: observed meridional sections of (a) dissolved inorganic carbon, DIC ($\mu\text{mol kg}^{-1}$), (b) phosphate ($\mu\text{mol kg}^{-1}$), and (c) silica ($\mu\text{mol kg}^{-1}$) versus depth (m); see Sections 2.3, 2.4, 6.4, 11.3, 11.4 and 12.1.

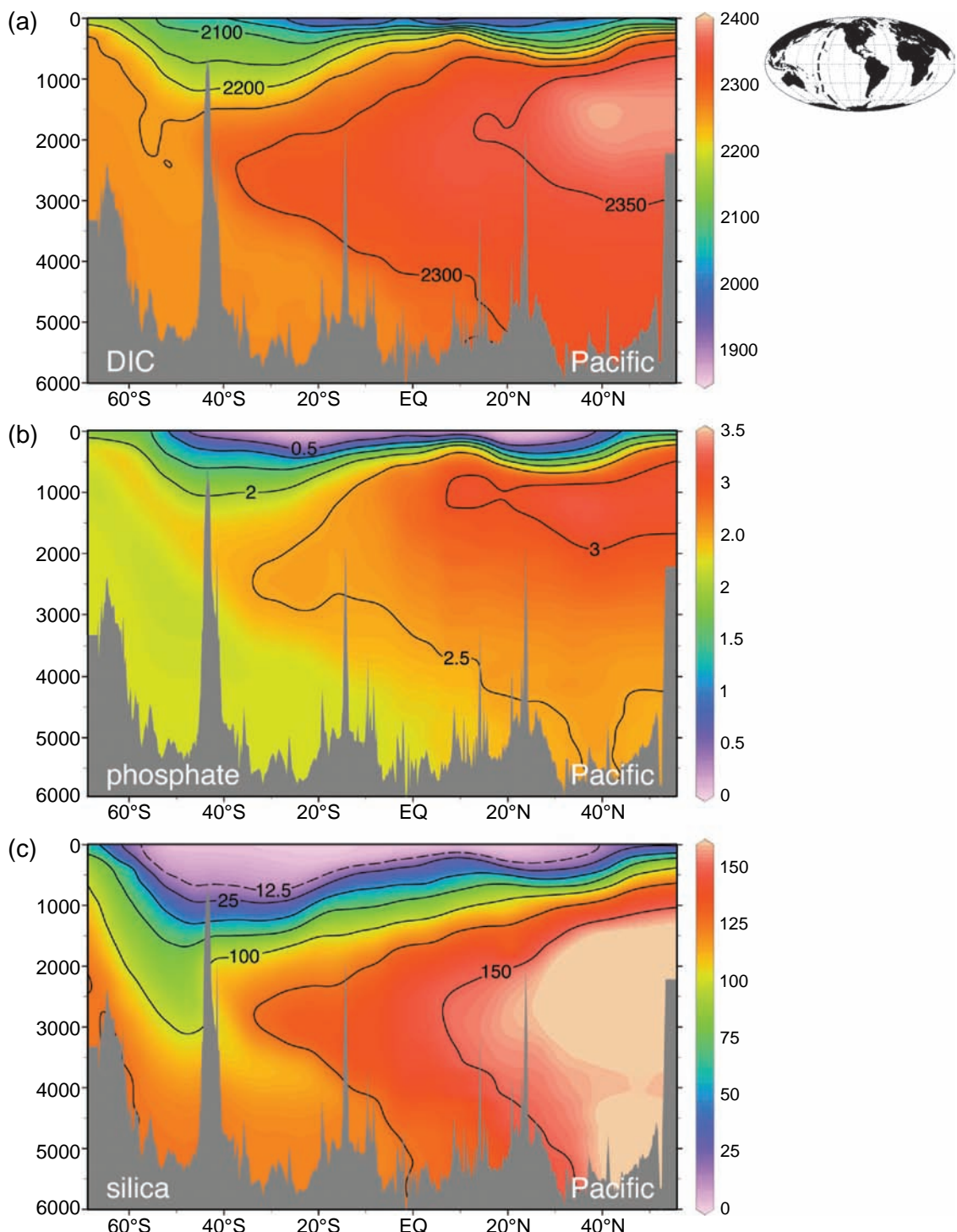


Plate 7. Biogeochemical properties for the Pacific along 170°W: observed meridional sections of (a) dissolved inorganic carbon, DIC ($\mu\text{mol kg}^{-1}$), (b) phosphate ($\mu\text{mol kg}^{-1}$), and (c) silica ($\mu\text{mol kg}^{-1}$) versus depth (m); see Sections 2.3, 2.4, 6.4, 11.3, 11.4 and 12.1.

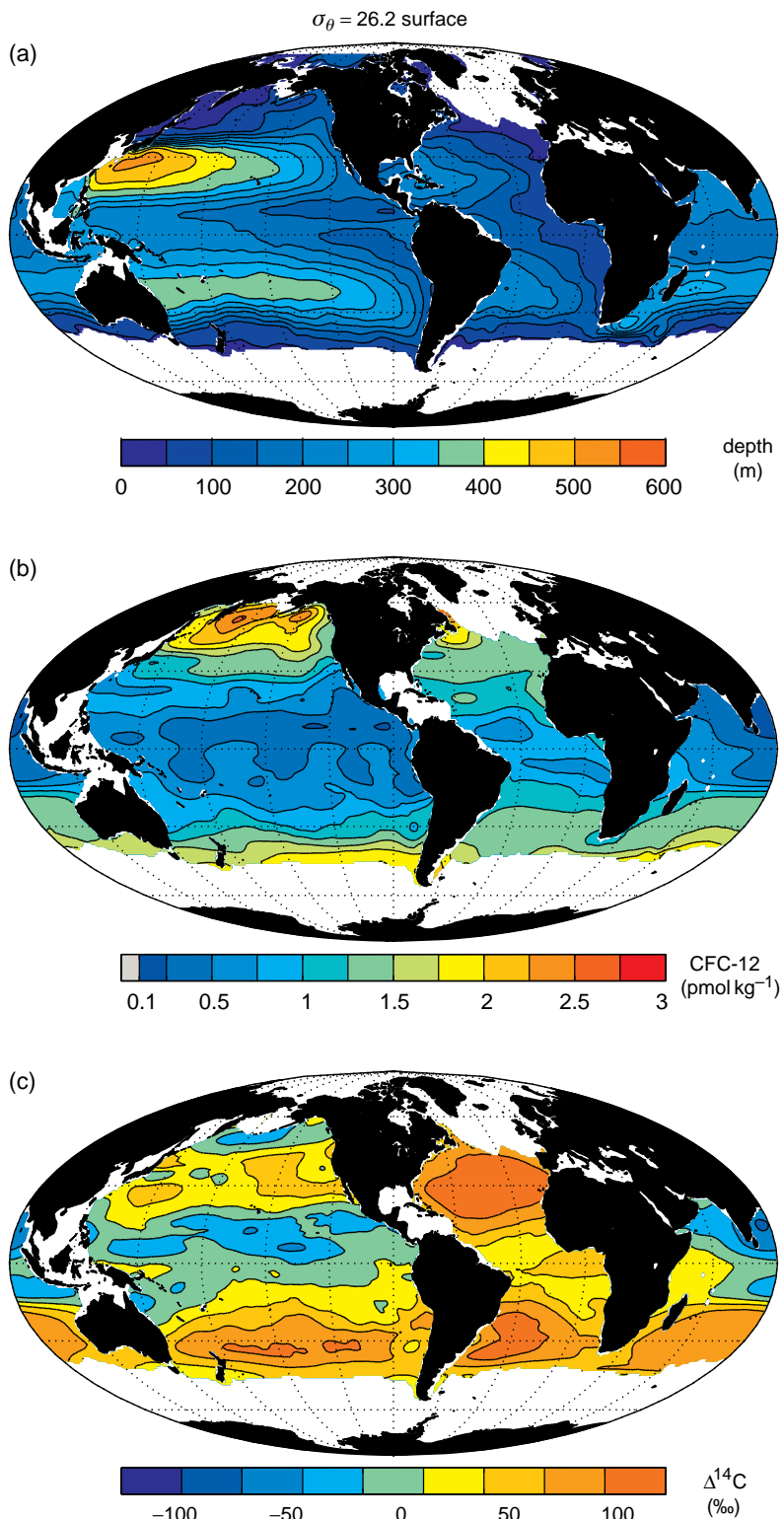


Plate 8. Properties along $\sigma_\theta = 26.2$ surface: (a) depth (m) (white is where the surface is not present), (b) CFC-12 (dichlorodifluoromethane, CCl_2F_2 ; $10^{-12} \text{ mol kg}^{-1}$), and (c) radiocarbon, $\Delta^{14}\text{C}$ (‰); see Section 10.1.

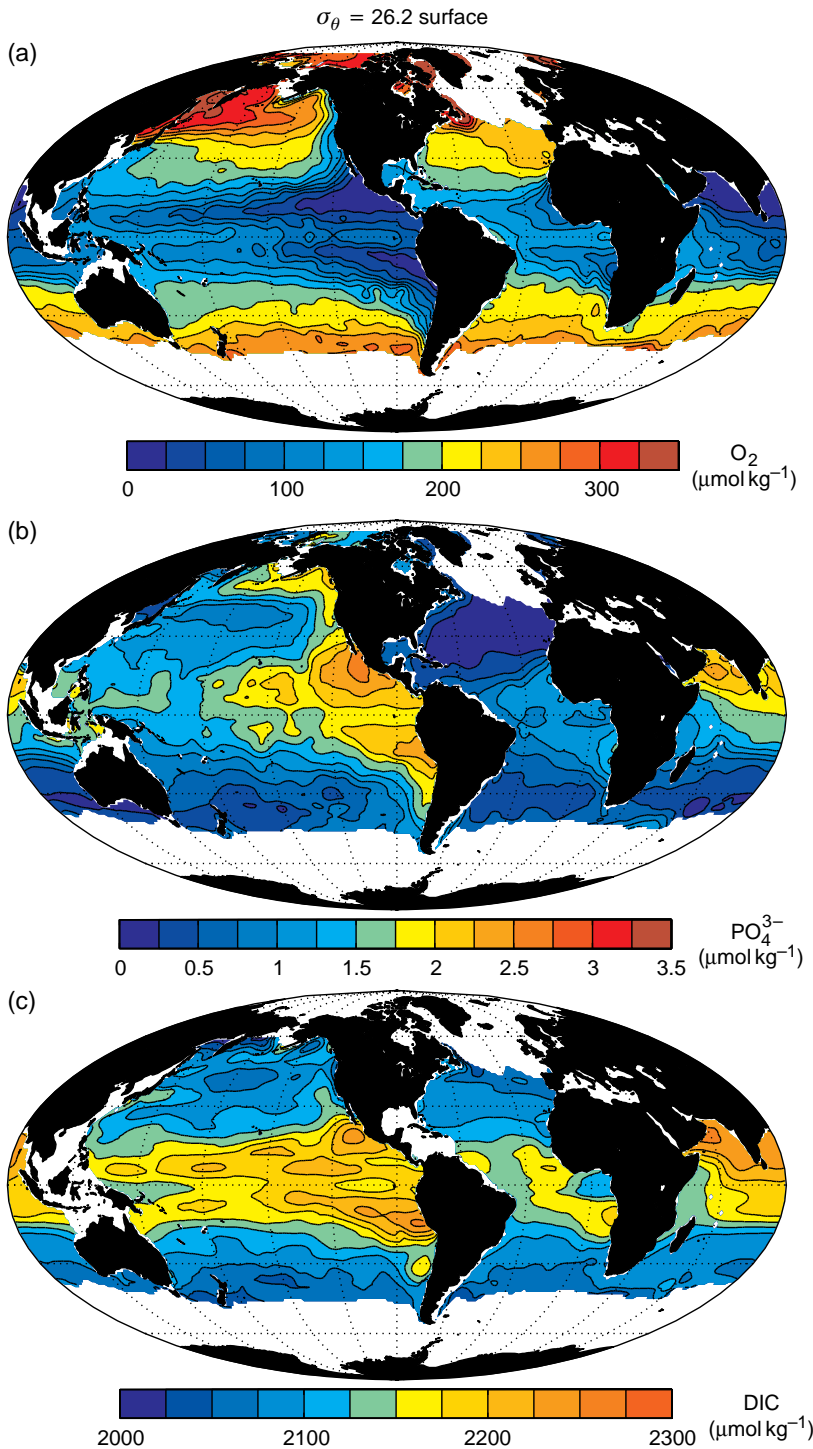


Plate 9. Properties along $\sigma_\theta = 26.2$ surface: (a) dissolved oxygen, O_2 ($\mu\text{mol kg}^{-1}$), (b) phosphate ($\mu\text{mol kg}^{-1}$) and (c) dissolved inorganic carbon, DIC ($\mu\text{mol kg}^{-1}$); see Section 10.1.

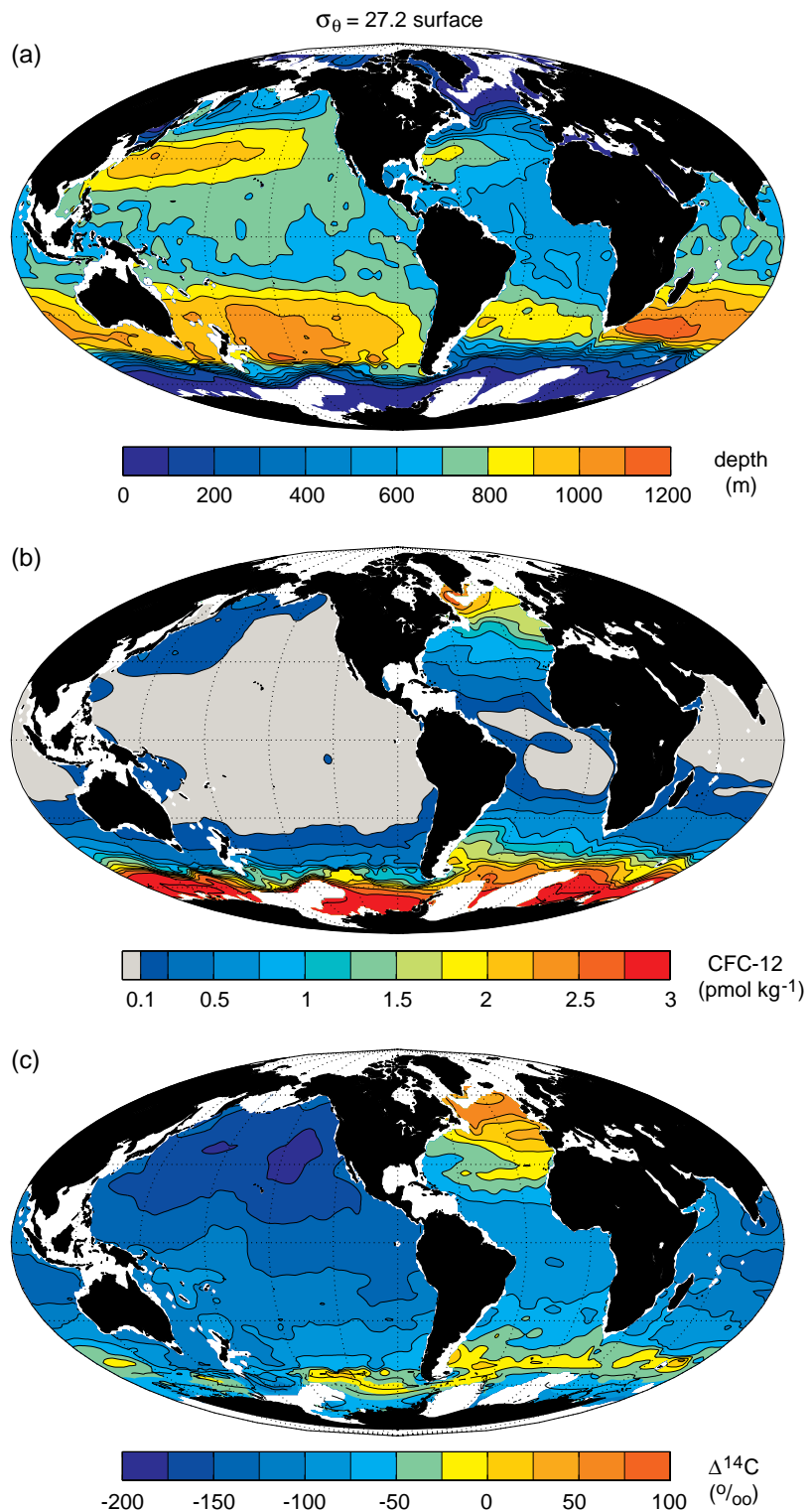


Plate 10. Properties along $\sigma_\theta = 27.2$ surface: (a) depth (m), (b) CFC-12 (dichlorodifluoromethane, CCl_2F_2 ; $10^{-12} \text{ mol kg}^{-1}$), and (c) radiocarbon, $\Delta^{14}\text{C}$ (\textperthousand); see Section 10.1.

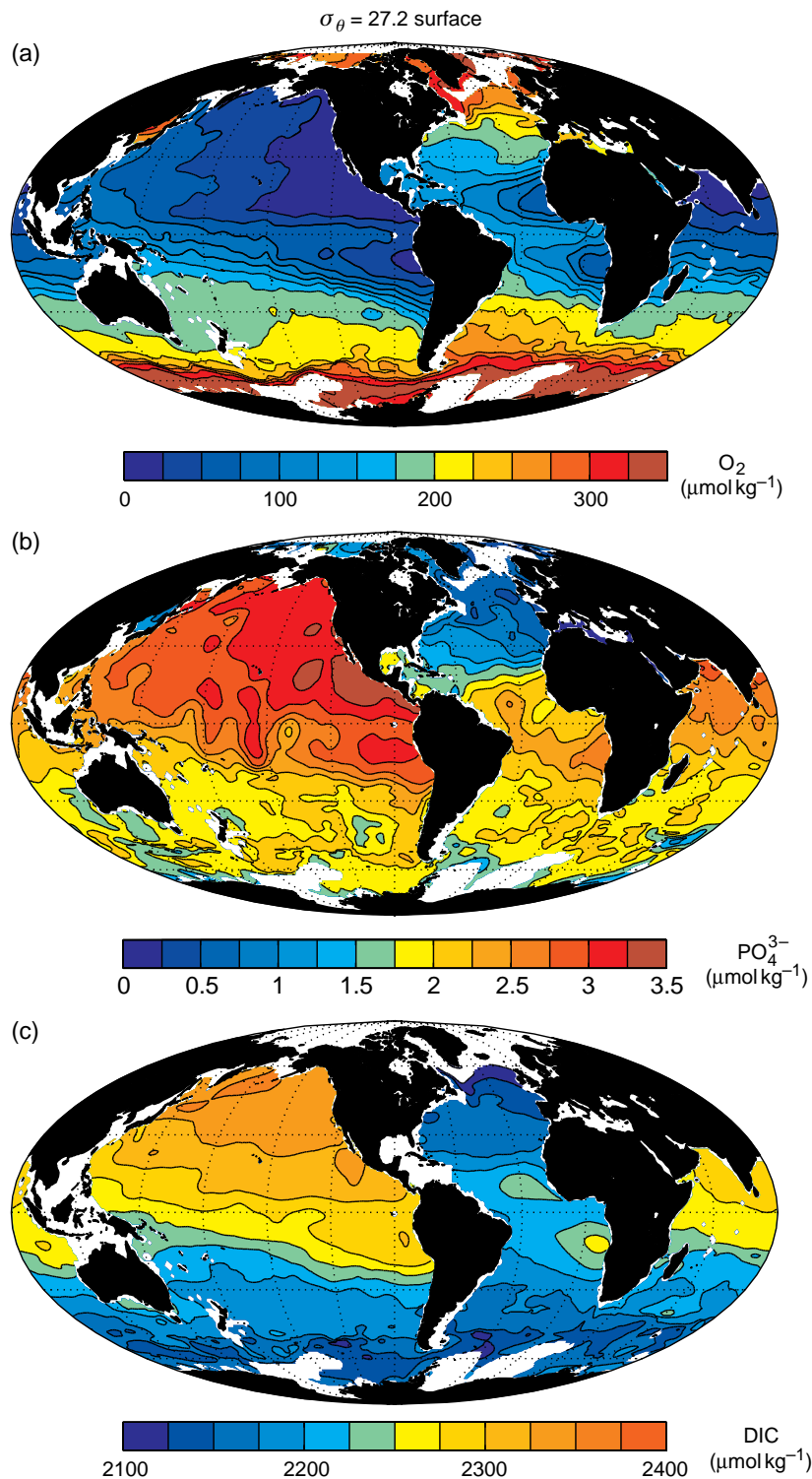


Plate III. Properties along $\sigma_\theta = 27.2$ surface: (a) dissolved oxygen, O_2 ($\mu\text{mol kg}^{-1}$), (b) phosphate ($\mu\text{mol kg}^{-1}$) and (c) dissolved inorganic carbon, DIC ($\mu\text{mol kg}^{-1}$); see Section 10.1.

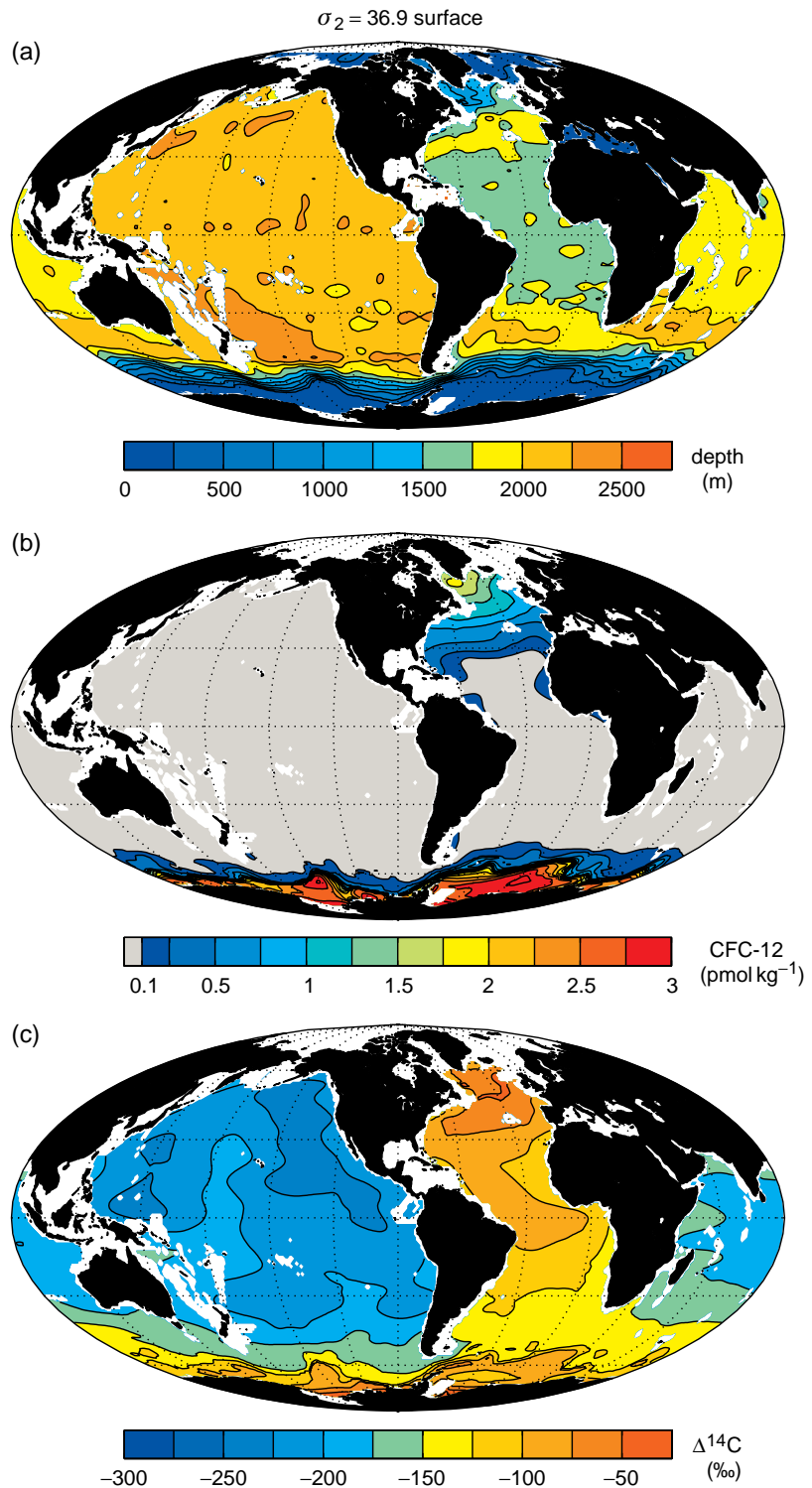


Plate 12. Properties along $\sigma_2 = 36.9$ surface: (a) depth (m), (b) CFC-12 (dichlorodifluoromethane, CCl_2F_2 ; $10^{-12} \text{ mol kg}^{-1}$), and (c) radiocarbon, $\Delta^{14}\text{C}$ (‰); see Section 10.1.

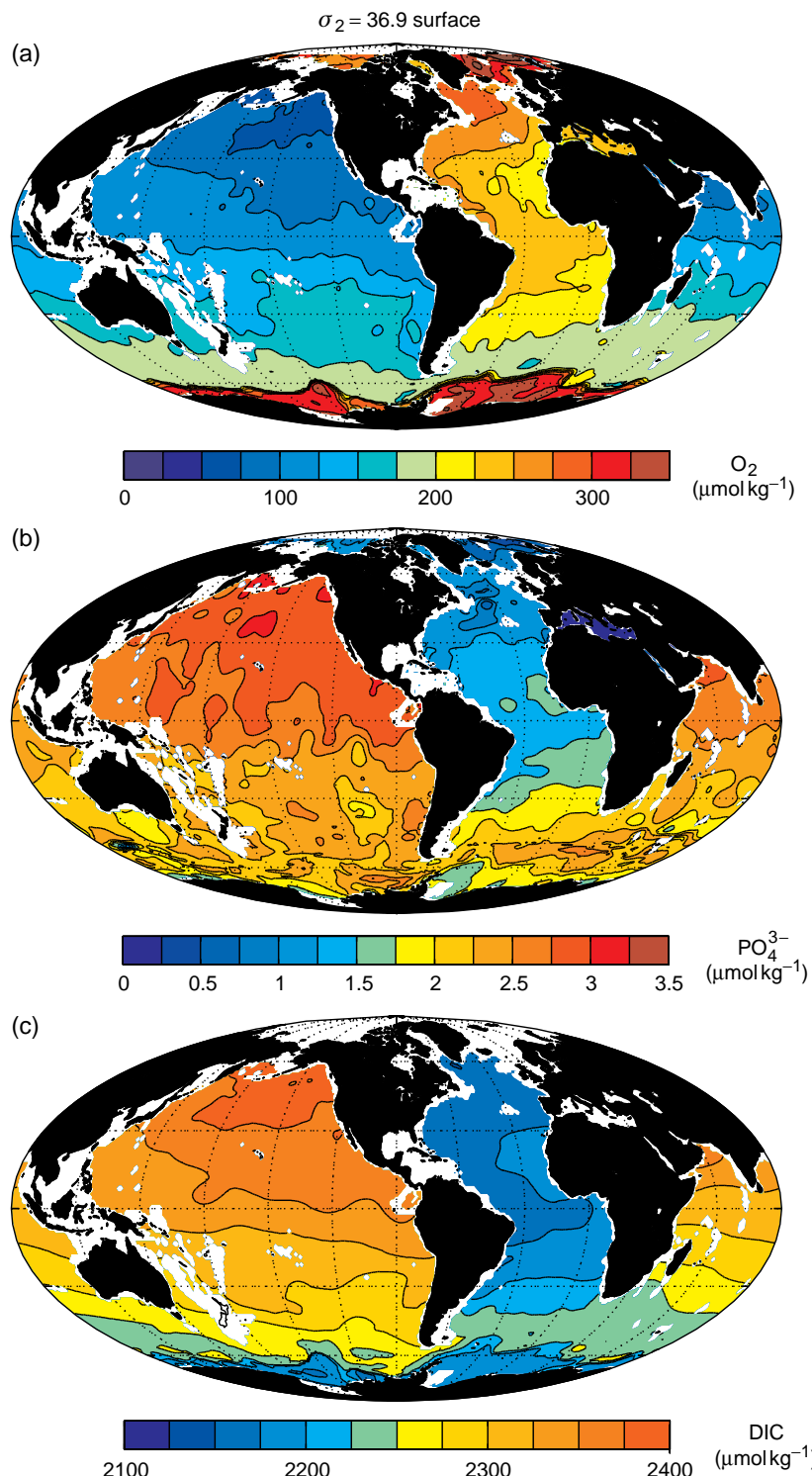


Plate 13. Properties along $\sigma_2 = 36.9$ surface: (a) dissolved oxygen, O_2 ($\mu\text{mol kg}^{-1}$), (b) phosphate ($\mu\text{mol kg}^{-1}$) and (c) dissolved inorganic carbon, DIC ($\mu\text{mol kg}^{-1}$); see Section 10.1.

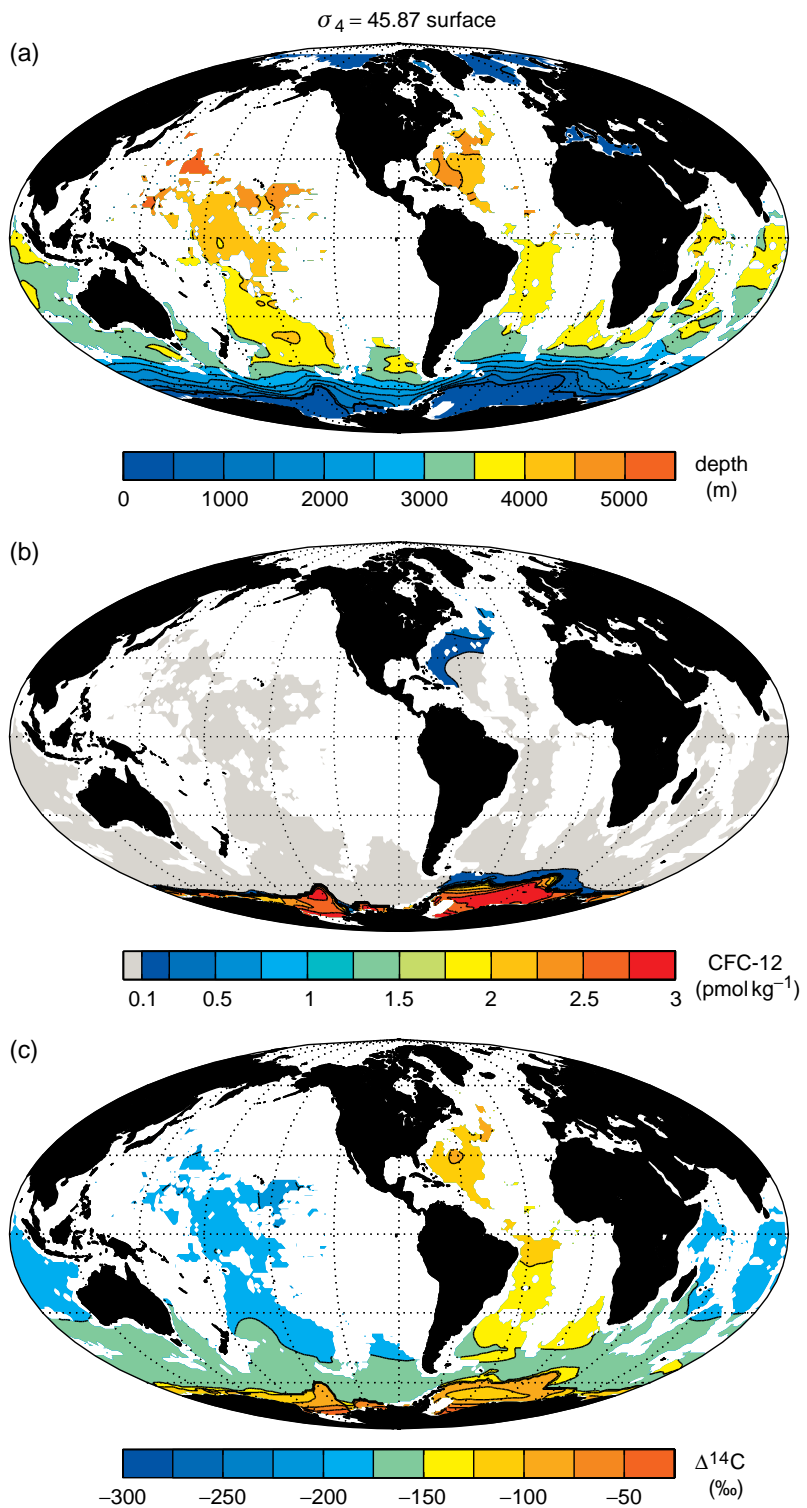


Plate 14. Properties along $\sigma_4 = 45.87$ surface: (a) depth (m), (b) CFC-12 (dichlorodifluoromethane, CCl_2F_2 ; $10^{-12}\text{mol kg}^{-1}$), and (c) radiocarbon, $\Delta^{14}\text{C}$ (‰); see Section 10.1.

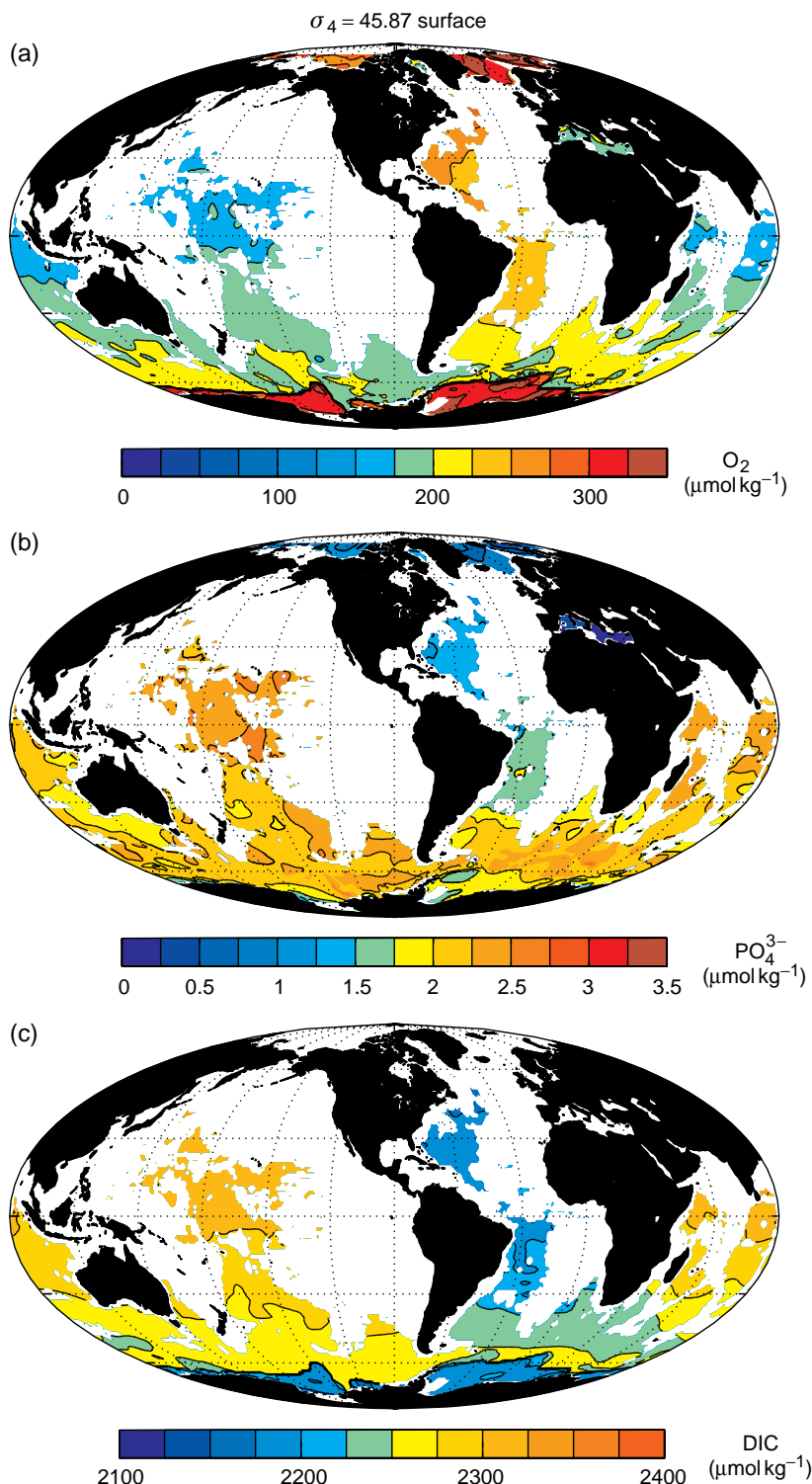


Plate 15. Properties along $\sigma_4 = 45.87$ surface: (a) dissolved oxygen, O_2 ($\mu\text{mol kg}^{-1}$), (b) phosphate ($\mu\text{mol kg}^{-1}$) and (c) dissolved inorganic carbon, DIC ($\mu\text{mol kg}^{-1}$); see Section 10.1.

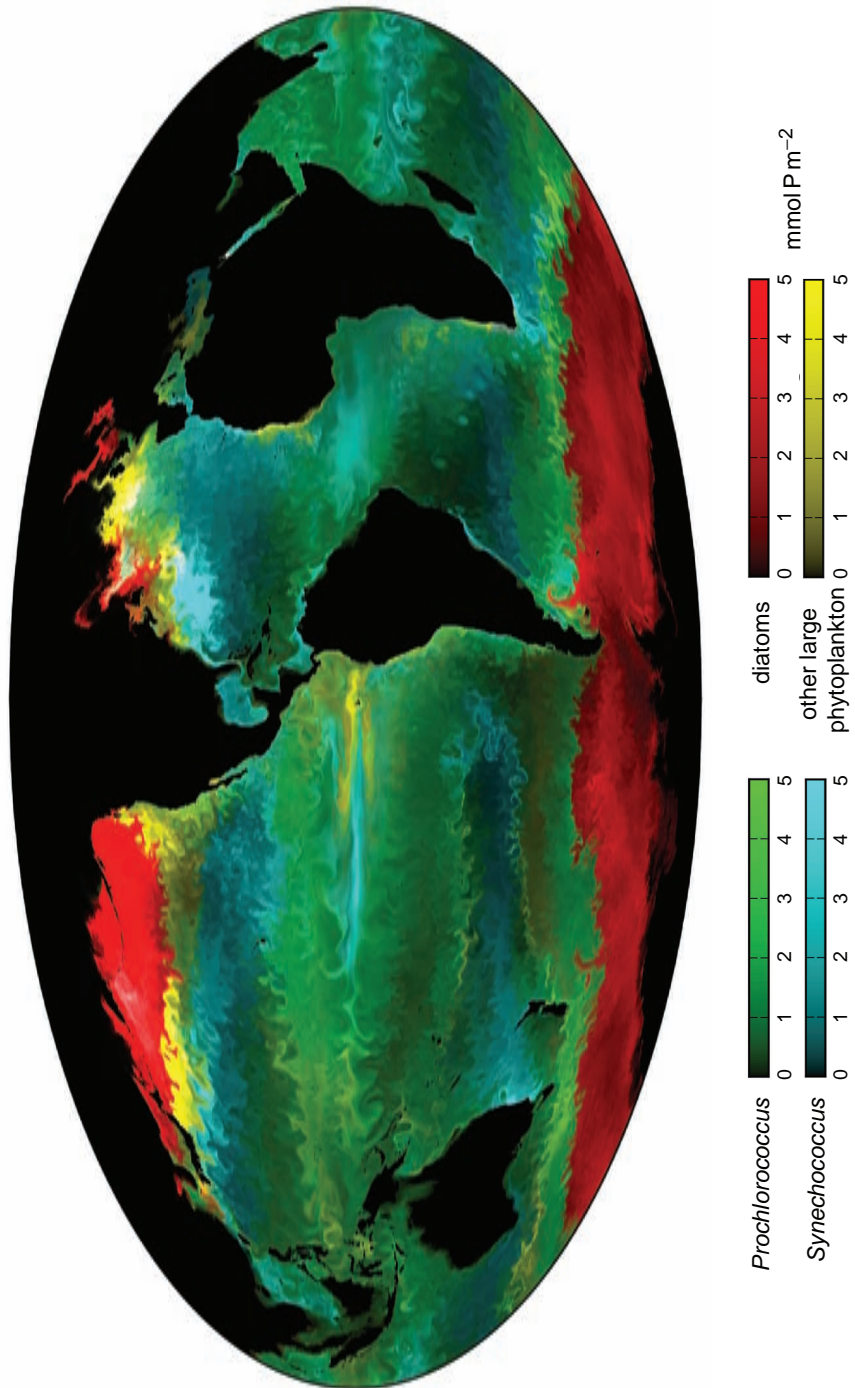


Plate 16. Snapshot of simulated surface phytoplankton community structure on a day in April (analogue of Prochlorococcus (green), Synechococcus and pico-eukaryotes (blue), diatoms (red) and other large phytoplankton (yellow) all in mmol P m^{-2}) from an integration of the MIT gem ocean model, configured with 18 km horizontal resolution to explicitly capture geostrophic eddies (physical configuration – Menemenlis et al., 2005; ecological model – Follows et al., 2007). Figure courtesy of Oliver Jahn. Linked animations at www.cambridge.org/williamsandfollows.

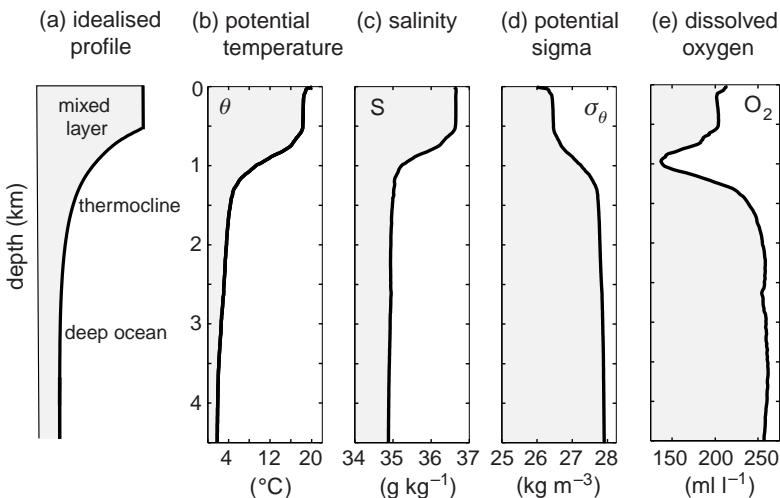


Figure 2.4 (a) A schematic vertical profile identifying the mixed layer, thermocline and deep ocean, together with actual profiles to the east of the Gulf Stream (74.28°W , 35.65°N) in May 2005, (b) potential temperature, θ ($^{\circ}\text{C}$), (c) salinity, the concentration of salt (g kg^{-1}), (d) potential density minus 1000 kg m^{-3} , σ_{θ} and (e) dissolved oxygen (ml l^{-1}) versus depth (km). The mixed layer is very thin in summer, perhaps less than 30 m, and there is a weak seasonal thermocline over the upper 100 m. The mixed layer has previously been thick in winter, as suggested by the relatively uniform properties from 100 m to 500 m; in this case, with temperatures of 18°C and high oxygen content. Below this seasonal boundary layer, there is a permanent thermocline, halocline and pycnocline with strong vertical gradients, extending from 500 m to 1200 m, together with an oxygen minimum zone. Below, in the deep ocean, there are relatively uniform physical properties and higher oxygen concentrations in the colder waters.

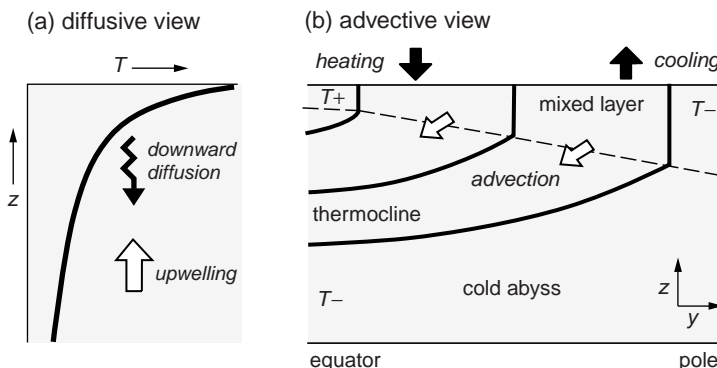


Figure 2.5 A schematic figure showing different views as to how the thermocline is sustained: (a) a diffusive view where there is a downward diffusion of heat (curly arrow) competing with an upward advection of cold, deep water (white arrow), and (b) an advective view where the thermocline is formed by the tilting of the surface temperature contrast into the vertical, involving both vertical and horizontal advection (white arrows).

warming by the penetrating rays of the Sun during summer, but weakens and becomes eroded by surface cooling during winter. The rest of the thermocline can persist over the entire year and there is no direct heating at these depths.

- In the deep ocean, there are relatively weak vertical gradients in temperature and density, such as seen below 1500 m in Fig. 2.4.

Why is there a thermocline?

In many ways, one of the most surprising features in the ocean is the thermocline, the region of

warm waters with a large vertical temperature gradient. The persistence of the thermocline over the ocean is thought-provoking given the tendency of diffusion to erode property gradients and make tracers more uniform.

Traditionally, the thermocline has been explained in terms of a balance between the upward movement of cold water and downward diffusion of heat (Fig. 2.5a). However, there is little observational support for this view, since upwelling of cold water is too small to be measured and the vertical diffusivity turns out to be very small within the thermocline.

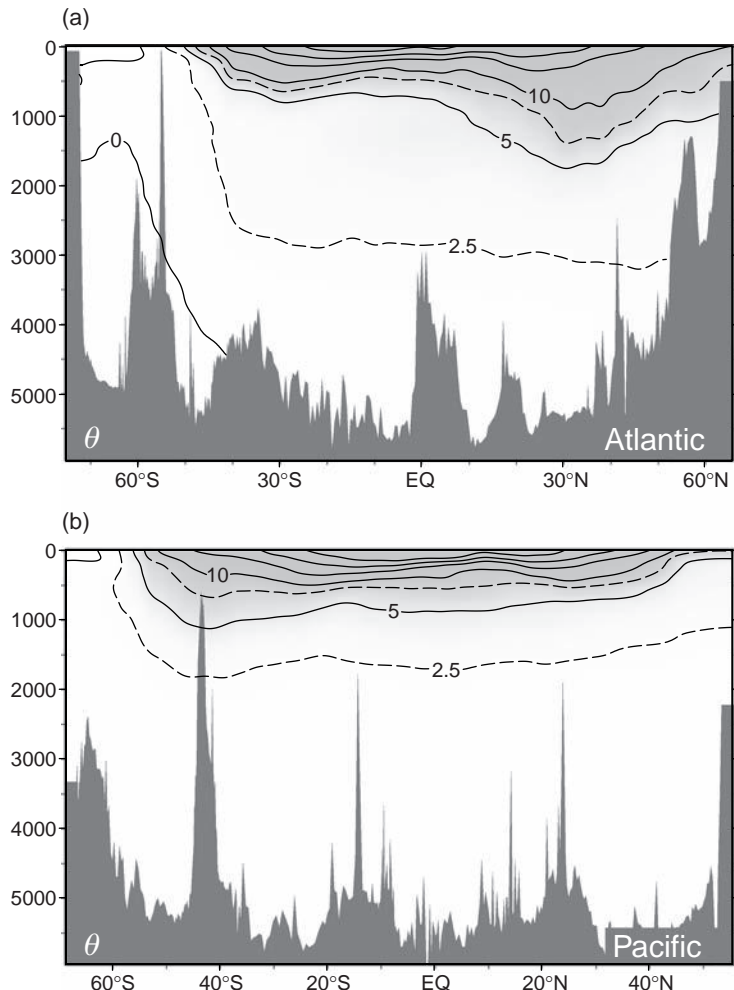


Figure 2.6 Observed meridional sections, latitude versus depth (m), of potential temperature, θ (°C), for (a) the Atlantic along 20°W, and (b) the Pacific along 170°W; see Plates 2a and 3a for colour and cruise track. There is generally a warm upper layer, referred to as the thermocline, overlying cold deep waters. The cold waters connect to the surface over the Southern Ocean. The sea floor is shaded in dark grey, revealing ridges and fracture zones. This section and many others are plotted from hydrographic data using Ocean Data View developed by Reiner Schlitzer.

Instead, the thermocline is a consequence of the three-dimensional circulation, effectively the surface temperature gradient is tilted into the vertical by the vertical and horizontal flows (Fig. 2.5b).

Over the globe, the thermocline is shallow in the tropics, deep at the mid latitudes, and eventually disappears at high latitudes (Fig. 2.6). This thermocline variation reflects the pattern of the atmospheric forcing and the resulting horizontal circulation. At mid latitudes, a thickening of the thermocline is associated with the subtropical gyres rotating anticyclonically (Fig. 2.3a), while at high latitudes, a poleward thinning and eventual vanishing of the thermocline is associated with the subpolar gyres rotating cyclonically and the strong eastward flow in the Antarctic Circumpolar

Current (Fig. 2.3b); this dynamical connection is discussed further in Sections 8.1.2, 8.4.1 and 10.2.3.

2.1.3 How do water masses spread over the globe?

Inferring the interior circulation is more challenging than might be expected due to the difficulty of measuring the flow below the surface. Clues as to the interior circulation are provided by the distribution of water masses, defined in terms of a collection of physical and biogeochemical properties, including temperature, salinity, dissolved oxygen and nutrient concentrations.

Water masses are formed in the surface mixed layer where their properties are determined

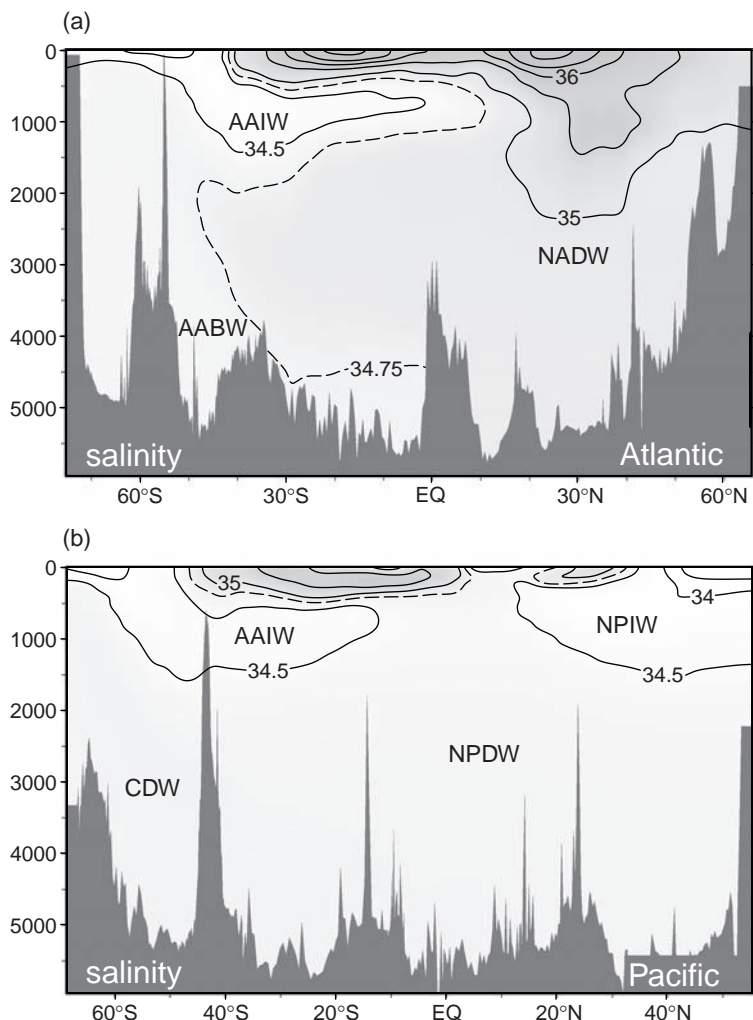


Figure 2.7 Observed meridional sections of salinity, S (g kg^{-1}), the concentration of salt in (a) the Atlantic along 20°W , and (b) the Pacific along 170°W ; see Plates 2b and 3b. The salt distribution is used to define the major water masses: AAIW, Antarctic Intermediate Water; AABW, Antarctic Bottom Water; CDW, Circumpolar Deep Water; NADW, North Atlantic Deep Water; NPIW, North Pacific Intermediate Water; and NPDW, North Pacific Deep Water. These water masses are formed in discrete regions so that the water at any particular location is usually a composite of several water masses.

through the exchange of heat, moisture and dissolved gases with the atmosphere and, in polar regions, with ice, as well as biogeochemical properties affected by biological activity (Fig. 2.4).

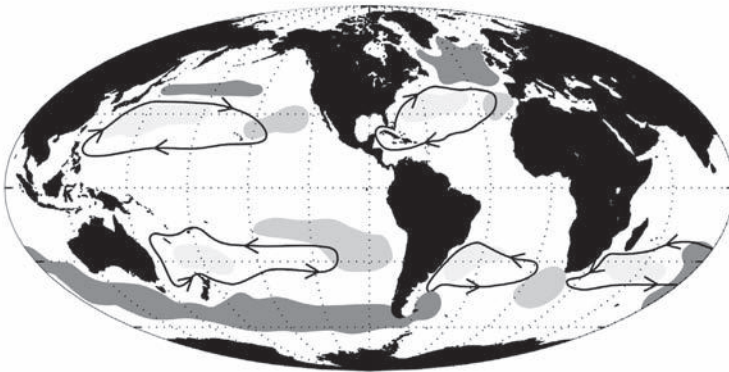
Once the water masses spread in the ocean interior (Fig. 2.5b), they preferentially conserve their salinity, as well as pressure-corrected variants of temperature and density, referred to as potential temperature and potential density, respectively. There are striking contrasts in surface salinity between subtropical and subpolar gyres, as well as between the Atlantic and Pacific basins. Consequently, the interior salinity distribution is very useful in revealing how water masses spread. For example, salinity sections through the Atlantic and Pacific, as depicted in Fig. 2.7, reveal the following pathways:

- Plumes of low salinity suggest a northward spreading at mid depths and along the bottom from the Southern Ocean into the Atlantic and Pacific basins, as well as a southward spreading in upper waters from high latitudes in the northern Pacific.
- Broader regions of higher salinity suggest a southward spreading over several kilometres depth in the Atlantic, as well as a more localised salty intrusion spreading at a depth of typically 1 km, ultimately originating from the Mediterranean Sea.

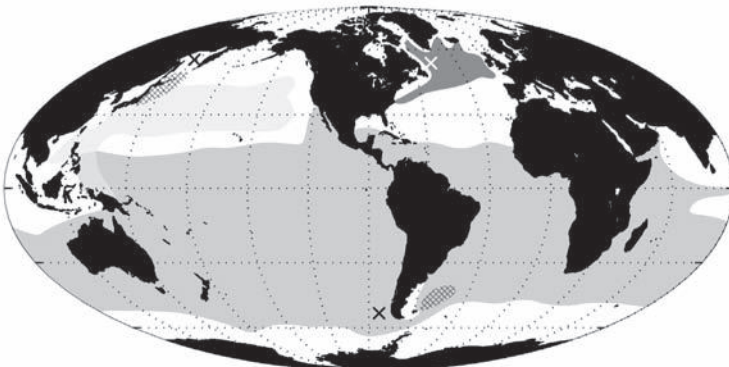
Spreading of mode waters

The water-mass distribution can be viewed as layers of water with nearly uniform properties,

(a) subtropical mode waters



(b) fresh intermediate waters



(c) dense bottom waters

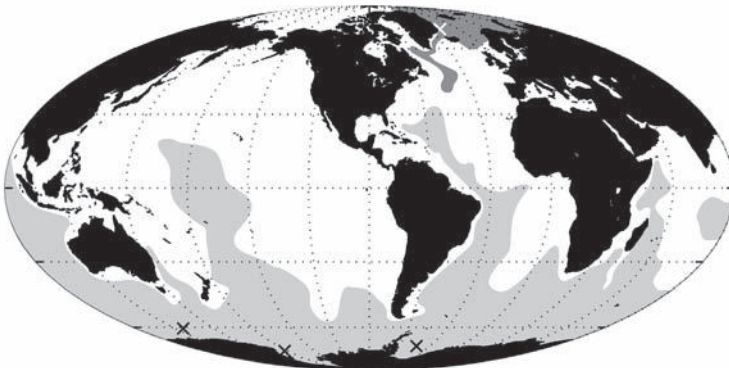


Figure 2.8 Global distribution of mode waters: (a) subtropical mode waters formed on the western side (light shading), eastern side (medium shading) and the poleward side (dark shading) of the gyre, including subpolar mode water in the North Atlantic, North Pacific central mode water and Sub-Antarctic mode water in the southern hemisphere, together with cartoons of the gyre circulation. (b) Fresh intermediate mode waters including Labrador Sea Water (dark shading, $\sigma_\theta = 27.8$), North Pacific Intermediate Water (light shading, $\sigma_\theta = 27.0$) and Antarctic Intermediate Water (medium shading, $\sigma_\theta = 27.1$), together with their formation sites ('X's) and neighbouring regions of strong mixing (hatching). (c) Spreading of dense bottom waters originating from the Antarctic (dark shading) or the North Atlantic (light shading), as defined by the $\sigma_4 = 45.92$ surface (formation sites are marked by X's). Redrawn from figures courtesy of Lynne Talley; further details see Talley (1999).

referred to as mode waters, stacked on top of each other; the lightest mode waters lying above denser mode waters. The distribution of mode waters then provides clues as to the underlying interior circulation over the globe, as illustrated in Fig. 2.8 from Talley (1999):

- Light mode waters are formed in the mid latitudes, generally within the wind-driven subtropical gyres (Fig. 2.8a). For example, in the North Atlantic, the subtropical mode water is formed within the mixed layer close to the Gulf Stream, as illustrated by the 18 °C water in Fig. 2.4b, then

spreads into the thermocline over the western side of the subtropical gyre.

- Intermediate mode waters form in high latitudes or in neighbouring semi-enclosed seas, and spread at depths of typically 1 to 2 km (Fig. 2.8b). For example, in the North Atlantic, warm and salty Mediterranean Sea Water spreads out from the Straits of Gibraltar (after experiencing much mixing) at a depth of ~1200 m, while the colder and fresher Labrador Sea Water spreads at depths ranging from 500 m to 2000 m. In the southern hemisphere, Antarctic Intermediate Water, formed in the southeast Pacific, spreads around the Southern Ocean and extends northward, reaching as far as the tropics of the northern hemisphere (Fig. 2.8b).
- Dense mode waters making up the bottom waters over the globe are formed in the high latitudes of the North Atlantic and off Antarctica (Fig. 2.8c). Their spreading is steered by topography and their properties are gradually diluted by mixing, particularly in fracture zones and regions of rough topography.

Schematic view of the overturning

Based on these water-mass distributions (as in Figs. 2.7 and 2.8), a simplified cartoon view of the ocean overturning can be constructed, as schematically set out in Fig. 2.9:

- Light or less dense water circulates in upper ocean cells associated with the wind-driven gyre circulations, which are confined within the mixed layer and upper thermocline. These cells provide a poleward transport of warm water from the tropics to high latitudes.
- Dense water circulates in a bottom cell and spreads from the Southern Ocean into the northern basins.
- Between these two cells, there is a northward transport of water from the Southern Ocean at mid depths, as well as a southward transport of mid-depth and deep waters from the northern basins.

The relative extent of each of the overturning cells varies within each basin. In the Atlantic, there is

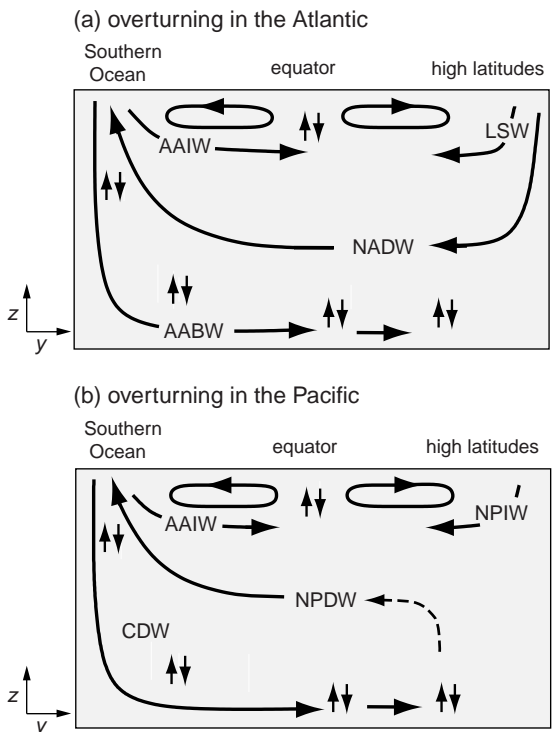


Figure 2.9 A schematic figure depicting a highly idealised, zonally averaged view (depth versus latitude) of the meridional circulation for (a) the Atlantic, and (b) the Pacific. Transport pathways (full lines) are based upon the preceding water-mass sections revealing characteristic water masses (definitions given in Fig. 2.7 together with Labrador Sea Water, LSW). Possible regions of strong vertical mixing (pairs of vertical arrows) are in the Southern Ocean, in the bottom waters and at the equator. The dominant components of the circulation are: subtropical gyre circulations in the upper ocean; a southward spreading of intermediate waters (LSW, NPIW) from the northern high latitudes; a southward spreading of dense water (NADW) in the Atlantic; and a northward spreading of intermediate water (AAIW) and dense bottom water (AABW, CDW) from the Southern Ocean. The bottom water in the Pacific lightens and forms deep water (NPDW) somewhere over the basin (dashed line).

a southward spreading of deep water, overlying a more limited northward spreading of bottom water originating from Antarctica (Fig. 2.9a). In contrast, in the Pacific, there is a much weaker southward spreading of water masses formed in the northern basin, together with deep and bottom water spreading northward from the Antarctic Circumpolar Current (Fig. 2.9b).

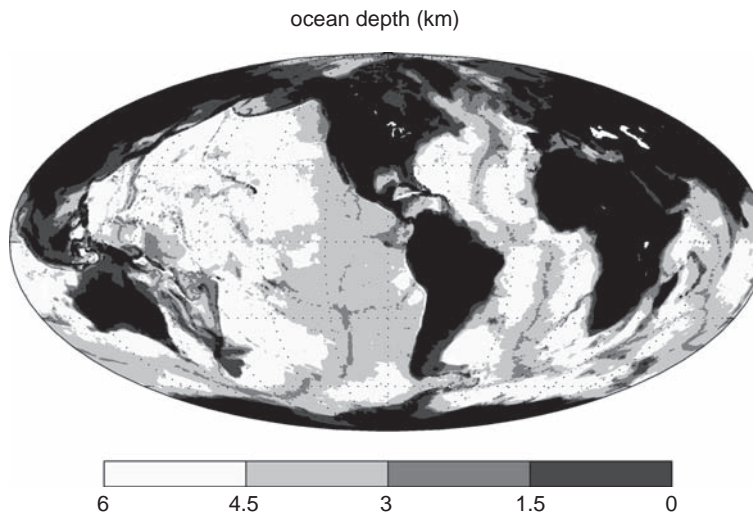


Figure 2.10 Map of ocean topography (km). The deepest ocean basins (unshaded) are defined by the position of topographic ridges (shaded), such as the mid-Atlantic ridge (30°W) and East Pacific Rise (110°W). The topography affects how the deep and bottom waters spread over the global ocean.

2.1.4 What is the effect of topography?

Topography affects the pattern of the deep circulation over the globe, sometimes providing a barrier that prevents water spreading into particular regions, as revealed by comparing the depth of the ocean and extent of bottom water (Figs. 2.10 and 2.8c). The effect of the topography on the surface circulation is less clear and consistent (Fig. 2.2a): the surface flow is not strongly deflected by the mid-Atlantic ridge (along 30°W) or by the East Pacific Rise (along 110°W), yet is deflected by ridges in the Southern Ocean.

Why does the topography appear to affect the surface flow in some cases and not in others? The answer lies in how the thermocline separates the surface and deep flows. When there is a thermocline and strong vertical contrasts in density, the surface and deep flows can be very different, even flowing in opposite directions, so that surface flows do not resemble the pattern of the underlying topography. Conversely, when there is no thermocline and vertical contrasts in density are weak, the surface and deep circulations flow in the same direction, hence such top to bottom circulations pass around ridges or bumps in the sea floor.

2.1.5 Summary

The ocean circulation is due to a combination of mechanical and density forcing, involving the surface winds, exchanges of heat, fresh water and salt, as well as tide-inducing gravitational accel-

erations. The ocean circulation can be viewed in the horizontal in terms of recirculating gyres and boundary currents within basins and near zonal flows close to the equator and in the Southern Ocean, as well as in the vertical by overturning cells connecting each of the basins with the Southern Ocean. Clues as to the interior circulation are provided by the distribution of water masses and tracers over the globe (see colour plates and later Section 10.1).

2.2 | Atmospheric circulation

While this book focusses on the role of the ocean, it is important to consider how the atmosphere circulates in order to understand the primary forcing of the ocean and how the atmosphere and ocean interact in the climate system.

2.2.1 How does the atmosphere circulate?

Remotely sensed pictures of the planet, such as in Fig. 2.11, provide clues from the pattern of clouds as to how the atmosphere circulates. There is always persistent high cloud in the tropics (23°S to 23°N), contrasting with normally cloud-free skies outside the tropics (at typically 30°N and 30°S), and more variable cloud cover at mid and high latitudes. Clouds form as moist air rises; air cools with height, holding less water vapour, leading to water condensing and forming cloud drops.

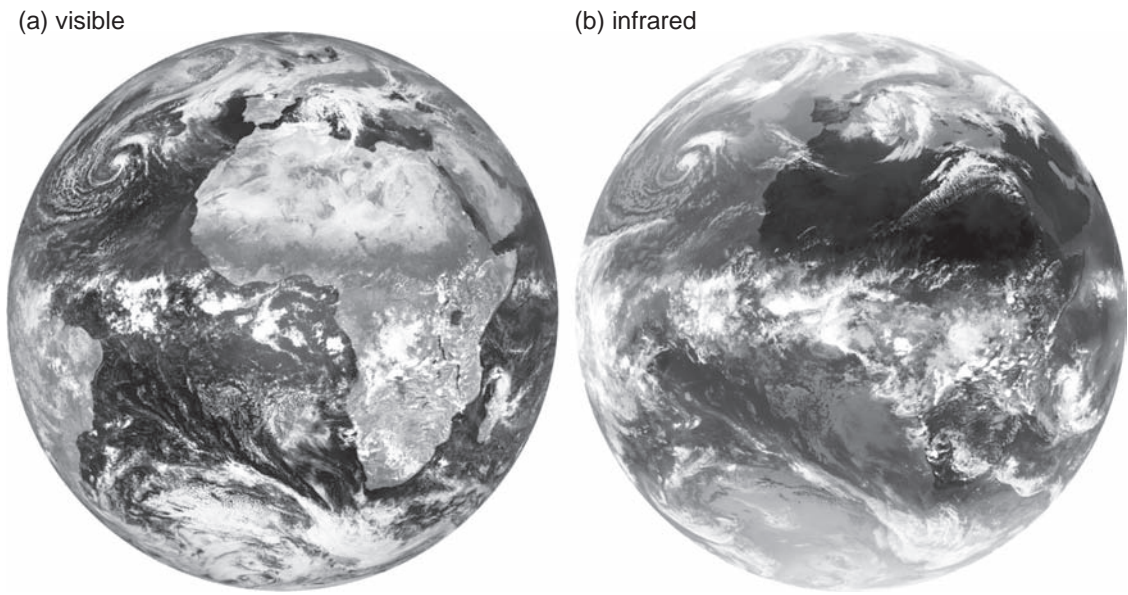


Figure 2.11 Atmospheric cloud revealed over the Atlantic sector for 6 March 2008 at 1200 UTC: (a) visible image of reflected light where white represents high reflectance from cloud (0.74–0.88 μm band) and (b) infrared image of long-wave radiation emitted, where white represent cold and dark represents warm temperatures, such as over the land (11–13 μm band). There is a band of cold, high clouds over the tropics, identifying the Intertropical Convergence Zone, together with clearer sky over northern Africa. At mid and high latitudes, there are variable cloud structures associated with the weather systems, such as the spiral cloud of a cyclone over the North Atlantic. From Meteosat Second Generation satellite MSG-2, image copyright: EUMETSAT, NERC Satellite Receiving Station, University of Dundee.

Conversely, sinking air is often associated with an absence of clouds. Individual bands of moving clouds also reveal the presence of fast-moving jets or storms, as seen when watching animated weather forecasts.

Consider now how the atmospheric circulation is controlled over the globe.

OVERTURNING CELLS

The atmospheric circulation is ultimately driven by the latitudinal variation of the Sun's heating over the globe. Heating leads to a narrow band of warm, moist air rising over the tropics, indicated by thick cloud and strong precipitation (Fig. 2.11). This warm air moves poleward at heights of 10–20 km and is replaced by equatorward moving air in the lower few kilometres – an overturning referred to as the Hadley cell, as depicted in Fig. 2.12.

This overturning cell does not extend in a simple manner over the entire globe. Instead the circulation is strongly constrained by the

Earth's rotation. The warm tropical air initially moves poleward aloft, but is deflected by the Earth's rotation into fast-moving, westerly upper air jets (Fig. 2.12; see Q2.4). The tropical air eventually descends just outside the tropics (typically 30°N and 30°S); hence, the Hadley cell only extends from the equator to just outside the tropics. The descending air warms and any water remains in vapour form, leading to clear skies and little precipitation (Fig. 2.11); thus, the great desert belts are formed along these latitude bands over the globe.

MID-LATITUDE JETS AND WEATHER SYSTEMS

In the mid latitudes, the fast-moving westerly jets are naturally expected to transfer heat zonally, rather than poleward. Hence, there is a problem: how does the atmosphere continue to move heat towards the poles across the mid latitudes?

These westerly jets turn out to be unstable, meandering and forming weather systems on horizontal scales of a thousand kilometres, as

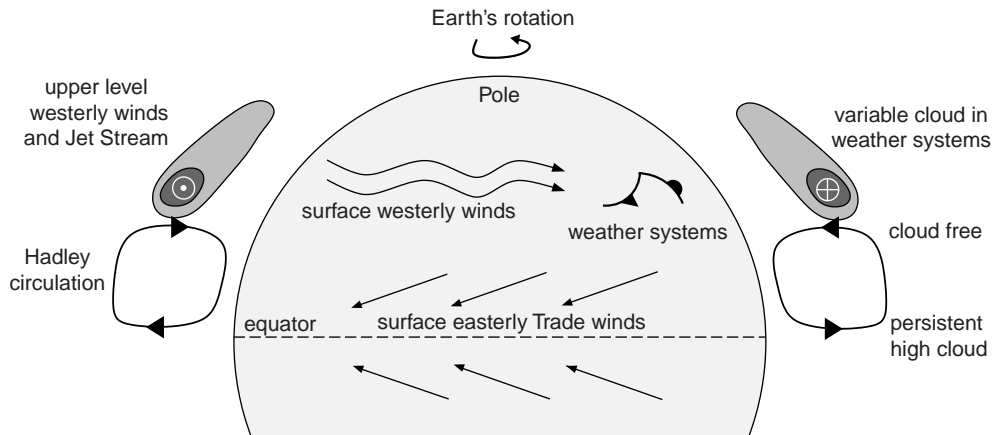


Figure 2.12 A schematic of the atmospheric general circulation. Heating in the tropics leads to rising warm air and persistent high cloud. This tropical air moves poleward aloft, but is deflected eastward and eventually descends at 30°N and 30°S , leading generally to cloud-free regions; this air is replaced on the ground through easterly Trade winds and towards the equator. On the poleward flank of this overturning cell (called the Hadley circulation), there are fast moving, upper level, westerly winds with the core of the subtropical Jet Stream (shading represents strong eastward flow); the surface winds at mid latitudes are also westerly. These fast jets in the mid latitudes are unstable, forming weather systems containing warm and cold fronts, associated with variable cloud, and lead to a polewards heat flux. Modified from article published in Marshall and Plumb (2007), © Elsevier.

illustrated by the cyclones with spiralling high cloud over the North Atlantic in Fig. 2.11. There is an exchange of air within these weather systems linked to the warm and cold fronts: warm air rises and moves poleward at the warm front, while cold air sinks and moves equatorward at the cold front. Hence, the instability of the zonal jets and formation of weather systems leads to a poleward heat flux at mid latitudes over the planet.

At mid latitudes, you can see the passage of these fronts from their characteristic cloud structures: early warning of an oncoming warm front is given by the arrival of high-level ice clouds (cirrus), identified by a hooked or hair-like profile from falling ice crystals in the sky. The later approach of the warm and cold fronts is associated with thickening grey cloud and drizzle, and the onset of the cold front by heavy rain. The eventual passing of the cold front is heralded by colder air, sometimes scattered showers, and clearer visibility.

In summary, the atmospheric general circulation is driven by the Sun's differential heating over the globe, although the response is constrained by the rapid rotation of the planet (Fig. 2.12). Heat is transferred poleward in the atmosphere

by a combination of the Hadley overturning cell, extending from the equator to just outside the tropics, and then by eddy circulations formed along the zonal jets in mid and high latitudes.

2.2.2 How do the atmosphere and ocean transfer heat together over the globe?

Both the atmosphere and ocean lead to a poleward heat transport, reaching 5 PW at mid latitudes as displayed in Fig. 2.13. The heat gained in the tropics is transported to the mid and high latitudes, where the heat is ultimately radiated back to space at the top of the atmosphere (Fig. 1.3a). The atmosphere provides the dominant contribution, reaching more than 4 PW at mid latitudes (Fig. 2.13, dashed line). The ocean provides a smaller heat transport reaching 1 to 2 PW in the tropics (at $\pm 20^{\circ}\text{N}$) and decreasing to less than half this value by the mid latitudes ($\pm 40^{\circ}\text{N}$) (Fig. 2.13, full line).

Concomitant with these transport patterns, the ocean gains heat in the tropics, but releases heat to the atmosphere at mid and high latitudes (Fig. 2.14). The strongest release of heat to the atmosphere occurs over the western side of the

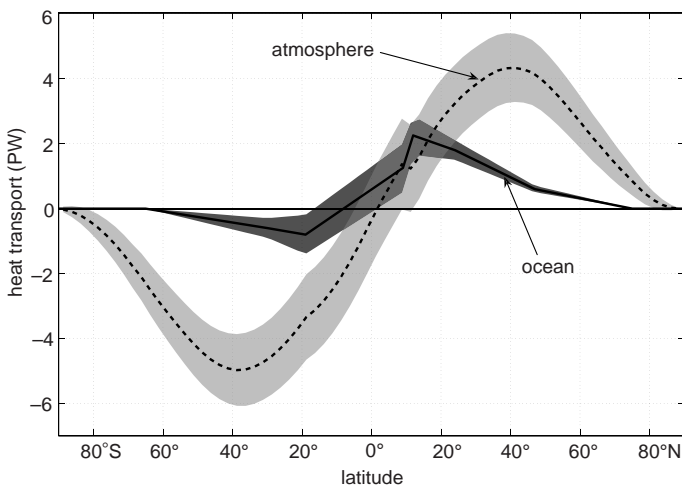


Figure 2.13 The northward transfer of heat ($\text{PVW} \equiv 10^{15}$ watts) over the globe by the atmosphere (dashed line) and ocean (full line), with shading for the error range. The ocean transport is diagnosed using a global inverse model based upon ocean section measurements, while the atmospheric transport is diagnosed as a residual using a heat budget from the mismatch between the measured radiation at the top of the atmosphere (from the Earth Radiation Budget Experiment over 3 years from 1987 to 1989) and these ocean measurements. From C. Wunsch; further details, see Wunsch (2005).

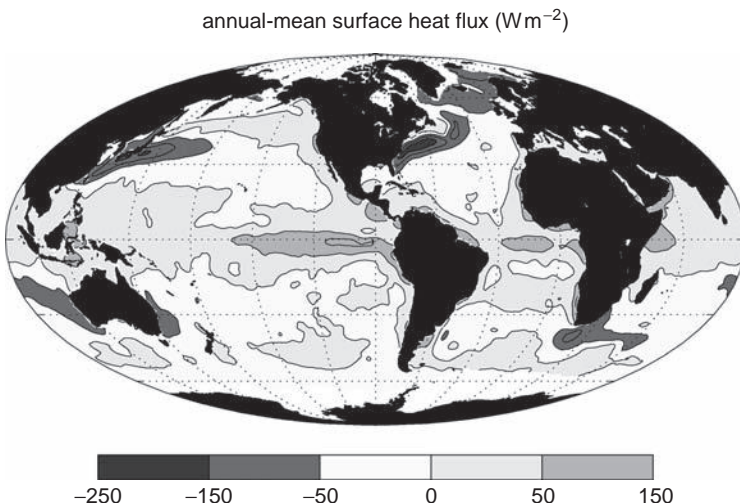


Figure 2.14 Air-sea heat flux into the ocean (W m^{-2}) from the NOCS climatology (Josey et al., 1999) with contours every 50 W m^{-2} . There is a heat input in the tropics (light shading) and a heat loss over high latitudes and the western side of basins at mid latitudes (dark shading).

ocean basins in the mid latitudes, where cold, dry air passes from the continents over the warm waters in the ocean boundary currents.

The overall poleward heat transport by both fluids can partly be viewed as a relay race where the ocean transports heat poleward at low latitudes, passing the heat onto the atmosphere at mid latitudes, which is then transferred further poleward by the atmosphere, until ultimately the heat is radiated back to space.

2.2.3 Summary

The atmosphere and ocean combine together to transfer heat poleward, reducing latitudinal temperature contrasts and making the Earth's cli-

mate more equitable. There are some common phenomena in both fluids: the strong jet streams in the atmosphere and the intense currents in the ocean, including the Antarctic Circumpolar Current, equatorial currents and western boundary currents. Instability of these intense flows leads to strong temporal variability, generating weather systems in the atmosphere and ocean eddies on the horizontal scale of several tens of kilometres.

There are also some important differences between the atmosphere and ocean: the continents provide barriers to zonal flow in the ocean, leading to gyre circulations within ocean basins; and the fluids are heated at opposing boundaries,

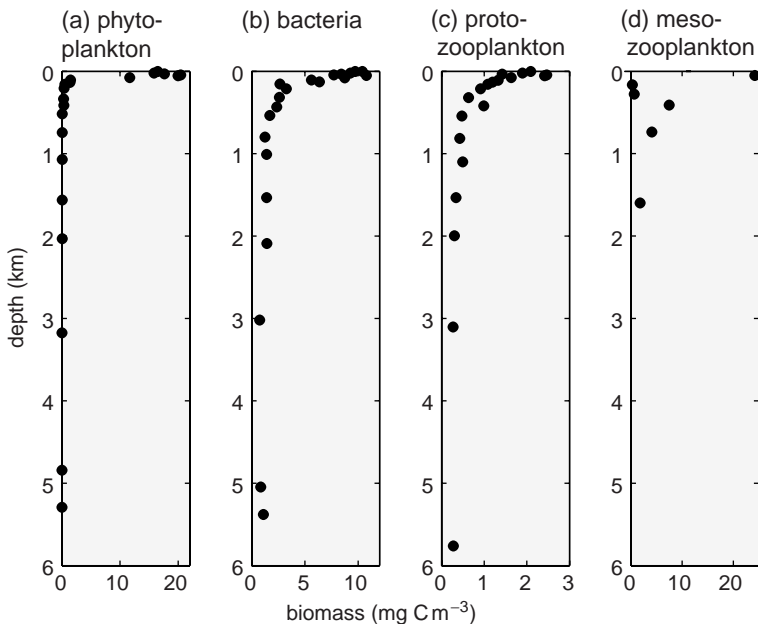


Figure 2.15 Observed vertical profiles of biomass (mg C m^{-3}) over the full water column depth in the North Pacific Ocean ($39^\circ\text{N}, 147^\circ\text{E}$): (a) phytoplankton, $0.2\text{--}200\ \mu\text{m}$, which perform photosynthesis; (b) bacteria, $0.2\text{--}2\ \mu\text{m}$, which respire organic detritus; (c) protozooplankton, unicellular and small predators, $2\text{--}200\ \mu\text{m}$, which consume bacteria and phytoplankton; and (d) mesozooplankton, $200\text{--}2000\ \mu\text{m}$, including tiny shrimp-like copepods, which prey upon the smaller organisms. Phytoplankton are restricted to the surface waters where sunlight can penetrate. Bacteria and their protozooplankton predators are ubiquitous, since organic detritus is found throughout the water column. They are more abundant at the surface in the region where photosynthesis provides a strong source of new organic material. Mesozooplankton are seen here throughout the upper water column (although observations were not made in the deepest waters). Replotted from Yamaguchi *et al.* (2002).

the atmosphere at its lower boundary and the ocean at its upper boundary. This contrast leads to the strongest atmospheric convection in the tropics, while the strongest ocean convection is at high latitudes.

Following these descriptive views of how the atmosphere and ocean circulate, we now turn to questions of how the ocean ecosystem and the carbon cycle operate.

2.3 Life and nutrient cycles in the ocean

The oceans sustain an enormous diversity of living creatures. While we are most familiar with the larger organisms, such as fish or whales, the vast majority of the living biomass is in the form

of microbes; tiny creatures that cannot be seen without the aid of a microscope.

Phytoplankton are the tiny plants of the ocean performing photosynthesis, converting the energy in light to chemical energy through the formation of organic molecules. They produce chlorophyll and other pigments in order to absorb light. Since light penetrates only 100 m or so in seawater, phytoplankton are confined to live in near-surface waters, as revealed in Fig. 2.15a. They are extremely diverse in form and function, ranging in size from one to several hundred microns.

Bacteria and archaea are also extremely small, typically less than a micron in size. They acquire energy and nutrients by breaking down and respiring pre-existing organic matter. They live throughout the water column since particles of organic detritus continually rain down from the

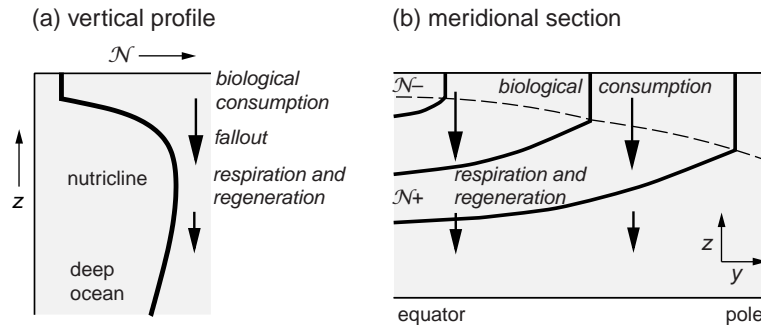


Figure 2.16 A schematic view of the biological cycling of nutrients in the ocean: (a) a vertical profile, and (b) a meridional section for a typical inorganic nutrient, \mathcal{N} , such as nitrate, phosphate and carbon. The nutrient profile is separated into a mixed layer overlying the nutricline and the deep ocean. Inorganic nutrients are consumed within the surface, sunlit ocean, then organic particles fall out of the surface layer. Most of the organic fallout is respired, leading to inorganic nutrients being regenerated and forming a subsurface maximum in concentration within the mid depths of the water column. In addition, the physical circulation also transports nutrients along density surfaces (black lines), leading to lower nutrient concentrations in younger waters (more recently in contact with the mixed layer) and higher concentrations in older waters.

productive surface layers, providing them with a means of sustenance (Fig. 2.15b).

Both phytoplankton and bacteria are eaten, or grazed, by zooplankton; unicellular grazers, perhaps some tens of microns in size, prey upon them. Some of these grazers also perform photosynthesis, hedging their bets for survival. Larger zooplankton, like submillimetre-sized shrimp, have more complex physiologies, and a variety of hunting strategies, and may mechanically break down particles of detritus. Like the bacteria, zooplankton can thrive throughout the water column (Fig. 2.15c,d).

2.3.1 Biological cycling of nutrients

Phytoplankton and other organisms need carbon, nitrogen, phosphorus, sulphur, iron and other elements to create their structural and functional organic molecules. The elemental composition of phytoplankton, in a bulk average sense, is relatively uniform ($C:N:P = 106:16:1$) reflecting the common biochemical molecules from which they are made.

Phytoplankton die through viral infection or are grazed by zooplankton, which in turn provide a food source for fish. This organic matter eventually either sinks or is transported from the sunlit, surface waters into the dark interior. As particles sink, they aggregate and disaggregate. They

are consumed by zooplankton and filter feeders like jellyfish which, in turn, produce new detritus. They are inhabited by colonies of bacteria which attack and respire their organic components. Nearly all of the organic matter is oxidised within the water column. Less than one per cent of the sinking organic matter reaches the sea floor, where most of the remaining organic material is rapidly reworked by the benthic ecosystem.

Surface waters transferred into the interior ocean contain inorganic nutrients and dissolved organic material. As these waters move through the deeper ocean, the respiration of dissolved organic matter and sinking organic particles leads to a regeneration of inorganic nutrients, increasing the concentrations of phosphate and nitrate, as illustrated schematically in Fig. 2.16.

The effect of the interior source of inorganic nutrients varies according to the elapsed time since the waters were in the surface mixed layer. In the Atlantic, deep waters are relatively young (having been relatively recently formed in the mixed layer) and the nitrate distribution resembles that of a physical tracer, such as salinity; compare Figs. 2.17a and 2.7a. Conversely, in the deep Pacific, the deep waters are relatively old and the accumulated effect of biological fallout and respiration has created strong gradients in nitrate compared with salinity; compare Figs. 2.17b and 2.7b.

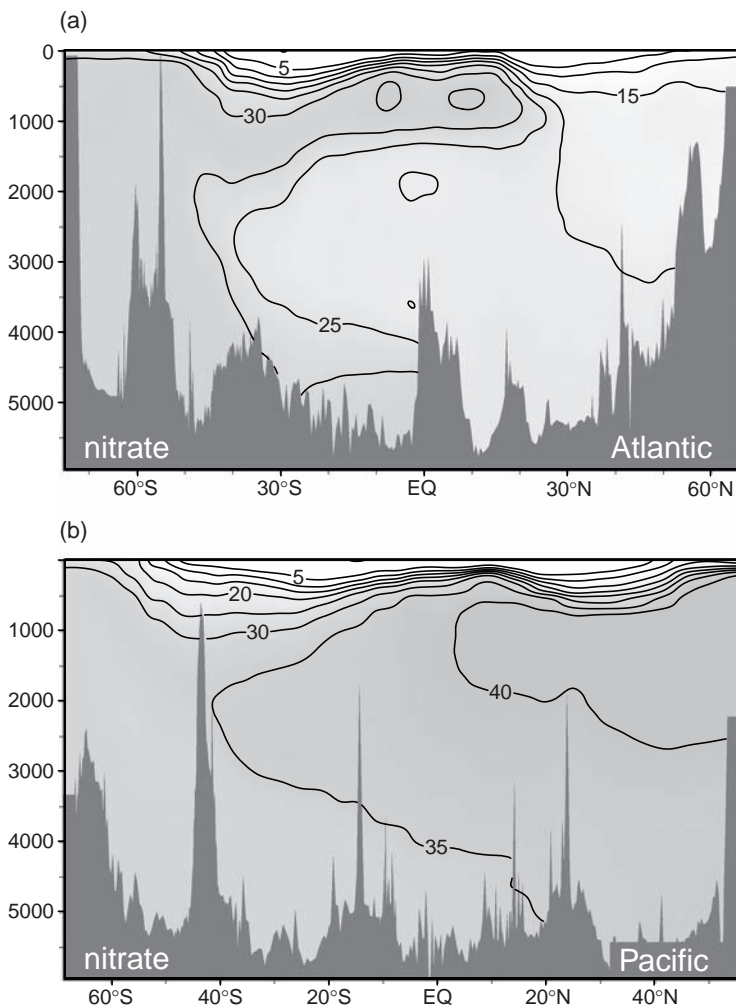


Figure 2.17 Observed meridional sections of nitrate (NO_3^- ; $\mu\text{mol kg}^{-1}$) for (a) the Atlantic along 20°W , and (b) the Pacific along 170°W . The nitrate concentrations are generally depleted at the sea surface and increase to a mid-depth maximum. There is a strong vertical gradient in the upper waters, referred to as the nitracline, which undulates in the same manner as the thermocline. Horizontal contrasts in the nitrate concentrations reflect the physical transport of water masses, as revealed by salinity (Fig. 2.7).

Consequently, there are strong contrasts between the distributions of inorganic nutrients in the Atlantic and Pacific.

2.3.2 Where is organic matter produced?

Light is essential for photosynthesis, but visible wavelengths are absorbed very effectively by seawater, as well as any suspended particles, within a few tens of metres from the sea surface. Hence, organic matter is produced only close to the surface of the ocean. Phytoplankton absorb sunlight using pigments, notably chlorophyll *a*, which absorb visible light most effectively in blue and red wavelengths. Thus, the ocean appears with a green tinge in waters where phytoplankton are abundant. The ‘greenness’ of the ocean, measured by comparing the relative transmission and

backscattering of green and blue wavelengths, can then be used to infer the concentration of chlorophyll and, hence, provide a gross measure of the surface phytoplankton distribution, as depicted in Fig. 2.18a.

Though the incident solar radiation increases towards the tropics, the highest surface concentrations of chlorophyll are in the shelf seas and high-latitude open ocean. Phytoplankton require not only sunlight, but also inorganic nutrients. Hence, the chlorophyll distribution broadly resembles the underlying nitrate distribution, with high concentrations in the high latitudes, shelf seas and parts of the tropics, and low or depleted concentrations in the mid latitudes (Fig. 2.18b); this connection is explored further in Sections 7.2 and 11.1.

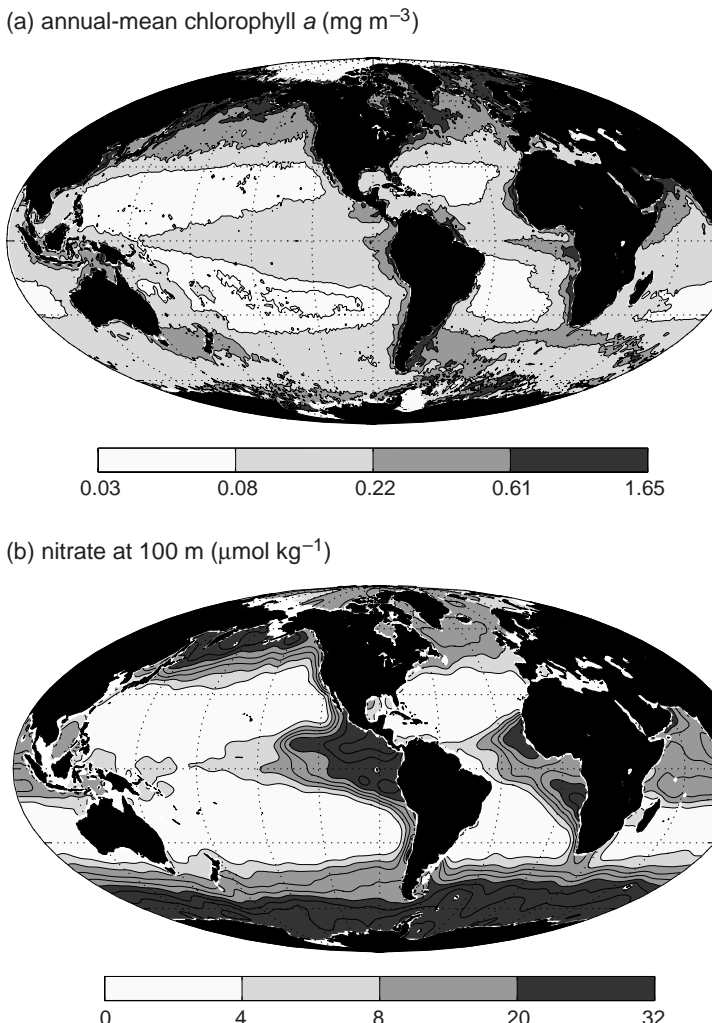


Figure 2.18 (a) The global distribution of phytoplankton inferred from annual-mean concentration of the green pigment, chlorophyll a ($\text{C}_{55}\text{H}_{72}\text{O}_5\text{N}_4\text{Mg}$; mg m^{-3}), inferred from remotely sensed backscatter of light observations (from NASA Sea-viewing Wide Field-of-view Sensor, SeaWiFS) at 1° resolution for 2006. Phytoplankton growth requires a supply of nutrients, so the pattern of chlorophyll broadly resembles (b) the distribution of nitrate at 100 m (contours every $4 \mu\text{mol kg}^{-1}$) (Conkright et al., 2002). There are higher concentrations of nitrate and chlorophyll a at high latitudes and the tropics, and along the coast, but much lower values over the open ocean in the mid latitudes.

2.3.3 Diversity in phytoplankton types

Many different types of phytoplankton contribute to the gross measure of phytoplankton distribution provided by remotely sensed chlorophyll (Fig. 2.18a). Each phytoplankton group and species has evolved to exploit slightly different conditions, some preferring relatively stable situations and others preferring regions of strong seasonality.

For example, diatoms are a fast growing group requiring silica to form parts of their protective shell (Fig. 2.19a). Thus, their distribution reflects that of the surface silica distribution, which has higher concentrations in high latitudes

and parts of the tropics, but very low concentrations in the subtropics (Fig. 2.19b). In contrast, tiny *Prochlorococcus* cells are found mainly in the stable, nutrient-depleted subtropical waters over the globe; the diversity of phytoplankton types and the effect of seasonality is explored further in Sections 5.4 and 7.2.

2.3.4 Summary

This interplay of life and nutrient cycling in the ocean is very different from on land. As terrestrial plants grow, they take up nutrients and trace metals from the soil. When they die these elements are returned to the soil as the organic matter is

(a) diatoms

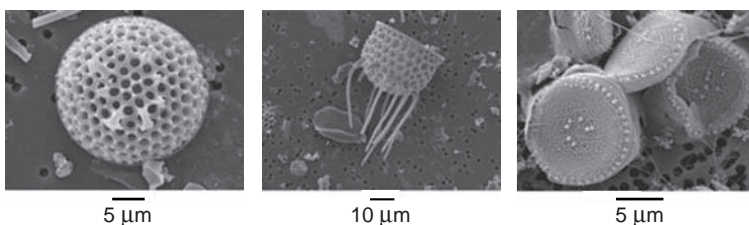
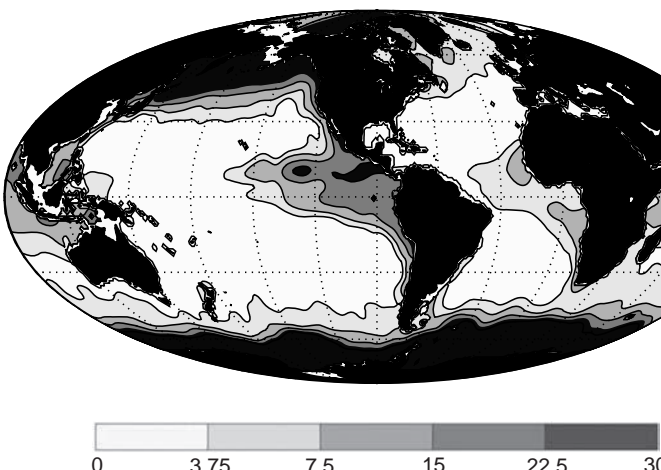
(b) silicate at 100 m ($\mu\text{mol kg}^{-1}$)

Figure 2.19 (a) Electron micrographs of the silica-based structural parts of fossil and modern diatoms (images courtesy of Zoe Finkel). There are thousands of species of diatom, spanning several orders of magnitude in cell size, some forming chain-like colonies. The availability of silicic acid in surface waters shapes their habitat. (b) Climatological, annual silicate concentration ($\mu\text{mol kg}^{-1}$) at a depth of 100 m (Conkright *et al.*, 2002).

respired locally by bacteria, and are assimilated the next year, and so the cycle goes on. In the oceans, sunlight is rapidly absorbed with depth and most of the water column is dark. When phytoplankton grow in the thin, sunlit surface layer, they consume inorganic nutrients. Most of the organic matter formed in the surface ocean is recycled locally, but a small fraction sinks through the water column, appearing like falling snow. Ultimately this organic matter is respired and regenerates inorganic nutrients at depth. This biological cycling then acts to transfer nutrients from the surface to the deep ocean and, ultimately, photosynthesis ceases unless nutrients can be returned to the sunlit surface layer. This resupply of nutrients to the surface ocean is principally achieved by physical processes acting within the ocean.

2.4 | The carbon cycle in the ocean

Carbon dioxide dissolves and reacts in seawater forming dissolved carbon dioxide, CO_2^* (defined

by the sum of the aqueous form of carbon dioxide, CO_2^{aq} , and carbonic acid, H_2CO_3), bicarbonate ions, HCO_3^- , and carbonate ions, CO_3^{2-} , which collectively are referred to as dissolved inorganic carbon, DIC:

$$\text{DIC} = [\text{CO}_2^*] + [\text{HCO}_3^-] + [\text{CO}_3^{2-}], \quad (2.1)$$

where square brackets denote concentrations in seawater defined per unit mass in $\mu\text{mol kg}^{-1}$.

While carbon is exchanged between the atmosphere and ocean in the form of carbon dioxide, most of the carbon dioxide is transferred into bicarbonate and carbonate ions within the ocean, such that typically 90% of DIC is made up of bicarbonate ions, about 9% as carbonate ions, and only a small remainder, up to 1%, as dissolved carbon dioxide (Fig. 2.20).

This transfer of carbon dioxide into bicarbonate and carbonate ions then leads to the ocean holding 50 times as much carbon as in the overlying atmosphere. This inorganic carbon in the ocean is about 40 times larger than the amount held as organic carbon.

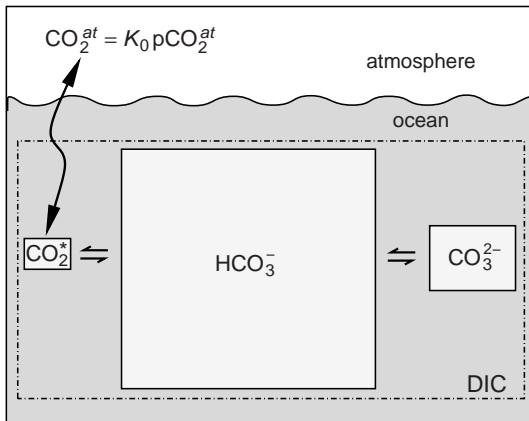


Figure 2.20 Carbon dioxide dissolves in and reacts with seawater, making up three dissolved inorganic forms of carbon: dissolved carbon dioxide, CO_2^* , bicarbonate, HCO_3^- , and carbonate CO_3^{2-} ions, which together make up dissolved inorganic carbon, DIC. For the present day, most of the dissolved inorganic carbon is in the form of bicarbonate ions. The air-sea exchange of carbon dioxide depends on the difference in the dissolved concentration of carbon dioxide in the ocean and the atmosphere, CO_2^{at} , which is related to the solubility, K_0 , and the partial pressure of carbon dioxide, $p\text{CO}_2^{at}$.

2.4.1 The vertical distribution of carbon

Dissolved inorganic carbon generally increases in concentration with depth, as depicted in Fig. 2.21 (solid line) with vertical contrasts of typically $200 \mu\text{mol kg}^{-1}$ and a much larger depth average of nearly $2300 \mu\text{mol kg}^{-1}$. Two factors maintain the vertical gradient in DIC:

- At equilibrium with the atmosphere, cooler waters hold more DIC. Since the density structure over the globe is largely controlled by temperature, cool, carbon-rich waters slide under warm, carbon-depleted waters. This physical enhancement of the carbon stored in the deep ocean is referred to as the solubility pump; discussed further in Section 6.3.
- In addition, phytoplankton take up carbon dioxide in the sunlit surface waters, creating organic matter by photosynthesis. A small fraction of this organic carbon sinks to the deep ocean before being respiration and returned to inorganic form by bacteria, which then increases DIC at depth. This biological enhancement of the carbon stored in the deep ocean is referred to as the biological pump; discussed further in Sections 5.5 and 6.4.

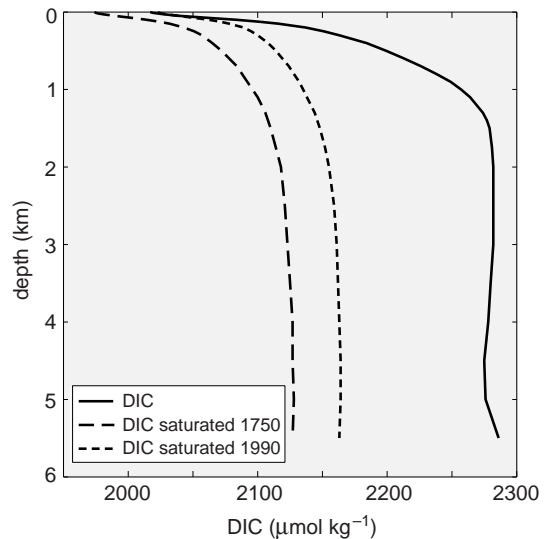


Figure 2.21 Vertical distribution of dissolved inorganic carbon, DIC ($\mu\text{mol kg}^{-1}$): globally averaged: observed vertical profile (solid line), together with equilibrium profiles if there were no biological processes and surface waters were in complete equilibrium with an atmospheric carbon dioxide for the pre-industrial era (long dashed line) or 1990 (short dashed line).

If there was no biological cycling of carbon, then the interior DIC distributions would resemble their equilibrium values given by their temperature and salinity at depth and an atmospheric value of carbon dioxide; as depicted for the pre-industrial or present era by dashed and dotted lines in Fig. 2.21, respectively. The actual DIC profile (in Fig. 2.21, full line) is greater than the equilibrium profiles, but comparable in magnitude. Hence typically 90% of the carbon stored in the ocean is due to the reactivity of carbon dioxide in seawater and the solubility pump, while the remaining 10% is due to the biological pump.

Atlantic and Pacific contrasts in DIC

The DIC distribution differs in each basin: in the Atlantic, there is a layered structure resembling that of physical tracers (Fig. 2.22a), while in the Pacific there is a relatively large vertical contrast (Fig. 2.22b). These DIC distributions are again due to a combination of physical transport and biological transfers:

- The physical transfer leads to the layering structure. Surface waters carry their properties with them as they pass from the mixed layer

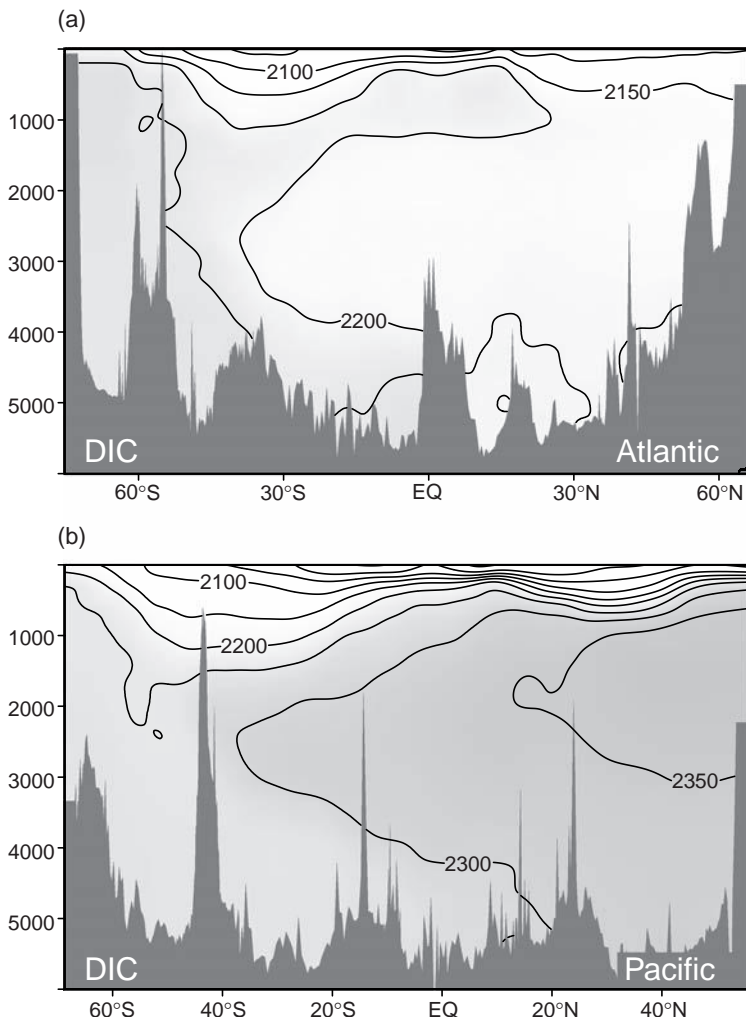


Figure 2.22 Observed meridional sections of dissolved inorganic carbon, DIC ($\mu\text{mol kg}^{-1}$) in (a) the Atlantic, approximately along 20°W, and (b) the Pacific, approximately along 170°W; see Plates 6a and 7a. DIC generally increases with depth, reflecting both the higher solubility of CO_2 in cold waters and the biological formation of sinking organic particles, which are respiration and regenerated to inorganic nutrients and carbon at depth. Large-scale structures partly reflect physical tracers, like salinity.

into the ocean interior. Cool waters originating in the high latitudes bring high concentrations of DIC, while warmer waters originating in the mid latitudes bring low concentrations of DIC.

- The accumulated effect of the biological cycling and regeneration of carbon gives rise to the strong Atlantic-Pacific contrast in deep DIC, such that younger waters in the deep Atlantic have low DIC and older waters in the deep Pacific have high DIC.

2.4.2 Air-sea exchange of carbon dioxide

The atmosphere and ocean reservoirs of carbon are connected through air-sea exchange of carbon dioxide. Ocean uptake of CO_2 occurs over much

of the mid and high latitudes and, conversely, ocean outgassing of CO_2 occurs in the tropics (Fig. 2.23, light and dark shades, respectively). The transfer of carbon between the atmosphere, the surface mixed layer and ocean interior involves the effects of physical transport, solubility, and biological cycling, as depicted respectively in Fig. 2.24a,b:

- At high latitudes, cooling increases the solubility and there is high biological productivity, both processes drawing down CO_2 from the atmosphere into the ocean.
- In the tropics, warming decreases the solubility and induces outgassing of CO_2 . In addition, an upward transfer of deep waters to the surface can either enhance biological productivity from

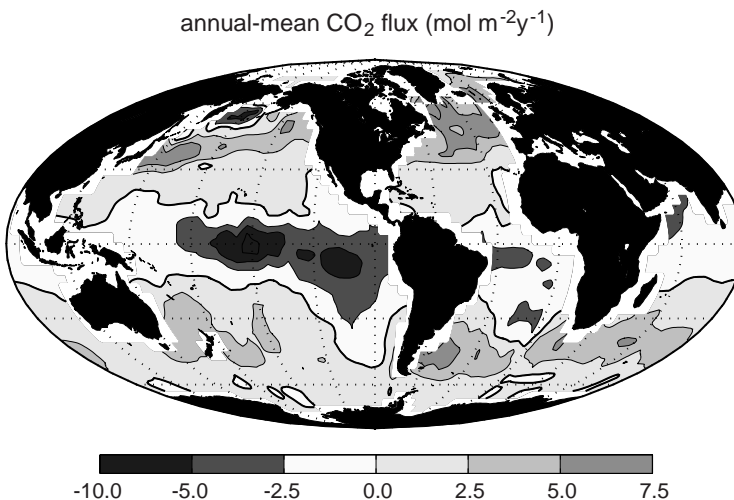
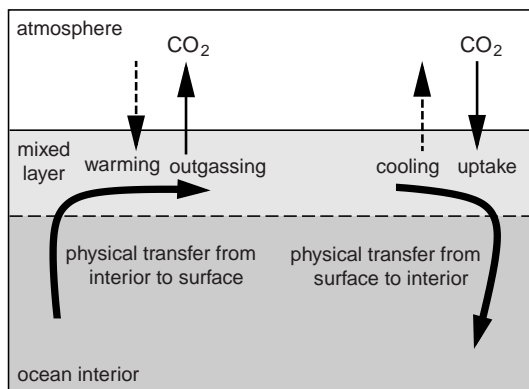


Figure 2.23 Climatological, annual-mean map of air-sea flux of CO₂ into the ocean (mol m⁻² y⁻¹), data from Takahashi *et al.* (2002). There is an ocean uptake of CO₂ (light shading) in the high latitudes and an ocean outgassing in the tropics (dark shading); however, there is considerable uncertainty in the direction of the flux over the Southern Ocean. This estimate is based on a compilation of about a million measurements of surface-water pCO₂ obtained since the International Geophysical Year of 1956–59. The climatology represents mean non-El Niño conditions with a spatial resolution of 4° × 5°, normalised to reference year 1995.

(a) physical transport and solubility



(b) physical transport and biology

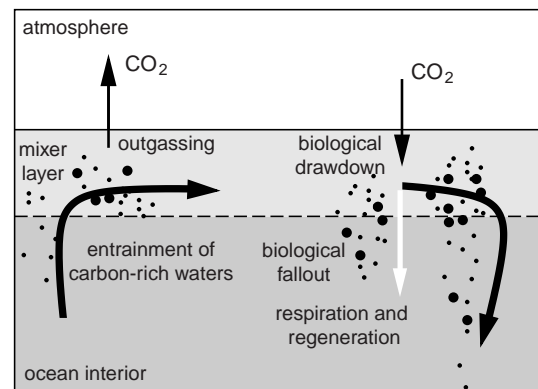


Figure 2.24 A schematic figure depicting how air-sea exchange of CO₂ is affected by an interplay of physical and biological processes involving the cycling and transport of DIC. In (a), warming of surface waters leads to an outgassing of CO₂, while a cooling of surface waters leads to an ocean uptake of CO₂. The physical transport (thick black arrows) of surface waters into the interior is then associated with an uptake of CO₂, while the return of deep waters to the surface leads to an outgassing of CO₂. In (b), the biological formation of organic matter leads to an ocean drawdown of atmospheric CO₂, which is then transferred to the ocean interior through the fallout of organic matter (white arrow). The respiration of the organic matter then regenerates the inorganic nutrients and carbon, increasing their concentrations in the deep waters. The return of deep water to the surface leads to an outgassing of CO₂.

the supply of nutrient-rich waters leading to an ocean uptake of CO₂ or, conversely, the supply of carbon-rich waters can lead to an outgassing of CO₂.

The air-sea fluxes of carbon dioxide integrated over the separate outgassing and uptake regions of the globe approximately balance each other, typically reaching 90 Pg Cy⁻¹ in each direction

(based upon Fig. 2.23). In comparison, the anthropogenic increase in atmospheric CO₂ leads to a net air-sea flux directed into the ocean of 2 Pg Cy⁻¹, much smaller than the regional variations in the annual flux. This anthropogenic increase may, though, tip the balance over parts of the Southern Ocean, possibly changing a pre-industrial net outgassing to a present-day or future uptake.

2.5 | Summary

This chapter provides a preliminary view of the open ocean. The ocean circulation is driven by mechanical forcing from the surface winds and tides, as well as by pressure gradients from density differences formed through surface exchanges of heat, fresh water and salt. The ocean circulation can be viewed in terms of a horizontal circulation confined between the continents, made up of recirculating gyres and western boundary currents, together with intense, near-zonal currents running along the equator and circumnavigating the Southern Ocean. In addition, there is a vertical overturning with dense water sinking at high latitudes, especially in the North Atlantic and Southern Ocean, spreading over the globe at depth and replaced by lighter surface waters from lower latitudes.

The imprint of the physical circulation is seen in how a range of physical and biogeochemical properties resemble each other: plumes of fresh and nutrient-rich water spread northward from the Southern Ocean and the thickness of the relatively warm and nutrient-depleted, thermocline waters undulate together; as illustrated in the meridional sections in colour plates 2 to 6.

Phytoplankton absorb visible wavelengths of light and use the energy, along with nutrients containing essential elements, to create new organic molecules or reproduce by producing a copy of the cell. The organic matter provides the ultimate source of energy and nutrients for all other living creatures in the ocean. Phytoplankton growth leads to the consumption of inorganic nutrients in surface waters; some of the organic matter gravitationally sinks through the water column and is respired to regenerate inorganic nutrients at depth.

Carbon is stored within the ocean predominantly as dissolved inorganic carbon, consisting mainly of bicarbonate and carbonate ions with less than one per cent held as dissolved carbon dioxide. The ocean inventory of carbon is typically fifty times larger than the atmospheric inventory of carbon dioxide.

Carbon dioxide is exchanged between the atmosphere and ocean: the ocean takes up carbon

dioxide when surface waters cool and sink, and when phytoplankton grow, forming new organic matter. Conversely, carbon dioxide is returned to the atmosphere when surface waters warm and when carbon and nutrient-rich deep waters are returned to the surface. Carbon is transferred into the ocean interior by the physical transfer of cold, carbon-rich surface waters and by the biological transfer of organic matter, falling through the water column and being respired at depth.

Following this descriptive overview, these themes are taken forward in a set of fundamental chapters addressing the controlling processes in more detail: how tracers are transported by the circulation; how the ocean circulates and is forced by the atmosphere; how phytoplankton cells grow and their implications for biogeochemistry; and how carbon dioxide is cycled in the ocean and exchanged with the atmosphere.

2.6 | Questions

Q2.1. Heat storage of the atmosphere and ocean.

Estimate the thickness of the ocean that holds as much heat as the overlying atmosphere, where the amount of heat Q required to raise the temperature of the atmosphere or ocean by ΔT is given by

$$Q = \rho C_p A D \Delta T, \quad (2.2)$$

where ρ is density (kg m^{-3}), C_p is heat capacity ($\text{J kg}^{-1} \text{K}^{-1}$), A is horizontal area (m^2), and D is the vertical scale (m).

Assume $\rho \sim 1 \text{ kg m}^{-3}$ for the atmosphere and 10^3 kg m^{-3} for the ocean, $C_p \sim 1000 \text{ J kg}^{-1} \text{ K}^{-1}$ for the atmosphere and $4000 \text{ J kg}^{-1} \text{ K}$ for the ocean, a vertical scale, D , of 10 km for the atmosphere (where the bulk of the atmosphere resides), $\Delta T = 1 \text{ K}$ and a horizontal area $A = 1 \text{ m}^2$.

Q2.2. Radiative heating and equilibrium temperature.

(a) For a planet with no atmosphere, derive how the equilibrium temperature, T , in kelvin, depends on the incident solar radiation, S_c , and the albedo, α , the fraction of reflected sunlight,

$$T = \left(\frac{(1 - \alpha)S_c}{4\sigma_{sb}} \right)^{1/4}, \quad (2.3)$$

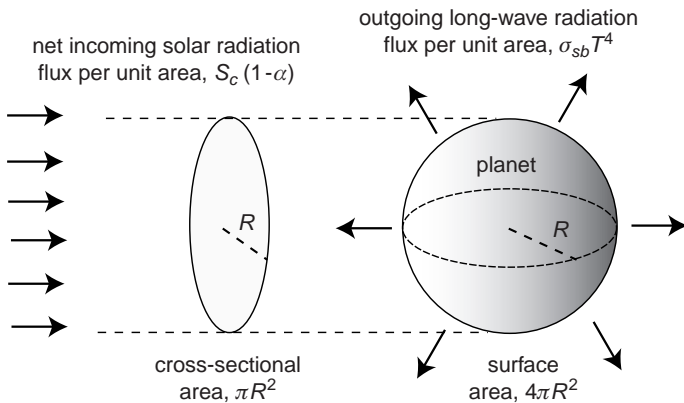


Figure 2.25 A schematic figure of the net incident solar radiation per unit horizontal area, the incident minus the reflected, $S_c(1 - \alpha)$, which is absorbed over the cross-sectional area of a planet with radius R . The outgoing long-wave radiation, $\sigma_{sb} T^4$, is radiated over the entire surface area of the planet.

where σ_{sb} is the Stefan-Boltzmann constant. Assume a radiative balance, as depicted in Fig. 2.25, where (i) the net solar radiation is absorbed over a circular disc with a cross-sectional area of the planet, and (ii) the outgoing long-wave radiation per unit horizontal area in W m^{-2} is given by the Stefan-Boltzmann law, $\sigma_{sb} T^4$, integrated over the surface area of the planet.

(b) Estimate this equilibrium temperature in kelvin for Venus, Earth and Mars assuming that S_c is 2600, 1400 and 590 W m^{-2} , and their albedos, α , are 0.8, 0.3 and 0.15, respectively, and $\sigma_{sb} = 5.7 \times 10^{-8} \text{ W m}^{-2} \text{ K}^{-4}$. How do these temperatures compare with their respective observed surface values of typically 750 K, 280 K and 220 K? Why might there be a mismatch in some cases?

(c) If the planet is now assumed to have an atmosphere that is transparent to solar radiation, but absorbs and re-radiates long-wave radiation, then a local radiative balance suggests that the absorbed solar and long-wave radiation at the ground balances the outgoing long-wave radiation. The surface temperature is then given by

$$T = \left(\frac{(1 - \alpha)S_c}{2\sigma_{sb}} \right)^{1/4}. \quad (2.4)$$

Use this relationship to estimate the implied temperature contrast between the tropics and the high latitudes. For simplicity, in the tropics, assume that the incident radiation is given by S_c , while at the high latitudes, the incident radiation is given by $S_c/3$. How does this estimate compare with the actual meridional temperature contrast of typically 30 K for the Earth?

Q2.3. Anthropogenic heating of the ocean by the increase in atmospheric CO₂.

Increasing atmospheric CO₂ leads to increasing radiative heating, $\Delta\mathcal{H}$ (in W m^{-2}), which varies logarithmically with the increase in mixing ratio for atmospheric CO₂ (as the effect of increasing CO₂ on the absorption and emission of long-wave radiation gradually saturates),

$$\Delta\mathcal{H} = \alpha_r \ln(X_{\text{CO}_2}(t)/X_{\text{CO}_2}(t_0)), \quad (2.5)$$

where $\alpha_r = 5.4 \text{ W m}^{-2}$ depends on the chemical composition of the atmosphere and $X_{\text{CO}_2}(t_0)$ and $X_{\text{CO}_2}(t)$ are the mixing ratios for CO₂ at times t_0 to t .

(a) Estimate the increase in implied radiative heating, $\Delta\mathcal{H}$, over the 50 years between 1958 and 2008 assuming an increase in X_{CO_2} from 315 ppmv to 386 ppmv; compare your answer with Fig. 1.11b.

(b) Given these estimates of radiative heating, then estimate how much the upper ocean might warm over 50 years. Assume that the temperature rise of the ocean is given from a simple heat balance by

$$\Delta T \sim \frac{\overline{\Delta\mathcal{H}} T}{\rho C_p h},$$

where $\overline{\Delta\mathcal{H}}$ is the average extra heating over the time period, T , of 50 years (convert to seconds) and h is the thickness of the upper ocean, taken as 500 m; ρ and C_p are as in Q2.1. Compare this estimate with the reported change for the global warming of the Earth over the last 50 years (IPCC, 2007).

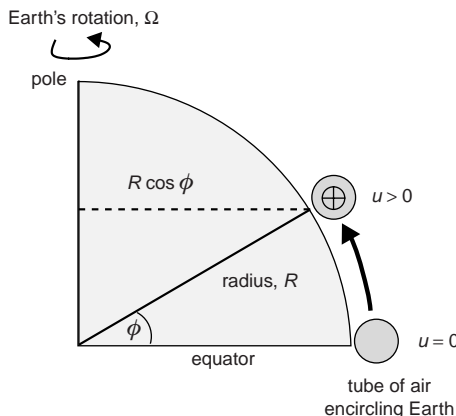


Figure 2.26 A schematic figure depicting a tube of air (dark shading) encircling the Earth along a latitude circle with the Earth rotating at an angular velocity Ω . The tube is at a distance $R \cos \phi$ from the rotational axis where R is the radius and ϕ is the latitude. As the tube moves from the equator towards the pole, the tube increases its zonal velocity, u , so as to conserve angular momentum. Adapted from Green (1981).

Q2.4. Atmospheric zonal jets and angular momentum.

Consider a tube of air circling the Earth at its equator that is uniformly displaced poleward, as depicted in Fig. 2.26. The angular momentum of the tube is given by

$$L_{\text{ang}} = (u + \Omega R \cos \phi) R \cos \phi, \quad (2.6)$$

where u is the zonal velocity, Ω is the angular velocity, R is the radius of the Earth, and ϕ is the latitude. $R \cos \phi$ represents the effective radius of the tube to its rotational axis, $\Omega R \cos \phi$ represents the velocity of the spinning Earth relative to a fixed point in space and u represents the velocity of the air relative to the Earth.

(a) Derive an expression giving the zonal velocity, u , as a function of latitude, ϕ , by assuming that angular momentum L_{ang} is conserved and the initial zonal velocity at the equator is zero.

(b) Calculate the implied zonal velocity for every 10° from the equator to 30°N for the Earth, assuming $\Omega = 2\pi/\text{day}$ and $R = 6340\text{ km}$. What are the implications of your result?

2.7 Recommended reading

A descriptive view of the ocean circulation is provided in L. D. Talley, G. L. Pickard, W. J. Emery and J. H. Swift, *Descriptive Physical Oceanography: An Introduction*. 6th edition, Academic Press (due for publication 2011).

A comprehensive view of the ocean, including observations, theory and modelling, is provided in G. Siedler, J. Church and J. Gould (2001). *Ocean Circulation and Climate: Observing and Modelling the Global Ocean*. San Diego, CA: Academic Press, 693pp.

An introductory view of the physical processes operating in the atmosphere and ocean, drawing on laboratory experiments and relevant theory, is provided by J. Marshall and R. A. Plumb (2008). *Atmosphere, Ocean and Climate Dynamics: An Introductory Text*. Burlington, MA: Academic Press Elsevier, 319pp.

An introductory view of marine chemical processes is provided by S. Emerson and J. Hedges (2008). *Chemical Oceanography and the Marine Carbon Cycle*. Cambridge: Cambridge University Press, 468pp.

An advanced view of the biogeochemistry and carbon cycle is provided by J. L. Sarmiento and N. Gruber (2006). *Ocean Biogeochemical Dynamics*. Princeton, NJ: Princeton University Press, 526pp.

Part II

Fundamentals

Chapter 3

Transport fundamentals

The atmosphere and ocean are never at rest and continually move, whether it is the random walk of individual molecules or the grand meanders of the atmospheric Jet Stream. This movement transports fluid properties and tracers on all scales over the globe. You can see this transport in action whenever you watch a cloud passing aloft or water being swept along in a stream. Sometimes this transfer occurs in a simple manner, like the languid drift of a leaf down a calm river; other times it is more complicated, like waves sweeping a floating stick back and forth out at sea. The transfer becomes even more chaotic in a turbulent flow, as in how a rising smoke plume fragments into a series of turbulent eddies, and fluid follows apparently random paths.

The spreading of tracers can be understood in terms of how tracers are carried by the flow, diffused and eventually diluted. These processes apply equally to a dye spreading in a glass of spinning water, where narrow filaments of dye are initially drawn out before eventually being diluted, and tracers spreading over the ocean and atmosphere. For example, there are spiralling flows over the surface ocean suggesting active stirring, as illustrated in Fig. 3.1. This stirring then leads to tracers having patchy distributions, sometimes dragged out into filaments and sometimes forming coherent blobs or vortices.

In this chapter, we explain how tracers spread, describing how they are advected and diffused, and how to represent these processes more formally within a tracer budget. The effects of time-varying circulations in providing tracer fluxes is then addressed, including examples ranging from

the effect of waves breaking on a beach and ozone being transported in the upper atmosphere.

3.1 | How do tracers spread?

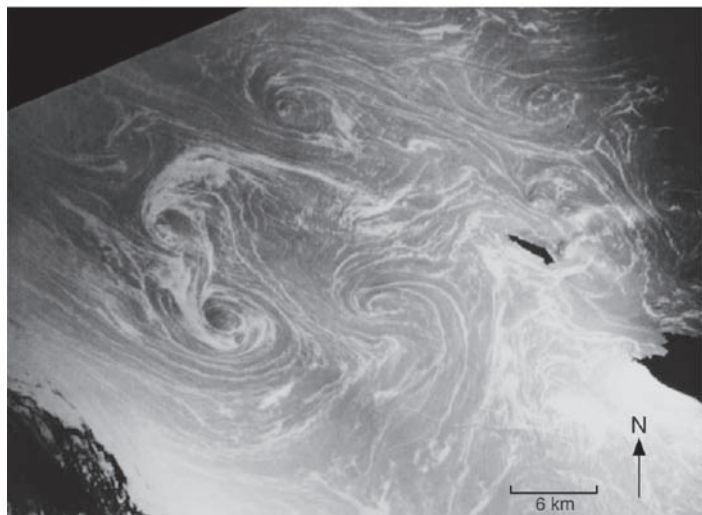
Tracers are transported through a range of processes: advection is the transfer of a tracer through the movement of fluid particles by the background flow; stirring involves how patches of tracer are drawn into narrow filaments by contrasts in advection; diffusion is the systematic transfer of tracer from high to low concentration, achieved by fine-scale correlations in the velocity and tracer concentration, provided on the smallest scale by the random motion of molecules; and mixing involves the irreversible transfer of fluid across a tracer contrast, which is ultimately achieved by diffusion on a molecular scale. Each of these processes are now described in more detail.

3.1.1 Advection

Advection is the translation of the fluid and any accompanying particles or tracers by the background flow. A simple example of advection is the motion of a small, untethered helium balloon blown along in the wind, where the balloon path is determined by the strength, direction and variability of the wind.

If a collection of balloons is released, then the centre of mass for all the balloons is displaced by their average advection (Fig. 3.2a). Each balloon is advected on a different individual pathway. The balloons gradually increase in separation from each other, leading to a spreading (or

(a)



(b)

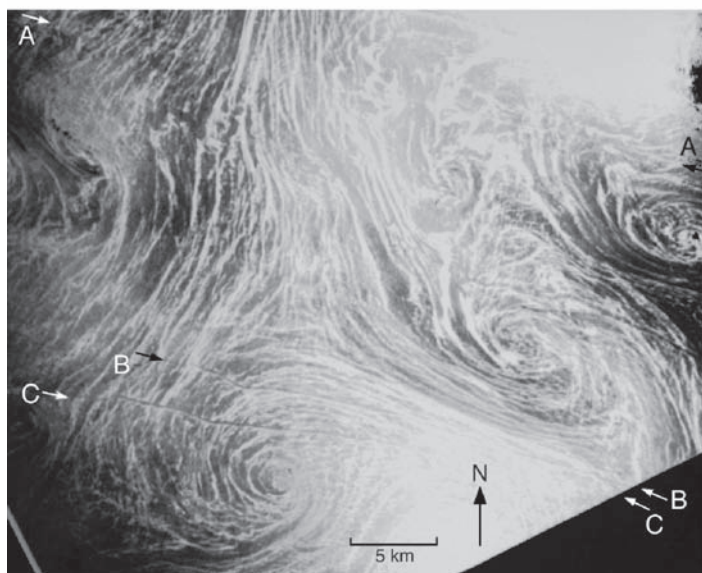


Figure 3.1 Spiral eddies seen in the sun glitter from the surface in the Mediterranean Sea detected from the Space Shuttle on 7 October 1984: (a) south of Crete, and (b) northwest of Crete (labels A, B and C refer to ship tracks). The spirals are on the scale of 10 km and suggest active stirring. Reproduced from Munk *et al.* (2000), courtesy of The Royal Society, London.

dispersion) away from the centre of mass of the balloons (Fig. 3.2b). If there are sufficient balloons, they might be considered in terms of a continuous tracer representing the concentration of balloons. For the same spreading pattern, now represented by a tracer, the centre of mass of the tracer is displaced by the average advection and the tracer is drawn out into narrow filaments away from the centre of mass by horizontal variations in velocity (Fig. 3.2c).

An ocean example of this advection and dispersion process is provided by floats spreading along the Gulf Stream (Fig. 3.3). In this experiment, floats were released at Cape Hatteras off the coast of North America and were tracked as the floats followed density surfaces within the upper ocean (Bower and Rossby, 1989). While individual float trajectories were chaotic and no two trajectories were alike, a general picture still emerged: floats were initially closely clustered near their release

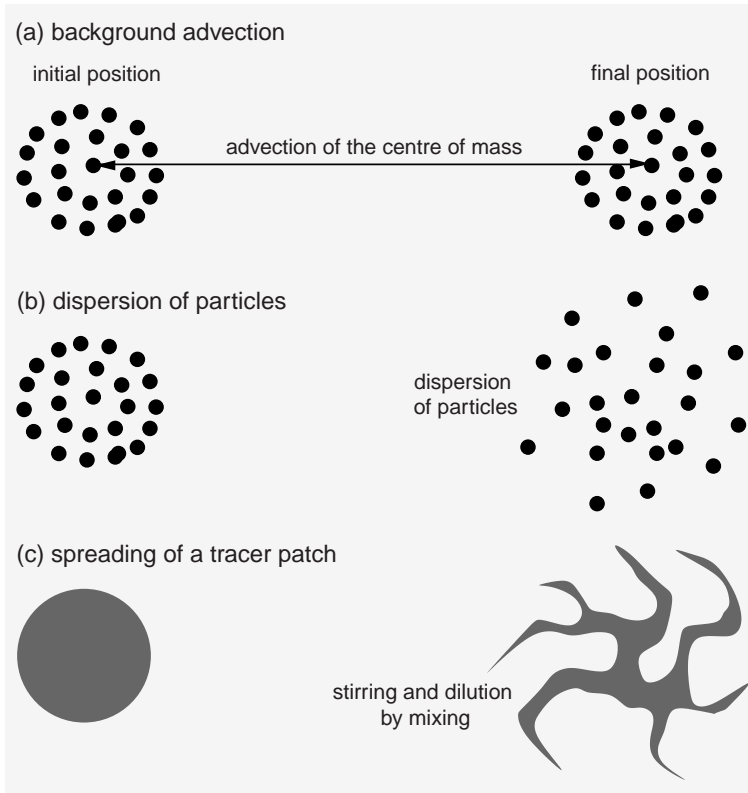


Figure 3.2 Schematic views of how particles and tracers spread: (a) the particles move to a new position through an advective displacement of the centre of mass; (b) the particles spread away or disperse from the centre of mass; (c) a tracer view of the same problem where the centre of mass of the tracer is displaced by advection and the tracer becomes stretched into narrow filaments through stirring. Eventually its concentration becoming diluted through finer-scale mixing.

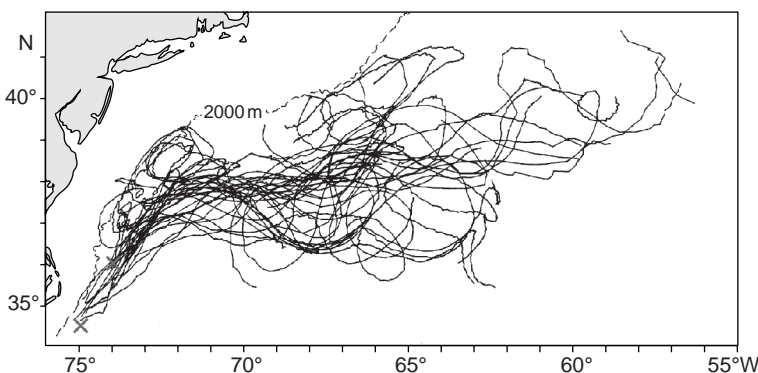


Figure 3.3 Float trajectories in the Gulf Stream: a composite of 37 isopycnal floats launched at different sites off Cape Halteras (34.5°N , 75°W to 36°N , 74°W ; grey crosses) at thermocline depths, between 400 m and 700 m, and tracked for up to 45 days. Redrawn from Bower and Rossby (1989).

point, swept downstream by the Gulf Stream and dispersed due to meandering circulations.

Flux of properties

It is often useful to consider the flux of a property as given by the amount of a property passing through a fixed area per unit time. In the previous Gulf Stream example, one can define a flux of floats given by the number of floats passing through a particular cross-sectional area in a

unit time. In an analogous manner, fluid parcels are expected to follow similar trajectories as the floats, carry their own properties, such as temperature, nutrients and carbon, and so provide fluxes of these properties.

3.1.2 Molecular diffusion

Molecular diffusion refers to the systematic transfer of a tracer from high to low concentration, which is achieved by the random motion of

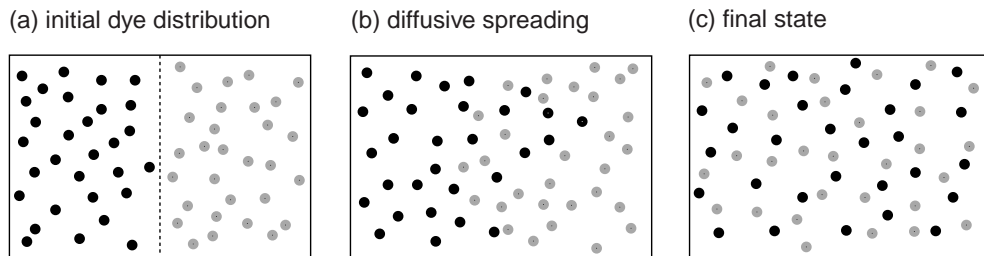


Figure 3.4 A thought experiment illustrating diffusion: (a) a fluid is separated by a partition with the same mass on either side of the partition, but with particles dyed black on one side and dyed grey on the other; (b) when the partition is removed, the particles move in a random manner and lead to black particles moving on average from left to right and the reverse for grey particles; (c) the near final state has approximately a uniform concentration of black and grey particles throughout the entire fluid.

molecules. For example, when macroscopic particles such as pollen are suspended in water, each pollen grain moves in a ‘random walk’ manner induced through the accumulated collisions with the smaller water molecules; this process is referred to as Brownian motion following its observation by Robert Brown in 1827. This random walk spreading of particles leads to any tracer contained in a fluid being transferred from high to low concentration. This concept of diffusion based upon a view of molecular transfers can also be applied to larger-scale phenomena.

To understand the distinction between advection and molecular diffusion, consider a simple experiment where a fluid is at rest and separated into two regions with particles marked by different dyes on either side of a partition (Fig. 3.4a). Assume that there is the same mass on either side of the partition. If the partition is gently removed with the minimum of disturbance, there is no mass flux and no advection by any large-scale flow. As one approaches smaller and smaller scales, there are always fine-scale variations in the flow, which are correlated with fluctuations in dye concentration. This correlation in the variations in velocity and dye concentration leads to a flux of dye, directed on average from high to low concentration (Fig. 3.4b). Eventually, this diffusive transfer leads to the dye acquiring a nearly uniform concentration (Fig. 3.4c).

When is molecular diffusion important?

Molecular diffusion is only important on very small length scales (typically less than a millime-

tre) and usually its effects are masked by larger-scale eddy transfers of tracers. Molecular diffusion does play a significant role in the following small-scale examples:

1. Cloud drops are formed through the diffusion of water vapour onto condensation nuclei. While this diffusion controls the initial growth of the cloud drop, the subsequent growth and eventual formation of rain drops is controlled by larger drops falling through the cloud, collecting up and combining with the smaller drops in the cloud, a process referred to as coalescence.
2. The molecular diffusivity of heat is greater than that of salt, which can lead to instability of the water column. For example, if warm, salty water overlies cold, fresh water, then the temperature contrast is removed faster than the salt contrast, leading to dense water overlying light water, which then leads to convective overturning. This process is referred to as double diffusion and, for example, is important beneath the salty Mediterranean water spreading into the North Atlantic (see later Fig. 3.10).
3. Phytoplankton cells need inorganic nutrients to grow whenever there is sufficient light for photosynthesis. These inorganic nutrients are diffused towards the cell wall from the surrounding water. When there is available light, the growth rate of the phytoplankton is then controlled by the rate of this diffusion; see later Sections 5.3.2 and 5.3.3.

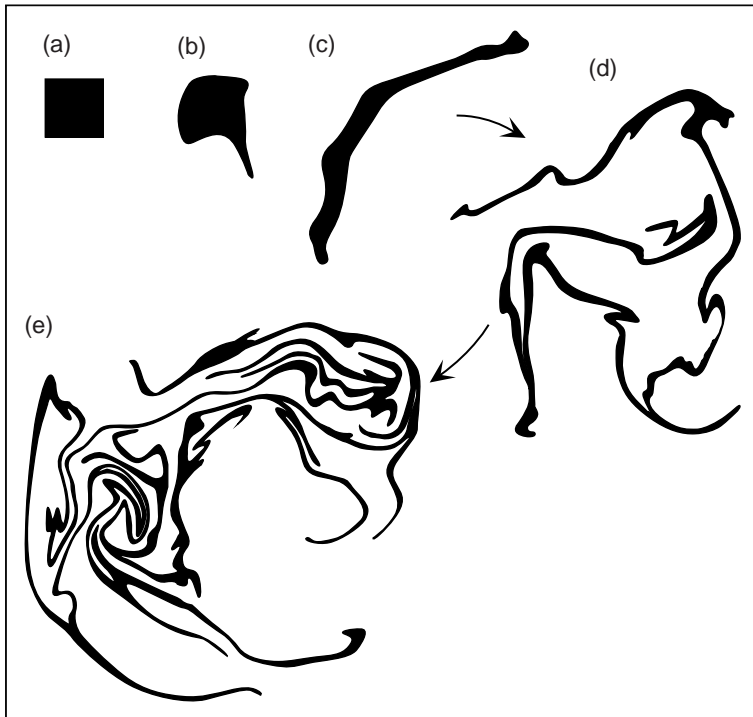


Figure 3.5 A series of snapshots illustrating the stirring process by showing the observed deformation of a small coloured square element of a fluid surface in a laboratory experiment. The experiment involved a rectangular vessel filled with water and a surface film of butanol, which was divided into square elements using a metal grid. One of the square elements was coloured with methyl-red and the water was set into horizontal motion with a slow basic rotation. The snapshots reveal how the patch of tracer was drawn out into filaments, which progressively increased in length and became folded. In this example, stirring dominates and the diffusive mixing is not yet evident. Redrawn from Welander (1955).

3.1.3 Stirring and mixing

Molecular diffusion is usually too weak to be important over the large-scale ocean. Instead, variations in advection can lead to tracers being stirred, which can then lead to molecular diffusion becoming significant. The best way to understand these processes is to try a simple dye experiment yourself: release a few drops of ink in a glass of water that is either motionless or has been stirred, then watch how the ink spreads from its source. In the unstirred case, blobs of ink initially persist before eventually becoming diluted. In the stirred case, the ink is drawn out into narrow filaments and rapidly spreads over the whole glass, again eventually becoming diluted.

How a dye spreads was firstly elegantly explained by Eckart (1948), in terms of how cream is stirred into a cup of coffee. There are three distinct stages in this process:

- Initially, there are distinct, separate regions of coffee and cream; there are sharp gradients at the interfaces of these tracers, but elsewhere

the gradient is practically zero. If motion of the liquid is avoided, then this state persists for a considerable time (as only diffusion is acting).

- If the cup is stirred, the masses of the cream and coffee are distorted and filaments are drawn out; there is a rapid increase in the extent of the interfacial regions where there are high gradients in tracer. The average value of the tracer gradient is increased in the cup.
- Finally, the coffee and cream become homogenised in the cup; the tracer gradients disappear, apparently quite suddenly and spontaneously by mixing.

In support of this conceptual view, Welander (1955) illustrated how tracers were stirred in a laboratory experiment (Fig. 3.5). Initially, there was a weak diffusive spreading of the tracer, then filaments of tracer were drawn out by gradients in velocity. These tracer filaments became folded and undulated, and eventually irreversible mixing occurs across them. Hence, stirring increases the length of tracer interfaces and leads to tracer

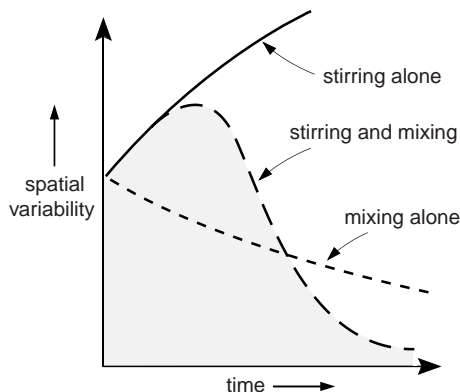


Figure 3.6 The evolution of the spatial variability in tracer (as measured by mean squared, tracer gradient) when stirring (full line) or mixing (dotted line) occurs alone and when stirring and mixing are simultaneously present (dashed line). Stirring always leads to an increase in the mean squared, tracer gradient through the folding and lengthening of tracer filaments, while mixing always reduces the mean squared, tracer gradient by removing tracer contrasts. The tracer gradient is removed more rapidly if the fluid is both stirred and mixed, rather than if mixing alone takes place. Redrawn from Salmon (1998).

contrasts being more rapidly eroded and removed by mixing than if the fluid is quiescent (Fig. 3.6).

Oceanic and atmospheric examples of stirring
Consider the movement of tracers on the scale of ocean and atmospheric flows. A summer bloom of phytoplankton reveals a patchy distribution, concentrated in isolated blobs or drawn out into

narrow filaments (Fig. 3.7). These spatial variations turn out to be partly linked to the circulation: isolated patches of phytoplankton are contained within recirculating eddy flows, while long, thin filaments of phytoplankton are drawn out between these eddy flows; also see Q3.1b addressing the stirring of an iron-induced, phytoplankton bloom.

This process of stirring and mixing also occurs on the planetary scale in the upper atmosphere, as vividly seen for the polar vortex (Fig. 3.8). During the prolonged winter night, a strong vortex is formed with a rapid circulation, isolating an inner core of polar air from the mid latitudes. Ozone becomes depleted within the polar vortex through chemical reactions involving CFCs. In the spring, this polar vortex weakens and its ozone-depleted air is exchanged with ozone-rich air in the mid latitudes. This exchange is revealed in two snapshots in Fig 3.8 showing ozone-depleted air confined in the central vortex (dark) together with a long filament being drawn out (Fig 3.8a), folded and mixed with the surrounding ozone-rich air (Fig 3.8b). This elongation and undulation of tracer filaments leads to a smearing out of tracer contrasts outside the polar vortex; consequently, there can be intermittent, spring intrusions of ozone-depleted polar air reaching the mid latitudes, which bring with them increased risk of harmful ultraviolet radiation penetrating to the ground.

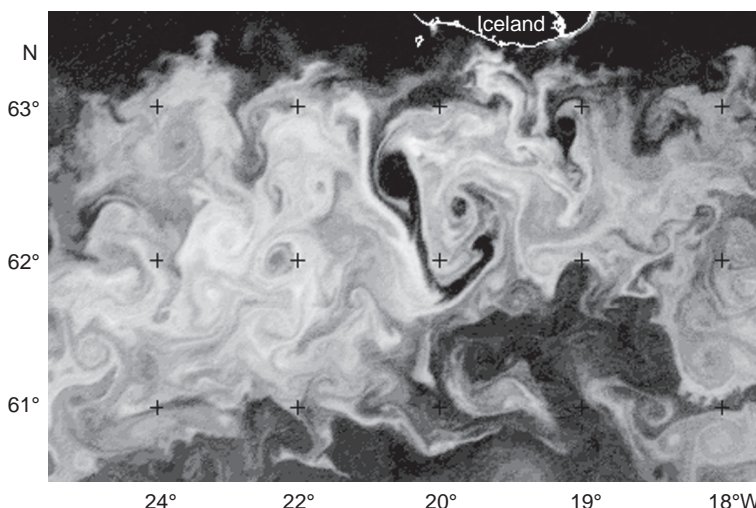


Figure 3.7 A phytoplankton bloom made up of isolated patches and drawn out filaments linked to mesoscale eddy circulations around 20°W , 62°N (higher reflectance and chlorophyll concentration is lighter), detected south of Iceland on 17 June 1991 from the NOAA Advanced Very High Resolution Radiometer (AVHRR); see detailed discussion by Martin (2003). This patchy tracer distribution is a consequence of advection by the background flow and spatial variations in phytoplankton growth and consumption. Image provided by Steve Groom, NEODAAS, Plymouth.

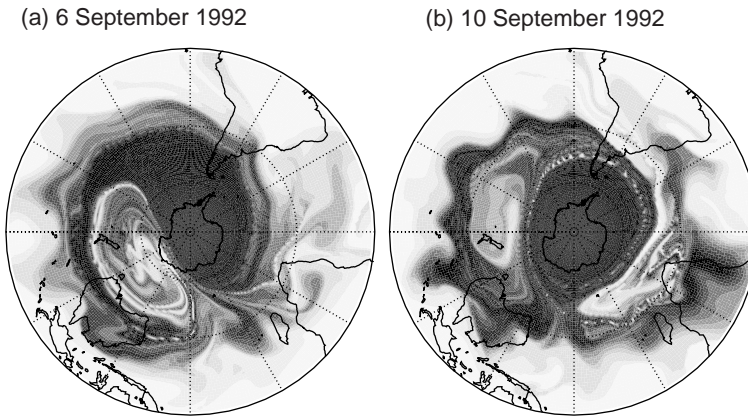


Figure 3.8 Snapshots of the ozone distribution for 6 and 10 September 1992 where dark shading denotes air with depleted ozone and high stratification, and light shading denotes air with higher concentrations of ozone and reduced stratification, diagnosed from observations and model-trajectory-based calculation (Waugh, 1993). A filament of ozone-depleted air (dark) is being stretched out from the polar vortex, reflecting stirring and mixing with ozone-rich air from mid latitudes. Images provided by Darryn Waugh.

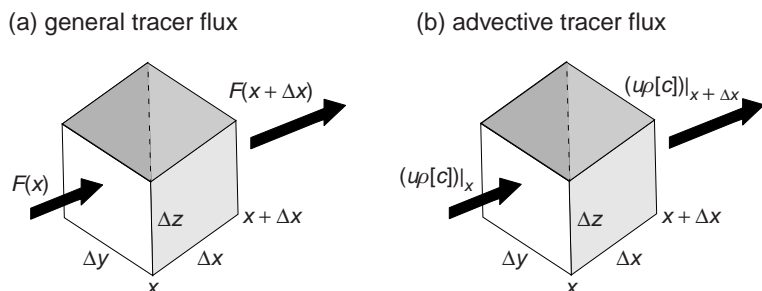


Figure 3.9 Divergence of tracer fluxes into and out of a small section of pipe for (a) generic representation of a tracer flux, F , and (b) an advective tracer flux, $u\rho[c]$, where u is velocity, ρ is the density and $[c]$ is the tracer concentration defined by the amount of a substance per unit mass. If the flux exiting the volume is greater than that entering, there is a net reduction of the tracer in the volume. Conversely, if the flux entering the volume is greater than that exiting, then there is a net increase of tracer in the volume. In (a), the tracer fluxes through the faces x and $x + \Delta x$ are written generically as $F(x)$ and $F(x + \Delta x)$, while in (b), the advective tracer fluxes are written as $(u\rho[c])|_x$ and $(u\rho[c])|_{x+\Delta x}$, respectively.

This description of stirring has focussed mainly on the effect of horizontal gradients in the velocity field, which is appropriate for much of the atmosphere and ocean. This view becomes more complicated in surface and bottom boundary layers where there is three-dimensional turbulence; fluid trajectories become more convoluted and tracers are stirred by both the vertical and horizontal gradients in velocity.

these processes are represented mathematically in a tracer conservation equation.

3.2.1 Generic tracer budget

Consider how a tracer evolves in a semi-enclosed pipe (Fig. 3.9a) containing a fluid with a volume, V , in m^3 and mass, ρV , in kg, where ρ is the density in kg m^{-3} . The amount of tracer in the pipe is then $[c]\rho V$ in moles where $[c]$ is the tracer concentration per unit mass in moles kg^{-1} .

The only tracer fluxes are through the ends of the pipe, given by FA where F is the flux of the tracer per unit horizontal area and A is the cross-sectional area. F is given by the product of tracer concentration, $[c]$, density and velocity (m s^{-1}) and so has units of $\text{moles kg}^{-1} \times \text{kg m}^{-3} \times \text{m s}^{-1} = \text{moles m}^{-2} \text{s}^{-1}$.

3.2 Tracer conservation and transport

To progress further in understanding how tracers are transported, it is necessary to consider the effects of advection and diffusion, and how

Table 3.1 Units for different properties and their fluxes.

Property and units	Concentration per unit mass, $[c]$	Property flux $u\rho[c]$
Tracer, mol	mol kg^{-1}	$\text{mol s}^{-1} \text{m}^{-2}$
Mass, kg	l	$\text{kg s}^{-1} \text{m}^{-2}$
Volume, m ³	$\text{m}^3 \text{kg}^{-1}$	$\text{m}^3 \text{s}^{-1} \text{m}^{-2}$
Heat, J	J kg^{-1}	$\text{J s}^{-1} \text{m}^{-2} = \text{W m}^{-2}$

If the tracer flux entering the pipe exceeds the flux out of the pipe, then there is a local increase in the amount of tracer within the pipe, which is expressed mathematically by

$$\frac{\partial}{\partial t}(\rho[c]V) = -(F(x + \Delta x) - F(x))A,$$

which, assuming that volume V is conserved, can be written more conveniently as

$$\frac{\partial}{\partial t}(\rho[c]) = -(F(x + \Delta x) - F(x))\frac{A}{V} = -\frac{\partial F}{\partial x}, \quad (3.1)$$

where the flux divergence is represented by the gradient $\partial F/\partial x = (F(x + \Delta x) - F(x))/\Delta x$, the area $A = \Delta y \Delta z$, and the volume, $V = \Delta x \Delta y \Delta z$.

Now consider, more precisely how the tracer fluxes, F , are represented.

3.2.2 Advection

The bulk movement of the fluid provides an advective flux of any tracer down the pipe given by the velocity, u , multiplied by the density and the property concentration, $\rho[c]$,

$$F = u\rho[c], \quad (3.2)$$

which applies for any property (Table 3.1).

Combining with (3.1) leads to the tracer equation,

$$\frac{\partial}{\partial t}(\rho[c]) = -\frac{\partial}{\partial x}(u\rho[c]), \quad (3.3a)$$

with the tracer concentration increasing in time when there is a convergence in the tracer flux, $u\rho[c]$. This tracer budget can equivalently be writ-

ten in terms of a tracer concentration defined per volume, $\{c\}$ in mol m^{-3} , where $\{c\} = \rho[c]$, such that

$$\frac{\partial}{\partial t}\{c\} = -\frac{\partial}{\partial x}(u\{c\}), \quad (3.3b)$$

and this version of the tracer equation is used henceforth.

Mass conservation

If the tracer is taken to represent the concentration of mass per unit volume, then (3.3b) becomes equivalent to mass conservation,

$$\frac{\partial \rho}{\partial t} = -\frac{\partial}{\partial x}(\rho u). \quad (3.4)$$

If there is a convergence in the mass fluxes, ρu , then the concentration of mass within the volume increases.

3.2.3 Molecular diffusion

Molecular diffusion leads to a systematic transfer of molecules from regions of high to low concentration, which occurs even if there is no movement of the bulk fluid (Fig. 3.4). The diffusive flux is usually parameterised in terms of a transfer down the concentration gradient, such that

$$F = -\kappa \frac{\partial \{c\}}{\partial x}, \quad (3.5)$$

where κ is a molecular diffusivity of the tracer with units of length \times velocity ($\text{m}^2 \text{s}^{-1}$); this relationship is called Fick's law and was derived by Adolf Fick in 1855.

The diffusive flux can be viewed in terms of fine-scale fluctuations in velocity correlating with the tracer concentration.

It is convenient to separate the definitions of advection and diffusion, such that the centre of mass is only displaced by advection and is not affected by diffusion. In this case, a velocity can be defined on the macroscopic scale to take in the effect of finer-scale correlations in velocity and mass, such that $u = \sum m_i u_i / \sum m_i$, which is a mass-weighted average of all the velocities of the molecules within a control volume, where m_i is the mass of molecule i and u_i is its velocity (Salmon, 1998).

In most large-scale situations, advection is much more important than molecular diffusion; see the scaling in Box 3.1.

Box 3.1 | Relative importance of advection and molecular diffusion

The general tracer equation (3.1) depends on contributions from both advective (3.2) and diffusive (3.5) fluxes,

$$\frac{\partial c}{\partial t} = -\frac{\partial}{\partial x}(uc) + \frac{\partial}{\partial x}\left(\kappa\frac{\partial c}{\partial x}\right), \quad (3.6)$$

where c is henceforth taken as the tracer concentration per unit volume, $\{c\}$. The relative importance of the advective and diffusive transfer can be estimated by comparing the size of the first and second terms on the right-hand side of (3.6). An order of magnitude estimate of the advective transfer is given by

$$-\frac{\partial}{\partial x}(uc) \sim \frac{UC}{L}, \quad (3.7)$$

and the diffusive transfer by

$$\frac{\partial}{\partial x}\left(\kappa\frac{\partial c}{\partial x}\right) \sim \frac{\kappa C}{L^2}, \quad (3.8)$$

where $\partial/\partial x \sim 1/L$ and L represents a typical horizontal scale, and U represents the magnitude of the horizontal velocity. Taking the ratio of these estimates, (3.7) and (3.8), gives the non-dimensional Peclet number,

$$Pe = \frac{UL}{\kappa}, \quad (3.9)$$

measuring the relative importance of advection to diffusion. In most practical situations, the Peclet number is very large and advection is much more important than molecular diffusion. This scaling can be repeated on the larger scale where the molecular diffusivity is replaced by a larger eddy diffusivity representing the effect of larger-scale eddies, leading to a smaller Peclet number.

3.2.4 Tracer spreading examples for salt and potential temperature

Salinity and potential temperature are tracers commonly employed to identify spreading pathways in the ocean, since they do not have interior sources or sinks. These water masses spread away from their formation regions by the three-dimensional advection and, ultimately, on fine scales by molecular diffusion (Box 3.2).

One of their most striking signals is in how salty, warm water spills out of the Mediterranean and spreads at mid depths over the North Atlantic (Fig. 3.10). The salty, warm water preferentially spreads northward along the eastern boundary, linked to a persistent, slope current, and is transferred westward by the overlying clockwise gyre circulation. This salty, warm water is also

transferred by the time-varying circulation, most vividly through subsurface eddies (called Meddies, which drift westward), which are rotating lenses of salty, warm water. As the water mass spreads away from its source over the Atlantic basin, it gradually becomes diluted through molecular diffusion and mixing. Given these tracer spreading patterns, now consider more carefully how tracers are transferred by a time-varying circulation.

3.2.5 Eddy transfer of tracers

The ocean has a time-varying circulation, which is often much vibrant than the background, time-averaged flow and nearly always more important than the effects of molecular diffusion. This time-varying circulation is very important in transferring tracers, as seen in the horizontal

Box 3.2 Three-dimensional forms of mass and tracer conservation

In three dimensions, *mass conservation* is given by

$$\frac{\partial \rho}{\partial t} + \frac{\partial}{\partial x}(\rho u) + \frac{\partial}{\partial y}(\rho v) + \frac{\partial}{\partial z}(\rho w) = 0, \quad (3.10a)$$

or in vector notation (see Appendix 1.1) by

$$\frac{\partial \rho}{\partial t} + \nabla \cdot (\rho \mathbf{u}) = 0, \quad (3.10b)$$

where there is no internal source or sink of mass, and no molecular diffusion of mass. In practice, density variations are relatively small in the ocean and mass conservation can be approximated by *volume conservation*,

$$\nabla \cdot \mathbf{u} = \frac{\partial u}{\partial x} + \frac{\partial v}{\partial y} + \frac{\partial w}{\partial z} = 0. \quad (3.11)$$

Tracer conservation is expressed in terms of the divergence of the advective and diffusive tracer fluxes,

$$\frac{\partial c}{\partial t} + \nabla \cdot (\mathbf{u}c) = \nabla \cdot (\kappa \nabla c) + S_c, \quad (3.12)$$

representing how tracers are advected by the flow, diffused down gradient and can have internal sources; where c is the tracer concentration per unit volume, κ is the tracer molecular diffusivity and S_c is a tracer source. For any model application, the molecular diffusivity, κ , is replaced by a much larger eddy transfer coefficient, K , representing the effect of larger-scale turbulence, which can vary spatially.

The tracer evolution can be interpreted in terms of the rate of change following a fluid parcel, referred to as the Lagrangian rate of change, using the definition

$$\frac{Dc}{Dt} \equiv \frac{\partial c}{\partial t} + \mathbf{u} \cdot \nabla c, \quad (3.13)$$

where D/Dt is the material or substantial derivative (see Appendix 1.2).

spreading of salty, warm water from the Mediterranean (Fig. 3.10).

To understand this effect of the time-varying circulation, again consider the advective flux of tracer along a pipe, $F = uc$, where c is the tracer concentration per unit volume. Now separate the velocity and tracer concentrations at any given moment into a time-mean part and an eddy part, such that

$$c = \bar{c} + c', \quad (3.14)$$

$$u = \bar{u} + u',$$

where the time-mean is defined by

$$\bar{c} = \frac{1}{\Delta t} \int_0^{\Delta t} c dt, \quad (3.15)$$

and the time-varying part, c' , is given by the departure from the time-mean and its own time-mean vanishes by definition, $\bar{c}' = 0$. The tracer flux can then be written as

$$F = uc = (\bar{u} + u')(\bar{c} + c') = \bar{u}\bar{c} + \bar{u}c' + u'\bar{c} + u'c',$$

and then applying a time average leads to

$$\bar{F} = \bar{u}\bar{c} = \bar{u}\bar{c} + \bar{u}\bar{c}' + \bar{u'}\bar{c} + \bar{u'}\bar{c}' \equiv \bar{u}\bar{c} + \bar{u'}\bar{c}', \quad (3.16)$$

where product terms with only a single time-varying component vanish, $\bar{u}c' \equiv 0$, but the product of two time-varying variables, $\bar{u'}c'$, need not vanish, as the two time-varying variables might

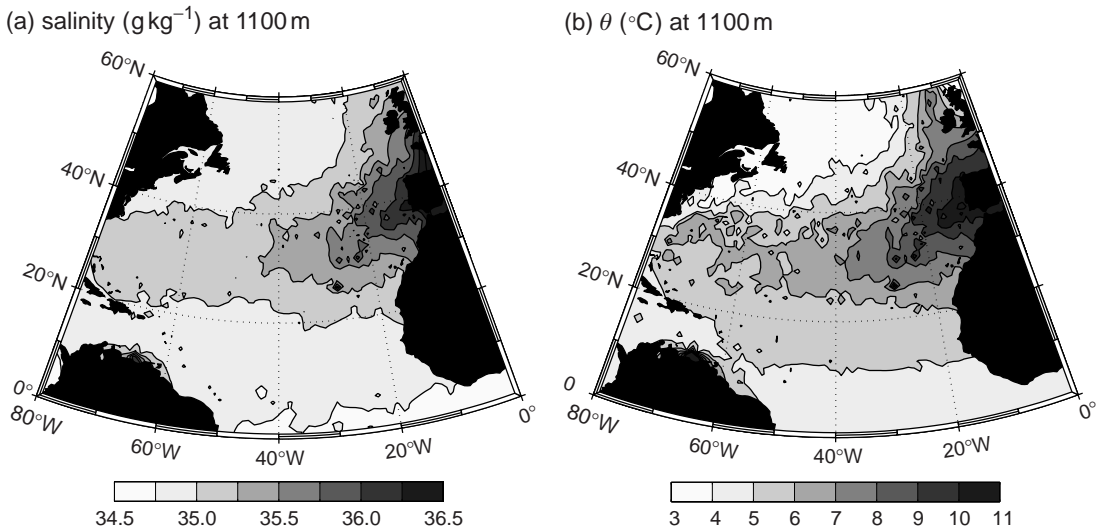


Figure 3.10 The spreading of warm, salty water from the Mediterranean over the North Atlantic: (a) salinity, S (g kg^{-1}), measuring the concentration of salt as the number of grams of salt in a kilogram of seawater, and (b) potential temperature, θ ($^{\circ}\text{C}$), the temperature a fluid parcel has if moved adiabatically to the surface, both at a constant depth of 1100 m; diagnosed from the Reid compilation of data. As the salty, warm water spreads, its properties become diluted through diffusion and mixing.

be correlated with each other. This latter term $\bar{u}'c'$ is referred to as an eddy flux.

To understand how this eddy flux might be formed, consider a simple problem of an oscillating velocity, v' , either varying as a cosine or a sine function in time together with temperature, T' , varying as a sine function (Fig. 3.11a,b). Both v' and T' separately average to zero over a single period. Now consider the northward temperature flux, $v'T'$; if $v' > 0$ and $T' > 0$, then their flux is positive, $v'T' > 0$, and likewise if $v' < 0$ and $T' < 0$, then the flux remains positive $v'T' > 0$, leading to the time average of the eddy flux $\bar{v'}T'$ being positive over a single wave period. Hence, the eddy flux can average to a non-zero value as long as the v' and T' contributions correlate with each other, as depicted in Fig. 3.11c.

Repeating this separation into mean and eddy terms in the tracer equation (3.3a) leads to

$$\frac{\partial \bar{c}}{\partial t} + \frac{\partial c'}{\partial t} = -\frac{\partial}{\partial x}(\bar{u}c) - \frac{\partial}{\partial x}(\bar{u}c') - \frac{\partial}{\partial x}(u'\bar{c}) - \frac{\partial}{\partial x}(u'c'),$$

then averaging in time leads to a prognostic equation for the time-mean component of the

tracer, \bar{c} :

$$\frac{\partial \bar{c}}{\partial t} = -\bar{u} \frac{\partial \bar{c}}{\partial x} - \frac{\partial}{\partial x}(\bar{u}'c'), \quad (3.17)$$

where the first term on the right is re-expressed in an advective form using continuity of volume ($\frac{\partial \bar{u}}{\partial x} = 0$ for the pipe). The first term on the right represents the advection of the mean tracer gradient by the mean flow, while the second term represents the divergence of the eddy tracer fluxes.

More generally for flows varying in three dimensions, the time-averaged tracer equation (now without molecular diffusion or a tracer source included) is written as

$$\frac{\partial \bar{c}}{\partial t} + \bar{\mathbf{u}} \cdot \nabla \bar{c} = -\nabla \cdot (\bar{u}'c'), \quad (3.18)$$

where $\bar{u}'c'$ represents an eddy flux of tracer. The time-mean tracer evolves through advection by the time-mean flow and from the divergence of the eddy tracer fluxes.

3.2.6 How are eddy fluxes represented?

In applying the time-averaged tracer transport equations, one has to think carefully about what the ‘eddy flux’, $\bar{u}'c'$, actually represents. The

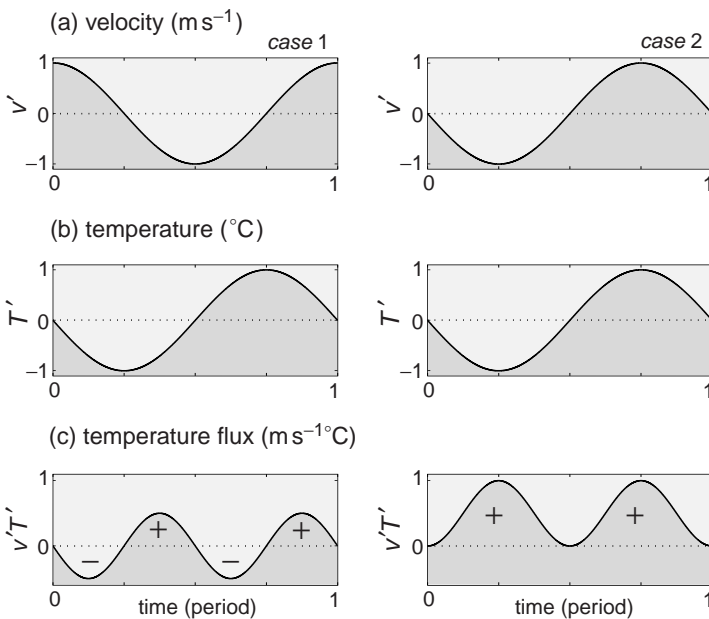


Figure 3.11 An idealised example illustrating how fluctuating velocity and temperature provide a temperature flux. Consider (a) the velocity $v'(t)$ either oscillating as a cosine or sine wave (cases 1 and 2) with time t , together with (b) temperature $T'(t)$ varying as a sine wave in time, and (c) their product, a temperature flux, $v'T'$, varying in time. In case 1, v' and T' are out of phase by $1/4$ of a wavelength, and their flux oscillates in sign and its time average $\overline{v'T'} = 0$ over an entire period. In case 2, v' and T' are in phase: positive v' is correlated with positive T' and negative v' is correlated with negative T' leading to the time average of their product, $v'T'$, always being positive (for this case, $\overline{v'T'} = 0.5 \text{ m s}^{-1} \text{ }^{\circ}\text{C}$).

physical interpretation of what the eddy represents depends on the temporal and spatial averaging applied. For example, consider three different choices:

1. For the smallest time and space scales, one might consider the Brownian motion of molecules and how their random walk leads to a molecular diffusion of a tracer, which is represented by a down-gradient closure in (3.5).
2. On timescales of a few seconds to hours, one can instead consider turbulent events within the mixed layer, and how the turbulence affects the evolution of the bulk properties of the mixed layer.
3. On timescales of days to months, one can consider oceanic mesoscale and atmospheric synoptic-scale eddies (with a characteristic horizontal scale of 50–100 km or 1000 km, respectively), and how their transfer of heat and tracers affect the background state of the ocean and atmosphere.

The eddy tracer flux is often parameterised in terms of the background tracer gradient,

$$\overline{u'c'} = -K \frac{\partial \bar{c}}{\partial x}, \quad (3.19)$$

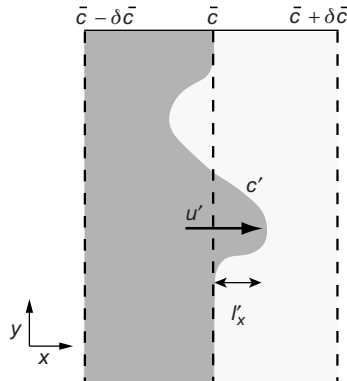


Figure 3.12 Perturbations in the flow field, u' , distort the instantaneous tracer field (shading) away from the time-mean distribution (dashed lines) leading to a tracer anomaly of concentration c' . In the time-mean, the integrated effect of the correlation of velocity and tracer anomalies leads to a flux of tracer given by $\overline{u'c'}$, where the overbar represents a time average. This tracer anomaly penetrates a distance l'_x into a region where there is a larger mean concentration, such that $c' \sim -l'_x \frac{\partial \bar{c}}{\partial x}$.

as illustrated in Fig. 3.12 and expanded upon in Box 3.3, where K represents an eddy transfer coefficient or eddy diffusivity ($\text{m}^2 \text{ s}^{-1}$), representing a product of an eddy velocity and eddy length scale (Box 3.3).

Box 3.3 How is the eddy tracer flux related to the background tracer gradient?

Consider a fluid in which there is a time-averaged, large-scale gradient of tracer (Fig. 3.12, dashed lines). At any instant, eddy circulations distort the tracer field (Fig. 3.12, shading) forming a tracer anomaly, c' , relative to the time-mean distribution. For small displacements, the tracer anomaly can be related to the distance, l'_x , that the tracer contour has been displaced from its time-mean position, such that

$$c' \sim -l'_x \frac{\partial \bar{c}}{\partial x}. \quad (3.20)$$

An eddy flux is given by the correlation of velocity and tracer perturbations, $\overline{u'c'}$, which can then be related to the displacements of fluid parcels and the background tracer gradient:

$$F = \overline{u'c'} \sim -\overline{u'l'_x} \frac{\partial \bar{c}}{\partial x}. \quad (3.21)$$

These eddy fluxes are partly analogous to the tracer transport by molecular diffusion involving the Brownian motion of molecules. Consequently, the transfer properties of the fluid, $\overline{u'l'_x}$, are often represented as

$$\overline{u'c'} \sim -\overline{u'l'_x} \frac{\partial \bar{c}}{\partial x} \sim -K \frac{\partial \bar{c}}{\partial x}, \quad (3.22)$$

where $K \sim \overline{u'l'_x}$ is an eddy transfer coefficient with the same mathematical form as molecular diffusivity, but having much larger values.

This closure (3.22) can be generalised in three dimensions to relate the three-dimensional eddy tracer fluxes to the three-dimensional tracer gradient,

$$\overline{\mathbf{u}'c'} = -K \nabla \bar{c}, \quad (3.23)$$

where K can take different values in the horizontal or vertical components.

How does the eddy diffusivity compare with molecular diffusivity?

The form of the eddy tracer flux closure (3.19) is analogous to that employed for molecular diffusion (3.5). However, it is important not to confuse the eddy transfer coefficient or diffusivity, K , with molecular diffusivity, κ . The molecular diffusivity is isotropic and tiny, such that the molecular diffusivity of salt in seawater, κ_s , only reaches $1.5 \times 10^{-9} \text{ m}^2 \text{ s}^{-1}$ at a temperature of 25°C . In contrast, the eddy transfer coefficient, K , is many orders of magnitude larger than κ and is anisotropic: K is much smaller in the vertical than in the horizontal; the vertical component, K_v , is typically $10^{-5} \text{ m}^2 \text{ s}^{-1}$ in the thermocline and increases to $10^{-4} \text{ m}^2 \text{ s}^{-1}$ or more near boundaries or above rough topography; while in the

horizontal, K_h , typically reaches 10^2 to $10^3 \text{ m}^2 \text{ s}^{-1}$ over the large-scale ocean. More physically, this anisotropic nature of K can be related to the position of density surfaces with a much larger component directed along density surfaces, than directed across them.

3.3 What is the effect of a time-varying, eddy circulation?

The preceding tracer view emphasises how tracers are advected by the time-mean circulation and transferred by the time-varying, eddy circulation, as well as diffused on the smallest scale by molecular processes. The transfer by the time-varying

circulation can be understood in terms of both an advective and diffusive transfer.

The diffusive transfer by eddies is simple to understand given how the eddy closure appears analogous to the down-gradient closure for molecular diffusion.

The advective transfer by eddies is more difficult to understand and we address this aspect in two different ways: firstly, considering how particles are transferred in a time-varying flow and, secondly, how eddies provide an additional volume flux.

3.3.1 Particle transfer by the time-varying circulation

To gain more physical insight into this problem, consider how particles move and their relation to the time-averaged circulation. This choice immediately simplifies the problem, as we only need to consider the effect of advection on a particle, rather than include the effect of diffusion (as required when considering a tracer). Ultimately, any views of how particles are transported need to be equivalent to the preceding view of how tracers spread, since a tracer can be viewed in terms of a concentration of many particles (Fig. 3.2).

It is useful to consider different time-averaged views of the circulation, rather than instantaneous snapshots. The most straightforward time average is at a fixed point in space, referred to as an Eulerian average; for example, as employed when measuring how fast the clouds are swept past you when sitting outside or how fast the sea moves past a pier. Although easy to apply, this Eulerian average can often be misleading in understanding how particles are transported, particularly when there are strong oscillating flows.

Alternatively, a time average following a moving object can be applied, referred to as a Lagrangian average; for example, as employed when measuring the average velocity of an untethered balloon moving in the sky or a freely moving buoy in the sea. While this averaging might be more difficult to apply, this approach is physically more revealing, as the movement of actual particles is followed.

To understand these different views, consider a floating stick drifting down a river. The Eulerian estimate of the velocity is given by how quickly

the stick passes a fixed point along the bank; this Eulerian estimate varies in position and time. The Lagrangian estimate of the velocity is instead given by the velocity of the stick following its movement down the river. At any instant, the Lagrangian and Eulerian velocities are the same, but over sufficient time can become very different as the stick moves down the river and experiences a different flow.

These different definitions of the average velocity become more apparent when considering the effect of oscillating flows in advecting particles. To illustrate this distinction, next consider how particles move in waves off the seashore.

3.3.2 What is the effect of waves on how particles move by the seashore?

Everyone is familiar with the sight of waves on the sea where the surface bobs up and down. As the waves move towards the coast, the lines of wave crests and troughs become parallel to the shore, and the waves eventually break, as depicted in Fig. 3.13. If a stick is thrown into the sea, the stick is swept back and forth by the passing waves. After several cycles of passing waves, there is usually an overall drift of the stick towards the shore.

To understand why the stick is usually swept onshore, consider the effect of waves on how particles move out at sea. If one watches the oscillations of the sea surface, the wave crests and troughs propagate in the same direction, moving much faster than the actual water particles (and the floating stick). The water velocity moves in the same direction as the wave when a wave crest passes, but reverses in direction when the wave trough passes (Fig. 3.14a,b). If there is no background current (as chosen in Fig. 3.14), the water velocity averages to zero over an entire wave period at any fixed position. However, the velocity does *not* average to zero following a particle moving back and forth in the waves. Instead the passing waves lead to particles rising as a wave crest approaches, then are swept forwards in the direction of the wave, then fall as a trough approaches and are swept backwards. As the wave motion decays with depth, the forward movement is greater than the backward movement of the particle. Hence, over an entire wave period, the particles do not exactly return to their starting



Figure 3.13 A photograph from a 100 m high cliff overlooking a beach at Torrey Pines, Southern California, revealing wave breaking over a surf zone, 100 to 200 m wide, together with an offshore plume of sediment and foam extending a similar distance out to sea (white arrow). There is an onshore transport associated with the waves, which is returned in a narrow rip current, several tens of metres wide, and leading to the offshore plume. In this case, the rip current is associated with reduced wave breaking. The return flow in rip currents is often coincident with channels, but in this case the rip current emerged spontaneously, lasting tens of minutes. Photograph courtesy of Brad Murray. For further examples and details of how rip currents spontaneously form, see Murray et al. (2003).

position, but drift slightly in the direction of the wave motion (depicted as left to right in Fig. 3.14c) and, thus, the Lagrangian velocity is non zero. This process can be seen in how a floating stick usually drifts onshore through the action of the waves.

In general, the average velocity following the particle, the Lagrangian velocity, can be very different to the average velocity at a fixed position, the Eulerian velocity; the difference between these two velocities is called the Stokes' drift velocity (Box 3.4), in recognition of George Stokes, who first explained this phenomenon for water waves in 1847. The Stokes' drift velocity induced by an oscillating wave is generally given by $v_{\text{Stokes}} = v_0^2/(2c)$, where v_0 is the amplitude of the oscillating horizontal velocity in the water (induced by the passing wave) and c is the wave

speed, measuring the speed of individual crests or troughs.

3.3.3 Relationship to eddy volume flux

The additional advection provided by time-varying eddy flows is represented by the Stokes' drift velocity. This effect can be seen by the systematic transfer of particles by waves, either out at sea or by the shore. Now consider a complementary view of how time-varying flows lead to an additional advection, which can be understood in a more physical manner than the Stokes' drift correction.

Consider a layer of fluid with an oscillating velocity and thickness, such as for a shallow-water wave approaching the shore (Fig. 3.15a) or for a density layer within the open ocean (Fig. 3.16a). For simplicity, assume that the velocity does not

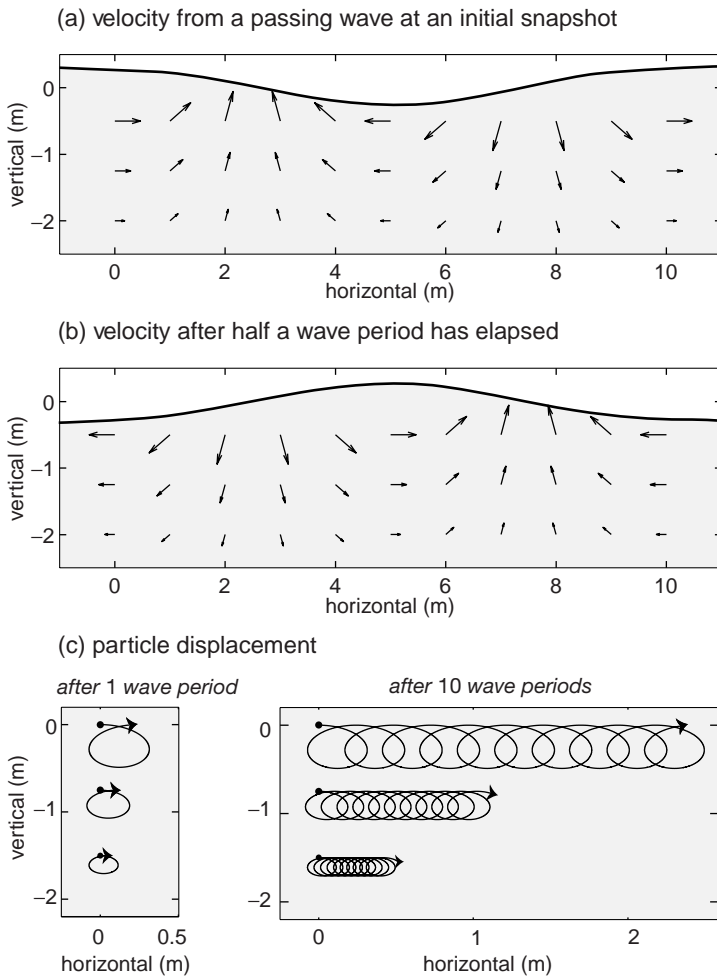


Figure 3.14 A figure depicting the horizontal velocity and particle displacement for waves in deep water: the water velocity (arrow) and sea surface height (full line) oscillate with the passage of a surface wave, depicted versus position in (a) for an initial snapshot at time, $t = 0$, and in (b) at $1/2$ a wave period. The velocity reverses in direction between these two times, as well as decays with depth, such that the time-averaged Eulerian velocity is zero. In (c), the Lagrangian displacement of particles (full line) is depicted in this oscillating flow. The particles follow an orbital motion along an elliptical path, starting at a horizontal position = 0 (denoted by a black circle) and drift horizontally in the direction of the wave motion (from left to right, denoted by the arrowhead). This wave-induced displacement is referred to as a Stokes' drift. These solutions are for deep-water waves, satisfying $v(y, z, t) = v_0 \exp(kz) \cos(ky - \omega t)$ and $w(y, z, t) = v_0 \exp(kz) \sin(ky - \omega t)$, assuming a wavelength $2\pi/k = 10$ m, a period $2\pi/\omega = 2.5$ s, a wave speed 3.95 m s^{-1} , a water speed $v_0 = 0.7 \text{ m s}^{-1}$, and a Stokes' drift velocity, $v_0^2/(2c)$, at the surface of 0.06 m s^{-1} .

vary with depth within the layer. The meridional transport within this layer (defined here as per unit horizontal length, so in $\text{m}^2 \text{s}^{-1}$) is

$$V = hv,$$

where h is the thickness of the layer and v is its meridional velocity. Splitting the thickness and velocity into time-mean and time-varying components, $h = \bar{h} + h'(t)$, $v = \bar{v} + v'(t)$, the time-mean transport is

$$\bar{V} = \bar{h}\bar{v} + \bar{h}'v'. \quad (3.24)$$

This total transport consists of the transport from the time-mean velocity, $\bar{h}\bar{v}$, and an additional eddy transport, $\bar{h}'v'$. This eddy transport relies on

an eddy correlation between layer thickness and velocity, and is non-zero when a greater volume of water mass moves meridionally in one direction than returns in the opposite direction (as sketched in Figs. 3.15a and 3.16a). The total transport can be rewritten in terms of a ‘transport velocity’ after dividing by the mean layer thickness,

$$(\bar{v} + v^*) = \bar{v} + \frac{\bar{h}'v'}{\bar{h}}, \quad (3.25)$$

where the eddy-induced velocity is given by

$$v^* = \frac{1}{\bar{h}} \bar{h}'v', \quad (3.26)$$

and will henceforth be referred to as the ‘bolus velocity’.

Box 3.4 The generic Stokes' drift for shallow-water waves

Any time-varying flow can lead to a particle displacement even if the velocity at a fixed position averages to zero. In order to illustrate this process, consider a wave motion leading to sinusoidal variations in water velocity,

$$v(y, t) = v_0 \sin(ky - \omega t). \quad (3.27)$$

The particle displacement, y_p , over a wave period τ is given by the time average of the water velocity following the particle (the Lagrangian velocity),

$$y_p(\tau) = \int_0^\tau v(y_p(t), t) dt. \quad (3.28)$$

The velocity following the particle (based upon a Taylor expansion for small perturbations in position, Appendix A.I.1) can be approximated by

$$v(y_p, t) = v(0, t) + y_p(t) \left. \frac{\partial v}{\partial y} \right|_{y=0} + \dots,$$

which allows (3.28) to be expressed as

$$y_p(\tau) = \int_0^\tau \left(v(0, t) + y_p(t) \left. \frac{\partial v}{\partial y} \right|_{y=0} + \dots \right) dt. \quad (3.29)$$

Again approximating $y_p(t)$ in the same manner on the right-hand side of (3.29), using (3.28) for a time interval of t , leads to the particle displacement being given by

$$y_p(\tau) = \int_0^\tau \left(v(0, t) + \left. \frac{\partial v}{\partial y} \right|_{y=0} \left(\int_0^t v(0, \tau) d\tau + \dots \right) \right) dt. \quad (3.30)$$

Substituting the sinusoidal choice for the flow (3.27) in (3.30) leads to the first term (the Eulerian velocity) averaging to zero, but a correlation in the second term gives an additional particle displacement, $y_p(\tau)$ in the time τ , corresponding to an additional velocity,

$$v_{Stokes} \equiv \frac{v_0^2}{2c}, \quad (3.31)$$

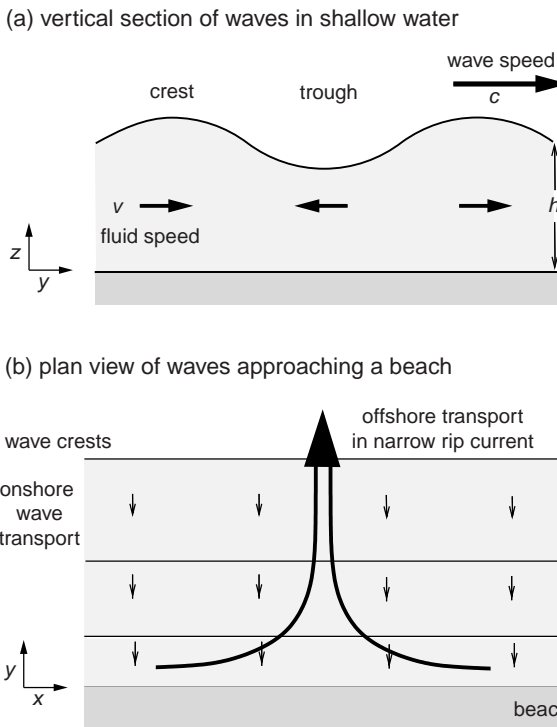
where $c = \omega/k$ is the phase speed of the wave and higher-order contributions have been neglected. This additional velocity is called the Stokes' drift velocity and represents the difference between the Lagrangian and Eulerian velocities.

Wave transfer in shallow seas

For shallow-water waves approaching the shore, at any instant, there is a greater volume flux, v_h , in wave crests directed onshore than returned in wave troughs (Fig. 3.15a). This phase relationship between velocity and thickness of the water column corresponds to the bolus velocity, v^* , being directed onshore (Fig. 3.15b). The bolus velocity provides an important contribution to the more

generic Stokes' drift velocity, $v_0^2/2c$, illustrated in Fig. 3.14 (Box 3.4). In this special case, both velocities are identical (see Q3.4), although this formal equivalence breaks down for more complicated flows.

This onshore flux cannot continue indefinitely everywhere, as otherwise the coast would be flooded. Instead, the water swept onshore by the action of the waves is returned offshore within



narrow currents, called ‘rip currents’ (Fig. 3.15b). The rip current can be seen where the surface water moves out to sea; carefully watch for where the surface ripples move, rather than be distracted by the passing waves. If the waves are particularly strong, then the rip current can be more clearly seen through narrow plumes of foam being swept out to sea (such as in Fig. 3.13, white arrow).

3.3.4 Eddy transfer in the open ocean

Now consider the bolus velocity over the open ocean. For simplicity, assume that the ocean is represented as two layers of fluid, light overlying dense fluid, and that the lighter layer is thicker in the tropics and thinner in the polar regions, reflecting the effect of surface heating in the tropics and cooling in the poles. The flow can extract energy from this background state when density layers slump, leading to eddies forming through a process referred to as baroclinic instability. During this slumping of density layers, thick blobs of light fluid preferentially move poleward, while thin blobs of light fluid move equatorward, leading to a poleward flux of light fluid (Fig. 3.16a).

Figure 3.15 A schematic figure depicting the transport associated with waves in shallow water: (a) the water velocity v and thickness h oscillate with the passage of the wave with v in the same direction as the wave speed c in the crests, and the opposite direction in the troughs. For simplicity, assuming that the velocity is constant with depth, then since the water column is thicker in the crests, there is an overall volume flux directed in the direction of the wave crests; (b) as the waves approach the shore, there is an overall onshore transport induced by the waves (thin arrows). This onshore transport sets up a narrow rip current to provide the necessary return transport (thick arrow).

Hence, there is an eddy bolus flux, directed poleward in the light layer and equatorward in the dense layer (Fig. 3.16b); see later model examples in Section 9.3.4.

3.3.5 Large-scale examples of tracer transport over the globe

Now consider larger-scale atmospheric and oceanic examples of tracer transport, where again the time-varying circulation provides an important contribution.

Atmospheric example

This effect of time-varying flows providing an advection of particles and tracers occurs at all scales over the globe. To illustrate this advective transfer, consider the distribution of ozone molecules in the upper atmosphere. Ozone is both formed and destroyed by the absorption of ultraviolet radiation in the stratosphere, providing both a photochemical source and sink. There are several stages in this closed set of reactions: (i) an oxygen molecule absorbs ultraviolet radiation, dissociates and forms two oxygen atoms;

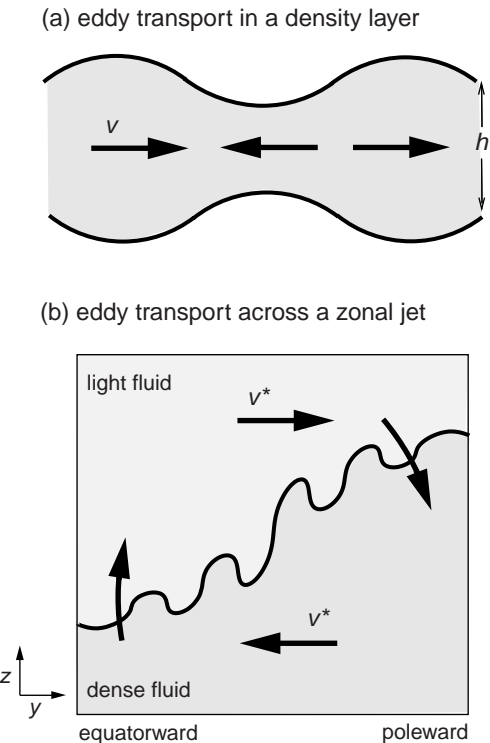


Figure 3.16 Schematic diagram of eddy transport for (a) a single density layer with the layer thickness h and the horizontal velocity \mathbf{u} . The time-averaged meridional volume flux in this undulating layer, $\bar{hv} = \bar{hv} + \bar{h'}v'$, depends on advection by the time-mean meridional velocity \bar{v} , and an eddy transport from the time-averaged correlation of the temporal deviations in velocity v' and layer thickness h' . (b) A two-layer representation of the ocean with light fluid overlying dense fluid. The slumping of the density interface (black line) leads to the eddy transport and associated bolus velocity, $v^* = \bar{h'}v'/\bar{h}$, being poleward in the light, upper layer, and equatorward in the dense, lower layer. Reproduced from Lee et al. (1997), courtesy of *J. Marine Res.*, Yale University.

(ii) an oxygen atom then combines with an oxygen molecule to form an ozone molecule; (iii) the ozone molecule absorbs ultraviolet radiation, dissociates and forms an oxygen molecule and oxygen atom; and (iv) two oxygen atoms combine to form an oxygen molecule.

Given these reactions, one might expect the maximum in ozone concentration to be at the tropics, where there is more incident ultraviolet radiation and, thus, a greater photochemical source and sink. However, surprisingly, the ozone maximum is *not* in the tropical source and instead

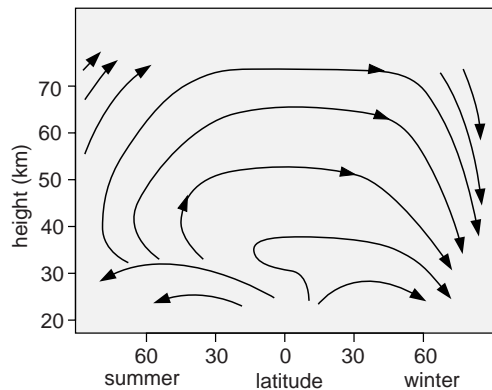


Figure 3.17 Schematic streamlines of the solstice diabatic circulation in the middle atmosphere, as diagnosed by Murgatroyd and Singleton (1961). In the stratosphere above 10–20 km, the transport is directed from the summer to the winter hemisphere. Ozone is both formed and destroyed by the photochemistry in the stratosphere. The circulation transports ozone-rich air from the tropics into the mid and high latitudes of the darker, winter hemisphere. This transport leads to the column-integrated ozone being greater in the mid latitudes during winter. This tracer transport is primarily due to the advection by the time-varying circulation, rather than the time-averaged Eulerian circulation or background diffusion. Redrawn from Andrews et al. (1987).

is shifted towards the mid latitudes in the winter hemisphere.

This puzzling distribution is explained by the circulation advecting ozone-rich air from its photochemical source in the tropics into the winter hemisphere (as depicted in Fig. 3.17), where the ozone accumulates as there is less ultraviolet radiation and a weaker photochemical sink in the darker hemisphere; note that in the polar regions there is also a reduction in stratospheric ozone through chemical reactions involving CFC compounds during the extremely cold, polar winter. This tracer transport from the summer to the winter hemisphere is *not* achieved either by the Eulerian time-averaged velocity that is very weak or any background down-gradient diffusion acting to remove tracer contrasts. Instead, time-varying eddies within the stratosphere provide an advective transfer of the tracer, directed poleward in the winter hemisphere.

Hence, in the same manner as a stick drifts in an oscillating wave field, eddy circulations lead to a systematic advection of particles and tracers over the globe (Fig 3.17).

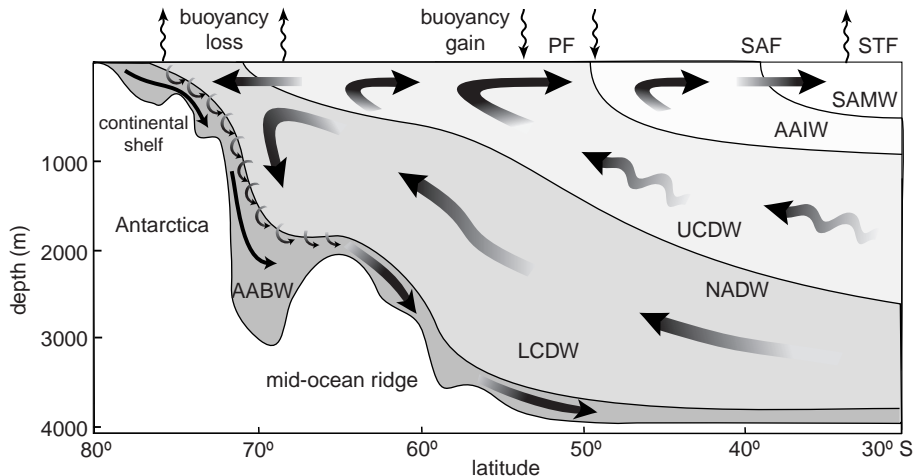


Figure 3.18 A schematic view of the overturning circulation in the Southern Ocean. There are two meridional overturning cells. An upper cell is primarily formed by a northwards Ekman transport beneath strong westerly winds and southwards eddy transport of tracers in Upper Circumpolar Deep Water (UCDW). A lower cell is primarily driven by the formation of dense Antarctic Bottom Water (AABW) near the Antarctic Continent. Other notation: PF, Polar Front; STF, Subtropical Front; SAMW, Sub-Antarctic Mode Water; AAIW, Antarctic Intermediate Water; NADW, North Atlantic Deep Water; LCDW, Lower Circumpolar Deep Water. From Speer *et al.* (2000).

Southern Ocean example

Tracers in the Southern Ocean, such as salinity, dissolved oxygen and nutrients, reveal meridional overturning cells (Fig. 3.18), involving a northward transfer of surface, intermediate and bottom waters together with a southward transfer of deep waters. This tracer transport is controlled by a combination of the advection by the time-mean Eulerian flow, the advection by the time-varying eddies (represented by the bolus velocity) and the down-gradient diffusion by the time-varying eddies.

For this Southern Ocean example and the earlier stratospheric example (Fig. 3.17), the tracer spreading is often understood in terms of a zonally and time averaged circulation. For these cases, the mean and eddy circulations are often opposing and the weaker net circulation is referred to as a ‘residual’ circulation. Tracers are advected by this ‘residual’ circulation [like in (3.25)], and diffused down gradient by the eddies; see later Section 9.3.4.

through a combination of advection and molecular diffusion, where advection displaces the centre of mass and molecular diffusion erodes tracer gradients. Variations in advection lead to tracers being stirred and drawn out in narrow filaments, leading to tracer gradients increasing, until these contrasts are removed through diffusion. This process can be seen in the patchy distribution of phytoplankton blooms and the spreading of ozone-depleted air in the upper atmosphere (in Figs. 3.19 and 3.8).

Individual particles are advected by the velocity following their movement (the Lagrangian circulation), which can be separated into contributions by the time-mean velocity at a fixed point (the Eulerian circulation) plus the integrated effect of the time-varying velocity (the Stokes’ drift contribution). Examples of the Stokes’ drift contribution from oscillating waves lead to an onshore volume flux, as seen in a floating stick usually being swept onshore, and this volume flux is returned offshore within narrow rip currents (Fig. 3.13).

Tracer transport is often separated into the effect of the time-averaged and time-varying circulations. The time-mean circulation simply advects the tracer, while the time-varying circulation both diffuses the tracer down gradient and advects the

3.4 | Summary

Tracers reveal transport pathways within the ocean and atmosphere. They are transported

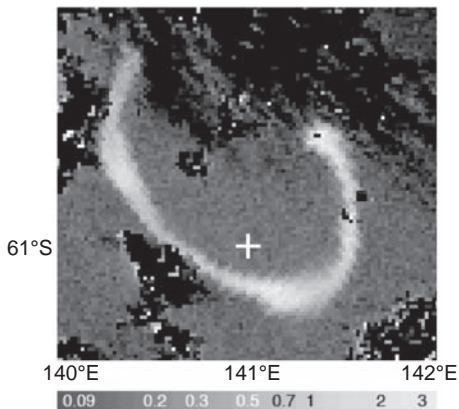


Figure 3.19 Snapshot of sea-surface chlorophyll *a* bloom formed from the Southern Ocean iron-release experiment taken from the NASA SeaWiFS ocean colour satellite on 23 March 1999. There is a patch of elevated chlorophyll concentrations (light shading) extending in a filament 150 km long after 6 weeks; see Abraham *et al.* (2000) and Martin (2003) for further details. Image courtesy of Steve Groom, NEODAAS, Plymouth.

tracer. The additional eddy advection of a tracer can be understood in terms of the eddy bolus velocity (involving correlations in velocity and thickness of a fluid layer) and is directly analogous to the additional advection of particles in a time-varying flow (the Stokes' drift contribution).

This transport of tracers plays a central role in determining the distribution of physical and biogeochemical properties over the globe. Tracer distributions in the atmosphere and ocean are rarely determined simply by local sources and sinks; instead, the patterns of tracers reflect the interplay of the circulation and these sources and sinks. This interplay makes any tracer pattern a real challenge to unravel and, ultimately, makes the atmosphere and ocean fascinating to study. These transport concepts are taken further in addressing the role of eddies (Chapter 9) and applied in understanding tracer distributions (Chapters 10 to 12).

3.5 | Questions

Q3.1. Stirring of tracers.

(a) Conduct a simple dye experiment. Release a few drops of food dye in a glass container filled with water, which is at rest. Watch how the dye

spreads over the next minute or so, and look at its surface pattern and the vertical plumes of dye.

Repeat the exercise, but this time make the water smoothly rotate in the container before adding the dye. Again watch how the dye spreads in the horizontal and vertical. How do the dye patterns differ in each case?

(b) In a similar manner on a grander scale, an iron-fertilisation experiment led to a phytoplankton bloom with subsequent stirring over the open ocean as illustrated in Fig. 3.19: iron was artificially supplied to a patch of ocean 7 km in diameter, which led to a local phytoplankton bloom reaching unusually high chlorophyll *a* concentrations of 3 mg m^{-3} . The bloom rapidly expanded through a combination of stirring and diffusion of the patch, as well as the growth of phytoplankton: the fertilised patch expanded to a horizontal length scale of 30 km long after 9 days and further to 150 km after 42 days. Based on these length scales, estimate the effective strain rate, γ_e , for the two periods from (i) initial release to 9 days; and (ii) from 9 days to 42 days, using

$$\Delta x(t) = \Delta x_0 \exp(\gamma_e t),$$

where $\Delta x(t)$ and Δx_0 are the length scales of the patch at the elapsed time t and the initial time. Do you expect the strain rate to increase or decrease as the length scale inflates?

Q3.2. Patchy tracers distributions and the flow pattern.

Tracers often have a patchy distribution, either confined in blobs or stretched out in narrow filaments, which reflects the effect of the flow pattern. Consider the spreading of a blob of tracer (Fig. 3.20a) either by a rotational or convergent flow (Fig. 3.20b,c). In (b), the rotational flow merely leads to the patch being rotated and there is no change in symmetry, while in (c), the tracer patch is compressed by the flow in the y -axis and stretched in the x -axis. Whether rapid stirring occurs or not can be diagnosed from the gradients in velocity, where the flow follows streamlines as marked in Fig. 3.20 (full lines).

(a) Assuming the streamfunction, ψ , for the flows in Fig. 3.20b,c are given by (i) $\psi = a(x^2 + y^2)/2$

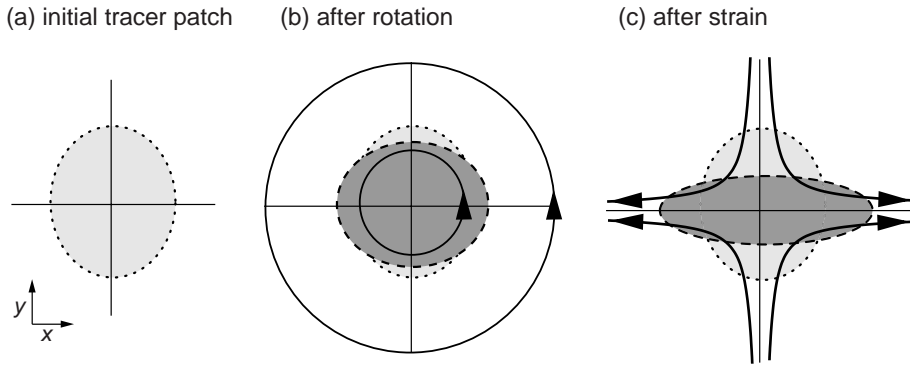


Figure 3.20 A schematic figure depicting (a) an elliptical patch of tracer (light shading) and the displacement of the patch (dark shading) after advection involving either (b) rotation or (c) pure strain (streamlines are full lines).

and (ii) $\psi = -axy$, respectively, then derive expressions for the velocities, $u \equiv -\partial\psi/\partial y$ and $v \equiv \partial\psi/\partial x$ for both cases.

(b) Based on these velocities, evaluate the vorticity, ζ ,

$$\zeta = \frac{\partial v}{\partial x} - \frac{\partial u}{\partial y}, \quad (3.32)$$

and the strain rate, γ , by

$$\gamma^2 = \left(\frac{\partial u}{\partial x} - \frac{\partial v}{\partial y} \right)^2 + \left(\frac{\partial v}{\partial x} + \frac{\partial u}{\partial y} \right)^2, \quad (3.33)$$

for both cases.

(c) Whether there is rapid stirring depends on the relative size of the strain rate, γ , and the vorticity, ζ , a measure of the rotation, as given by the parameter,

$$\gamma^2 - \zeta^2. \quad (3.34)$$

Assuming that the spacing between tracer contours increases at a rate given by $\exp(\pm(\gamma^2 - \zeta^2)^{1/2}t)$, discuss the implications for how the tracer spreads for cases (i) and (ii).

Q3.3. Time-varying tracer fluxes.

(a) Construct two time series for velocity, $u(t)$, and tracer concentration, $c(t)$, based on random choices for each variable. For example, take a dice and throw it 50 times and record the values for u , and then repeat the process and record the values for c .

(b) Evaluate the time-mean value for velocity \bar{u} and the time-mean value of tracer \bar{c} .

(c) Construct a time series for $u'(t) = u(t) - \bar{u}$ and $c'(t) = c(t) - \bar{c}$.

(d) Evaluate the separate contributions to the products of velocity and tracer concentrations for each time, $u(t)c(t)$, $\bar{u}\bar{c}$, $u'(t)\bar{c}$, $\bar{u}c'(t)$, $u'(t)c'(t)$.

At each time, check that the tracer flux is given by $u(t)c(t) = \bar{u}\bar{c} + u'(t)\bar{c} + \bar{u}c'(t) + u'(t)c'(t)$.

(e) Evaluate the time-averaged contributions of each of the terms, $\bar{u}(t)c(t)$, $\bar{u}\bar{c}$, $\bar{u}'(t)\bar{c}$, $\bar{u}c'(t)$, and $u'(t)c'(t)$.

Identify which terms contribute to the time-averaged flux, $\bar{u}(t)c(t)$, and identify what each term represents.

Q3.4. Bolus velocity and Stokes' drift in shallow-water waves.

(a) For shallow-water waves, there is local balance between the temporal acceleration and the horizontal pressure gradient (dependent on the thickness of the water column, h), such that

$$\frac{\partial v}{\partial t} = -g \frac{\partial h}{\partial y}, \quad (3.35)$$

where g is gravity. Assuming a sinusoidal wave form for the velocity in the water column associated with the wave,

$$v(y, t) = v_0 \sin(ky - \omega t), \quad (3.36)$$

then show that the thickness of the water column, h , varies in a similar sinusoidal manner:

$$h(y, t) = \bar{h} + h_0 \sin(ky - \omega t), \quad (3.37)$$

where \bar{h} is the time-mean thickness of the column, h_0 is the amplitude of the oscillating wave, k is the wavenumber, and ω is the angular frequency for the wave. Identify how v_0 and h_0 are related.

Given the sinusoidal variations for v and h , how does the volume flux vh vary in magnitude and direction in the crest and trough of the wave?

(b) Integrate over a wave period τ at a fixed position $y = 0$, and show that the time-integrated volume flux using (3.36) and (3.37) is given by

$$\begin{aligned} & \int_0^\tau v(0, t)h(0, t)dt \\ &= \int_0^\tau v_0 \sin(-\omega t)(\bar{h} + h_0 \sin(-\omega t))dt \\ &= \frac{v_0 h_0}{2} \tau \end{aligned} \quad (3.38)$$

Hence, infer the direction of the volume flux associated with the wave motion.

(c) For the special case of shallow-water waves approaching the shore, show how the implied bolus velocity, $v^* = \bar{h}' v' / \bar{h}$, from (3.38) is equivalent to the Stokes' drift velocity, $v_0^2 / 2c$, from (3.28)

assuming a wave speed $c = (g\bar{h})^{1/2}$ for shallow-water waves, and the relationship between v_0 and h_0 (from part (a)).

3.6 | Recommended reading

A comprehensive derivation of mass and tracer budgets is provided by A. E. Gill (1982).

Ocean–Atmosphere Dynamics. New York: Academic Press, 662pp; see Section 4.3.

An accessible discussion of stirring and mixing is in W. R. Young (1999). Lectures on stirring and mixing, delivered at the 1999 WHOI Summer Program in Geophysical Fluid Dynamics.

A description of how stirring and mixing affect phytoplankton distributions is provided by A. P. Martin (2003). Phytoplankton patchiness: the role of lateral stirring and mixing. *Progr. Oceanogr.*, **57**, 125–174.

A mathematical discussion of the concepts of advection, diffusion, mixing and stirring processes is provided in R. Salmon (1998). *Lectures on Geophysical Fluid Dynamics*. New York: Oxford University Press, 378pp; see Sections 1.9 and 1.14.

A high-level discussion of atmospheric transport and the different representations of eddies is in D. G. Andrews, J. R. Holton and C. B. Leovy (1987). *Middle Atmosphere Dynamics*. Orlando, FL: Academic Press, 489pp; see Chapters 7 and 10 for the middle atmosphere circulation and the ozone distribution.

Chapter 4

Physics fundamentals

The ocean circulates, redistributing heat, carbon and tracers over the globe. This advective transfer can be seen in how seaweed, floating debris and sediments are swept along the shoreline, as well as on a grander scale in how warm water is moved from the tropics for thousands of kilometres by the ocean before releasing its warmth to the atmosphere. Currents occur in a range of guises: as narrow, fast jets; meandering boundary currents; spinning vortices and vibrant eddies; as well as broad and weak interior flows.

Ocean currents are mainly driven by the frictional drag from the wind blowing over the sea and the air-sea exchange of heat and fresh water. While this forcing is comparatively easy to understand, the ocean's response is more complex. The crucial point to grasp is that the ocean flows take a long time to move any significant distance over the globe and, during that time, the spinning Earth completes many rotations around its axis; for example, even for fast currents, like the Gulf Stream moving at over 1 m s^{-1} , the Earth completes 10 rotations in the time a water parcel takes to travel 1000 km. Consequently, the effects of the Earth's rotation need to be considered in order to understand the motion of any ocean current lasting a day or longer.

In this chapter, we explain how the ocean circulates, responding to accelerations on a rotating planet, in a broadly descriptive manner; accompanying mathematical expressions are summarised in boxes. The physical balances are used to define the different parts of the circulation and relate the interior circulation to the density distribution. Finally, we describe the patterns of atmospheric

forcing, mapping out the variations in wind stress and air-sea fluxes of heat and fresh water over the globe.

4.1 Which forces are important for the ocean circulation?

In order to understand the ocean circulation, it is important to understand how fluid is accelerated by forces. Let's start by considering the external forces and then move onto the apparent forces arising from the Earth's rotation; accompanying mathematical derivations are provided in Appendix A.2.

4.1.1 What are the external forces?

Intuitively, one can expect there to be several forces that are important for a fluid:

- Gravity always acts to accelerate masses towards each other, whether it is raindrops falling towards the ground, water cascading in a breaking wave on the seashore or the orbital movement of the Moon around the Earth. The gravitational acceleration is independent of the mass of the object and, for the Earth, varies inversely with the square of the distance from the centre of the Earth. The gravitational force on an object is then its mass multiplied by the gravitational acceleration.
- Pressure contrasts affect the flow. For fluids, the pressure is defined as the force per unit area against a normal surface, where the force is given by the weight of the overlying fluid. Not

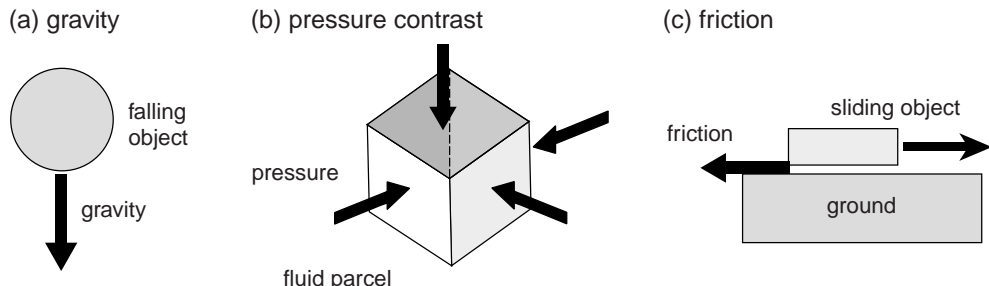


Figure 4.1 A schematic figure denoting examples of external forces: (a) gravity provides a downward acceleration (black arrow) on a falling object towards the Earth; (b) pressure contrasts acting on a parcel of fluid, the pressure (black arrow) is directed inwards on each face of the parcel; and (c) friction (black thick arrow) acts to oppose the movement of an object sliding over the ground.

surprisingly, pressure increases with depth in the ocean, such that if a metal can is dropped in the ocean, the can becomes compressed and crushed as it falls to greater depths and the overlying weight of water becomes greater. Fluid motion depends on the contrast in pressure, such that fluid is accelerated from high to low pressure.

- A frictional force can act either to decelerate moving objects, such as when a book slides across a table or water moves near the sea floor, or conversely to accelerate the flow, such as when the wind blows over a calm lake, exciting waves and the movement of water.

In summary, we expect a fluid to be accelerated (i) by gravity towards a large mass, (ii) from high to low pressure, and (iii) in the direction of a frictional acceleration.

In most everyday situations, these forces are sufficient to explain the motion of a fluid. However, additional forces need to be taken into account to understand the motion on the spinning Earth; these additional forces are important whenever the motion persists long enough for the Earth to rotate a significant distance about its own axis.

4.1.2 What is the effect of rotation?

To understand the effect of rotation, consider an everyday situation of three children playing with a ball in a park, where two of the children, A and C, are standing on the ground in the park, while the other child B is on a spinning merry-go-round (Fig. 4.2a).

Consider what is seen when a ball is thrown from child A to C. From their perspective, there are no surprises: the ball moves in a straight line from A to C (Fig. 4.2b), consistent with our intuition. However, child B sitting on the spinning merry-go-round sees a completely different picture: the ball instead appears to move in a curved path, its velocity changing direction and so being accelerated during its flight (Fig. 4.2c). The apparent acceleration of the moving ball is a consequence of the rotation of the merry-go-round: if the merry-go-round spins in an anticlockwise sense, the moving ball appears to be deflected in a clockwise direction; while if the merry-go-round spins in a clockwise sense, then the ball appears to be deflected in an anticlockwise direction; finally, if the merry-go-round spins faster, then there is a larger apparent deflection.

For the child watching in the rotating frame, there is a real problem in understanding why the ball appears to follow a curved path. During the flight of the ball, no external forces are acting to deflect the horizontal velocity; gravity simply makes the ball fall towards the ground, air resistance slows the ball down, but does not deflect the ball into a curved path, and pressure contrasts in the air are relatively unimportant for the moving ball. Instead, for the child in the rotating frame, the trajectory of the ball can only be explained by invoking *apparent accelerations*, which take into account the rotation of the merry-go-round.

The apparent acceleration of the ball (as seen by the child on the merry-go-round) is made up of two contributions:

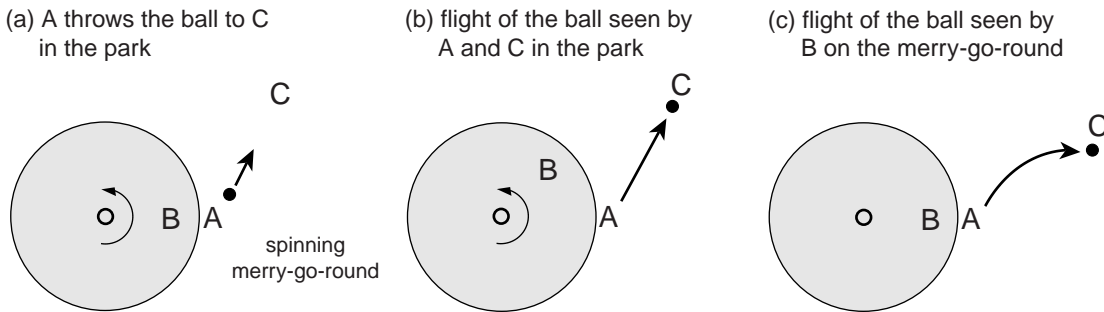


Figure 4.2 A schematic figure depicting why there are apparent accelerations. Consider three children playing with a ball in a park with children A and C standing on the ground and child B on a spinning merry-go-round (grey): (a) initially, A throws a ball towards C and at that instant A and B are alongside each other; while at a later time, (b) and (c), A sees the ball move in a straight line to C (while at the same time, B moves away from A), but conversely, B on the merry-go-round sees the ball moves in a curved path to C.

- The centrifugal acceleration provides an outward acceleration, depending on the distance of the ball from the rotational axis and the rotation rate of the merry-go-round (but is independent of the ball's velocity). This acceleration is always outward, irrespective of which way the merry-go-round spins.
- The Coriolis acceleration, which depends on the velocity of the ball and the rotation rate of the merry-go-round, provides a deflection perpendicular to the velocity of the ball. This deflection is to the right of its motion when the merry-go-round rotates in an anticlockwise sense and to the left when the merry-go-round rotates in a clockwise sense.

Hence, the child in the rotating frame sees the ball accelerated outward by the centrifugal acceleration and deflected perpendicular to its motion by the Coriolis acceleration.

In a similar manner, an observer on the spinning Earth sees the effects of these apparent accelerations for any moving particles. In most everyday situations, the motion usually only persists for a short time and the apparent deflections are not noticeable. However, if the motion lasts for a day or more, then the moving particles appear to be deflected in the same manner as in the merry-go-round example; for a derivation of the apparent accelerations, see Appendix A.2.2.

4.1.3 What are the balances of the forces?

When viewed from the rotating Earth, the atmosphere or ocean is accelerated by a combination

of external forces consisting of gravity, pressure contrasts and friction, as well as by the two apparent accelerations, Coriolis and centrifugal (Box 4.1). To begin with this system appears to be rather difficult to understand, but thankfully in many situations only a few of the forces dominate and for practical purposes can be grouped together:

- In the horizontal plane, the dominant forces are from horizontal pressure contrasts and the apparent Coriolis acceleration, together with frictional stresses near boundaries.
- In the vertical plane, the dominant forces are from gravity and the vertical pressure gradient. The apparent centrifugal acceleration also plays a minor role, deforming the shape of the Earth, which is accommodated by the gravitational acceleration, g , varying with latitude (Appendix A.2.2).

4.2 | How is the surface circulation determined?

Given the forces acting on the ocean, now consider how the surface circulation is determined in relation to observational diagnostics. The surface circulation is revealed by drifters spreading at a typical depth of 15 m over the North Atlantic (Fig. 4.3), highlighting the intense western boundary current, as well as the weaker, broadly clockwise circulation over the basin interior. This surface circulation involves a complicated response

Box 4.1 | The momentum equations

Newton's second law, force equals mass times acceleration, $F = ma$, is used to relate the rate of change of velocity in a fluid to accelerations from gravity, the pressure gradient, friction, Coriolis and centrifugal (derived in Appendix A.2):

$$\frac{Du}{Dt} + 2\Omega w \cos \phi - 2\Omega v \sin \phi + \frac{1}{\rho} \frac{\partial P}{\partial x} = \mathcal{F}_x \quad (4.1a)$$

$$\frac{Dv}{Dt} + 2\Omega u \sin \phi + \frac{1}{\rho} \frac{\partial P}{\partial y} = \mathcal{F}_y \quad (4.1b)$$

$$\underbrace{\frac{Dw}{Dt} + g}_{\text{local acceleration}} - \underbrace{2\Omega u \cos \phi}_{\text{centrifugal}} + \underbrace{\frac{1}{\rho} \frac{\partial P}{\partial z}}_{\text{pressure gradient}} = \underbrace{\mathcal{F}_z}_{\text{friction}} \quad (4.1c)$$

where the velocity (m s^{-1}) is separated into components u , v and w in the eastward x , northward y and vertical z directions; D/Dt represents the rate of change following the flow (s^{-1}), g represents the gravitational acceleration (m s^{-2}) including the attraction of masses to each other and a weaker contribution from the centrifugal acceleration, $\Omega = 2\pi/\text{day}$ is the angular velocity of the Earth (s^{-1}), ϕ is latitude, P is pressure ($\text{N m}^{-2} = \text{kg m}^{-1} \text{s}^{-2}$), ρ is density (kg m^{-3}) and \mathcal{F} represents the frictional acceleration (m s^{-2}).

For large-scale ocean and atmospheric flows, there are two important simplifying approximations to these momentum equations:

(a) The vertical velocity is relatively small compared with the horizontal velocity, such that terms involving w can be ignored ($2\Omega w \cos \phi$ and Dw/Dt). In the vertical component, the dominant remaining terms in (4.1c) lead to a hydrostatic balance,

$$\frac{\partial P}{\partial z} = -\rho g, \quad (4.2)$$

with the vertical pressure gradient balancing the gravitational acceleration.

(b) The slowness of the large-scale motion leads to the local accelerations, Du/Dt and Dv/Dt , being relatively small, so that there is a three-way balance between the Coriolis acceleration, the horizontal pressure gradient and frictional acceleration in (4.1a,b) in the horizontal plane,

$$-fv + \frac{1}{\rho} \frac{\partial P}{\partial x} = \frac{1}{\rho} \frac{\partial \tau_x}{\partial z}, \quad (4.3a)$$

$$fu + \frac{1}{\rho} \frac{\partial P}{\partial y} = \frac{1}{\rho} \frac{\partial \tau_y}{\partial z}, \quad (4.3b)$$

where the Coriolis parameter is $f = 2\Omega \sin \phi$ in s^{-1} and the frictional acceleration is written in terms of a vertical gradient of a frictional stress, τ (N m^{-2}).

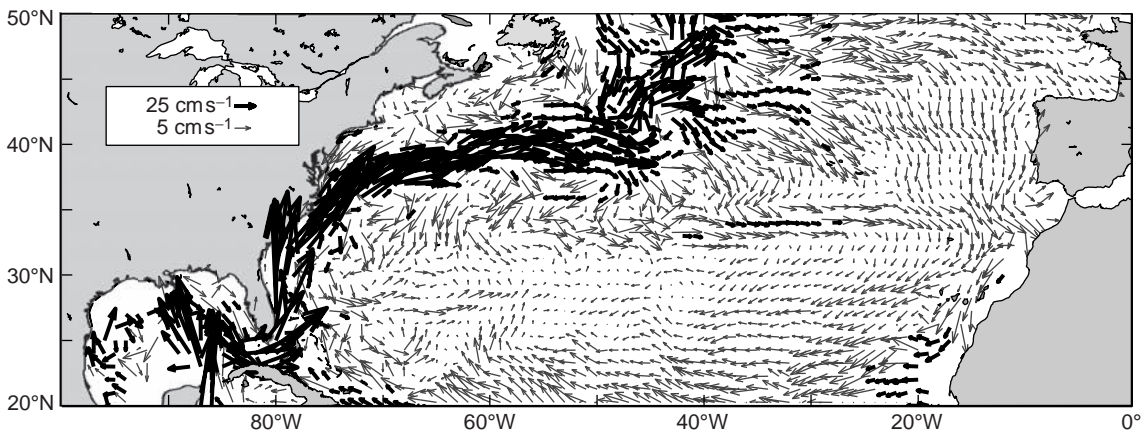
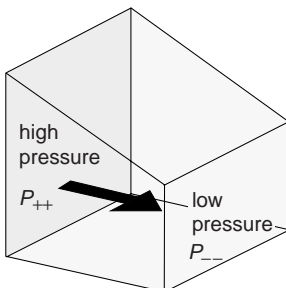


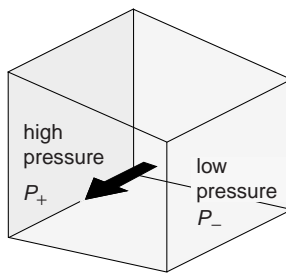
Figure 4.3 Time-mean velocity of surface drifters (cm s^{-1}) in the subtropical North Atlantic from October 1989 to April 2004: a separate scale is used for velocities exceeding 10 cm s^{-1} with velocities greater or less than 10 cm s^{-1} denoted by dark or light vectors, respectively. Courtesy of Rick Lumpkin; for full details of these Lagrangian measurements, see Lumpkin and Pazos (2006).

(a) initial response to a pressure contrast



initial flow $u > 0$

(b) response after several days



geostrophic flow $v < 0$

Figure 4.4 A schematic figure displaying (a) the initial response to a pressure contrast within a fluid (represented by a different thickness in the fluid), where the flow moves from high to low pressure and this redistribution of mass acts to reduce the pressure contrasts; (b) the counterintuitive response after a day or longer, where the flow is directed parallel to the pressure contours with high pressure to the right in the northern hemisphere. This flow along the pressure contours is referred to as the geostrophic flow.

to the action of the surface wind stress and horizontal pressure gradient, which is constrained by the rotation of the planet. Accordingly, the surface circulation can be separated into different components, each defined by their own dynamical balance: a geostrophic component related to a balance between the Coriolis acceleration and pressure gradient; and an Ekman component related to a balance between the Coriolis acceleration and the effect of the wind stress. Now consider each of these components in turn.

4.2.1 Geostrophic balance

Start by considering how water flows in response to a pressure contrast, such as formed by water piling up on one side of a bath or ocean basin. After this pressure contrast is created, the water naturally responds by starting to move from high

to low pressure (Fig. 4.4a). Within a bath, this adjustment takes a few seconds and the water surface quickly becomes flat, the pressure contrast disappears and the flow ceases.

Within the ocean, the adjustment process usually takes much longer, requiring perhaps many days for the water to move from a region of high to low pressure. Consequently, when viewed from the rotating Earth, the moving water appears to become deflected by an apparent acceleration, the Coriolis acceleration, directed to the right of flow in the northern hemisphere and to the left in the southern hemisphere (as in the merry-go-round example in Fig. 4.2). This deflection then leads to the water moving parallel to pressure contours (Fig. 4.4b), rather than moving from high to low pressure; the same balance occurs in the atmosphere with air moving along pressure contours.

Box 4.2 | How does fluid move in response to pressure contrasts?

How fluid responds to a pressure gradient on a rotating planet can be defined in terms of the relative size of the local accelerations, Du/Dt and Dv/Dt , and the Coriolis accelerations, $-fv$ and fu , as measured by the non-dimensional Rossby number,

$$Ro \equiv \frac{U}{fL}, \quad (4.4)$$

where U is the typical magnitude of the horizontal velocity, L is the typical horizontal length scale and f is the Coriolis parameter. To understand the different regimes, for simplicity, assume that frictional accelerations are neglected.

(a) For most everyday situations, such as throwing a ball in a park or water moving in a bath, the motion lasts only for a few seconds and the Coriolis acceleration from the Earth's rotation is unimportant (as the Earth has not rotated far in such a short time); this regime is defined by the Rossby number being large, $Ro \gg 1$. In this case, the Coriolis acceleration is relatively small and the horizontal momentum equations (4.1a,b), with friction neglected, reduce to

$$\frac{Du}{Dt} + \frac{1}{\rho} \frac{\partial P}{\partial x} \simeq 0,$$

$$\frac{Dv}{Dt} + \frac{1}{\rho} \frac{\partial P}{\partial y} \simeq 0,$$

and fluid is accelerated from high to low pressure.

(b) For timescales of a day or longer, the Coriolis acceleration becomes important due to the significant rotation of the Earth during that time; this regime is defined by the Rossby number being relatively small, $Ro \ll 1$. The horizontal momentum equations (4.1a,b), with friction neglected, instead reduce to a geostrophic balance,

$$-fv + \frac{1}{\rho} \frac{\partial P}{\partial x} \simeq 0,$$

$$fu + \frac{1}{\rho} \frac{\partial P}{\partial y} \simeq 0,$$

where fluid moves along pressure contours (high P to right of motion where $f > 0$), rather than from high to low pressure. This geostrophic balance is used to infer the large-scale circulation from the pressure field.

This geostrophic velocity is defined by this balance between the pressure gradient and Coriolis acceleration (Box 4.2), as given by

$$u_g = -\frac{1}{\rho f} \frac{\partial P}{\partial y}, \quad (4.5a)$$

$$v_g = \frac{1}{\rho f} \frac{\partial P}{\partial x}, \quad (4.5b)$$

where u_g and v_g are the eastward and northward geostrophic velocities (m s^{-1}), ρ is density

(kg m^{-3}) and P is the pressure (N m^{-2}). The Coriolis parameter is defined by $f = 2\Omega \sin \phi$ in s^{-1} , where $\Omega = 2\pi/\text{day}$ is the angular velocity and ϕ is the latitude: f increases poleward with latitude, ranging from 2Ω at the North Pole, 0 at the equator and -2Ω at the South Pole. The units of (4.5a,b) are given by

$$\text{m s}^{-1} = \frac{\text{N m}^{-2}}{(\text{kg m}^{-3})(\text{s}^{-1})(\text{m})},$$

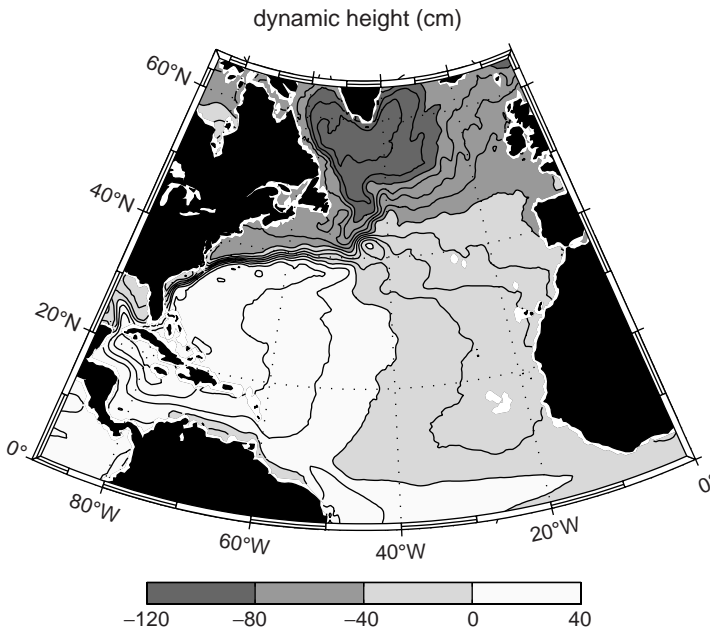


Figure 4.5 Map of dynamic height (contours with an interval of 10 cm) for the North Atlantic (with a Lambert projection). The surface geostrophic flow is aligned along dynamic height contours with high dynamic height to the right of the motion in the northern hemisphere. Ocean mean dynamic height was taken from a combined dataset integrating information from surface drifters, satellite altimetry, surface winds and the GRACE gravity mission (Niiler et al., 2003; Maximenko and Niiler, 2005).

which are equivalent (remembering $N \equiv \text{kg m s}^{-2}$).

The geostrophic flow is directed along pressure contours with high pressure to the right of the motion in the northern hemisphere and reversing to the left of the motion in the southern hemisphere. For example, in the northern hemisphere, there is an eastward geostrophic flow when pressure decreases northward, $\partial P / \partial y < 0$, and a southward geostrophic flow when pressure decreases eastward, $\partial P / \partial x < 0$ (Fig. 4.4b); in both these cases, high pressure is to the right of the flow. This geostrophic flow represents the dominant contribution to the time-mean velocity of the surface drifters in Fig. 4.3.

Dynamic height

For the ocean, the geostrophic flow (4.5a,b) can equivalently be defined in terms of the horizontal gradient in dynamic height, η , in m:

$$u_g = -\frac{g}{f} \frac{\partial \eta}{\partial y},$$

$$v_g = \frac{g}{f} \frac{\partial \eta}{\partial x},$$

where the dynamic height represents the vertical displacement of a pressure surface above a refer-

ence surface called the geoid (a surface of constant gravitational acceleration).

Geostrophic currents flow along contours of dynamic height with higher dynamic height to the right of the flow in the northern hemisphere. For example, a map of dynamic height over the North Atlantic (Fig. 4.5) reveals the broadly clockwise circulation over the mid latitudes (10°N to 40°N) changing to an anticlockwise circulation at higher latitudes (40°N to 65°N). The flow strengthens when contours of dynamic height are closely spaced, as occurring along the Gulf Stream and its extension into the basin (30°N to 40°N).

4.2.2 Ageostrophic and Ekman flow

While the ocean circulation is often close to the geostrophic flow, there are other contributions to the flow, collectively referred to as ageostrophic flow (denoted by subscript ag) as defined by the difference between the actual flow and the geostrophic flow:

$$u = u_g + u_{ag},$$

$$v = v_g + v_{ag}.$$

The ageostrophic contributions are associated with frictional acceleration and local accelerations; these ageostrophic contributions can

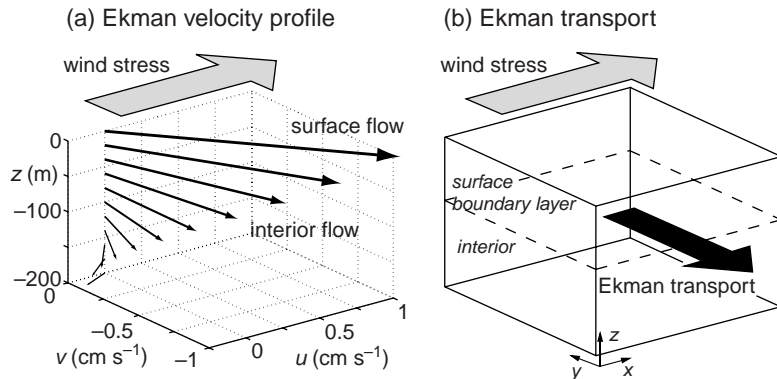


Figure 4.6 The effect of the wind stress on the interior flow: (a) the Ekman velocity rotates and weakens with depth. Theory suggests that the surface velocity is at 45° to the right of the wind stress and spirals in a clockwise manner in the northern hemisphere; (b) the surface stress drives a horizontal Ekman transport within a thin surface boundary layer, directed to the right of the wind in the northern hemisphere. In (a), the velocity profile is calculated for an eastward wind stress, $\tau_x^s = 0.1 \text{ N m}^{-2}$, and an interior stress assumed to follow $\tau = \rho A_v \partial \mathbf{u} / \partial z$ with a constant eddy viscosity, $A_v = 0.5 \text{ m}^2 \text{ s}^{-1}$ and $f = 10^{-4} \text{ s}^{-1}$, using $u(z) = u_0 e^{z/d} \cos(z/d - \pi/4)$ and $v(z) = u_0 e^{z/d} \sin(z/d - \pi/4)$ with $u_0 = \sqrt{2\tau_x^s}/(\rho f d)$ and $d = (2A_v/f)^{1/2}$ is taken as the thickness of the Ekman layer; see Vallis (2006) for further details of the analytical solution.

equivalently be defined by the terms in (4.1a,b) which have been neglected in forming the geostrophic balance (4.5a,b). The most important ageostrophic contribution involves the frictional acceleration imparted at the boundary, involving either a wind stress from air moving over the ocean or a bottom stress from fluid moving over the sea floor.

Focussing on the surface ocean, the wind stress at the sea surface is communicated by turbulent mixing over a thin boundary layer and drives an ageostrophic velocity, called the Ekman velocity,

$$u_{ek} = \frac{1}{\rho f} \frac{\partial \tau_y}{\partial z}, \quad (4.6a)$$

$$v_{ek} = -\frac{1}{\rho f} \frac{\partial \tau_x}{\partial z}, \quad (4.6b)$$

where u_{ek} and v_{ek} are the eastward and northward Ekman velocities, and τ_x and τ_y represent the frictional and turbulent stresses acting within the water column (N m^{-2}), directed eastward and northward.

The Ekman velocity is defined by a balance between the frictional acceleration and the Coriolis acceleration (from (4.3a,b) in Box 4.1). The frictional acceleration depends on the vertical gradient in stress and drives an Ekman velocity to the right of the stress in the northern hemisphere. Assuming a simple form as to how the stress varies

with depth suggests that the Ekman velocity spirals and weakens with depth (Fig. 4.6a).

The effect of this frictional deflection was first reported by Fridtjof Nansen who, while in his ship, the *Fram*, trapped in the Arctic ice, noticed how icebergs drifted 20° to 40° to the right of the wind; the mathematical description of the velocity spiral providing this drift was subsequently provided by Vagn Ekman in 1902. The details of the predicted velocity spiral (such as in Fig. 4.6a) are rarely seen though, only appearing under calm conditions under sea ice or when long time averages are applied to velocity profile measurements.

Ekman transport

While the details of the Ekman velocity profile are difficult to verify, there is a robust relationship between the wind stress and the depth integral of the Ekman velocities given by

$$U_{ek} \equiv \int_{-D}^0 u_{ek} dz = \frac{\tau_y^s}{\rho f}, \quad (4.7a)$$

and

$$V_{ek} \equiv \int_{-D}^0 v_{ek} dz = -\frac{\tau_x^s}{\rho f}, \quad (4.7b)$$

where U_{ek} and V_{ek} represent the Ekman volume flux per unit length, having units of $\text{m}^2 \text{ s}^{-1}$ from the depth integral of velocity, and D represents the

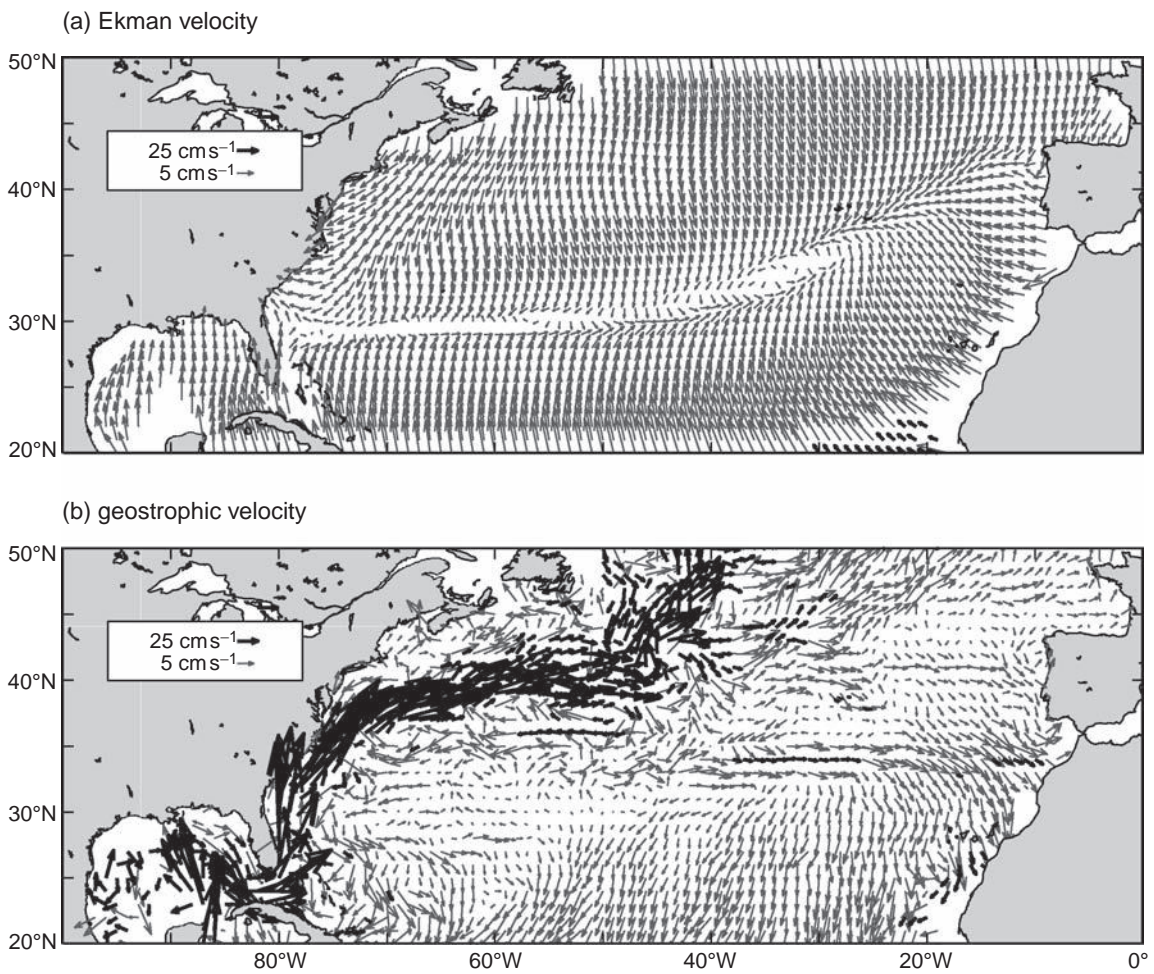


Figure 4.7 Time-mean velocity (cm s^{-1}) of surface drifters (as in Fig. 4.3) separated into (a) an Ekman component predicted from the wind stress and (b) a geostrophic component from the difference between the time-mean velocity and the Ekman velocity. Courtesy of Rick Lumpkin; for further details, see Lumpkin and Pazos (2006).

thickness of the surface boundary layer, extending from the surface to a depth of several tens of metres to 100 m. An Ekman transport in $\text{m}^3 \text{s}^{-1}$ is then given by the horizontal integral of the Ekman volume flux, which is directed at right angles to the imposed wind stress (Fig. 4.6b): an eastward wind stress, $\tau_x^s > 0$, imparts an equatorward transport, $V_{ek} < 0$, and a northward wind stress, $\tau_y^s > 0$, imparts an eastward transport, $u_{ek} > 0$, in the northern hemisphere.

North Atlantic drifter example

Returning to the drifter trajectories over the North Atlantic (Fig. 4.3), their average velocities can be separated into Ekman and geostrophic velocity

components; the Ekman component is diagnosed from the surface winds, assuming a simple form for how the stress is communicated (as in Fig. 4.6a). The Ekman drift of the drifters, as depicted in Fig. 4.7a, varies from southward along the northern flank of the subtropical gyre, where there is an eastward wind stress, to northward along its southern flank, where there is a westward wind stress. There is a stronger geostrophic velocity over much of the subtropical gyre, revealing again a clockwise circulation and an intense western boundary current (Fig. 4.7b).

Ekman upwelling along the coast

The wind stress also drives vertical motion, referred to as Ekman upwelling or downwelling:

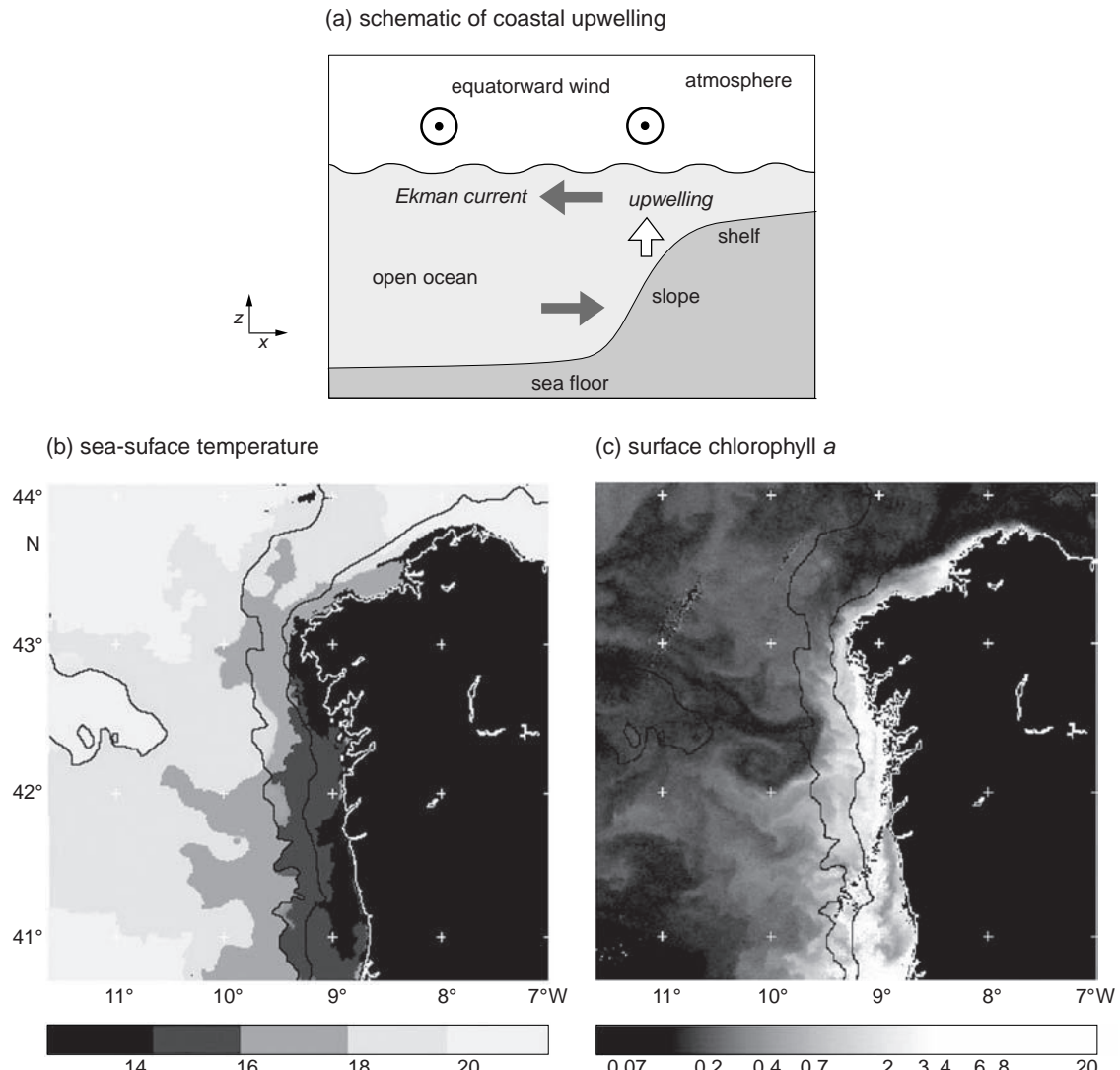


Figure 4.8 (a) A schematic figure of the Ekman upwelling; satellite pictures off Spain during an upwelling event on 3 August 1998 for (b) sea-surface temperature ($^{\circ}\text{C}$) and (c) chlorophyll a (mg m^{-3}) revealing surface cold, nutrient-rich waters off the coast supporting elevated concentrations of phytoplankton. Satellite measurements courtesy of Steve Groom, NEODASS, Plymouth.

upwelling occurs whenever there is horizontal divergence, defined by when the horizontal volume flux leaving the surface boundary layer is greater than that entering (discussed further in Section 10.2.3).

This effect of the winds in driving upwelling is particularly apparent along the coast. Along an eastern boundary, an equatorward wind drives an offshore Ekman transport (Fig. 4.8a). This water swept offshore has to be supplied somehow and the only option is for cold, deep water to be

upwelled along the coast; as evident in surface waters off the western coast of Spain being relatively cold and nutrient-rich and, thus, supporting high concentrations of phytoplankton (Fig. 4.8b,c). If the winds change to poleward, there is instead an onshore transport and downwelling along the eastern boundary. In a similar manner, along the western boundary, there is an offshore Ekman transport and upwelling for a poleward wind, and an onshore Ekman transport and downwelling for an equatorward wind.

Table 4.1 Variation of potential temperature, *in situ* and potential density with temperature and pressure for a salinity of 35 g kg⁻¹.

Temperature <i>T</i> (°C)	Pressure <i>P</i> (mbar)	Potential temperature θ (°C)	<i>In situ</i> density –1000 kg m ⁻³ σ (kg m ⁻³)	Potential density –1000 kg m ⁻³ σ_θ (kg m ⁻³)
20	0	20	24.8	24.8
10	0	10	27.0	27.0
5	0	5	27.7	27.7
5	2000	4.8177	36.7	27.7
5	4000	4.5828	45.4	27.7

4.3 How is the interior circulation determined?

Given how the surface flow is affected by pressure contrasts and surface stresses, now consider the deep, interior flow. Frictional stresses are confined to surface, bottom and side boundaries, so are relatively unimportant for much of the ocean interior. Instead the deeper flow is affected primarily by how the horizontal pressure gradients vary with depth, which themselves alter with changes in density. Consequently, we now consider how density and pressure vary with depth, and their relationship to the interior flow.

4.3.1 How does density vary with depth?

Density is defined as the mass per unit volume. *In situ* density, ρ , is the locally measured density and increases with increasing pressure, P , decreasing temperature, T , and increasing salinity, S (Table 4.1). The weight of overlying water compresses water at depth, increasing *in situ* density, which even reaches 1070 kg m⁻³ in the deepest part of the world's ocean, the Mariana Trench (Fig. 4.9a).

Potential density provides a pressure-corrected measure of density (Table 4.1), so at the base of the same trench, the potential density referenced to the sea surface only reaches 1028 kg m⁻³ (Fig. 4.9c). These two definitions of density serve different purposes: *in situ* density is the correct density to use when calculating the weight of the fluid, while potential density (or its more accurate relation, a neutral density surface) is the appropriate vari-

able to employ when inferring how water masses spread (Box 4.3).

4.3.2 How does pressure vary with depth?

The weight of the overlying fluid always leads to pressure increasing with depth, as described by the hydrostatic balance (4.2),

$$\frac{\partial P}{\partial z} = -\rho g,$$

where P is in N m⁻², z in m, ρ in kg m⁻³ and g in m s⁻². This background increase in pressure with depth is by itself unimportant for the circulation, since the geostrophic flow depends on horizontal gradients in pressure.

Crucially, there is a larger pressure increase with depth in dense water than in light water, since the overlying weight is greater in dense water. Hence, horizontal gradients in density lead to horizontal gradients in pressure changing with depth.

4.3.3 How does the geostrophic flow vary with depth?

The geostrophic flow depends on horizontal pressure gradients. Given how the depth variation in pressure alters with density, the vertical shear in geostrophic velocity depends on horizontal density gradients (see Q4.2):

$$\frac{\partial u_g}{\partial z} = \frac{g}{\rho f} \frac{\partial \rho}{\partial y}, \quad (4.8a)$$

$$\frac{\partial v_g}{\partial z} = -\frac{g}{\rho f} \frac{\partial \rho}{\partial x}. \quad (4.8b)$$

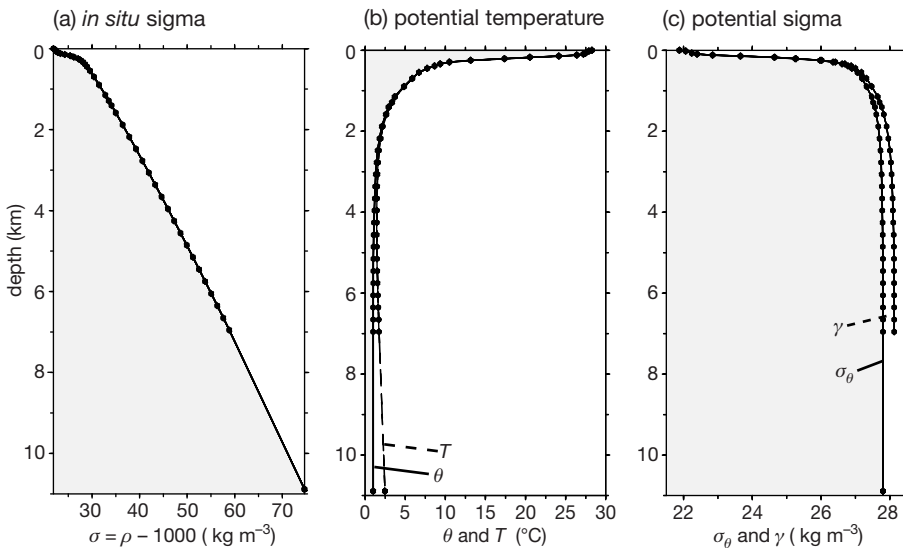


Figure 4.9 Vertical profiles of (a) *in situ* density minus 1000 kg m^{-3} , (b) potential and *in situ* temperature, θ and T ($^{\circ}\text{C}$), and (c) potential density referenced to the sea surface minus 1000 kg m^{-3} , σ_θ , and neutral density, γ (kg m^{-3}), in the deepest part of the ocean (a depth of 10924 m) in the Mariana Trench of the North Pacific (142.167°E , 11.333°N) evaluated from the Pacific Ocean database collated by J. L. Reid and A. W. Mantyla. The weight of overlying fluid compresses the fluid leading to an increase in the *in situ* density with depth in (a), as well as a slight increase in the *in situ* temperature with depth in (b). This adiabatic warming is accounted for by using potential temperature, θ . In (c), the vertical variations in potential density are much smaller than that of *in situ* density, taking into account the compression of water with depth. The neutral density surface, γ , usually closely follows that of potential density, differing for large depth excursions.

The units of the equation are given by

$$\frac{(\text{m s}^{-1})}{\text{m}} \sim \frac{(\text{m s}^{-2})}{(\text{kg m}^{-3})(\text{s}^{-1})} \frac{(\text{kg m}^{-3})}{(\text{m})},$$

simplifying to s^{-1} on each side. In the northern hemisphere, a northward increase in density implies that the eastward component of the geostrophic flow becomes stronger towards the surface (4.8a), while an eastward increase in density implies that the southward component of the geostrophic flow becomes stronger towards the surface (4.8b) (Fig. 4.10). These inferred flow directions reverse in the southern hemisphere with the change in sign of the Coriolis parameter.

This balance (4.8a,b) is referred to as thermal wind, reflecting its application in the atmosphere where the vertical shear in horizontal velocity is controlled by horizontal temperature gradients, as seen in how the eastward moving Jet Stream depends on the poleward decrease in air temperature.

These vertical shear relations (4.8a,b) form the basis of historical observational attempts to infer the circulation, where the geostrophic flow at a depth z is related to that at a constant reference depth, z_{ref} , by

$$u_g(z) = u_g(z_{ref}) + \frac{g}{\rho f} \int_{z_{ref}}^z \frac{\partial \rho}{\partial y} dz, \quad (4.9a)$$

$$v_g(z) = v_g(z_{ref}) - \frac{g}{\rho f} \int_{z_{ref}}^z \frac{\partial \rho}{\partial x} dz. \quad (4.9b)$$

Thus, the geostrophic flow across a section can be inferred from a depth integration of the horizontal density gradients along the section, subject to reference velocities, $u_g(z_{ref})$ and $v_g(z_{ref})$, being either measured independently or assumed. The choice of the reference velocity only makes a slight difference to the surface velocity, but can significantly alter the volume transport when integrated with depth over the water column.

Now consider this thermal-wind method applied across the subtropical North Atlantic.

Box 4.3 | Equation of state, density and salinity

In situ density, ρ , is the locally measured density and is related to the *in situ* temperature, salinity and pressure through an empirical equation of state,

$$\rho = \rho(P, T, S), \quad (4.10)$$

where ρ increases with increasing pressure, P , decreasing temperature, T , and increasing salinity, S , as illustrated in Table 4.1; σ is used as a convenient shorthand, such that $\sigma_T = \rho - 1000 \text{ kg m}^{-3}$. Density nearly always increases with depth, due to the increasing weight of the fluid, which slightly compresses the fluid (Fig. 4.9a). In turn, the *in situ* density alters the weight of the overlying fluid and, thus, how pressure varies with depth in (4.2).

Salinity has traditionally been defined in terms of the number of grams of salt per kilogram of seawater (g kg^{-1}), as well as defined in terms of a practical salinity based on the conductivity of seawater. Absolute salinity is now the recommended choice, defined by the concentration of dissolved material in seawater in g kg^{-1} , which more exactly relates to the thermodynamic properties of seawater (McDougall et al., 2009).

The change in density, $\Delta\rho$, at a particular depth may be related to the change in temperature, ΔT , and salinity, ΔS , using a linearised version of the equation of state,

$$\Delta\rho/\rho = -\alpha_T \Delta T + \beta_S \Delta S, \quad (4.11)$$

where the density expansion coefficient for temperature is $\alpha_T = -\frac{1}{\rho} \frac{\partial \rho}{\partial T}$ and the density contraction coefficient for salinity is $\beta_S = \frac{1}{\rho} \frac{\partial \rho}{\partial S}$.

Potential density is a pressure-corrected density, defined as the density of a fluid parcel after moving adiabatically (without any heat exchange) from its depth to a reference depth; the corresponding σ_θ is the potential density minus 1000 kg m^{-3} . Fluid parcels approximately move along potential density surfaces when there is adiabatic motion and there are limited depth changes, so this surface is useful to denote how water masses spread. However, the non-linearity of the equation of state (4.10) means that fluid parcels do not exactly follow potential density surfaces if there are large depth excursions.

Instead, fluid parcels more closely follow neutral density surfaces during adiabatic motion; these surfaces can be viewed as a continuous analogue of potential density referenced to a discrete set of reference depths (Jackett and McDougall, 1997).

Gulf Stream and North Atlantic example

Over the North Atlantic subtropical gyre, there is a westward deepening of potential density surfaces, which is particularly pronounced in the upper 1 km of the water column (Fig. 4.11). This westward decrease in density, $\partial\rho/\partial x > 0$, implies a negative velocity shear, $\partial v_g/\partial z < 0$, from (4.8b). Assuming that the deep flow is weak and approaches zero, then this vertical shear implies that the upper waters are moving southward in the interior. Con-

versely, along the western boundary, there is a pronounced westward shallowing of potential density surfaces, with $\partial\rho/\partial x < 0$ implying $\partial v_g/\partial z > 0$ and the upper flow is directed northward across the section.

Now estimate the northward velocity in the Gulf Stream along the western boundary from the west-east density gradient at 36°N using (4.9b),

$$\Delta v_g \sim -\frac{g}{\rho f} \frac{\Delta\rho}{\Delta x} \Delta z.$$

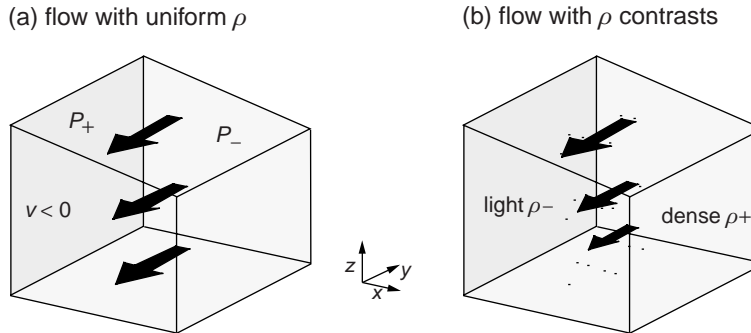


Figure 4.10 A schematic figure displaying how the geostrophic flow varies with depth for (a) uniform density where the flow and horizontal pressure gradient do not vary with depth, and (b) with a horizontal density contrast where the flow is decreasing with depth. For this example, a southward flow is depicted with surface pressure decreasing to the east and, in (b), the density is assumed to increase to the east leading to this flow weakening with depth.

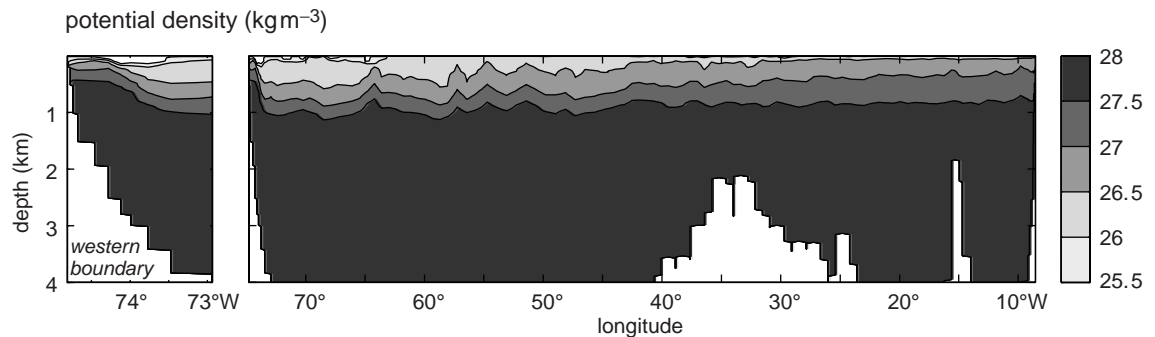


Figure 4.11 Zonal section along 36°N for potential density referenced to the sea surface, σ_{θ} (kg m^{-3}), in the North Atlantic in May 2005 for the western boundary (left panel) and the entire basin (right panel) over the upper 4 km. There is a general westward deepening of the isopycnals over the upper 1 km, together with a rapid shoaling along the western boundary.

Assuming a horizontal density contrast, $\Delta\rho \sim -1 \text{ kg m}^{-3}$ over an east–west distance $\Delta x \sim 100 \text{ km}$ and a depth change $\Delta z \sim 1 \text{ km}$ implies a change in the northward velocity over this depth range of typically

$$\Delta v_g \sim -\frac{(10 \text{ m s}^{-2})(-1 \text{ kg m}^{-3}) (10^3 \text{ m})}{(10^3 \text{ kg m}^{-3})(10^{-4} \text{ s}^{-1})(10^5 \text{ m})} \\ \sim 1 \text{ m s}^{-1},$$

where $f \sim 10^{-4} \text{ s}^{-1}$. This northwards velocity estimate is in accord with the measured geostrophic flow reaching between 1 and 2 m s^{-1} in the surface core of the Gulf Stream (Fig. 4.12).

Volume transport

The associated meridional volume transport crossing a zonal section is given by

$$\int_{x_1}^{x_2} \int_{z_1}^{z_2} v \, dx dz,$$

where x_1, x_2 and z_1, z_2 represent the longitude and depth ranges of the integration; the units of volume transport are given by the product of velocity (m s^{-1}) with cross-sectional area (m^2), thus, volume per second ($\text{m}^3 \text{ s}^{-1}$) and usually expressed in sverdrups ($1 \text{ Sv} \equiv 10^6 \text{ m}^3 \text{ s}^{-1}$).

This integration can be performed in different ways to reveal either the strength of the meridional overturning circulation or the horizontal recirculation:

- The overturning is estimated if the integration is applied from the surface to a mid depth (typically 1500 m) and over the entire width of the basin. For this 36°N section in Fig. 4.11, there is a northward, upper ocean transport reaching 18 Sv, which is returned southward in the deeper ocean.
- The horizontal circulation is estimated if the integration is performed over the full depth

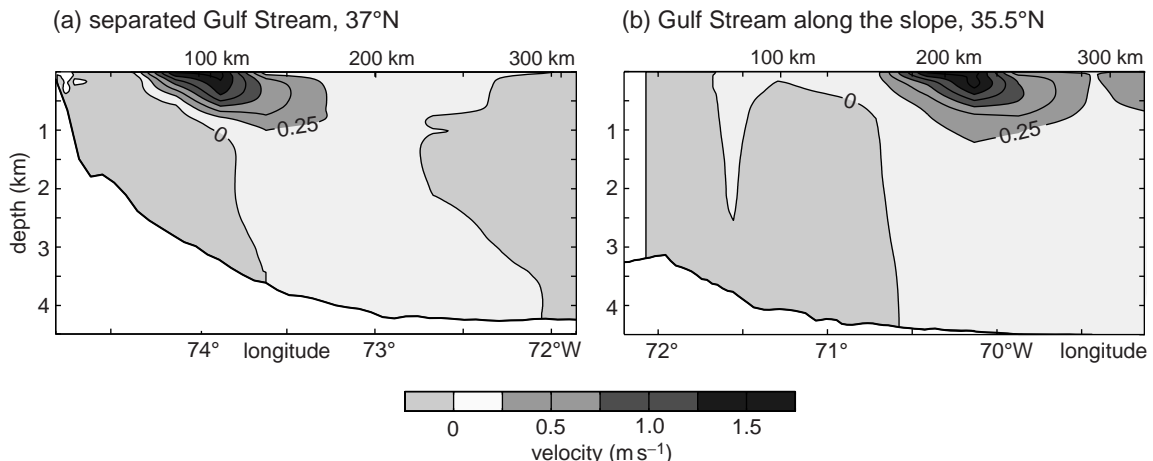


Figure 4.12 Northward geostrophic velocity (m s^{-1}) associated with (a) the Gulf Stream having separated from the coast at 37°N , and (b) the Gulf Stream running along the continental slope at 35.5°N . Data collected in May 2005; velocity data supplied by Elaine McDonagh.

range and the width of the basin interior, but excluding the western boundary. Again for the 36°N section, there is a southward, interior gyre transport reaching -50 Sv , which is returned northward as part of the Gulf Stream in the western boundary.

These transport estimates from ocean sections provide one of the key foundations of physical oceanography. There are, though, uncertainties in calculating the reference velocity and in how representative a single section is, given the seasonal and inter-annual variability in the ocean. This approach can be extended to provide the transport of associated properties, such as heat, nutrients and carbon, by melding the velocity measurements with coincident property measurements.

4.4 Global-scale patterns of atmospheric forcing

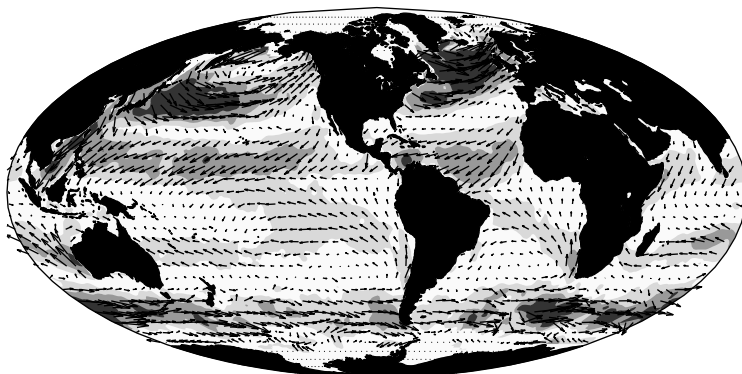
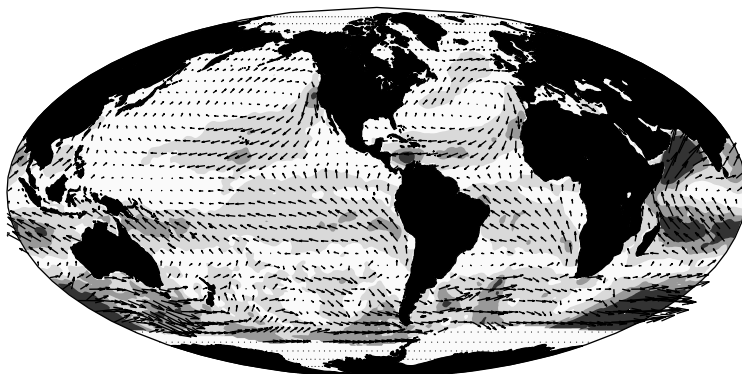
Given the preceding discussions of the physical balances in the ocean, we now return to the surface and consider the patterns of the large-scale atmospheric forcing, which ultimately drive nearly all the circulation over the globe.

4.4.1 Surface circulation and wind forcing

The atmospheric winds provide the most important forcing for the surface circulation. There is a characteristic pattern of easterly Trade winds in the tropics and westerly winds at mid latitudes (Fig. 4.13a,b). This pattern of winds provides a surface torque, a twisting force, which drives recirculations in the ocean basins between the continents, referred to as gyres, as revealed in the nearly closed contours for dynamic height (Fig. 4.13c). Over the Southern Ocean, the winds provide a momentum input driving an eastward transport in the Antarctic Circumpolar Current, as revealed in the tightly spaced contours for dynamic height (with high values of dynamic height to the left of the flow).

There is a strong seasonal cycle in the surface winds: the pole-equator temperature contrast in the atmosphere is much greater in winter, leading to a stronger eastward flow in the upper atmosphere (from thermal-wind balance), with a more vigorous Jet Stream and more frequent mid-latitude storms. Accordingly, this seasonal strengthening of the winds leads to a stronger surface stress and torque being imparted to the ocean in winter, compared with in summer (Fig. 4.13a,b).

Now consider the global patterns for the surface fluxes of heat and fresh water.

(a) January wind stress (N m^{-2})(b) July wind stress (N m^{-2})

(c) dynamic height (cm)

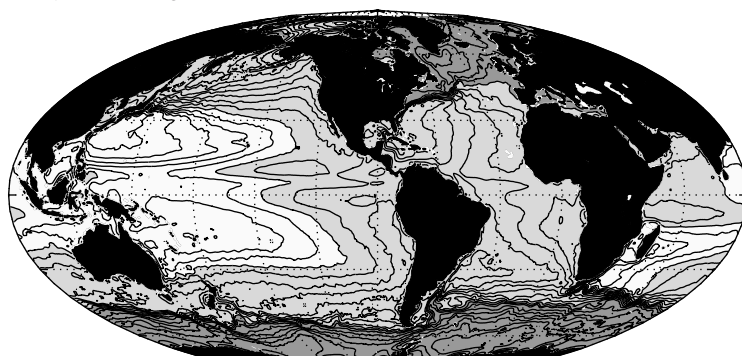
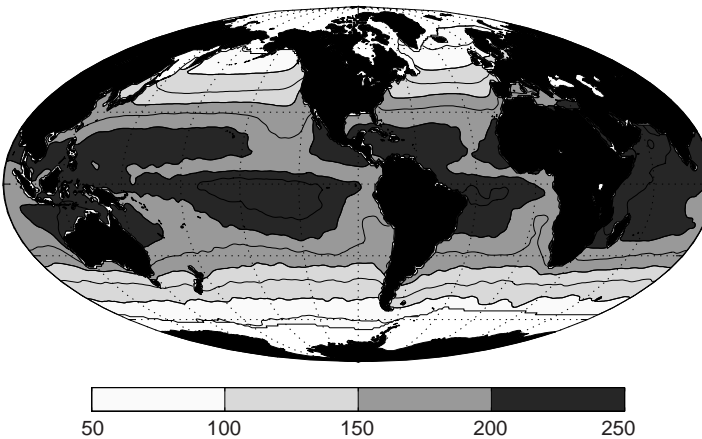
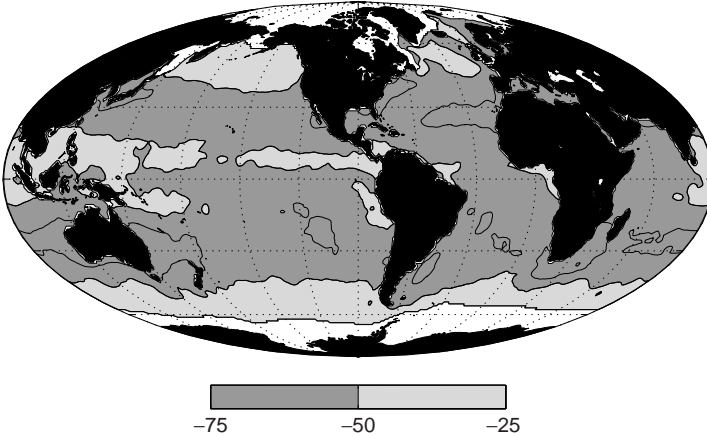


Figure 4.13 Global maps of surface-wind stress (N m^{-2}) for (a) January and (b) July from the NOCS climatology (Josey *et al.*, 2002), with (c) ocean mean dynamic height (contours with an interval of 10 cm and increased to 20 cm over the Southern Ocean); dynamic height details are given in Fig. 4.5 (Niiler *et al.*, 2003; Maximenko and Niiler, 2005). There is a much stronger wind-stress forcing (darker shading) in the winter hemisphere, reflecting the effect of the overlying jet stream and the pole-equator temperature gradient being stronger in winter. The surface geostrophic flow is aligned along dynamic height contours with high dynamic height to the right of the motion in the northern hemisphere.

(a) annual-mean solar flux (W m^{-2})(b) annual-mean long-wave heat flux (W m^{-2})

4.4.2 Air-sea exchange of heat

The surface heat flux into the ocean has several components,

$$\mathcal{H} = \mathcal{H}_{\text{solar}} + \mathcal{H}_{\text{long}} + \mathcal{H}_{\text{latent}} + \mathcal{H}_{\text{sensible}}, \quad (4.12)$$

where the heat flux is defined by rate of energy supply per unit area, so the units are in energy per unit area and time, $\text{J m}^{-2} \text{s}^{-1} = \text{W m}^{-2}$, and the subscript identifies each component. The solar component, $\mathcal{H}_{\text{solar}}$, represents the radiative heat flux from the incoming solar radiation minus that reflected. This net solar heat input at the sea surface ranges from 250 W m^{-2} in the tropics to 50 W m^{-2} over the high latitudes when averaged over the year (Fig. 4.14a). This differential solar

Figure 4.14 Annual-mean surface maps of (a) net solar heat flux from incoming minus reflected (contours every 25 W m^{-2}), and (b) net long-wave or infrared heat flux from incoming minus outgoing (contours every 12.5 W m^{-2}) from the NOCS climatology (Josey et al., 1999). Positive values represent a heat flux into the ocean and polar regions have no data (white).

heating over the globe is the powerhouse of the atmosphere and ocean, driving a physical circulation that redistributes heat over the globe. The long-wave component, $\mathcal{H}_{\text{long}}$, represents the radiative heat flux over the range of wavelengths emitted from the sea surface, dominated by infrared radiation; the sign is again defined by incoming minus outgoing radiation, so that $\mathcal{H}_{\text{long}}$ is negative. The net outgoing long-wave radiation, $\mathcal{H}_{\text{long}}$, typically only reaches from -25 to -75 W m^{-2} (Fig. 4.14b), much smaller than the net solar heat input.

Hence, the radiative flux from the sum of these two components, $\mathcal{H}_{\text{solar}} + \mathcal{H}_{\text{long}}$, is directed into the ocean, varying from nearly 200 W m^{-2} in the tropics to less than 50 W m^{-2} at high latitudes

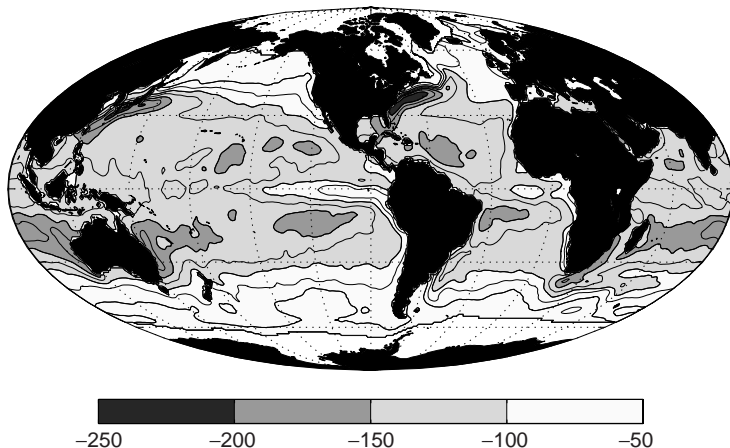
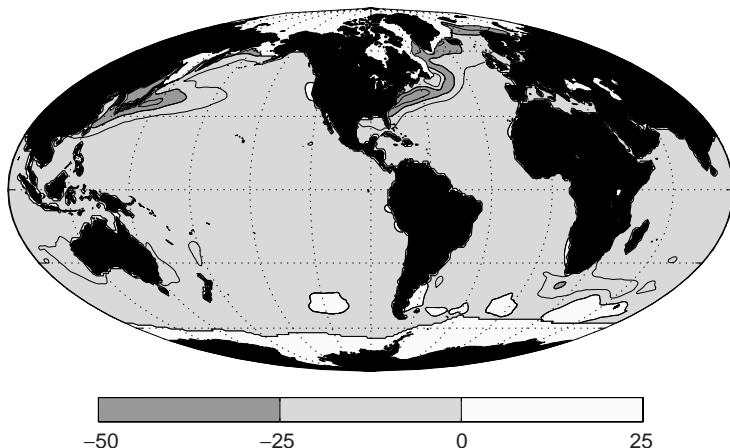
(a) annual-mean latent heat flux (W m^{-2})(b) annual-mean sensible heat flux (W m^{-2})

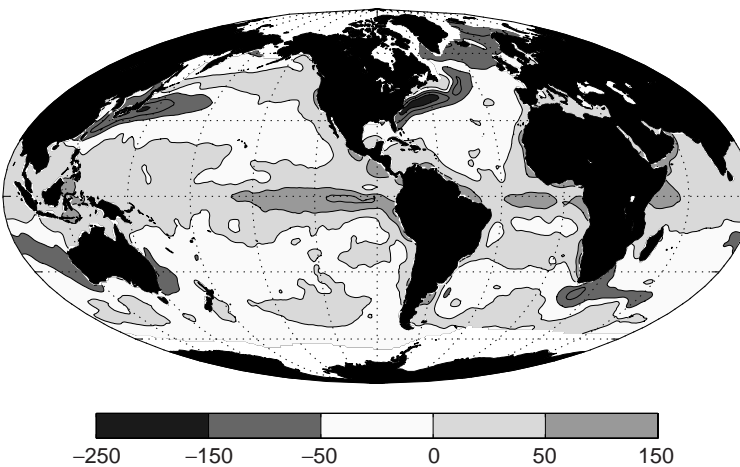
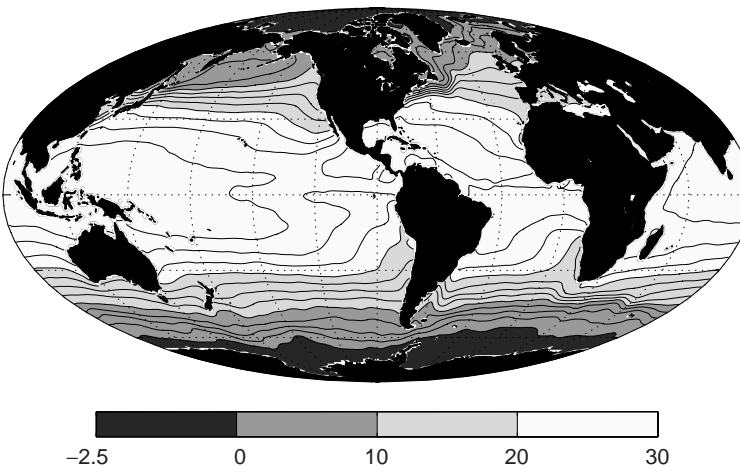
Figure 4.15 Annual-mean surface maps of (a) latent heat flux (contours every 25 W m^{-2}), and (b) sensible heat flux (contours every 12.5 W m^{-2}) from the NOCS climatology (Josey et al., 1999). These negative values represent a heat transfer from the ocean to the atmosphere.

(Fig. 4.14). The radiative heating broadly decreases with latitude, but is modified by cloud cover with enhanced heat input occurring north and south of the equator, where there is reduced cloud cover.

This overall radiative heat input into the ocean is offset by the air-sea transfer of heat achieved through the sensible and latent contributions, $\mathcal{H}_{\text{sensible}} + \mathcal{H}_{\text{latent}}$ (each shown in Fig. 4.15). The air-sea heat flux by sensible heat is achieved by a turbulent transfer of heat across the sea surface depending on the air-sea temperature differences, while the latent heat flux is achieved by a turbulent transfer of evaporated water, where heat is used to enable the phase change from a liquid to a vapour. Stronger winds increase

the surface cooling and evaporation from the ocean.

The latent exchange nearly always dominates over the sensible exchange, reflecting how much heat is stored and utilised in the phase changes of water. The sum of the sensible and latent heat fluxes varies typically from -250 W m^{-2} to -50 W m^{-2} (Fig. 4.15). This air-sea heat loss has a more complicated pattern than the radiative heat input. The maximum heat loss is over the western boundary currents, which is affected by how dry and cold is the air swept from the land relative to the warm ocean. Conversely, the minimum heat loss to the atmosphere is often far from the land, either in the Southern Ocean or the eastern side of

(a) annual-mean surface heat flux (W m^{-2})(b) surface temperature ($^{\circ}\text{C}$)

the basins, where the air-sea contrasts in humidity and temperature are smaller.

In summary, at the sea surface, the warming of the ocean by solar heating is opposed by cooling from long-wave radiation and latent and sensible heat fluxes to the atmosphere. This upward heat flux warms the atmosphere and heat is transferred upward through the atmosphere by a combination of long-wave radiation and convection. At the top of the atmosphere, the outgoing long-wave radiation then balances the net incoming solar radiation when integrated over a year and the entire surface area of the planet.

Figure 4.16 Map of (a) annual-mean, air-sea heat flux (contours every 50 W m^{-2}) into the ocean from the NOCS climatology (Josey et al., 1999) and (b) sea-surface temperature (contours every $2.5 ^{\circ}\text{C}$) from the World Ocean Atlas 2001 (Conkright et al., 2002). There are significant uncertainties in this net heat flux, perhaps ranging from 10% to 20% for each component making up the net flux.

Air-sea heat flux and surface temperature

The net surface heat flux, \mathcal{H} , into the ocean is defined by the sum of the warming from the solar heat input and cooling from the combination of long-wave radiation, latent and sensible heat exchange. There is *not* a local heat balance and, instead, there is a gain in heat over the expansive area of the tropics of typically 50 W m^{-2} versus a more localised loss of heat at high latitudes and over the western boundaries at mid latitudes, reaching -250 W m^{-2} (Fig. 4.16a). These heat fluxes drive a corresponding temperature change over a surface mixed layer of thickness

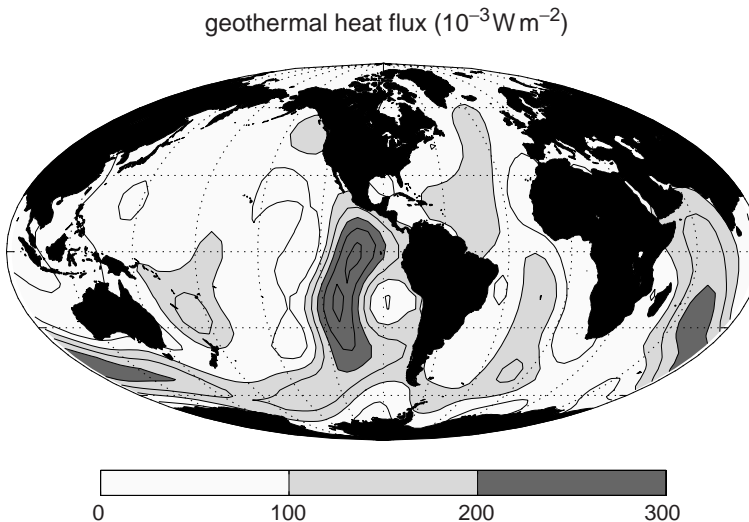


Figure 4.17 Geothermal heat flux at the sea floor (contours every $50 \times 10^{-3} \text{ W m}^{-2}$). The heat flux is small and positive, acting continuously to warm the bottom waters. The estimate of geothermal heating is based on direct observations over the globe (with very few data in the Southern Ocean), which is then mapped with spherical harmonics on a 5° grid; replotted from Pollack et al. (1993) using data from <http://www.ngdc.noaa.gov/Data>.

h given by,

$$\frac{DT}{Dt} = \frac{1}{\rho C_p} \frac{\mathcal{H}}{h}, \quad (4.13)$$

where for simplicity any penetration of heat below the mixed layer is ignored, as well as entrainment or mixing; C_p is the heat capacity for seawater at a constant pressure in $\text{J kg}^{-1} \text{ K}^{-1}$. The surface heat flux is measured in W m^{-2} , so the units on each side of (4.13) are the same and given by

$$\frac{K}{s} = \frac{(\text{J s}^{-1} \text{ m}^{-2})}{(\text{kg m}^{-3})(\text{J kg}^{-1} \text{ K}^{-1})(\text{m})}.$$

At mid latitudes, the boundary currents provide a poleward transport of warm water leading to a westward increase in sea-surface temperature, while at high latitudes, the boundary currents provide an equatorward transport of cold water leading to a westward decrease in sea-surface temperature (Fig. 4.16b).

The annual gain in heat in the tropics and loss at high latitudes is generally offset by an ocean heat transport, directed poleward in the global average. However, the exception to this general rule is in the Atlantic, where the heat transport is directed northward even in the southern hemisphere: cold, deep water is transported southward and warm, surface water is transported northward over the entire basin, as part of the overturning circulation.

Geothermal heat flux from the sea floor

While the surface heat flux is the most important thermal forcing for the ocean, there is also a much smaller geothermal heating from the sea floor typically reaching 0.1 W m^{-2} (Pollack et al., 1993). This geothermal heating is supplied by conduction from the lithosphere and is enhanced over topographic ridges (Fig. 4.17), particularly where there is hydrothermal activity. While this geothermal heat flux is several orders of magnitude smaller than the surface heat flux, the heat flux along the sea floor is always unidirectional, acting to warm the bottom waters and reduce their stratification.

4.4.3 Air-sea freshwater flux and surface salinity

Salinity, defined by the concentration of salts and dissolved matter, is altered by the exchange of fresh water and salt with the atmosphere, land or ice: salt becomes more concentrated when there is a surface freshwater loss and, conversely, more diluted when there is a freshwater gain. Changes in the actual inputs of the salts are usually unimportant, apart from beneath ice sheets where ejection of salt during freezing leads to sinking plumes of dense, salty water.

Fresh water is exchanged between the atmosphere and ocean via precipitation, \mathcal{P} , and evaporation, \mathcal{E} (Fig. 4.18a,b), as well as provided by river

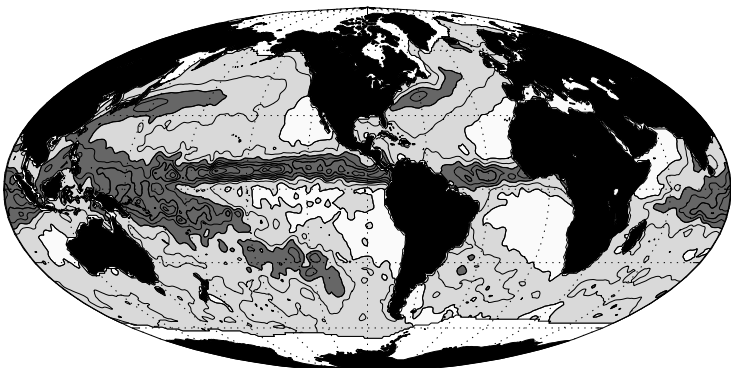
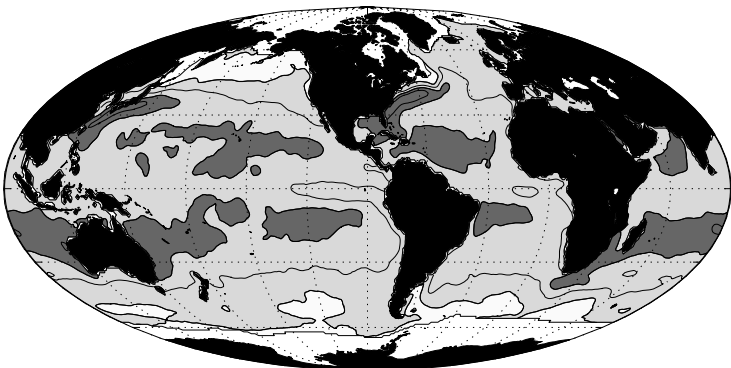
(a) annual-mean precipitation (m y^{-1})(b) annual-mean evaporation (m y^{-1})

Figure 4.18 Maps of climatological, annual-average (a) precipitation into the ocean, and (b) evaporation out of the ocean (contours every 0.5 m y^{-1}) from the NOCS climatology (Josey et al., 1999) with larger magnitudes denoted by dark shading.

run-off from land and exchanged through melting and freezing of ice; the units for the air-sea freshwater flux are given as m y^{-1} from the volume flux of fresh water ($\text{m}^3 \text{ y}^{-1}$) exchanged per unit horizontal area (m^2). There is an overall input of fresh water to the ocean along a narrow band in the tropics, a loss of fresh water in the subtropics and an input of fresh water at mid and high latitudes (Fig. 4.19a).

The pattern of air-sea exchange of fresh water is rather more complicated than that for heat. The air-sea exchange of fresh water is controlled by (i) how precipitation increases with vertical ascent in the atmosphere, as seen along the inter-tropical convergence zone in the tropics and the atmospheric storm belts at mid latitudes (Fig. 4.18a), and (ii) how evaporation increases in warmer waters in the mid latitudes and where relatively

dry air passes from the continents over the warm, ocean boundary currents (Fig. 4.18b).

A transfer of fresh water from the ocean to the atmosphere increases the concentration of salts and dissolved matter remaining in surface ocean, as measured by the salinity (Fig. 4.19b),

$$\frac{DS}{Dt} = S \frac{(\mathcal{E} - \mathcal{P})}{h}, \quad (4.14)$$

where the surface ocean is assumed to be well mixed over a thickness h and ignoring entrainment and mixing. If salinity is measured in g kg^{-1} and the freshwater fluxes as a volume flux per unit area in $\text{m}^3 \text{ s}^{-1} \text{ m}^{-2}$, then the units of each side of (4.14) are identical,

$$\frac{\text{g kg}^{-1}}{\text{s}} = (\text{g kg}^{-1}) \frac{(\text{m}^3 \text{ s}^{-1} \text{ m}^{-2})}{(\text{m})}.$$

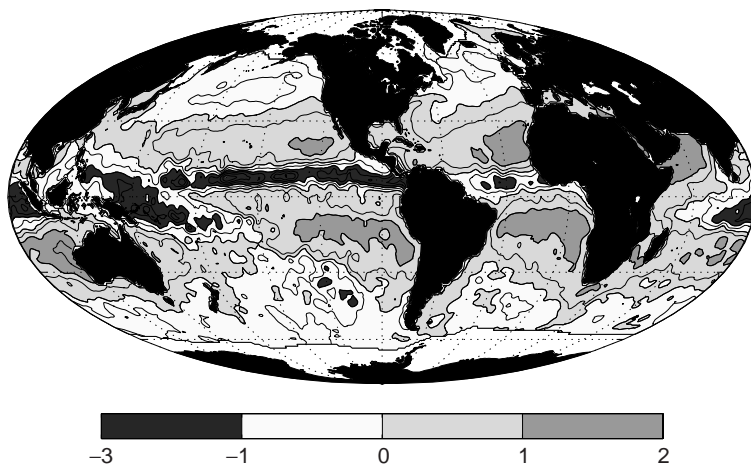
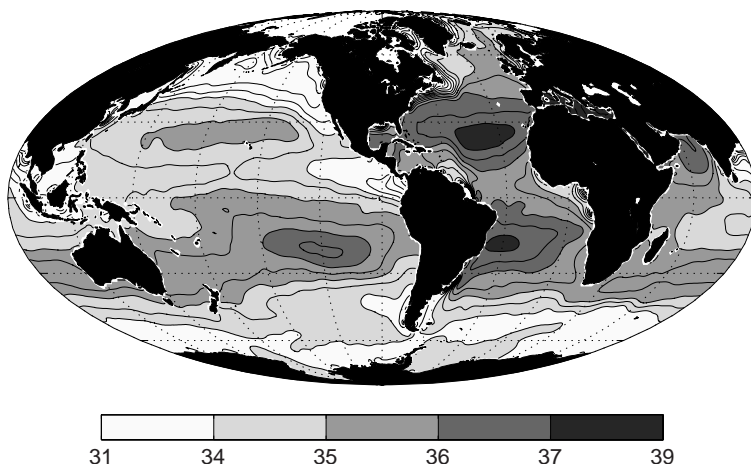
(a) annual-mean freshwater flux (m y^{-1})

Figure 4.19 Maps of climatological, annual-average (a) freshwater flux out of the ocean (contours every 0.5 m y^{-1}) from the NOCS climatology (Josey et al., 1999), shading emphasises extremes, positive flux is dark, negative is light, and (b) sea-surface salinity (contours every 0.5 g kg^{-1}) from the *World Ocean Atlas 2001* (Conkright et al., 2002). There are significant uncertainties in this net freshwater flux, perhaps ranging from 10% to 20% for each component making up the net flux.

(b) surface salinity (g kg^{-1})

The annual-mean salinity is highest in concentration in low-latitude, semi-enclosed seas, such as the Mediterranean and the Red Sea, where evaporation is strong over warm waters and there is relatively little precipitation. Over the open ocean, salinity is relatively low in concentration along the tropics where precipitation is strong, then becomes greater over the subtropics reflecting a loss of fresh water from both enhanced evaporation and lack of precipitation (Fig. 4.19a,b). Salinity then weakens poleward at mid and high latitudes reflecting the effect of increased freshwater input from precipitation and ice melt (Fig. 4.19a,b).

The Pacific is much fresher than the Atlantic through an overall freshwater gain over the Pacific compared with the Atlantic, which is partly a consequence of enhanced precipitation over the tropical Pacific and enhanced evaporation over the subtropical Atlantic; this is discussed further in Section 12.1.3.

4.4.4 Air-sea forcing of surface density

The combination of the surface heat and freshwater fluxes alters the surface density: warming or freshening acts to lighten surface waters, while cooling or evaporation acts to increase the surface density. The forcing of surface density, \mathcal{D} ,

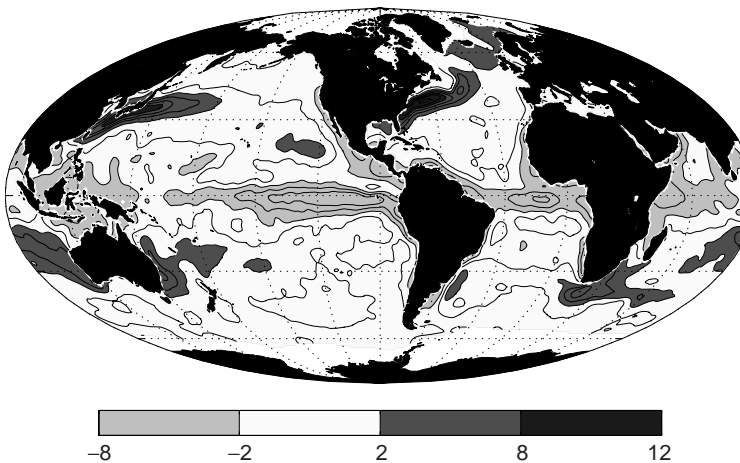
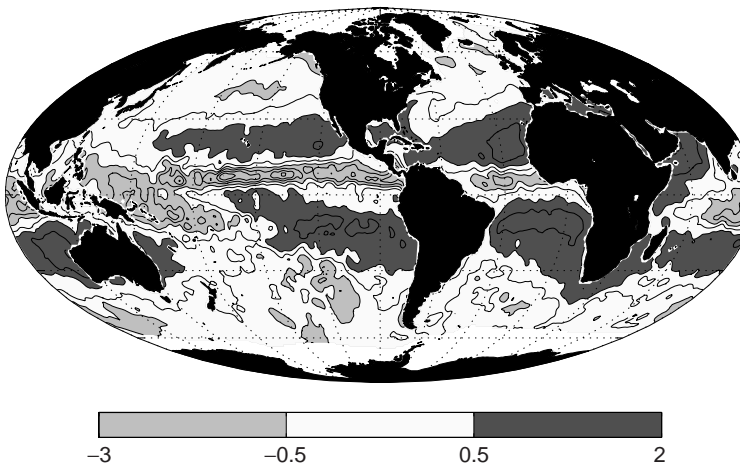
(a) density flux from heat ($10^{-6} \text{ kg m}^{-2} \text{s}^{-1}$)(b) density flux from fresh water ($10^{-6} \text{ kg m}^{-2} \text{s}^{-1}$)

Figure 4.20 Maps of the contribution to the climatological, surface density forcing, \mathcal{D} , from (a) surface heat fluxes, $-\frac{\alpha_T}{C_p} \mathcal{H}$ (contours every $2 \times 10^{-6} \text{ kg m}^{-2} \text{s}^{-1}$), and the weaker contribution from (b) surface freshwater fluxes, $\rho \beta_S S(\mathcal{E} - \mathcal{P})$ (contours every $0.5 \times 10^{-6} \text{ kg m}^{-2} \text{s}^{-1}$), which are evaluated monthly using air-sea fluxes from NOCS (Josey et al., 1999) and temperature and salinity from the *World Ocean Atlas 2001* (Conkright et al., 2002). Note that the range is four times larger in (a) than in (b), and the shading is chosen to identify extremes for surface density input (dark) or loss (light).

can be defined in terms of the density effects of the surface heat and and freshwater fluxes given by

$$\mathcal{D} = -\frac{\alpha_T}{C_p} \mathcal{H} + \rho \beta_S S(\mathcal{E} - \mathcal{P}), \quad (4.15)$$

where \mathcal{D} has units of mass per unit area and unit time, $\text{kg m}^{-2} \text{s}^{-1}$; α_T is the density expansion coefficient for temperature and β_S is the density contraction coefficient for salinity from the linearised equation of state (4.11); this surface forcing is often equivalently written in terms of a buoyancy flux, given by $-g\mathcal{D}/\rho$ with units of $\text{m}^2 \text{s}^{-3}$.

The surface density forcing is mainly provided by surface heat fluxes (Fig. 4.20a) and there is a

smaller contribution by a factor of four or more from freshwater fluxes (Fig. 4.20b, note different scale). Evaporation leads to an increase in density over the central part of the subtropical gyre with $\mathcal{D} \sim 1 \times 10^{-6} \text{ kg m}^{-2} \text{s}^{-1}$, while the precipitation over the equator leads to a lightening of $-2 \times 10^{-6} \text{ kg m}^{-2} \text{s}^{-1}$. The freshwater contribution only becomes comparable to the thermal forcing over the eastern sides of ocean basins outside the tropics, as well as the Southern Ocean (Fig. 4.20b).

The relative importance of a thermal perturbation versus a saline perturbation in forcing density changes varies over the global ocean. To understand this variation, consider how

Table 4.2 Variation of density expansion coefficients, $\alpha_T = -\frac{1}{\rho} \frac{\partial \rho}{\partial T}$ and $\beta_S = \frac{1}{\rho} \frac{\partial \rho}{\partial S}$, with temperature and pressure for a fixed salinity of 35 g kg^{-1} ; evaluated from CSIRO SEAWATER library.

Temperature T ($^{\circ}\text{C}$)	Pressure P (mbar)	Ratio of expansion coefficients α_T / β_S
20	0	0.3466
10	0	0.2198
5	0	0.1472
5	2000	0.2117
5	4000	0.2748

fractional density changes, $\Delta\rho$, from (4.11) are related to temperature and salinity changes, ΔT and ΔS , by

$$\frac{\Delta\rho}{\rho} = -\alpha_T \Delta T + \beta_S \Delta S,$$

where the relative contributions of ΔT and ΔS are measured by α_T and β_S . For given temperature and salinity changes, their relative importance in forcing density changes varies according to the ratio, α_T / β_S , which varies strongly with temperature, as well as pressure (Table 4.2). For the same temperature perturbation, the resulting density change in warm waters is twice as large as that induced in cold polar waters; conversely, a salinity perturbation becomes more important in controlling density changes in cold waters.

How might the evolution of thermal and freshwater anomalies differ?

While thermal forcing is generally more important in determining the surface density than freshwater forcing, there are some important subtleties. Thermal anomalies in the surface ocean can easily become damped by air-sea interaction: a warm surface anomaly increases the local heat loss to the atmosphere from long-wave, latent and sensible heat loss. Hence, a warm surface anomaly cools more rapidly than its neighbouring environment, so that the surface anomaly can be damped and removed; conversely, a cool, surface anomaly preferentially warms and again is damped. Ultimately, the importance of this air-sea damping varies with the horizontal scale of

the anomaly: the atmosphere can easily dampen surface temperature signals associated with ocean eddies on scales of tens of kilometres over several weeks or months, but this damping is less rapid for ocean anomalies on much larger horizontal scales.

In contrast, freshwater or salinity anomalies are not damped by air-sea interaction: a surface increase in salinity does not directly alter the air-sea flux of fresh water. Hence, once a salinity anomaly is formed in the surface ocean, the salinity anomaly can persist for much longer than a thermal anomaly; indeed, it is for this very reason that salinity is a very useful tracer, identifying the origin of water-mass properties.

Over the global scale, contrasts in freshwater forcing turn out to be very important in leading to different surface density conditions between different ocean basins, leading to contrasting overturning circulations in the North Atlantic and North Pacific (Section 12.1.3).

4.5 | Summary

The physical balances operating in the ocean and atmosphere are more unintuitive than one might initially expect. The ocean moves in response to external accelerations involving gravity, contrasts in pressure and frictional stresses, as well as in response to two apparent accelerations, the centrifugal and Coriolis, depending on the rotation of the Earth. The centrifugal acceleration is an outward acceleration deforming the shape of the Earth from a perfect sphere to an ellipsoid. The Coriolis acceleration provides a deflection, directed to the right of the motion in the northern hemisphere and to the left in the southern hemisphere. This Coriolis effect is revealed in how atmospheric cyclones spin in an anticlockwise manner in the northern hemisphere and in a clockwise manner in the southern hemisphere. Despite popular myth, how water drains around a plug hole is not a reliable indicator, as the timescale is too short for the Coriolis acceleration to be significant.

The dominant physical balances for the ocean circulation turn out to be very different in the vertical and horizontal. In the vertical, gravitational

acceleration is balanced by vertical pressure contrasts, with pressure increasing with depth given the increasing weight of overlying fluid. In the horizontal, there is a three-way balance between Coriolis acceleration, horizontal pressure gradients and frictional stresses. The Coriolis acceleration acts to deflect the flow such that fluid either moves parallel to pressure contours or perpendicular to frictional stresses. This three-way balance is usually separated into a geostrophic balance between the Coriolis acceleration and the pressure gradient, together with an Ekman balance confined close to the surface and sea floor between the Coriolis acceleration and the frictional stress.

The effect of the Coriolis acceleration is very profound. Away from boundaries, fluid does not simply move from high to low pressure, but rather along pressure contours. Since the pressure contrasts driving the flow are not easily removed, flows tend to keep moving and, hence, the ocean and atmosphere are full of persistent currents and jets! Eventually, frictional stresses at the surface and bottom boundaries do become important and the atmospheric and ocean flows become damped, but the rate at which these currents spin down is much slower than one might initially expect.

The ocean circulation is primarily forced by this movement of the atmosphere via air-sea exchanges of momentum, heat and fresh water. The surface wind pattern provides the frictional forcing of the surface ocean, evident in the sense of rotation of the ocean gyres within the basins and the direction of the zonal currents in the tropics and the Southern Ocean. The surface heat flux leads to the expected surface temperature contrasts: warming in the tropics and cooling at high latitudes, apart from the surprise that the maximum surface cooling occurs over the western side of ocean basins where there are warm boundary currents. The surface freshwater flux has a more complex pattern: precipitation occurs where air is rising in the tropics or in mid-latitude weather systems, while evaporation increases where waters are warmer. The combination of the surface heat and freshwater forcing alters the surface density of the ocean; thermal contribution is usually the controlling factor, apart from at high latitudes where the freshwater contribution becomes increasingly important.

These physical concepts of how the ocean circulates are taken further in subsequent chapters addressing specific phenomena: how ocean gyres circulate, how ocean eddies form, how the ocean is ventilated and how the deep ocean circulates.

4.6 | Questions

Q4.1. Apparent accelerations.

When particles are viewed in a rotating frame, they appear to be deflected by apparent accelerations. Consider the case of a particle initially moving only in the x -direction on the rotating Earth, which is deflected by the Coriolis acceleration. The particle travels a distance of 100 m in the x -direction in a time of either (i) 10 s or (ii) 10^4 s.

For each case, (a) calculate the Coriolis acceleration to the right of the motion in the y -direction given by $-fu$, where u is the zonal velocity in the x -direction and f is the Coriolis parameter; $f = 2\Omega \sin \phi$, where $\Omega = 2\pi/\text{day}$ and ϕ is the latitude, which assume here is at 45°N.

(b) calculate the displacement in the y -direction using $s = \frac{1}{2}at^2$ from the Coriolis acceleration, where s is the displacement, a is the Coriolis acceleration in the y -direction, and t is time.

(c) Comparing the x and y displacements, calculate the angle of flight (relative to the initial path).

(d) Compare your answers for (i) and (ii), and discuss in which cases the Coriolis effect appears to be more important.

(e) How might the situation change in the southern hemisphere?

Q4.2. Thermal-wind balance across the Antarctic Circumpolar Current.

Thermal-wind balance relates the vertical shear in geostrophic velocity to the horizontal density gradient, which for the eastward flow is given by

$$\frac{\partial u}{\partial z} = \frac{g}{\rho f} \frac{\partial \rho}{\partial y}.$$

(a) Derive thermal-wind balance by differentiating geostrophic balance (4.5a) with depth and substituting hydrostatic balance (4.2).

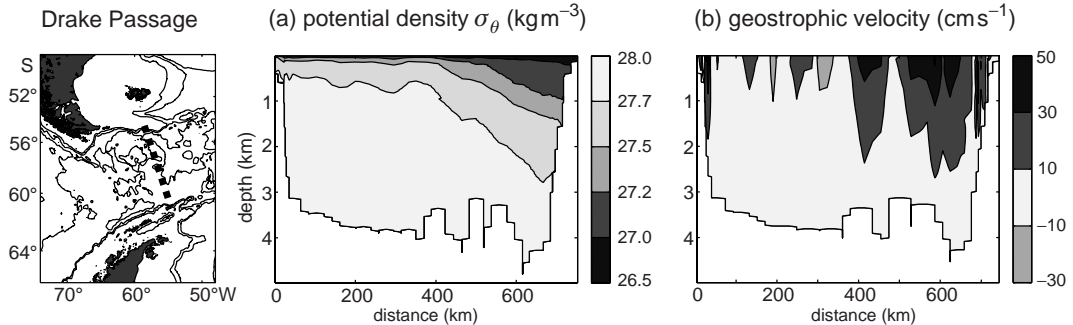


Figure 4.21 Section through Drake Passage between South America and Antarctica in the Southern Ocean for (a) potential density referenced to the sea surface minus 1000 kg m^{-3} , σ_θ , and (b) eastwards geostrophic velocity (cm s^{-1}), relative to an assumed zero flow on the sea floor versus depth together with a map of bathymetry and position of section (dashed line) in the left panel. The distance along the section increases northward. Data collected between 30 December 1997 and 7 January 1998 with a maximum station spacing of 17 km. Data supplied by Brian King; for further details, see Cunningham et al. (2003).

(b) Consider the density variations across the Drake Passage in the Southern Ocean (Fig. 4.21). Estimate the change in eastward velocity, Δu_g , associated with the northward change in density, $\Delta\rho$, over a depth scale Δz using a differenced-version of thermal wind,

$$\Delta u_g \sim \frac{g}{\rho f} \frac{\Delta \rho}{\Delta y} \Delta z.$$

Take $\Delta\rho$ at $y = 600 \text{ km}$ in Fig. 4.21a over a north-south distance $\Delta y \sim 200 \text{ km}$ and a depth change $\Delta z \sim 2 \text{ km}$ with $f \sim -10^{-4} \text{ s}^{-1}$. Check the units and sign of your answer. Compare your answer to the observed geostrophic velocity in Fig. 4.21b.

Q4.3. Scaling of terms in the momentum equation for a Gulf Stream ring.

(a) Consider the flow associated with an ocean eddy formed by the meandering of the Gulf Stream. Assume that the typical magnitude for the current speed is given by $U \sim 0.5 \text{ m s}^{-1}$ and a horizontal length scale $L \sim 100 \text{ km}$ and vertical height scale $H \sim 500 \text{ m}$, then estimate (i) the advective timescale given by L/U ; and (ii) an upper bound for the vertical velocity from $W < U H/L$.

(b) The x -component of the unforced, momentum equation (4.1a) is given by

$$\frac{Du}{Dt} - 2\Omega v \sin \phi + 2\Omega w \cos \phi + \frac{1}{\rho} \frac{\partial P}{\partial x} = 0.$$

Crudely estimate the magnitude of the first three terms, assuming that the rate of change following

the motion is typically given by $Du/Dt \sim U^2/L$, the horizontal velocities are $u \sim v \sim U$ and the vertical velocity $w \sim W$; assume the angular velocity $\Omega = 2\pi/86400 \text{ s}$ and a latitude $\phi \sim 35^\circ \text{ N}$.

Hence, identify which term balances the horizontal pressure gradient.

(c) Show how the relative importance of the temporal acceleration and the Coriolis acceleration is given by the non-dimensional Rossby number,

$$Ro = \frac{U}{fL}.$$

Calculate how large the Rossby number is for the ocean ring.

Q4.4. Divergence and curl.

(a) For the velocity fields for a circulating flow and a reversing jet, depicted in Fig. 4.22, speculate on whether there is (i) any horizontal divergence, i.e., whether more fluid leaves a unit area than enters the unit area (where more fluid leaving a region is defined as positive divergence), and (ii) any rotation of the velocity field, i.e., defined by how a paddle wheel placed in the flow will rotate (where an anticlockwise rotation is defined as a positive rotation). In each case, identify the sign of your answer.

(b) More formally, now evaluate the horizontal divergence, $\frac{\partial u}{\partial x} + \frac{\partial v}{\partial y}$, and the relative vorticity measuring the rotation of the fluid, $\zeta = \frac{\partial v}{\partial x} - \frac{\partial u}{\partial y}$, corresponding to the velocity fields depicted in Fig. 4.22.

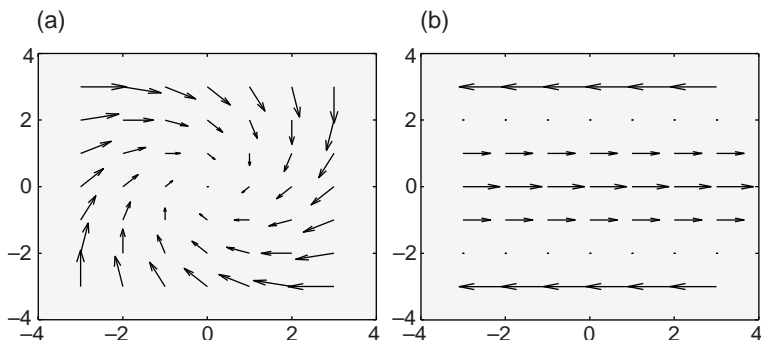


Figure 4.22 Velocity fields for (a) a circulating flow, and (b) a reversing jet. The horizontal divergence is denoted by whether more fluid leaves a horizontal area than enters it. The relative vorticity, ζ , is denoted by whether a paddle wheel placed in the flow rotates in an anticlockwise manner.

Assume that the eastward velocity, u , and northward velocity, v , vary in x and y in the following manner: (i) $u = y - x$ and $v = -x - y$; and (ii) $u = 2 - 0.5y^2$ and $v = 0$.

4.7 | Recommended reading

There are a range of excellent and comprehensive texts which carefully discuss the equations of motion and derive the relevant balances:

- B. Cushman-Roisin (1994). *Introduction to Geophysical Fluid Dynamics*. Englewood Cliffs, NJ: Prentice Hall, 320pp.
- A. E. Gill (1982). *Atmosphere–Ocean Dynamics*. New York: Academic Press, 692pp.
- J. Marshall and A. R. Plumb (2007). *Atmosphere, Ocean and Climate Dynamics*. Burlington, MA: Academic Press/Elsevier, 319pp.
- J. Pedlosky (1987). *Geophysical Fluid Dynamics*. New York: Springer-Verlag, 710pp.
- G. K. Vallis (2006). *Atmospheric and Oceanic Fluid Dynamics: Fundamentals and Large-Scale Circulation*. Cambridge: Cambridge University Press, 745pp.

Chapter 5

Biological fundamentals

The ocean is teeming with life. In sunlit surface waters, every millilitre may contain hundreds of thousands of phytoplankton (Fig. 5.1a). These tiny plants, some as small as a micron, use chlorophyll to capture energy from sunlight to create the organic molecules that make up their bodies and fuel the biochemical reactions that support almost all marine life. While most individual phytoplankton cells are invisible to the naked eye, collectively their chlorophyll colours the water. If you take a cruise from the tropics to the high latitude oceans, the surface waters turn from a clear blue to an opaque greenish tinge. This change in colour reflects how the abundance of phytoplankton increases with the availability of essential nutrients, sunlight, temperature and the predators which eat them.

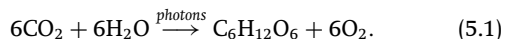
Phytoplankton are at the bottom of the food chain: they create fresh organic matter from dissolved nutrients, carbon dioxide, and energy from sunlight. Many of the phytoplankton are eaten by other plankton (Fig. 5.1a) which in turn are consumed by larger organisms, ultimately sustaining large fish and mammals at the top of the food chain. Eventually some of the organic matter sinks to the deeper, dark waters either as dead cells or faecal pellets. This organic matter is utilised by a host of organisms, including bacteria, which recover the last of the energy originally captured by the phytoplankton and, in the process of respiration, convert organic molecules back to inorganic form.

In this chapter, we discuss the biological processes which are particularly relevant to the marine carbon cycle, as depicted in Fig. 5.1b. We

begin at the scale of molecules and individual living cells, describing some fundamental aspects of biochemical reactions, cellular composition and physiology. We discuss how phytoplankton populations acquire the nutrients and light they need to create new organic molecules, as well as the variety of strategies which allows them to thrive in diverse environments. We address where organic carbon is formed in the open ocean and its subsequent fate in surface and deep waters, and finally discuss how slight differences in the biological role and processing of nutrient elements affects their utilisation and distributions over the ocean.

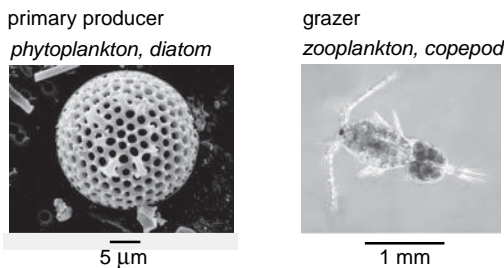
5.1 Photosynthesis and respiration

In a simple view, photosynthesis is the conversion of electromagnetic energy into chemical energy through the formation of organic molecules (Fig. 5.1b). A simple, schematic representation of this process is a chemical reaction where carbon dioxide and water are converted to glucose, $C_6H_{12}O_6$, and molecular oxygen, using energy from photons:

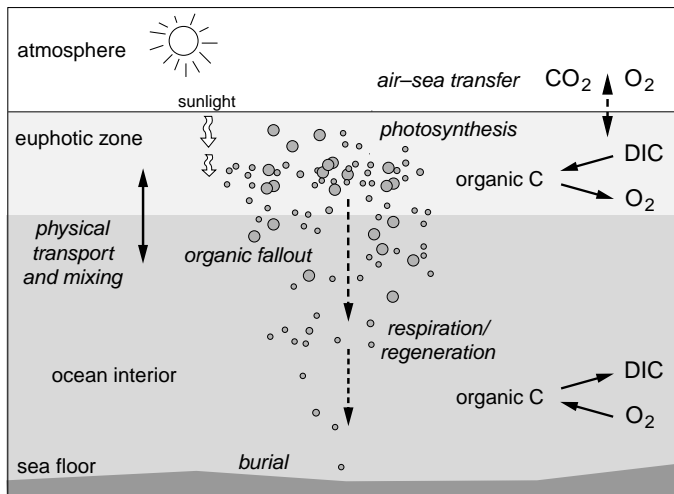


The creation of organic matter from inorganic compounds is called primary production. The primary producers in the ocean are phytoplankton, single cells or colonies of cells living freely in the water column. Organisms which make a living by photosynthesis are called phototrophs.

(a) marine plankton

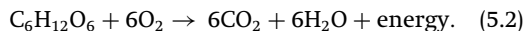


(b) carbon pathways in the ecosystem



The energy for photosynthesis comes from the absorption of visible wavelengths of light. Electromagnetic radiation is rapidly absorbed in seawater; even in very clear water the downward flux of light decays exponentially with depth, limiting viable phytoplankton growth to within typically 200 m of the surface. This region where photosynthesis is viable is called the euphotic layer.

Respiration, the oxidation of organic matter, is the reverse of photosynthesis (Fig. 5.1b). Oxygen is consumed and energy released to fuel biochemical reactions and mechanical work:



Organisms which obtain energy exclusively by harvesting and respiring live or dead organic matter are called heterotrophs. In the ocean they include submicron-scale bacteria, zooplankton preying on phytoplankton, bacteria and smaller zooplankton, as well as fish. Mixotrophs are organisms which adopt both strategies, obtaining

Figure 5.1 (a) Examples of marine plankton: phytoplankton, the plants of the ocean, are single cells or colonies ranging from about one to 100s of microns in cell size. Copepods are larger zooplankton, typically on the order of a millimetre or more in size, which graze on phytoplankton, bacteria and smaller zooplankton. (b) Photosynthesis by phytoplankton occurs in the sunlit, surface waters, producing organic matter and oxygen. Much of the organic matter is respiration back to inorganic form within the euphotic zone, but a significant fraction is transported down, or sinks gravitationally into the deep ocean. Respiration by zooplankton, bacteria and archaea returns the organic material to inorganic forms, including dissolved inorganic carbon. Diatom image courtesy of Zoe Finkel.

energy and essential elements both by photosynthesis and the harvesting and respiration of existing organic matter.

5.2 What are marine microbes made of?

Microbes are those organisms which are too tiny to observe with the naked eye and include phytoplankton and heterotrophic bacteria. In order to reproduce and create new individuals, microbes need to maintain a complex set of biochemical machinery, depicted schematically in Fig. 5.2a,b. All these living microbes are made up of molecules which can be classified into a few broad biochemical categories:

- Carbohydrates, such as glucose, are basic organic molecules composed only of carbon, hydrogen and oxygen (see Table 5.1). They

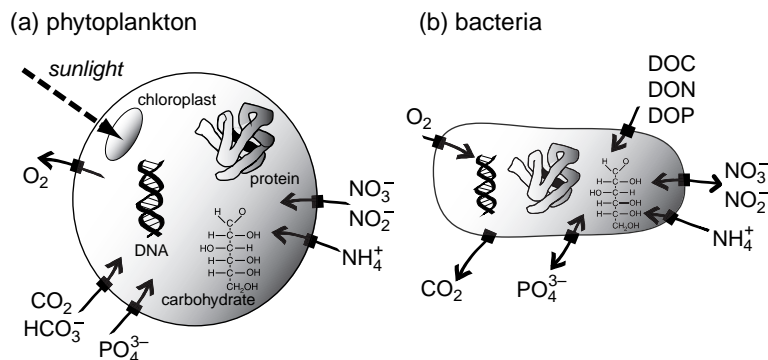


Figure 5.2 Schematic depiction of an idealised (a) phytoplankton, and (b) bacterium. The common physiological demands of resource acquisition and reproduction mean that all microbes manufacture proteins, lipids and nucleic acids. Phytoplankton take up inorganic nutrients, forming carbohydrates by photosynthesis and expelling oxygen as a by-product. Chloroplasts contain the pigments which harvest energy from photons. Bacteria import oxygen and organic matter, acquiring energy through respiration, and return inorganic compounds to the environment.

Table 5.1 Representative biochemical composition of phytoplankton cells: inferred mean molecular composition of major cell components and average contribution to the cell by dry organic weight.
Evaluated by Anderson (1995).

Metabolite	Elemental composition	% cell
Protein	C _{3.83} H _{6.05} O _{1.25} N	54.4
Carbohydrate	C ₆ H ₁₀ O ₅	25.5
Lipid	C ₄₀ H ₇₄ O ₅	16.1
Nucleic acid	C _{9.625} H ₁₂ O _{6.5} N _{3.75} P	4.0

provide a store of energy and basic building blocks for more complex cellular components.

- Lipids are largely composed of carbon, hydrogen and oxygen, but do incorporate other elements. They provide an energy store and form the basis for important membranes in the cell.
- Proteins provide structural components and perform key functions as enzymes, catalysing the complex biochemical reactions that occur in the cell.
- Nucleic acids are the reproductive machinery of the cell. DNA holds the blueprint of the living organism, while RNA takes that blueprint and creates new proteins, melding together component molecules.

In marine microbes, half of the dry-weight biomass is accounted for by proteins, followed by carbohydrates and lipids, while nucleic acid contributes only a small fraction (Table 5.1).

Each of these components has a different elemental composition, so that most of the cellular nitrogen content is in proteins, while a large fraction of the phosphorus is in nucleic acids (Table 5.1). Trace metals are also incorporated into some proteins, enabling specific enzymatic functions.

5.2.1 How does the elemental composition of microbes vary?

The relative abundance of elements in living cells reflects the abundance and elemental composition of the molecules from which they are composed. There can be significant variations in the biochemical composition of microbial cells within and between species (Table 5.2), even over the lifetime of an individual cell, since cells can alter their biochemical composition as they acclimate or adjust their physiology to cope with a changing environment. For example:

- Some microbes can fix nitrogen, converting nitrogen gas, N₂, into organic form. They use the enzyme nitrogenase which has a significant iron content, so nitrogen fixers have a high cellular iron quota.
- When cells are growing and dividing rapidly, they produce extra RNA, which transcribes the blueprint of DNA into proteins, increasing their phosphorus content.
- Some phytoplankton maintain an internal store of nutrient elements, acquiring nutrients from

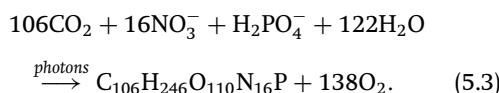
Table 5.2 The ratios of key elements in dissolved inorganic form in the water column and in marine phytoplankton and zooplankton (^aRedfield *et al.*, 1963). The cultured phytoplankton data are the average of 15 species of estuarine, coastal and open ocean phytoplankton grown under controlled laboratory conditions (^bHo *et al.*, 2003). *Prochlorococcus* MED4 is a strain of tiny phytoplankton (about a micron in scale). Elemental ratios were measured in *Prochlorococcus* cultures grown under phosphorus replete and phosphorus limited conditions (^cBertilsson *et al.*, 2003). Ranges of values are also shown for isolated marine bacteria grown under various conditions of nutrient limitation (^dVrede *et al.*, 2002).

Reservoir	C	N	P
^a Marine inorganic nutrients		15	—
^a Bulk marine organic matter	106	16	—
^b Cultured phytoplankton	147 ± 19	16 ± 2	— ± 0.2
^c <i>Prochlorococcus</i> MED4 (P-replete)	121 ± 17	21.2 ± 4.5	—
^c <i>Prochlorococcus</i> MED4 (P-limited)	464 ± 28	62.3 ± 14.1	—
^d Marine bacteria	35–178	7–18	—

the environment when they are plentiful, but utilising the store when the environment is depleted.

Redfield ratios

Despite the variations within and between species, there is a general consistency in the elemental composition of bulk marine phytoplankton and zooplankton (Table 5.2). This consistency reflects how all marine plankton utilise some common molecular machinery. Incorporating the contributions of nitrogen and phosphorus, the simple representation of photosynthesis in (5.1) can be extended to



The elemental ratios in the idealised organic molecule formed by photosynthesis, C : N : P : O₂ = 106 : 16 : 1 : -138, are referred to as the ‘Redfield ratio’ (Table 5.2), reflecting the bulk measurements of Redfield and colleagues (Redfield *et al.*, 1963). They measured the C : N : P ratio in marine phytoplankton and zooplankton, and estimated the corresponding oxygen production/consumption ratio, P : O₂ = 1 : -138, by calculating the requirement to oxidise the organic molecules of the measured composition to CO₂, NO₃⁻ and PO₄³⁻. More recent studies have evaluated the oxygen ratio empirically, finding P : O₂ = 1 : -170 (Takahashi *et al.*, 1985; Anderson and

Sarmiento, 1994). The mismatch can be explained by assuming a slightly different balance between the major classes of biochemical molecules in the organisms (Anderson, 1995), or by adopting a more complex view of photosynthesis than (5.3).

This view of the elemental composition of organic matter and the effect on ocean biogeochemistry is revisited in Section 5.6. Now consider the chemical reactions in which simple molecules are combined to form complex organic substances.

5.2.2 How are organic molecules produced in a cell?

The complex organic molecules of a living cell are the result of chemical reactions between component compounds. The necessary reactions are catalysed by special proteins called enzymes, without which they would proceed very slowly or not at all. While enzymes facilitate reactions, they are not consumed in the process.

Enzymatic reactions can be described as a sequence of stages, as illustrated in Fig. 5.3a:

- Molecules A and B become bound, or complexed, to the enzyme E (panels (i) to (iii)).
- A reaction proceeds between A and B, while attached to the enzyme, forming a product C (panel (iv)).
- The product C is released, freeing the enzyme to repeat the function (panel (v)).

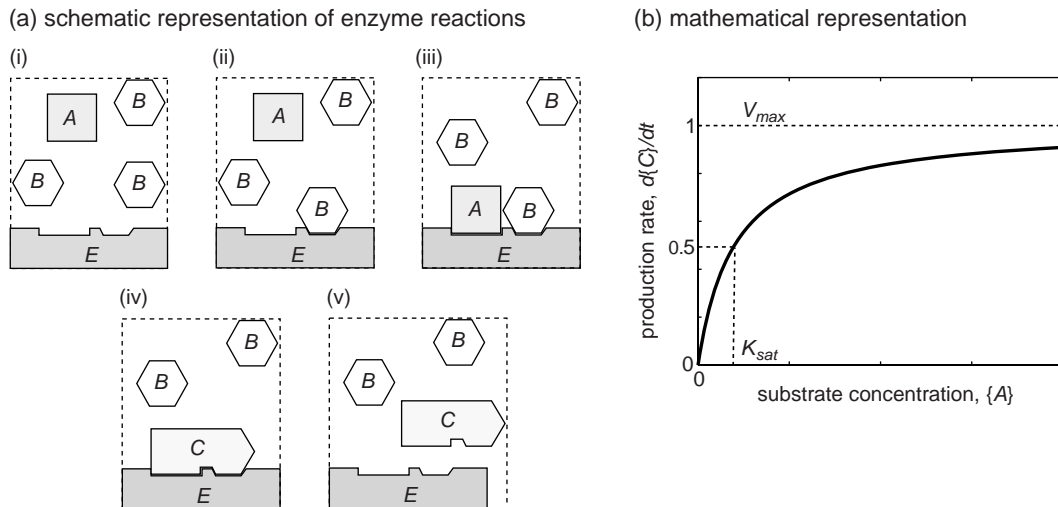
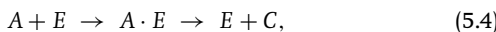


Figure 5.3 Enzymatic reactions: (a) a schematic view, and (b) a mathematical representation. Enzymes are organic molecules which catalyse biochemical reactions, including the production of organic compounds from simpler molecules or substrates. In (a), the enzyme \$E\$ captures molecules of substrates \$A\$ and \$B\$ at receptor sites (i)–(iii), synthesises the product, \$C\$, (iv) and (v), the product \$C\$ is released, allowing the enzyme to perform this function again. In (b), the relationship between the rate of production of the product \$\{C\}\$ and the concentration of \$\{A\}\$ per unit volume (referred to as a substrate), described by \$\frac{d\{C\}}{dt} = V_{max}\{A\}/(K_{sat} + \{A\})\$, where \$V_{max}\$ is the maximum rate of production, and \$K_{sat}\$ is the half saturation; this relationship follows the Michaelis–Menten model of enzyme reactions.

The Michaelis–Menten model of an enzymatic reaction

Now consider how the simplest form of enzymatic reaction can be represented as a sequence of chemical reactions. Assume that molecules of \$A\$ are less abundant than \$B\$ and are limiting the reactions (as depicted in Fig. 5.3a). The sequence of reactions for the molecule \$A\$ (referred to as a substrate) then follows



where molecule \$A\$ becomes bound to a free enzyme, \$E\$; the pair forming a complex, \$A \cdot E\$. Here we consider the simplest case where \$A\$ does not become detached again. After some time, the complex produces a molecule of the product \$C\$, which is released and the enzyme is free to start the cycle again. The two phases are awaiting the ‘arrival’ of the substrate and its subsequent ‘handling’ to form the product.

The rate of production of \$C\$ from the complex is described by

$$\frac{d\{C\}}{dt} = k_p\{A \cdot E\}, \quad (5.5)$$

where curly brackets, \$\{\cdot\}\$, denote concentration per unit volume (\$\text{mol m}^{-3}\$) and \$k_p\$ (\$\text{s}^{-1}\$) is the rate constant of formation of the product. Usually we are interested in how the rate of formation of product \$C\$ depends upon the concentration of the substrate, \$\{A\}\$, rather than \$\{A \cdot E\}\$ as in (5.5). Thus, we need to find the relationship between \$\{A\}\$ and \$\{A \cdot E\}\$. To make this connection, consider the rate of change of the enzyme-substrate complex, \$A \cdot E\$, in (5.4): this complex increases in concentration when the substrate \$A\$ binds to the free enzyme \$E\$, but decreases in concentration when the product \$C\$ is formed, which can be written as

$$\frac{d\{A \cdot E\}}{dt} = k_f\{A\}\{E\} - k_p\{A \cdot E\}, \quad (5.6)$$

where \$k_f\$ is the rate constant of the forward reaction, \$\{A\} + \{E\} \rightarrow \{A \cdot E\}\$ in units of \$(\text{mol m}^{-3})^{-1} \text{s}^{-1}\$. If an equilibrium is reached where the amount of complexed enzyme is unchanging, \$d\{A \cdot E\}/dt = 0\$, then

$$\{A \cdot E\} = \frac{k_f}{k_p}\{A\}\{E\}. \quad (5.7)$$

If the total enzyme concentration, $\{E_T\}$, defined by the sum of the free and complexed forms, remains constant,

$$\{E_T\} = \{E\} + \{A \cdot E\}, \quad (5.8)$$

then (5.7) and (5.8) can be combined to find

$$\{A \cdot E\} = \frac{\{E_T\} \{A\}}{(k_p/k_f + \{A\})}. \quad (5.9)$$

The rate of production of $\{C\}$ can now be expressed in terms of $\{A\}$ by combining (5.5) and (5.9), so that

$$\frac{d\{C\}}{dt} = k_p\{E_T\} \frac{\{A\}}{k_p/k_f + \{A\}}, \quad (5.10)$$

where $\{A\}$ appears in both the numerator and denominator on the right-hand side. This enzymatic relation (5.10) is usually re-expressed as

$$\frac{d\{C\}}{dt} = V_{max} \frac{\{A\}}{K_{sat} + \{A\}}, \quad (5.11)$$

depicted in Fig. 5.3b, where $V_{max} = k_p\{E_T\}$ (in units of $\text{mol m}^{-3} \text{s}^{-1}$) represents the maximum rate of production which is reached, in theory, when all of the enzyme is constantly in complexed form; and $K_{sat} = k_p/k_f$ (in units of mol m^{-3}) is the half saturation, the substrate concentration at which production is half of that maximum. This form is referred to as Michaelis–Menten kinetics after Michaelis and Menten (1913).

This parameterisation of a two-stage chemical reaction fits empirical data for enzymatic reactions very well. This model turns out to be very relevant for other ecosystem processes including nutrient uptake by cells, light harvesting and predator–prey interactions. Next we consider their relevance for phytoplankton growth.

5.3 How is phytoplankton growth affected by the environment?

What is the relationship between phytoplankton growth and nutrient abundance, light and temperature of the local environment? To grow and reproduce, phytoplankton need light for energy, and dissolved forms of essential elements, including carbon, nitrogen, phosphorus, and trace metals. There is an abundance of dissolved inorganic carbon throughout the ocean, with concentrations typically greater than $1900 \mu\text{mol kg}^{-1}$,

but the inorganic forms of nitrogen and phosphorus can become severely depleted (less than $10^{-9} \text{ mol kg}^{-1}$) over large areas of the surface ocean. In the euphotic layer, the availability of either nitrogen, phosphorus, silicon or a trace metal often becomes the limiting factor for phytoplankton growth. Since phytoplankton need these elements in appropriate ratios to build specific molecules, one element usually becomes depleted before all others and impedes growth and reproduction.

5.3.1 Population growth and nutrient limitation

In regions of the ocean with strong seasonal variations, blooms of phytoplankton occur in the spring and summer, as observed in the Norwegian Sea and illustrated in Fig. 5.4a,b: a rapid increase in phytoplankton abundance, indicated by the concentration of chlorophyll *a*, a pigment which all phytoplankton produce to harvest light, is accompanied by the consumption of nitrate and other nutrients within the euphotic layer. In this case, nitrate is completely depleted at the height of the bloom and growth is halted. Consumption of the phytoplankton by predators continues, so the abundance of chlorophyll subsequently declines rapidly.

Blooms arrested by nutrient limitation are also seen in laboratory populations. Consider a vessel of nutrient-enriched, sterilised seawater seeded with a living culture of phytoplankton cells illustrated in Fig. 5.5: during the early stages of growth, there is an exponential increase in population density, X (cells ml^{-1}), such that $X(t) \sim X(0)e^{\mu t}$ and cells divide roughly once a day (Fig. 5.5a); here μ is a population growth rate (s^{-1}) and t is time (s). Nitrate is consumed rapidly during the growth phase and the C : N ratio of the cells decreases as plentiful nitrate is rapidly imported. After three days, nitrate is completely depleted (Fig. 5.5b), rapid growth is halted and the C : N ratio of the cells increases (Fig. 5.5c). In contrast to the bloom observed in the ocean (Fig. 5.4), the laboratory population does not immediately decline when nitrate is depleted, but persists. This difference in response reflects the lack of predators in the laboratory study, where the loss of living phytoplankton cells is much reduced.

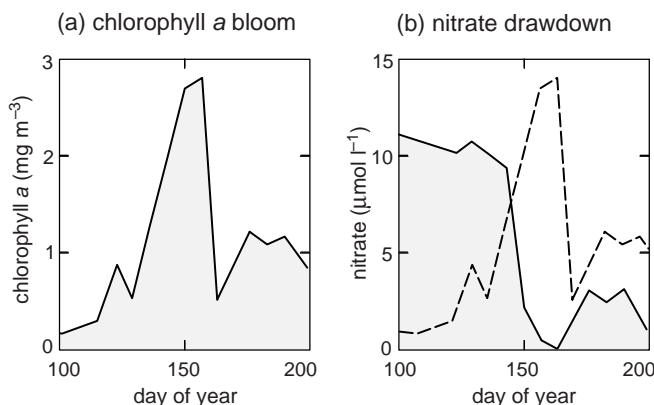


Figure 5.4 An observed phytoplankton bloom: (a) bloom of surface chlorophyll a (mg m^{-3}), and (b) drawdown of surface nitrate ($\mu\text{mol l}^{-1}$, full line, and chlorophyll repeated as dashed line) at Ocean Weather Station M in the Norwegian Sea (66°N , 2°E) in 1992. Redrawn from Dale et al. (1999); data provided by Francisco Rey.

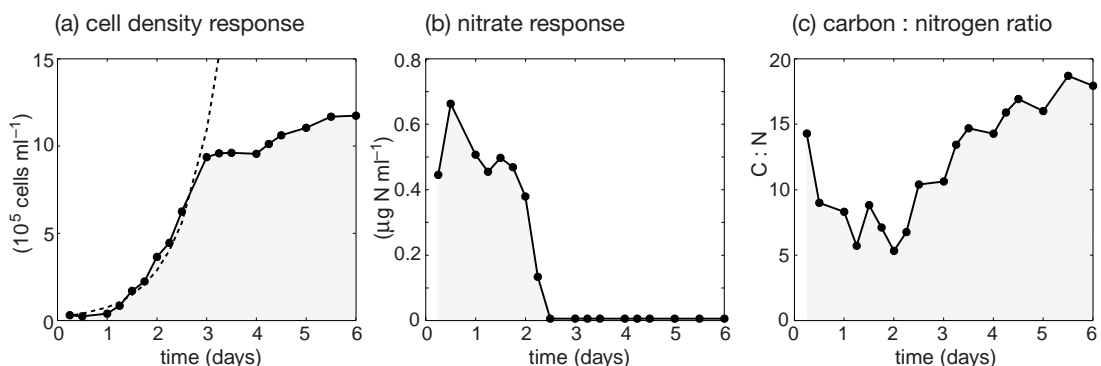


Figure 5.5 The rate of change of (a) cell number density (X , $10^5 \text{ cells ml}^{-1}$), (b) nitrate concentration ($\mu\text{g N ml}^{-1}$) and (c) carbon : nitrogen ratio in the cells from a laboratory batch culture of the marine diatom *Thalassiosira pseudonana*. A seed population was introduced into a nutrient-rich, well-lit medium. The phytoplankton population increased exponentially, consuming nitrate and other nutrients. Eventually nitrate was depleted to a limiting concentration and the population ceased to grow. The initial growth phase can be described by an exponential increase and the laboratory data in (a) are overlaid by a dashed curve with an exponential growth rate $\mu = 0.75 \text{ day}^{-1}$. Note that the carbon to nitrogen ratio of these particular cells is typically greater than the Redfield ratio and varies over the course of the experiment, acquiring extra nitrogen for pigments or protein production when it is plentiful. (Data provided by Keith Davidson; Davidson et al., 1999.)

Next we consider in more detail how phytoplankton and other microbes bring dissolved nutrients into the cell, and how the uptake rate is related to the nutrient concentration in the environment.

5.3.2 How do microbes acquire dissolved nutrients from the water?

The uptake of dissolved nutrients by microbial cells can be viewed in terms of two stages, as depicted schematically in Fig. 5.6a: molecules of nutrient near the cell surface are captured by transporter proteins in the cell wall and then transferred into the interior of the cell. This

uptake creates a gradient in the nutrient concentration within a narrow layer of fluid adjacent to the cell wall, which leads to a transfer of more nutrient molecules towards the cell by molecular diffusion (Fig. 5.6b).

Laboratory cultures reveal that cellular uptake of dissolved nutrients varies with the ambient nutrient concentration in the environment following a saturating function (Fig. 5.6c): when the nutrient is scarce, uptake is linearly dependent on its concentration, and when the nutrient is abundant, uptake saturates to a maximum value.

We now consider nutrient transport into and towards the cell in more detail.

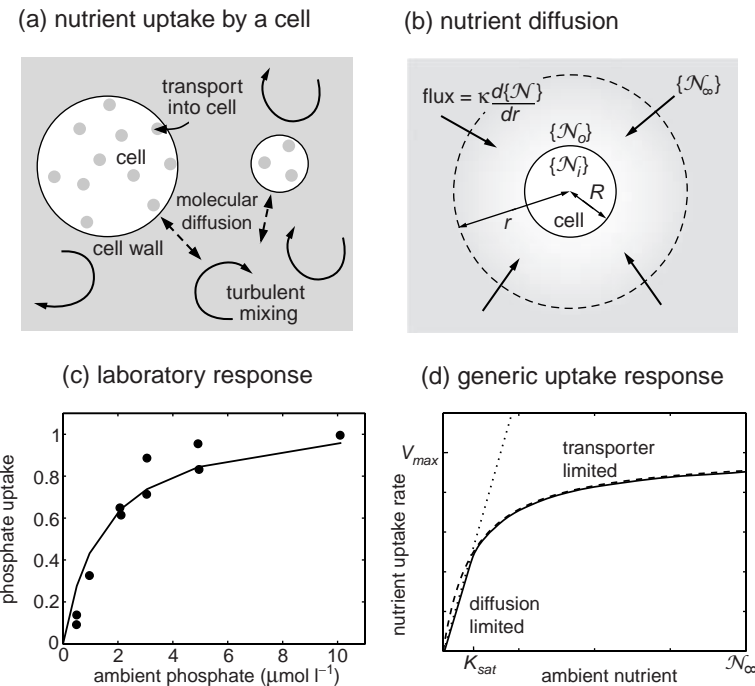
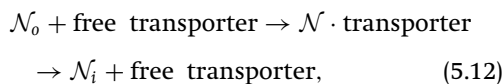


Figure 5.6 (a) A schematic view of the transfer of nutrient molecules into a microbial cell. Nutrients are transferred by the turbulence in the background environment and molecular diffusion near the cell wall. Molecules encountering transporter proteins at the cell wall are trapped and transferred inside, depleting the concentration near the cell surface. (b) The gradient in nutrient concentration drives molecules towards the cell by molecular diffusion. The concentration of the nutrient (mol m^{-3}) far from the cell is $\{N_\infty\}$, just outside the cell wall is $\{N_o\}$, and inside the cell is $\{N_i\}$. Close to the cell, the diffusive flux of N towards the cell is $\kappa d\{N\} / dr$ where κ is the molecular diffusivity and r is the radius from the centre of the cell. (c) Observed relationship between the cellular uptake of phosphate ($\text{pmol P cell}^{-1} \text{h}^{-1}$) and its ambient concentration in a laboratory culture of phytoplankton. A Michaelis–Menten curve is superimposed, with maximum uptake rate $V_{max} = 1.1 \text{ pmol P cell}^{-1} \text{ h}^{-1}$ and half-saturation coefficient $K_{sat} = 1.5 \mu\text{mol PO}_4^{2-} \text{l}^{-1}$. Redrawn from Yamamoto and Tarutani (1999), © Wiley. (d) Cellular nutrient uptake ($\text{mol cell}^{-1} \text{s}^{-1}$) as a function of the ambient nutrient concentration in the surrounding medium. At high concentrations uptake is limited by the density and efficiency of transporters in the cell wall (dashed line). At low concentrations uptake is limited by the rate of diffusion towards the cell (dotted line). The combined result (solid black line, lesser of the dashed and dotted curves) reflects the form of the Michaelis–Menten curve, which is often fitted empirically.

Nutrient transfer across the cell wall

Transporter proteins in the cell wall capture nutrient molecules and pass them into the cell, as depicted simply in Fig. 5.6a: each transporter site is either unoccupied and ready to accept a nutrient molecule or is already engaged in the process of transport through the cell wall. Schematically, the uptake of a nutrient resource N can be represented as a two-stage process,



where N_0 is a nutrient molecule just outside the cell, $N \cdot \text{transporter}$ represents a transporter occu-

pied by a nutrient molecule and N_i is the nutrient molecule in the cell. This two-stage nutrient uptake in (5.12) is analogous to the enzymatic reaction (5.4); also see Q5.2. Following the steps in Section 5.2.2, an analogy of the Michaelis–Menten relationship emerges between the cellular rate of uptake and the near-surface, external nutrient concentration, $\{N_0\}$:

$$\text{uptake of } N = V_{max} \frac{\{N_0\}}{K_{sat} + \{N_0\}}. \quad (5.13)$$

Here, the maximum uptake rate, $V_{max} = E_T K_p$, depends on the density of transporters in the cell wall, E_T , and the rate at which captured ions are transferred into the cell, K_p . However, this

Box 5.1 | Diffusion of nutrients towards a cell

Consider the down-gradient diffusion of nutrient molecules towards a spherical cell of radius R (m) where the ambient nutrient concentration in the fluid is $\{\mathcal{N}_\infty\}$ (mol m^{-3}) and the concentration just outside the cell wall is $\{\mathcal{N}_o\}$, as depicted in Fig. 5.6b. The diffusive flux of nutrients ($\text{mol m}^{-2} \text{ s}^{-1}$) towards the cell along a radial line normal to its surface is given by

$$\kappa \frac{d\{\mathcal{N}\}}{dr},$$

where an outward increase in \mathcal{N} leads to an inward diffusive flux and κ is the molecular diffusivity of \mathcal{N} in seawater ($\text{m}^2 \text{ s}^{-1}$) (see Section 3.2.3). Integrating the flux over the surface of a sphere of radius much greater than the cell, $r > R$, then the area-integrated flux of \mathcal{N} towards the cell (mol s^{-1}) is

$$4\pi r^2 \kappa \frac{\partial\{\mathcal{N}\}}{\partial r}. \quad (5.14)$$

Applying boundary conditions for $\{\mathcal{N}\}$ far away from the cell of $\{\mathcal{N}_\infty\}$ and at the cell surface of $\{\mathcal{N}_o\}$, then the area-integrated flux of \mathcal{N} arriving at the cell surface is

$$4\pi R \kappa (\{\mathcal{N}_\infty\} - \{\mathcal{N}_o\}). \quad (5.15)$$

At the same time, the volume of the cell varies as $(4/3)\pi R^3$, so that the diffusive supply of nutrients per unit volume of the cell is given by

$$3\kappa (\{\mathcal{N}_\infty\} - \{\mathcal{N}_o\})/R^2. \quad (5.16)$$

Hence, the diffusive supply is more efficient in sustaining the growth and division of cells with a small radius R , than a large radius.

relationship is couched in terms of the nutrient concentration just outside the cell wall, $\{\mathcal{N}_o\}$, rather than the ambient concentration in the medium, $\{\mathcal{N}_\infty\}$, which is measured in the field or laboratory, as in Fig. 5.6b. How are the near-surface nutrient concentration, $\{\mathcal{N}_o\}$, and ambient concentration, $\{\mathcal{N}_\infty\}$, related?

Molecular diffusion toward the cell

We assume that nutrients diffuse across a thin molecular boundary layer surrounding a spherical cell (Pasciak and Gavis, 1974; Armstrong, 2008), although fine-scale turbulence, sinking or swimming can also be important for larger cells. The cellular uptake of \mathcal{N} is sustained by the diffusive flux into the cell surface, which (as described in Box 5.1 also see Q5.3) can be represented as

$$\text{uptake of } \mathcal{N} = 4\pi R\kappa(\{\mathcal{N}_\infty\} - \{\mathcal{N}_o\}), \quad (5.17)$$

where R is the radius of the cell.

The two views of nutrient uptake described by (5.13) and (5.17) must, in reality, be consistent and the near-cell concentration, $\{\mathcal{N}_o\}$, will adjust to reflect this. The two expressions can be combined to eliminate \mathcal{N}_o , solving for uptake in terms of \mathcal{N}_∞ , transporter density and molecular diffusion characteristics (see Armstrong, 2008). Here, more simply, we consider two limits:

- If diffusion towards the cell is the rate-limiting process, then the near-cell concentration will become strongly depleted so $\{\mathcal{N}_\infty\} \gg \{\mathcal{N}_o\}$ and, from (5.17), the uptake rate is given by

$$4\pi R\kappa \{\mathcal{N}_\infty\}. \quad (5.18)$$

This limit is most likely to occur at low ambient nutrient concentrations. Uptake is linearly dependent on the ambient concentration of the nutrient and is not limited by the density of transporters (represented by V_{max}).

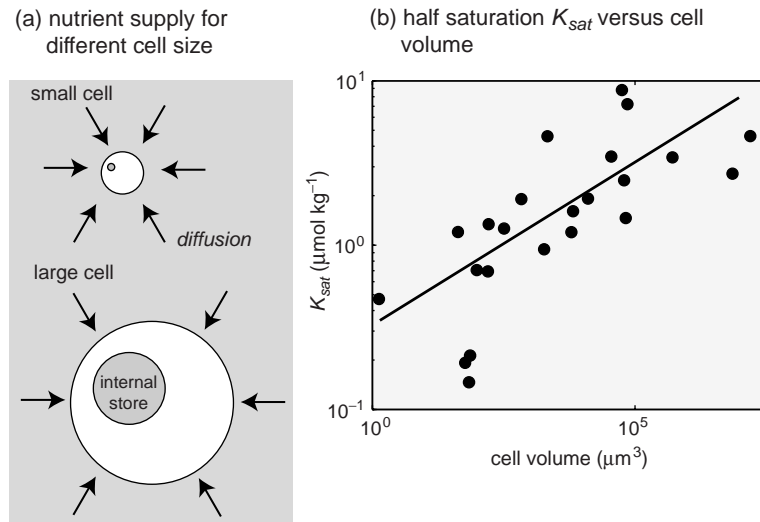


Figure 5.7 The effect of cell size on nutrient uptake and storage. (a) Schematic view: nutrients used for growth are supplied either externally by diffusion into the cell (arrows) or from an internal store of previously acquired nutrient. Diffusion is more efficient for smaller cells. Larger cells can accommodate a larger, easily accessible internal store of nutrients. (b) The half-saturation coefficient, K_{sat} ($\mu\text{mol kg}^{-1}$), for the nitrate uptake rate ($\text{mol N cell}^{-1} \text{s}^{-1}$) by phytoplankton as a function of cell volume, based on a compilation of laboratory culture studies. Smaller cells have lower half saturations and are more effective at directly obtaining nutrients from the environment. Redrawn from Litchman *et al.* (2007).

- At high ambient nutrient concentrations, the diffusive flux towards the cell can supply more nutrient than the cell wall transporters can process, which reduces the deficit in the near-cell nutrient concentration, and decreases the gradient of \mathcal{N} across the boundary layer until $\{\mathcal{N}_\infty\} \sim \{\mathcal{N}_0\}$. In this limit (5.13) can be rewritten in terms of the ambient nutrient concentration

$$\text{uptake of } \mathcal{N} = V_{max} \frac{\{\mathcal{N}_\infty\}}{K_{sat} + \{\mathcal{N}_\infty\}}. \quad (5.19)$$

In this case, uptake of nutrients is proportional to V_{max} and so depends on the density of transporters and the rate at which captured ions are transferred into the cell. Cells may acclimate, adjusting the density of transporters according to the ambient nutrient concentration.

Hence, these limit cases suggests that cellular nutrient uptake is either limited at low ambient nutrient concentrations by diffusion towards the cell (5.18) or at high nutrient concentrations by the density of the transporters in the cell wall (5.19). This combined response is illustrated in Fig. 5.6d and is consistent with the form of the illustrated laboratory study (Fig. 5.6c). The math-

ematical similarity with enzyme kinetics arises, in part, because both can be described as a multi-stage process characterised by an ‘arrival stage’ and a ‘handling stage’. In this case, the arrival of nutrients at the transporter sites is modulated by the diffusive boundary layer, which is ultimately affected by larger-scale turbulence.

5.3.3 Nutrient uptake and population growth

There is an enormous diversity of phytoplankton cells. Cell size is one important factor which affects the uptake of nutrients and growth rates. Now we consider how nutrient uptake varies with size and then how nutrient uptake and growth are related.

Nutrient uptake and cell size

Cell size affects the diffusive supply of nutrients, as depicted in Fig. 5.7a: for an idealised, spherical cell at low nutrient concentrations, the diffusive supply of nutrients increases with cell radius R (5.18), but at the same time the cell volume increases as $(4/3)\pi R^3$. Thus, the diffusive supply of nutrients per unit volume is largest for cells with small R and smallest for cells with large R ; see

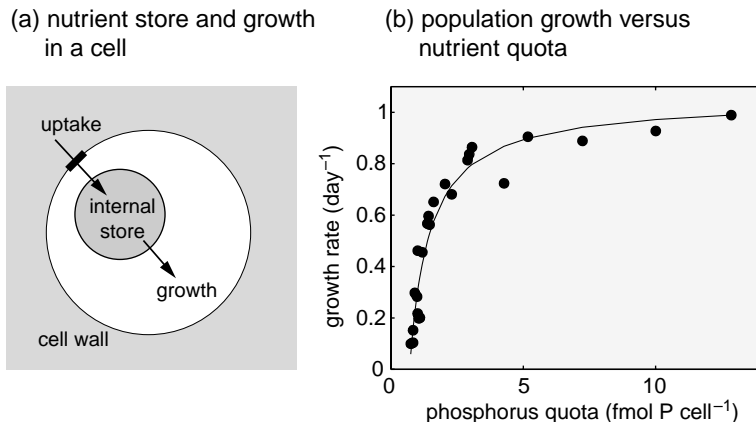


Figure 5.8 Reproduction of phytoplankton cells depends on the internal store of nutrients within the cell, as well as the uptake of nutrients from the environment. (a) A schematic view: nutrients are taken up across a cell wall into an internal store. This rapidly accessible reservoir within the cell can sustain rapid growth even when the direct uptake is insufficient at the time. (b) A laboratory view of the population growth rate, μ (day^{-1}), in continuous cultures of the phytoplankton *Monochrysis lutheri* as a function of the average phosphorus content of the cells (data from Burmester, 1979); the solid curve is described by $\mu = \mu^{\max} \frac{\Delta Q_p}{\Delta Q_p + K_{Q_p}}$, where $\mu^{\max} = 1.05 \text{ day}^{-1}$, $K_{Q_p} = 0.75 \text{ fmol P cell}^{-1}$, $\Delta Q_p = Q_p - Q_p^{\min}$ and $Q_p^{\min} = 0.702 \text{ fmol P cell}^{-1}$; note $\text{fmol} = 10^{-15} \text{ moles}$. Larger phosphorus content implies a larger internal store, facilitating rapid growth. It may also be associated with a high concentration of RNA, which synthesises new proteins.

Box 5.1 and Q5.3. In accord with this view, laboratory studies reveal the nitrate uptake half saturation is smaller for smaller volume cells, illustrated in Fig. 5.7b, enhancing their ability to compete for nutrients at low concentrations.

Hence, if phytoplankton growth only depended on the diffusive supply of nutrients, then the fastest growing and most competitive phytoplankton species would always be the smallest cells. However, this is not the case and large cells dominate some environments.

Decoupling of nutrient uptake and growth

The uptake of nutrients and growth of new cells need not always be tightly coupled. Instead cells may acquire nutrients into an internal store then synthesise new proteins later (Fig. 5.8a). This process is analogous to a piper playing the bagpipes: the piper blows into the instrument, supplying air which does not immediately make a note, but is stored in a reservoir and used to produce notes at a later time.

Larger phytoplankton cells can accommodate an internal store of nutrients within their greater volume. When there are appropriate conditions for growth, such as sufficient sunlight, larger phytoplankton cells can utilise this store to

grow much faster than smaller cells, which are constrained by the external diffusive supply of nutrients. Laboratory studies reveal growth rate increasing with the phosphorus content of the cells, referred to as cell quota, as illustrated in Fig. 5.8b. There is a minimum cell quota, Q_p (mol cell^{-1}), necessary for survival and then cell division rate increases with cell quota, saturating at an upper bound.

Hence, growth rate increases when the cell has an internal store of phosphorus which may be accessed rapidly (Droop, 1968; Caperon, 1968). This decoupling of uptake and growth provides a mechanism by which large cells, in some circumstances, can be more viable and outcompete smaller cells. This mechanism can be described in relatively simple model structures, as in Box 5.2.

Now we consider other environmental factors affecting phytoplankton growth, and their distribution in the ocean.

5.3.4 How does light affect microbial growth?

Phytoplankton obtain energy by absorbing photons with light-harvesting pigments, as illustrated in Fig. 5.9a. Light-harvesting pigments are occupied for a finite time as the energy is passed into

Box 5.2 A basic model of phytoplankton population growth

The biomass of phytoplankton with respect to element \mathcal{N} , $B_{\mathcal{N}}$ (mol m^{-3}), is the product of the cell quota, $Q_{\mathcal{N}}$ (mol cell^{-1}), and the number density of cells, X (cells m^{-3}):

$$B_{\mathcal{N}} = Q_{\mathcal{N}}X. \quad (5.20)$$

The rate of change of biomass, $\dot{B}_{\mathcal{N}}$ ($\text{mol m}^{-3} \text{s}^{-1}$), depends on the balance between the acquisition of nutrient \mathcal{N} by the cell from the environment following a saturating relationship and loss processes, including mortality due to viral infection or predation,

$$\frac{dB_{\mathcal{N}}}{dt} = V_{\mathcal{N}}^{\max} \frac{\{\mathcal{N}\}}{\{\mathcal{N}\} + K_{\mathcal{N}}} X - mB_{\mathcal{N}}, \quad (5.21)$$

where $\{\mathcal{N}\}$ is the nutrient concentration (mol m^{-3}) in the environment, $K_{\mathcal{N}}$ is the half-saturation rate (mol m^{-3}), $V_{\mathcal{N}}^{\max}$ is the cellular uptake rate ($\text{mol cell}^{-1} \text{s}^{-1}$) and the loss of biomass is represented by a simple, linear decay, with constant m (s^{-1}).

The rate of change of number density of cells, X , is described as the balance between production due to cell division, with exponential growth rate, μ (s^{-1}), and losses due to mortality, m ,

$$\frac{dX}{dt} = \mu X - mX. \quad (5.22)$$

This simplified framework is completed by relating the growth rate, μ , to the cell quota, $Q_{\mathcal{N}}$, assuming a saturating relationship (Fig. 5.8b) following Caperon (1968),

$$\mu = \mu^{\max}(T, l) \frac{\Delta Q_{\mathcal{N}}}{\Delta Q_{\mathcal{N}} + K_{Q_{\mathcal{N}}}}, \quad (5.23)$$

where $\mu^{\max}(T, l)$ is the maximum growth rate and $\Delta Q_{\mathcal{N}} = Q_{\mathcal{N}} - Q_{\mathcal{N}}^{\min}$ is the excess of nutrient element \mathcal{N} relative to its minimum subsistence quantity, and $K_{Q_{\mathcal{N}}}$ is a half-saturation coefficient. The maximum growth rate may be modulated by other environmental variables, including temperature (T) and light (l).

the cell before being able to absorb additional photons; see Falkowski and Raven (1997) for a detailed exposition on aquatic photosynthesis. Primary production, the creation of organic matter, generally increases with the incident flux of photons at low light levels, but saturates at high photon fluxes, as illustrated in Fig. 5.9b. Conceptually the form of this relationship is analogous to an enzymatic reaction with an arrival stage and a handling stage.

Phytoplankton adjust the abundance of pigment in the cell, the chlorophyll concentration, to optimise light harvesting. In reduced irradiance,

the cells produce a higher concentration of chlorophyll (Fig. 5.9c), reflected in the increasing chlorophyll content of phytoplankton with depth through the euphotic zone, as observed in the tropical Atlantic in Fig. 5.10, even though carbon biomass remains uniform over the same layer. This acclimation of chlorophyll in phytoplankton alters the elemental composition of the cells, since pigments used for light harvesting are rich in nitrogen (Geider *et al.*, 1997).

Conversely, if irradiance is very strong, the cellular chlorophyll concentration is reduced. Under some circumstances, the increased incidence of

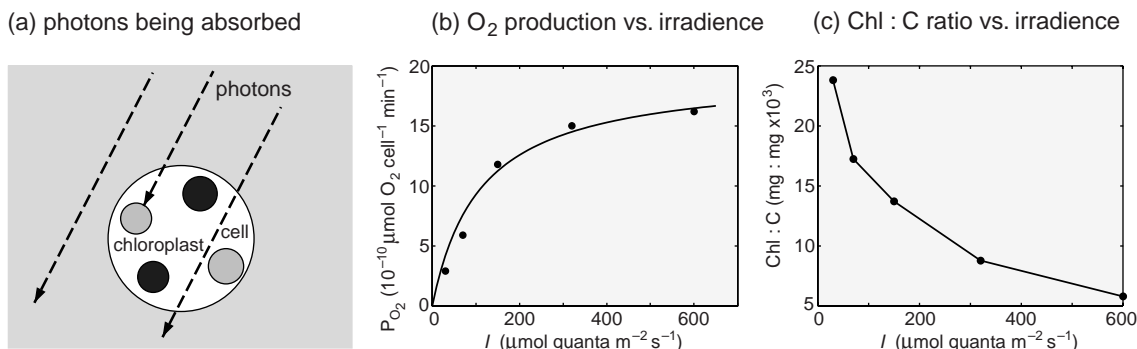


Figure 5.9 (a) A schematic view of the absorption of photons by pigments within cells; (b) the relationship between gross photosynthesis measured in terms of oxygen production, P_{O_2} ($10^{-10} \mu\text{mol O}_2 \text{ cell}^{-1} \text{ min}^{-1}$), and irradiance, I ($\mu\text{mol quanta m}^{-2} \text{ s}^{-1}$) by visible wavelength radiation in equilibrated laboratory cultures of *Isochrysis galbana*; and (c) the acclimated ratio of cell chlorophyll to carbon content, Chl : C ($\text{mg : mg} \times 10^3$), in the same cultures. At low light, the cells increase chlorophyll content in an effort to maintain light-harvesting capability. Data from Falkowski *et al.* (1985).

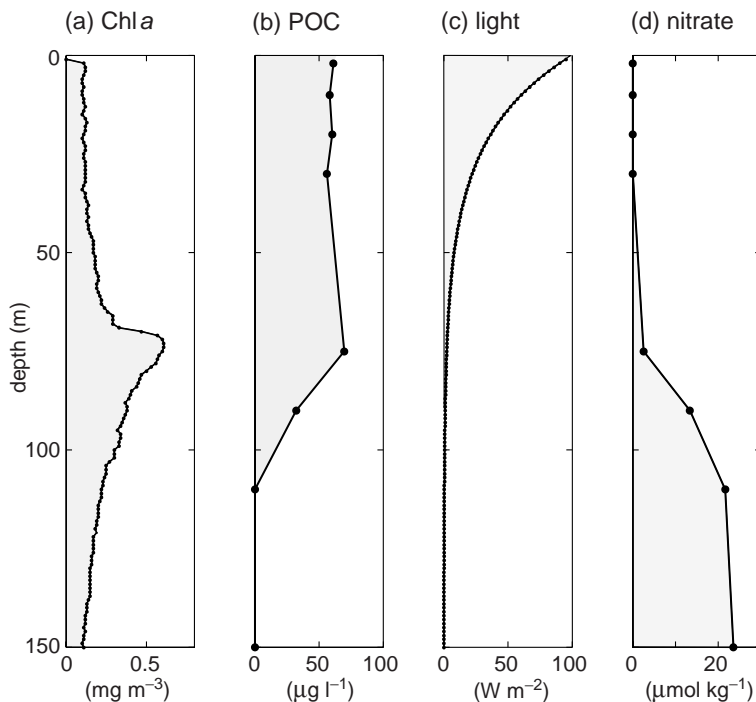


Figure 5.10 Vertical profiles of (a) chlorophyll *a* (mg m^{-3}) and (b) particulate organic carbon, POC ($\mu\text{g l}^{-1}$), including total phytoplankton and zooplankton biomass, (c) the downward flux of visible wavelength solar radiation (W m^{-2}) and, (d) nitrate concentration ($\mu\text{mol kg}^{-1}$) in the equatorial Atlantic Ocean (2.5°N , 24.4°W). Data from Atlantic Meridional Transect 15; figure courtesy of Anna Hickman.

photons is damaging and photosynthesis becomes less efficient as light exposure increases. In this case, resources within the cell are diverted to form photo-protection pigments, which dissipates the excess energy and protects the cell, at the price of a reduced rate of photosynthesis and population growth.

5.3.5 How does temperature affect phytoplankton growth?

Biochemical reactions proceed more rapidly at warmer temperatures; accordingly laboratory studies reveal maximum phytoplankton growth rates increase with temperature (Fig. 5.11). In the ocean, the effects of nutrient availability,

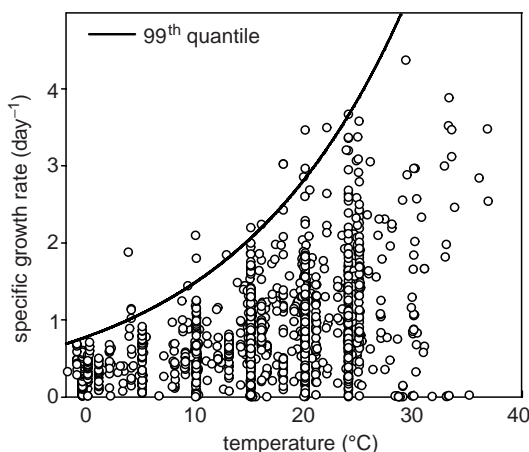


Figure 5.11 Marine phytoplankton, maximum growth rate (day^{-1}) as a function of temperature (circles), each point represents the measured growth rate of a phytoplankton culture at a particular temperature from a dataset of 1501 samples, together with the 99th regression quantile (full line). The envelope of highest maximum growth rates increases exponentially with temperature, reflecting the underlying temperature sensitivity of biochemical reaction rates; for details of the data set, see Bissinger et al. (2008), which updates the study of Eppley (1972). Figure courtesy of David Montagnes, © 2008 by the American Society of Limnology and Oceanography.

irradiance and temperature combine to regulate phytoplankton growth rates and primary production of organic matter.

Next we consider how diverse functional types of phytoplankton flourish in different regions of the ocean, examining how their physiological adaptations make them successful.

5.4 Phytoplankton community structure

There is a vast diversity in phytoplankton species in the oceans with cell sizes ranging from one to hundreds of microns and a wide variety of physiological specialities:

- Diatoms can form large internal stores, grow very quickly and bloom when resources are plentiful. They create silicon-based structural parts, spanning a wide range of cell size from

a few microns to hundreds of microns, and may be unicellular or form colonies. A significant fraction of the fresh organic matter created by diatoms ends up in large particles ballasted by mineral silicon which sink rapidly to depth.

- Coccolithophorids form calcium carbonate platelets with a high reflectance of sunlight, so their blooms are easily detected from space, as seen in Fig. 5.12. They are typically a few microns in size. The formation of mineral calcium carbonate has a significant effect on surface ocean chemistry and provides ballast to particles, enhancing the sinking flux of organic matter.
- Tiny pico-phytoplankton dominate the ecosystem over large regions of the surface ocean. These micron-scale cells have no mineral structure and are grazed by tiny predators, so most of the organic matter they produce is efficiently recycled to inorganic form in the surface ocean and the nutrients can be reused for photosynthesis.
- Diazotrophs are organisms which have the ability to fix dissolved nitrogen gas, N_2 which, though energetically costly, can be an advantage for phytoplankton when the availability of dissolved inorganic nitrogen is limiting phytoplankton growth. Diazotrophy is associated with cells types spanning a wide range of size and functionality.
- Flagellates have protrusions (flagella) which can be whipped, enabling active movement which can be an advantage in seeking out scarce resources. Many dinoflagellates (with dual flagella) are mixotrophic; they can perform photosynthesis and prey upon other cells. Some coastal varieties are known for their production of toxins which can taint shellfish. Flagellates range from a few microns to hundreds of microns in size.

Each of these key phytoplankton groups is composed of many hundreds or thousands of species and physiological variants. Next we consider in more detail the relationships between light, nutrients, phytoplankton abundance and community structure.

(a) coccolithophore (b) coccolithophore bloom

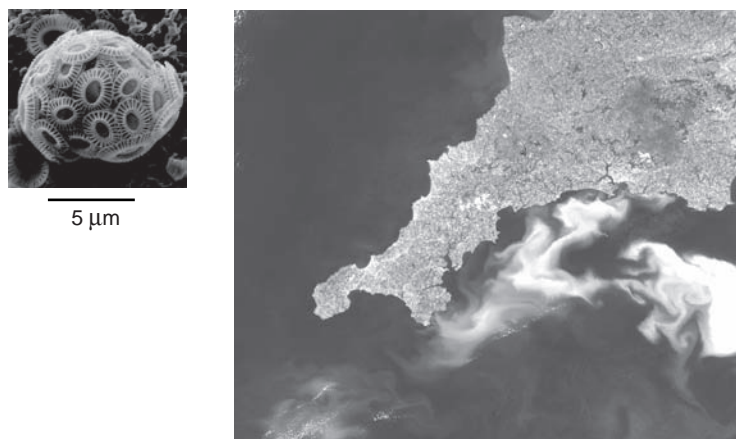


Figure 5.12 (a) Electron-micrograph of coccolithophores; unicellular marine phytoplankton which form calcium carbonate platelets, perhaps as protection from grazers. Image from Karl-Heinz Baumann Universität Bremen (<http://www.geo.uni-bremen.de/cocco>). The species *Emiliania huxleyi* can bloom, reaching high concentrations. (b) Landsat image of a coccolithophore bloom off the coast of southwest England on 24 July 1999 (lighter is more reflectance). The high-reflectance patch (white) covered 16 000 km² at its greatest extent and lasted approximately 3 weeks before being dispersed by unsettled weather in August. The bloom can be seen from space due to the high concentration of external calcite platelets or coccoliths that become detached as the bloom develops. Figure courtesy of Steve Groom, Plymouth Marine Laboratory; see Smyth et al. (2002).

5.4.1 How does phytoplankton community structure vary with the environment?

How do nutrients, light and temperature shape the phytoplankton population? We examine the relationships between chlorophyll, carbon biomass, and phytoplankton community structure along a meridional transect passing through the Atlantic (Aiken *et al.*, 2000).

The chlorophyll concentration is greatest near the surface in the tropics and subpolar latitudes (Fig. 5.13a), but deepens to a subsurface maximum at depths of 100 m or more in the subtropics. This chlorophyll distribution is a consequence of both light and nutrient availability. The depth at which the downward flux of solar radiation is reduced to 1% of its surface value is often used as a measure of the euphotic layer depth, and varies from a few metres, where phytoplankton pigments or suspended sediments are abundant, to as much as 200 m in the clearest waters of the open ocean, where most of the photons are absorbed by water molecules (Fig. 5.13, dashed line). Below

this layer, there is insufficient light to sustain photosynthesis and few phytoplankton are present.

In the upwelling tropical and subpolar regimes, nutrient-rich waters are delivered into the euphotic zone, sustaining phytoplankton growth and high chlorophyll concentrations near the surface, at least on a seasonal basis. In turn, the high concentration of surface pigment absorb light, making the euphotic layer thinner and restricting production at depth.

In the subtropics, the subsurface chlorophyll maximum broadly follows the nitracline, the sharp increase in nitrate with depth (Fig. 5.13b), which is also coincident with the base of the euphotic zone (Fig. 5.13, dashed line), suggesting close co-regulation of phytoplankton growth by nutrient and light availability.

How does phytoplankton community structure vary?

Along a similar meridional section, the near-surface carbon biomass closely follows the

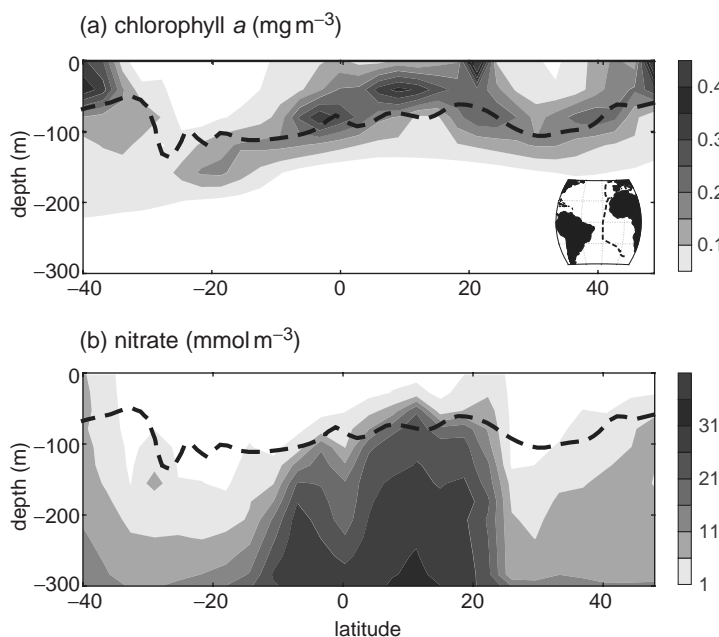


Figure 5.13 Observed (a) chlorophyll *a* (mg m^{-3}), and (b) nitrate (mmol m^{-3}) with depth along the Atlantic Meridional Transect (AMT15, September 2004) from 50°N to 40°S in the Atlantic Ocean. Dashed contours indicate the depth at which irradiance is 1% of the incident surface flux, sometimes used as an indicator of the depth of the euphotic zone. Figure courtesy of Anna Hickman.

near-surface chlorophyll *a* distribution (Fig. 5.14a), which reflects the contribution of different phytoplankton species (Fig. 5.14b):

- Diatoms occur in the nutrient-rich, surface waters of the tropics, subpolar latitudes and off coastal upwelling sites.
- Pico-cyanobacteria, including *Prochlorococcus* and *Synechococcus*, as well as flagellates dominate in the nutrient-depleted regions of the subtropics.
- Coccolithophorids are ubiquitous, but typically account for only 2 to 10% of total phytoplankton biomass along this transect (Marañón *et al.*, 2000).
- Nitrogen-fixing phytoplankton have been observed over the tropics and subtropics, extending up to latitudes of typically 30°, though they make a very minor contribution to biomass.

Now we consider in more detail why the phytoplankton community structure varies with the environment in this way along the Atlantic Meridional Transect, and as illustrated in a global ecosystem model in Plate 16.

5.4.2 What regulates the pattern of community structure?

The biogeography of the marine ecosystem, what lives where and when, is determined by the relative fitness of all of the possible organism physiologies in different environments. We can make a broad brush interpretation by classifying many phytoplankton into one of two types: “gleaners” adapted to low nutrient conditions, and “opportunists” which can most efficiently exploit resources when they become plentiful (MacArthur and Wilson, 1967).

Gleaners and low nutrient conditions

Gleaners specialise in efficiently acquiring resources when they are sparse. Near-surface waters over the subtropical oceans are depleted in dissolved inorganic nutrients, as illustrated in Fig. 5.13b, while irradiance remains strong in these clear waters. The smallest phytoplankton, the cyanobacterium *Prochlorococcus*, dominate this stable environment (Fig. 5.14). Their small size makes them efficient gleaners, with low half-saturation coefficients and efficient diffusive uptake of nutrients (Box 5.3). Flagellates are also

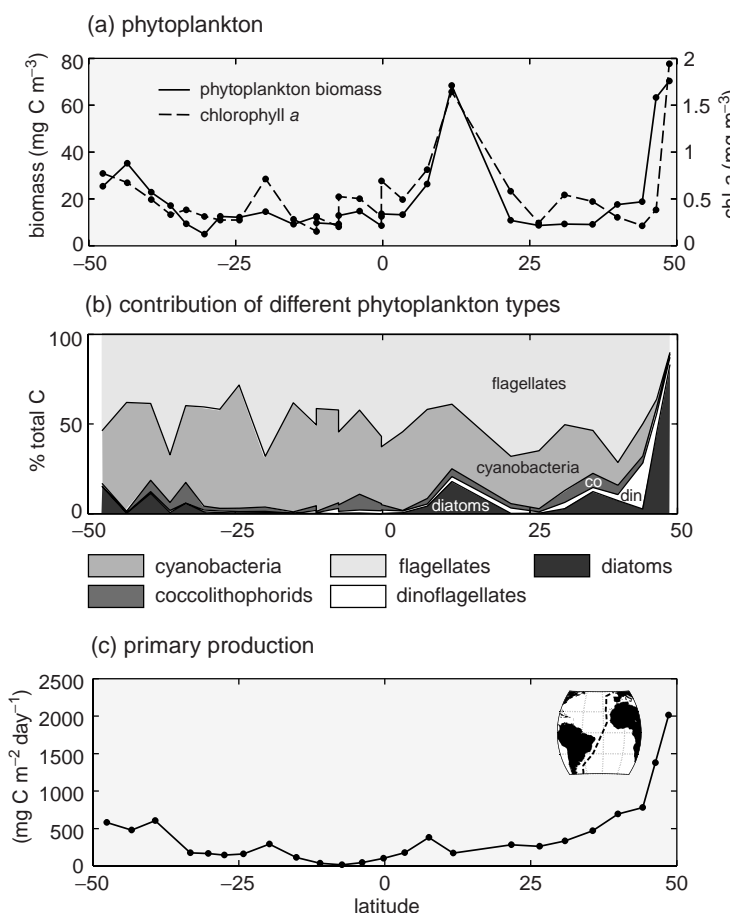


Figure 5.14 Observed phytoplankton community characteristics at 7 m depth along the Atlantic Meridional Transect (AMT2, May 1996): (a) phytoplankton biomass (mg C m^{-3} , full line) and chlorophyll *a* concentration (mg m^{-3}); (b) contributions to biomass of functional groups (mg C m^{-3}), cyanobacteria (mid grey), coccolithophorids (dark grey), flagellates (light grey) and dinoflagellates (white), and diatoms (very dark grey); (c) primary production ($\text{mg C m}^{-2} \text{ day}^{-1}$). Redrawn from Marañón *et al.* (2000), with help from X. Irigoien.

abundant in the subtropics. Their flagella provide a means to move and escape a locally depleted nutrient environment at scales close to their own size.

Opportunists and high nutrient conditions

In contrast, opportunists are organisms which can grow rapidly when resources are plentiful. The mid- and high-latitude oceans are strongly seasonal: winter mixing supplies nutrients to the surface and in the following spring, when the water column warms and irradiance increases, there is a window of opportunity when all resources are replete. These optimal conditions fuel a bloom of opportunists, typically fast-growing diatoms, as illustrated in Fig. 5.4. On shorter timescales, the surface ocean is also regularly disturbed by

the passage of weather systems and ocean eddies, which can enable opportunistic phytoplankton to thrive intermittently.

Alternative strategies

There are also other ecologically successful strategies. For example, mixotrophic dinoflagellates combine photosynthesis with an ability to prey upon other cells; they are successful in environments where neither fast-growing opportunists nor more efficient gleaners survive, and can thrive in barren periods by eating their competitors (Thingstad *et al.*, 1996). Nitrogen fixers also flourish in nitrate-depleted, subtropical waters, where they relieve nitrogen limitation by expending energy to break the triple bond in nitrogen gas at the price of reduced growth rate.

Box 5.3 | Diversity and optimal nutrient strategies

Consider the simple model of phytoplankton growth outlined in Box 5.2 for two contrasting regimes, an equilibrium state where seasonal variability is relatively small and a time-varying state.

Consider the equilibrium solution for the rate of change of biomass (5.21) in a tightly coupled state, where growth and mortality balance,

$$\frac{dB_N}{dt} = V_N^{\max} \frac{\{N\}}{\{N\} + K_N} X - m Q_{N,N} X \sim 0, \quad (5.24)$$

which can be rearranged to define the equilibrium concentration of the limiting nutrient, $\{N\}$, in terms of the physiology of the phytoplankton community,

$$\{N\} = \frac{K_N m}{V_N^{\max}/Q_{N,N} - m}. \quad (5.25)$$

In this limit, the organism which can exist at the lowest equilibrium nutrient concentration draws the nutrient down to this concentration $\{N\}$, which is below the subsistence level of their competitors (Stewart and Levin, 1973; Tilman, 1977). The equilibrium nutrient concentration is a function of the physiological characteristics of the phytoplankton and a low nutrient uptake half saturation, K_N , is advantageous for a gleaner (see Fig. 5.7b).

Alternatively, in a time-varying environment, opportunists can instead thrive. Consider the rate of change of number density, combining (5.22) and (5.23):

$$\frac{dX}{dt} = \mu^{\max} \frac{\Delta Q_N}{\Delta Q_N + K_{Q,N}} X - m X. \quad (5.26)$$

In a variable environment, the fittest opportunist is the organism which capitalises most effectively on the availability of an intermittent resource, boosting their population during the plentiful periods in preparation for the barren periods. From (5.26), the per capita net growth rate for a population of phytoplankton is described as

$$\frac{1}{X} \frac{dX}{dt} = \mu^{\max} \frac{\Delta Q_N}{\Delta Q_N + K_{Q,N}} - m. \quad (5.27)$$

The organism with the highest per capita growth rate is the most effective opportunist. This optimal response can be achieved in a variety of ways: to have a large maximum growth rate, μ^{\max} ; to maintain a large internal store of readily available nutrient resources, ΔQ_N ; or to reduce mortality, m , by defence against predators.

Now we turn to the integrated effect of these different phytoplankton species on the formation of organic carbon and its subsequent fate.

5.5 Primary production and the fate of organic matter

The production of organic carbon, referred to as primary production, depends upon several fac-

tors: the abundance of chlorophyll and irradiance, the availability of essential nutrients and temperature. Primary production is separated into two components: new production utilises nutrients recently arrived into the euphotic layer, while recycled production utilises nutrients derived from respired organic matter which never left the euphotic layer (Fig. 5.15). The relative contributions of new and recycled production varies according to how much ‘new’ nutrients are

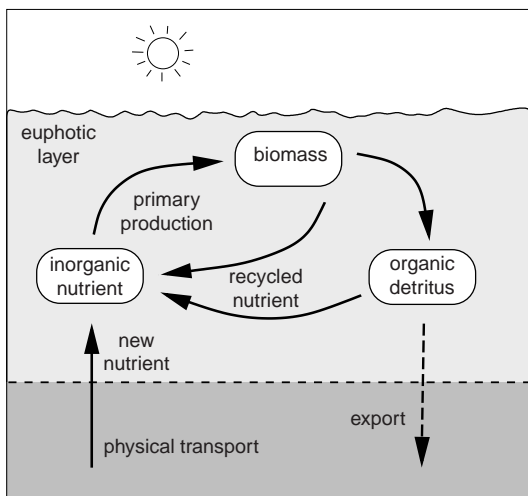


Figure 5.15 Primary production of organic matter may be fuelled in part by 'new' inorganic nutrients which have recently arrived in the local euphotic layer through physical transport or atmospheric deposition. In addition, local respiration of organic matter by bacteria or zooplankton returns living biomass and detritus to the form of inorganic nutrients, and these recycled nutrients also contribute to primary production. A fraction of organic matter, either living or in detrital form, leaves the euphotic layer; this fraction is referred to as export production.

supplied and the phytoplankton community structure.

Some of the organic matter leaves the euphotic zone and passes into the dark interior; this downwards flux of organic matter is referred to as export production. For a steady state, new production and export production have to balance each other when averaged over large space and time scales (Fig. 5.15), although this balance need not hold locally.

5.5.1 Estimating primary productivity

The rate of primary production can be evaluated using *in situ* observations, such as by measuring the rate of uptake of radiocarbon-labelled dissolved inorganic carbon or the rate of production of oxygen in a closed sample. For example, primary production measured along the Atlantic Meridional Transect in Fig. 5.14c varies from less than $300 \text{ mg C m}^{-2} \text{ day}^{-1}$ over the subtropical gyres to more than 500 and up to $2000 \text{ mg C m}^{-2} \text{ day}^{-1}$ over the subpolar latitudes.

Primary production varies strongly with the abundance of chlorophyll. More chloro-

phyll means more light energy harvested and more organic molecules produced. A productivity model using remotely sensed chlorophyll and temperature suggests that primary productivity is largest in the coastal seas, over parts of the tropics and the high latitudes, while primary productivity is lowest in the subtropical gyres and parts of the Southern Ocean (Fig. 5.16; Behrenfeld and Falkowski, 1997).

Integrated over the globe, estimates of the annual primary production range between 35 and 75 Pg Cy^{-1} (Carr *et al.*, 2006). Thus, the photosynthetic production of organic matter in the euphotic layer integrated over a year is of similar order of magnitude to the total living microbial biomass in the entire global ocean (see Q5.1). Thus the global standing stock of biomass in the ocean is refreshed about once a year and the global standing stock of phytoplankton biomass is renewed every couple of weeks.

5.5.2 What is the fate of the organic matter produced by phytoplankton?

Production of organic matter by phytoplankton forms the base of the marine food chain. The subsequent fate of the organic matter is very complex (as depicted in Fig. 5.17), involving the interactions of a vast diversity of organisms and life strategies, from virus to whale. Consequently, it is very difficult to characterise and quantify the fluxes and fate of organic carbon in the marine ecosystem.

Phytoplankton ultimately die through infection by virus, consumption by predators or sinking out of the euphotic layer into the dark waters. Each of these processes leads to the formation of particulate and dissolved organic detritus, which is ultimately reworked and respired by heterotrophs, including zooplankton and bacteria.

- **Viral Infection.** A virus penetrates the cell wall and hijacks the genetic material and nutrient resources of the host cell in order to replicate. After some time the host is burst, releasing the new generation of virus and leaving the remaining portions of the cell to sink or be consumed by other organisms.
- **Predation.** The smallest, micron-scale phytoplankton, such as *Prochlorococcus*, are preyed upon by unicellular predators which can

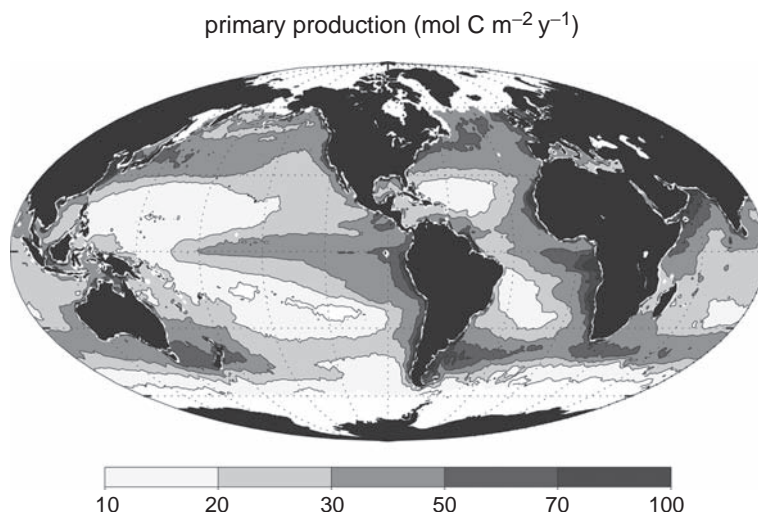


Figure 5.16 Primary production ($\text{mol C m}^{-2} \text{y}^{-1}$), the rate of production of organic matter by photosynthesis, as inferred from remotely sensed estimates of surface chlorophyll and temperature for the year 2005 using the vertically generalised productivity model of Behrenfeld and Falkowski (1997a,b).

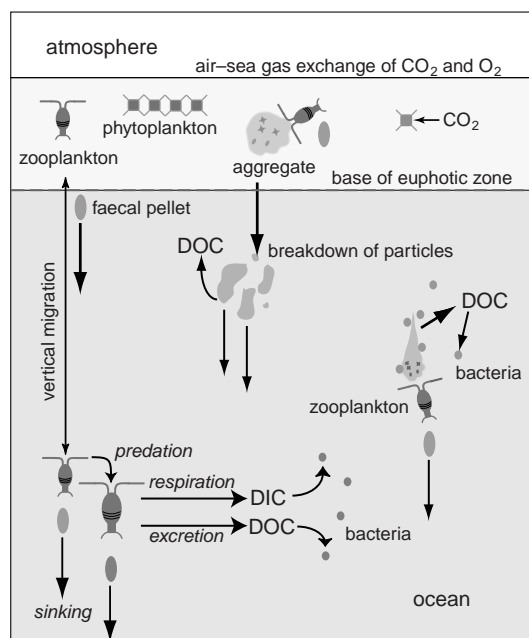


Figure 5.17 Schematic depiction of processes which regulate the export of organic matter from the euphotic layer into the deep ocean. These include primary production of organic carbon, grazing and sinking of phytoplankton cells, respiration and reworking of sinking particulates by bacteria and zooplankton. Modified from Burd *et al.* (2002).

engulf whole cells and digest them. These tiny predators, or micro-zooplankton, excrete dissolved organic matter (DOM), organic detritus consisting of single molecules or tiny, neutrally buoyant particles, which in turn provide a source of nutrients and energy to bacteria.

Larger cells, including diatoms, coccolithophorids, and the micro-zooplankton are preyed upon by larger grazers, including millimetre-scale, shrimp-like copepods and jelly-like, filter-feeding salps. These predators also release DOM and sinking particulate organic matter, POM, through sloppy feeding and the production of faecal pellets.

The grazing of prey by predators can be described as a two-stage process with an interesting analogy to enzyme kinetics. Prey are captured by a predator (Fig. 5.18a), then must be ingested before another capture can occur (Holling, 1959), leading to the characteristic saturating functional form associated with arrival and handling. Laboratory studies reveal the ingestion of prey by a zooplankton increases with prey density, then saturates, as illustrated in Fig. 5.18b. This relationship can be modified by the behaviour of the predators; for example, when prey is scarce, more energy can be spent finding food than is consumed, so that a predator may stop feeding or switch to a different prey.

- **Sinking.** Small phytoplankton cells and organic matter are easily suspended by turbulence, while larger phytoplankton cells and clumps of organic matter sink more quickly. This response is analogous to how small cloud droplets in the atmosphere remain suspended until they coalesce together and form larger droplets which fall out of the cloud as rain. However,

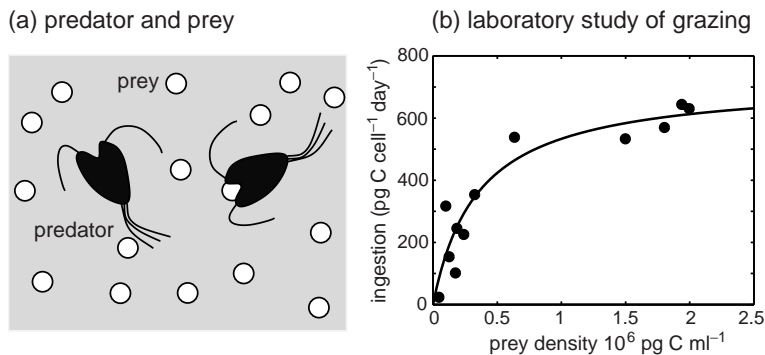


Figure 5.18 Predator-prey relationships: (a) a schematic view of a predator hunting prey, and (b) a laboratory study revealing the rate of ingestion of prey by a dinoflagellate, *Karlodinium armiger*, versus prey density of a phytoplankton, *Rhodomonas salina*; redrawn from Berge et al. (2008) courtesy of Inter-Research. These data can be described by a saturating curve (Holling, 1959); here the solid line indicates a curve with half-saturation prey density of $0.35 \times 10^6 \text{ pg C ml}^{-1}$ and maximum ingestion rate of $720 \text{ pg C cell}^{-1} \text{ day}^{-1}$.

living cells can counteract negative buoyancy by forming a vacuole or a reservoir of low density organic compounds. In contrast, the dense mineral components of diatoms and coccolithophorids promote sinking. In the late stages of diatom blooms, the cells excrete carbon-rich organic matter which sticks together, forming sinking aggregates and marine snow (see later Fig. 5.20a). As the sinking material falls, suspended material is swept up (like falling cloud drops growing into rain drops), and provide a source of nutrition for heterotrophs living at depth.

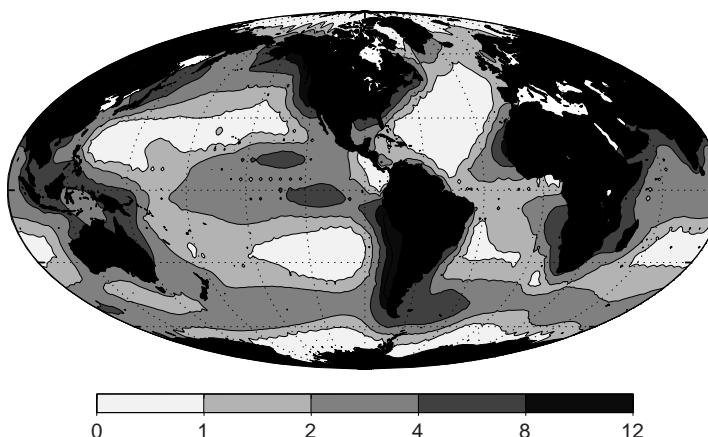
5.5.3 Export production

Most of the organic matter produced by phytoplankton is respired by bacteria or zooplankton within the sunlit euphotic layer. However, a significant fraction of organic matter is transported into the underlying dark waters. The organic matter leaves the euphotic zone either as sinking particles or suspended and transported by the circulation. The organic matter is separated into particulate organic matter (POM) and dissolved organic matter (DOM), which is operationally defined as passing through a $0.45 \mu\text{m}$ filter. DOM includes contributions from compounds consumed within hours, perhaps amino acids which can be used by other cells, to very long-lived compounds, including structural proteins, which circulate within the ocean for hundreds of years or more.

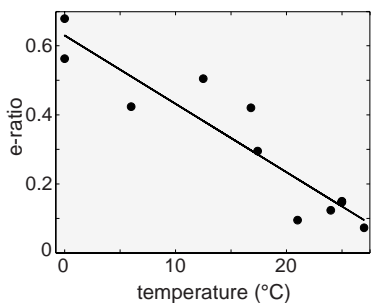
Export production, the rate at which particulate organic carbon sinks across the base of the euphotic layer, varies with patterns of primary production and the efficiency of recycling (Fig. 5.15). Based on an inverse model of ocean circulation and nutrient fluxes, export production is largest over the coastal seas, upwelling regimes in the tropics and subpolar gyres, and lowest over the subtropical gyres, as illustrated in Fig. 5.19a. This pattern broadly suggests reduced export in regions of low primary production (Fig. 5.16). In support of this view, observations with sediment traps, suspended cups which catch sinking particles, suggest that between 10% and 70% of primary production is exported from the euphotic layer as sinking particles (Fig. 5.19b,c; Laws et al., 2000), with highest export efficiencies in the colder, nutrient-rich, productive waters.

Phytoplankton community composition also affects the efficiency of recycling and the resulting export production:

- Small cells without mineral parts sink more slowly and are more likely to be consumed and recycled within the euphotic layer or the upper water column. Phytoplankton with small cells preferentially flourish in the nutrient-depleted surface waters of the subtropical gyres. Hence, the ratio of export to primary production, the e-ratio, is low over the subtropical gyres, as illustrated in Fig. 5.19b,c.
- Larger cells, such as diatoms or coccolithophores, with mineral parts, lead to more

(a) export production ($\text{mol C m}^{-2} \text{y}^{-1}$)

(b) e-ratio versus temperature



(c) e-ratio versus latitude

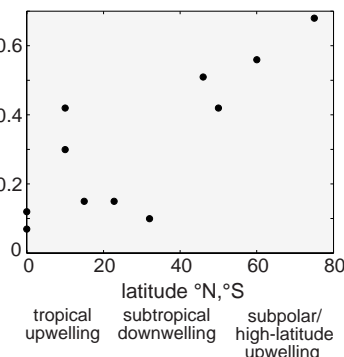


Figure 5.19 (a) Export production: the downward flux of organic carbon across the 133 m depth horizon ($\text{mol C m}^{-2} \text{y}^{-1}$) is estimated using an inverse model for the physical transport of temperature, salinity, nutrients and carbon (Schlitzer, 2000; data from export estimate provided by R. Schlitzer). In (b) and (c), the e-ratio (dimensionless) is defined as the fraction of export production (from measurements of sinking particles) divided by primary production plotted against (b) temperature ($^{\circ}\text{C}$) and (c) latitude (north or south). There is a clear relationship for the e-ratio with temperature (full line), but a more complex variation with latitude, reflecting the dynamical regime: low e-ratios in the latitude band for downwelling, subtropical gyres and larger e-ratios over the upwelling zones of the tropics, subpolar gyres and high latitudes. Data in (b) and (c) compiled by Laws *et al.* (2000) from regional process studies.

rapid sinking with their silica or calcium-carbonate mineral components deterring efficient grazing. If they are grazed, the faecal pellets of the grazers are then packed with ballast from the undigested mineral material. Larger cells tend to flourish in nutrient-rich upwelling regions, such as the tropics and subpolar waters, which then have high export relative to primary productivity, a high e-ratio (Fig. 5.19c).

Hence, the export of organic matter from the euphotic zone is affected by both the primary productivity and the phytoplankton community structure. Now we consider the subsequent fate of the organic matter.

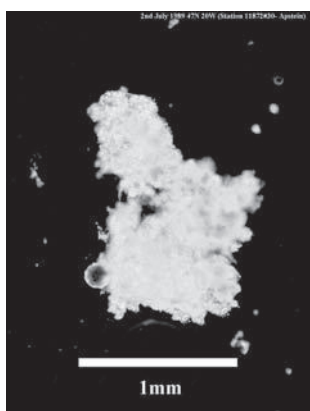
5.5.4 What is the fate of exported organic carbon?

Marine microbes have evolved to efficiently utilise the energy available from organic matter created

by primary producers. Almost all of the organic material leaving the sunlit layer is respired by heterotrophs. Immediately below the euphotic layer, the downward flux of organic matter decreases rapidly, with an e-folding length scale, z^* , of typically 100 m to 200 m (Fig. 5.20b). Only about 1% of the export from the euphotic layer reaches the sea floor, where the organic matter may be respired by benthic organisms or buried in the sediments.

Larger and denser particles sink faster and are respired at greater depth than smaller or less dense particles. A sinking speed of 100 m per day implies a particle leaves the euphotic layer within a day or two, and might take several weeks to reach the sea floor. Mineral ballast increases sinking speed and protects some of the associated organic material from bacterial respiration, leading to slower and deeper regeneration. The

(a) marine snow



(b) sinking flux of POC

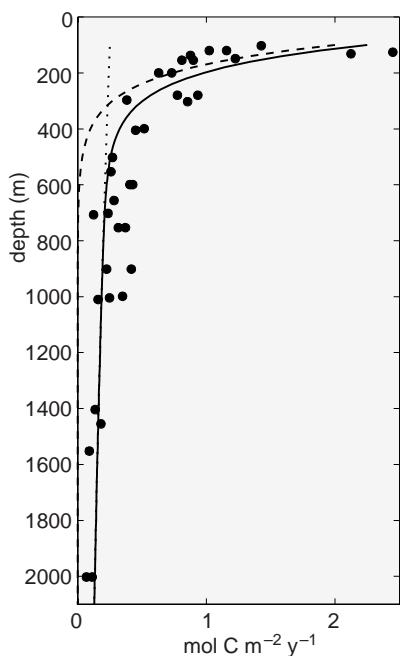


Figure 5.20 (a) Photograph of marine snow collected 2 July 1989 at 47°N, 20°W. This organic detritus, collected below the surface sunlit layer, includes aggregates of organic matter from dead organisms and faecal matter, mineral material from phytoplankton cell structures and dust particles blown from the land; courtesy of Richard Lampitt (Watson *et al.*, 2001). (b) A vertical profile of the sinking flux of particulate organic carbon in the subtropical Pacific Ocean, as measured by sediment traps; redrawn from Martin *et al.* (1987). Filled circles represent the measured data. The solid line represents the total downward flux, and dashed and dotted lines indicate modelled fluxes of unprotected and protected particle organic carbon, respectively: the curves are $F_{POC}(z) = F_{POC}(z_0)e^{-(z-z_0)/z^*}$, where $F_{POC}(z_0)$ is 2.0 and 0.25 mol C m⁻² y⁻¹ respectively, z^* is 100 and 2500 m respectively, and the reference depth, z_0 , is 100 m (see Box 5.4).

ratio of organic carbon to calcium carbonate in sinking particles decreases from around 80% at the base of the euphotic zone to about 5% at 1000 m and deeper depths. Most of the organic carbon in the particles is readily accessible to bacteria and quickly respired, while about 5% is protected from the bacteria by the matrix of mineral material (Armstrong *et al.*, 2002); see Fig. 5.20b, dashed and dotted lines, and Box 5.4 for a mathematical representation.

Conceptually, the sinking organic particles can be separated into material protected by ballast and that which is not (Armstrong *et al.*, 2002): the two components are respiration at different rates reflecting how accessible the organic matter is to bacteria. The downward flux of organic carbon can then be described as the sum of two exponentially decaying components with depth, one with a longer regeneration length scale (slower regeneration rate) than the other (curves on Fig. 5.20b). This simple model reflects some important processes, but is still highly idealised, since the rate of respiration of organic carbon depends on complex interactions with the organisms in the environment.

5.6

Consequences for ocean biogeochemistry

The recycling of exported organic matter has a major impact on the large-scale distribution and cycling of biologically active tracers in the ocean. As Redfield (1934) first noted, there is a close correspondence between the average elemental ratios in the plankton and those of the dissolved inorganic nutrients in the water column (Table 5.2).

Primary production creates organic matter with average elemental ratios of C : N : P = 106 : 16 : 1. This organic matter passes through the food web, some of it eventually sinking to the deep ocean to be respiration by heterotrophs, returning the elements to dissolved inorganic form in approximately the same ratio. Recent inferences of the elemental ratios in sinking particles find C : N : P : O₂ = 117(±14) : 16(±1) : 1 : 170(±10) (Anderson and Sarmiento, 2004).

The observed relationships between dissolved inorganic carbon, nitrate and phosphate in the global ocean are thus broadly consistent with the elemental ratios of the plankton population, as

Box 5.4 A simple model of particle respiration and regeneration

Consider a one-dimensional vertical balance for organic matter in sinking particles, $\{\text{POC}\}$ (mol C m^{-3}), ignoring lateral transfers. Below the euphotic layer, the rate of change in the concentration of particles depends upon the divergence of the vertical sinking flux and respiration of the organic matter;

$$\frac{\partial \{\text{POC}\}}{\partial t} = -w_{\text{sink}} \frac{\partial \{\text{POC}\}}{\partial z} - \lambda_{\text{POC}} \{\text{POC}\}, \quad (5.28)$$

where w_{sink} (m s^{-1}) is the sinking speed of the particles, and λ_{POC} (s^{-1}) the rate of respiration of the organic matter. Assuming a steady state, then rearranging (5.28) reveals

$$\frac{1}{\{\text{POC}\}} \frac{\partial \{\text{POC}\}}{\partial z} = -\frac{\lambda_{\text{POC}}}{w_{\text{sink}}} = -\frac{1}{z^*}. \quad (5.29)$$

The solution for the particle concentration as a function of depth, $\{\text{POC}(z)\}$, is

$$\{\text{POC}(z)\} = \{\text{POC}(z_0)\} e^{-(z-z_0)/z^*}, \quad (5.30)$$

where $\{\text{POC}(z_0)\}$ is the concentration at a reference depth, z_0 , perhaps the base of the euphotic layer; and $z^* = w_{\text{sink}}/\lambda_{\text{POC}}$ is the e-folding length scale of regeneration, the vertical distance over which the particle concentration decreases by a factor e . This simple model suggests an exponential decrease in particle concentration with depth, subject to λ_{POC} and w_{sink} being taken as constant.

The downward flux of particles, F_{POC} ($\text{mol C m}^{-2} \text{s}^{-1}$), is simply given by

$$F_{\text{POC}}(z) = w_{\text{sink}} \{\text{POC}(z)\} = F_{\text{POC}}(z_0) e^{-(z-z_0)/z^*}, \quad (5.31)$$

where $F_{\text{POC}}(z_0) = w_{\text{sink}} \{\text{POC}(z_0)\}$.

Particles associated with mineral material are denser, sink faster and reach a greater depth before complete respiration. Mineral ballast protects part of the organic matter and effectively reduces the respiration rate, λ_{POC} , and so increases the depth at which the organic material becomes regenerated, z^* . Particles originating in communities dominated by diatoms or coccolithophores have a higher sinking speed, w_{sink} , and deeper regeneration length scale, z^* , driven by the dense mineral components.

In reality, sinking particles are a mixture of accessible and mineral protected organic matter (see Fig. 5.20b, dashed and dotted lines).

illustrated in Fig. 5.21, where the scatterplot of inorganic nutrients is more or less aligned with the dashed lines reflecting the canonical Redfield ratios.

The concept of ‘fixed’ Redfield ratios is a useful device with which to develop simple frameworks to interpret the relationship of the carbon cycle and those of other elements. However, in addition to the variability in elemental ratios between and within phytoplankton species (Table 5.2), there is a

significant spread of ocean data points away from this canonical relationship in Fig. 5.21. Notably the slope of the nitrate : phosphate scatterplot is slightly shallower than 16, reflecting a global deficit of nitrogen relative to phosphorous compared to a Redfield balance.

Variations in the nutrient cycles lead to departures in the nutrient ratios from the canonical Redfield values. Next we consider the differences in the cycling of some key elements.

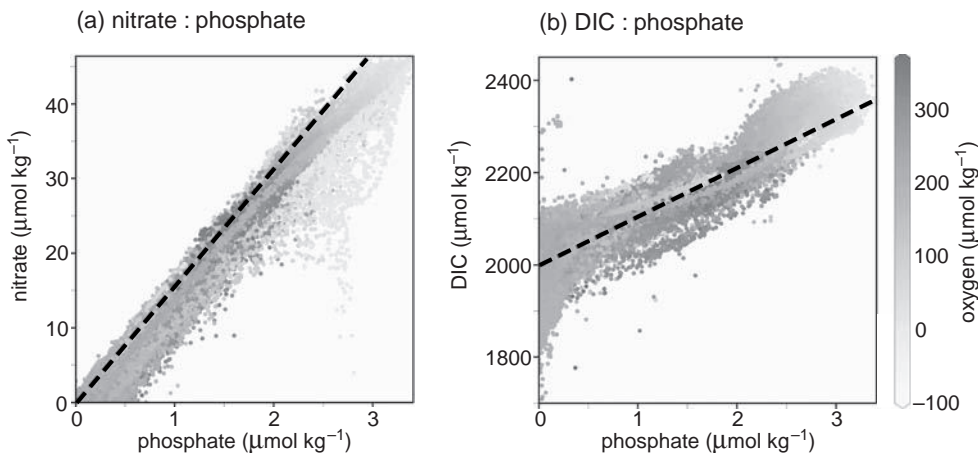


Figure 5.21 Relationships between observed concentrations of (a) nitrate and phosphate, and (b) dissolved inorganic carbon (DIC) and phosphate ($\mu\text{mol kg}^{-1}$) in the global ocean. Grey shading indicates the dissolved oxygen concentration ($\mu\text{mol kg}^{-1}$). The data reveal the close relationship between ocean nutrient ratios and those of ‘average’ marine plankton or Redfield ratios (dashed lines) of $\delta\text{DIC} : \text{NO}_3^- : \text{PO}_4^{3-} = 106 : 16 : 1$. δDIC is the difference in dissolved inorganic carbon from a reference value. Data from Key *et al.* (2004).

5.6.1 Contrasts in nutrient cycles

Nutrients are incorporated into organic matter in the surface ocean and regenerated in deeper waters. The global distributions of nutrients are primarily controlled by a combination of the biological cycling and physical transport and mixing processes. Circulation and biological export come into a global equilibrium over a few thousand years. Differences in the sources and sinks of the key elements, phosphorus, nitrogen, silica and iron, affect the phytoplankton community structure and cycling of organic matter, as illustrated schematically in Fig. 5.22:

- Phosphorus trickles into the ocean from rivers and atmospheric deposition, and is buried in sediments (Fig. 5.22a). These fluxes are small relative to the physical and biological transfers within the water column. Phosphorus has a lifetime of about 100 000 years in the ocean. Silicon also has riverine sources and a loss due to burial. It is utilised by some organisms to provide mineral structural material, which sinks and is redissolved, but more slowly than the remineralisation of most organic matter.
- Nitrogen likewise has sources from rivers and atmospheric deposition, but is also supplied to

the ocean through biological fixation of soluble nitrogen gas. Nitrogen is ultimately lost from the ocean in low oxygen waters and sediments through denitrification (Fig. 5.22b). In a low oxygen state, microbes use nitrate to provide the oxidising agent for organic matter, eventually returning nitrogen to gaseous form, which is lost from the ocean. Due to these additional sources and sinks, nitrogen has a lifetime on the order of 10 000 years in the ocean (Gruber, 2004), much shorter than that of phosphorus. The departure from Redfield ratio of nitrate and phosphate can be quantified by

$$\text{DIN}_{xs} = \text{NO}_3^- - 16\text{PO}_4^{3-} \quad (5.32)$$

(Hansell *et al.*, 2004), and the close variant, N^* , which adds a constant (Gruber *et al.*, 1996). This tracer provides a clue as to the relative sizes of the sources and sinks of nitrogen to and from the ocean: higher values indicate an overall nitrogen supply to the ocean, such as from nitrogen fixation, while lower values represent an overall loss from the ocean, such as from denitrification; as illustrated in Fig. 5.23b.

- Iron is carried as windborne dust from the continents and deposited on the ocean, where a

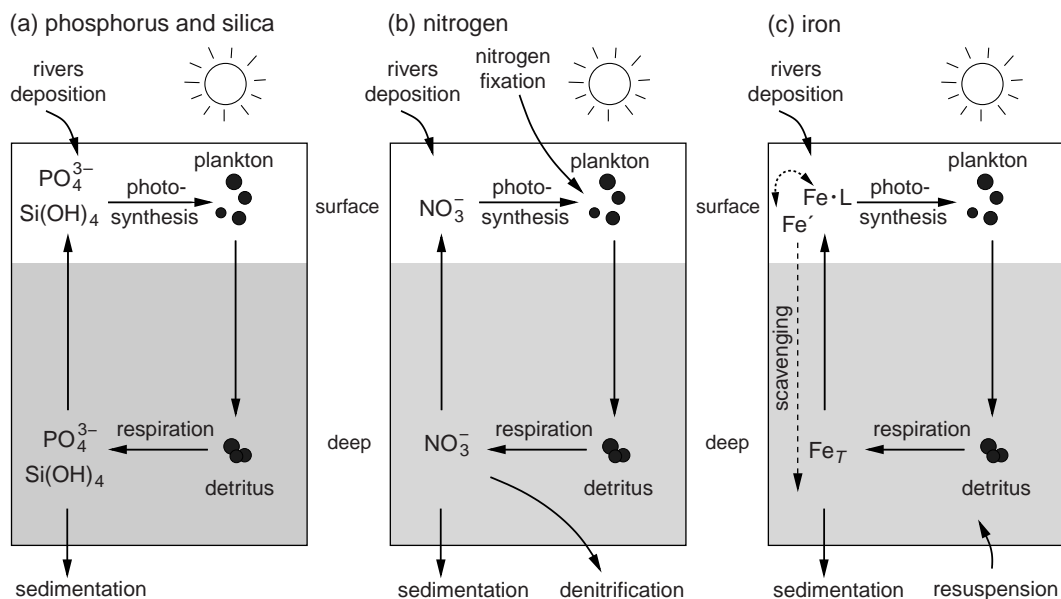


Figure 5.22 Contrasting global nutrient cycles for (a) phosphorus and silica, (b) nitrogen and (c) iron. In (a), phosphorus and silica pass into the ocean from rivers and atmospheric deposition and are buried in sediments. In (b), nitrogen is also fixed from nitrogen gas in the surface ocean and returned to gaseous form through denitrification in low oxygen waters and sediments. In (c), the total dissolved iron, Fe_T , is made up of free iron, Fe^+ , and a complex from, $\text{Fe} \cdot \text{L}$, bound to a ligand. The free iron sticks to sinking particles and is quickly scavenged from the water column, leaving most of the dissolved iron in the complex form. Iron is supplied to the ocean through windborne dust from the continents, and released from sediments and hydrothermal vents. Adapted from a figure by F. Monteiro.

fraction enters the dissolved phase (e.g., Mahowald *et al.*, 2009). Iron is also released from sediments and hydrothermal vents. Dissolved iron is in a highly oxidised state which has extremely low solubility. Iron is incorporated into organic matter, exported and regenerated along with other elements. However, unlike nitrate and phosphate, dissolved iron has a very low solubility, sticks to sinking particles and is rapidly scavenged from the water column and lost to the sea floor (Fig. 5.22c). Nearly all of the dissolved iron is bound to organic ligands, molecules with appropriate binding sites (Johnson *et al.*, 1997), which provide some protection from scavenging (see Box 5.5). The concentration of dissolved iron is on the order of 1 nmol kg^{-1} in seawater. Iron is an essential nutrient for phytoplankton, playing a key role in light harvesting and nitrogen-fixing enzymes, but is a minor contributor to the mass of phytoplankton cells. The observed $\text{Fe} : \text{C}$ ratio varies widely from $1 : 10^3$ to $1 : 10^6$ (Boyd *et al.*, 2007). Iron has a very dynamic

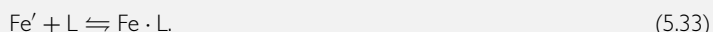
cycle in the ocean, with an average lifetime on the order of 100 years (Bruland *et al.*, 1994).

The contrasting cycles of nitrogen, phosphorus, iron and silicon lead to subtle differences in the distributions of their dissolved inorganic forms, observed along a meridional section in the North Atlantic ocean, illustrated in Fig. 5.23. Nitrate is very depleted throughout the surface (Fig. 5.23a) and the nitracline is depressed by downwelling in the subtropics. Tropical upwelling fuels primary and export production, and leads to an accumulation of regenerated nitrate at a few hundred metres below the surface. The contrast between nitrate and phosphate, measured by DIN_{xs} (Fig. 5.23b), shows higher values to the north and a decline to the south. This signal reveals how the North Atlantic is a region of nitrogen fixation, sustained by the atmospheric deposition of iron-rich dust from the Sahara, which elevates the tropical surface iron concentration, even though nitrate is completely depleted (Fig. 5.23c), and

Box 5.5 | Complexation maintains the dissolved ocean iron inventory

Iron in the ocean can be separated into particulate and dissolved forms, defined by the passage through an 0.4 µm filter. Total dissolved iron, Fe_T , is composed of free iron, Fe' , and a complexed form, $\text{Fe} \cdot \text{L}$, bound to organic ligands, which accounts for 99% of the total (Gledhill and van den Berg, 1994). Free iron, Fe' , has a very low solubility and is easily scavenged, and were it not for complexation, the concentration of iron would be even lower than observed.

Consider this complexation in more detail: free iron atoms, Fe' , bind with a ligand, L , to form a complex $\text{Fe} \cdot \text{L}$,



The complex is held together by relatively weak intermolecular bonds and Fe' may eventually detach from $\text{Fe} \cdot \text{L}$, perhaps through thermal excitation or photodissociation. The rate of change of the concentration of free iron, $\{\text{Fe}'\}$ (mol m⁻³), is represented in the forward and backward reactions of (5.33), which can also be described by the kinetic equation

$$\frac{d\{\text{Fe}'\}}{dt} = -k_f \{\text{Fe}'\}\{\text{L}\} + k_b \{\text{Fe} \cdot \text{L}\}, \quad (5.34)$$

where the rate of the forward reaction (leading to a loss of $\{\text{Fe}'\}$) is defined by k_f in s⁻¹ (mol m⁻³)⁻¹, and the rate of the reverse reaction is defined by k_b in s⁻¹. If a thermodynamic equilibrium is reached, then the rate at which the substrate binds with the ligand must equal the rate at which the substrate detaches from the complex, so that the concentrations of unbound substrate, ligand and complex become constant in time. Setting $d\{\text{Fe}'\}/dt = 0$ in (5.34), then the partitioning of iron is given by

$$\frac{\{\text{Fe} \cdot \text{L}\}}{\{\text{Fe}'\}\{\text{L}\}} = \frac{k_f}{k_b} = \beta_{\text{Fe}}. \quad (5.35)$$

This ratio is determined by the relative magnitude of the rate constants for the forward and backward reactions. For example, if the forward, binding reaction occurs with a much higher probability than the reverse, release reaction, $k_f \gg k_b$, then the equilibrium concentration of the complex is much higher than that of the substrate and free ligand. For iron binding to ligands in the ocean, β_{Fe} is very large (on the order of 10^{11} (mol kg⁻¹)⁻¹), so almost all of the dissolved iron is in complexed form. The concentration of iron-binding ligands in the ocean is about 1 nmol kg⁻¹ or so, maintaining the dissolved iron concentration at a similar order. The sources, sinks and controls on the ligand concentration are still very unclear.

also has a signature of deeper regeneration. Silicic acid (Fig. 5.23d) is very depleted in the surface and its tropical, subsurface maximum is notably deeper than that of nitrate and iron, suggesting a slower rate of remineralisation relative to sinking organic matter, as well as being displaced southward, reflecting the effect of ocean transport and changes in the overlying phytoplankton community.

5.6.2 Modulation of regional productivity by iron: High Nitrate Low Chlorophyll regimes

Our first-order view is that primary production is restricted to the surface waters by light limitation and its basin-scale variations are controlled by the physical supply of macro-nutrients (nitrate and phosphate) to the euphotic layer. This view is modified by the

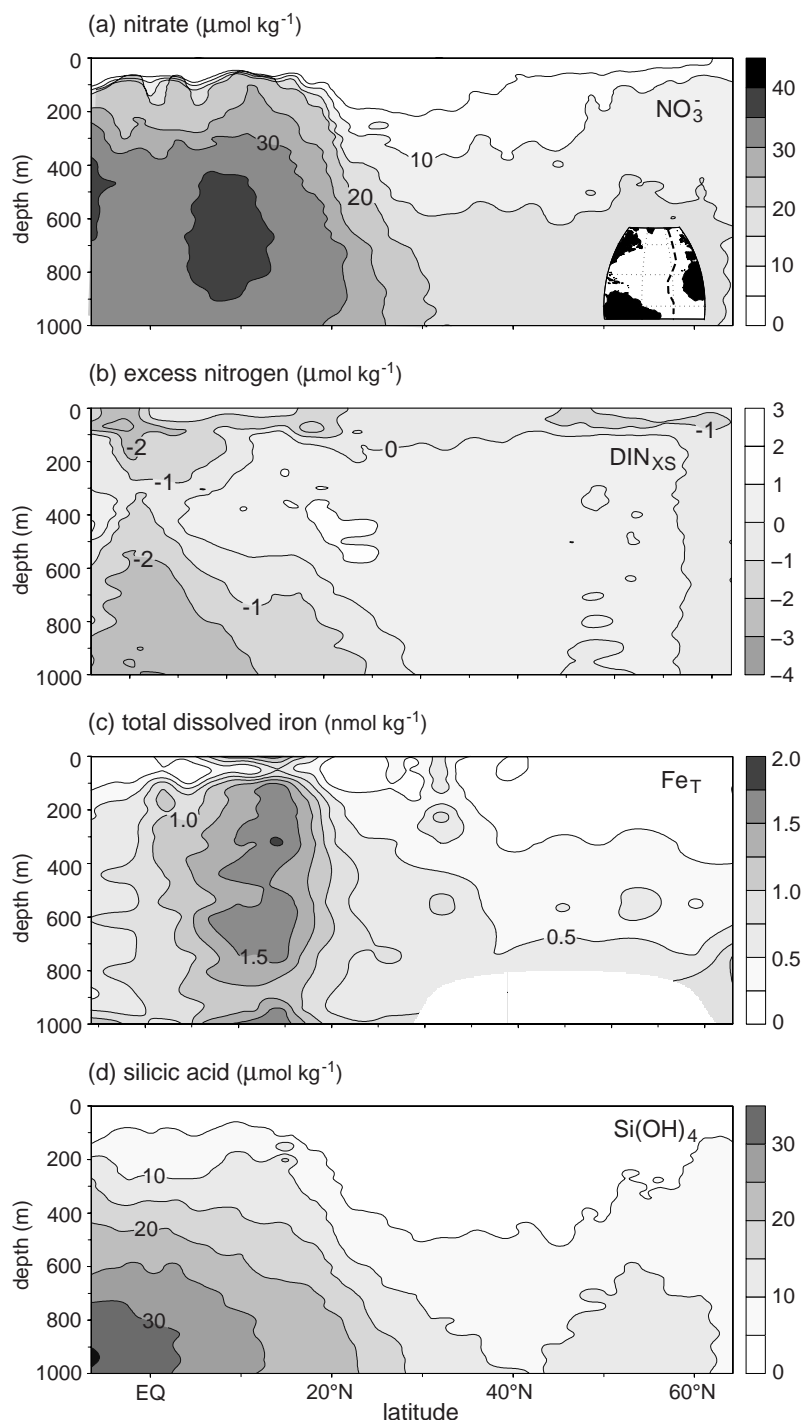


Figure 5.23 (a) Nitrate, NO_3^- ($\mu\text{mol kg}^{-1}$), (b) excess nitrogen $\text{DIN}_{XS} = \text{NO}_3^- - 16\text{PO}_4^{3-}$ ($\mu\text{mol kg}^{-1}$), (c) total dissolved iron, Fe_T (nmol kg^{-1}) and (d) silicic acid Si(OH)_4 ($\mu\text{mol kg}^{-1}$) measured on a transect through the North Atlantic at approximately 20°W. (A16N CLIVAR Repeat Hydrography, 2003.)

essential role, but low abundance, of iron in the ocean.

In the mid and high latitudes of the North Atlantic, there is a striking seasonal phytoplankton bloom (Fig. 5.4) where phytoplankton rapidly grow and reduce nitrate concentrations to sub-micromolar concentrations in a few days. In contrast, in the Sub-Arctic Pacific, tropical Pacific and Southern Ocean, chlorophyll concentrations are never as intense, and micromolar concentrations of nitrate and phosphate persist in the surface waters all year round. In other words, the macro-nutrients are not completely utilised by the phytoplankton so primary and export production are not as vigorous in these areas as might be expected given the macro-nutrient concentrations; these regions are referred to as High Nitrate Low Chlorophyll (HNLC) regions.

Why does complete nutrient utilisation occur in the North Atlantic, but not in the Sub-Arctic Pacific or the Southern Ocean? A prevailing view is that the consumption of macro-nutrients is limited by the low availability of dissolved iron in the surface waters of the HNLC regions. In the deep ocean, free dissolved iron readily sticks to sinking particles and is scavenged from the water column rapidly. Dissolved iron concentrations are maintained at roughly nanomolar concentrations (10^{-9} mol kg $^{-1}$) through complexation with organic ligands (see Box 5.5). Upwelling waters have a deficit in dissolved iron relative to nitrate and phosphate, relative to the requirements for phytoplankton growth: they carry 30 $\mu\text{mol kg}^{-1}$ NO_3^- and 1 nmol kg $^{-1}$ of dissolved iron, which has an Fe : N ratio of 1 : 30 000, far short of the 1 : 2000 ratio in laboratory-grown phytoplankton cultures (Ho *et al.*, 2003). Thus, productivity in the subpolar and tropical regions of wind-driven upwelling is potentially limited by iron availability.

Part of this iron deficit can be compensated by atmospheric transport and deposition of iron-rich dust from the continents (Mahowald *et al.*, 2009). In regions like the North Atlantic, Saharan dust storms frequently deliver soluble, bio-available iron to the surface waters, elevating iron concentrations in the subtropics, in contrast to nitrate and silicic acid, and compensating for iron scavenging (see Fig. 5.23; also Measures *et al.*, 2008). In these iron-replete regions, the produc-

tion of iron-rich enzymes that enable nitrogen fixation; the associated signature of nitrogen fixation and enhanced iron supply over the tropical Atlantic can be seen in the increase in DIN_{XS} in Fig. 5.23b and in later Fig. 11.14. In coastal waters, the release of dissolved iron from sediments also provides a significant source to the local surface ocean (Johnson *et al.*, 1999).

In contrast, in deep-water areas far from major continental dust sources, such as the Sub-Arctic Pacific and the Southern Ocean, the supply of iron from airborne and sedimentary sources is too weak to compensate for the deficit in upwelling waters, and limits the growth of phytoplankton. Martin and Fitzwater (1988) demonstrated this deficit by adding bio-available iron to water samples from the Sub-Arctic North Pacific, stimulating phytoplankton blooms. Subsequent open ocean iron-enrichment studies have shown similar responses in the water column (see earlier Fig. 3.19; Boyd *et al.*, 2007), supporting the view of iron limitation. However, efficient grazing or lack of light thick mixed layers caused by relatively may also play a role in limiting primary production in the HNLC regions.

5.7 | Summary

Phytoplankton produce organic matter by photosynthesis in the surface ocean, converting electromagnetic energy into chemical energy. The organic matter, a fraction of which sinks into deeper waters, provides the source of energy for almost all living creatures in the ocean, including bacteria, zooplankton and fish. Phytoplankton gather energy from sunlight and the elements to build organic molecules from dissolved forms. The rate of production of organic matter by phytoplankton is thus controlled by the rate of supply of photons and essential nutrients into the cell, the rates of essential biochemical reactions, and the rate at which predation or viral infection control the phytoplankton population. In turn, nutrient and light availability to phytoplankton is regulated by ocean circulation and mixing processes. Biochemical reaction rates are affected by the temperature of the environment.

The elemental ratios in marine plankton reflect the collection of organic molecules which facilitate the functions of life. Though elemental ratios vary between species and with acclimation to the local environment, the average elemental composition of the plankton is C : N : P : O₂ = 106 : 16 : 1 : –170, referred to as the ‘Redfield ratio’. These elemental ratios are broadly preserved in both production and respiration of organic matter. In turn, these ratios are reflected in the ratios of the inorganic nutrients within the water column.

Sunlight is rapidly absorbed in seawater so primary production is confined to the upper 200 m of the water column. Regional variations in primary production strongly mirror the pattern of upwelling of macro-nutrient enriched deeper waters. The vigour of production is reduced in some upwelling regimes because of a deficit of dissolved iron, relative to the requirements of phytoplankton. Global ocean primary production of organic carbon is estimated to be between 35 and 70 Pg Cy⁻¹. Most of this organic matter is consumed and respired by zooplankton and bacteria mostly within the euphotic layer, but between 10 and 20 Pg Cy⁻¹ passes into the deeper, dark ocean where organic carbon, too, is respired and returned to inorganic forms. Only a very small fraction of the exported organic carbon reaches the sea floor.

The effects of the ecosystem on the ocean carbon cycle are addressed further in Chapter 6, the role of seasonal variations in modulating production in Chapter 7, and how the interplay of biological transfers and physical transport determines nutrient and carbon distributions is discussed in Chapter 11.

5.8 Questions

Q5.1. How much carbon is in the microbes of the ocean?

Marine bacteria are typically on the order of 1 μm³ in volume and have a carbon content of about 50 × 10^{–15} g C cell^{–1}. Bacteria are found throughout the whole water column with a population density of about 10⁵ cells ml^{–1}. The smallest phytoplankton, *Prochlorococcus*, are of similar size and

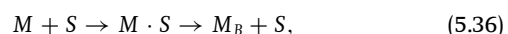
carbon content, and there are also as many as 10⁵ cells ml^{–1} in the surface waters of the subtropical gyres, about half the ocean surface area, but restricted over the upper 250 m. Larger organisms typically occur at lower number densities, so most of the living organic carbon in the ocean is in the form of these smallest cells.

- (a) Approximately how many bacterial cells are in the global ocean and how many *Prochlorococcus* cells? Assume that the volume of the global ocean is about 1.4 × 10¹⁸ m³.
- (b) Make an order of magnitude estimate of the amount of carbon in living microbes in the global ocean.
- (c) If each *Prochlorococcus* cell divides once a day or less, provide an upper bound for the global rate of primary production (Pg Cy^{–1}) by this organism?

Q5.2. Analogy of Michaelis–Menten type, two-stage process

Consider a simple everyday example of a two-stage process involving children collecting marbles (inspired by Runge *et al.*, 2006). A teacher releases a large number of marbles, which spill across the floor in a gym, and asks the children to collect the marbles one by one and drop them into a single bucket. There are two stages, the first involves a child finding a single marble on the floor and the second involves the child carrying the marble to the bucket and dropping it in, which is then repeated.

We can write a pseudo-reaction to describe this game. To begin with, there are M uncollected marbles and S schoolchildren searching for an uncollected marble. Marbles being carried by the children are represented by $M \cdot S$ and marbles released into the bucket are represented by M_B . This process of collection and transfer of marbles is represented by



where the total number of schoolchildren, S_T , is given by the sum of the children searching for a marble, S , and those carrying a marble, $M \cdot S$,

$$S_T = S + M \cdot S. \quad (5.37)$$

The rate of change of the number of uncollected marbles, M , is described by a loss, proportional to the number of uncollected marbles and the number of schoolchildren searching for a marble,

$$\frac{\partial M}{\partial t} = -k_{find} M S, \quad (5.38)$$

where the product $(k_{find} S)^{-1}$ represents the time for a single marble to be found and the product $(k_{find} M)^{-1}$ as the time for an individual child to find a marble.

(a) Assume that the rate of change of the number of marbles in the bucket, M_B , is given by the source, depending on the number of marbles being carried by a child divided by the time, T_{drop} , to return the marble to the bucket and drop the marble in,

$$\frac{\partial M_B}{\partial t} = \frac{M \cdot S}{T_{drop}}. \quad (5.39)$$

Then show that the rate of change in the number of marbles being dropped into the bucket, M_B , is related to the number of uncollected marbles, M , by

$$\frac{\partial M_B}{\partial t} = \frac{S_T}{T_{drop}} \frac{M}{(T_{drop} k_{find})^{-1} + M}. \quad (5.40)$$

(b) Consider the limit when there are very few marbles on the floor. What is the process limiting the rate of increase in the marbles being dropped in the bucket? How is the rate of change of M_B written in this limit?

(c) Now consider the opposing limit when there are a lot of marbles on the floor. What is the process limiting the rate of increase in the marbles being dropped in the bucket? How is the rate of change of M_B written in this limit?

Q5.3. Nutrient diffusion towards the cell.

Consider the down-gradient diffusion of nutrient molecules, \mathcal{N} , towards a spherical cell of radius R . The transport or area-integrated flux towards the cell ($\text{mol s}^{-1} \text{cell}^{-2}$) through any sphere of radius $r > R$, can be described as

$$\int F(r)dA = 4\pi r^2 \kappa \frac{\partial \mathcal{N}}{\partial r}, \quad (5.41)$$

where κ is a molecular diffusivity ($\text{m}^2 \text{s}^{-1}$), $F(r)$ is the diffusive flux per unit area ($\text{mol s}^{-1} \text{m}^{-2}$) and

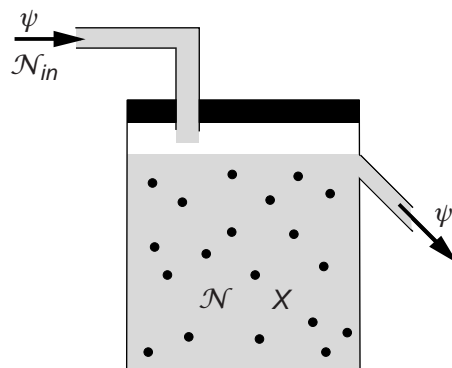


Figure 5.24 Schematic view of chemostat apparatus.

$\int dA$ is the surface area of the cell ($\text{m}^2 \text{cell}^{-1}$) taken to be asphere of radius R .

Assume that a quasi-equilibrium state is reached in which the cell is acquiring nutrients at a constant rate and the transport of nutrient towards the cell through any sphere around the cell is also constant. By continuity, $\int F(R)dA$ is the rate of transport of nutrient into the cell which is facilitated by the cell-wall transporters.

(a) Derive an expression for the cell's rate of nutrient uptake in terms of R , $\mathcal{N}(R) = \mathcal{N}_0, \mathcal{N}_\infty$ and κ by re-arranging (5.41) and integrating from the radius R far away from the cell.

(b) Under what circumstances might the near-cell concentration of the nutrient become almost depleted such that $\mathcal{N}_0 \ll \mathcal{N}_\infty$?

(c) For the regime discussed in (b), if the average cellular content of \mathcal{N} is constant, Q_N (mol cell^{-1}), write a simple expression for the population growth rate, μ (s^{-1}) in terms of cell radius.

(d) If you initialised a batch culture study in the laboratory with two individual cells, one 5 microns in diameter and the other 50 microns, would the number density of the smaller or larger cells increase more rapidly?

Q5.4. Nutrient content and growth of phytoplankton.

The chemostat is an experimental apparatus used to study the physiology of phytoplankton and bacteria. The vessel is filled with a nutrient-replete medium (e.g., filtered seawater) and a seed population of the organism of interest. The vessel is

stirred and aerated, and temperature and light are regulated. A nutrient-replete medium is introduced at a continuous flow rate ψ with concentration of the limiting nutrient element N_{in} . The volume of medium, V , is held constant by an equal rate of outflow (see Fig. 5.24). The number density of cells, X , and the nutrient concentration, N , in the outflow are monitored and the system is run to equilibrium. The biomass of phytoplankton, B , is the product of the number density of cells in the vessel, X , and the average ‘cell quota’, Q_N (quantity of nutrient element N per cell), of the cells in the vessel:

$$B = Q_N X. \quad (5.42)$$

Conservation equations can be written for the nutrient,

$$\frac{dN}{dt} = -\rho_N X - D(N - N_{in}), \quad (5.43)$$

the biomass,

$$\frac{dB}{dt} = \rho_N X - DB, \quad (5.44)$$

and the number density in the vessel,

$$\frac{dX}{dt} = \mu X - DX, \quad (5.45)$$

where the ‘dilution rate’, D , is determined by the flow rate and the volume of medium, $D = \psi/V$. The inflowing medium contains no phytoplankton, so that $X_{in} = 0$ and $B_{in} = 0$, whereas there is an input of the limiting nutrient, N_{in} . The variables are: D (s^{-1}), the dilution rate; N (mol m^{-3}), the concentration of the limiting nutrient in the vessel; Q_N (mol cell^{-1}), the ‘cell quota’ of element N ; X (cell m^{-3}), the number density of cells in medium; V (m^3), the volume of medium in the vessel; ρ_N ($\text{mol cell}^{-1} s^{-1}$), the cellular uptake rate of dissolved nutrient element N ; μ (s^{-1}), the exponential growth rate of population; and ψ ($\text{m}^3 s^{-1}$), the rate of inflow/outflow.

(a) Without measuring the composition of the cells directly, how would you estimate the

cell quota, Q_N , of element N in the cells at equilibrium?

(b) How would you control the experimental system to examine the relationship between growth rate, μ , and cell quota, Q_N ?

(c) Using a chemostat, Burmaster (1979) evaluated the relationship between exponential population growth rate and cell quota of phosphorus, Q_P , under equilibrium conditions, as illustrated in Fig. 5.8. Why is the intercept with the x -axis not at $Q_P = 0$?

(d) The cell quota of phosphorus varies by an order of magnitude across the set of experiments. What underlying processes might this reflect? Why would a high cell quota be associated with higher growth rate?

(e) Speculate on which physical regimes a chemostat system might be a useful analogy in understanding how an oceanic phytoplankton population is controlled?

5.9 | Recommended reading

For a comprehensive, mechanistic description of the physiology of light harvesting and photosynthesis in marine phytoplankton, read P. G. Falkowski and J. Raven (1997). *Aquatic Photosynthesis*. Princeton, NJ: Princeton University Press.

An excellent, mechanistic discussion of how plankton live in their fluid environment is provided by T. Kiørboe (2009). *A Mechanistic Approach to Plankton Ecology*. Princeton, NJ: Princeton University Press.

An introductory overview of biological oceanography is provided by C. B. Miller (2004). *Biological Oceanography*. Malden, MA: Blackwell, 416pp.

A comprehensive review of nutrient and carbon cycles is provided by J. L. Sarmiento and N. Gruber (2006). *Ocean Biogeochemical Dynamics*. Princeton, NJ: Princeton University Press, 526pp.

Chapter 6

Carbonate chemistry fundamentals

The carbon cycle plays an important role in the Earth's climate system: atmospheric carbon dioxide increases the absorption and emission of long-wave radiation (Fig. 1.2), enhancing the radiative heating of the Earth's surface. The amount of carbon dioxide in the atmosphere is determined by the exchange of carbon between the atmosphere, ocean and terrestrial reservoirs. The ocean stores about 60 times as much carbon as the atmosphere. Fifteen per cent or more of the atmospheric inventory passes into and out of the ocean on an annual basis, so that the two reservoirs communicate rapidly. However, the deeper ocean takes much longer to equilibrate with the atmosphere, perhaps several thousands of years, due to the length of time for its properties to be reset over the entire globe by ocean overturning. Exchanges with the much larger carbon reservoir of sedimentary rocks occur on even longer timescales of many tens and hundreds of thousand years. Changes in how carbon is partitioned between the ocean and atmosphere are implicated in the glacial and interglacial cycles of atmospheric carbon dioxide, the carbon system providing a positive feedback for radiative heating and amplifying any climate perturbations.

Over an annual cycle, the ocean absorbs carbon dioxide from the atmosphere at high latitudes and returns carbon dioxide in the tropics. The large fluxes into and out of the ocean almost balance on an annual basis. However, over the past century, carbon emissions due to human activities have rapidly increased the atmospheric inventory, driving a net flux of carbon dioxide from the atmosphere into the ocean. At present, about one

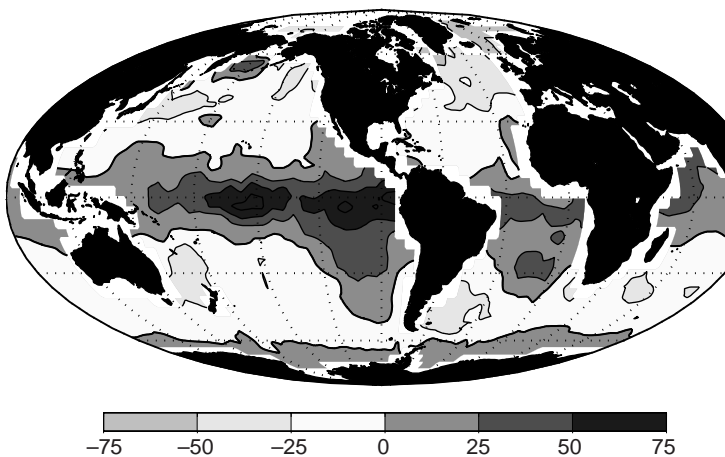
third of annual emissions of anthropogenic carbon dioxide finds their way into the ocean, reducing the impact on radiative heating.

In this book, we consider how the carbon cycle operates over the globe: why is there so much more carbon in the ocean than the atmosphere; what controls the pattern and rates of air-sea exchange of carbon dioxide (Fig. 6.1a); and how might the ocean uptake vary given the ongoing rise in atmospheric carbon dioxide (Fig. 6.1b)? In this chapter, we develop tools to address these questions, drawing on the basic concepts of carbonate chemistry in seawater and charge balance in the ocean, and discuss the physical, chemical and biological processes involved in air-sea exchange and cycling of carbon within the ocean.

6.1 Solubility of carbon dioxide

Carbon dioxide dissolves in seawater and the aqueous form, CO_2^{aq} , reacts with water to form carbonic acid, H_2CO_3 . These species, $[\text{CO}_2^*] = [\text{CO}_2^{\text{aq}}] + [\text{H}_2\text{CO}_3]$, are referred to as dissolved CO_2 , where square brackets denote concentrations in seawater in terms of the amount per unit mass ($\mu\text{mol kg}^{-1}$). Molecules of CO_2 continually pass across the air-sea interface and there is a flux of the gas ($\text{mol C m}^{-2} \text{s}^{-1}$) both into and out of the water. When the flux in each direction is of identical magnitude, the air and water reservoirs of CO_2 are in equilibrium.

The abundance of carbon dioxide in the surface atmosphere is measured in terms of a partial pressure, $p\text{CO}_2^{\text{at}}$ (μatm), the pressure imparted

(a) annual-mean $\Delta p\text{CO}_2$ (μatm)

(b) historical changes

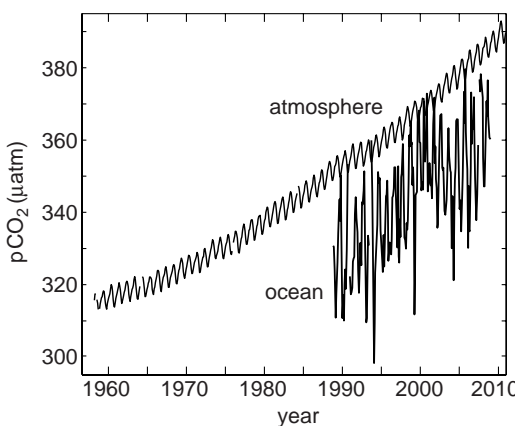


Figure 6.1 (a) The annual-mean difference in surface ocean and lower-atmosphere partial pressure of carbon dioxide, $\Delta p\text{CO}_2 = p\text{CO}_2 - p\text{CO}_2^{\text{at}} (\mu\text{atm})$ from Takahashi *et al.* (2002). There is ocean uptake of CO_2 (light shading) over parts of the high latitudes where the partial pressure in the atmosphere is greater than in the ocean. Conversely, there is ocean outgassing (dark shading) in the tropics and possibly over parts of the Southern Ocean. This climatology represents a large compilation of surface ocean observations normalised to reference year 1995 (non-El Niño conditions) and mapped onto a grid of $4^\circ \times 5^\circ$; white regions around continents are areas with no ocean data due to the coarse-grained gridding. (b) Observed changes in surface ocean (0–20 m) $p\text{CO}_2$ at the Hawaii Ocean Time-Series station and atmospheric $p\text{CO}_2$ observed at Mauna Loa, Hawaii. Surface ocean $p\text{CO}_2$ follows the rise in atmospheric $p\text{CO}_2$ due to air-sea exchange. For this region, surface ocean $p\text{CO}_2$ is always lower than in the atmosphere, driven away from a local equilibrium by ocean circulation and biological activity, and so there is a local ocean uptake of CO_2 (ocean data from Dore, 2009; atmospheric data from NOAA/ESRL).

by that gas at the Earth's surface; see Box 6.1 for a summary of definitions used here. The partial pressure in the surface atmosphere is relatively uniform, reaching almost 370 μatm in 2000, as recorded at Mauna Loa, Hawaii (Fig. 6.1b). Seasonal and regional variations of $p\text{CO}_2^{\text{at}}$ are less than 10 μatm , even though there are large variations in the carbon exchanges and emissions over the globe, reflecting the effect of rapid transport and mixing within the atmosphere.

There is an effective partial pressure of carbon dioxide, $p\text{CO}_2$ (μatm) in seawater: the partial pressure that the gas would have in the overlying atmosphere if an equilibrium is reached with the concentration of dissolved carbon dioxide, $[\text{CO}_2^*]$, in surface water. The ratio between $[\text{CO}_2^*]$ and the

effective partial pressure, $p\text{CO}_2$, is described by the solubility, K_0 ($\text{mol kg}^{-1} \text{ atm}^{-1}$), defined as

$$\frac{[\text{CO}_2^*]}{p\text{CO}_2} = K_0. \quad (6.1)$$

Solubility in a simple system

To understand solubility in a simple system, consider the air-water exchange of a soluble gas in a closed vessel containing seawater and an airspace above (Fig. 6.2; definitions in Box 6.1). Molecules of a soluble gas, c , continually pass in each direction across the air-water interface. The concentration in water is $[c]$ ($\mu\text{mol kg}^{-1}$), and the partial pressure in the airspace is p_c (μatm). The flux of molecules into the water is proportional to the partial

Box 6.1 | Definitions for soluble gases

For a generic, soluble gas, c , we define the following:

- The *mixing ratio* of a gas in air, X_c , is the number of moles of the gas per mole of air. This ratio is dimensionless and, for carbon dioxide, often expressed as parts per million by volume (ppmv).
- The *concentration* of the gas in air can be defined either as the number of moles per unit volume, $\{c_a\}$ (mol m^{-3}) or the number of moles per unit mass, $[c_a]$ (mol kg^{-1}), where $\{c_a\} = [c_a]\rho_a$ and ρ_a is the density of air at local temperature and pressure. The concentration is related to the mixing ratio by $\{c_a\} = \frac{X_c\rho_a}{M_a}$, where M_a is the mean molecular mass per unit mole of air (kg mol^{-1}).
- The *partial pressure*, pc^{at} , of the gas in air is the contribution of that gas constituent to the total atmospheric pressure, p , given by $pc = X_c p$, and, for carbon dioxide is often expressed in terms of micro-atmospheres (μatm).
- The *fugacity*, fc^{at} (μatm), is an effective partial pressure, corrected to account for the non-ideal nature of real gases; for carbon dioxide the correction is typically $< 1\%$ (Zeebe and Wolf-Gladrow, 2001).
- The *concentration* of the dissolved gas in water is either expressed per unit volume, $\{c\}$ (mol m^{-3}), or unit mass, $[c]$ (mol kg^{-1}), where $\{c\} = [c]\rho_w$ and ρ_w is the density of water at the given pressure, temperature and salinity.
- The *solubility*, K_0^c , quantifies the ratio of the concentration of the dissolved gas in seawater and the partial pressure in the air when they are in equilibrium: $K_0^c \equiv [c]/pc$.

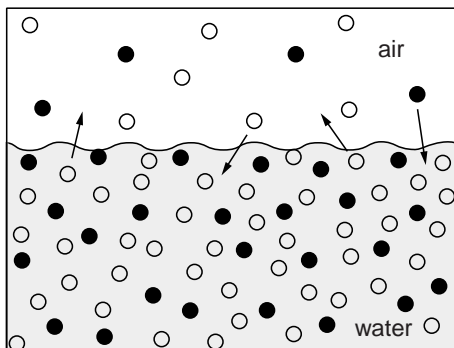


Figure 6.2 Schematic view of a simple closed vessel which contains seawater and an airspace above. Molecules of all soluble gases (filled and open circles), continually pass across the air–water interface in both directions. Filled circles represent a soluble gas, c , which has concentration in water $[c]$ ($\mu\text{mol kg}^{-1}$) and a partial pressure in the airspace pc (μatm).

pressure, pc , in the airspace. The greater the abundance of molecules of c in the air, the greater the likelihood of one crossing into the water. Thus, the flux into the water is proportional to the partial

pressure, pc ,

$$\text{Flux in} = K_{in} pc,$$

and the flux out of the water is proportional to the dissolved concentration $[c]$,

$$\text{Flux out} = -K_{out}[c],$$

where K_{in} and K_{out} are constants of proportionality (with different units). At equilibrium, the flux in must exactly balance the flux out, and pc and $[c]$ are unchanging. In this case,

$$\frac{[c]}{pc} = \frac{K_{in}}{K_{out}} = K_0^c,$$

where K_0^c ($\text{mol kg}^{-1} \text{ atm}^{-1}$) is the solubility for a general gas c ; we will use K_0 to denote the solubility of CO_2 . The solubility reflects the relative efficiency with which molecules pass into and out of the water, and varies with environmental factors, including temperature and salinity (empirically evaluated by Weiss, 1974). For example, the kinetic energy of molecules in solution increases at higher temperatures and, thus, dissolved gas

molecules are more likely to have sufficient energy to cross the air-sea interface. Hence, the solubility of a dissolved gas decreases with increasing temperature.

Air-sea contrasts in partial pressure

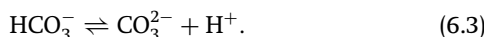
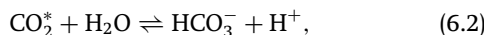
If the effective partial pressure, $p\text{CO}_2$, in seawater is greater than the partial pressure in the overlying atmosphere, $p\text{CO}_2^{at}$, CO_2 outgasses from the ocean: gas molecules are statistically more likely to pass out of the water than into it. Conversely, if the surface seawater partial pressure is lower than that of the overlying atmosphere, there is a net flux of CO_2 into the ocean.

The annual-mean difference in the partial pressure of carbon dioxide across the air-sea interface, $\Delta p\text{CO}_2 = p\text{CO}_2 - p\text{CO}_2^{at}$ (μatm), varies between typically $-75 \mu\text{atm}$ at high latitudes and $+75 \mu\text{atm}$ in the tropics, as illustrated in Fig. 6.1a. Ocean uptake occurs over parts of the high latitudes and ocean outgassing over the tropics. Almost nowhere is the surface ocean's effective partial pressure the same as that in the overlying atmosphere: there is not a local equilibrium between the surface ocean and atmosphere for CO_2 .

The atmospheric partial pressure, $p\text{CO}_2^{at}$, is relatively homogeneous, so that the air-sea flux of CO_2 is controlled by regional and seasonal variations in $p\text{CO}_2$, which in turn depend upon the variations in $[\text{CO}_2^*]$ and K_0 (6.1). To understand these surface patterns for the carbonate system, we consider first how carbon dioxide and its associated species react in seawater and second, the effects of temperature and alkalinity.

6.2 What are the reactions of the carbonate system in seawater?

Dissolved carbon dioxide, CO_2^* , reacts with water to form bicarbonate ions, HCO_3^- , which in turn dissociate to form carbonate ions, CO_3^{2-} :



This reaction of carbon dioxide with water produces hydrogen ions, which by definition, makes

carbon dioxide an acid. Conversely, a compound which when dissolved in water reduces the concentration of hydrogen ions is termed a base.

Kinetic equations and equilibrium

We can provide an alternative description of the carbonate system by writing equations describing the temporal changes for each of the component species as a function of their sources and sinks. For example, the temporal changes of $[\text{CO}_2^*]$ in a water parcel, due to reactions (6.2) and (6.3), can be described by the ordinary differential equation:

$$\frac{d[\text{CO}_2^*]}{dt} = -K_F[\text{CO}_2^*] + K_B[\text{HCO}_3^-][\text{H}^+], \quad (6.4)$$

where the left-hand side represents the rate of change in time of $[\text{CO}_2^*]$. There is a balance between the loss of CO_2^* due to its reaction with water (first term on the right) and a gain of CO_2^* due to the reaction of HCO_3^- with hydrogen ions (second term on the right); where K_F (s^{-1}) and K_B ($(\text{mol kg}^{-1})^{-1} \text{s}^{-1}$) are reaction rate constants for the forward and backward reactions, respectively. It is intuitive that the magnitude of the forward reaction should depend upon the concentration of CO_2^* ; the concentration of water is effectively constant and this factor is folded into the definition of K_F . Likewise, the backward reaction is assumed to be proportional to both $[\text{HCO}_3^-]$ and $[\text{H}^+]$. If the concentration of one of the reactants is increased, the likelihood of encounters between ions is also enhanced, and so too the rate of the reaction; for a detailed discussion of the kinetics, see Zeebe and Wolf-Gladrow (2001).

At equilibrium, there is a dynamic transfer in each direction, the rates of the forward and backward reactions exactly balance. This dynamic equilibrium is typically reached in a matter of minutes for the seawater carbonate system. Setting the left-hand side of (6.4) to zero, the equilibrium partitioning of carbon between these species is related to the ratio of the forward and backward reaction rates:

$$\frac{[\text{HCO}_3^-][\text{H}^+]}{[\text{CO}_2^*]} = \frac{K_F}{K_B} = K'_1, \quad (6.5)$$

where the forward and backward reaction rate constants are combined into a single equilibrium coefficient, K'_1 (mol kg^{-1}).

Table 6.1 | Carbonate system constants and parameter values evaluated for seawater at $T = 20^\circ\text{C}$ and $S = 34.5 \text{ g kg}^{-1}$.

Parameter	Description	Value	Units
K_0	Solubility of CO_2	0.033	$\text{mol kg}^{-1} \text{ atm}^{-1}$
K'_1	Thermodynamic equilibrium	1.3×10^{-6}	mol kg^{-1}
K'_2	Thermodynamic equilibrium	9.1×10^{-10}	mol kg^{-1}
pCO_2^{at}	Atmospheric partial pressure for CO_2 (in 2005)	380	μatm
X_{CO_2}	Atmospheric mixing ratio for CO_2 (in 2005)	380	ppmv
pH	$-\log_{10}([\text{H}^+])$ surface ocean	8.06	
$[\text{H}^+]$	Hydrogen ions	8.7×10^{-9}	mol kg^{-1}

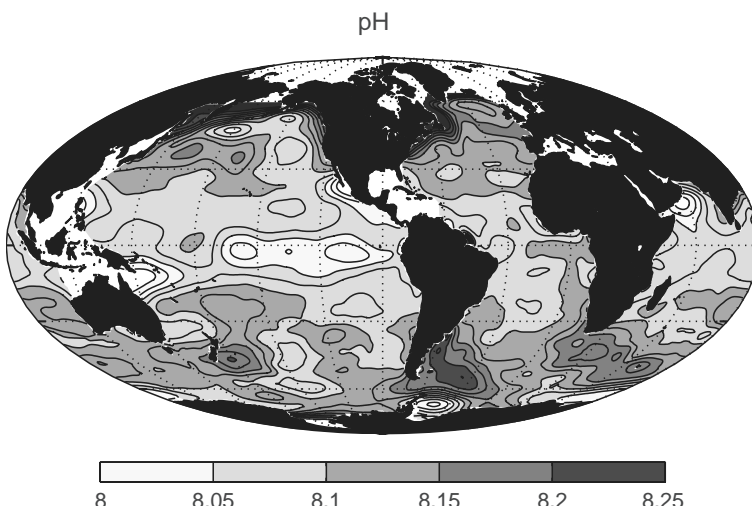


Figure 6.3 Global surface distribution of $\text{pH} = -\log_{10}([\text{H}^+])$, where $[\text{H}^+]$ is hydrogen ion concentration, determined assuming thermodynamic equilibrium between the components based on climatological DIC and alkalinity (Key et al., 2004), and using annual-mean surface climatologies of temperature, salinity, phosphate, silicic acid (Conkright et al., 2002).

Similar equilibrium expressions and coefficients can be obtained for any set of chemical reactions in seawater. Provided that the timescale for the chemical system to come to equilibrium is short relative to other processes, for example, mixing or the consumption of the reactants by microbes, the system is assumed to have reached chemical equilibrium.

Thermodynamic equilibrium

The relative abundances of the carbonate species at thermodynamic equilibrium are defined by coefficients K'_1 and K'_2 ,

$$K'_1 = \frac{[\text{HCO}_3^-][\text{H}^+]}{[\text{CO}_2^*]}, \quad (6.6)$$

$$K'_2 = \frac{[\text{CO}_3^{2-}][\text{H}^+]}{[\text{HCO}_3^-]}, \quad (6.7)$$

which vary with temperature and salinity. These equilibrium coefficients have been evaluated for

seawater in the laboratory over the range of ocean temperatures, salinities and pressures (e.g., Millero, 1995); typical values for the subtropical surface ocean are provided in Table 6.1.

The hydrogen ion concentration in natural waters is typically described in terms of $\text{pH} = -\log_{10}[\text{H}^+]$; see later Section 6.3.6. The pH of the surface ocean is observed to be rather uniform, only varying between 8.0 and 8.2, as illustrated in Fig. 6.3. Assuming that $\text{pH} = 8.06$ and using reasonable surface ocean values for K'_1 and K'_2 (Table 6.1), then equilibrium relationships (6.6) and (6.7) imply that

$$\frac{[\text{HCO}_3^-]}{[\text{CO}_2^*]} = \frac{K'_1}{[\text{H}^+]} \sim 149,$$

and

$$\frac{[\text{CO}_3^{2-}]}{[\text{CO}_2^*]} = \frac{K'_1 K'_2}{[\text{H}^+]^2} \sim 16.$$

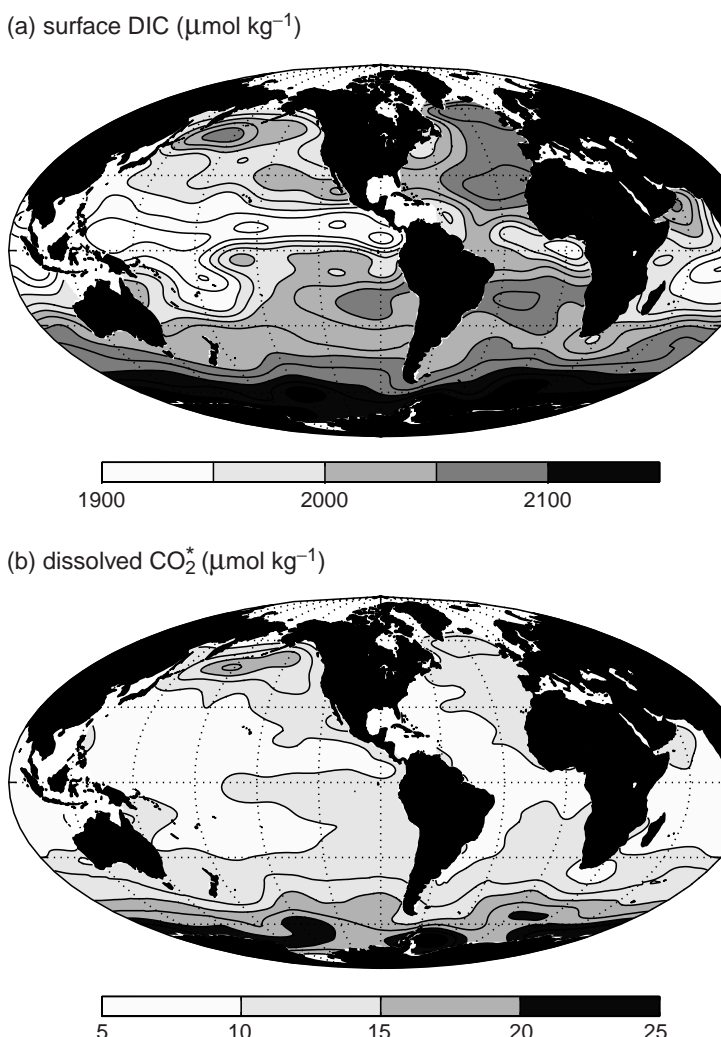


Figure 6.4 Global surface distributions of carbonate system components ($\mu\text{mol kg}^{-1}$): (a) Dissolved inorganic carbon, DIC = $[\text{CO}_2^*] + [\text{HCO}_3^-] + [\text{CO}_3^{2-}]$, (b) dissolved carbon dioxide, $[\text{CO}_2^*]$ (c) bicarbonate ion $[\text{HCO}_3^-]$ and (d) carbonate ion $[\text{CO}_3^{2-}]$. The components have been determined assuming thermodynamic equilibrium between the components based on climatological DIC and alkalinity (Key *et al.*, 2004) using annual-mean surface climatologies of temperature, salinity, phosphate and silicic acid (Conkright *et al.*, 2002).

These ratios reveal that the carbon dissolved in the ocean is predominantly in the form of HCO_3^- , about 10% as CO_3^{2-} and only 0.6% as CO_2^* . While the proportion in CO_2^* is relatively small, this is the only form that directly communicates with the atmospheric reservoir. These ratios vary with temperature, salinity and other factors, but are representative for the present day.

Hence, the reaction of carbon dioxide with seawater enhances the ocean's storage of carbon by more than a hundred-fold. If CO_2 did not react with seawater, but still dissolved with the same solubility, the atmospheric and oceanic inventories of carbon would be of a similar magnitude: a dramatic contrast to the world we live in, where

the oceanic inventory is more than 60 times that of the atmosphere.

6.2.1 Dissolved inorganic carbon

The total concentration of carbon in dissolved inorganic form in seawater, referred to as dissolved inorganic carbon, DIC, is defined as the sum of the concentrations of the three carbonate species (Fig. 6.4):

$$\text{DIC} = [\text{CO}_2^*] + [\text{HCO}_3^-] + [\text{CO}_3^{2-}]. \quad (6.8)$$

The relative size of $[\text{CO}_2^*]$ and DIC can be estimated from the following scaling. $[\text{CO}_2^*]$ is typically about $12.5 \mu\text{mol kg}^{-1}$ in surface waters based

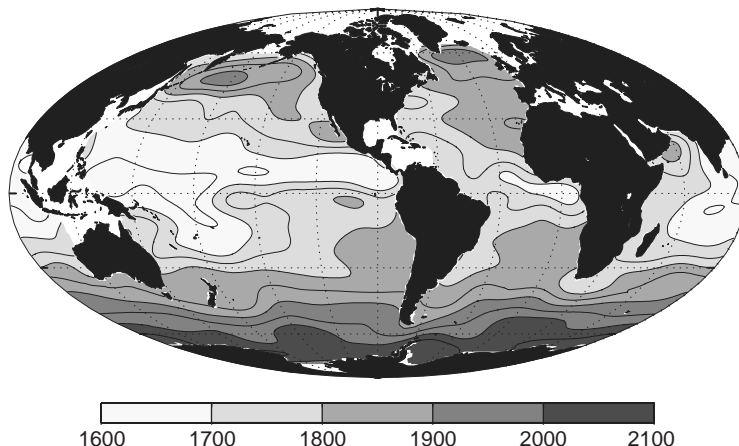
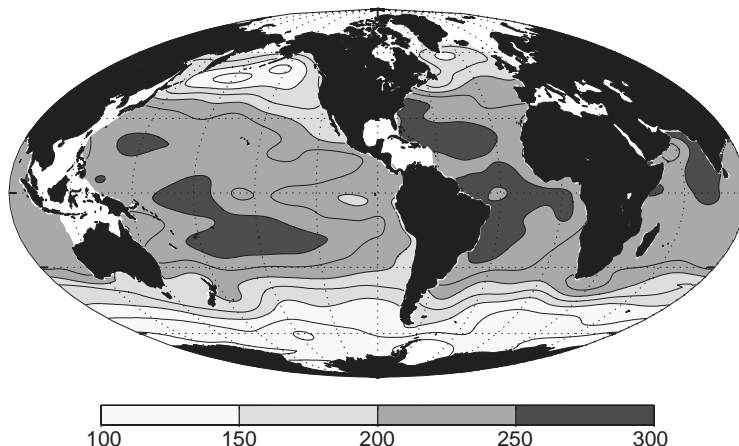
(c) surface $[\text{HCO}_3^-]$ ($\mu\text{mol kg}^{-1}$)

Figure 6.4 (cont.)

(d) surface $[\text{CO}_3^{2-}]$ ($\mu\text{mol kg}^{-1}$)

upon the solubility K_0 at equilibrium with a surface atmospheric pCO_2 of $380 \mu\text{atm}$; using $[\text{CO}_2^*] = K_0 \text{ pCO}_2$ and values in Table 6.1. For $\text{pH} = 8.06$, relationships (6.6)–(6.8), suggest that $\text{DIC} \sim 2075 \mu\text{mol kg}^{-1}$, again more than two orders of magnitude larger than $[\text{CO}_2^*]$.

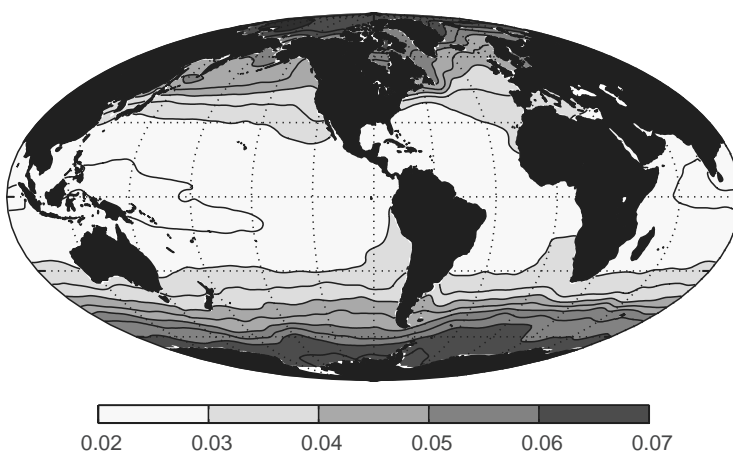
Surface observations reveal comparable values of DIC, varying from less than $2000 \mu\text{mol kg}^{-1}$ in the tropics to more than $2100 \mu\text{mol kg}^{-1}$ in the high latitudes (Fig. 6.4a). Most of the surface DIC is accounted for by $[\text{HCO}_3^-]$ (Fig. 6.4c), followed by $[\text{CO}_3^{2-}]$ (Fig. 6.4d), while $[\text{CO}_2^*]$ accounts for less than 1% (Fig. 6.4b). The patterns of DIC and its carbon components are not identical over the globe: there is a general increase in DIC, $[\text{HCO}_3^-]$ and $[\text{CO}_2^*]$ with

latitude (Figs. 6.4a,b,c), but an opposing decrease in $[\text{CO}_3^{2-}]$ (Fig. 6.4d).

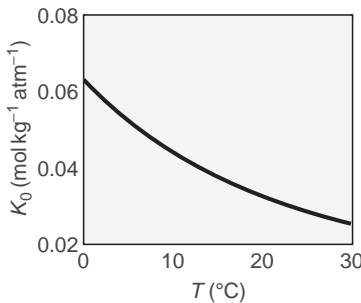
What controls these regional patterns of surface ocean DIC and its component species? Next we consider how temperature affects solubility, how charge balance constrains ocean chemistry, and their combined influence on the component species of DIC.

6.3 What controls DIC in the surface ocean?

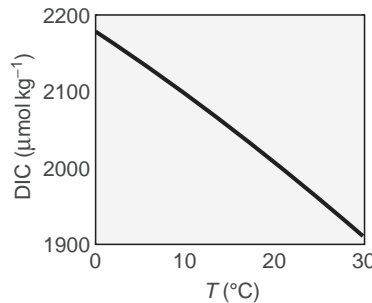
For a parcel of surface ocean water at equilibrium with a given atmospheric pCO_2 , the capacity to

(a) solubility ($\text{mol kg}^{-1} \text{ atm}^{-1}$)

(b) solubility versus temperature



(c) DIC versus temperature



store carbon as DIC depends on two key influences: the temperature of the water and the alkalinity, which can be understood as an expression of charge balance.

6.3.1 Temperature, solubility and surface DIC

For all soluble gases, the solubility increases with decreasing water temperature. The colder the water, the slower the average speed associated with the Brownian motion of dissolved gas molecules and the lower the probability that they escape across the air–water interface. The solubility of CO_2 in seawater decreases by more than a factor of two as temperature increases across the range of surface ocean waters (Fig. 6.5a,b).

To understand this effect, consider a vessel of seawater initially at equilibrium with an airspace above: increasing the temperature of the water reduces the solubility of CO_2 , increases pCO_2 and

drives carbon dioxide into the airspace. In contrast, the equilibrium coefficients K'_1 and K'_2 , determining the partitioning between carbonate species, both increase with temperature. Warming the system pushes reaction (6.2) to the right, moving carbon from $[\text{CO}_2^*]$ into $[\text{HCO}_3^-]$, which reduces the partial pressure, opposing the effect of changing solubility. However, solutions for the complete carbonate system reveal that the solubility effect dominates and, at equilibrium with a fixed pCO_2 , cooler waters hold more DIC (Fig. 6.5c). The relationship between DIC at equilibrium and temperature is relatively linear over the range of ocean temperatures; a feature which we exploit in Chapter 13.

How does this temperature control of solubility then affect the observed regional changes in surface ocean DIC and $[\text{CO}_2^*]$, mapped in Fig. 6.4a,b? The atmosphere is relatively well mixed with regard to carbon dioxide and surface atmospheric

Figure 6.5 (a) Global distribution of solubility of carbon dioxide ($\text{mol kg}^{-1} \text{ atm}^{-1}$) inferred from temperature and salinity distributions, which have been corrected for non-ideal gas behaviour for carbon dioxide, and temperature dependence of (b) the solubility of CO_2 (K_0 , $\text{mol kg}^{-1} \text{ atm}^{-1}$) and (c) the saturated DIC of seawater at equilibrium with a fixed $\text{pCO}_2^{at} = 280 \mu\text{atm}$ (where salinity $S = 34.5 \text{ g kg}^{-1}$, total alkalinity $A_T = 2350.0 \mu\text{mol kg}^{-1}$, and total boron concentration $B_T = 409.8 \mu\text{mol kg}^{-1}$).

$p\text{CO}_2$ is to a first approximation uniform. Thus, surface waters in the cool, high latitudes and warm, low latitudes are both equilibrating with the same $p\text{CO}_2$. If the surface ocean were at equilibrium with the overlying atmosphere, surface DIC should increase by about $250 \mu\text{mol kg}^{-1}$ from low to high latitudes (based on Fig. 6.5c), because of the surface temperature gradient. This meridional contrast in DIC predicted by a local equilibrium with the atmosphere is indeed close to that observed in surface DIC (as suggested by the similar ranges in Figs. 6.5c and 6.4a).

The solubility of CO_2 and the coefficients of thermodynamic equilibrium also vary with salinity. However, across the range of salinities encountered in the open ocean, 32.5 to 37.5 g kg^{-1} , the equilibrium DIC concentration at fixed $p\text{CO}_2$ varies by only $20 \mu\text{mol kg}^{-1}$, a relatively small change compared to the temperature effect. In coastal waters, there are large changes in the salinity, between fresh water in river outflows and the much saltier ocean, and then salinity can play a more significant role for variations in $p\text{CO}_2$; henceforth in this chapter, we neglect the relatively weak effect of salinity in the open ocean on the thermodynamic coefficients of the carbonate system.

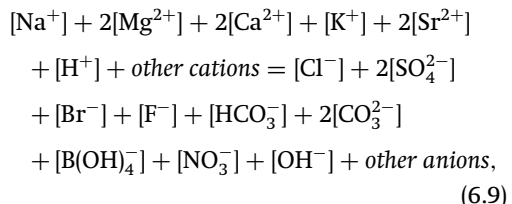
6.3.2 Charge balance and alkalinity

To understand how the partitioning of carbon between the carbonate species is controlled, as well as the enhanced capacity of seawater to hold DIC, we next consider the concept of charge balance and alkalinity.

Seawater cannot maintain a net charge due to its high conductivity, so the charge contributions from all cations and anions must balance. Now consider the ocean as a large vessel in which a variety of electrolytes (compounds which dissociate into positive and negative ions in water) are dissolved. Strong electrolytes have high equilibrium coefficients (e.g., $K'_c = [c^-][\text{H}^+]/[\text{Hc}]$) favouring complete ionisation in all conditions. Weak electrolytes are not completely ionised in water.

For seawater, a statement of charge balance can be written taking into account the contributions of the most abundant ions, derived from strong and weak electrolytes, both acids and

bases:

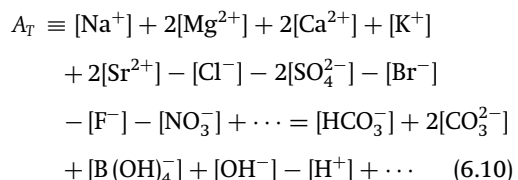


where factors of 2 reflect the contributions of the doubly charged ions.

Total alkalinity

The charge balance in seawater can be separated into two contributions: conservative ions, derived from strong electrolytes which are effectively completely ionised under all conditions, and non-conservative ions, derived from weak electrolytes and whose concentrations and degree of ionisation do vary with changes in temperature, salinity or pH; the concentrations of the most abundant conservative and non-conservative ions are listed in Tables 6.2 and 6.3, respectively.

The charge balance in seawater (6.9) can be rearranged by collecting together the charge contribution from the conservative ions and defining total alkalinity, A_T :



Total alkalinity, A_T , is set by the net charge contribution from the collected conservative anions and cations, quantified in Table 6.2, and is a conservative property of a water parcel. A_T has a value of about $+2300 (\pm 200) \mu\text{mol kg}^{-1}$ in surface seawater, increasing to $2370 \mu\text{mol kg}^{-1}$ in the global, full-depth mean. There cannot be a net charge in seawater, so this value *must* be balanced by the sum of the charges associated with the ions from the weak acids and bases, as in (6.10); for further discussion, see Zeebe and Wolf-Gladrow (2001) and Morel and Hering (1993).

The global-mean concentrations of the conservative ions depend only upon the magnitude of their sources and sinks: global-mean alkalinity is set by the balance between sources from rivers

Table 6.2 Concentrations of the major conservative ions in surface seawater (mmol kg^{-1}) and their associated charge concentrations. For this dataset, the difference between the total charge concentrations of the conservative cations and anions, or total alkalinity, $A_T = 2.319 \text{ mmol kg}^{-1}$. Data from Pilson (1998).

Cations	Conc.	Charge conc.	Anions	Conc.	Charge conc.
Na^+	468.96	468.96	Cl^-	545.88	-545.88
Mg^{2+}	52.83	105.66	SO_4^{2-}	28.23	-56.46
Ca^{2+}	10.28	20.56	Br^-	0.844	-0.844
K^+	10.21	10.21	F^-	0.068	-0.068
Sr^{2+}	0.0906	0.181			
Total		+605.571			-603.252

Table 6.3 Typical values for the concentrations of the most abundant non-conservative ions in surface seawater (mmol kg^{-1}). Their concentrations vary significantly with temperature, salinity, pressure and pH (unlike the conservative ions in Table 6.2) and are evaluated here for surface subtropical waters with temperature of 20°C , salinity 34.5 g kg^{-1} , $\text{pH} = 8.06$ and with $\text{pCO}_2 = 380 \mu\text{atm}$. Here, $A_T = 2.319 \text{ mmol kg}^{-1}$ is imposed for consistency with the sum of conservative cations and anions in Table 6.2.

Cations	Conc.	Charge conc.	Anions	Conc.	Charge conc.
H^+	8.71×10^{-6}	8.71×10^{-6}	HCO_3^-	1.839	-1.839
			CO_3^{2-}	0.196	-0.392
			B(OH)_4^-	0.084	-0.084
			OH^-	0.00445	-0.00445
Total		$+8.71 \times 10^{-6}$			-2.319

and the atmosphere, and sinks, such as burial in sediments. For many of the conservative ions, the source and sink rates are very slow and their lifetime in the ocean, the average time spent by a single ion in the ocean between arrival and departure, can be many millions of years; see Q6.1 for lifetimes of sodium. Calcium ions have more rapid sources and sinks due to the formation and dissolution of calcium carbonate sediments (Section 6.4) and modulate global ocean alkalinity on timescales of tens of thousands of years. Since the global ocean overturns and resets its deep properties on a timescale of several thousand years, salinity and alkalinity have relatively small variations around their mean ocean values.

6.3.3 What controls total alkalinity in the surface oceans?

Total alkalinity varies between 2100 and $2500 \mu\text{mol kg}^{-1}$ in the surface open ocean, with highest concentrations in the middle of the subtropical gyres (Fig. 6.6a), which broadly resembles

the salinity pattern. This close correspondence is due to evaporation and precipitation (Fig. 4.18), respectively, acting to dilute and concentrate alkalinity and salinity, which then leads to a nearly linear relationship between them in surface waters, as illustrated in Fig. 6.6b.

6.3.4 How does alkalinity affect DIC?

The relationship between A_T and DIC is now considered in a qualitative manner; while a more formal perspective is provided in Box 6.2.

Negatively charged non-conservative ions are needed to balance the net positive charge of the conservative ions, A_T . In seawater, this negative charge is largely accommodated by bicarbonate and carbonate ions, although there are small contributions from other anions, including $[\text{B(OH)}_4^-]$, accounting for a few per cent of the demand. Hence,

$$[\text{HCO}_3^-] + 2[\text{CO}_3^{2-}] \lesssim A_T. \quad (6.11)$$

There are two consequences of this relationship:

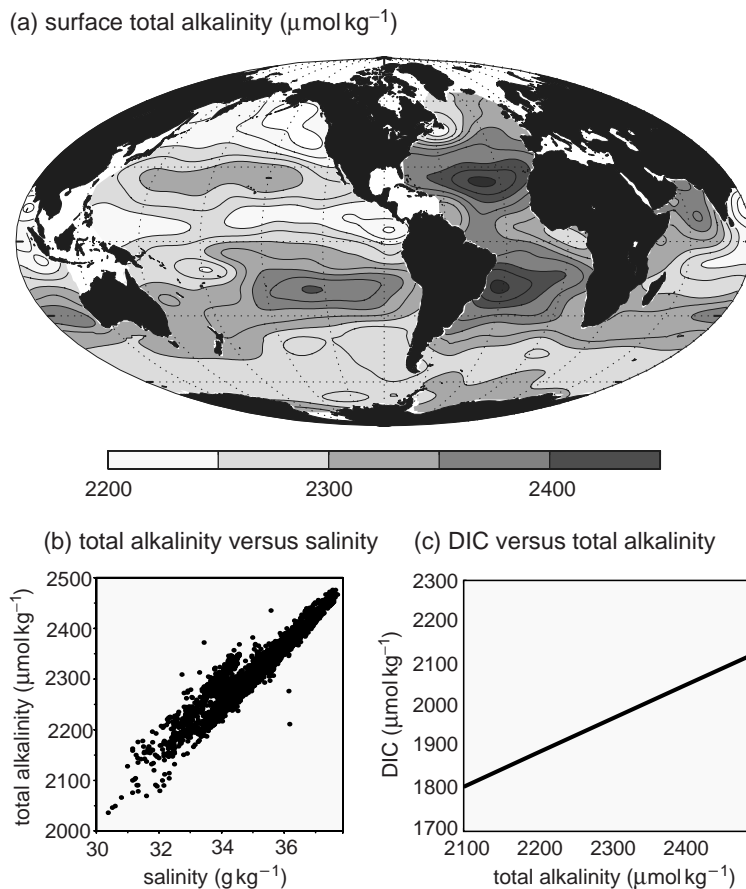


Figure 6.6 (a) Annual-mean surface map of total alkalinity ($\mu\text{mol kg}^{-1}$), together with (b) total alkalinity versus salinity (g kg^{-1}) in the uppermost 25 m of the ocean from data (Key *et al.*, 2004), and (c) the equilibrium relationship of DIC ($\mu\text{mol kg}^{-1}$) to total alkalinity A_T with $p\text{CO}_2 = 278 \mu\text{atm}$, $T = 20^\circ\text{C}$ and $S = 34.5 \text{ g kg}^{-1}$.

- Since DIC is largely composed of singly charged bicarbonate ions, the equilibrium concentration of DIC (for fixed $p\text{CO}_2$) scales almost linearly with A_T , as illustrated in Fig. 6.6c.
- Since $A_T \gg \text{CO}_2^* = K_0 p\text{CO}_2^{at}$, then $[\text{HCO}_3^-] + [\text{CO}_3^{2-}] \gg [\text{CO}_2^*]$. In other words, the alkalinity and charge balance of the oceans dictates that most of the DIC is accounted for by negatively charged bicarbonate and carbonate ions. Hence, the carbon storage of the ocean is two orders of magnitude greater than if only CO_2^* was present.

Carbonate alkalinity

More than 95% of the total alkalinity is accounted for by the carbonate species (see Table 6.3). Their contribution is formally defined as the carbonate alkalinity, A_C :

$$A_C = [\text{HCO}_3^-] + 2[\text{CO}_3^{2-}]. \quad (6.12)$$

The assumption that $A_C \sim A_T$ is a useful device to interpret the seawater carbonate system, which together with the definition of DIC (6.8) and equilibrium relationships (6.6) and (6.7) allows a simplified version of the carbonate system to be solved; see Box 6.3.

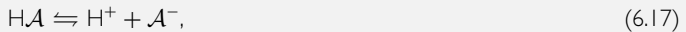
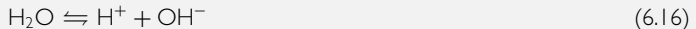
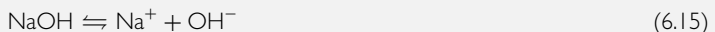
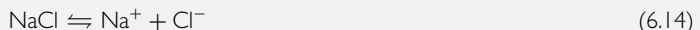
6.3.5 What controls regional variations in surface HCO_3^- and CO_3^{2-} ?

Now we return to the question of how the carbonate components vary spatially. The solubility of CO_2 increases in cooler waters, leading to the poleward increase in $[\text{CO}_2^*]$ and $[\text{HCO}_3^-]$, as seen in Fig. 6.4b,c. In contrast, alkalinity generally decreases poleward and is highest in the salty subtropical gyres due to the net freshwater loss to the atmosphere. Neglecting the very small contribution of $[\text{CO}_2^*]$ to DIC,

$$\text{DIC} \simeq [\text{HCO}_3^-] + [\text{CO}_3^{2-}], \quad (6.13)$$

Box 6.2 | Alkalinity and buffering in a simple system

Consider a simple system in which NaCl and NaOH are dissolved in pure water, providing sources of conservative sodium and chloride ions. A soluble gas, \mathcal{A} , with fixed partial pressure in the airspace, $p\mathcal{A}$ (μatm), invades the water and forms a weak acid, $\text{H}\mathcal{A}$ (mol kg^{-1}), which partially ionises. This system (discussed also by Zeebe and Wolf-Gladrow, 2001) can be described by the reactions:



where (6.16) and (6.17) can be described by the equilibrium relationships

$$K_w = [\text{H}^+][\text{OH}^-], \quad K_{\mathcal{A}} = \frac{[\text{H}^+][\mathcal{A}^-]}{[\text{H}\mathcal{A}]} \quad (6.18)$$

At equilibrium, $[\text{H}\mathcal{A}] = K_0^{\mathcal{A}} p\mathcal{A}$, and the total abundance of \mathcal{A} in the water is $\mathcal{A}_{\text{tot}} = [\text{H}\mathcal{A}] + [\mathcal{A}^-]$. Enforcing charge balance and rearranging to separate the conservative ions, we define the total alkalinity A_T^s ,

$$A_T^s = [\text{Na}^+] - [\text{Cl}^-] = [\mathcal{A}^-] + [\text{OH}^-] - [\text{H}^+] \quad (6.19)$$

With some analogies to CO_2 , assume that $K_0^{\mathcal{A}} = 10^{-2} \text{ mol kg}^{-1} \text{ atm}^{-1}$, $p\mathcal{A} = 350 \mu\text{atm}$, $K_{\mathcal{A}} = 10^{-6} \text{ mol kg}^{-1}$ and $K_w = 10^{-14} (\text{mol kg}^{-1})^2$. Combining (6.19) with the relationships in (6.18) leads to a quadratic in $[\mathcal{A}^-]$ which, when $K_w/(K_{\mathcal{A}}[\text{H}\mathcal{A}]) \ll 1$, has the solution

$$[\mathcal{A}^-] \sim \frac{A_T^s}{2} + \frac{\left((A_T^s)^2 + 4K_{\mathcal{A}}[\text{H}\mathcal{A}] \right)^{1/2}}{2} \quad (6.20)$$

There are two interesting limits for alkalinity:

(i) $A_T^s = 0$; if NaCl is dissolved, then $[\text{Na}^+] = [\text{Cl}^-]$. For the given equilibrium coefficients, $[\mathcal{A}^-] \sim (K_{\mathcal{A}}[\text{H}\mathcal{A}])^{1/2}$. With a relatively small pool of negative ions, the capacity to buffer changes in pH is low.

(ii) $A_T^s > 0$; if both NaCl and NaOH are dissolved, then $[\text{Na}^+] > [\text{Cl}^-]$. In the limit $(A_T^s)^2 \gg 4K_{\mathcal{A}}[\text{H}\mathcal{A}]$, we find that $[\mathcal{A}^-] \sim A_T^s$. \mathcal{A}_{tot} is then dominated by the ionic form so that $[\text{H}\mathcal{A}] \ll [\mathcal{A}^-]$. The positive charge of the conservative ions, A_T^s , demands to be balanced by $[\mathcal{A}^-]$, which sets the capacity to buffer changes in $[\text{H}^+]$. This limit is similar to the ocean carbonate system, where bicarbonate and carbonate ions dominate DIC, provide a significant buffer for pH, and DIC is of similar magnitude to A_T^s .

which, in combination with the definition of carbonate alkalinity (6.12), reveals that

$$\begin{aligned} [\text{CO}_3^{2-}] &\simeq A_C - \text{DIC}, \\ &\simeq A_T - \text{DIC}. \end{aligned} \quad (6.21)$$

The $[\text{CO}_3^{2-}]$ variation can then be inferred from the opposing contributions from variations of A_C and DIC with latitude as is evident in Fig. 6.4d: A_T and A_C generally decrease poleward due to freshwater fluxes at the sea surface, while DIC

Box 6.3 | Solving the carbonate system: a simplified view

The carbonate system can be understood in terms of mass conservation, charge balance and thermodynamic equilibrium. Consider a simplified carbonate system in which only carbonate contributions to alkalinity are considered. First we write down the basic conservation laws and thermodynamic equilibria:

Mass conservation for dissolved inorganic carbon

$$\text{DIC} = [\text{CO}_2^*] + [\text{HCO}_3^-] + [\text{CO}_3^{2-}], \quad (6.22)$$

Charge balance and carbonate alkalinity

$$A_C = [\text{HCO}_3^-] + 2[\text{CO}_3^{2-}], \quad (6.23)$$

Thermodynamic equilibrium for the carbonate species

$$K'_1 = \frac{[\text{HCO}_3^-][\text{H}^+]}{[\text{CO}_2^*]}, \quad (6.24)$$

$$K'_2 = \frac{[\text{CO}_3^{2-}][\text{H}^+]}{[\text{HCO}_3^-]}. \quad (6.25)$$

There are four equations. Providing values for K'_1 and K'_2 , and with knowledge of DIC and A_C , we are left with four unknowns, $[\text{CO}_2^*]$, $[\text{HCO}_3^-]$, $[\text{CO}_3^{2-}]$ and $[\text{H}^+]$, and the system can be fully solved. In this case combining (6.22)–(6.25), and defining $\gamma = \text{DIC}/A_C$, leads to a quadratic function of $[\text{H}^+]$ where the positive root is the appropriate solution:

$$[\text{H}^+] = \frac{1}{2} \left((\gamma - 1)K'_1 + \{(\gamma - 1)^2 K'^2_1 - 4K'_1 K'_2(1 - 2\gamma)\}^{\frac{1}{2}} \right). \quad (6.26)$$

The value of $[\text{H}^+]$ can be used to solve for $[\text{CO}_2^*]$, $[\text{HCO}_3^-]$ and $[\text{CO}_3^{2-}]$. Other permutations can be solved in a similar manner; say, if $[\text{CO}_2^*]$ and pH are known instead of DIC and A_T . More complete descriptions of the carbonate system, retaining more terms for alkalinity, result in a higher-order polynomial for $[\text{H}^+]$, which can be solved iteratively (e.g., Follows et al., 2006); see Appendix A.3.

increases poleward as temperature decreases and solubility increases and thus $[\text{CO}_3^{2-}]$ decreases poleward.

6.3.6 How does pH affect buffering and the partitioning of DIC?

The abundance of negatively charged carbonate and bicarbonate ions causes seawater to have a strong negative feedback, or buffering, against changes in hydrogen ion concentration. If an acid is added to seawater, $[\text{H}^+]$ instantaneously increases with the consequence of driving reactions (6.2) and (6.3) to the left, rapidly consuming the additional hydrogen ions again. Changes in

the partitioning of carbonate species in seawater with pH for a fixed A_T and DIC are illustrated in Fig. 6.7.

Consider the effect of an addition of CO_2 to seawater: DIC increases and H^+ ions are produced as reactions (6.2) and (6.3) are moved to the right. Combining equilibrium relationships (6.6) and (6.7) leads to the ratio in concentrations of carbonate ions and dissolved carbon dioxide being expressed by

$$\frac{[\text{CO}_3^{2-}]}{[\text{CO}_2^*]} = \frac{K'_1 K'_2}{[\text{H}^+]^2}, \quad (6.27)$$

so an increase in $[\text{H}^+]$ (and a decrease in pH) increases the relative contribution of $[\text{CO}_2^*]$ to DIC

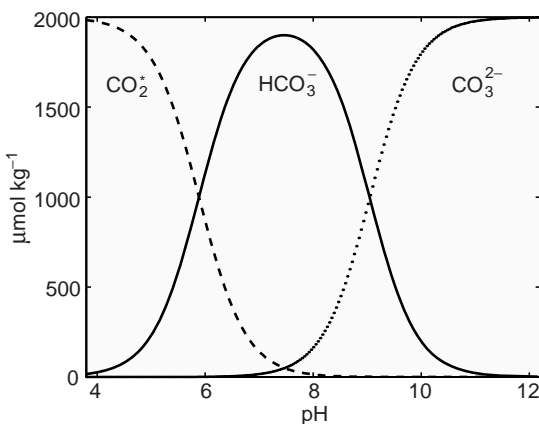


Figure 6.7 The Bjerrum plot reveals the partitioning of carbonate species as a function of pH. Dissolved inorganic carbon, DIC, is partitioned between CO_2^* (dashed line), HCO_3^- (full line) and CO_3^{2-} (dotted line). Lower pH indicates a higher $[\text{H}^+]$, pushing reactions (6.2) and (6.3) to the left, consuming CO_3^{2-} and favouring CO_2^* . For this plot, the carbonate system was solved (Appendix A.3) at fixed T , S , A_T and DIC, while varying pH.

at the expense of $[\text{CO}_3^{2-}]$, as indicated by their opposing trends in Fig. 6.7.

At pH close to the modern surface ocean value of 8.1, most of the DIC is in the form of HCO_3^- . At low pH, most of the DIC is instead held as CO_2^* , since the high concentration of hydrogen ions pushes reactions (6.2) and (6.3) to the left, consum-

ing carbonate ions. Conversely, at high pH, there is low $[\text{H}^+]$ leading to CO_3^{2-} being more abundant.

6.3.7 Regulation of DIC by temperature and alkalinity in the surface ocean

When in equilibrium with a fixed atmospheric pCO_2 , DIC varies strongly, and almost linearly, with temperature (Fig. 6.5c) and total alkalinity (Fig. 6.6c). Over the surface ocean, observations reveal two different regimes for how DIC varies with temperature and alkalinity, as illustrated in Fig. 6.8:

- In the extratropics, surface waters are cool and have low alkalinity, and DIC follows the trend expected from a temperature-controlled equilibrium with the atmosphere (Fig. 6.8a, dark dots).
- Conversely, in the tropics and subtropics, surface waters are warm and have high alkalinity, and DIC follows the linear trend expected from an alkalinity-controlled equilibrium with the atmosphere (Fig. 6.8b, pale dots).

While both temperature and alkalinity affect surface DIC, the dominant effect is temperature, since surface DIC is higher in the cooler, lower alkalinity waters of the high latitudes (as displayed earlier in Fig. 6.4a), than in the warmer, higher alkalinity waters of the tropics.

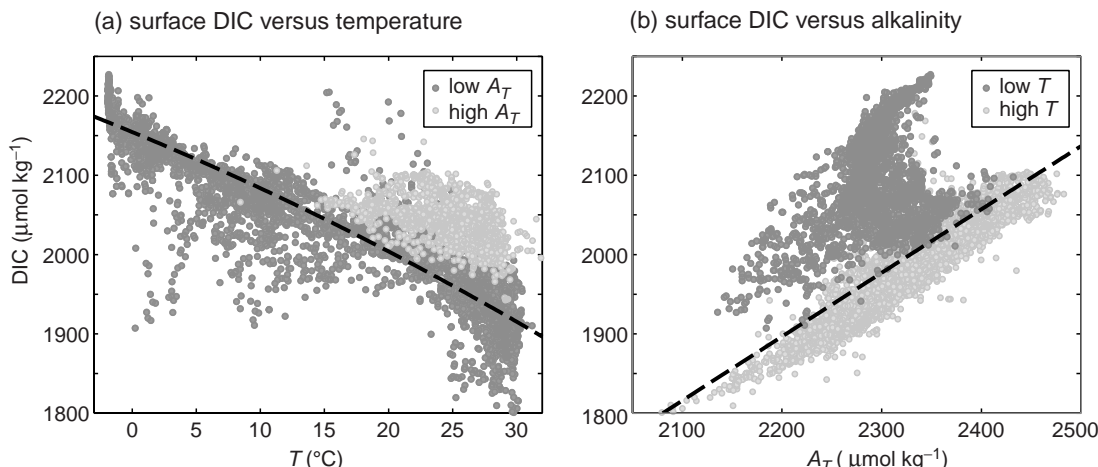


Figure 6.8 Observed relationships between DIC ($\mu\text{mol kg}^{-1}$), temperature, T ($^\circ\text{C}$), and alkalinity, A_T ($\mu\text{mol kg}^{-1}$), over the surface ocean (0–25 m): (a) DIC versus T separated into low alkalinity (dark grey) ($A_T < 2350 \mu\text{mol kg}^{-1}$) and high alkalinity water (light grey); and (b) DIC versus A_T for cold waters (dark grey) and warm waters (light grey; $T > 20^\circ\text{C}$). In both (a) and (b), the theoretical equilibrium DIC (thick dashed line) is included for $\text{pCO}_2 = 360 \mu\text{atm}$ (a value typical of the surface atmosphere in the 1990s, when most of the ocean data were collected) as a function of T (with fixed $A_T = 2280 \mu\text{mol kg}^{-1}$) or A_T (with fixed $T = 25^\circ\text{C}$). Data from Key *et al.* (2004).

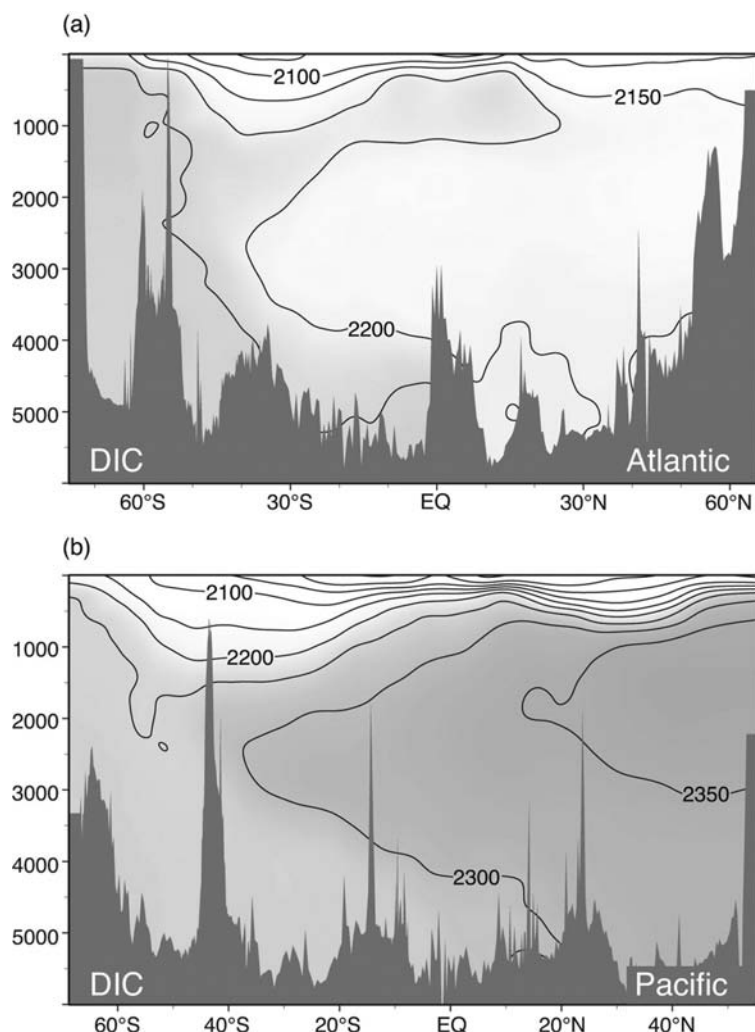


Figure 6.9 Observed meridional sections of dissolved inorganic carbon, DIC ($\mu\text{mol kg}^{-1}$) in (a) the Atlantic, approximately along 20°W , and (b) the Pacific, approximately along 170°W ; see Plates 6a and 7a.

6.4 Coupling of DIC and alkalinity cycles with depth

The focus so far has been on the carbon chemistry in the surface ocean, but this is only part of the story. Now consider how DIC and alkalinity vary with depth, examining meridional sections passing through the Atlantic and Pacific.

6.4.1 Variation of DIC with depth

DIC generally increases with depth, as depicted in Fig. 6.9, through a combination of physical, biological and chemical processes:

- There is a physical transfer of carbon-rich, cold waters from the surface mixed layer in high latitudes to the deep ocean, enhancing DIC at depth (Sections 2.4.1 and 6.3); referred to as the solubility pump.
- There is a biologically driven formation of organic matter in the sunlit, surface ocean, some of which eventually sinks or is transferred downward by the circulation to be respired at depth (Sections 2.4.1 and 5.5), enhancing deep DIC. This transfer of carbon is referred to as the biological soft-tissue pump.
- Carbon is also transported vertically through the formation, sinking and dissolution of calcium carbonate, supplying calcium ions and DIC at depth; referred to as the carbonate pump.

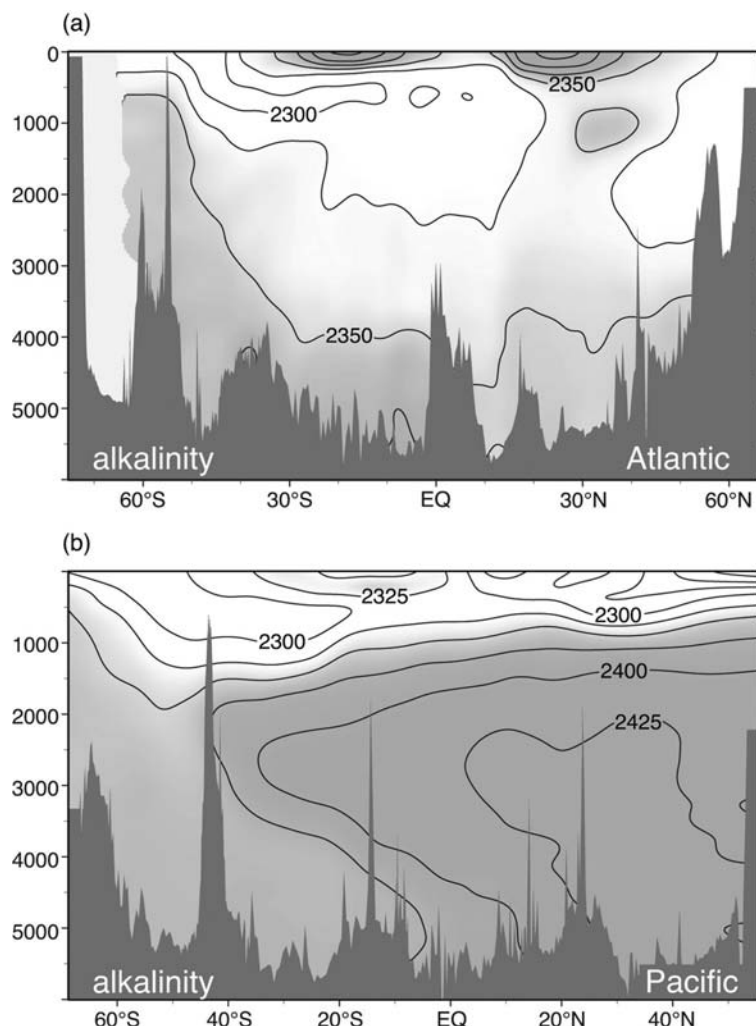


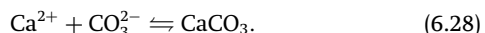
Figure 6.10 Observed distribution of total alkalinity A_T ($\mu\text{mol kg}^{-1}$) in the Atlantic and Pacific Oceans. The average total alkalinity in the global ocean is about $2370 \mu\text{mol kg}^{-1}$.

6.4.2 Variation of alkalinity with depth

Alkalinity likewise varies over the globe, as depicted in Fig. 6.10, also depending on the interplay of physical, biological and chemical processes:

- There is a physical transfer of low-alkalinity, fresher waters from the high-latitude surface into the deep ocean. This physical transfer leads to a layered structure, revealed in the imprint of fresh, low-alkalinity intermediate waters spreading northward from the Southern Ocean at depths of a few hundred metres (Fig. 6.10a,b).
- Alkalinity is strongly affected by the formation and dissolution of calcium carbonate, which

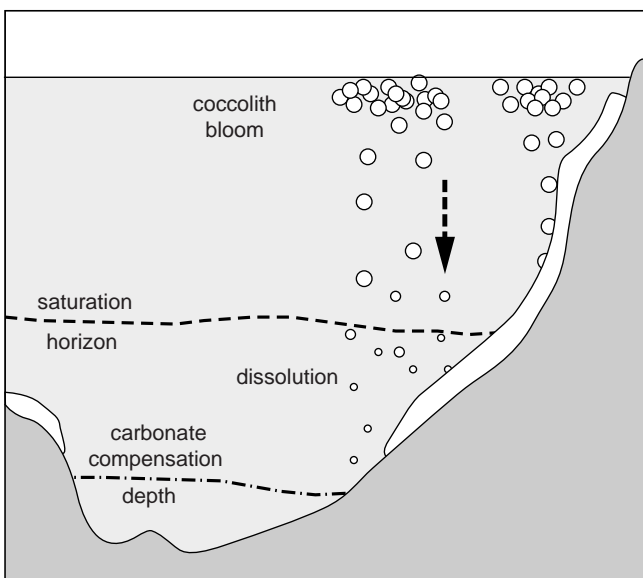
removes or supplies calcium ions:



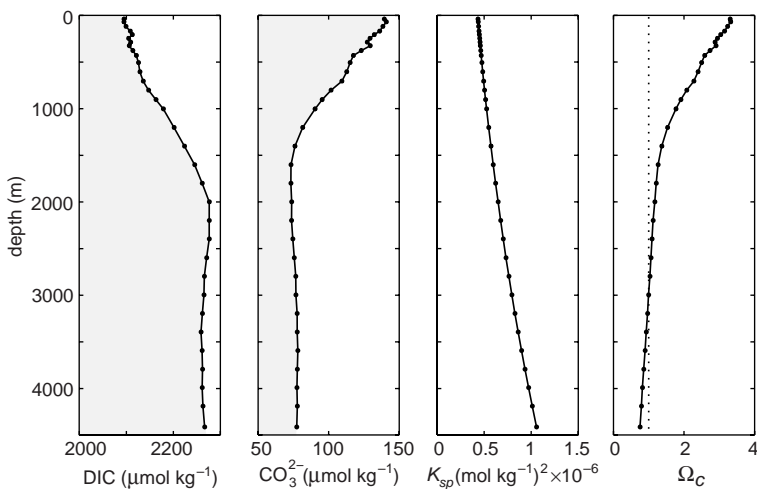
Some plankton create mineral calcium carbonate structural and defensive body parts, which then removes calcium ions and reduces alkalinity in surface waters. This inorganic matter sinks and dissolves at depth, returns calcium and carbonate ions to the water column, and increases alkalinity in deep waters (Fig. 6.10a,b).

- There is a minor opposing contribution from the biological transfer of nitrate, which makes a negative contribution to total alkalinity, as indicated in (6.10). Nitrate is rapidly consumed by phytoplankton and increasing the

(a) calcium carbonate cycling



(b) South Pacific profiles



alkalinity in surface waters. Nitrate is regenerated at depth as sinking organic matter is respiration and reducing alkalinity in deep waters. The alkalinity effect of the biological transfer of nitrate opposes, and is weaker, than that of calcium carbonate.

Given the effect of calcium carbonate cycling on both DIC and alkalinity, now we consider how calcium carbonate cycling varies with depth.

6.4.3 What determines the depth at which sinking calcium carbonate dissolves?

Sinking calcium carbonate either eventually completely dissolves in the water column or is buried in sediments, as depicted in Fig. 6.11a.

The depth at which calcium carbonate dissolves depends on the solubility of solid calcium carbonate in seawater. Consider a beaker of seawater in which there is a lump of solid calcium

Figure 6.11 Calcium carbonate cycling in the ocean: (a) a schematic view, and (b) vertical profiles of DIC, $[CO_3^{2-}]$ (both $\mu\text{mol kg}^{-1}$), calcite (calcium carbonate) solubility product, K_{sp} ($(\text{mol kg}^{-1})^2$) and the non-dimensional ratio, Ω_C from (6.29) in the South Pacific ($150.5^\circ\text{W}, 47.5^\circ\text{S}$). In (a), organisms in the surface waters produce calcium carbonate body parts, which eventually sink into the dark abyss. Solid CaCO_3 begins to dissolve below a depth referred to as the saturation horizon. Dissolution is not instantaneous and the downward flux continues to the depth where dissolution completely consumes the downward flux, the carbonate compensation depth. The depth above which the sediments are observed to be rich in CaCO_3 is called the lysocline.

carbonate: there is a dynamic exchange of calcium and carbonate ions between the solid and aqueous forms as CaCO_3 is continuously formed and dissolved. Eventually an equilibrium is reached in which the formation and dissolution rates are equal, and the lump of calcium carbonate neither grows nor shrinks.

At this equilibrium, a solubility product can be defined, $K_{sp}(T, S, p) = [\text{Ca}^{2+}][\text{CO}_3^{2-}] (\text{mol}^2 \text{kg}^{-2})$: the product of the dissolved calcium and carbonate ion concentrations in the presence of solid CaCO_3 . Different regimes can be represented by a non-dimensional ratio, Ω_C , given by the product of the calcium and carbonate concentrations divided by the solubility product:

$$\Omega_C = \frac{[\text{Ca}^{2+}][\text{CO}_3^{2-}]}{K_{sp}}. \quad (6.29)$$

By definition, $\Omega_C = 1$ at equilibrium; $\Omega_C < 1$ reflects undersaturation favourable for dissolution of solid calcium carbonate; and $\Omega_C > 1$ reflects supersaturation favourable for calcium carbonate to precipitate out of solution. In the present ocean, even in supersaturated waters, precipitation of calcium carbonate is usually biologically mediated.

The depth range over which CaCO_3 either dissolves or forms is determined by the variations in $[\text{CO}_3^{2-}]$ and the solubility product K_{sp} in (6.29), rather than the variation in $[\text{Ca}^{2+}]$ ions which are relatively uniform in the ocean. $[\text{CO}_3^{2-}]$ generally decreases with depth as DIC increases (Figs. 6.9 and 6.11b). Since CO_2 is a weak acid, the additional DIC lowers pH and favours $[\text{CO}_3^*]$ at the expense of $[\text{CO}_3^{2-}]$ in the deeper waters. The solubility of calcium carbonate, K_{sp} , increases with higher pressure and lower temperature (Fig. 6.11b).

For the illustrated profiles in the South Pacific (Fig. 6.12b), there is supersaturation in the upper ocean, $\Omega_C > 1$, favourable for the formation of mineral CaCO_3 (as depicted in Fig. 6.11b). Ω_C reduces with depth due to declining $[\text{CO}_3^{2-}]$ and increasing K_{sp} with depth. In the deeper ocean, waters eventually become undersaturated, $\Omega_C < 1$, and mineral CaCO_3 dissolves, adding calcium and carbonate ions, further increasing alkalinity and DIC.

6.5 How are changes in pCO_2 related to changes in DIC?

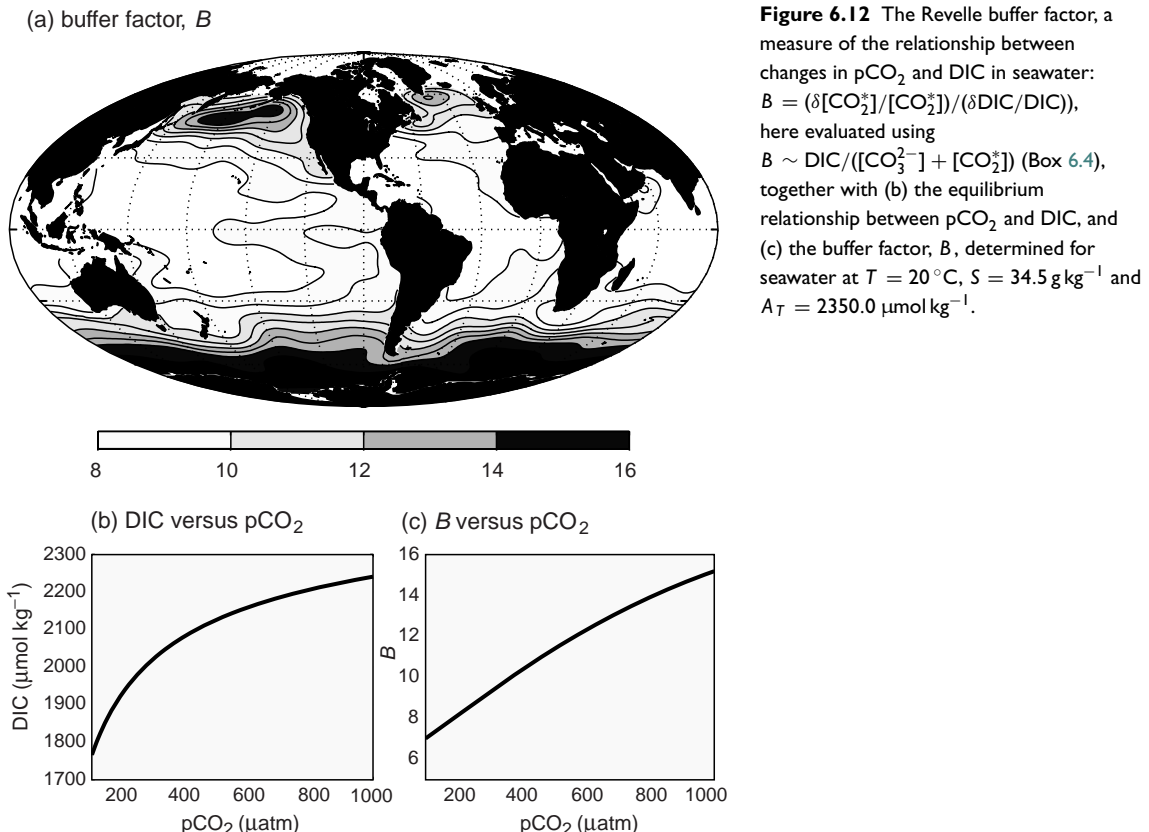
The air-sea exchange of carbon dioxide depends on the partial pressure, pCO_2 , or concentration of CO_2^* in the surface waters, while the global ocean storage of carbon is measured by DIC. How are changes in these parameters related?

6.5.1 Buffering of the seawater carbonate system

Changes in DIC are buffered with respect to changes in pCO_2 . In other words, there are negative feedbacks in the carbonate system which dampen the impact of perturbations on the total dissolved inorganic carbon pool. On the other hand, this ocean feedback amplifies changes in atmospheric pCO_2 in response to changes in ocean DIC.

Consider a thought experiment revealing the nature of buffering: air and seawater are contained in a closed vessel. The partial pressures of two gases, inert CFC-11 and reactive CO_2 , are held fixed in the airspace. The gases dissolve in the seawater and the air and water reservoirs come into equilibrium. If the partial pressure of CFC-11 in the airspace is then increased by 10%, molecules are preferentially transferred into the seawater until the concentration of dissolved CFC-11 and the inventory of CFC-11 in the water have both also increased by 10%.

If the partial pressure of CO_2 in the airspace is likewise increased by 10% (and held at that value), CO_2 molecules are also driven across the surface into the seawater. Much of the newly dissolved CO_2 is rapidly transferred into the other carbonate species. The exchange of CO_2 across the surface ceases when the concentration of dissolved CO_2^* in the seawater has increased by 10%. At this point DIC has also increased, as expected, but only by about 1%. Why does DIC not also increase by 10%? DIC would increase by the same amount if the partitioning between carbonate species were fixed, but the addition of CO_2 also lowers the pH, and the partitioning of carbonate species shifts in favour of CO_2^* , as indicated by the equilibrium relationship (6.27). pCO_2 and pCO_2^{at} come back into



balance, even though DIC has changed by much less than 10%. Thus, the carbonate system is buffered against changes to DIC.

The Revelle buffer factor

The relationship between fractional changes in $p\text{CO}_2$ and DIC is formally expressed in terms of the *Revelle buffer factor*, B , which is defined as the ratio of the relative changes in $p\text{CO}_2$ and DIC (Bolin and Erickson, 1959),

$$B = \frac{\delta p\text{CO}_2}{p\text{CO}_2} / \frac{\delta \text{DIC}}{\text{DIC}} = \frac{\delta [\text{CO}_2^*]}{[\text{CO}_2^*]} / \frac{\delta \text{DIC}}{\text{DIC}}. \quad (6.30)$$

The buffer factor can be formally written and evaluated as a function of the equilibrium coefficients and $[\text{H}^+]$ by differentiating the equations defining DIC and A_T , and assuming that changes in alkalinity are negligible (Bolin and Erickson, 1959). The relationship between equilibrium DIC and $p\text{CO}_2$ at fixed T and A_T is illustrated in Fig. 6.12b, with the Revelle buffer factor related to the slope of the curve. Since the DIC– $p\text{CO}_2$ relationship is non-

Figure 6.12 The Revelle buffer factor, a measure of the relationship between changes in $p\text{CO}_2$ and DIC in seawater: $B = (\delta [\text{CO}_2^*]/[\text{CO}_2^*]) / (\delta \text{DIC}/\text{DIC})$, here evaluated using $B \sim \text{DIC}/([\text{CO}_3^{2-}] + [\text{CO}_2^*])$ (Box 6.4), together with (b) the equilibrium relationship between $p\text{CO}_2$ and DIC, and (c) the buffer factor, B , determined for seawater at $T = 20^\circ\text{C}$, $S = 34.5 \text{ g kg}^{-1}$ and $A_T = 2350.0 \mu\text{mol kg}^{-1}$.

linear, the Revelle buffer factor is not constant, changing by a factor of two over the range of $p\text{CO}_2$, as depicted in Fig. 6.12c.

How does the Revelle buffer factor vary?

In today's surface ocean, B varies from 8 in the tropics to 16 in high latitudes (Fig. 6.12a). What controls this mean value and its variations?

In Box 6.4, we derive an approximate expression for B in terms of the carbonate system components, which reveals that B depends on the ratio of DIC and the concentration of carbonate ions,

$$B \sim \frac{\text{DIC}}{[\text{CO}_3^{2-}]} \sim 10. \quad (6.31)$$

Hence, fractional changes in $p\text{CO}_2$ are typically 10 times larger than the corresponding changes in surface DIC. The buffering, or ability to respond to change, is controlled by the relative size of the carbonate ion reservoir, which in turn is related to the alkalinity. Combining (6.31) and the definition of carbonate alkalinity (6.12), $[\text{CO}_3^{2-}] \sim A_C - \text{DIC}$,

Box 6.4 | Why is the buffer factor on the order of 10?

In order to understand the value of the buffer factor, start by combining the equilibrium relationships (6.6) and (6.7), eliminating $[H^+]$:

$$[CO_2^*] = \frac{K'_2}{K'_1} \frac{[HCO_3^-]^2}{[CO_3^{2-}]} . \quad (6.32)$$

An expression for fractional changes in $[CO_2^*]$ can be obtained by differentiating (6.32) and applying a product rule (where for a general expression $h = f^m g^n$, the changes in each variable are related by $\delta h/h = m\delta f/f + n\delta g/g$), such that

$$\frac{\delta[CO_2^*]}{[CO_2^*]} = 2 \frac{\delta[HCO_3^-]}{[HCO_3^-]} - \frac{\delta[CO_3^{2-}]}{[CO_3^{2-}]} . \quad (6.33)$$

Assuming that the carbonate alkalinity is constant ($\delta A_c = 0$), differentiating its definition (6.23) leads to

$$\delta A_c = 0 = \delta[HCO_3^-] + 2\delta[CO_3^{2-}] . \quad (6.34)$$

Substituting (6.34) into (6.33) leads to

$$\frac{\delta[CO_2^*]}{[CO_2^*]} = - \frac{\delta[CO_3^{2-}]}{[CO_3^{2-}]} \left(1 + \frac{4[CO_3^{2-}]}{[HCO_3^-]} \right) = - \frac{\delta[CO_3^{2-}]}{[CO_3^{2-}]} \beta_c , \quad (6.35)$$

where, in the modern ocean, $\beta_c = (1 + 4[CO_3^{2-}]/[HCO_3^-]) \sim 1.4$, is of order 1. The fractional changes in $[CO_2^*]$ and $[CO_3^{2-}]$ are approximately equal and opposite. Now differentiating the definition for DIC (6.22), assuming that A_c is constant, and dividing through by DIC leads to

$$\frac{\delta DIC}{DIC} = \frac{\delta[CO_2^*] - \delta[CO_3^{2-}]}{DIC} . \quad (6.36)$$

The Revelle buffer factor is defined as (6.35) divided by (6.36). Since $\beta_c \sim 1$ and using $\delta[CO_2^*] \ll \delta[CO_3^{2-}]$ which follows from (6.35) for typical ocean conditions, we obtain

$$B \simeq \frac{DIC}{[CO_3^{2-}]/\beta_c + [CO_2^*]} \sim \frac{DIC}{[CO_3^{2-}]} \sim 10 . \quad (6.37)$$

then the buffer factor B can be expressed in terms of A_c ($\sim A_T$) and DIC:

$$B \sim \frac{1}{A_c/DIC - 1} . \quad (6.38)$$

In the surface ocean DIC generally increases with latitude, while alkalinity generally decreases with latitude (Figs. 6.4a and 6.6a), and so B increases with latitude.

This gradient in B implies that changes in atmospheric pCO₂ have a weaker impact on surface DIC at high latitudes, relative to low latitudes. Conversely, changes in surface DIC at high lati-

tudes have a larger impact on surface pCO₂, and likewise atmospheric pCO₂, relative to a change in surface DIC in low latitudes.

Buffering and changes in atmospheric pCO₂

The buffer factor also varies with how much carbon is held in the atmosphere and ocean, as illustrated in Fig. 6.12c. As carbon is added to seawater, the pH decreases, reducing the relative contribution of $[CO_3^{2-}]$ to DIC and increasing B .

This variation in B is important for the climate response to anthropogenic increases in

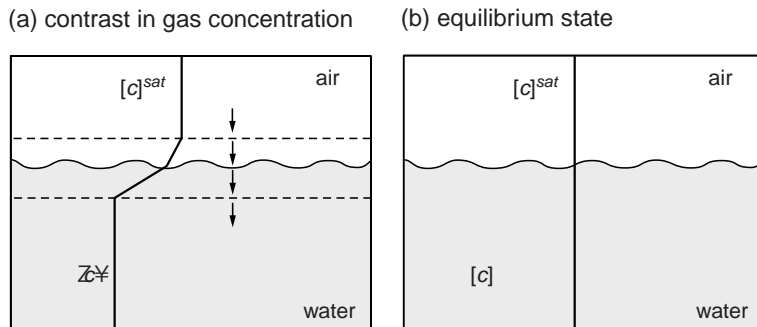


Figure 6.13 The relationship between the air-sea difference in the concentration of a gas and its flux across the sea surface. $[c]^{\text{sat}}$ is the concentration that the ocean would have if it came to equilibrium with the atmosphere at its current pCO_2 . $[c]^{\text{sat}}$ is related to the partial pressure of the gas by $[c]^{\text{sat}} = K_0 \rho c$, where K_0 is the solubility. Initially, (a) there is an air-sea difference in the concentration (or partial pressure) and gas fluxes into the ocean. At equilibrium, (b), there is no net gas exchange and $[c] = [c]^{\text{sat}}$.

atmospheric pCO_2 . The ocean is absorbing carbon dioxide from the atmosphere, reducing the radiative warming effects, but also increasing the buffer factor. The increase in B is then reducing the efficiency with which the ocean can absorb future carbon emissions and so a larger fraction of these emissions will remain in the atmosphere.

Up to now, we have largely considered the carbon system in terms of equilibrium behaviour, both between the carbonate components and between air and water reservoirs. However, the air-sea flux of CO_2 is driven by disequilibrium across the sea surface. In the following sections we consider how the surface ocean is driven away from equilibrium and the implications for air-sea exchange.

6.6 Air-sea exchange of carbon dioxide

All soluble gases, including oxygen and carbon dioxide, are exchanged across the air-sea interface, connecting the atmosphere and ocean reservoirs. The air-sea flux of a gas is difficult to measure directly, but can be related to the departure from equilibrium of the air and water reservoirs.

From the ocean perspective (Fig. 6.13), the air-sea flux is naturally understood in terms of the dissolved gas concentration, $[c]$ (where c is

a generic, soluble gas), and saturated concentration, $[c]^{\text{sat}}$, that the ocean would have if it came to equilibrium with the overlying atmosphere with its current partial pressure, ρc . The air-sea flux of the gas, \mathcal{F} ($\text{mol c m}^{-2} \text{s}^{-1}$), is then related to the difference between the current and saturated concentrations,

$$\mathcal{F} = -\rho_0 K_g ([c] - [c]^{\text{sat}}), \quad (6.39)$$

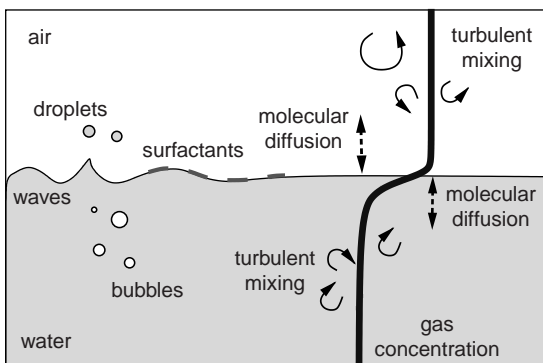
where ρ_0 is a reference density for seawater (kg m^{-3}) and K_g (m s^{-1}) is the air-sea gas transfer coefficient, measuring the efficiency with which gas exchange occurs (Fig. 6.14b); here a positive flux is defined as directed into the ocean. If the saturation concentration, $[c]^{\text{sat}}$, is greater than the aqueous phase concentration, $[c]$, there is an influx of the gas into the ocean until equilibrium is reached.

Alternatively, from an atmospheric perspective, the air-sea contrast in gas concentration is understood in terms of the partial pressure of the gas in the atmosphere, ρc^{at} (μatm), and the effective partial pressure in the ocean,

$$\mathcal{F} = -\rho_0 K_g K_0 (\rho c - \rho c^{\text{at}}), \quad (6.40)$$

where the solubility of the gas, $K_0 = [c]/\rho c$ in units of $\text{mol kg}^{-1} \mu\text{atm}^{-1}$. Thus, if the partial pressure of the atmosphere, ρc^{at} , is greater than the effective value in the ocean, then the air-sea flux is again directed into the ocean, increasing the ocean concentration $[c]$ and ρc .

(a) physical processes affecting air-sea transfer



(b) air-sea gas transfer versus wind speed

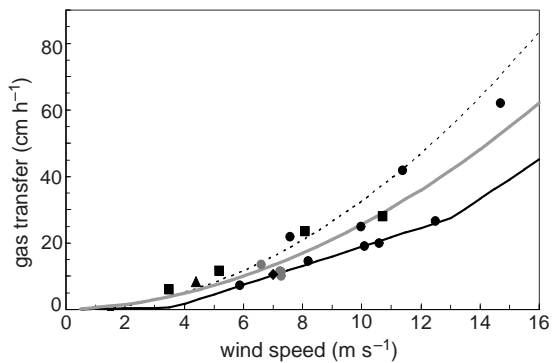


Figure 6.14 (a) Schematic view of the physical processes regulating the air-sea transfer of a dissolved gas. The concentration of the gas (solid line) varies in the vertical and drives a net flux of gas molecules across the sea surface. The efficiency of gas transfer is a function of the rate of molecular diffusion within a very thin layer of each fluid at the air-sea interface, and the rate of replacement of those layers due to turbulent mixing. The ejection of spray and entrainment of bubbles can enhance the net rate of exchange. A very thin thermal 'skin' and organic surfactants at the surface of the water can also modify the effective solubility, surface tension and efficiency of gas exchange. (b) Air-sea gas transfer coefficient, K_g (cm h^{-1}) as a function of wind speed at 10 m, based on observations in laboratory, lakes and ocean; a value of 20 cm h^{-1} is equivalent to $5 \times 10^{-5} \text{ m s}^{-1}$. The data points depict results from dual tracer experiments in the equatorial Pacific (grey circles), North Sea (black circles), Florida Shelf (black triangle), Georges Bank (black squares) and Atlantic Ocean (black diamond). The curves indicate different parameterisations of how K_g varies with wind speed at 10 m based upon Liss and Merlivat (1986) (thin black line), Wanninkhof and McGillis (1999) (dashed line) and a best fit to dual tracer data by Nightingale et al. (2000) (grey line). Figure supplied by Phil Nightingale; further details, see Nightingale et al. (2000).

6.6.1 What controls the rate of gas transfer?

The effectiveness of the air-sea gas transfer is determined by a complex set of physical processes, including molecular diffusion, turbulent mixing, surface waves, bubbles and spray (Fig. 6.14a; see review by Jähne and Haussecker, 1998). The air-sea gas transfer coefficient, K_g , crudely measures the combined effect of all of these processes; K_g is empirically found to vary between 10^{-5} to 10^{-3} m s^{-1} , and increases with wind speed (Fig. 6.14b). After accounting for temperature-driven changes in molecular diffusion and viscosity, polynomial relationships have been fitted between K_g and wind speed (Fig. 6.14b, lines) based on several field experiments; there is significant scatter reflecting the complexity of the physical processes and the difficulty in obtaining field data at high wind speeds.

6.6.2 The air-sea flux of CO₂

The air-sea flux of CO₂ has been estimated using (6.40), as illustrated in Fig. 6.15a from Takahashi

et al. (2002), based upon compiled measurements of surface ocean pCO₂, observed atmospheric pCO₂^{at}, solubility K_0 (or fugacity, accounting for non-ideal gas effects), and a wind-speed-dependent model of K_g .

The regional variations in the sign of the air-sea flux are mainly due to the pattern of surface ocean pCO₂ (Fig. 6.1), since CO₂ is relatively well mixed in the lower atmosphere. The magnitude of the annual air-sea flux typically reaches several mol C m⁻² y⁻¹. Air-sea exchange increases when there is large disequilibrium and efficient exchange, encapsulated in K_g , which is enhanced in strong winds, such as over the mid-latitude storm tracks.

In the tropics, the partial pressure of carbon dioxide, pCO₂, in the ocean exceeds the atmospheric partial pressure, pCO₂^{at}, driving outgassing (Fig. 6.15a, dark shading). Conversely, in the northern high latitudes, the pCO₂ in the ocean is less than that in the atmosphere, leading to an influx of CO₂ (Fig. 6.15a, light shading). In the Southern Ocean, the annual flux is relatively weak and suggests a regional uptake of CO₂ by the ocean from the atmosphere.

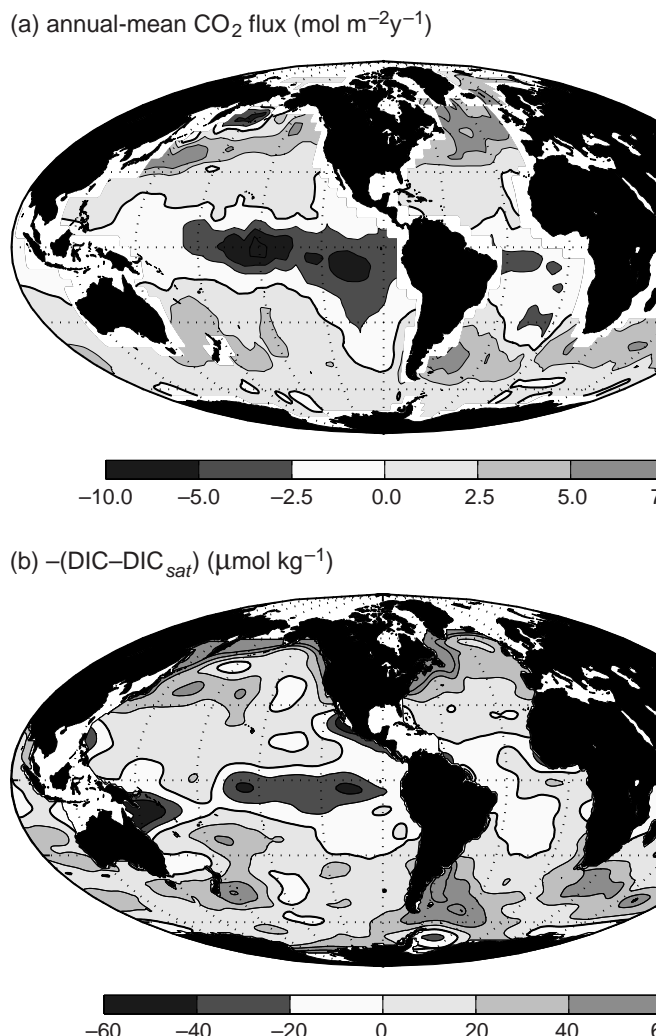


Figure 6.15 Global distribution of (a) air-sea flux of CO_2 into the ocean ($\text{mol m}^{-2}\text{y}^{-1}$) based on a compilation of surface ocean observations from Takahashi *et al.* (2002). There is an ocean uptake of CO_2 (light shading) in the high latitudes and an ocean outgassing in the tropics (dark shading). The thick, solid line indicates the zero contour. However, there is considerable uncertainty in the direction of the flux over the Southern Ocean. This evaluation is based on a compilation of about a million measurements of surface-water pCO_2 obtained since the International Geophysical Year of 1956–59. The climatology represents mean non-El Nino conditions with a spatial resolution of $4^\circ \times 5^\circ$, normalised to reference year 1995. (b) An evaluation of the associated disequilibrium in DIC ($\Delta\text{DIC} = \text{DIC} - \text{DIC}_{\text{sat}}$, $\mu\text{mol kg}^{-1}$) inferred from an independent global climatology of DIC and A_T . Ocean uptake of CO_2 is implied when ΔDIC is negative (light shading) and, conversely, an outflux of CO_2 whenever ΔDIC is positive (dark shading). ΔDIC is evaluated by differencing mapped DIC and estimated DIC_{sat} , based upon ocean DIC, A_T , T and S using the climatologies of Key *et al.* (2004) and Conkright (2002). In (b), pCO_2^{at} was assumed to be 360 μatm .

6.6.3 What prevents a local air-sea equilibrium?

The air-sea flux acts to erode the air-sea difference in pCO_2 . Why then, is surface ocean pCO_2 so far from pCO_2^{at} ? Other ocean processes are continually acting to move surface ocean pCO_2 away from equilibrium, as depicted in Fig. 6.16.

Surface heating and solubility forcing

Surface heating and cooling of the upper ocean drive air-sea fluxes of CO_2 by modifying the solubility. Surface warming increases pCO_2 , favour-

ing an outflux of CO_2 from the ocean, while cooling decreases pCO_2 , favouring an influx of CO_2 . Since, at equilibrium with a given pCO_2 , DIC is almost linearly dependent on temperature (Fig. 6.5c), the ‘potential’ air-sea flux of CO_2 due to surface heat fluxes can be estimated assuming an instantaneous response to the change in solubility (Murnane *et al.*, 1999). This estimate of the thermally forced air-sea flux is mapped in Fig. 6.17 and broadly resembles the observed actual CO_2 flux (Fig. 6.15b). Hence, surface heat fluxes significantly regulate the broad-scale patterns of the net air-sea carbon flux; see Q6.4. However, this potential air-sea flux does not account for the long

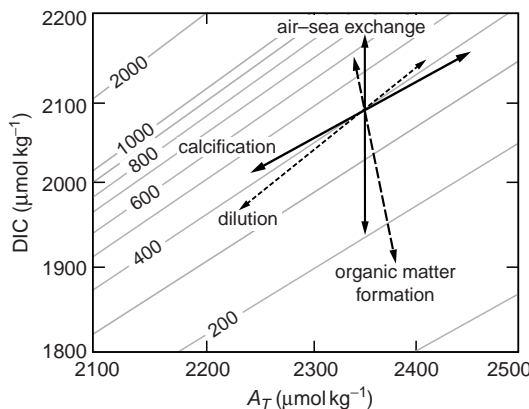
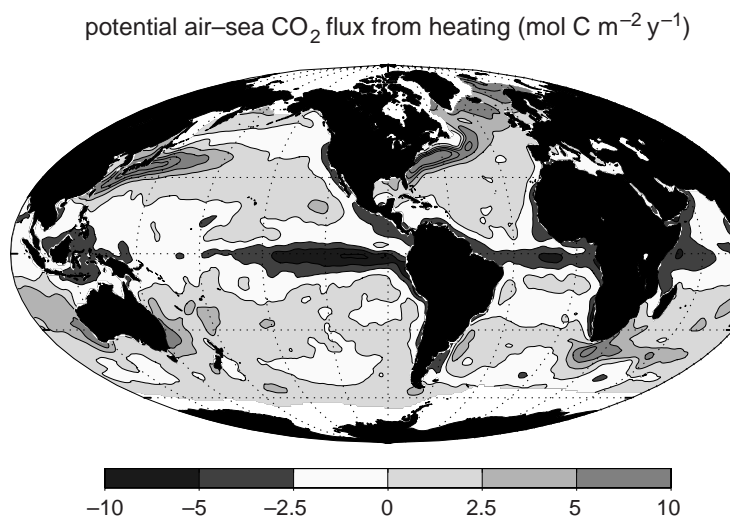


Figure 6.16 Surface ocean $p\text{CO}_2$ (contours, μatm) as a function of A_T and DIC ($T = 20^\circ\text{C}$, $S = 34.5 \text{ g kg}^{-1}$). Vectors indicate the relative changes in A_T and DIC associated with various processes, along with changes in $p\text{CO}_2$ relative to an initial $p\text{CO}_2$ of $400 \mu\text{atm}$. Temperature changes modulate solubility, driving air-sea gas exchange, which affect DIC but have no impact on A_T . Evaporation and precipitation cause concentration and dilution of both A_T and DIC with relatively little net effect on $p\text{CO}_2$: the trajectory is almost parallel to the isolines of $p\text{CO}_2$. The formation of organic matter decreases DIC, reducing $p\text{CO}_2$, and consuming nitrate which leads to a small increase in alkalinity. Here it is assumed that nitrate is the nitrogen source and that carbon and nitrogen are consumed in the Redfield ratio of $106:16$. The formation of calcium carbonate is a particularly interesting case: DIC and A_T are consumed in a $1:2$ ratio so the change in alkalinity dominates the impact on $p\text{CO}_2$, causing $p\text{CO}_2$ to increase even though DIC is consumed. In the open ocean, the formation of calcium carbonate and organic matter occur together as coccolithophorids bloom.



timescale for the air-sea equilibration of CO_2 (Section 6.6.5), which delays the response to heating/cooling.

Production and respiration of organic matter

The production and export of organic matter from the surface ocean consumes DIC and decreases $p\text{CO}_2$, potentially driving a local uptake of CO_2 from the atmosphere. Primary and export production in the open ocean are largest in the high latitudes and tropics, where the supply of macro-nutrients to the euphotic zone from the deep ocean is most vigorous. In the high-latitude surface waters, biological consumption of DIC reinforces the reduction of $p\text{CO}_2$ due to surface cooling, potentially enhancing the uptake of carbon dioxide from the atmosphere. In the tropics, biological consumption of DIC also reduces $p\text{CO}_2$, here counteracting the effect of surface warming.

Upwelling of deep, carbon-rich waters

Organic carbon is eventually respired (with oxygen consumed) and returned to DIC, mostly within the dark ocean interior. When carbon-enriched deep waters return to the surface, $p\text{CO}_2$ increases, driving an outgassing from the ocean to the atmosphere, such as in the tropics and Southern Ocean. Waters returning to the surface are enriched in both nutrients and carbon from respired organic matter. When the nutrients

Figure 6.17 Potential air-sea CO_2 flux ($\text{mol m}^{-2} \text{ y}^{-1}$) implied from surface heating, where heating drives an outflux of CO_2 (dark shades) and cooling drives an influx (light shades). This is the flux that would occur if air-sea exchange instantly compensated for the changes in solubility (Murnane *et al.*, 1999). The relationship between the air-sea heat flux, \mathcal{H} (W m^{-2}), and the potential carbon flux, $\mathcal{F}_C^{\text{pat}}$, ($\text{mol m}^{-2} \text{ y}^{-1}$) is $\mathcal{F}_C^{\text{pat}} = \mathcal{H}\gamma_T / C_p$, where $\gamma_T = -9.0 \mu\text{mol C kg}^{-1} \text{ K}^{-1}$ is the slope of a linear fit to the equilibrium DIC-T relationship (Fig. 6.5c), $C_p = 3992 \text{ J kg}^{-1} \text{ K}^{-1}$ is the heat capacity of seawater at $T = 15^\circ\text{C}$ and $S = 34.5 \text{ g kg}^{-1}$; see Q6.4 for more detail.

are consumed again, the associated consumption of DIC is, at least in part, compensated by the upwelled carbon. Thus, ocean transport and the biological consumption of carbon in the surface tend to compensate one another in terms of driving an air-sea flux.

Production of mineral calcium carbonate

Some phytoplankton (coccolithophorids) produce mineral calcium carbonate along with their organic soft-tissue parts. This production of calcium carbonate consumes further DIC, but also removes calcium ions and alkalinity. The reduction of alkalinity increases $p\text{CO}_2$. The formation of one mole of calcium carbonate removes one mole of DIC and two moles of A_T , so has the net effect of reducing $p\text{CO}_2$. This effect is illustrated in Fig. 6.16, where the calcification vector crosses to lower $p\text{CO}_2$. In the open ocean, calcium carbonate is produced in association with organic carbon. The net effect on $p\text{CO}_2$ depends upon the relative rate of production of organic matter and mineral CaCO_3 . Observations of the relative change in DIC and A_T in the open ocean (Fig. 6.18; Robertson *et al.*, 1994) indicate, for one particular bloom of coccolithophorids, almost equal rates of production of organic carbon and calcium carbonate, with the net effect of reducing $p\text{CO}_2$. The relative amount of organic and inorganic (i.e., CaCO_3) carbon in sinking particles is called the rain ratio. In a coccolithophore bloom, illustrated in Fig. 6.18, the rain ratio is observed to be about 1:1. However, coccolithophores only make up a small fraction of the total phytoplankton community, and so the rain ratio from the surface ocean for a global average is more typically about 5:1 (organic to inorganic; Broecker and Peng, 1982).

Dilution and concentration

A net source of fresh water to the surface, due to rainfall or river run-off, leads to an equivalent dilution of both DIC and A_T in surface waters: the dilution of DIC effectively reduces $p\text{CO}_2$, while the dilution of A_T shifts carbon from carbonate and bicarbonate into $[\text{CO}_2^*]$, and increases $p\text{CO}_2$. Hence, the impact of freshwater forcing on DIC

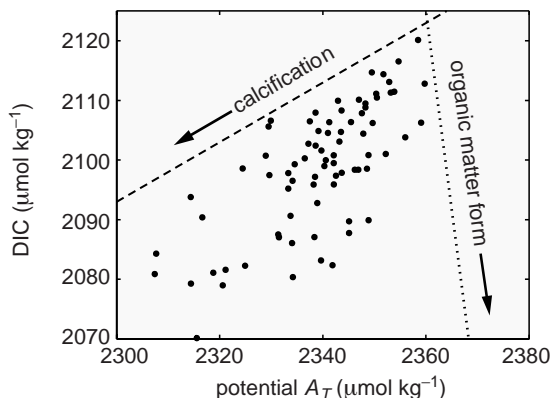


Figure 6.18 The observed relationship between surface ocean DIC and alkalinity during a bloom of coccolithophorids *Emiliania huxleyi* in the North Atlantic in June 1991. The bloom was also observed from space (as illustrated in Fig. 3.7). The formation of organic carbon reduces DIC with little effect on alkalinity. The formation of one mole of calcium carbonate removes two moles of alkalinity and one mole of dissolved inorganic carbon from a water parcel. Redrawn from Robertson *et al.* (1994). The relationship between changes in surface alkalinity and DIC indicate the formation of organic carbon and calcium carbonate in a ratio of about 1:1.

and A_T almost compensate in terms of the net change in $p\text{CO}_2$; the dilution concentration vector in Fig. 6.16 almost follows the contours of $p\text{CO}_2$ and, thus, freshwater fluxes play a relatively minor role in affecting the pattern of air-sea CO_2 flux.

Ocean circulation

Finally, ocean circulation plays a crucial role in redistributing heat, nutrients and DIC. For example, the cooling and heating patterns driving changes in $p\text{CO}_2$ are in turn controlled by the movement of warm, tropical surface waters to mid latitudes, where they lose heat to the cool atmosphere. For example, there is a strong heat loss over the swift western boundary currents, which drives an ocean uptake of carbon dioxide, occurring both locally and downstream. Likewise, the ocean circulation redistributes nutrients and sustains the production of organic matter. The circulation returns inorganic nutrients to the surface, as well as DIC including the carbon that was lost from the surface as sinking inorganic particles.

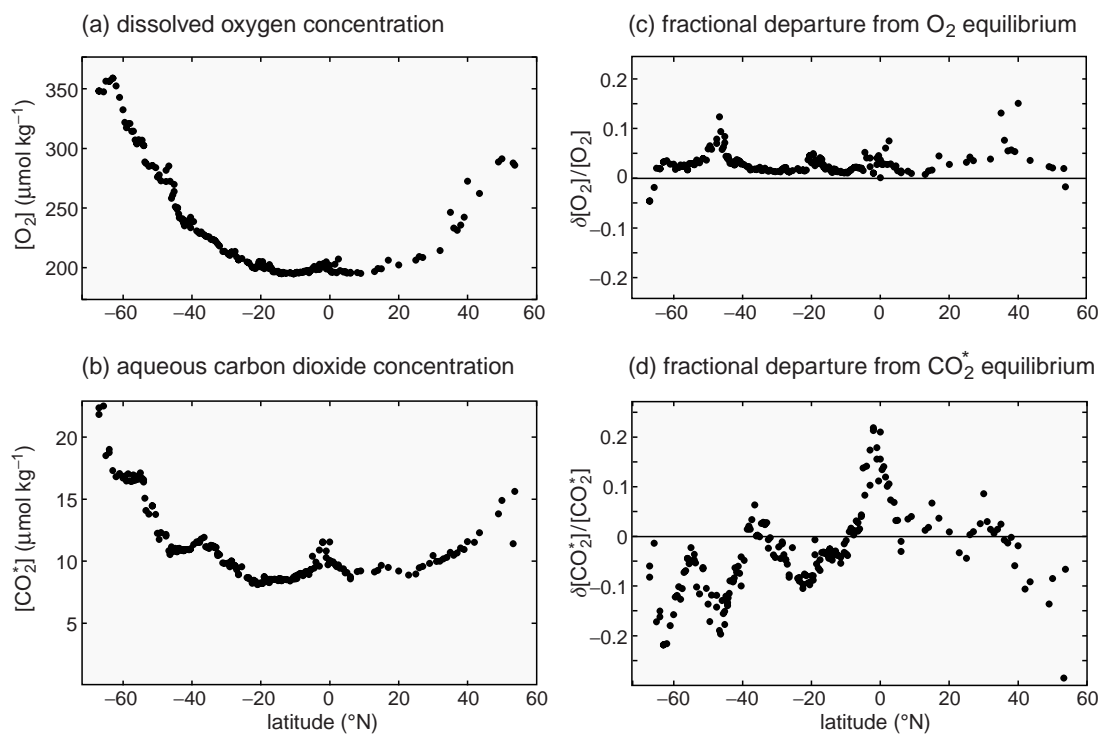


Figure 6.19 Surface concentrations of (a) dissolved oxygen (O_2 , $\mu\text{mol kg}^{-1}$), and (b) aqueous carbon dioxide (CO_2^* , $\mu\text{mol kg}^{-1}$) in the mixed layer (0–25 m) along 170°W in the Pacific Ocean (WOCE P15), together with (c) the fractional departure from equilibrium for dissolved oxygen, $(O_2 - O_{2,\text{sat}})/O_2$, and (d) the fractional departure from equilibrium for carbon dioxide, $(DIC - DIC_{\text{sat}})/[CO_2^*]$, where $O_{2,\text{sat}}$ and DIC_{sat} represent the equilibrium values based upon temperature and alkalinity. Data from Key *et al.* (2004).

6.6.4 Departures from a local equilibrium for surface DIC

An alternative way to describe the disequilibrium between the surface ocean and atmospheric carbon reservoirs is to separate DIC into ‘saturation’ and ‘disequilibrium’ components, DIC_{sat} and ΔDIC , respectively:

$$DIC = DIC_{\text{sat}} + \Delta DIC.$$

Here DIC_{sat} is the concentration of dissolved inorganic carbon that the surface ocean would have if it were in equilibrium with the pCO_2 of the local, overlying atmosphere. ΔDIC is defined similarly as the difference between the actual DIC and DIC_{sat} , and is mapped in Fig. 6.15b. An air-sea flux of CO_2 directed into the ocean is inferred whenever ΔDIC is negative (light shading) and, conversely, an outflux of CO_2 whenever ΔDIC is positive (dark shading). The broad-scale pattern of disequilibrium and the implied direction of the

air-sea flux are broadly in accord with the estimate from a largely independent dataset, based on many more measurements of pCO_2 (Fig. 6.15a).

Variations of disequilibrium in the Pacific Ocean

Consider the concentrations of dissolved oxygen, $[O_2]$, and carbon dioxide, $[CO_2^*]$, along a north-south transect in the Pacific basin. The dissolved oxygen concentration increases with latitude driven by changes in solubility (Fig. 6.19a). The dissolved oxygen is relatively close to saturation, with a fractional departure from saturation, $([O_2] - [O_{2,\text{sat}}])/[O_2]$, of 0.05 or less over most of the transect (Fig. 6.19c). In contrast to oxygen, there are large-scale patterns of significant disequilibrium in surface $[CO_2^*]$, with supersaturation in the tropics and undersaturation at higher latitudes (Fig. 6.19b). The fractional departure from saturation, $([CO_2^*] - [CO_2^*]_{\text{sat}})/[CO_2^*]$, varies between

–0.2 in the high latitudes to 0.2 in the tropics (Fig. 6.19d). For both gases, the disequilibrium is largely driven by the same set of processes, including changes in temperature and solubility, the production and respiration of organic matter, and ocean transport. Why do they show such different signatures of disequilibrium?

The degree of disequilibrium is the result of a competition between the time taken for air-sea exchange to erode anomalies in partial pressure and the timescale of the processes driving the system away from that equilibrium. The observations (Fig. 6.19c,d) reflect how O₂ equilibrates across the sea surface much more quickly than CO₂. We next evaluate the equilibration timescales and show how the difference is set by the reactivity of CO₂ in seawater.

6.6.5 Timescale of air-sea equilibration

The efficiency with which the air-sea contrast is eroded, and the time taken for the surface mixed layer to reach an equilibrium with the atmosphere, depend on processes encapsulated by the gas transfer coefficient, K_g, the thickness of the surface mixed layer of the ocean, and the chemistry of the gas in seawater. We now compare this timescale for oxygen and carbon dioxide.

Exchange timescale for a non-reactive gas

For a non-reactive gas, such as dissolved oxygen or chlorofluorocarbons, the air-sea exchange timescale depends on the mixed-layer thickness, *h*, divided by the gas transfer coefficient, K_g (see the reasoning in Box 6.5),

$$\tau = \frac{h}{K_g}. \quad (6.41)$$

The gas transfer coefficient, K_g, is typically $3 \times 10^{-5} \text{ m s}^{-1}$, so assuming a mixed-layer thickness of 100 m, the characteristic timescale for air-sea exchange, τ_c , is $3 \times 10^6 \text{ s}$, about one month. Consider a case where the oxygen concentration in the surface ocean is in equilibrium with the atmosphere: if the mixed layer becomes supersaturated with oxygen due to a rapid bloom of phytoplankton, the resulting oxygen disequilibrium takes a month to be eroded by air-sea exchange.

Exchange timescale for carbon dioxide

The air-sea exchange of carbon dioxide is more complicated than that of a non-reactive gas because CO₂^{*} is closely connected to the large reservoir of other carbonate species. Consider a situation where the carbon system in the surface ocean is in equilibrium with the overlying atmosphere. A phytoplankton bloom consumes DIC and pCO₂ is correspondingly reduced. The difference in surface ocean and atmospheric pCO₂ now drives a flux of CO₂ into the ocean, returning the system to equilibrium. However, most of the newly absorbed CO₂ is rapidly converted into HCO₃[−] and CO₃^{2−} on a timescale of minutes, so that the disequilibrium remains until much more carbon is added and all of the carbonate components reach their equilibrium values.

Thus, the equilibrium timescale is much longer for surface pCO₂ to equilibrate than surface pO₂, since most of the carbon added to the CO₂^{*} passes into the other carbonate species. [CO₂^{*}] represents only about 1/200th of DIC, so intuition suggests that it might take 200 times as long to equilibrate pCO₂ than a non-reactive gas. However, this response is *not* the case due to buffering. As carbon is added to surface water through air-sea exchange, the pH decreases and the relative sizes of the carbonate pools adjust, with the concentration of CO₂^{*} increasing at a greater rate than DIC (see Section 6.5.1). The equilibration timescale of CO₂ is increased by a factor, DIC/[B[CO₂^{*}]], relative to a non-reactive gas, so that the exchange timescale for carbon dioxide is

$$\tau_c = \frac{h}{K_g} \frac{\text{DIC}}{B [\text{CO}_2^*]}, \quad (6.42)$$

where the ratio DIC/[CO₂^{*}] is on the order of 10², the buffer factor, *B*, is on the order of 10, and τ_c is about 1 year for a mixed-layer thickness of 100 m; a derivation is presented in Box 6.6. Hence, carbon dioxide takes about 10 times as long to equilibrate between the surface ocean and atmosphere compared to oxygen or chlorofluorocarbons.

Returning to the disequilibrium signals in Fig. 6.19, we can now understand why the relative disequilibrium for CO₂ is greater than for O₂. Both gases are perturbed in the surface ocean by similar processes, such as seasonal heating and cooling and blooms of phytoplankton. Oxygen

Box 6.5 Air-sea exchange timescale for non-reactive gases

The rate of change of the surface concentration of a generic, non-reactive gas, $[c]$ (mol kg^{-1}), following a moving water column can be viewed as being controlled by the air-sea flux, \mathcal{F} (mol c m s^{-1}), into the ocean divided by the mixed-layer thickness, h (m),

$$\frac{D[c]}{Dt} = \frac{\mathcal{F}}{h}, \quad (6.43)$$

where the air-sea flux is defined either by the contrast in partial pressure, $p_c - p_c^{at}$, or equivalently by the contrast in concentration, $[c] - [c^{sat}]$, such that

$$\begin{aligned} \mathcal{F} &= -K_g K_0 (p_c - p_c^{at}) \\ &= -K_g ([c] - [c^{sat}]), \end{aligned} \quad (6.44)$$

where K_0 is the saturation and K_g is the exchange velocity for the gas. The surface concentration of the gas, $[c]$, can be expressed as the sum of the saturated concentration, $[c^{sat}]$, and a disequilibrium contribution, $[\Delta c]$:

$$[c] = [c^{sat}] + [\Delta c]; \quad (6.45)$$

where $[c^{sat}]$ is the concentration the gas would have at equilibrium with the overlying atmosphere. By combining (6.43) to (6.45), the rate of change in surface concentration of $[c]$ can be expressed as

$$\frac{D[c]}{Dt} = \frac{D}{Dt} ([c^{sat}] + [\Delta c]) = -\frac{K_g}{h} [\Delta c] \equiv -\frac{1}{\tau} [\Delta c]. \quad (6.46)$$

In the limit that $[c^{sat}]$ does not rapidly change, then (6.46) defines how the departure from saturation of the gas, $[\Delta c]$, evolves in time,

$$\frac{D}{Dt} [\Delta c] \approx -\frac{1}{\tau} [\Delta c], \quad (6.47)$$

which implies that the disequilibrium contribution decays exponentially in time, such that $[\Delta c(t)] = [\Delta c(0)] \exp(-t/\tau)$, where the exchange timescale $\tau \equiv h/K_g$ in units of s.

re-equilibrates with the atmosphere in about a month and always appears close to equilibrium. In contrast, anomalies of pCO_2 persist for months or even years and other processes may intervene before the anomalies are fully eroded by air-sea equilibration.

The slow equilibration timescale for CO_2 also affects the relationship between the surface heat fluxes and solubility forcing, and the resulting air-sea exchange. The one-year timescale induces a significant lag between forcing and response; a water parcel in the surface ocean may have moved several hundreds to a thousand kilometres in that time interval. Thus, the air-sea CO_2 flux response

to the cooling of the western boundary currents is relatively smeared out; compare the actual CO_2 flux and the implied potential flux from surface cooling in Figs. 6.15a and 6.17.

6.7 | Summary

Carbon dioxide is a weak acid, and dissolves and reacts with water to produce bicarbonate, carbonate and hydrogen ions. In seawater, more than 90% of dissolved inorganic carbon, DIC, is in the form of bicarbonate ions. The ionic forms of DIC are more abundant because of the alkalinity, which

Box 6.6 Air-sea exchange timescale for a reactive gas, carbon dioxide

The rate of change of the surface concentration of DIC through air-sea exchange of carbon dioxide is given by

$$\frac{D}{Dt} \text{DIC} = -\frac{K_g}{h} ([\text{CO}_2^*] - [\text{CO}_2^{*\text{SAT}}]) = -\frac{K_g}{h} [\Delta\text{CO}_2^*]. \quad (6.48)$$

Evaluating the timescale for air-sea exchange is now more difficult than for a non-reactive gas through DIC appearing on the left-hand side and $[\Delta\text{CO}_2^*]$ on the right-hand side of (6.48). This difficulty can be solved by exploiting the relationship between small changes in $[\text{CO}_2^*]$ and DIC described by a discrete form of the buffer factor (6.30),

$$\frac{[\Delta\text{CO}_2^*]}{[\text{CO}_2^*]} = B \frac{\Delta\text{DIC}}{\text{DIC}},$$

such that $[\Delta\text{CO}_2^*]$ in (6.48) is expressed as

$$\frac{D}{Dt} \text{DIC} = -\frac{K_g}{h} B \frac{[\text{CO}_2^*]}{\text{DIC}} \Delta\text{DIC} \equiv -\frac{\Delta\text{DIC}}{\tau_c}, \quad (6.49)$$

where the exchange timescale for carbon is now given by

$$\tau_c \equiv \frac{h}{K_g} \frac{\text{DIC}}{B [\text{CO}_2^*]}. \quad (6.50)$$

The surface DIC can be separated into saturated and disequilibrium components, $\text{DIC} = \text{DIC}_{\text{sat}} + \Delta\text{DIC}$, so that (6.49) can be expressed as

$$\frac{D}{Dt} (\text{DIC}_{\text{sat}} + \Delta\text{DIC}) = -\frac{\Delta\text{DIC}}{\tau_c}, \quad (6.51)$$

and assuming that the saturated component is not changing, then gives

$$\frac{D}{Dt} \Delta\text{DIC} \approx -\frac{\Delta\text{DIC}}{\tau_c}. \quad (6.52)$$

Hence, the timescale for any surface anomaly in DIC, as well as anomalies in $[\text{CO}_2^*]$ and pCO_2 , to be damped and equilibrate with the overlying atmosphere by air-sea exchange is given by

$$\tau_c = \frac{h}{K_g} \frac{\text{DIC}}{B [\text{CO}_2^*]}. \quad (6.53)$$

is the net positive charge associated with conservative ions in the ocean. For overall charge balance, there must be an equal net negative charge in the non-conservative ions, which is met largely by bicarbonate and carbonate ions.

At equilibrium with a given atmospheric pCO_2 , DIC increases almost linearly with increasing alkalinity and decreases almost linearly with increasing water temperature. However, pCO_2 and DIC have a complex relationship. There are much larger fractional changes in pCO_2 than in DIC. This

relationship is encapsulated by the Revelle buffer factor, defined as $B = (\delta[\text{CO}_2^*]/[\text{CO}_2^*]) / (\delta\text{DIC}/\text{DIC})$ and of order 10 in the ocean. The large reservoir of carbonate ions connected to CO_2 and its buffering chemistry extends the air-sea equilibration timescale for CO_2 to about one year, an order of magnitude longer than for a non-reactive gas, such as oxygen.

The ocean takes up CO_2 from the atmosphere at mid and high northern latitudes, where cooling enhances the capacity of surface waters to

hold DIC and where there is biological consumption of DIC due to photosynthesis. The ocean outgasses CO₂ in the tropics, where surface warming reduces the capacity of the water to hold DIC and upwelling returns carbon-rich waters to the surface. The sign of the air-sea flux is not reliably known over the Southern Ocean, where there is a complex interplay of upwelling of carbon-rich waters, biological consumption, and regions of cooling and warming.

In subsequent chapters, we explore how the seasonal cycle affects the surface ocean carbon cycle, the pathways by which carbon is transported between the surface ocean and the interior, and how carbon is partitioned between the atmosphere and ocean integrated over the globe.

6.8 | Questions

Q6.1. Sources, sinks and residence time of ocean tracers.

Sodium, Na⁺, is one of the major conservative ions in the ocean. Sodium is delivered to the sea in rivers and lost through burial, evaporation or in sea-salt aerosol associated with spray. The concentration of sodium in the ocean, [Na⁺], is measured to be 470×10^{-3} mol kg⁻¹. The average concentration of sodium in rivers flowing into the sea, [Na⁺]_R, is significantly lower, about 280×10^{-6} mol kg⁻¹. The global delivery of river water to the oceans, ψ_R , is about 1 Sv (10^6 m³ s⁻¹).

- (a) What is the source, S_{Na^+} , in moles y⁻¹, of sodium to the global ocean?
- (b) What is the global ocean inventory, I_{Na^+} , of sodium ions (moles)?
- (c) What is the residence time spent by a sodium ion in the global ocean, τ_{Na^+} , in years?
- (d) If the the inventory of sodium in the ocean is not changing, what can we say about the rate at which losses are occurring from the ocean?

Assume the density of seawater $\rho_0 = 1024.5$ kg m⁻³, and an ocean volume $V_0 = 1.4 \times 10^{18}$ m³.

Q6.2. How much carbon is in the ocean?

Dissolved inorganic carbon is defined as

$$\text{DIC} = [\text{CO}_2^*] + [\text{HCO}_3^-] + [\text{CO}_3^{2-}], \quad (6.54)$$

and the carbonate species are related by thermodynamic equilibria,

$$K'_1 = \frac{[\text{HCO}_3^-][\text{H}^+]}{[\text{CO}_2^*]}, \quad K'_2 = \frac{[\text{CO}_3^{2-}][\text{H}^+]}{[\text{HCO}_3^-]}. \quad (6.55)$$

(a) Find the equilibrium relationship between DIC and [CO₂^{*}] in terms of K'_1 , K'_2 and [H⁺].

(b) Assume that pH = 8.18, pCO₂^{at} = 278 μatm, and the mean ocean temperature is 3.9 °C. Stating additional assumptions, estimate how much carbon (Pg C) is in the global ocean as DIC.

(c) What other contributions does this estimate miss?

Here use the following values: T = 3.9 °C, S = 34.5 g kg⁻¹, $K_0 = 5.4 \times 10^{-2}$ mol kg⁻¹ atm⁻¹, $K'_1 = 8.8 \times 10^{-7}$ mol kg⁻¹, $K'_2 = 4.8 \times 10^{-10}$ mol kg⁻¹, ocean volume $V_0 = 1.4 \times 10^{18}$ m³, reference density of seawater $\rho_0 = 1024.5$ kg m⁻³.

Q6.3. Solving the carbonate system.

Using the definitions for DIC in (6.54) and the thermodynamic equilibria, K'_1 and K'_2 in (6.55), then outline how the carbonate system can be solved to evaluate [H⁺], [CO₂^{*}], [CO₃²⁻], and [HCO₃⁻]. Assume that you know the values of dissolved inorganic carbon, DIC, and the total alkalinity, A_T , and that $A_T \sim A_C = [\text{HCO}_3^-] + 2[\text{CO}_3^{2-}]$.

Q6.4. Air-sea flux of heat and carbon dioxide

Surface heating and cooling lead to air-sea differences in the effective partial pressure of carbon dioxide, or the effective concentrations of dissolved inorganic carbon, DIC. In turn, these differences drive, and are eroded by, air-sea gas exchange. Consider following a water column with a surface mixed layer of thickness, h (m), and assume there is no biological activity.

(a) Write an expression for the rate of temperature change in the mixed layer, $\partial T / \partial t$ in K s⁻¹, due to a heat flux across the sea surface, \mathcal{H} in W m⁻²; see Chapter 4.

(b) Write an expression for the rate of change of DIC in the mixed layer in terms of the air-sea flux of carbon dioxide, \mathcal{F}_C in $\text{mol m}^{-2} \text{ s}^{-1}$; split DIC into its saturated and disequilibrium components, $\text{DIC} = \text{DIC}_{\text{sat}} + \Delta\text{DIC}$.

(c) Taking advantage of the almost linear relationship between saturated dissolved inorganic carbon, DIC_{sat} , and temperature (see Fig. 6.6c), with slope $\partial\text{DIC}_{\text{sat}}/\partial T \simeq \gamma_T$, relate the rate of change in DIC_{sat} in the mixed layer to a surface heat flux, \mathcal{H} (W m^{-2}).

(d) Hence, write down a relationship between air-sea heat and carbon fluxes. What is the relationship when the disequilibrium carbon concentration ΔDIC , is not changing in time? This relationship defines the “potential carbon flux” due to changes in temperature and solubility, $\mathcal{F}_C^{\text{pot}}$.

(e) Estimate the “potential carbon flux” across the sea surface (i.e. the flux that would occur in response to a heat gain or loss in order to maintain air-sea equilibrium in partial pressures) in response to a surface warming of 100 W m^{-2} in the tropical Atlantic and surface cooling of -200 W m^{-2} in the vicinity of the Gulf Stream (see Fig. 4.17); assume that $C_p = 4000 \text{ J kg}^{-1} \text{ K}^{-1}$ and $\gamma_T = -9.0 \mu\text{mol kg}^{-1} \text{ K}^{-1}$.

(f) Why do measured air-sea carbon fluxes (Fig. 6.16) differ from the “potential carbon flux” (Fig. 6.18)?

atmosphere and sea due to fossil fuel combustion. In *The Atmosphere and the Sea in Motion: Scientific Contributions to the Rossby Memorial Volume*, ed. B. Bolin. New York: Rockefeller Institute Press, pp. 130–142.

A wide-ranging and data-rich discussion of the distributions and cycling of trace elements, including carbon, in the ocean is given by W. S. Broecker and T.-H. Peng (1982). *Tracers in the Sea*. New York: Eldigio Press, 690pp.

An informative review discussing the concept of alkalinity, with a historical perspective, is provided by A. G. Dickson (1992). The development of the alkalinity concept in marine chemistry. *Mar. Chem.* 40, 49–63.

A thorough documentation of the carbonate system, extremely useful when you need the nuts and bolts, is detailed by DOE (Department of Energy) (1994). *Handbook of Methods for the Analysis of the Various Parameters of the Carbon Dioxide System in Sea Water*, Version 2, ed. A. G. Dickson and C. Goyet, ORNL/CDIAC-74.

A mechanistic review of the processes of gas exchange across an air-water interface by B. Jähne and H. Haussecker (1998). Air-water gas exchange. *Annu. Rev. Fluid Mech.*, 30, 443–468.

An accessible introduction to the chemistry of the carbonate system in seawater from a chemist's perspective is provided by J. Murray (2004). Ocean carbonate chemistry: the aquatic chemistry fundamentals. In *The Ocean Carbon Cycle and Climate*, ed. M. Follows and T. Oguz, NATO Science Series, IV, Vol. 40. Dordrecht: Kluwer Academic Publishers.

A comprehensive textbook examining the marine carbonate system in detail from a chemical and physical perspective is provided by R. E. Zeebe and D. Wolf-Gladrow (2001). *CO₂ in Seawater: Equilibrium, Kinetics and Isotopes*. Elsevier Oceanography Series. Amsterdam: Elsevier, 346pp. If you need to get down to the nitty gritty, this is the book.

6.9 Recommended reading

A clear derivation and application of the Revelle buffer factor is provided by B. Bolin and E. Eriksson (1958). Changes in the carbon dioxide content of the

Part III

**Physical Phenomena and their
Biogeochemical Signals**

Chapter 7

Seasonality of the upper ocean

One of the most striking features on the planet is the seasonal variation in sunlight, longer days in summer and shorter days in winter outside the tropics, as marked by the spring unfolding of leaves and their later autumn colour change and fall. Seasonal changes in sunlight likewise affect the upper ocean. Surface waters warm in summer and cool in winter, reaching their highest and lowest temperatures close to the autumn and spring equinoxes, respectively, as illustrated in Fig. 7.1a.

The marine ecosystem also responds to the progression of the seasons, affected by variations in sunshine and the availability of nutrients in surface waters. There are, however, some surprises. At high latitudes, phytoplankton bloom in summer when daylight is greatest, while at mid latitudes they flourish in winter or spring when nutrients are most plentiful. During summer, phytoplankton concentrations diminish in the subtropics and tropics near the surface and instead become more abundant at depths of 100 m where sunlight penetrates weakly, but there are nutrient-rich waters (Fig. 7.1b).

In turn, these physical and biological changes affect the carbon cycle: seasonal warming and cooling drive an ocean outgassing of carbon dioxide in summer and an uptake in winter; while seasonal growth of phytoplankton drives a consumption of dissolved inorganic carbon in surface waters, often leading to an ocean uptake of carbon dioxide and, conversely, a later decay of organic matter leads to the reverse process and an outgassing of carbon dioxide.

In this chapter, we describe the seasonal cycle of the open ocean, the repeating cycle of warming and cooling throughout the year, accompanied by periods of reduced and enhanced mixing in the upper ocean. We describe how seasonality in mixing affects phytoplankton blooms, and alters the air-sea exchange of carbon dioxide. Finally, we discuss how the seasonal response differs in the shelf seas from the open ocean, primarily due to enhanced mixing in the shallower waters.

7.1 | Seasonality in the physics

The surface ocean is a crucial interface between the atmosphere and ocean interior. Fluxes of heat, moisture, momentum and dissolved gases are exchanged through the sea surface, affecting the evolution of properties, such as temperature, freshwater content, velocity and gas concentration, for both fluids. The extent to which this surface forcing is communicated over the upper ocean depends on the vigour of turbulence and mixing.

7.1.1 Turbulence and the surface mixed layer

Three-dimensional turbulence in the ocean is rarely homogeneous, but is instead concentrated at the surface or the sea floor where mechanical stresses are large. A measure of the turbulence is provided by the dissipation of kinetic energy, typically varying between 10^{-7} and $10^{-8} \text{ W kg}^{-1}$ in the surface layer and decreasing by two orders

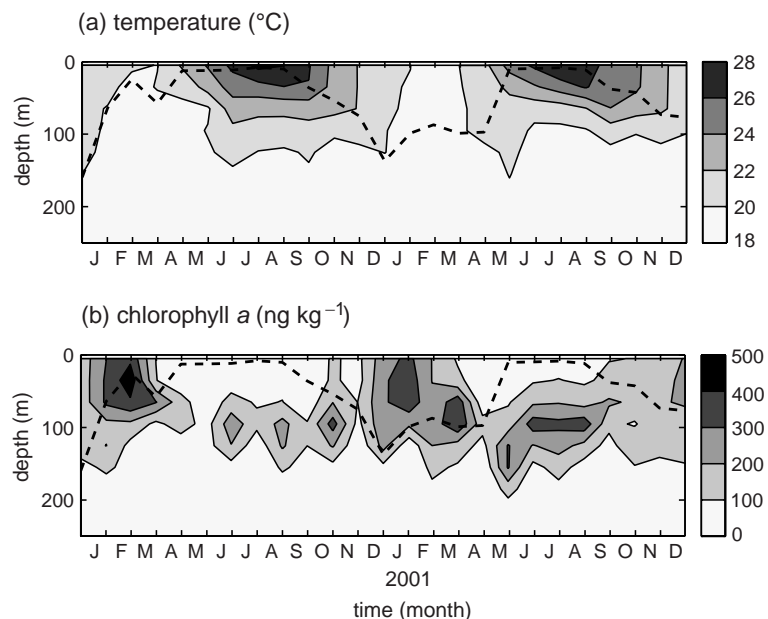


Figure 7.1 Time evolution versus depth of (a) *in situ* temperature ($^{\circ}\text{C}$) and (b) chlorophyll a concentration (ng kg^{-1}) at the Bermuda Atlantic Time-Series Study ($31.7^{\circ}\text{N}, 64.2^{\circ}\text{W}$) over the upper 250 m using monthly data from January 2000 to December 2001. Increased concentrations of chlorophyll a are indicative of greater concentrations of phytoplankton. The thickness of the mixed layer (dashed line) is diagnosed from the depth where σ_{θ} increases by 0.125 kg m^{-3} from the surface. Data supplied by the Bermuda Atlantic Time-Series Study, courtesy Nick Bates.

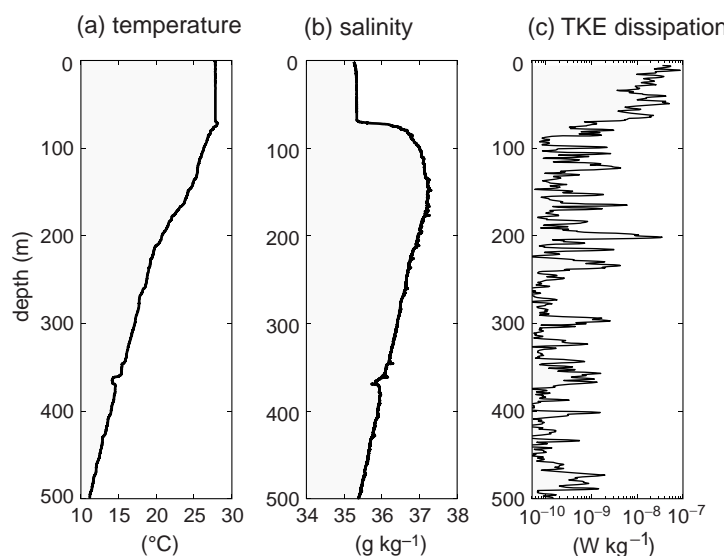


Figure 7.2 Observed profiles for (a) potential temperature ($^{\circ}\text{C}$), (b) salinity (g kg^{-1}), and (c) turbulent kinetic energy (TKE) dissipation (W kg^{-1} ; log scale) over the upper 500 m in the western boundary of the North Atlantic, next to the Caribbean Sea ($17.23^{\circ}\text{N}, 61.18^{\circ}\text{W}$). A surface mixed layer extends over the upper 70 m, as indicated by the vertically uniform temperature and salinity. The TKE dissipation over the mixed layer is typically two orders of magnitude greater than over much of the interior. Data supplied by Alberto Naveira-Garabato.

of magnitude to between 10^{-9} and $10^{-10} \text{ W kg}^{-1}$ in the thermocline over much of the open ocean (Fig. 7.2). Given this vertical variation in turbulence, it is useful to separate the upper ocean into a surface mixed layer, where there is more vigorous mixing, and a stratified and more quiescent interior.

While a mixed layer should in principle be defined as where turbulence is enhanced, this

identification is often difficult to achieve without detailed measurements of very fine scale velocity structures. Instead, the mixed layer is usually interpreted in a more ad hoc manner in terms of the underlying property profile. For example, a surface mixed layer of 70 m thickness is suggested by the vertically uniform temperature and salinity in the profiles in Fig. 7.2. More generally, the base of the mixed layer is diagnosed by the underlying

density profile, such as by the depth at which the density increases by a particular amount from the surface (as applied in Fig. 7.1, dashed line). However, one must be cautious when interpreting the mixed layer solely from a density profile since well-mixed features need not represent ongoing mixing but, instead, reflect the effect of past mixing events.

7.1.2 Mixed-layer physics

The surface ocean is mechanically forced by the stresses imparted by winds and tides moving over the sea floor, thermodynamically by solar radiation and heat exchange with the atmosphere, as well as by freshwater exchange with the atmosphere, any overlying ice or neighbouring land.

This combination of mechanical and surface density forcing (Fig. 7.3a) can either compete or reinforce each other in altering the mixed layer and structure of the upper ocean:

1. Surface heat input makes the mixed layer warmer, lighter and thinner, and increases the underlying stratification. A surface freshwater input likewise makes the mixed layer fresher and lighter; in each case, the depth-integrated heat and freshwater content is increased.
2. Conversely, mechanical forcing from the winds and tides make the mixed layer thicker and denser through the entrainment of denser water below the mixed layer. The mechanical forcing does not alter the depth-integrated heat or salt content, but does change their vertical profiles.
3. Surface heat loss makes the mixed layer cooler and denser and, likewise, a surface freshwater loss makes the mixed layer saltier and denser; decreasing the depth-integrated heat and freshwater content, respectively. This increase in surface density leads to convection, involving a vertical overturning of water parcels, and the fluid rearranges itself to a state where the density progressively increases with depth. Sometimes during this rearrangement, sinking dense water overshoots its naturally buoyant level and leads to further entrainment.

Given this mechanistic view of how the mixed layer is forced, now consider the seasonal variability of the mixed layer.

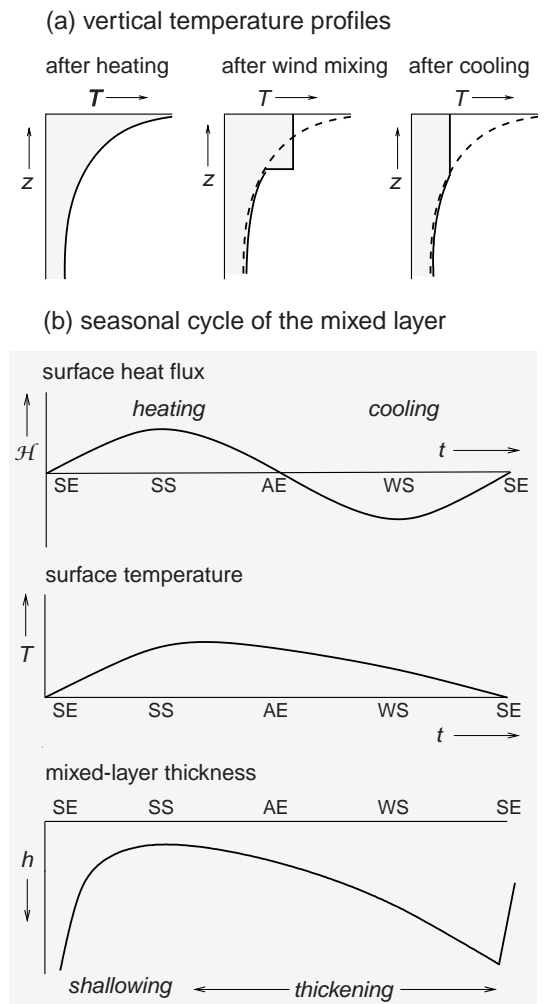


Figure 7.3 A schematic figure depicting (a) vertical temperature profiles after surface heating, wind mixing and surface cooling (the dashed line repeats the profile after surface warming), and (b) an idealised seasonal cycle in surface heat flux, temperature and thickness of the mixed layer (SE, SS, AE and WS denote the spring equinox, summer solstice, autumn equinox and winter solstice, respectively). There are three phases in the seasonal cycle: increasing heating from SE to SS leads to warming and thinning of the mixed layer; decreasing heating from SS to AE leads to a thickening of the mixed layer, a subsequent warming and then cooling; and a cooling from AE to SS leads to the mixed-layer cooling and thickening.

Idealised seasonal and diurnal cycles

At the simplest level, consider an idealised, sinusoidally varying, thermal forcing for the open ocean over the year (with mechanical forcing from the winds remaining constant), such that

Box 7.1 | Mixed-layer model

A simple description of the mixed-layer cycle and vertical temperature profile is provided by a one-dimensional model by Kraus and Turner (1967). The mixed-layer temperature, T_m , is controlled by a heat equation (ignoring any advection),

$$h \frac{\partial T_m}{\partial t} = \frac{\mathcal{H}}{\rho C_p} - \wedge \Delta T \frac{\partial h}{\partial t}, \quad (7.1)$$

where the mixed layer warms from a surface heat input (first term on right-hand side) and cools from entrainment of underlying thermocline waters (second term on right-hand side); \mathcal{H} is the surface heat flux (W m^{-2} and taken as positive into the ocean) and ΔT is the temperature difference between the mixed layer and thermocline. Entrainment only occurs when the mixed layer thickens (represented by $\wedge = 1$ when $\partial h / \partial t > 0$ and otherwise $\wedge = 0$).

The thickness of the mixed layer is solved from a mechanical energy balance,

$$\wedge h \Delta T \frac{\partial h}{\partial t} = \frac{2mu_*^3}{g\alpha_T} - \frac{\mathcal{H}h}{\rho C_p}, \quad (7.2)$$

where potential energy from a thickening of the mixed layer (left-hand term) is increased through a mechanical input of turbulent kinetic energy (first term on right-hand side) and opposed by surface warming (second term on the right-hand side); u_* is the friction velocity (m s^{-1}), defined in terms of the surface stress $\tau = \rho u_*^2 = c_d \rho_{air} u_{air}^2$, where c_d is the drag coefficient, ρ_{air} is the air density, u_{air} is the air velocity at a height of 10 m, $m = m_e(\rho / (c_d \rho_{air}))^{1/2}$ and m_e is the efficiency of wind mixing (typically 1.5×10^{-3} ; Kato and Phillips, 1969). Given appropriate surface forcing, the mixed-layer temperature and thickness can be solved using (7.1) and (7.2), as seen in Fig. 7.4. The mixed-layer cycle has two distinct regimes:

Thinning of the mixed layer. When the mixed layer thins, its thickness can be diagnosed from the effects of warming balancing wind mixing (from the right-hand side of (7.2) with $\wedge = 0$),

$$h = \frac{2mu_*^3}{g\alpha_T \mathcal{H}/(\rho C_p)}. \quad (7.3)$$

Increasing surface heat input inhibits turbulence and makes the mixed layer thinner, while increasing mechanical forcing makes turbulence more vigorous and thickens the mixed layer.

Thickening of the mixed layer. When the mixed layer is thickening, the rate of increase in h in (7.2) is enhanced by a net increase in the mechanical forcing, mu_*^3 , or a surface heat loss ($\mathcal{H} < 0$), but decreased by a heat input ($\mathcal{H} > 0$).

The effect of advection. The surface heat fluxes nearly always exceed the advective supply of heat at any particular time and, thus, control much of the seasonal response. However, there is a smaller residual surface heat input or loss when averaged over the year, $\bar{\mathcal{H}}$, which is usually balanced by an advective transfer of heat over the seasonal boundary layer (taken as the thickness of the end of winter mixed layer; H), such that

$$\int_{-H}^0 \mathbf{u} \cdot \nabla T dz \sim \frac{\bar{\mathcal{H}}}{\rho C_p}. \quad (7.4)$$

For example, an advection of warm water, $\mathbf{u} \cdot \nabla T < 0$, can sustain an annual surface heat loss to the atmosphere.

there is warming between the spring and autumn equinoxes, and cooling over the other half of the year; see Box 7.1 for accompanying theoretical balances. The annual cycle is then made up of three distinct regimes (Figs. 7.3b and 7.4):

1. From the spring equinox to the summer solstice, increasing surface heating warms and thins the mixed layer. The mixed-layer thickness is controlled by the competition between heating, acting to thin the mixed layer, and mechanical forcing, acting to thicken the mixed layer. Hence, the mixed layer is thinnest when the amount of sunlight and surface heating become largest at the summer solstice; see (7.3) in Box 7.1.
2. From the summer solstice to the autumn equinox, the mixed layer thickens as the surface heat input weakens. The mixed layer continues to warm for part of this time, but eventually cools from the entrainment of cooler, deeper waters; the overall heat content of the upper ocean continues to increase over this entire period.
3. From the autumn equinox to the spring equinox, the mixed layer progressively cools and thickens with surface cooling and mechanical forcing acting together. The mixed layer reaches a maximum thickness and minimum temperature at the spring equinox. Subsequently, there is surface warming and the seasonal cycle repeats itself.

In a similar manner, the mixed layer also follows a diurnal cycle: the mixed layer is thinnest at noon when there is maximum heat input, warmest at dusk when the daytime heating ceases, and thickest and coldest at dawn after the accumulated night-time cooling (Fig. 7.4a,c, full and dashed lines). These responses can be generalised to include the effects of freshwater fluxes and salinity variations by considering the density changes in the water column.

7.1.3 Mixed-layer cycle in the subtropical North Atlantic

Following this idealised view of the mixed-layer cycle, now consider the response in the subtropical North Atlantic: in summer, there is the expected warming, lightening and thinning of

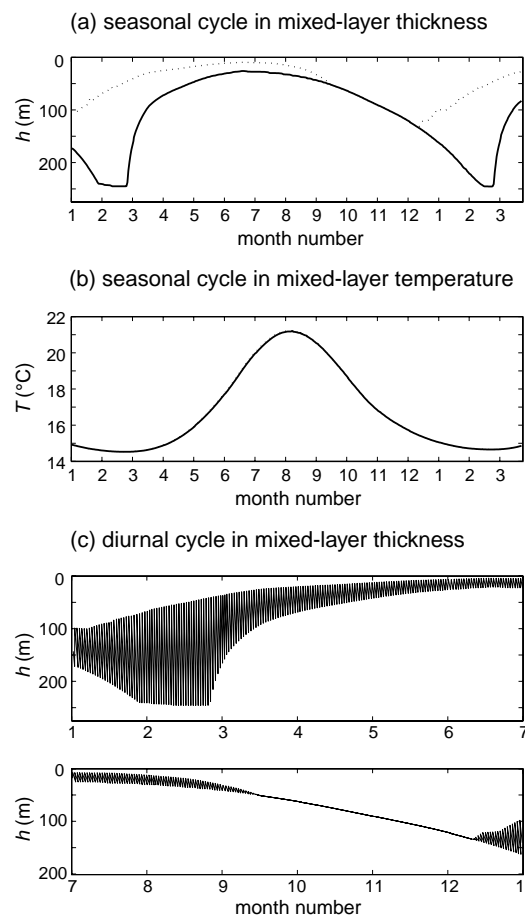
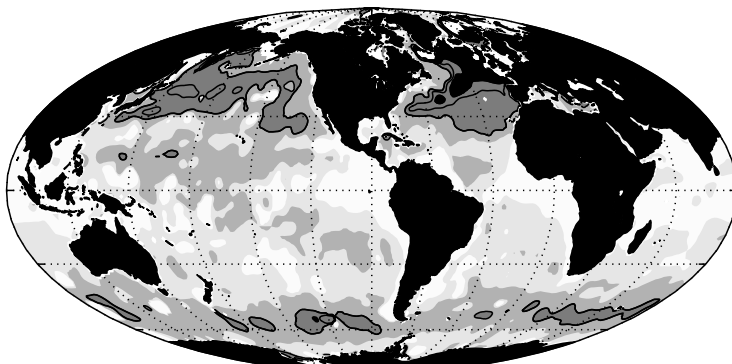


Figure 7.4 Annual cycle of (a) mixed-layer thickness (m), and (b) temperature (°C) from a one-dimensional mixed-layer model integrated using surface fluxes at 40°N, 25°W in the North Atlantic (where the surface heat fluxes nearly balance over an entire year); the model balances are the same as in Box 7.1. There is a characteristic seasonal cycle of mixed-layer warming and thinning in summer followed by cooling and thickening in winter. In (c), there is also a diurnal cycle of a thinner mixed layer during the daytime when there is surface warming and a thicker mixed layer at night-time when there is surface cooling; this is also illustrated in (a) by a dotted line for noon and full line for dusk.

the mixed layer, followed in winter by the mixed layer cooling, increasing in density and thickening (Fig. 7.1a, dashed line). This seasonal cycle is primarily a response to the changes in surface heat flux, although mechanical forcing maintains a thin mixed layer during summer heating and thickens the mixed layer whenever atmospheric storms pass; see examples later in Fig. 7.15b,d.

(a) March mixed-layer thickness (m)



(b) June mixed-layer thickness (m)

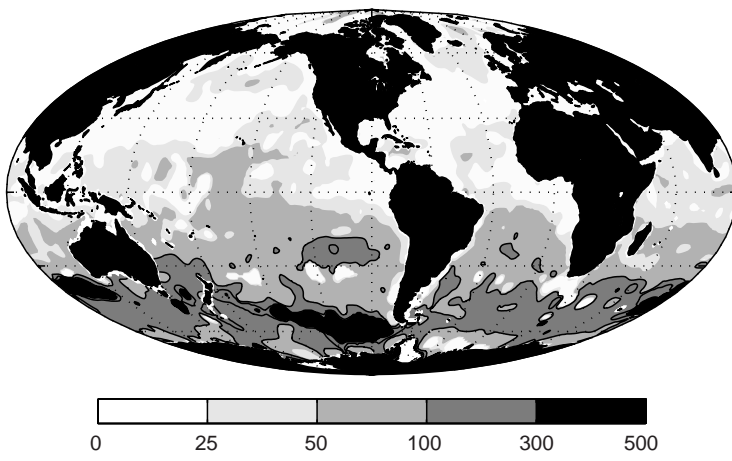


Figure 7.5 Mixed-layer thickness (m) for (a) March, (b) June, (c) September, and (d) December (with a contour for every 100 m) diagnosed from the World Ocean 2001 climatology (Conkright *et al.*, 2002) based upon an increase in potential density from the surface of 0.125 kg m^{-3} . The mixed layer is thickest in the spring equinox and thinner in the autumn equinox outside of the tropics.

Now we consider the mixed-layer variations over the rest of the globe.

7.1.4 Seasonal mixed-layer cycle over the global ocean

The mixed-layer variations over the globe are primarily forced by the variations in surface heat flux: the mixed layer is thinnest at the summer solstice when the summer heating is a maximum and thickest at the spring equinox after the accumulated winter cooling (Fig. 7.5a-d). The mixed layer is relatively uniform in thickness during summer, typically less than 50 m over most of the ocean and increasing to 100 m or more over the Southern Ocean. In contrast, the mixed layer strongly varies in thickness at the end of winter, thickening to more than 300 m over

the northern North Atlantic and Southern Ocean (Fig. 7.5a,c), while remaining relatively shallow in the subtropics.

7.2 Seasonality in phytoplankton

The marine ecosystem is affected by the seasonal changes in sunlight, surface heating and surface winds, which are illustrated here by remotely sensed variations in near-surface chlorophyll (Fig. 7.6a,b).

The seasonal contrast in chlorophyll is generally more marked in mid and high latitudes than in the tropics. Now we consider first the variability in the mid and high latitudes and, second, in the tropics and low latitudes.

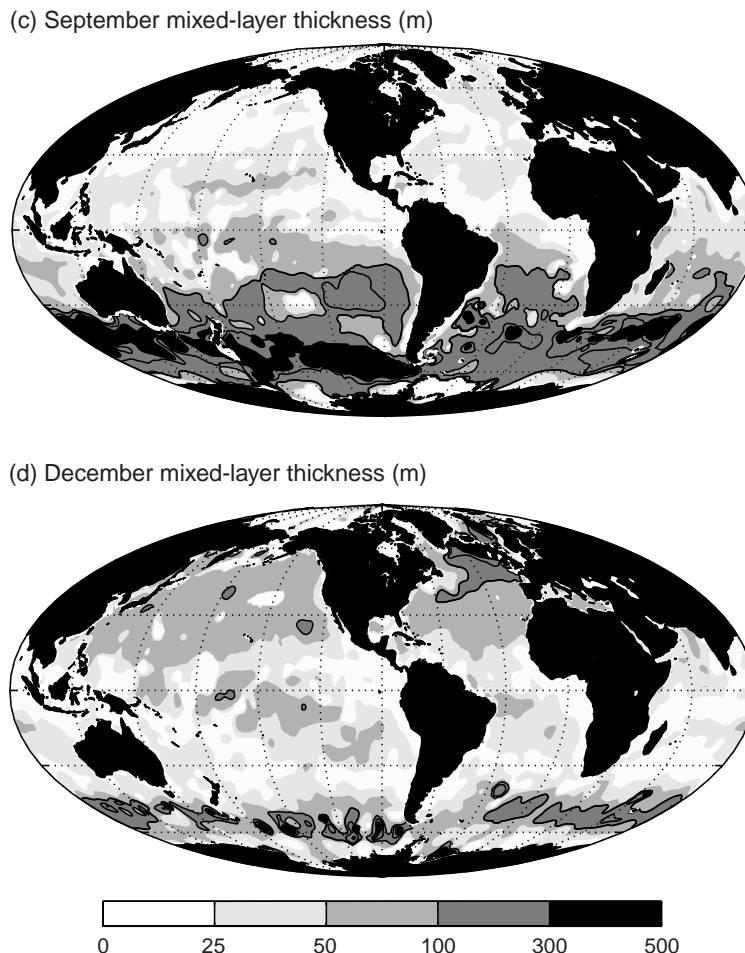


Figure 7.5 (continued) mixed-layer thickness (m) for (c) September, and (d) December (contours every 100 m).

7.2.1 Mid- and high-latitude variability

The timing and intensity of the annual bloom varies with latitude and from basin to basin. Typically, the subtropics are characterised by a weak seasonal cycle in chlorophyll, which has a late winter maximum when viewed from space (Fig. 7.6c,d,e; dotted lines). At subpolar latitudes, a more intense bloom occurs in the spring or summer and is complemented by a weaker increase in chlorophyll in the autumn (Fig. 7.6c,d,e; dashed and solid lines).

The intensity of the annual bloom also varies from basin to basin: the bloom is strongest in the mid and high latitudes of the North Atlantic and the high latitudes of the North Pacific. In contrast, the bloom is relatively subdued elsewhere, partic-

ularly the mid latitudes of the Pacific and much of the Southern Ocean (Fig. 7.6d–e). The absence of a stronger seasonal bloom and the underutilisation of macro-nutrients over these regions, referred to as High Nitrate Low Chlorophyll regimes, has presented rather a puzzle. The lack of a bloom is now usually viewed as being, at least in part, due to the low availability of iron in the surface waters (Section 5.6).

Next we consider the mechanisms affecting the seasonal blooms over the North Atlantic.

Spring bloom in the North Atlantic

The North Atlantic exhibits a vigorous spring bloom, as illustrated in seasonal maps of remotely sensed surface chlorophyll (Fig. 7.6c). In the

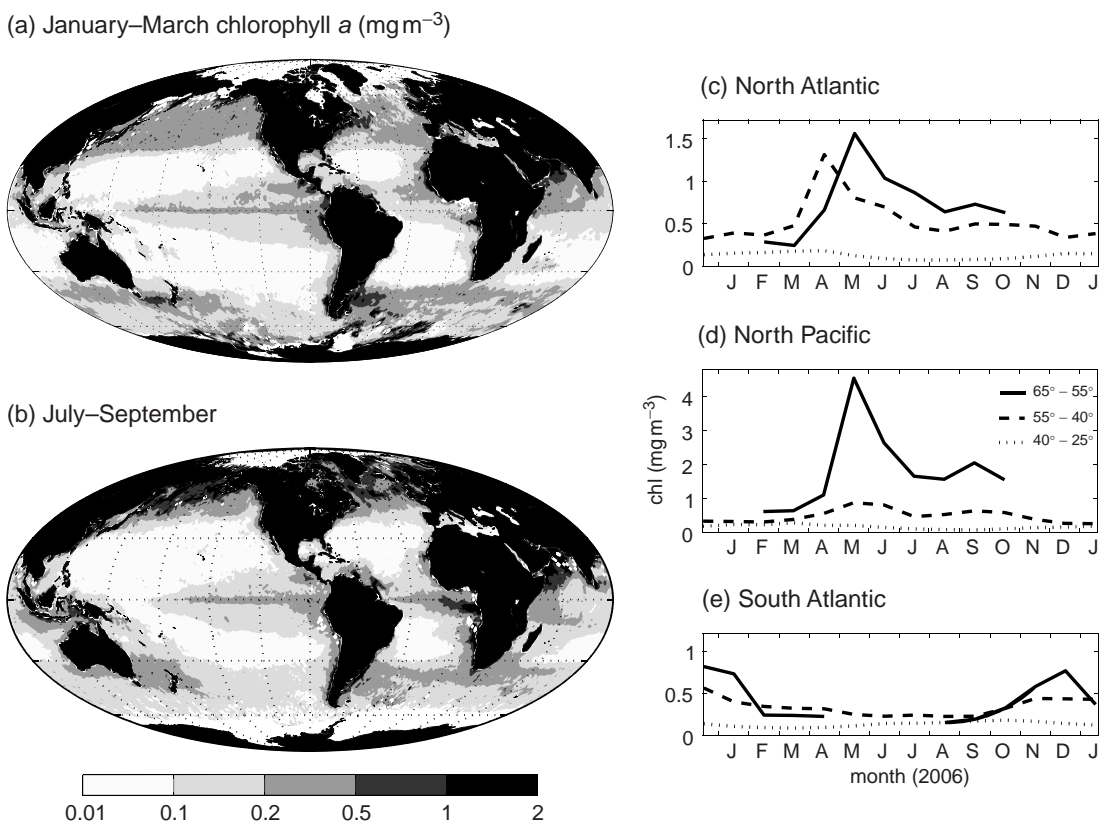


Figure 7.6 Seasonal variation of remotely sensed chlorophyll a (mg m^{-3}) for (a) January to March and (b) July to September for 2006, together with monthly time series for (c) the North Atlantic, (d) the North Pacific, and (e) the South Atlantic. Evaluated from monthly composite fields from SeaWiFS at 1° resolution evaluated from monthly data from NASA SeaWiFS on 1° grid; white in polar regions or off coasts represents missing data. In (c) to (e), the latitude bands of the regions are 65° to 55° (full line), 55° to 40° (dashed line) and 40° to 25° (dotted line), and the 40° wide longitude bands are 60°W to 20°W for the North Atlantic, 40°W to 0°W for the South Atlantic, and 160°E to 160°W for the Pacific. Note a different vertical scale is used for the Pacific due to the greater range at high latitudes.

mid-subtropical region and eastern North Atlantic (30 – 40°N), the bloom peaks in January and February, and subsequently fades away with an expansion of the low-chlorophyll, oligotrophic waters (Fig. 7.7a–d). Over the inter-gyre boundary, further north around 50°N , surface chlorophyll intensifies in March and April. In the higher latitudes, the bloom continues into summer, peaking from May to July, such as illustrated in the Norwegian Sea in Fig. 7.8.

During a bloom, phytoplankton abundance, as measured by chlorophyll, increases dramatically over a period of a few days, accompanied by a consumption of inorganic nutrients

and carbon in surface waters. Nutrients are recycled within the surface waters, maintaining high chlorophyll concentrations, but eventually surface nutrients become exhausted as organic matter is exported to deeper waters. Usually after a few weeks, phytoplankton growth is arrested either by complete utilisation of one or more key nutrients or the phytoplankton are consumed by increased grazing as the zooplankton population grows.

The relationship of the bloom and the annual (and inter-annual) variation of physical forcing can be understood in terms of distinct subtropical and subpolar regimes.

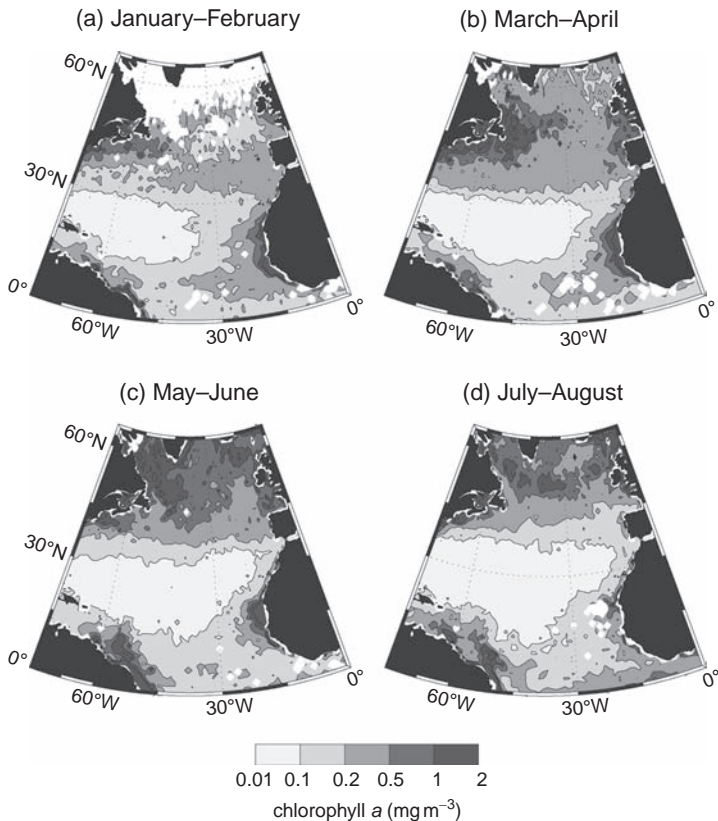


Figure 7.7 Bi-monthly maps for surface chlorophyll a (mg m^{-3}) during the bloom over the North Atlantic for (a) January to February, (b) March to April, (c) May to June, and (d) July to August. Evaluated from monthly composite fields from SeaWiFS at 1° resolution evaluated from monthly data from NASA SeaWiFS on 1° grid.

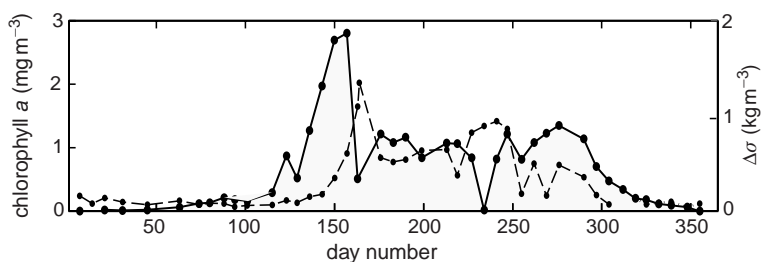


Figure 7.8 Time series for surface chlorophyll a (mg m^{-3} , full line) and vertical density contrast, $\Delta\sigma_t$, (kg m^{-3} , dashed line) between the surface and 75 m at the Ocean Weather Station M in the Norwegian Sea ($66^\circ\text{N}, 2^\circ\text{E}$) in 1992. There is a summer bloom, characteristic of the subpolar and high-latitude oceans. Replotted from Dale et al. (1999); data provided by Francisco Rey.

Mechanisms of the subpolar bloom

At high latitudes in winter, phytoplankton growth is usually limited by the availability of light (as in Fig. 7.8). Here the winter sun is low in the sky, day length is short, waters are cool, and surface heat loss and strong winds drive convection, maintaining a mixed layer that is much thicker than the euphotic zone. Hence, phytoplankton spend much of their time in the dark aphotic region, growth is suppressed, and sinking and predation

reduce their population. At the same time, convective mixing transfers nutrients to the surface.

In the spring, insolation and day length increase, the surface waters warm, and nutrients are plentiful from the previous winter mixing, stimulating enhanced growth of phytoplankton. Grazing is relatively weak due to the winter-time decline of zooplankton. Surface warming inhibits vertical mixing and so the turbulent transport of phytoplankton out of the euphotic layer is

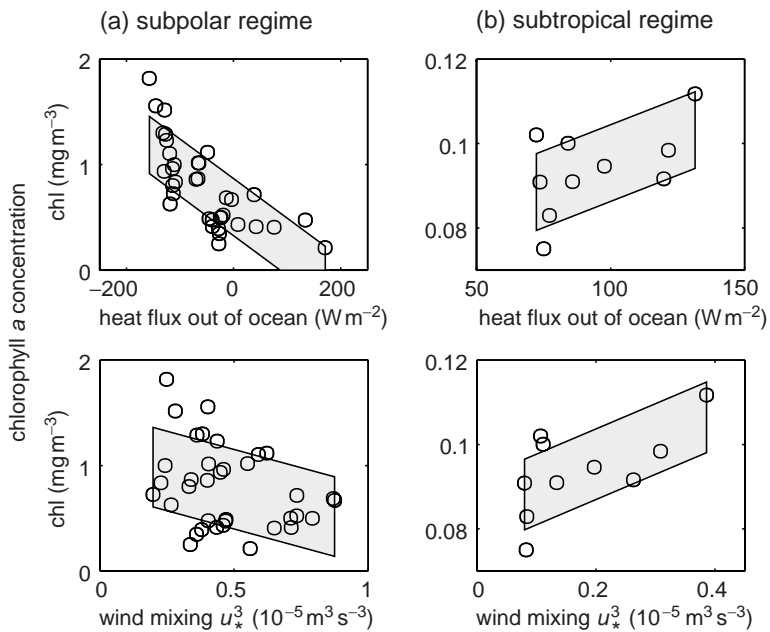


Figure 7.9 The relationship between chlorophyll *a* concentration (mg m^{-3}) from SeaWiFS and physical forcing of the mixed layer during the 1998 phytoplankton bloom for (a) subpolar, and (b) subtropical regimes of the North Atlantic. A surface heat loss (W m^{-2}) from the surface ocean or input of turbulent mixing energy by the wind given by the cube of the friction velocity, u_*^3 ($10^{-5} \text{m}^3 \text{s}^{-3}$), both lead to a thickening of the mixed layer. In (a), the subpolar region, the bloom is more intense when there is a surface gain of heat (i.e., negative heat loss) or weaker winds, enhancing the stratification and reducing light limitation. Conversely, in (b), the subtropics, there is a weaker bloom that strengthens with stronger heat loss and stronger winds, both driving enhanced entrainment of nutrients into the surface mixed layer. The scatterplots are for a bloom period (spanning a two-month window) based on diagnostics over 5° latitude bands, with shading representing one standard deviation from a linear least squares fit (Follows and Dutkiewicz, 2002).

reduced. Eventually, the mixed layer shoals and phytoplankton growth further increases, continuing as long as there are available nutrients and only a few grazers. Consequently, as light limitation is relieved, there is a late spring or early summer bloom; as first set out by Sverdrup (1953).

Hence, during the subpolar bloom, an enhancement in surface heating or a reduction in surface winds further thins the mixed layer, alleviating light limitation and enhancing the bloom; as illustrated in Fig. 7.9a.

Subtropical bloom

In contrast, in subtropical latitudes, the thermocline and associated nitracline are relatively deep. The waters are clearer and light penetration deeper, so the euphotic layer is often deeper than the mixed layer. Consequently, surface macro-nutrients are reduced to limiting con-

centrations: any slow trickle of nutrients into the euphotic zone is rapidly consumed by phytoplankton which, in turn, are rapidly consumed by grazers. During late winter, surface cooling and wind stirring thickens the mixed layer, entraining nutrient-rich waters from the thermocline. These nutrients are rapidly utilised, driving a late winter or spring bloom, as illustrated in Fig. 7.1 for near Bermuda; and explained by Menzel and Ryther (1961).

Hence, in subtropical latitudes, stronger surface heat loss or surface winds during the bloom further thickens the mixed layer, alleviating nutrient limitation and enhancing the winter bloom; as illustrated in Fig. 7.9b.

The effect of eddies on phytoplankton blooms

In addition to the seasonal cycle of sunlight and large-scale physical forcing, phytoplankton

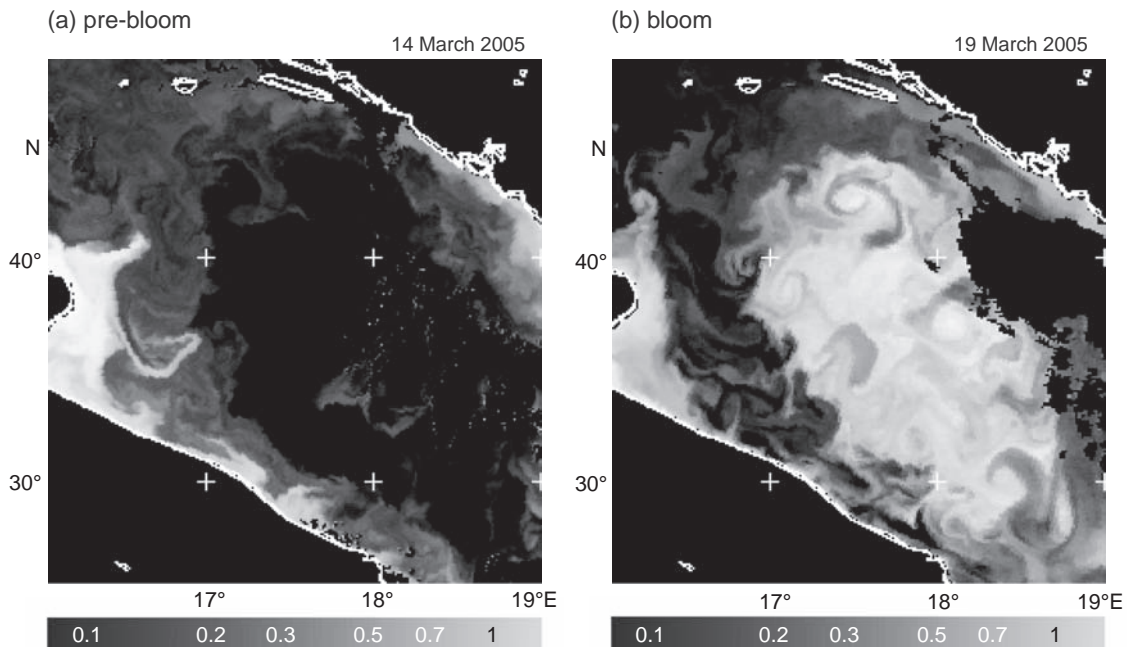


Figure 7.10 Spring phytoplankton bloom evolution during a convection event as revealed by MODIS chlorophyll α data (mg m^{-3}) in the Adriatic Sea: (a) pre-bloom in the convective patch (14 March 2005), and (b) bloom (19 March 2005). There is a region of low chlorophyll concentration (dark), coincident with where vigorous convection has occurred (centred at 41.5°N , 18°W), evolving five days later to a bloom (light). The bloom reveals a swirling pattern on the scale of a few tens of kilometres. Images and processing supplied by Rory Hutson, Plymouth Marine Laboratory; for further details of this event, see Civitarese *et al.* (2005).

blooms are affected by fine-scale physical phenomena, such as eddies, altering the circulation and the mixed layer and stratification. For example, eddy signals are revealed in the spring bloom of the Adriatic Sea in Fig. 7.10: initially enhanced convection during the spring inhibits phytoplankton growth through light limitation (Fig. 7.10a, dark), which is followed a few days later by the surface waters warming and stratifying, relieving light limitation and allowing a bloom to develop (Fig. 7.10b, light). In this bloom, eddies affect the swirling patterns of chlorophyll on scales of tens of kilometres by horizontal stirring, and by restratifying the upper water column and thinning the mixed layer.

After the winter–spring phytoplankton bloom
 Following a phytoplankton bloom, inorganic nutrients are usually very depleted in the mixed layer. The nutrient elements are locked up in organic form, some of which are respiration and recycled by zooplankton, mixotrophic phytoplankton

and bacteria, returning elements to inorganic form, which are quickly utilised. Overall, there is a net loss of nutrients from the euphotic layer as organic particles sink.

In the subtropics, phytoplankton continue to thrive below the mixed layer, as long as there is sufficient light penetrating from above and enough dissolved nutrients to sustain growth within the upper thermocline. For example, in the Sargasso Sea, after the surface winter bloom, a subsurface chlorophyll maximum forms at a depth of 100 m and persists throughout the summer and autumn (see Fig. 7.1b and later Fig. 7.14c).

7.2.2 Tropical and low-latitude variability

Tropical and low-latitude regions are generally characterised by relatively little seasonality (Fig. 7.11). A narrow band of elevated chlorophyll extends along the equator in the Atlantic and Pacific basins throughout the year, associated with the upwelling of nutrients (Fig. 7.6a,b).

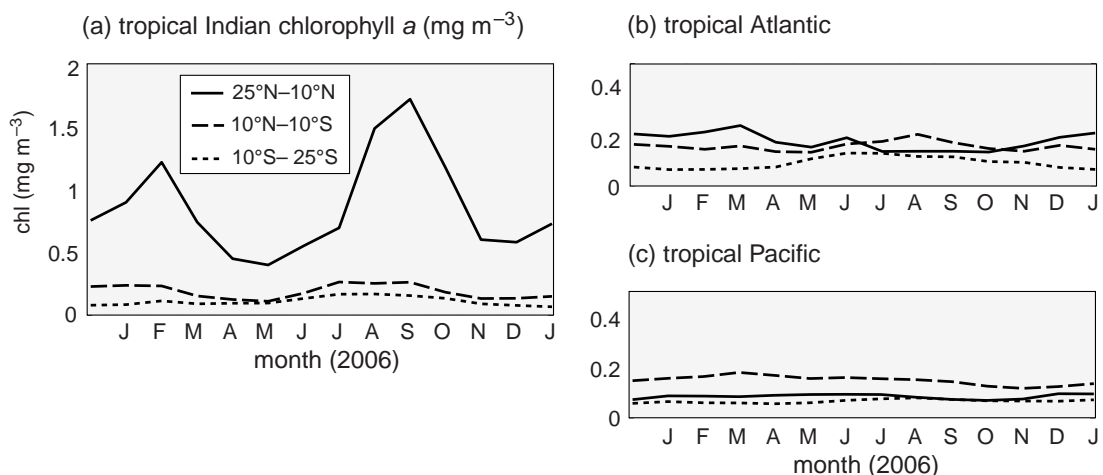


Figure 7.11 Time series of remotely sensed chlorophyll a (mg m^{-3}) during 2006 for tropical ocean regions: (a) Indian, (b) central Atlantic, and (c) central Pacific evaluated from monthly composite fields from SeaWiFS at 1° resolution; the latitude bands of the regions are 25° to 10°N (full line), 10°N to 10°S (dashed line) and 10°S to 25°S (dotted line), and the longitude bands are 55°E to 70°E for the Indian, 40°W to 20°W for the Atlantic, and 160° to 120°W for the Pacific.

This tropical signal is disturbed on timescales of a few weeks by the passage of eddies and tropical instability waves (waves which are perturbations in the sea-surface temperature fronts on either side of the equator).

Summer and winter blooms in the Indian Ocean

In contrast to the tropical Atlantic and Pacific, there is striking variability in the Indian Ocean, with phytoplankton flourishing in both summer and winter (Figs. 7.11a and 7.12): the summer bloom spreads over much of the Arabian Sea (15°N , 60°W), typically ranging from July to October, while the winter bloom is more restricted to the northern Arabian Sea, typically from January to February.

This double bloom is associated with the reversing winds linked to the Indian monsoon. During summer, there is enhanced warming and ascent of the air over the land relative to the sea, directing surface winds from the ocean onto the continent – like a giant ‘sea breeze’. Conversely, during winter, there is preferential cooling over the land and the wind pattern reverses direction.

How do these reversing monsoon winds lead to summer and winter blooms? At such low latitudes, there is nearly always sufficient light in the surface waters, so phytoplankton growth is limited by nutrient availability and grazing by

zooplankton. In summer, the winds are directed northeastward over the Arabian Sea, leading to coastal upwelling off the Arabian mainland, as well as widespread upwelling and thickening of the mixed layer over the centre of the Arabian Sea. Conversely, in winter, the winds are directed southwestward, inhibiting upwelling in the Arabian Sea, but the dryness of the air and the strength of the winds enhance convection and thicken the mixed layer over the northern Arabian Sea. Hence, the summer and winter blooms (Fig. 7.12) can be explained in terms of the increased nutrient supply into the mixed layer from the thermocline, involving a combination of wind-induced upwelling and mixed-layer thickening, possibly augmented by horizontal advection (Lévy *et al.*, 2007).

Longer-term variability in the equatorial Pacific

In the tropical Pacific, the most striking ecosystem changes are not related to the seasonal cycle (Fig. 7.13a), but instead are due to longer-term variability.

7.2.3 El Niño–Southern Oscillation

The most significant form of variability occurs in the tropical ocean, the El Niño–Southern Oscillation (ENSO), involving coupled changes in the

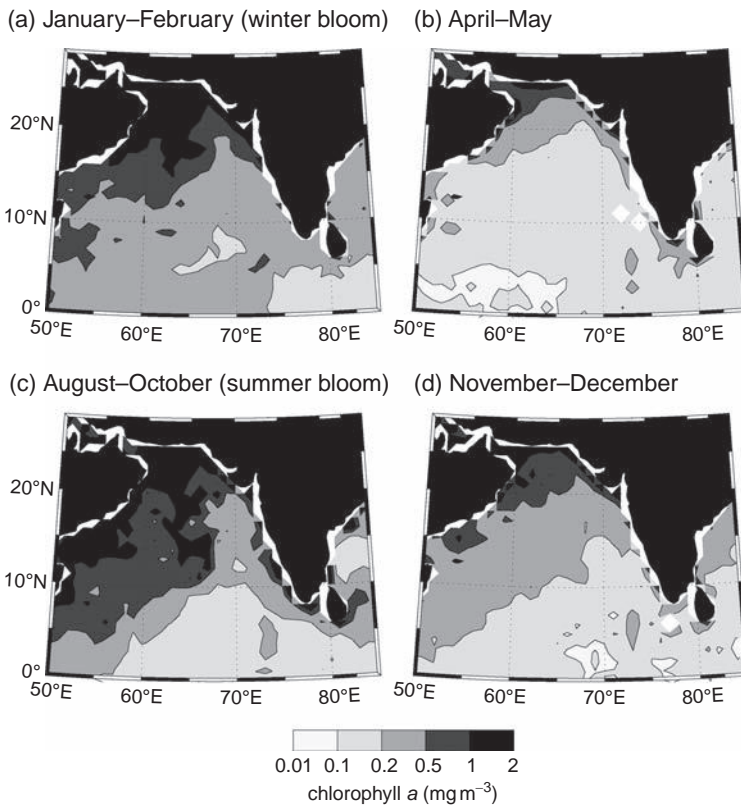


Figure 7.12 Composite maps for chlorophyll a (mg m^{-3}) over the Indian Ocean for (a) January to February representing the winter bloom; (b) April to May; (c) August to October representing the summer bloom; and (d) November to December. Monthly data from NASA SeaWiFS on 1° grid for 2006; missing data are indicated by white.

wind circulation and upwelling; see reviews by Philander (1990) and Godfrey *et al.* (2001).

In ‘normal’ periods, the surface waters of the eastern Equatorial Pacific are relatively cool and rich in macro-nutrients, sustained by a narrow band of equatorial and coastal upwelling. Conversely, during an El Niño event, the easterly Trade winds are reduced in strength, with the equatorial and coastal upwelling weakened or suppressed. The thermocline and nutricline become anomalously deep, and there is a reduced chlorophyll signal over the eastern Pacific, as illustrated for the 1997/1998 El Niño event in Fig. 7.13a,b. After the event ceased, there was a very intense bloom in the following summer, or La Niña (Fig. 7.13a,c), which was much more extensive than usually seen over a seasonal cycle of a typical year.

7.2.4 Seasonal succession in phytoplankton community structure

The seasonality of the upper ocean affects the composition of the phytoplankton community. Marine phytoplankton can be broadly viewed in

terms of two broad categories: ‘opportunists’, which grow fast and thrive when nutrients are intermittently plentiful, and ‘gleaners’, which are adapted to life in very low nutrient concentrations (McArthur and Wilson, 1967); see Section 5.4.2.

During winter convection in the subtropics and spring restratification at higher latitudes, there is a period of time when both light and nutrients are abundant in surface waters. Over this period, opportunism is advantageous, and efficient opportunists assimilate the available nutrients rapidly and reproduce quickly. After just a week or so, nutrients are drawn down to very low concentrations or the larger predators increase in number sufficiently to arrest their population growth. A seasonal succession of phytoplankton occurs, starting with fast-growing diatoms and moving onto populations of smaller cells adapted to low nutrient conditions.

Conversely, in the late summer, or all year round in the tropics, nutrients are strongly depleted in the mixed layer and euphotic zone. These conditions favour gleaners; phytoplankton adapted to competing for scarce resources. These

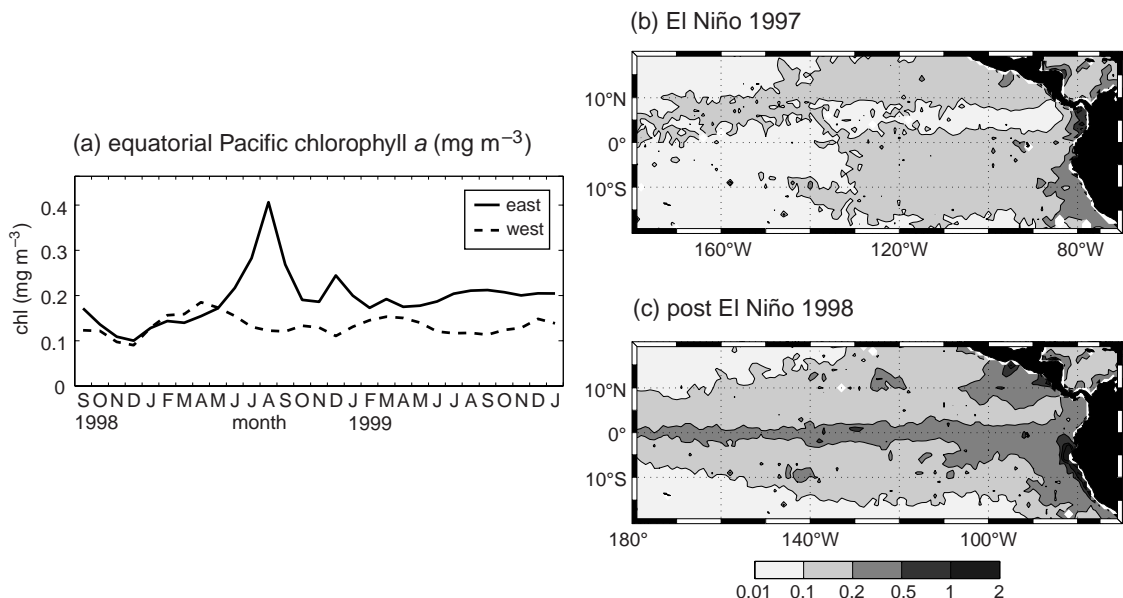


Figure 7.13 Chlorophyll a (mg m^{-3}) variation over the tropical Pacific: (a) a time series of the area-averaged concentration over the equator (5°N to 5°S) for eastern (140°E to 100°E ; full line) and western (140°W to 180° ; dashed line) regions from September 1998 to January 2000; and composite maps for (b) December 1997 to January 1998 when there was a vigorous El Niño, and (c) December 1998 to January 1999 after the El Niño had ceased; and evaluated using monthly data from NASA SeaWiFS on 1° grid.

are typically small cells, including micron-scale *Prochlorococcus*, which can eke out an existence at very low nutrient concentrations.

7.3 Seasonality in the carbon cycle

The surface ocean carbon cycle is driven by seasonality in the physics and ecosystem, but is unable to equilibrate in any one season due to the long equilibration time for air-sea exchange of CO_2 (Section 6.6.5). Physical processes affect the carbon system in a variety of ways. Seasonal changes in temperature alter the solubility of dissolved gases, driving an uptake of CO_2 in winter and an outgassing in summer. Air-sea transfer increases with stronger winds, particularly linked with the passage of atmospheric storms. The mixed layer thickens through surface heat loss or increased winds and the entrainment of thermocline waters enriches surface water with dissolved inorganic carbon concentrations.

The carbon system is also modulated by biological processes. Phytoplankton absorb dissolved

inorganic carbon, fixing it into organic form by photosynthesis within the surface euphotic zone. This photosynthesis lowers the concentration of DIC and pCO_2 in the near-surface waters. Conversely, organic detritus is respiration back to CO_2 by bacteria and zooplankton in the surface waters and as particles sink throughout the entire water column, increasing DIC and pCO_2 at depth.

These complex interactions are illustrated next for the subtropical North Atlantic and then later for the European shelf.

7.3.1 Seasonality in the subtropical North Atlantic

In the subtropical North Atlantic, there is a repeating seasonal cycle in the carbon system, connected to seasonal changes in physics and biology (Fig. 7.14).

Seasonality of DIC

Surface DIC concentrations are lower in summer and higher in winter following the seasonal changes in temperature (Fig. 7.14a,b). Seasonal changes in the ecosystem are revealed by the winter chlorophyll bloom and the subsequent

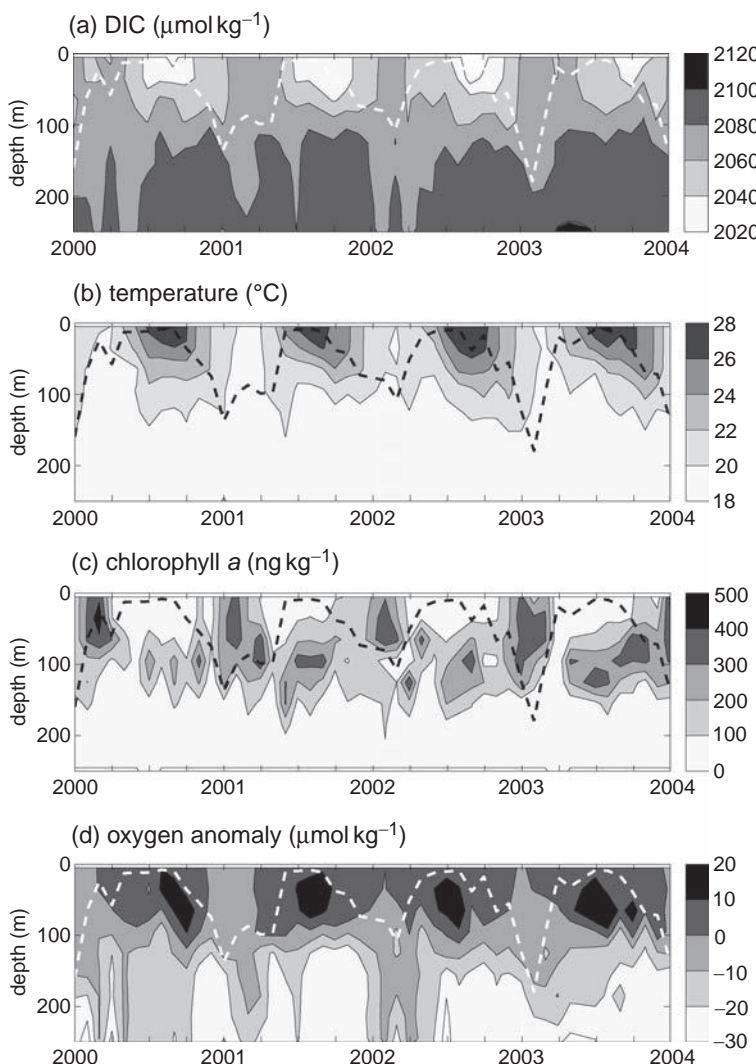


Figure 7.14 Time series of observed profiles for (a) dissolved inorganic carbon, DIC ($\mu\text{mol kg}^{-1}$), (b) potential temperature ($^{\circ}\text{C}$), (c) chlorophyll a (ng kg^{-1}), and (d) dissolved oxygen anomaly ($\mu\text{mol kg}^{-1}$), together with the thickness of the mixed layer (dashed line) at the Bermuda Atlantic Time-Series Study ($31.7^{\circ}\text{N}, 64.2^{\circ}\text{W}$) using monthly data from January 2000 to January 2004. For more details of analyses, see Bates (2001).

accumulation of oxygen just below the mixed layer driven by photosynthesis (Fig. 7.14c,d). There is an accompanying consumption of oxygen and enhancement of DIC deeper in the water column (below 100 m) due to the oxidation of sinking organic particles and subducted dissolved organic matter. The oxygen and DIC anomalies are inversely correlated (Fig. 7.14a,d), both are affected by winter mixing acting on their opposing gradients and respond in the opposite sense to photosynthesis and respiration.

Seasonality in the air-sea flux of CO₂

The seasonal changes in DIC affect the partial pressure of CO₂ and resulting air-sea transfer of CO₂

(Fig. 7.15a,c). Within the upper mixed layer, summer heating is associated with an outflux of CO₂ to the atmosphere, while winter cooling is associated with an influx of CO₂ into the ocean (Fig. 7.15a,b). However, there is a lag in this relationship, the CO₂ outflux in summer only starts one to two months after the onset of surface heating. This delayed response is due to a combination of the long equilibration timescale of CO₂ (Section 6.6.5) and, to a lesser extent here, the biological consumption of DIC.

To better understand their seasonal control we now compare the evolution of surface temperature and the partial pressure of CO₂ for a typical year (Fig. 7.16 from Bates *et al.*, 1996):

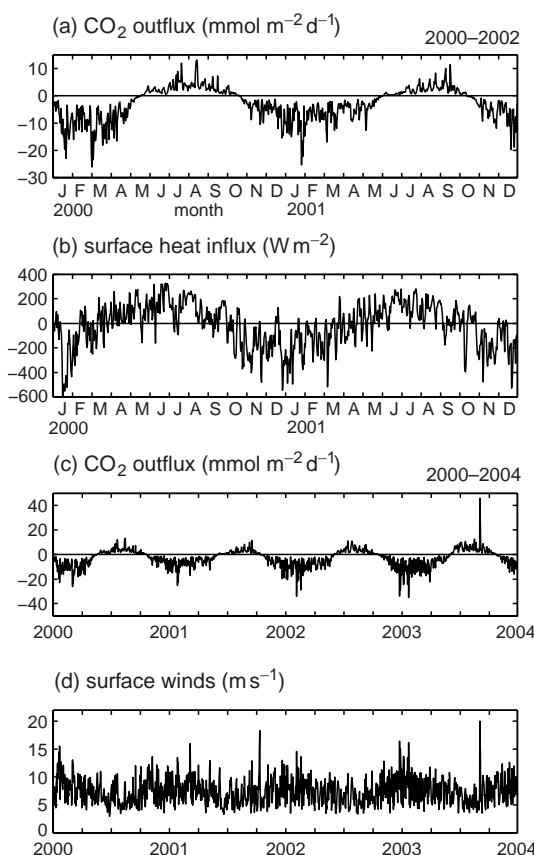


Figure 7.15 Time series of daily air-sea CO₂ flux out of the ocean (mmol m⁻² d⁻¹) for two different periods: (a) 2000 to 2002, and (c) 2000 to 2004, together with (b) surface heat flux into the ocean (W m⁻²) for 2000 to 2002, and (d) daily wind speed (m s⁻¹) for 2000 to 2004 from the Bermuda Atlantic Time-Series Study (31.7°N, 64.2°W). The CO₂ outflux broadly follows the surface heating cycle with a slight delay of 1–2 months. There is a local peak in the CO₂ outflux associated with the extreme winds of Hurricane Fabian (5 September 2003); for details of a previous hurricane, see Bates *et al.* (1998). Data supplied by BATS, courtesy of Nick Bates.

1. In late spring and summer (April to July), warming of the mixed layer reduces the solubility of CO₂, increasing pCO₂, and driving an outflux of CO₂ from the ocean;
2. Conversely, in the autumn and early winter (September to December), cooling of the mixed layer reduces pCO₂ and drives an influx of CO₂ from the atmosphere;
3. Finally, in the winter and early spring (December to April), the mixed layer continues to cool,

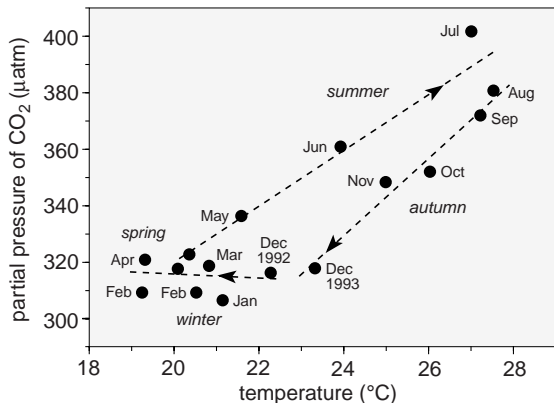


Figure 7.16 Seasonal progression of the partial pressure of CO₂ (μatm) versus temperature in the surface mixed layer at the Bermuda Atlantic Time-Series Study (BATS) from monthly data from December 1992 to December 1993. Reproduced from Bates *et al.* (1996).

but pCO₂ remains relatively constant. This surprising lack of change in pCO₂ is due to a three-way balance between cooling (increasing solubility and reducing pCO₂) and entrainment of nutrients driving a winter bloom (reducing surface DIC and pCO₂), which are both opposed by entrainment of carbon-enriched thermocline waters (acting to increase surface DIC and pCO₂).

Effect of extreme events

The air-sea transfer of CO₂ is also enhanced by severe winds linked with the passage of atmospheric storms, shown here for Hurricane Fabian (5 September 2003) passing close to Bermuda (Fig. 7.15d). The enhanced wind mixing and surface heat loss leads to a thickening of the mixed layer and the entrainment of DIC-rich thermocline waters, which then increases DIC in surface waters and drives an outflux of CO₂ (Fig. 7.15c). The entrainment of nutrients into the mixed layer is expected to drive a subsequent biological bloom with an opposing effect, acting to draw down CO₂ from the atmosphere.

Longer-term variability

There is also strong inter-annual variability over the upper ocean associated with atmospheric

anomalies often described in terms of circulation modes.

For example, in the North Atlantic, there is large-scale variability in the path and structure of the atmospheric Jet Stream, which often splits into a subtropical jet and an eddy-driven jet further to the north (Woolings, 2010). The resulting variability in surface winds is often crudely described in terms of the North Atlantic Oscillation (NAO), where a positive NAO index represents a stronger sea-level pressure difference between Iceland and Portugal (Hurrell *et al.*, 2003). In an NAO positive state, atmospheric winds drive enhanced winter surface heat loss and deep convection over the Labrador Sea (Dickson *et al.*, 1996), while in a negative NAO state, the winds change pattern and drive enhanced winter heat loss and convection over the Greenland Sea and Sargasso Sea. These physical changes drive corresponding changes in the nutrient supply, primary production and DIC anomalies, which are reflected in the observed time-series record at BATS (Bates, 2001).

7.4 Seasonality in the shelf and coastal seas

So far we have discussed the seasonality of the open ocean. Now consider the shelf seas, typically less than 200 m deep, and separating the land and the slope (where the topography rapidly deepens to several kilometres on the ocean side). All the physical and biogeochemical processes discussed so far still apply, but the response in the shelf seas is strongly affected by the shallow depths and the proximity to land.

The shelf seas are characterised by high levels of biological productivity. This enhanced activity reflects the greater recycling of organic nutrients and carbon from the sediments in the shallow waters, as well as the increased inputs of nutrients and trace metals from the land via river run-off and atmospheric transport. Despite their relatively small area, the shelf seas provide a significant fraction perhaps reaching 16% of globally integrated, annual primary production (Simpson and Sharples, not yet published).

7.4.1 Turbulence in the shelf seas

The vertical structure in the shelf seas is controlled by the competition between processes acting either to stratify or mix the water column: mechanical forcing acts to mix the water column, while surface heat or freshwater input acts to stratify the water column.

Turbulence is generated in a surface mixed layer from the mechanical forcing of the wind and convection by surface heating or evaporation, as well as in a bottom boundary layer by tidal currents flowing over the seabed. If the surface waters are lighter than the bottom waters, then these two boundary layers are separated by a thermocline, as seen during the summer, stratified part of the European shelf (Fig. 7.17a).

The concentration of mixing energy in the shelf seas is relatively large, often two to three orders of magnitude larger than seen in the thermocline of the open ocean; for example, the turbulent kinetic energy reaches $10^{-7} \text{ W kg}^{-1}$ in the English Channel (Fig. 7.17c), compared with only 10^{-10} to $10^{-9} \text{ W kg}^{-1}$ in the western Atlantic (Fig. 7.2c). If the mechanical inputs of mixing energy become sufficiently strong to offset surface heating or freshwater inputs, then the thermocline is eroded and the water column becomes vertically homogeneous.

For regions of strong tidal forcing, there can also be variations in the input of mixing energy and resulting density structure following the spring-neap cycle of tides. The spring and neap tides, respectively, refer to times when the tidal accelerations from the Sun and Moon either reinforce or oppose each other.

7.4.2 Shelf-sea regimes and fronts

There are different physical regimes over the shelf seas, reflecting the relative strength of the mechanical forcing (acting to mix the water column) and surface density forcing (acting to stratify the water column in summer). For example, observations from a section passing across the European shelf in summer reveals stratified waters in the open ocean, seasonally stratified waters over part of the shelf and permanently well-mixed waters near the coast (Fig. 7.18a).

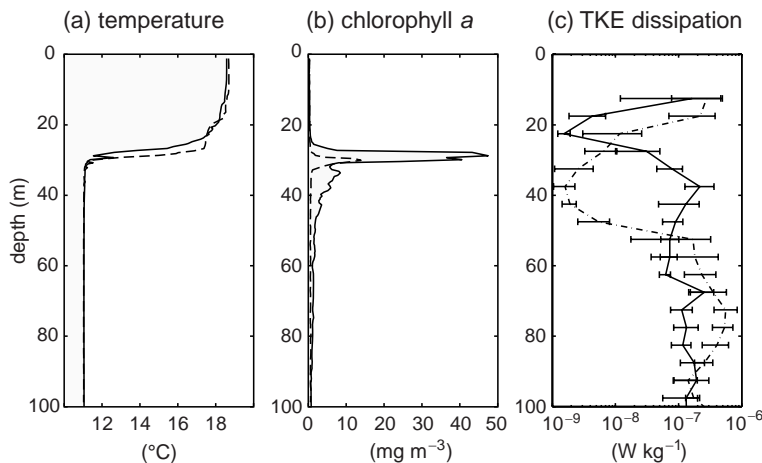


Figure 7.17 Vertical distributions of (a) temperature ($^{\circ}\text{C}$), (b) chlorophyll *a* (mg m^{-3}), and (c) turbulent kinetic energy dissipation (W kg^{-1} ; log scale with error bars for 95% confidence limits) in stratified waters of the western English Channel ($49^{\circ}\text{N}, 6^{\circ}\text{W}$) on 9 August 1999 at 03h25 (dashed line) and 06h15 (full line). There is a shallow thermocline at 30 m, separating the surface mixed layer and nearly homogeneous deeper waters, which is coincident with a subsurface chlorophyll maximum. There are high levels of turbulent kinetic energy being dissipated at the surface and above the sea floor. Between two time periods, 03h25 and 06h15, a patch of slightly cooler water with higher concentrations of chlorophyll along the thermocline moved into the domain. Enhanced mixing below the thermocline leads to a transfer of chlorophyll below the thermocline between 03h25 and 06h15. Data supplied by Jonathan Sharples; see Sharples *et al.* (2001) for full details. Original © 2001 by The American Society of Limnology and Oceanography.

Tidally mixed front

The tidally mixed front separates the stratified and well-mixed waters on the shelf, reflecting the outcrop of the thermocline (Fig. 7.18, at 550 km). The shelf waters remain well mixed throughout the year in regions of high tidal flow or shallow depth, while summer waters become stratified in regions of low tidal flow or large depth.

The position of the tidally mixed front varies with the competition between the mechanical forcing and surface density forcing during summer. The tidally mixed front moves offshore when there is increased mechanical forcing or when surface heating weakens.

Shelf-break front

The shelf-break front separates the open ocean and shelf water, located where the slope joins the shelf at the shelf edge. This front can often be revealed by contrasts in salinity: the shelf waters either fresher or saltier than the open ocean due to river inputs or net evaporation, respectively (Fig. 7.19a).

At the shelf break, the sharp changes in topography can lead to enhanced mixing, evident in cooler waters, and higher nutrient and chlorophyll *a* concentrations (Fig. 7.18 at 50 km and

Fig. 7.19b,c), which result from an internal tide interacting with the topography and generating internal-wave breaking.

7.4.3 Primary production in the shelf seas

Phytoplankton growth is again limited by sunlight and the availability of nutrients. The more vigorous turbulence in the shelf seas affects both these processes: enhanced bottom mixing leads to greater concentrations of suspended sediments making the waters more opaque and limiting the penetration of sunlight. Nutrients are mixed strongly in the vertical and there is both a burial of organic matter and resupply of inorganic nutrients from the sea floor.

Over the European shelf, there is an intense phytoplankton bloom every spring. The bloom only lasts several weeks as surface waters become nutrient depleted. Bottom waters remain nutrient rich, as there is insufficient light for phytoplankton growth. During the summer, any remaining phytoplankton growth is usually concentrated along a shallow thermocline, the sharp interface between the surface and bottom waters (Fig. 7.17b). This phytoplankton growth forms a

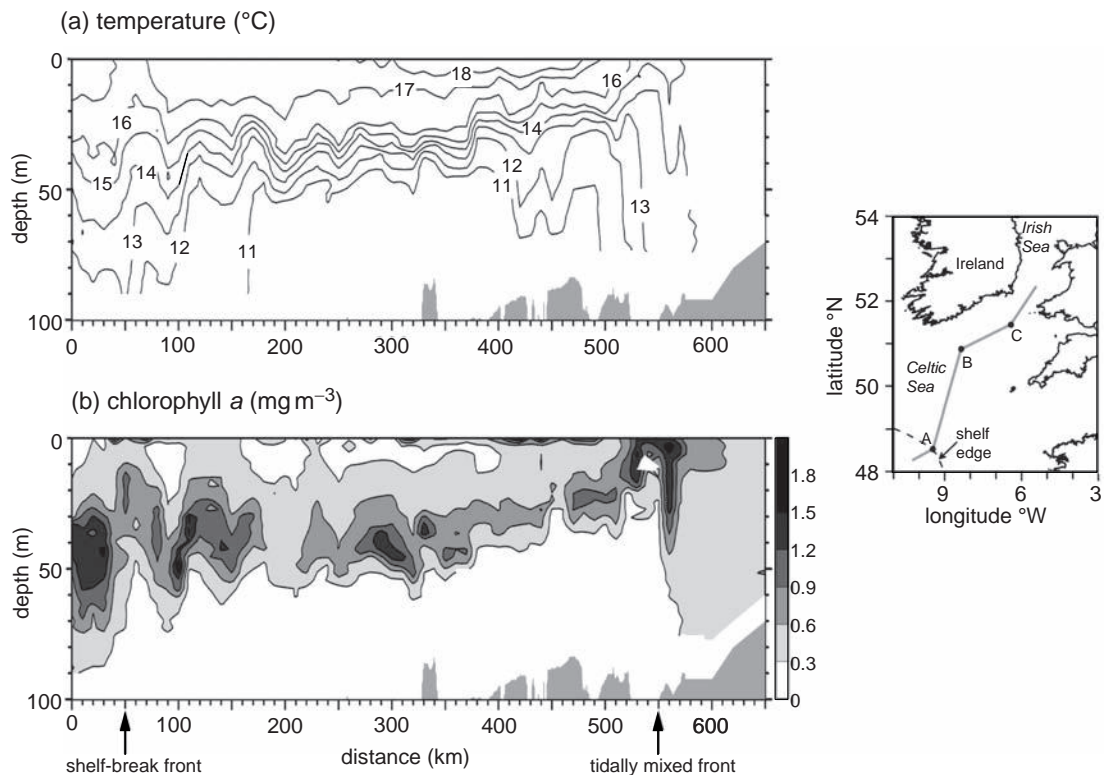


Figure 7.18 European Shelf Sea section of (a) temperature ($^{\circ}\text{C}$), and (b) chlorophyll *a* concentration (mg m^{-3}) along a section in July 2003 (marked on the map), starting in the stratified waters of the North Atlantic ($48^{\circ} 17' \text{N}$, $10^{\circ} 13' \text{W}$), crosses the shelf-break front at 50 km, passes through the stratified waters of the Celtic Sea, and reaches the tidally mixed front at 550 km ($51^{\circ} 28.4' \text{N}$, $6^{\circ} 25.8' \text{W}$) and a well-mixed station at 650 km ($52^{\circ} 34.01' \text{N}$, $5^{\circ} 28.02' \text{W}$). The first 600 km were carried out with a Seasorar and CTD casts at 625 and 650 km. The thermocline is typically 1 to 2 km thick over the open ocean, but thins dramatically over the shelf seas, gradually being eroded, and eventually outcrops at the sea surface. The subsurface chlorophyll maximum broadly follows the position of the thermocline over the shelf. Figure supplied by Jonathan Sharples; see Simpson and Sharples, not yet published.

widespread subsurface chlorophyll maximum persisting over summer, which tracks the thermocline, shoaling towards the coast in Fig. 7.18. The primary productivity associated with this subsurface chlorophyll maximum can become significant and comparable to that from the more intense, but short-lived surface bloom. Finally, as autumn cooling progresses and the surface mixed layer thickens, there can be another surface bloom, as nutrients are entrained into the surface mixed layer from the thermocline and bottom waters.

7.4.4 Seasonality in the carbon cycle: case study of the North Sea

We have previously discussed the seasonality of the carbon cycle in the North Atlantic (Sec-

tion 7.3.1). Now we consider the response in the shelf seas and the effect of these different mixing regimes for the North Sea on the European shelf.

The central and northern parts of the North Sea stratify during summer, while the shallower southern part remains well mixed over the entire year (Thomas *et al.*, 2004). There is an ocean uptake of CO₂ over the entire North Sea during late spring, which continues over the stratified regions during summer (Fig. 7.20b,c, dark shading), but instead reverses to an ocean outflux of CO₂ over the well-mixed regions (Fig. 7.20c, light shading).

Why is there this regionally varying response of the air-sea flux of CO₂ during summer? Over the stratified waters in the northern North Sea, photosynthesis leads to a progressive reduction in DIC in

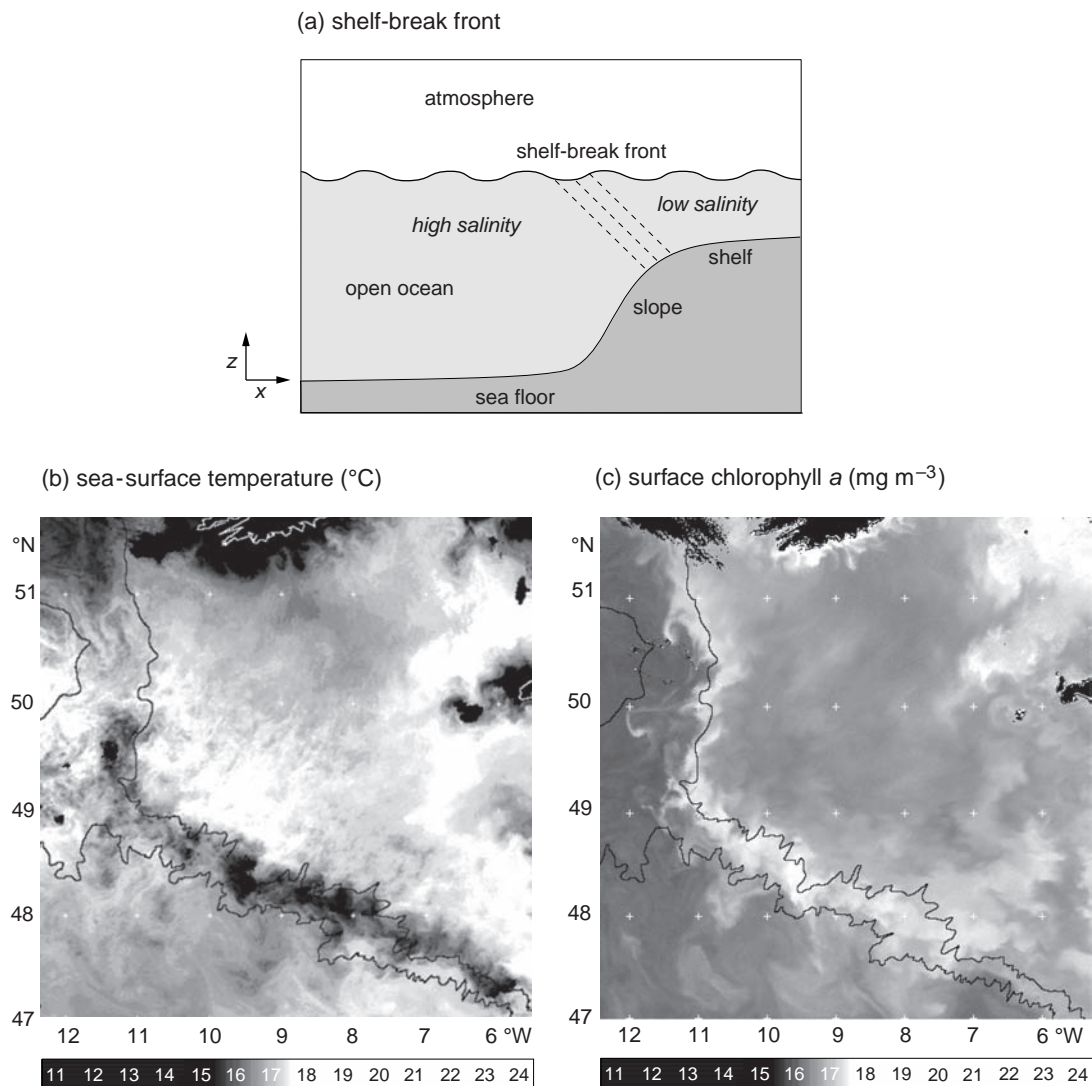


Figure 7.19 (a) A schematic figure of the shelf-break front; and remotely sensed pictures of the shelf-break front in the NW European shelf on 15 June 2004: (b) sea-surface temperature ($^{\circ}\text{C}$) and (c) surface chlorophyll (mg m^{-3}), together with two depth contours. Note how there is a lower temperature over the shelf-break front and a higher chlorophyll concentration. Courtesy of Steve Groom, NODAAS, Plymouth.

surface waters from winter to summer (Fig. 7.20e, light shading), as well as an associated increase in DIC in the deeper waters from the remineralisation of organic fallout (Fig. 7.20e, dark shading). The summer stratification isolates DIC in the deep waters from the surface and biological consumption in the surface continues to drive an uptake of atmospheric CO_2 .

In contrast, in the southern North Sea, the water column is well mixed, so the reduction

of DIC by photosynthesis is opposed by the increase in DIC by remineralisation. Hence, biological cycling of carbon does not have any net effect for the well-mixed waters during summer, so that the remaining effect of thermal warming on solubility leads to a summer outflux of CO_2 .

In summary, the physical contrasts in mixing across the shelf seas affect the detailed patterns for air-sea exchange of CO_2 .

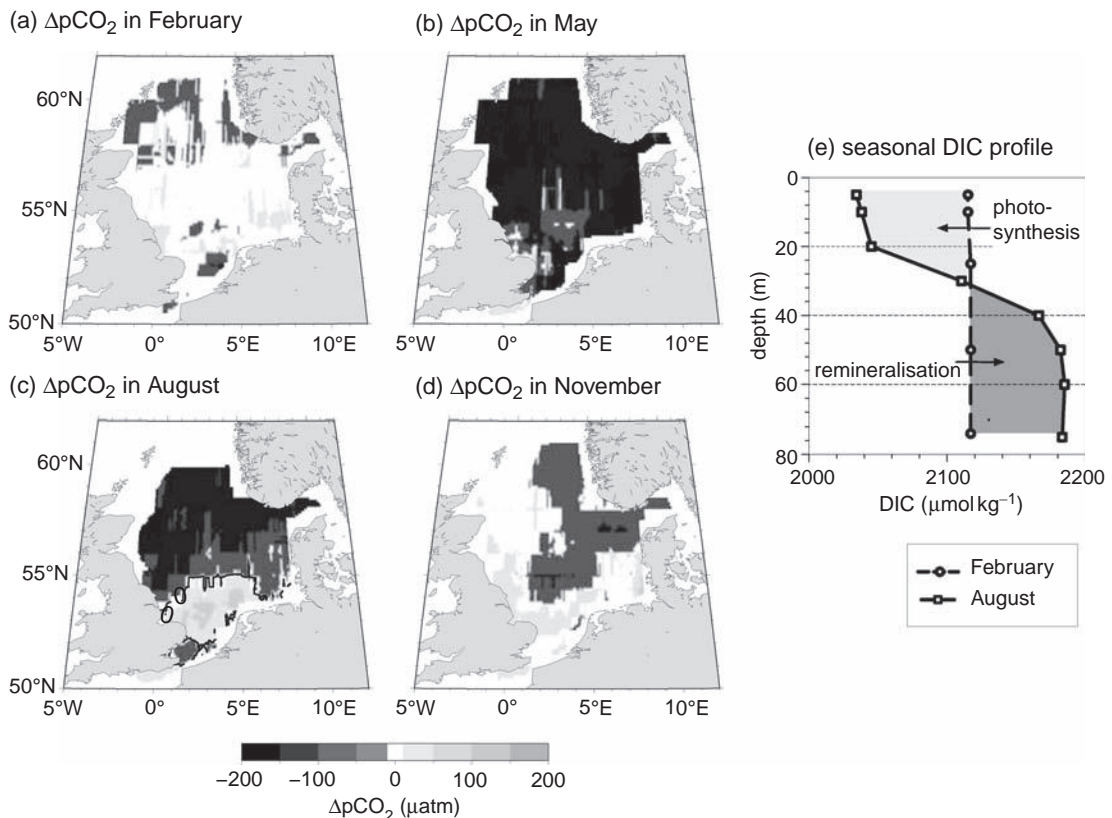


Figure 7.20 Seasonal variation of the carbon cycle over the North Sea. Data for August 2001 to May 2002: $\Delta p\text{CO}_2$ (μatm) for (a) winter (February), (b) spring (May), (c) summer (August), and (d) autumn (November), together with (e) the seasonal variation of dissolved inorganic carbon (DIC, $\mu\text{mol kg}^{-1}$) in the summer stratified part of the northern North Sea (57°N , 2.25°E). In (a) to (d), there is an ocean uptake of CO_2 (negative values for $\Delta p\text{CO}_2$, dark shading) in spring and summer over the stratified parts of the North Sea, and an outflux of CO_2 (light shading) over the well-mixed regions of the southern North Sea in summer and autumn. In (e), there is a summer reduction of DIC in the surface waters (light shading) from photosynthesis, leading to uptake of atmospheric CO_2 and a corresponding increase of DIC in deep waters (dark shading) due to the remineralised organic fallout. Figure courtesy of Helmuth Thomas (Thomas *et al.*, 2004), reprinted with permission from AAAS.

7.5 | Summary

The physical, chemical and biological properties of the upper ocean have a pronounced seasonal cycle outside the tropics, which reflects the effect of seasonal changes in solar forcing. One of the most marked changes is in the surface mixed layer: thinnest at the summer solstice when there is most solar heating and thickest at the spring equinox when surface cooling finally ceases.

The ecosystem is likewise affected by the seasonality in sunlight, and by the supply of nutrients

and trace metals. Over some parts of the globe, particularly the North Atlantic and the shelf seas, a phytoplankton bloom occurs whenever there is sufficient sunlight and nutrient-replete surface waters. The timing of the bloom varies from late winter or early spring in the subtropics to the summer in polar regions. However, over other parts of the globe, the bloom is rather subdued and probably limited by the availability of iron.

The surface carbon cycle is affected by both these physical and biological changes. The physics affects the surface carbon cycle in the following manner:

- Dissolved gases are more soluble in cold water, leading to a general uptake of CO₂ during winter and outgassing during summer.
- Surface cooling or stronger mechanical forcing leads to a thickening of the mixed layer and the entrainment of carbon-rich waters into the surface layer, providing outgassing (or reduced uptake) of CO₂.
- Stronger winds enhance the air-sea transfer of the dissolved gases.

Biological activity likewise affects the cycling of carbon:

- Photosynthetic growth forms organic carbon within the surface euphotic zone, which reduces the concentration of DIC in the surface waters and drives a surface drawdown of CO₂ from the atmosphere (or reduced outgassing). A by-product of this photosynthesis is the summer formation of oxygen within the euphotic zone.
- Conversely, organic carbon is converted back to CO₂ and increasing DIC. If this latter process occurs in the surface mixed layer, outgassing of CO₂ is enhanced. The respiration of sinking organic particles enhances DIC at depth.

In the shelf seas, there is more vigorous turbulence in the shallower water column, leading to suspended sediments and less light penetration. Biological productivity is, however, generally enhanced due to the availability of nutrients, provided by resuspension from the sediments, riverine or atmospheric inputs. There is usually an intense surface bloom in the spring, followed by summer production along a shallow thermocline and, sometimes, a weaker surface bloom in the autumn. The air-sea exchange of carbon dioxide is strongly affected by this biological cycling and by the distribution of summer stratification.

While the seasonal cycle provides the dominant variability at mid and high latitudes, there is also variability on longer timescales, which is often connected to dominant circulation modes, such as the El Niño–Southern Oscillation (ENSO) and the North Atlantic Oscillation (NAO). ENSO represents a coupled mode involving changes in the atmosphere and ocean, which feed back on each other, while NAO is mainly an atmospheric

mode forcing the ocean. These variations in atmospheric forcing alter the convection, stratification and circulation of the upper ocean, modulating the variations due to the seasonal cycle. There is also the possible long-term drift in the climate system.

These themes of seasonality are taken further in later chapters addressing how the ocean is ventilated, how nutrients and carbon are transported and cycled, as well as how dense waters form in the mixed layer ([Chapters 10 to 12](#)).

7.6 | Questions

Q7.1. Seasonality in temperature.

Consider the seasonal change in temperature for a body of water in a well-mixed sea of constant thickness, D , where the temperature evolution is given by

$$\frac{\partial T}{\partial t} = \frac{1}{\rho C_p} \frac{\mathcal{H}(t)}{D}, \quad (7.5)$$

and the surface heat flux is assumed to vary as $\mathcal{H}(t) = -\mathcal{H}_0 \cos(2\pi t/T)$, where the time t is 0 at the start of the year and T at the end of the year.

- When is $\partial T / \partial t$ most positive and negative?
- When is T likely to be largest and smallest over the year?
- Show that the seasonal temperature range is given by $\frac{\mathcal{H}_0}{\rho C_p D} \frac{T}{2\pi}$.
- How large is the implied seasonal cycle in temperature for a water thickness of $D = 100$ m, typical for a shelf sea, a surface heat flux of $\mathcal{H}_0 = 200 \text{ W m}^{-2}$, $\rho \sim 1000 \text{ kg m}^{-3}$, $C_p \sim 4000 \text{ J kg}^{-1} \text{ K}^{-1}$ and T is the number of seconds in a year. Check the units of your answer.

Q7.2. Summer mixed-layer thickness over the open ocean.

During the summer, the thickness of the mixed layer depends on the competition between wind mixing and surface heat input, and can often be predicted by

$$h = \frac{2m\mu_*^3}{g\alpha_T \mathcal{H}/(\rho C_p)}. \quad (7.6)$$

(a) Show that dimensionally the two sides of the equation are balanced, where the friction velocity u_* is in m s^{-1} , g in m s^{-2} , α_T in K^{-1} , \mathcal{H} in $\text{J s}^{-1} \text{m}^{-2}$, ρ in kg m^{-3} , C_p in $\text{J kg}^{-1} \text{K}^{-1}$ and m is non-dimensional.

(b) For a wind speed, u_{air} , of 10 m s^{-1} , estimate the magnitude of the surface stress, $\tau = \rho_{\text{air}} c_d u_{\text{air}}^2$, and diagnose the related friction velocity, u_* , defined by $\tau = \rho u_*^2$, assuming a drag coefficient, c_d , of 1.14×10^{-3} and air density, ρ_{air} , of 1.2 kg m^{-3} .

(c) Predict the summer thickness of the mixed layer, h , from (7.6) assuming a wind speed of 10 m s^{-1} and a surface heat flux of $\mathcal{H} \sim 200 \text{ W m}^{-2}$, together with $\alpha_T \sim 2 \times 10^{-4} \text{ K}^{-1}$, $\rho \sim 10^3 \text{ kg m}^{-3}$, $g = 9.81 \text{ ms}^{-2}$ and $m = m_e (\rho / (\rho_{\text{air}} c_d))^{1/2}$ with an efficiency of wind mixing, m_e , of 1.5×10^{-3} .

(d) How much does h alter if either (i) the wind speed doubles or (ii) the heat flux into the ocean doubles?

Q7.3. Mechanical forcing from winds and tides in a shelf sea.

In the shelf seas, there is often a front separating regions of stable and unstable stratification, which occurs at a depth given by

$$D = \frac{2}{g \alpha_T \mathcal{H} / C_p} (m_e c_d \rho_{\text{air}} u_{\text{air}}^3 + m_b c_b \rho u_b^3), \quad (7.7)$$

which is based upon the competition between the rate of input of mechanical energy available for mixing from the wind, $m_e c_d \rho_{\text{air}} u_{\text{air}}^3$, and the tides, $m_b c_b \rho u_b^3$, versus the stratifying effect of a surface heat flux, \mathcal{H} ; m_b is the efficiency in using tidal inputs of energy for mixing and c_b is the drag coefficient for the bottom, and u_b is a bottom velocity.

(a) Show that the previous mixed-layer balance (7.6) can be re-expressed as (7.7) assuming that (i) the mixed-layer thickness, h , becomes the same as the depth of the water column, D , and (ii) the mechanical energy input available for mixing from the wind, $m u_*^3$, is augmented to include the mechanical input from the tides, $m_b c_b u_b^3$.

(b) Compare the relative importance of the mechanical energy inputs available for mixing for a wind speed of 10 m s^{-1} and a bottom current of (i) for a strong tide, 1 m s^{-1} or (ii) a

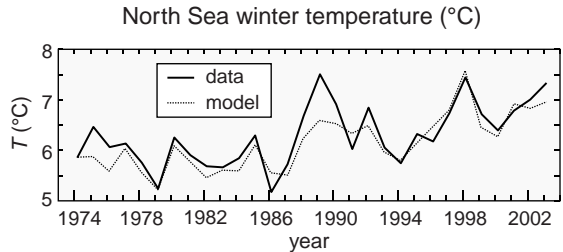


Figure 7.21 Observed and modelled time series of February temperature ($^{\circ}\text{C}$) in the North Sea (56.3°N , 1.7°W) of the European shelf from 1974 to 2003. The model simulation (dashed line) is from a one-dimensional mixed layer model driven by meteorological and tidal forcing (Sharples et al., 2006). The time series reveals both interannual variability and a longer-term warming trend. Data supplied by Jonathan Sharples.

weak tide, 0.1 m s^{-1} ; assume $m_b = 4 \times 10^{-3}$ and $c_b = 2.5 \times 10^{-3}$ (and values from Q7.2).

(c) For both the strong and weak tides, predict the thickness D of the well-mixed water column from (7.7) if there is a surface heat flux of 200 W m^{-2} .

Q7.4. Inter-annual variability and long-term warming in the shelf seas.

Winter temperature anomalies in the shelf seas are illustrated in Fig. 7.21, full line over the European shelf. These thermal anomalies are primarily due to the effect of the surface forcing, rather than horizontal exchange with the open ocean, since they are predicted reasonably well using a one-dimensional mixed-layer model (like Box 7.1) driven by meteorological and tidal forcing (Fig. 7.21, dashed line).

(a) Estimate the warming trend over the nearly three decades of data in Fig. 7.21.

(b) Assuming a one-dimensional heat balance (7.5), then estimate the surface heat flux, \mathcal{H} , needed to explain this warming trend; assume $\rho \sim 1027 \text{ kg m}^{-3}$, $C_p \sim 4000 \text{ J kg}^{-1} \text{ K}^{-1}$, and D is the depth of 60 m.

(c) How would your answer in (a) have altered if applied to a shorter record? What then are the implications for inferring long-term climate change?

7.7 | Recommended reading

Mixed-layer physical balances are described in P. P. Niiler and E. B. Kraus (1977). One-dimensional models of the upper ocean. In *Modeling and Prediction*

of the Upper Layers of the Ocean, ed. E. B. Kraus, New York: Pergamon, pp. 143–172.

A discussion of the physical and biological processes acting in the shelf seas is provided by J. H. Simpson and J. Sharples, *An Introduction to the Physical and Biological Oceanography of Shelf Seas*. Cambridge: Cambridge University Press, not yet published.

Ocean gyres and intense currents

The atmosphere and ocean share many similar dynamical features. Both fluids move easily over the globe. Together they respond to the latitudinal variation in Sun's heating over the Earth, transferring heat from the tropics to the poles. Over the scale of the planet, this fluid motion is relatively slow, so that winds and currents are strongly affected by the Earth's rotation. The atmosphere and ocean differ, though, in an important and obvious way: the atmosphere easily moves above the Earth's surface, including most of its mountain ranges, whereas the ocean flow is constrained by the land. This difference turns out to be of fundamental importance.

The atmosphere has a strong zonal character to its circulation, particularly at mid latitudes where there are strong upper-air, westerly winds, the Jet Stream. In contrast, the ocean has large-scale recirculations, called gyres, within each of the basins, since zonal flows are blocked by continental barriers. A similar circumpolar flow to the atmosphere only occurs in the Southern Ocean, where the eastward flowing Antarctic Circumpolar Current passes between the gaps in the continents and encircles the globe.

At the simplest level, how ocean gyres rotate can be understood in terms of the twisting force imparted by the surface winds. However, these gyre circulations are surprising in having much stronger flows along their western side than their eastern side. To understand this asymmetrical response, one has to consider how the ocean responds on the basin scale to wind forcing, taking into account that the Earth is a spinning sphere.

In this chapter, we start by describing the pattern of ocean gyres and western boundary currents, and then provide theoretical views as to how these phenomena form. We then describe the near-zonal flows in the Southern Ocean and discuss their control.

8.1 | What are ocean gyres?

Ocean gyres are large-scale recirculations within ocean basins. At the simplest level, gyres rotate according to the pattern of atmospheric winds, as depicted in Fig 8.1a. Subtropical gyres are forced by the persistent easterly Trade winds in the tropics and westerly winds at mid latitudes leading to an anticyclonic circulation, defined as clockwise in the northern hemisphere and anticlockwise in the southern hemisphere. Subpolar gyres have a cyclonic circulation, the opposite sense of rotation to subtropical gyres, and are confined poleward of the subtropical gyres, where the strong westerly winds weaken poleward and sometimes change to easterlies.

Associated with the gyre circulations, there are basin-scale undulations of sea-surface height and the underlying thermocline (Fig. 8.1b). The sea surface is preferentially raised over the subtropical gyre and depressed over the subpolar gyre. The thermocline is likewise thicker over the subtropical gyre and thinner or absent over the subpolar gyre.

Next we consider these sea-surface height and thermocline signals within ocean basins.

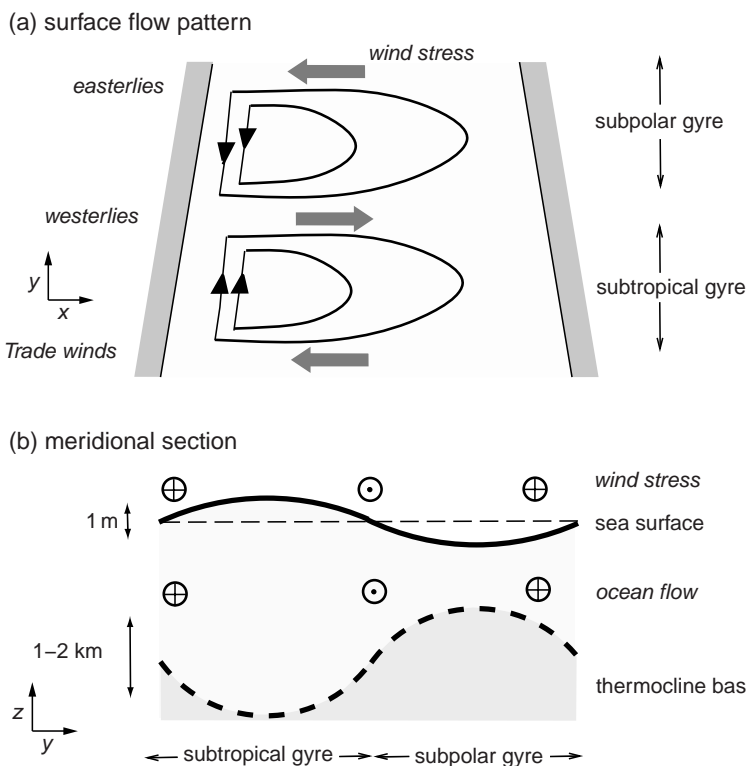


Figure 8.1 A schematic figure of ocean gyres within an idealised basin: (a) a plan view showing the wind stress pattern (grey arrows) and the resulting gyre circulation (black contours), with an anticyclonic circulation in the subtropical gyre and a cyclonic circulation in the subpolar gyre; (b) a vertical section showing the undulations of the sea surface and thermocline over the subtropical and subpolar gyres.

8.1.1 Surface signals

In the same way that surface winds generally follow pressure contours on a weather map, the surface currents broadly follow contours of dynamic height; more precisely, the geostrophic part of the surface flow follows contours of dynamic height η , involving a balance between the Coriolis acceleration and the pressure gradient (Section 4.2.1), such that

$$u_g = -\frac{g}{f} \frac{\partial \eta}{\partial y} \quad \text{and} \quad v_g = \frac{g}{f} \frac{\partial \eta}{\partial x}. \quad (8.1)$$

This surface flow is aligned such that high dynamic height is on the right of the flow in the northern hemisphere and to the left of the flow in the southern hemisphere. Now we consider how the surface flow, as revealed by patterns of dynamic height and geostrophic speed, varies over the major basins of the northern and southern hemisphere.

Northern hemisphere

In both the North Atlantic and Pacific basins, there are well-defined pairs of subtropical and subpolar

gyres (Figs. 8.2a and 8.3a): an anticyclonic circulation occurring within the subtropical gyre, typically between 15°N to 40°N , and a cyclonic circulation occurring within the subpolar gyre further to the north. These circulations extend across the entire width of the basin. The flows are generally weak over much of the basin, with speeds less than 5 cm s^{-1} , but become much stronger along the western boundary, with speeds reaching 50 cm s^{-1} or more (Figs. 8.2b and 8.3b).

In the North Atlantic, the Gulf Stream is directed northward along the western boundary of the subtropical gyre and separates from the coast around 36°N , and then flows offshore up to 40°W (Fig. 8.2), eventually extending northeastward across the basin interior, where the current is then referred to as the North Atlantic Current. Conversely, in the subpolar gyre, there is a southward flow in the Labrador Current along the western boundary.

In a similar manner in the North Pacific, the Kuroshio Current is directed northward on the western side of the subtropical gyre, then

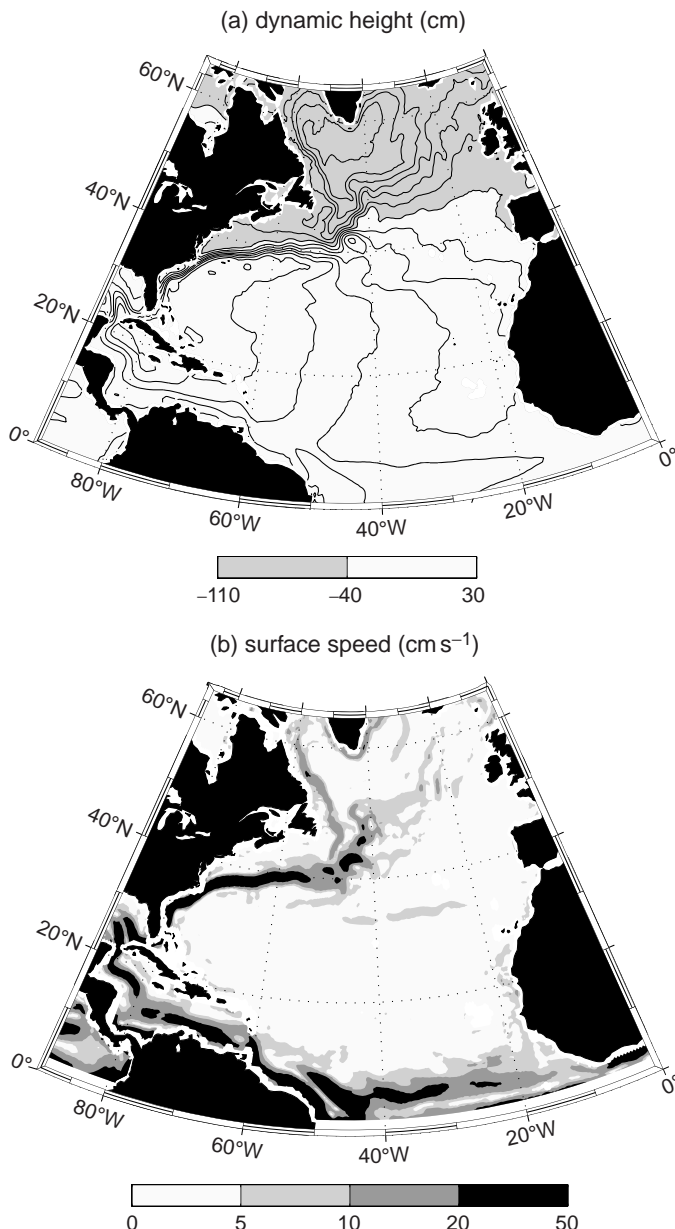


Figure 8.2 (a) Ocean mean dynamic height (cm; contours every 10 cm), and (b) geostrophic speed (cm s^{-1}) for the North Atlantic. The surface geostrophic flow is directed along the contours of dynamic height (with high values to the right of the flow in the northern hemisphere). There are large-scale recirculations in the basins, referred to as gyres, with an intense return flow along the western boundary: the Gulf Stream for the subtropical gyre and Labrador Current for the subpolar gyre. In addition, there are strong zonal flows in the tropics, associated with a westward flow in the North Equatorial Current and an eastward flow in the Equatorial Counter Current; the geostrophic speed is not calculated within 2° of the equator. The mean dynamic height was taken from a combined dataset integrating information from surface drifters, satellite altimetry, surface winds and the GRACE gravity mission (Niiler *et al.*, 2003; Maximenko and Niiler, 2005).

separates from the coast off Japan (Fig. 8.3), and to the north there is a southward flowing Oyashio Current on the western side of the subpolar gyre. These currents extend for several thousand kilometres into the basin interior and are referred to as the North Pacific Current.

Southern hemisphere

In the southern basins, the dominant signal is the eastward flowing, Antarctic Circumpolar Current

(Figs. 8.4a and 8.5a). There are weaker subtropical gyres, extending from the tropics to the northern flank of the Antarctic Circumpolar Current, typically ranging from 5°S to 40°S . However, there are no subpolar circulations between the equatorial region and the southern tip of the continents due to the westerly winds continuing to strengthen southward over this latitude range; the subpolar gyres (not shown here) are confined between Antarctica and the southern flank of the

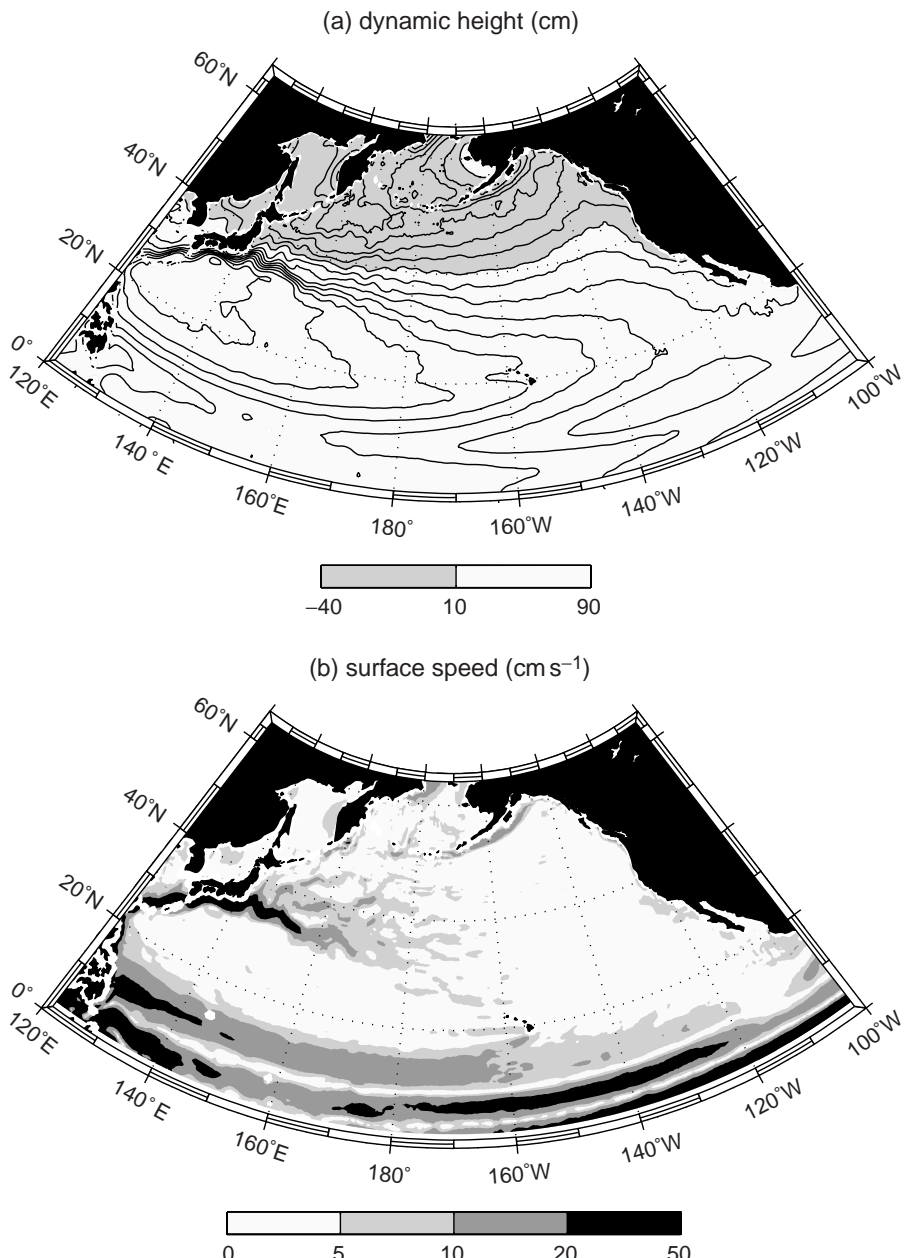


Figure 8.3 (a) Ocean mean dynamic height (cm; contours every 10 cm), and (b) geostrophic speed (cm s^{-1}) for the North Pacific; details as for Fig. 8.2. The western boundary currents are the Kuroshio Current for the subtropical gyre and the Oyashio Current for the subpolar gyre (although the latter is not clearly shown in these maps), as well as strong zonal flows in the tropics, associated with the North Equatorial Current and Equatorial Counter Current.

Antarctic Circumpolar Current: the Weddell and Ross gyres with clockwise circulations.

In the South Atlantic, the subtropical gyre circulation is relatively weak compared with the Antarctic Circumpolar Current. The anticyclonic

circulation leads to a southward flowing, western boundary current, called the Brazil Current, although the speeds are less than 20 cm s^{-1} in Fig. 8.4. There is also a northward influx of warm, salty water from the Indian Ocean into the South

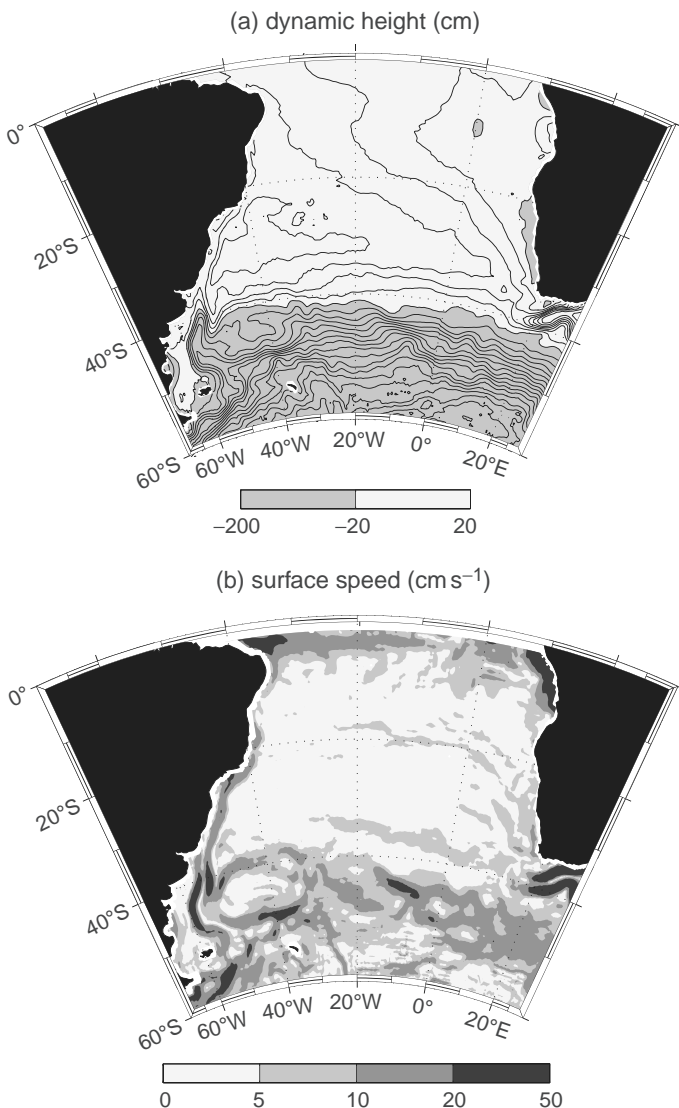


Figure 8.4 (a) Ocean mean dynamic height (cm; contours every 10 cm), and (b) geostrophic speed (cm s^{-1}) for the South Atlantic; details as for Fig. 8.2. The Antarctic Circumpolar Current flows eastward along the dynamic height contours (shaded) with high values to the left of the flow in the southern hemisphere, passing south of South America and South Africa, while the Brazil Current is the western boundary current of the subtropical gyre. There are also strong zonal flows in the tropics, associated with the South Equatorial Current and Equatorial Counter Current.

Atlantic gyre, as revealed by dynamic height contours extending from the tropics to south of Southern Africa; this influx is also facilitated through the transfer of intense rings and eddies, spawned from the Agulhas Current, into the South Atlantic.

In the South Pacific, there is again a gyre circulation extending over the entire basin. There is a western boundary current along the eastern side of Australia: the East Australian Current. This boundary current is relatively weak, only reaching 20 cm s^{-1} in Fig. 8.5, since the topography does not form a continuous barrier to the interior gyre flow.

Tropical gyres and equatorial flows

In the tropics, there is a different dynamical balance as the rotational control becomes weaker. On either side of the equator, the easterly Trade winds drive equatorial currents flowing to the west: the North and South Equatorial Currents. This westward flow leads to an accumulation of fluid along the western boundary. Persistent west-east pressure gradients cannot be supported along the equator due to the smallness of the Coriolis parameter, so that there is an eastward return flow, the Equatorial Counter Current, along the equator. These currents are fast moving with high surface speeds (Figs. 8.2–8.5). The precise location

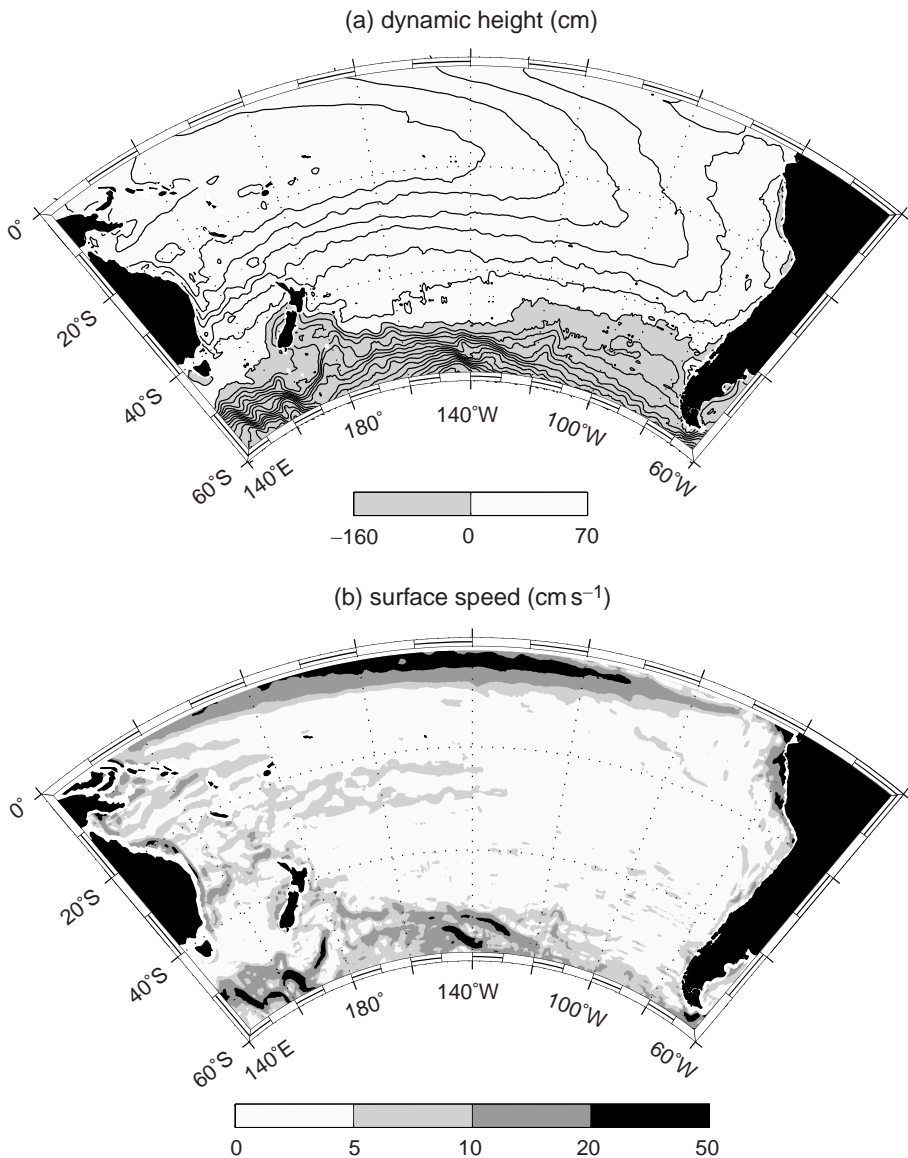


Figure 8.5 (a) Ocean mean dynamic height (cm; contours every 10 cm), and (b) geostrophic speed (cm s^{-1}) for the South Pacific; details as for Fig. 8.2. The Antarctic Circumpolar Current flows eastward along the dynamic height contours (shaded), passing south of Australia and South America. The East Australian Current is the western boundary current of the subtropical gyre and there are strong zonal flows in the tropics associated with the South Equatorial Current and Equatorial Counter Current.

of these zonal currents varies seasonally with the pattern of the surface winds and associated migration of the Inter-Tropical Convergence Zone.

The Indian Ocean reveals a particularly complex interplay of gyre recirculations and zonal equatorial currents (Fig. 8.6). South of the equator, there is an anticyclonic subtropical circulation,

together with a southward flow in a western boundary current along the southern flank of Africa, the Agulhas Current. The circulation becomes more complex north of the equator due to the seasonal changes in monsoon winds: the western boundary current, the Somali Current, is directed northeastward during late summer, but

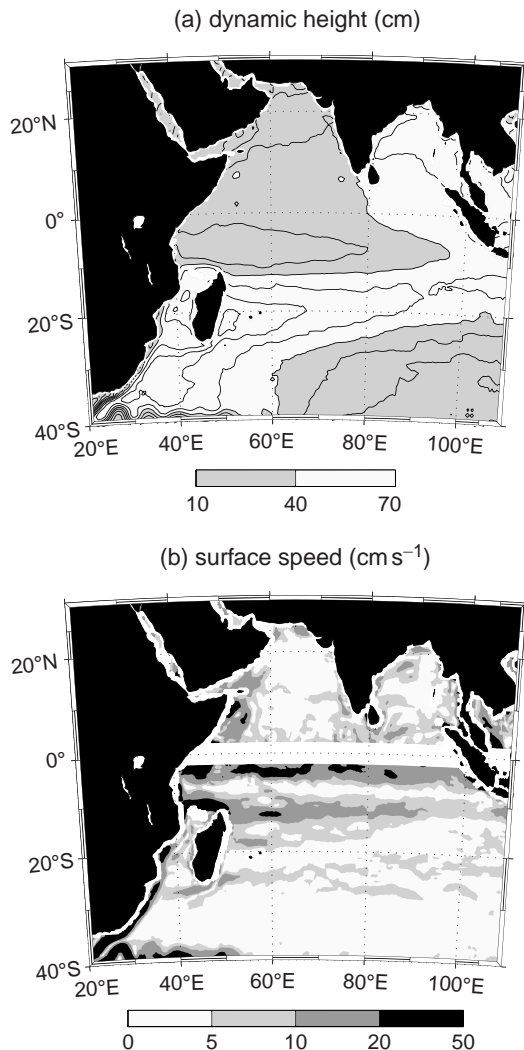


Figure 8.6 (a) Ocean mean dynamic height (cm; contours every 10 cm), and (b) geostrophic speed (cm s^{-1}) for the Indian Ocean; details as for Fig. 8.2. There are strong zonal flows in the tropics, a westward flow in the North and South Equatorial Currents, as well as an eastward return flow in the Equatorial Counter Current along the equator; the geostrophic speed is not calculated within 2° of the equator. South of the equator, there is an Agulhas Current running along the western boundary of the subtropical gyre, while north of the equator, the reversing pattern of winds associated with the monsoon lead to a seasonal reversal in the direction of the western boundary current, the Somali Current (which is not revealed in these annual-mean diagnostics).

reverses to southwestward during late winter and spring; hence, there is not a strong signal in the dynamic height in an annual average.

8.1.2 Interior signals

The gyre signatures are also evident in the accompanying undulations of the thermocline (Fig. 8.7): potential temperature surfaces are pushed down over the subtropical gyres (centred at typically 30°N and 30°S), and raised over the tropics and higher latitudes, together with similar undulations in salinity and potential density.

The resulting density gradients induce a vertical shear in the horizontal velocity from thermal-wind balance (Section 4.3), such that

$$\frac{\partial u_g}{\partial z} = \frac{g}{\rho f} \frac{\partial \rho}{\partial y} \quad \text{and} \quad \frac{\partial v_g}{\partial z} = -\frac{g}{\rho f} \frac{\partial \rho}{\partial x}. \quad (8.2)$$

Assuming a weak deep flow, the surface flow is directed eastward on the poleward flank of the subtropical gyre and westward on its equatorial flank. This gyre circulation extends at least to several kilometres and sometimes to the sea floor when the stratification is weak. A signature of the Antarctic Circumpolar Current is again evident over the Southern Ocean through the poleward shoaling and outcropping of the density surfaces; the southward increase in density is associated with a strong eastward flow at the surface, relative to the deep ocean, through thermal wind (8.2).

Given this view of gyres as generic features, now we consider in more detail their western boundary structure.

8.2 What are western boundary currents?

Western boundary currents, such as the Gulf Stream and Kuroshio, are some of the most striking features of the ocean circulation. They are intense flows along the western side of the ocean basins, with surface velocities often exceeding 1 m s^{-1} .

The structure of the Gulf Stream is now briefly described; while some of the details are specific to this current, many of its features are generic for other boundary currents.

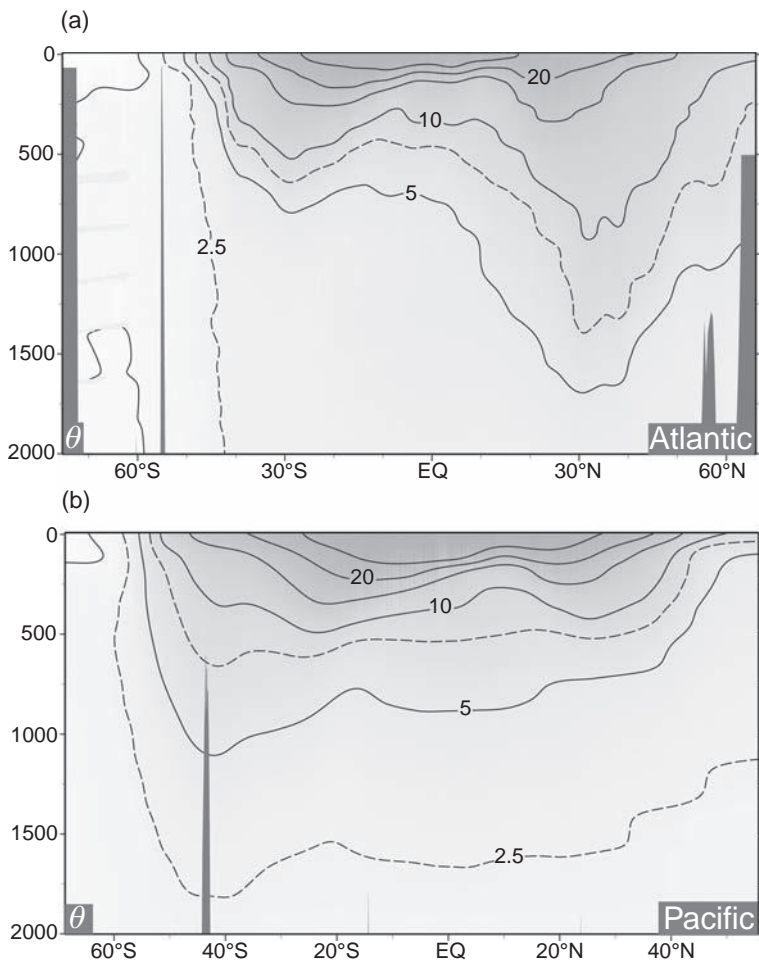


Figure 8.7 Observed meridional section of potential temperature ($^{\circ}\text{C}$) over the upper 2 km through (a) the Atlantic along 20°W , and (b) the Pacific along 170°W ; see Plates 2a and 3a. There is an upper layer of warm water with a strong vertical temperature gradient overlying the colder deep waters. This thermocline is thick over the subtropical gyres (centred at 30°N and 30°S), and thin over the equator and the subpolar gyres.

8.2.1 What is the structure and transport of the Gulf Stream?

The Gulf Stream flows northward between Florida Straits and Cape Hatteras as a western boundary current, then leaves the coast near 36°N , moving from the shelf into deeper water, and continues eastward as a separated jet into the ocean interior. At the surface, the Gulf Stream is apparent as a plume of warm waters, emanating from the tropics, running along the western boundary, then separating from the coast and meandering within the interior of the basin (Fig. 8.8). This plume is much warmer than the colder water to the north and even slightly warmer than waters immediately to the south. This warm signal is gradually eroded at the surface by intense surface heat loss to the atmosphere, especially during winter, and

horizontal exchange with the surrounding cooler waters.

Below the surface, the Gulf Stream is coincident with strong horizontal temperature and density gradients (Fig. 8.9a). These horizontal gradients reflect the northward shoaling and eventual outcropping of the main thermocline.

The Gulf Stream has large horizontal velocities, exceeding 1 m s^{-1} when averaged in a streamwise coordinate (Fig. 8.9b), such that an average is taken following any meanders of the current. This strong current is dynamically unstable. Meanders progressively develop, downstream, some of which amplify and break away forming eddies: meanders pinching off to the north form eddies with a warm core and an anticyclonic circulation, while those pinching off to the

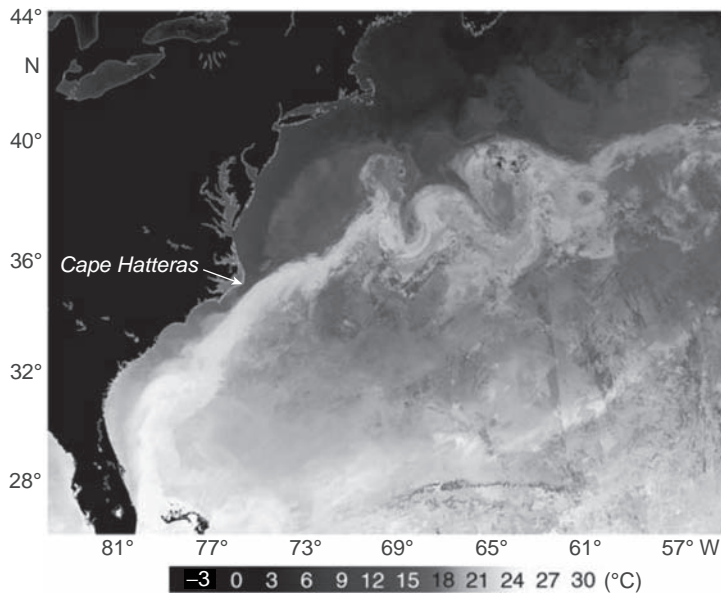


Figure 8.8 Remotely sensed image of sea-surface temperature (warm is light, cold is dark) from 13 to 21 May 2006 over the North Atlantic. The core of the Gulf Stream is apparent as the plume of warmest waters, leaving the coast at Cape Hatteras, and spreading into the interior of the basin. Details and processing as in Fig. 1.7.

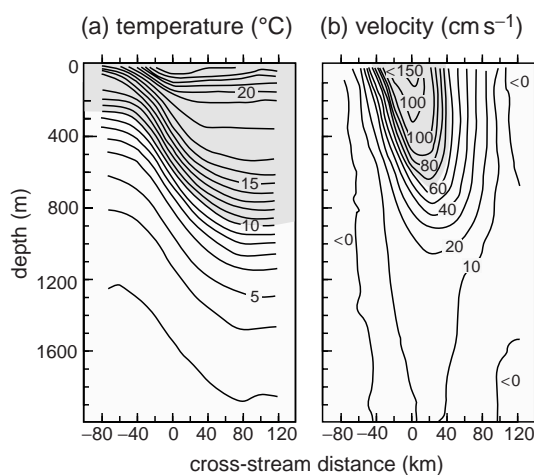


Figure 8.9 Cross-sections of (a) temperature ($^{\circ}\text{C}$), and (b) downstream velocity (cm s^{-1}) of the Gulf Stream, calculated along a transect crossing the stream east of Cape Hatteras at 73°W . This time-mean estimate is based upon 16 sections taken between September 1980 and May 1983 using a coordinate system following the centre of the stream. Redrawn from Halkin and Rossby (1985).

south form eddies with a cold core and a cyclonic circulation.

Despite this eddy formation and exchange, the Gulf Stream still retains its coherence after leaving the coast for several thousands of kilometres into the interior, as seen in the sea-surface temper-

ature signal in Fig. 8.8. Hence, the separated Gulf Stream can be viewed as a boundary current separating different water masses in the subtropical and subpolar gyres.

What is the transport of the Gulf Stream?

The Gulf Stream increases in transport from about 30 Sv off Florida to about 85 Sv when the current leaves the coast at Cape Hatteras, and increases further to 150 Sv south of Nova Scotia. This enhancement of the transport is associated with two localised recirculating gyres on either flank of the separated Gulf Stream: an anticyclonic recirculation to the south and a cyclonic recirculation to the north, between 55° and 70°W , as depicted in Fig. 8.10.

Following this observational view of gyres and boundary currents, we next consider why these phenomena form.

8.3 A theoretical view of ocean gyres and boundary currents

While ocean gyres are broadly forced by the atmospheric winds, the detailed response is rather unintuitive and depends on how fluid moves within a basin on the rotating, spherical

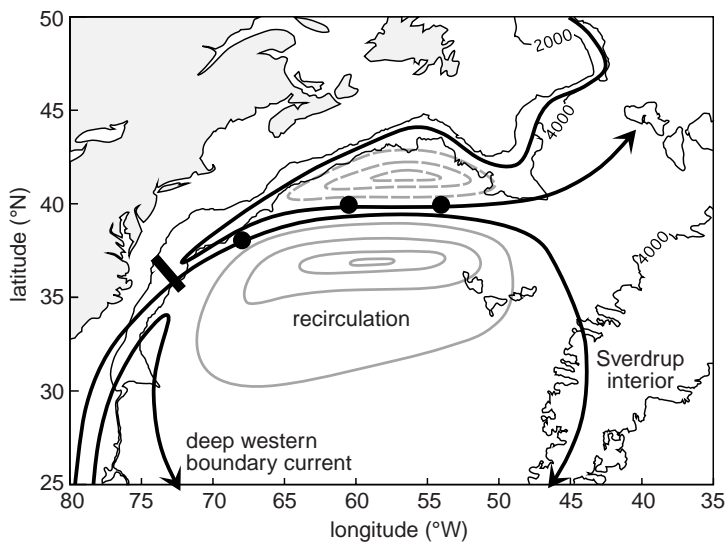


Figure 8.10 Schematic chart showing the average surface-to-bottom transport of the Gulf Stream and flanking recirculating gyres (grey lines; dashed for cyclonic, full for anticyclonic) with each contour representing 15 Sv. The three dots and line in the Stream mark locations where moored current meter arrays provide long-term measurements, and the fine contours mark depths of 2000 m and 4000 m. The depth-integrated pathways (black) include the wind-driven Sverdrup interior circulation, the recirculating gyres on either side of the Gulf Stream and the deep western boundary current (which lies further east along the continental slope). Redrawn from Hogg (1992).

Earth. To understand the detailed response, the spin of the fluid or its vorticity needs to be considered.

8.3.1 What is vorticity?

The vorticity measures the rate at which an object or fluid rotates about its own axis, where by definition the vorticity is positive for a cyclonic flow, rotating in the same sense as the Earth's rotation. For a spinning solid object, like a spinning top, the vorticity is simply twice the angular velocity, the rate at which the object rotates. For a more complicated flow, the sign of the vorticity can be understood by the direction a 'paddle wheel' would rotate when inserted into the flow. For example, in an eastward jet, the vorticity is positive on the northern side of the jet where the 'paddle wheel' rotates cyclonically and negative on the southern side where the 'paddle wheel' rotates anticyclonically, as illustrated in Fig. 8.11a.

How is vorticity defined on the rotating Earth?

On the rotating Earth, it is simplest to consider the vorticity associated with the spin around an axis perpendicular to the surface of the Earth. The vorticity of the fluid is due to the rotation of the fluid as seen from space. This vorticity, q , can be separated into components referred to as the relative vorticity, ζ , measuring how the fluid rotates relative to the solid Earth, and the planetary vor-

ticity, f , measuring how rapidly the solid Earth rotates:

$$q = \zeta + f. \quad (8.3)$$

The relative vorticity is formally defined by $\zeta = \partial v / \partial x - \partial u / \partial y$, where u and v are the eastward and northward velocities in the eastwards and northwards directions, x and y , respectively.

The planetary vorticity is twice the angular velocity of the solid Earth, which at the North Pole is given by 2Ω . Elsewhere, the components of the angular velocity and planetary vorticity normal to the surface Earth vary from that at the North Pole by a factor $\sin \phi$, where ϕ is the latitude (Fig. 8.11b). The sense of rotation, as measured by the angular velocity and planetary vorticity, relative to a normal vector (pointing outward from the Earth's surface), changes from being cyclonic and strongly positive at the North Pole, to zero at the equator and anticyclonic and strongly negative at the South Pole, as depicted in Fig. 8.11c.

Analogy with a spinning top

As a starting point, the rotation of ocean gyres can be thought of in a similar manner to a spinning top. If you spin a top, your fingers impart a twisting force or torque which spins up the object and supplies vorticity to the top. Friction acts against this motion and provides an opposing torque,

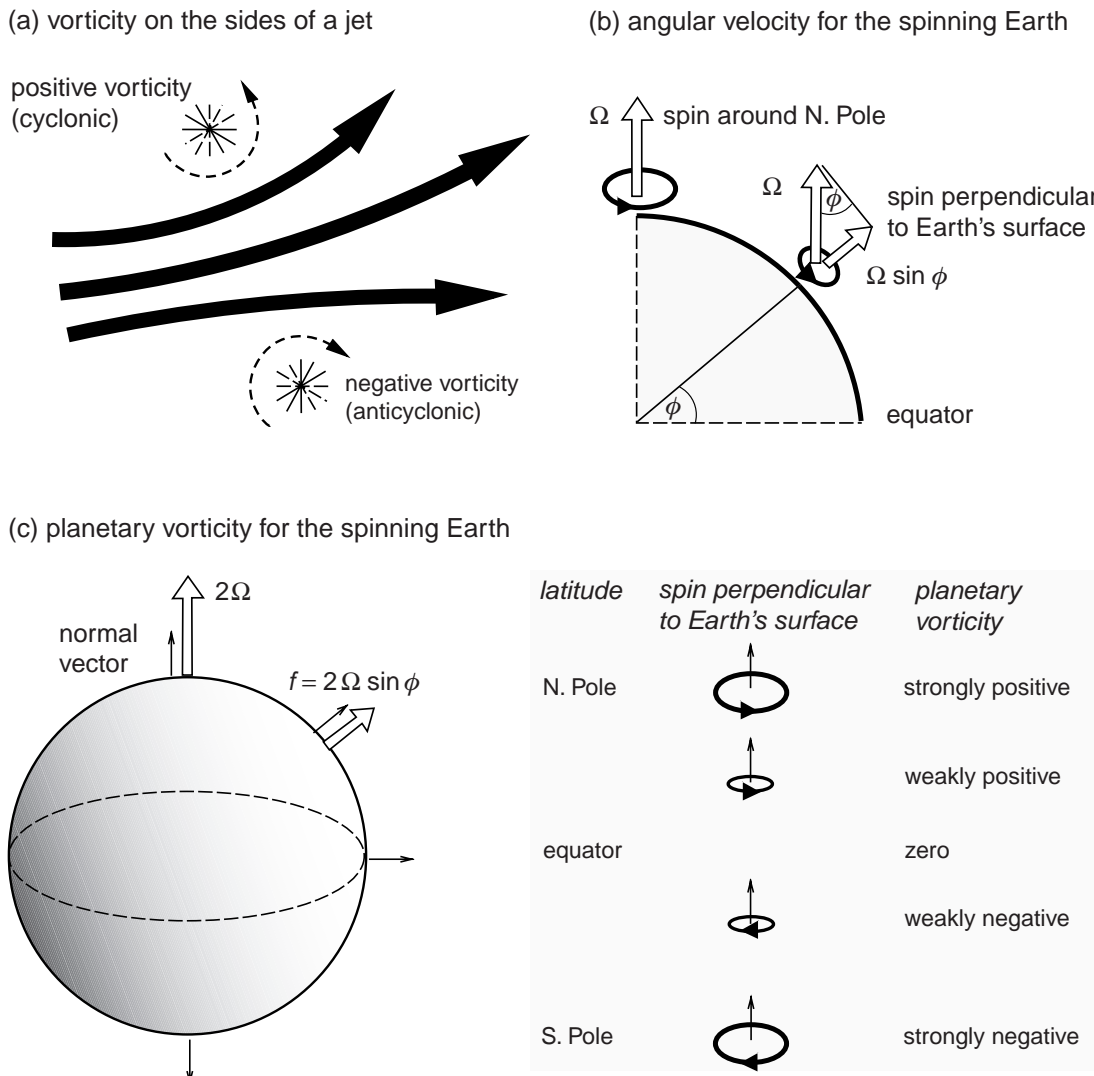


Figure 8.11 A schematic figure of (a) a current flow (thick lines) with positive (cyclonic) and negative (anticyclonic) vorticity on either side of the jet, as depicted by rotation (thin lines) of a hypothetical 'paddle wheel'; (b) angular velocity Ω over the spinning Earth, a vertical vector which has a component perpendicular to the surface of the Earth given by $\Omega \sin \phi$, where ϕ is the latitude, and a sense of rotation marked by the curved arrows; (c) planetary vorticity over the spherical Earth given by twice the angular velocity vector, 2Ω , which has a component perpendicular to the surface of the Earth, $f = 2\Omega \sin \phi$ (thick arrow). The spin around the normal vector (thin arrow) is given by the circles. The planetary vorticity and the sense of rotation around the normal vector changes from strongly positive at the North Pole, to 0 at the equator and strongly negative at the South Pole.

dissipating the vorticity and, in the absence of further inputs of vorticity, the top eventually ceases spinning. In a similar manner for the ocean, the pattern of atmospheric winds imparts vorticity, spinning up the subtropical and subpolar gyres, while friction provides an opposing torque acting to spin the gyres down.

There is a crucial difference, though, between a spinning top and spinning fluid. A fluid can move from one region to another region leading to a *redistribution* of vorticity. For the spinning top, at a steady state, there is an overall balance between the torque imparted by your fingers acting to increase the spin of the top

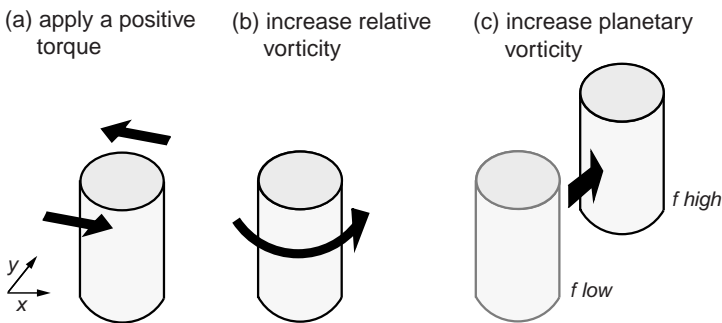


Figure 8.12 A schematic figure showing how (a) a fluid column responds to a vorticity input, either through (b) an increase in its local spin or relative vorticity, or (c) moving to a more northern latitude where the planetary vorticity f is larger.

and the opposing effect of friction to reduce the spin of the top. For the ocean, there is a similar overall balance, in that the overall input of vorticity from the wind has to balance an overall loss of vorticity from friction. However, this overall balance need not apply *locally* for the ocean: there is an input of vorticity from the wind making the ocean rotate, then this vorticity is redistributed within the ocean by the movement of water columns, and finally this vorticity is dissipated in a different location through the action of friction.

8.3.2 How does the ocean respond to an input of vorticity?

If there is a positive input of vorticity to the ocean, the absolute vorticity, q , has to increase either by an increase in relative vorticity, ζ , or by an increase in planetary vorticity, f (Fig. 8.12). An increase in ζ is associated with the fluid locally spinning more in a cyclonic sense, while an increase in f is associated with fluid moving to a more northern latitude. Conversely, a negative input of vorticity leads to the absolute vorticity decrease, with fluid either spinning in a more anticyclonic manner or moving to a more southern latitude.

How a fluid changes its vorticity when there is an input of vorticity, whether ζ or f alter, depends on the velocity and length scales of the problem. The key issue is how the rate of change of relative vorticity, $D\zeta/Dt$, compares with the rate of change of planetary vorticity, Df/Dt , following a moving water column as given by the ratio

$$\frac{D\zeta}{Dt} / \frac{Df}{Dt};$$

this non-dimensional quantity is analogous to a Rossby number, $Ro = \zeta/f$, but now refers to the ratio of rates of change of relative vorticity and planetary vorticity. This ratio can be estimated by scale analysis, where the magnitude of each term is crudely estimated: u and v are assumed to have a magnitude U , $\zeta = \partial v/\partial x - \partial u/\partial y$ a magnitude U/L , the advective rate of change is assumed $D/Dt \sim U/L$, so that $D\zeta/Dt \sim U^2/L^2$ and $Df/Dt \equiv \beta v \sim \beta U$. Applying these scales, then the ratio of the advection of relative vorticity and advection of planetary vorticity is given by

$$\frac{D\zeta}{Dt} / \frac{Df}{Dt} \sim \frac{U}{\beta L^2}. \quad (8.4)$$

Now consider two different regimes for this ratio (8.4): the frontal scale where $L \sim 10$ km and $U \sim 0.1 \text{ m s}^{-1}$ versus the basin scale where $L \sim 1000$ km and $U \sim 0.01 \text{ m s}^{-1}$, and assume mid-latitude values for β of $10^{-11} \text{ m}^{-1} \text{ s}^{-1}$. On the frontal scale, $U/(\beta L^2) \sim (0.1/(10^{-11}(10^4)^2)) = 10^2$. Hence, the rate of change in relative vorticity is much larger than the rate of change of planetary vorticity, which suggests that an input of positive vorticity leads to a water column locally spinning and increasing ζ , consistent with our intuition, as depicted in Fig. 8.12b.

On the basin scale, the larger length scale and smaller velocity instead leads to $U/(\beta L^2) \sim (10^{-2}/(10^{-11}(10^6)^2)) = 10^{-3}$. Hence, the rate of change in relative vorticity is small compared with the rate of change in planetary vorticity. This result is surprising and counterintuitive: an input of positive vorticity leads to a water column moving northward and increasing its planetary vorticity, f , as depicted in Fig. 8.12c, rather than locally increasing its rotation.

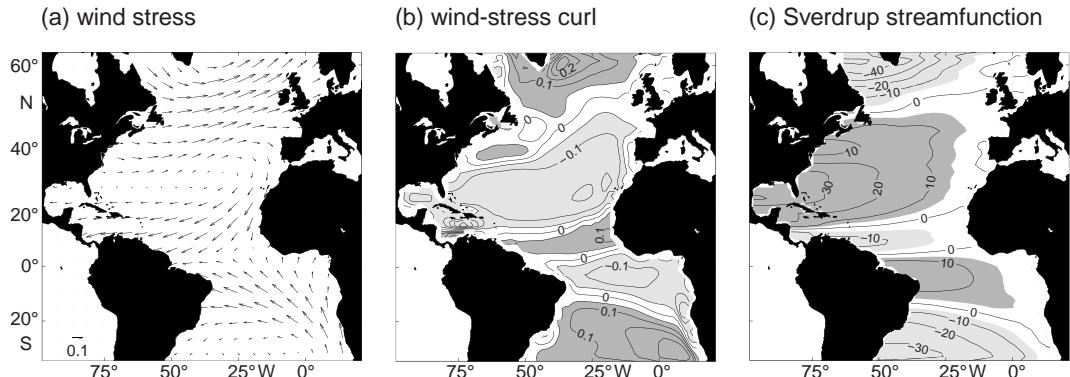


Figure 8.13 Sverdrup diagnostics for the North Atlantic: (a) wind stress vectors (reference arrow is for 0.1 N m^{-2}); (b) wind-stress curl (10^{-6} N m^{-3}); and (c) horizontal streamfunction ($1 \text{ Sv} \equiv 10^6 \text{ m}^3 \text{ s}^{-1}$) for the depth-integrated flow, assuming a Sverdrup balance (8.5) and $\partial\psi/\partial x \equiv \int_{-H}^0 v dz$. The pattern of atmospheric winds provides an anticyclonic torque over the subtropical gyre and an associated anticyclonic interior transport. The diagnostics are made using an annual-mean wind stress from the European Weather Centre ERA40 climatology.

This result turns out to be central in understanding why the ocean circulates in gyres and western boundary currents form. Now exploiting this large-scale response, we consider the effect of the winds' input of vorticity over a basin.

8.3.3 Sverdrup balance

Over the interior of ocean basins, the large-scale pattern of winds provide inputs of positive and negative vorticity over the ocean basins (Figs 8.13a and 8.14a, grey arrows). The input of positive vorticity again leads to a water column moving northward over the interior of the basin and an input of negative vorticity to a southward movement (Fig. 8.14a, black arrows). This relationship is formally expressed by the connection between the depth-integrated change in planetary vorticity and the twisting acceleration from the surface winds (Box 8.1),

$$\underbrace{\int_{-H}^0 \frac{Df}{Dt} dz}_{\text{depth-integrated change in planetary vorticity}} = \beta \int_{-H}^0 v dz = \underbrace{\frac{1}{\rho_0} \left(\frac{\partial \tau_y^s}{\partial x} - \frac{\partial \tau_x^s}{\partial y} \right)}_{\text{twisting acceleration from wind}}, \quad (8.5)$$

the depth of the ocean (m), τ^s is the surface wind stress (N m^{-2}) and the subscripts x and y denote the eastward and northward components.

What is the typical magnitude of the transport?

For the North Atlantic, the wind stress is typically 0.1 N m^{-2} from the westerlies at 45°N and -0.1 N m^{-2} in the easterly Trade winds at 15°N (Fig. 8.13a). This meridional contrast in wind stress leads to a clockwise torque and a negative vorticity input being applied to the subtropical gyre, with $\frac{\partial \tau_y^s}{\partial x} - \frac{\partial \tau_x^s}{\partial y}$, reaching $-0.1 \times 10^{-6} \text{ N m}^{-3}$ (Fig. 8.13b). Applying a zonal integral of (8.5) over the width of the basin, L , and dividing by β then estimates the meridional transport ($\text{m}^3 \text{ s}^{-1}$),

$$\begin{aligned} & \int_0^L \int_{-H}^0 v dz dx \\ &= \frac{L_x}{\beta \rho_0} \left(\frac{\partial \tau_y^s}{\partial x} - \frac{\partial \tau_x^s}{\partial y} \right) \\ &\sim \frac{3 \times 10^6 \text{ m} \times -0.1 \times 10^{-6} \text{ N m}^{-3}}{10^{-11} \text{ m}^{-1} \text{ s}^{-1} \times 10^3 \text{ kg m}^{-3}} \\ &\sim -30 \times 10^6 \text{ m}^3 \text{ s}^{-1}, \end{aligned}$$

as established by Sverdrup (1947) and referred to as Sverdrup balance; β is the meridional gradient in planetary vorticity ($\text{m}^{-1} \text{ s}^{-1}$), $\int_{-H}^0 v dz$ is the depth-integrated meridional velocity ($\text{m}^2 \text{ s}^{-1}$), H is

the negative sign indicating a southward transport, in accord with the diagnostics presented in Fig. 8.13c. If this transport is carried over the upper 1 km of the ocean and the basin is 3000 km

Box 8.1 | Sverdrup balance for meridional transport

Consider the horizontal momentum equations for the large-scale interior flow. On the large scale over the open ocean, the Rossby number is small, $Ro = U/(fL) \ll 1$, such that the temporal acceleration and advection of velocity terms are very small compared with the Coriolis acceleration. Consequently, the horizontal momentum equations reduce to a three-way balance between the Coriolis acceleration, the horizontal pressure gradient and the frictional acceleration:

$$-fv = -\frac{1}{\rho_0} \frac{\partial P}{\partial x} + \frac{1}{\rho_0} \frac{\partial \tau_x}{\partial z}, \quad (8.6)$$

$$fu = -\frac{1}{\rho_0} \frac{\partial P}{\partial y} + \frac{1}{\rho_0} \frac{\partial \tau_y}{\partial z}. \quad (8.7)$$

On the large scale, the continuity equation is given by

$$\frac{\partial u}{\partial x} + \frac{\partial v}{\partial y} + \frac{\partial w}{\partial z} = 0. \quad (8.8)$$

In order to focus on the large-scale response, it is important to recognise that the Coriolis parameter varies with y and not x , represented by $\beta \equiv df/dy$ and $df/dx = 0$. Then, applying $\partial/\partial x$ (8.7) $- \partial/\partial y$ (8.6) eliminates the pressure gradient term, and combining with (8.8) gives

$$\beta v = f \frac{\partial w}{\partial z} + \frac{1}{\rho_0} \left(\frac{\partial}{\partial x} \frac{\partial \tau_y}{\partial z} - \frac{\partial}{\partial y} \frac{\partial \tau_x}{\partial z} \right), \quad (8.9)$$

then rearranging the order of the differentiation of the stress term (using $\frac{\partial}{\partial x} \left(\frac{\partial A}{\partial z} \right) \equiv \frac{\partial}{\partial z} \left(\frac{\partial A}{\partial x} \right)$ where A is an arbitrary variable) gives the linear vorticity balance,

$$\beta v = f \frac{\partial w}{\partial z} + \frac{1}{\rho_0} \frac{\partial}{\partial z} \left(\frac{\partial \tau_y}{\partial x} - \frac{\partial \tau_x}{\partial y} \right), \quad (8.10)$$

which is used later in the extensions of the gyre theory. Integrating with depth over the water column, assuming $w = 0$ at the sea surface and at the sea floor, and neglecting the stress on the bottom leads to (8.10) becoming the Sverdrup balance,

$$\beta \int_{-H}^0 v dz = \frac{1}{\rho_0} \left(\frac{\partial \tau_y^s}{\partial x} - \frac{\partial \tau_x^s}{\partial y} \right), \quad (8.11)$$

which represents how the twisting acceleration from the wind stress leads to water columns moving meridionally and changing their planetary vorticity; here τ_x^s and τ_y^s denote the eastward and northward components of the wind stress. While the Sverdrup balance provides a key part of gyre theory, the neglect of w on the sea floor can become problematic; see later extension including w on the sea floor in Box 8.3.

wide, then the typical size of the interior velocity is 1 cm s^{-1} .

8.3.4 How is the gyre circulation completed?

In order for there to be a closed circulation, the meridional transport of fluid over the interior

of ocean basins needs to be returned somehow. Since the previous arguments focussed on the gyre response on the large scale (typically 1000 km or more), we expect these arguments to break down on the fine scale (typically 100 km or less) and, thus, the return flow to occur within narrow boundary layers.

There should be a poleward return current in the subtropical gyre and an equatorward return current in the subpolar gyre. However, it is unclear whether the narrow boundary current might occur on the western or eastern side of the ocean basin.

Intuitively, one can guess the correct response. Consider a subtropical gyre where the circulation is driven by the westerly winds at mid latitudes and the easterly winds at low latitudes. The gyre is expected to rotate in the same sense as the torque applied by the winds, rotating anticyclonically. If the interior transport is returned poleward in an eastern boundary, the overall circulation in the gyre is cyclonic, in the opposite sense to the torque provided by the winds. On the other hand, if the interior transport is returned poleward in a western boundary, the overall circulation in the gyre is anticyclonic, in the same sense as the torque applied by the winds. Obviously, this latter result is the more plausible answer. Now we consider a more formal explanation.

Vorticity argument and Stommel model

The pattern of winds provides a basin-scale input of vorticity, which has to be dissipated by friction somewhere for a steady state to be attained. For example, for a subtropical gyre in the northern hemisphere, the winds provide a negative input of vorticity, as depicted by the grey arrow in Fig. 8.14a. The friction from the sidewalls is always acting to decelerate the strong currents along the boundaries. If the boundary current is on the western side of the subtropical gyre, friction then provides an input of positive vorticity, as depicted by the grey arrow in Fig. 8.14b. Alternatively, if (unrealistically) the boundary current is on the eastern side, then friction provides a negative input of vorticity, as depicted in Fig. 8.14c. Hence, the negative input of vorticity from the winds is only offset by friction if the boundary current is on the western boundary, rather than the eastern boundary. Again, the sense of rotation of the gyre circulation is then in accord with the torque applied by the winds.

This vorticity argument was first made in a famous study by Stommel (1948). He examined the circulation in a subtropical gyre driven by winds in a rectangular box in three idealised thought

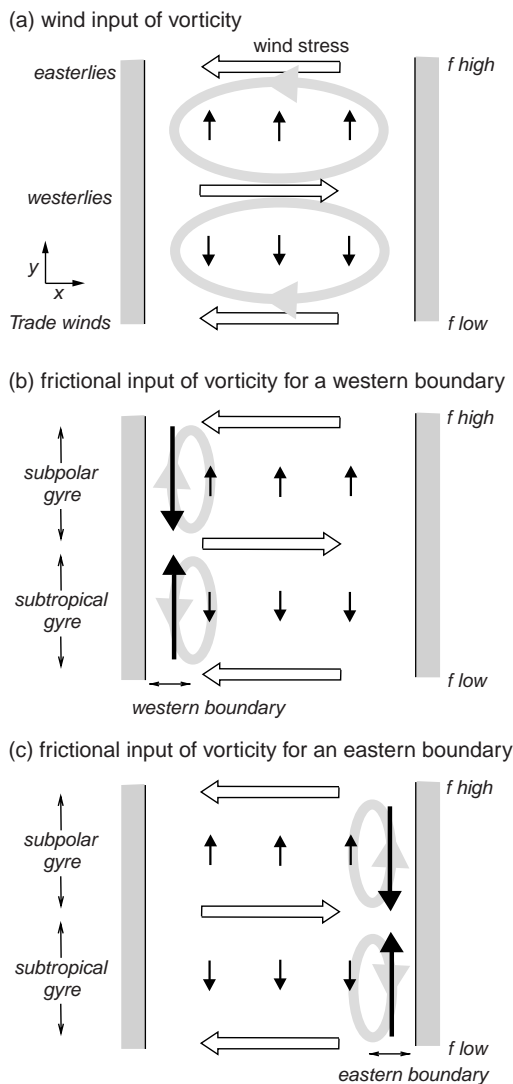


Figure 8.14 A schematic view of (a) a pair of wind-forced subtropical and subpolar gyres in the northern hemisphere together with the wind stress (white arrows), interior circulation response (black arrows) and sense of vorticity input (grey arrows). In (b), the interior flow is returned within a narrow boundary (long black arrows) along the western boundary. Within the subtropical gyre, this boundary flow has a negative relative vorticity (from the gradient in the black arrows). Friction (grey arrows) acts to dissipate the vorticity of the boundary current and, thus, leads to a positive input of vorticity here, which can then oppose the wind input of vorticity. In contrast, if the boundary current is in the eastern boundary as in (c), then frictional dissipation of the boundary current provides a negative input of vorticity here, which is the same sign as the wind input of vorticity, and thus cannot provide a steady-state solution.

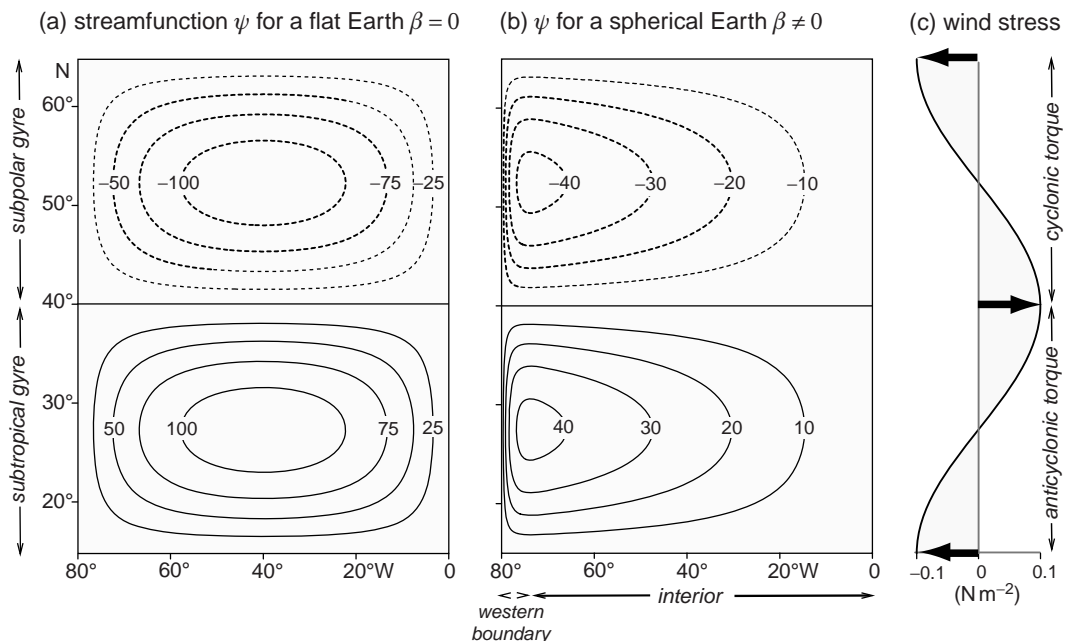


Figure 8.15 Model illustration of why there is western intensification in an ocean basin: the transport streamfunction, ψ ($\text{Sv} = 10^6 \text{ m}^3 \text{ s}^{-1}$), in a rectangular basin incorporating wind forcing and bottom friction for either (a) a flat Earth with $\beta = 0$, or (b) for a spherical Earth with $\beta \neq 0$, together in (c) with the imposed wind stress, τ (N m^{-2}). The winds impart a cyclonic torque on the northern half of the basin and an anticyclonic torque on the southern half, defining the location of the subpolar and subtropical gyres, respectively. In (a), the streamfunction is symmetric with longitude, with $\beta = 0$, but in (b) acquires a western intensification and a strong boundary current, with $\beta \neq 0$ in both gyres. The analytical solutions are for the Stommel (1948) model, extended to a double gyre (supplied by Vassil Roussenov).

experiments: (i) no rotation with the planetary vorticity, $f = 0$; (ii) a rotating ocean with constant f and $\beta = df/dy = 0$, appropriate for a flat Earth, and (iii) a rotating ocean with a variable f and non-zero β , appropriate for a spherical Earth.

In the case of no rotation, the winds simply drive a symmetric circulation, just as you might expect from stirring a tea cup. In the case of constant f , the solution is much the same; there is again a symmetric solution, fluid rotating cyclonically in a subpolar gyre and anticyclonically in a subtropical gyre without any western intensification, as depicted in Fig. 8.15a. However, in the case of variable f , appropriate for a rotating, spherical Earth, a different response occurs: the interior flow is directed equatorward in the subtropical gyre, in accord with Sverdrup balance (8.5), and the poleward return flow is concentrated in a narrow, western boundary current, as depicted in Fig. 8.15b. This response equally applies for a subpolar gyre and for either hemisphere.

Hence, western intensification requires the Earth to be a spinning sphere with planetary vorticity varying with latitude, referred to as the ' β effect'; see a more formal explanation in Box 8.2.

While this gyre theory has provided an explanation of western intensification, the theory has so far ignored the interaction of the flow with bottom topography, which is discussed next.

8.3.5 The effect of a sloping sea floor on the gyre circulation

There are significant variations in bottom topography over the ocean. One might expect that the gyre circulation would move around any topographical features, but this does not turn out to be the case over much of the ocean.

For example, over the North Atlantic subtropical gyre in Fig. 8.16, the dynamic height contours are not deflected by the presence of the

Box 8.2 | Stommel model

The Stommel solutions depicted in Fig. 8.15 can be understood by extending the derivation of the Sverdrup balance to include a bottom stress (τ_x^b , τ_y^b), such that a depth integral of (8.10) for a homogeneous fluid of constant density with a thickness H is given by

$$\beta \int_{-H}^0 v dz = \beta v H = \frac{1}{\rho_0} \left(\frac{\partial \tau_y^s}{\partial x} - \frac{\partial \tau_x^s}{\partial y} \right) - \frac{1}{\rho_0} \left(\frac{\partial \tau_y^b}{\partial x} - \frac{\partial \tau_x^b}{\partial y} \right). \quad (8.12)$$

This relationship can be re-expressed by assuming that the bottom stress depends on the velocity, such that $\tau_x^b = -\rho_0 H r u$ and $\tau_y^b = -\rho_0 H r v$, where r^{-1} represents the timescale for the flow to spin down, leading to

$$\underbrace{\frac{Df}{Dt}}_{\begin{array}{l} \text{change in} \\ \text{planetary vorticity} \end{array}} = \underbrace{\frac{1}{\rho_0 H} \left(\frac{\partial \tau_y^s}{\partial x} - \frac{\partial \tau_x^s}{\partial y} \right)}_{\begin{array}{l} \text{wind input} \\ \text{of vorticity} \end{array}} - \underbrace{r \zeta}_{\begin{array}{l} \text{frictional dissipation} \\ \text{of vorticity} \end{array}}. \quad (8.13)$$

The wind input of vorticity is from the twisting acceleration of the wind, while the dissipation of vorticity is from the frictional effect of the sea floor (referred to as a bottom drag). In the experiments with no rotation or constant f , $\beta = df/dy = 0$, so that the input of vorticity from the wind simply balances the opposing frictional dissipation everywhere (the two right-hand terms in (8.13) balance), leading to symmetric solutions.

In the case of variable f , $\beta = df/dy \neq 0$, appropriate for a rotating, spherical Earth, there are different balances in (8.13) for the interior and western boundary. Over most of the basin, fluid moves to a different latitude driven by the wind forcing, where fluid columns change their planetary vorticity from the input of vorticity from the wind (the left-hand and first right-hand terms balancing in (8.13)). The fluid columns return to their original latitude within a narrow western boundary, where their change in planetary vorticity is achieved by a frictional dissipation providing an input of cyclonic vorticity (the left-hand and second right-hand terms balancing in (8.13)).

Hence, the asymmetry between the western boundary and the interior results from the presence of β , reflecting the Earth as a rotating sphere. These balances are modified when topography is included, but the controlling role of β remains the same.

mid-Atlantic ridge, although there is more of an effect of the topography in the subpolar gyre. This general lack of a steering of the surface flow by the bottom topography is due to the presence of the strong thermocline and pycnocline (Fig. 8.7), leading to the gyre flow rapidly weakening with depth and having a weak bottom flow. The one exception to this weak interaction between the gyre circulation and the topography is along the topographical slope running around the continental barriers.

Now consider how water columns are forced meridionally along a topographical slope, which is represented by sloping sidewalls. If a water column stretches in the vertical, the water column increases its vorticity, $\zeta + f$ (Fig. 8.17a,b). This response occurs through conservation of potential vorticity, $Q = (\zeta + f)/h$, where h is a depth scale representing the thickness of the water column for an unstratified fluid or the vertical spacing between two potential density surfaces. The increase in $\zeta + f$ can again occur in two

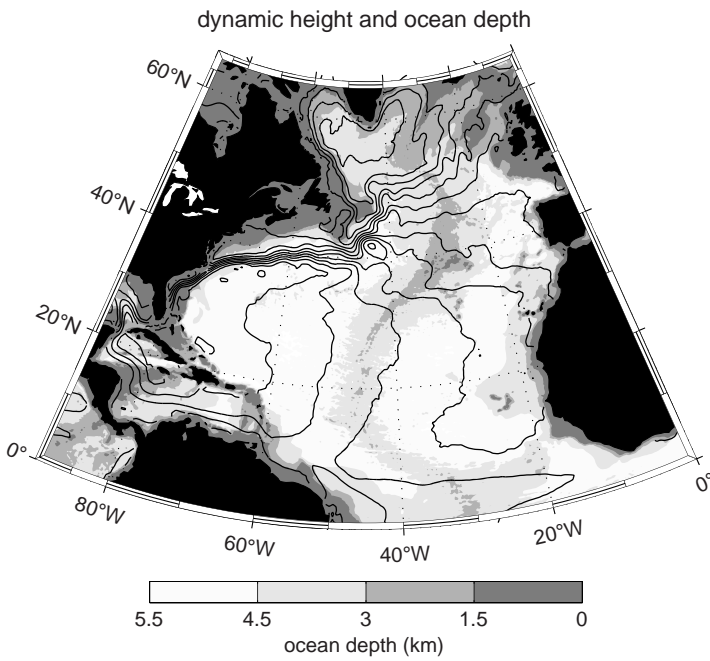
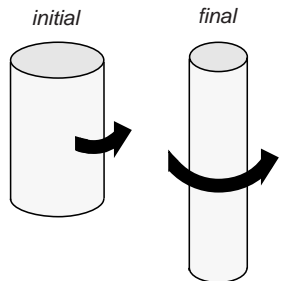
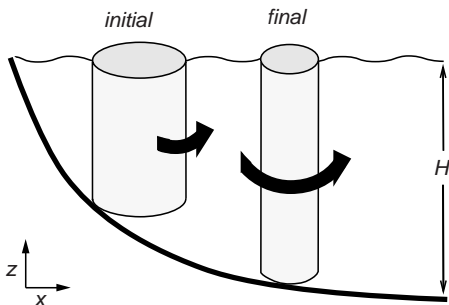


Figure 8.16 Ocean mean dynamic height (cm; contours every 10 cm) and ocean depth (km, shaded) for the North Atlantic. The surface flow does not appear to reflect the underlying topography over the mid latitudes, although there is a closer correspondence between the dynamic height contours and the ocean depth over the subpolar gyre. Details for dynamic height as in Fig. 8.2.

(a) stretching of a spinning fluid column



(b) column moving off the slope



(c) double gyre with sloping sidewalls

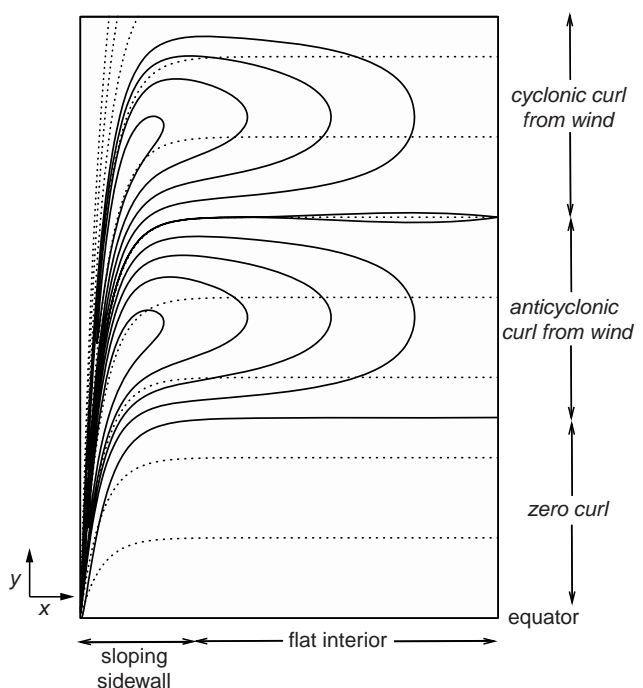


Figure 8.17 A schematic figure showing (a) an initially spinning water column, which spins faster if there is vertical stretching, a response which is directly analogous to how a spinning ice skater rotates faster when she pulls her arms in; and (b) a water column is stretched by moving from the slope into deeper water. In addition, analytical solutions (c) for the interior streamfunction, ψ (full lines) and the f/H contours (dotted lines) for a homogeneous fluid with a double gyre and a sloping sidewall on the western boundary. Along the sloping sidewall, the f/H contours (dotted lines) converge towards the equator, rather than follow latitude circles. The streamfunction pattern closely follows the f/H contours along the western boundary and, in this analytical model, crosses the f/H contours in the southwest corner of the model towards the equator. From Laura Jackson; see Salmon (1998) and Jackson et al. (2006) for further details.

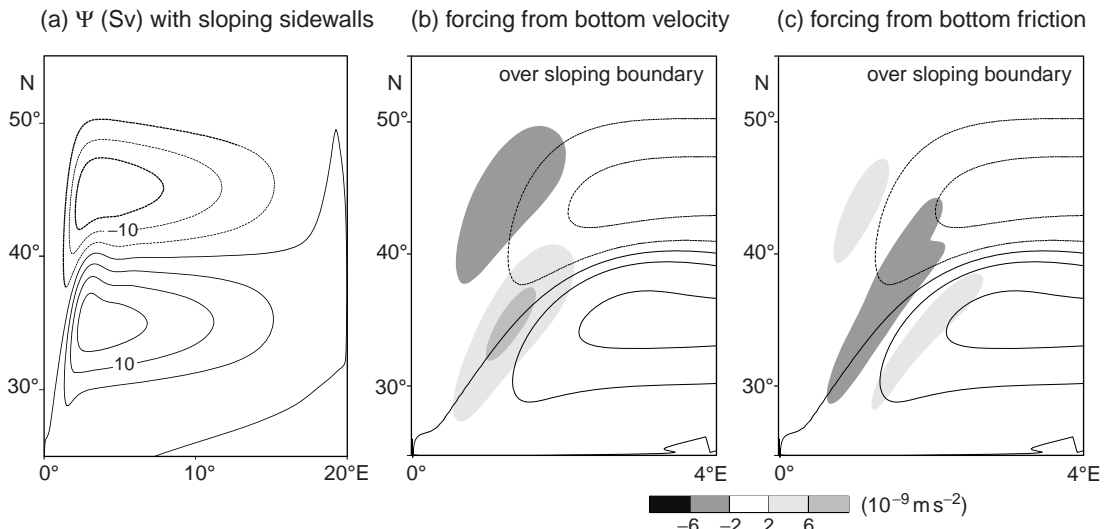


Figure 8.18 Numerical model solutions for an idealised double gyre with sloping sidewalls: (a) the streamfunction, Ψ ($10^6 \text{ m}^3 \text{ s}^{-1} \equiv 1 \text{ Sv}$), over the entire domain, together with maps over the western boundary depicting (b) the forcing from the vertical velocity on the sea floor (also referred to as bottom-pressure torque), evaluated above the base of the bottom Ekman layer, $-f w_b$ (10^{-9} m s^{-2} , shading), and (c) the twisting acceleration from bottom drag, $-\frac{1}{\rho_0} \left(\frac{\partial \tau_y^b}{\partial x} - \frac{\partial \tau_x^b}{\partial y} \right)$ (10^{-9} m s^{-2} , shading) together with Ψ (contours). From Laura Jackson; see Jackson et al. (2006).

different ways: on the small scale, the water column locally spins faster and increases its relative vorticity, ζ , while on the basin scale the water column moves poleward and increases the magnitude of its planetary vorticity, f .

Hence, on the basin scale, whenever a water column moves from the slope into deeper water, the water column becomes stretched in the vertical and moves poleward to a larger magnitude of planetary vorticity. This response then leads to a water column preferentially moving along f/H contours (Fig. 8.17c, dotted contours), where f is the planetary vorticity and H is the thickness of the water column,

$$\frac{f_2}{H_2} = \frac{f_1}{H_1}, \quad (8.14)$$

such that the new value of the planetary vorticity f_2 is given by the old value, f_1 , modulated by the thickness change H_2/H_1 .

For a basin with a uniform thickness and vertical sidewalls, f/H contours simply follow latitude circles. Water columns move meridionally across f contours only when there is a twisting acceleration either from the wind stress or bottom drag, as previously depicted in the Stommel solution (Fig. 8.15).

For a basin with sloping sidewalls, f/H contours converge towards the equator along the sidewalls (Fig. 8.17c). As fluid moves from shallow to deep along the sloping sidewalls, the water column becomes stretched and so the water column moves poleward to a larger magnitude in f (8.14).

A numerical model assessment of how fluid moves meridionally in a western boundary

When there is a vertical sidewall, there is the classical western intensification for both the subtropical and subpolar gyres (Fig. 8.15b). With a sloping sidewall, there is again a western intensification, but now there is an asymmetry between the subtropical and subpolar gyres (Fig. 8.18a). The western boundary current moves eastward along the slope in the subtropical gyre, while the boundary current in the subpolar gyre moves westward and overshoots the maximum wind-stress line at 40°N . Crucially, the movement of fluid in the boundary current is controlled by the vertical stretching of the water column (Fig. 8.18b), rather than by frictional dissipation (Fig. 8.18c); see Box 8.3 for a more formal explanation.

Box 8.3 | Vorticity balance with sloping topography

Again consider the linear vorticity equation (8.10) with relative vorticity neglected, as previously used in the derivation of (8.5) in the Sverdrup and (8.13) in the Stommel models,

$$\frac{Df}{Dt} = \beta v = f \frac{\partial w}{\partial z} + \frac{l}{\rho_0} \frac{\partial}{\partial z} \left(\frac{\partial \tau_y^s}{\partial x} - \frac{\partial \tau_x^s}{\partial y} \right). \quad (8.15)$$

Integrating with depth for the vertical velocity term (first term on the right) gives

$$\int_{-H}^0 f \frac{\partial w}{\partial z} dz = f (w_s - w_b),$$

where w_s and w_b are the vertical velocities at the sea surface and the bottom respectively (as defined on the interior side of the Ekman boundary layers). The vertical velocity at the sea surface is assumed to be negligible, but the vertical velocity at the sea floor can be significant when the water column varies in thickness. Now integrating all of the terms in (8.15) with depth and only neglecting w_s leads to a general relationship for the meridional volume flux driven by the twisting accelerations from the wind stress and bottom drag, and the vertical stretching of the water column:

$$\underbrace{\beta \int_{-H}^0 v dz}_{\text{depth-integrated change in planetary vorticity}} = \underbrace{\frac{l}{\rho_0} \left(\frac{\partial \tau_y^s}{\partial x} - \frac{\partial \tau_x^s}{\partial y} \right)}_{\text{effect of wind stress}} - \underbrace{\frac{l}{\rho_0} \left(\frac{\partial \tau_y^b}{\partial x} - \frac{\partial \tau_x^b}{\partial y} \right)}_{\text{effect of bottom drag}} - \underbrace{f w_b}_{\text{stretching of water column}}. \quad (8.16)$$

The balance between the meridional volume flux (left-hand term) and the twisting acceleration from the wind stress (first term on the right) is the same as the Sverdrup balance (8.5), while the inclusion of the twisting acceleration from the bottom drag (second term on the right) is equivalent to the Stommel balance (8.13). The new term is the vorticity contribution from the stretching of the water column, $-f w_b$, (also referred to as a bottom-pressure torque).

Now consider a numerical model assessment of how fluid moves meridionally in a western boundary, as depicted in Fig. 8.18. In the western boundary, there is a three-way balance between $\beta \int_{-H}^0 v dz$, the bottom drag, and stretching by the bottom vertical velocity, w_b . The northward transport of the boundary current in the subtropical gyre is achieved by the stretching by the bottom vertical velocity (Fig. 8.18b, light shading), while the bottom drag provides both southward and northward contributions to the transport on the western and eastern sides of the jet respectively (Fig. 8.18c, dark and light shading).

This view of western boundary currents being controlled by the stretching of the water column, rather than by friction, was shown theoretically by Salmon (1998) and demonstrated to hold in general circulation models by Hughes and de Cuevas (2001).

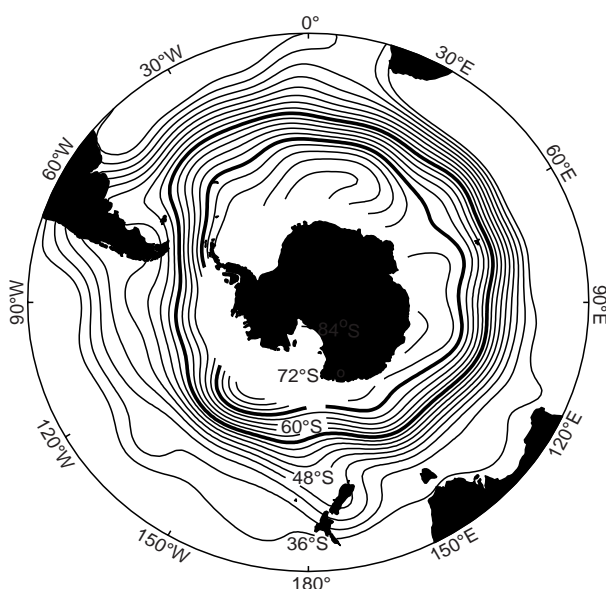
8.3.6 Gyre summary

Gyres are a ubiquitous circulation feature within ocean basins, consisting of a broad interior flow returned in an intense western boundary current. The gyre circulation and western intensification can be understood in several different ways:

- On the basin scale, a wind input of anticyclonic vorticity forces a water column equatorward in a subtropical gyre and, conversely, a wind input of cyclonic vorticity forces a water column poleward in a subpolar gyre.
- This vorticity input from the wind can be offset by dissipation in the western boundary.
- As fluid moves along a sloping sidewall, the water column becomes stretched, leading to the water column moving poleward. This response turns out to be important along western boundaries and can locally be more important than the effects of friction.

The individual circulation patterns of each gyre, depicted in Figs. 8.2 to 8.6, each differ according to the detailed wind forcing, extent of the basin and the bounding near-zonal currents in the equator and Southern Ocean, as well as by forcing by the eddies and interactions with the sea floor.

Next we consider a departure from this gyre view of how the ocean circulates.



8.4 How is the Southern Ocean different to the rest of the globe?

We now consider how the circulation differs in the Southern Ocean, where the Antarctic Circumpolar Current connects the Atlantic, Indian and Pacific basins.

8.4.1 How does the Antarctic Circumpolar Current vary?

The Antarctic Circumpolar Current is described in terms of a series of frontal bands, including the Antarctic Polar Front and Sub-Antarctic Front, encircling the globe, as depicted in Fig. 8.19. The path of the Antarctic Circumpolar Current and these frontal contrasts are affected by the underlying topography (Fig. 8.20): the current has to navigate the mid-Atlantic ridge extending southward towards Antarctica, the mid-Indian ridge running along 50°S in the Indian basin, passing south of Australia and joining the East Pacific ridge, and elevated plateaux, such as Kerguelan, at 80°E, 50°S.

The topography leads to a banded structure in the Antarctic Circumpolar Current, as shown

Figure 8.19 Geostrophic streamlines (thin lines) and approximate positions of the Antarctic Polar Front and the Sub-Antarctic Front (thick lines) where the streamlines are taken from a 4 year time average of dynamic sea-surface height from TOPEX-Poseidon altimetry at 2° resolution. From Ito et al. (2004b).

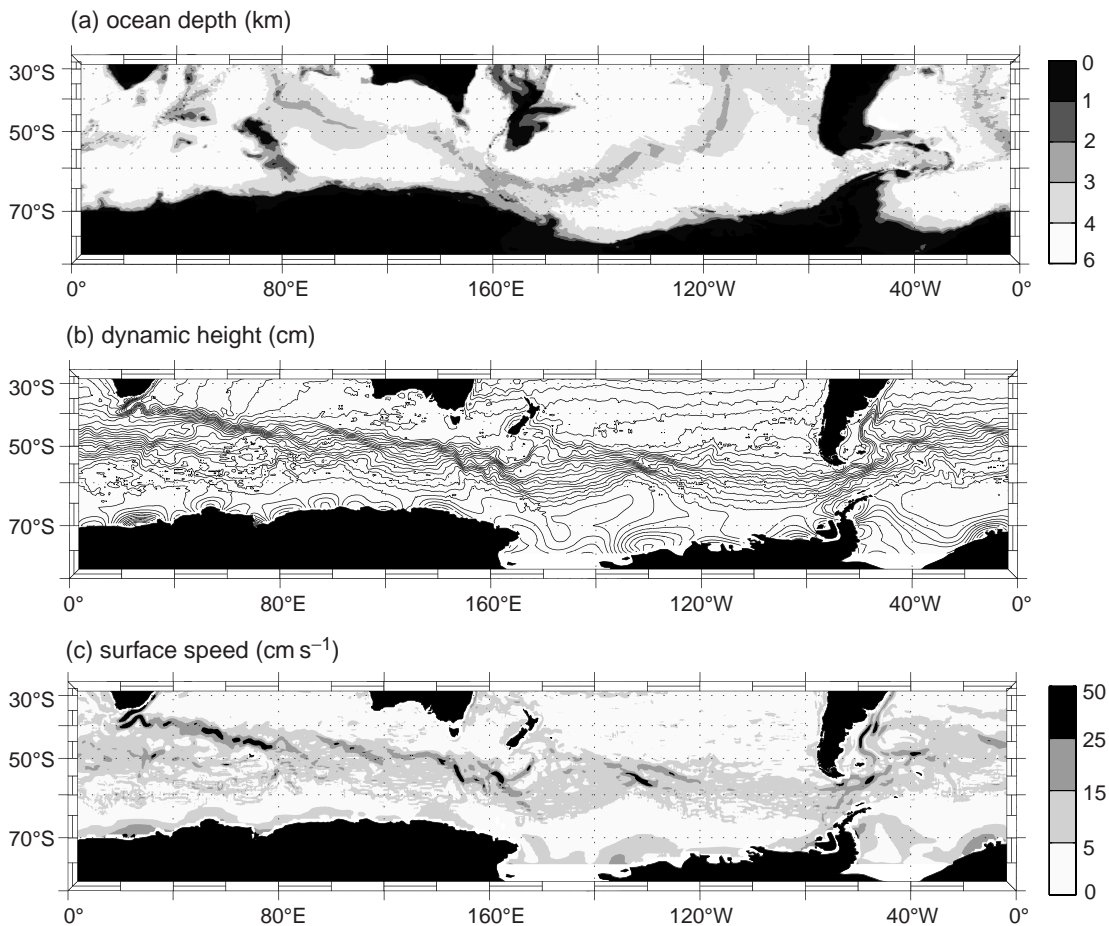


Figure 8.20 (a) Ocean depth (km), (b) mean dynamic height (cm; contours every 10 cm), and (c) geostrophic speed (cm s^{-1}) for the Southern Ocean. The surface geostrophic flow is directed along the contours of dynamic height (with high values to the left of the flow). Ocean mean dynamic height was taken from a combined dataset integrating information from surface drifters, satellite altimetry, surface winds and the GRACE gravity mission (Niiler et al., 2003; Maximenko and Niiler, 2005).

in dynamic height and speed (Fig. 8.20b,c), with strong flows south of South Africa and Australia, and latitudinal shifts in the core of the current coincident with the change in topography, such as at 80°E and 160°E. The frontal contrasts across the current vary downstream along the path of the current, with particular fronts merging or separating according to how the current moves around ridges in the topography.

These frontal bands with strong horizontal density gradients are dynamically unstable and create a vibrant geostrophic eddy field (discussed in Chapter 9). In turn, the geostrophic eddies are important in flattening density sur-

faces and in transferring properties both horizontally and vertically across the Southern Ocean.

How does the surface flow connect to the underlying density structure?

The eastward flow of the Antarctic Circumpolar Current is associated with a southward increase in density, which is sufficiently strong for all the dense isopycnals and accompanying potential temperature and salinity surfaces in the open ocean to shoal and reach the sea surface, as illustrated for Drake Passage in Fig. 8.21; there is also a signal of cold and fresh waters spreading

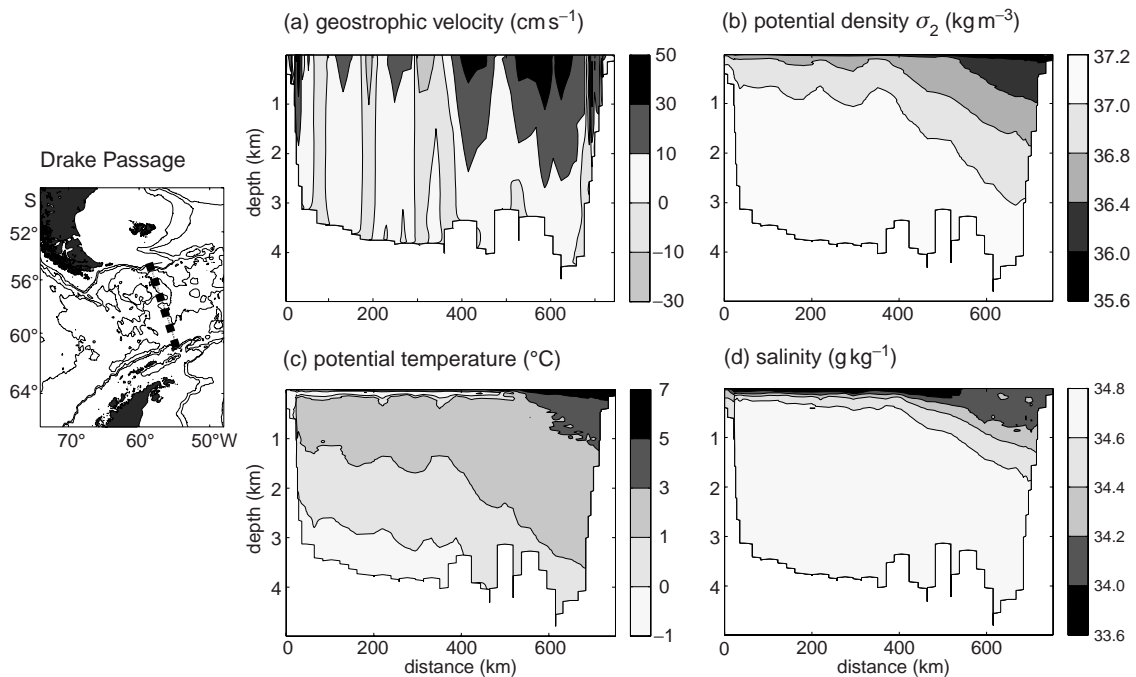


Figure 8.21 Geostrophic flow and water-mass properties across Drake Passage: (a) eastward geostrophic velocity (cm s^{-1}) versus depth, relative to assumed zero flow on the sea floor; (b) potential density minus 1000 kg m^{-3} referenced to a depth of 2 km, σ_2 (kg m^{-3}); (c) potential temperature ($^{\circ}\text{C}$); and (d) salinity (g kg^{-1}). The distance along the section increases northward with the section path (dashed line) displayed in the map insert. Data collected between 30 December 1997 and 7 January 1998 with a maximum station spacing of 17 km. Data supplied by Brian King; further details, see Cunningham et al. (2003).

northward from Antarctica within the upper 100 m (Fig. 8.21c,d).

How does the transport of the Antarctic Circumpolar Current compare to a western boundary current?

The surface speeds of the Antarctic Circumpolar Current are only several 10 cm s^{-1} , weaker than the intense flows of the western boundary currents reaching 50 cm s^{-1} or more. However, the Antarctic Circumpolar Current is much wider extending typically 1000 km or so, compared to the 100 km width of the western boundary currents. The flows in the Antarctic Circumpolar Current are also less surface intensified than the subtropical gyres and western boundary currents (Fig. 8.22), typically extending over the entire water column to the sea floor, rather than being more confined to the upper 1 to 2 km.

Combining these estimates of the characteristic velocity, width and thickness for the Antarctic Circumpolar Current suggests that the zonal transport is typically given by

$$\int_0^L \int_{-H}^0 u \, dy \, dz \sim LHU \\ \sim (1000 \times 10^3 \text{ m})(5 \times 10^3 \text{ m})(0.02 \text{ m s}^{-1}) \\ \sim 100 \times 10^6 \text{ m}^3 \text{ s}^{-1} \sim 100 \text{ Sv},$$

which is comparable to the 140 Sv diagnosed as passing through Drake Passage (Fig. 8.21). In comparison, there is a similar meridional transport in a western boundary current, assuming a stronger velocity, $U \sim 0.5 \text{ m s}^{-1}$, a narrower width, $L \sim 100 \text{ km}$ and a shallower depth scale $H \sim 2 \text{ km}$. This eastward transport of the Antarctic Circumpolar Current is typically an order of magnitude larger than the meridional overturning circulation, discussed later in Chapter 12.

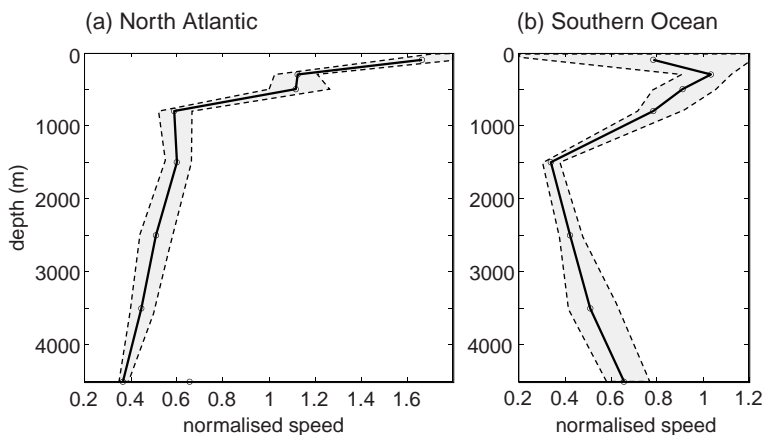


Figure 8.22 Profiles of normalised speed from current meter records, each lasting more than 180 days, in (a) the North Atlantic basin, and (b) the Southern Ocean (thick full line), together with 67% confidence limits (thin dashed lines). The profiles are calculated from a mean of 25 current moorings for the subtropical North Atlantic (179 current meters) from 20°N to 50°N and the same number for the Southern Ocean (104 current meters) from 40°S to 60°S. All current speeds have been normalised by the root mean square local surface speed obtained from satellite altimeter data. The profiles revealed that the flow in the Southern Ocean was less surface intensified than in the subtropical Atlantic. From Darran Furnival and Rob Scott. Further details in Scott *et al.* (2010).

8.4.2 Why is there an Antarctic Circumpolar Current?

At the simplest level, the Antarctic Circumpolar Current is forced eastward by the prevailing westerly winds. As there is not a continental barrier at all latitudes, the current is primarily zonal, rather than forced in gyre circulations within the basins. In this respect, the controlling dynamics of the Antarctic Circumpolar Current resembles the atmosphere, where the Jet Stream encircles the globe.

While surface winds provide the forcing, the Antarctic Circumpolar Current clearly does not continue to accelerate until its speed matches the atmosphere. Instead, the Antarctic Circumpolar Current reaches a steady state where the atmospheric input of momentum is offset by a sink of momentum (Box 8.4). Before this steady state is reached, a series of processes occur (based on ocean circulation model studies):

- Surface waters accelerate eastward through the input of momentum from the wind (Fig. 8.23). After a day or so, the sea-surface height decreases southward and isopycnals shoal southward; both are consequences of the geostrophic balance between the northward Coriolis acceleration (deflecting to the left in the southern hemi-

sphere) and the southward acceleration from the pressure gradient.

- The intense eastward current becomes dynamically unstable, forming geostrophic eddies. This instability process flattens the tilting isopycnals, reducing the vertical shear in velocity and transferring eastward momentum from the surface into the deep water.
- The eastward momentum within deep flows is ultimately transferred to the solid Earth (8.23) through pressure differences forming across topographic ridges: high pressure upstream and low pressure downstream of the ridge, referred to as form stress (Box 8.4). This pressure difference then acts to decelerate the ocean and, conversely, accelerate the solid Earth. In analogy, you experience a similar pressure contrast when you hold a barrier up against a strong wind: a high pressure upstream of the barrier and low pressure downstream, which attempts to flatten the barrier.

8.5 | Summary

The surface circulation consists of contrasting regimes: recirculating gyres and western

Box 8.4 | Zonal momentum balance in a channel

A zonal flow involves a balance between temporal acceleration, Coriolis, pressure gradient and frictional accelerations,

$$\frac{\partial u}{\partial t} - fv = -\frac{1}{\rho_0} \frac{\partial P}{\partial x} + \frac{1}{\rho_0} \frac{\partial \tau_x}{\partial z}, \quad (8.17)$$

where the non-linear advection terms are ignored here for simplicity. Applying a depth integral from the sea surface, η , to the sea floor, $z = -H$, to the density multiplied by velocity gives

$$U = \int_{-H}^{\eta} \rho_0 u dz \quad \text{and} \quad V = \int_{-H}^{\eta} \rho_0 v dz. \quad (8.18)$$

Depth integrating the frictional acceleration gives the surface stress minus the bottom stress,

$$\int_{-H}^{\eta} \frac{\partial \tau_x}{\partial z} dz = \tau_x^s - \tau_x^b. \quad (8.19)$$

The depth integral of the pressure gradient can be separated into two terms when there are depth variations in the sea floor,

$$\int_{-H}^{\eta} \frac{\partial P}{\partial x} dz = \frac{\partial}{\partial x} \int_{-H}^{\eta} P dz - P_b \frac{\partial H}{\partial x}, \quad (8.20)$$

where the second term on the right represents the bottom pressure multiplied by the gradient in thickness of the water column, referred to as the form stress; here a general relationship, $\frac{\partial}{\partial x} \int_b^a F dx = \int_b^a \frac{\partial F}{\partial x} dx + F(a) \frac{\partial a}{\partial x} - F(b) \frac{\partial b}{\partial x}$, is applied and $P_b \equiv P(-H)$. Substituting (8.18) to (8.20) into a depth integral of (8.17) gives

$$\frac{\partial U}{\partial t} - fv = -\frac{\partial}{\partial x} \int_{-H}^{\eta} P dz + P_b \frac{\partial H}{\partial x} + \tau_x^s - \tau_x^b. \quad (8.21)$$

Now integrating (8.21) around the entire longitudinal width, L , of the zonal channel, the northward transport over the entire channel, $\int_0^L V dx$, has to vanish to conserve mass (second term on left) and $\partial/\partial x (\int_{-H}^{\eta} P dz)$ (first term on right) has to vanish as the start and end points of integration are the same, such that

$$\underbrace{\int_0^L \frac{\partial U}{\partial t} dx}_{\text{zonal acceleration}} = \underbrace{\int_0^L P_b \frac{\partial H}{\partial x} dx}_{\text{form stress}} + \underbrace{\int_0^L (\tau_x^s - \tau_x^b) dx}_{\text{frictional stress}}. \quad (8.22)$$

Hence, if the winds blow over the channel, the zonal flow initially accelerates around the channel: a balance between the first term on the left and second on the right of (8.22). Eventually a steady state is reached where the zonal flow ceases to change and the frictional acceleration from the wind stress has to be balanced by the form stress and bottom drag (first and third terms on the right). Model studies suggest that the wind stress is balanced by the form stress from the variations in pressure across bumps, such that

$$\int_0^L P_b \frac{\partial H}{\partial x} dx + \int_0^L \tau_x^s dx \sim 0. \quad (8.23)$$

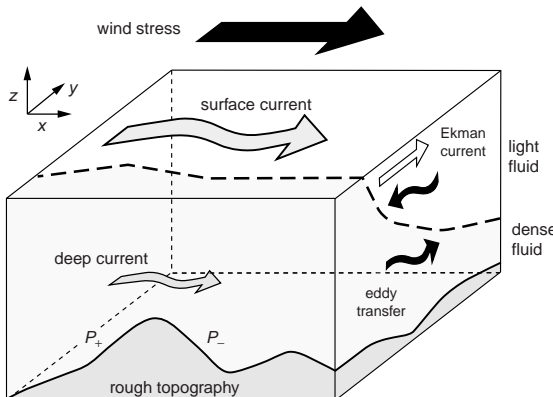


Figure 8.23 Schematic figure of the processes acting in the Southern Ocean. The surface wind stress (black arrow) accelerates the surface current eastward (grey arrow), as well as leading to a northward Ekman current (white arrow) and a southward shoaling of isopycnals (dashed line). This current is unstable, leading to eddy transfers that act to flatten the isopycnals (curly black arrows) and transfer momentum to the deep ocean. The deep currents lead to a high pressure P_+ upstream of a topographic ridge (hatched) and low pressure P_- downstream, which acts to decelerate the current and transfer momentum to the solid Earth.

boundary currents within basins, together with zonal flows in the tropics and Southern Ocean.

Ocean gyres are a consequence of the wind forcing over ocean basins, where the sense of rotation is dictated by the torque from the wind. In the northern hemisphere, the gyres are particularly dominant, with subtropical circulations extending over much of the mid-latitude basins and subpolar circulations confined to higher latitudes. In the North Indian Ocean, a permanent gyre signal is less clear due to the seasonal reversal in the monsoon winds. The subtropical circulations in the southern hemisphere appear relatively weak; the South Atlantic gyre is relatively confined, while the lack of a continuous land barrier leads to the western boundary current being less pronounced in the South Pacific.

Western boundary currents provide the return flow of the interior gyre circulation and are a consequence of the Earth being a rapidly rotating sphere. When the currents separate from the coast, they remain a coherent feature for several thousand kilometres, despite meandering and forming intense eddies and rings.

In the tropics, there are intense zonal flows, directed westward on either side of the equator together with an eastward return flow along the equator. These zonal flows are a consequence of the wind forcing and the smallness of the Coriolis parameter along the equator. Easterly Trade winds drive the Equatorial Currents flowing to the west on either side of the equator. Persistent west-east pressure gradients cannot be supported along the equator, leading to an eastward return flow, the Equatorial Counter Current, along the equator.

In the southern hemisphere, the prevailing westerly winds drive an eastward Antarctic Circumpolar Current, encircling the globe at high latitudes, and connecting the Atlantic, Indian and Pacific basins. The Antarctic Circumpolar Current is controlled by the momentum input by the surface winds, which is transferred through the water column to the sea floor. The momentum is thought to be taken out of the water column through pressure differences across ridges and bumps along the sea floor. The path of the Antarctic Circumpolar Current varies according to the topography, as well as being affected by the overlying winds.

This structure of ocean gyres and intense currents has a profound effect on the transport of tracers, including heat, salt, nutrients and carbon, as well as the functioning of the ecosystem and cycling of carbon, as discussed in Chapters 10 to 12.

8.6 Questions

Q8.1. What does the Stommel model suggest for the width of the western boundary current?

Based on the Stommel closure for the western boundary layer, the meridional velocity is determined by the balance between how fluid changes planetary vorticity, $Df/Dt = \beta v$, and dissipation of vorticity by bottom friction,

$$\beta v \simeq -r\zeta, \quad (8.24)$$

where $\zeta = \frac{\partial v}{\partial x} - \frac{\partial u}{\partial y}$. Assuming that west-east gradients are greater than north-south gradients,

(8.24) can be approximated to

$$\beta v \simeq -r \frac{\partial v}{\partial x}. \quad (8.25)$$

(a) Using scale analysis, estimate the characteristic width of the western boundary current. Assume $\beta = 10^{-11} \text{ m}^{-1} \text{s}^{-1}$ and a spin down timescale for the currents of $r^{-1} \sim 10$ days.

(b) What is the strength of the western boundary current assuming that the current returns the interior Sverdrup transport, $v_{int} H L_{int} \sim -50 \times 10^6 \text{ m}^3 \text{s}^{-1}$ (Fig. 8.13c) and a depth of $H \sim 10^3 \text{ m}$,

$$v_{bdry} H L_{bdry} + v_{int} H L_{int} = 0? \quad (8.26)$$

Q8.2. What does the Munk model suggest for the width of the western boundary current?

Munk (1950) provided an alternative to the Stommel (1948) model for ocean gyres, where the meridional flow in the western boundary is controlled by a horizontal diffusion of relative vorticity,

$$\beta v = K_h \left(\frac{\partial^2}{\partial x^2} + \frac{\partial^2}{\partial y^2} \right) \zeta, \quad (8.27)$$

where K_h is the horizontal diffusivity. Apply the scale analysis and diagnose how the width of the western boundary varies with β and K_h . What is the typical value for the boundary width for $\beta = 10^{-11} \text{ m}^{-1} \text{s}^{-1}$ and $K_h \sim 10^3 \text{ m}^2 \text{s}^{-1}$?

Q8.3. Derive the vorticity equation.

The momentum equations for a layer of constant density and variable thickness, h , are given by

$$\frac{Du}{Dt} - fv = -g \frac{\partial h}{\partial x} + \frac{1}{\rho_0} \frac{\partial \tau_x}{\partial z}, \quad (8.28)$$

$$\frac{Dv}{Dt} + fu = -g \frac{\partial h}{\partial y} + \frac{1}{\rho_0} \frac{\partial \tau_y}{\partial z}, \quad (8.29)$$

where $\frac{D}{Dt} = \frac{\partial}{\partial t} + u\frac{\partial}{\partial x} + v\frac{\partial}{\partial y}$ and represents the rate of change following a fluid parcel, and τ is the frictional stress.

Form a vorticity equation, taking $\partial/\partial x$ (8.29)– $\partial/\partial y$ (8.28) to obtain

$$\begin{aligned} \frac{D}{Dt} (\zeta + f) + (\zeta + f) \left(\frac{\partial u}{\partial x} + \frac{\partial v}{\partial y} \right) \\ = \frac{1}{\rho_0} \frac{\partial}{\partial z} \left(\frac{\partial \tau_y}{\partial x} - \frac{\partial \tau_x}{\partial y} \right), \end{aligned} \quad (8.30)$$

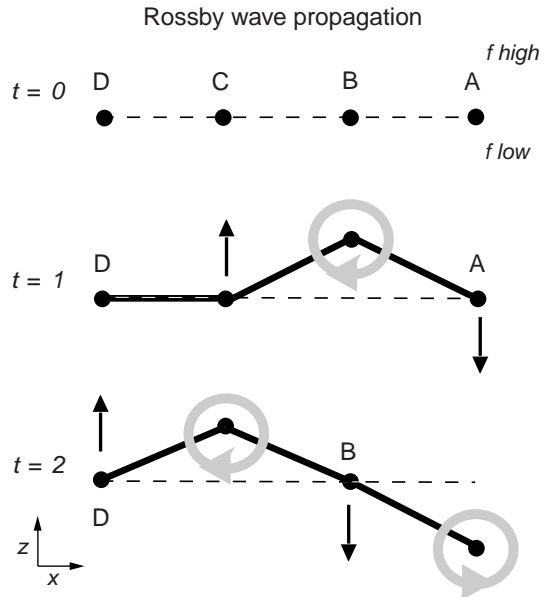


Figure 8.24 A schematic figure depicting how Rossby waves propagate westward; a plan view of a hypothetical string of particles labelled A to D, over a domain with a northward increase in planetary vorticity, f . Initially, the particles are orientated along a latitude circle ($t = 0$). If particle B is displaced northward, then a circulation with negative relative vorticity is acquired around B ($t = 1$). This circulation around particle B (marked by grey arrow) displaces particle C northward and particle A southward ($t = 2$).

where $Df/Dt = \beta v$ and represents the advection of planetary vorticity and $\zeta = \partial v / \partial x - \partial u / \partial y$ is the relative vorticity.

Q8.4. Rossby waves.

Over timescales longer than a day, the ocean supports a particular class of waves called Rossby waves or planetary waves, where the restoring force is provided by the meridional change in planetary vorticity over the globe; the motion in these planetary waves can be understood in terms of the fluid conserving potential vorticity, $Q = (\zeta + f)/h$.

(a) Firstly, on a small scale, ignore any variations in the thickness of the water column, h , and consider conservation of absolute vorticity, $q = \zeta + f$. Consider a string of hypothetical particles, labelled A to D, positioned from east to west, which are able to move, and assume that q is conserved for each of them (Fig. 8.24). If particle B is

perturbed northward to a larger f , explain why a circulation with a negative relative vorticity is created. Why is particle C then displaced northward and particle A southward? Explain what subsequently occurs.

(b) Secondly, consider the large-scale limit where relative vorticity, ζ , is small and f/h is conserved. Again, as particle B is displaced northward, and f increases, how does the thickness h vary? What is the circulation around particle B based upon geostrophy, $v = \frac{\zeta}{f} \partial h / \partial x$? Explain how this flow affects the movement of the particles C and A. What is the similarity with case (a)?

8.7 | Recommended reading

There are a number of excellent reviews of ocean circulation theory, often focussing on the mathematical balances:

- A. E. Gill (1982). *Atmosphere-Ocean Dynamics*. New York: Academic Press;
- J. Pedlosky (1987). *Geophysical Fluid Dynamics*. New York: Springer-Verlag;
- J. Pedlosky (1996). *Ocean Circulation Theory*. Berlin: Springer-Verlag, 453pp;
- G. K. Vallis (2006). *Atmospheric and Oceanic Fluid Dynamics: Fundamentals and Large-scale Circulation*. Cambridge: Cambridge University Press, 745pp.

In addition a complementary view drawing on laboratory experiments is provided by J. Marshall and R. A. Plumb (2008). *Atmosphere, Ocean and Climate Dynamics: An Introductory Text*. Burlington, MA: Academic Press/Elsevier, 319pp.

A comprehensive review of the Antarctic Circumpolar Current is provided by S. Rintoul, C. W. Hughes and D. Olbers (2001). The Antarctic Circumpolar Current System. In *Ocean Circulation and Climate: Observing and Modelling the Global Ocean*, ed. G. Siedler, J. Church and J. Gould, San Diego, CA: Academic Press, pp. 271–302.

Chapter 9

Ocean eddies

The ocean and atmosphere are full of swirling circulations, flows changing their velocity in time and/or space, which are generically referred to as eddies. Eddies are seen whenever we look at moving fluids, like small-scale vortices formed by a paddle moving in the water, in the turbulent wake of a river flowing around a rock, and on a grander scale like the weather systems where hook-like ice clouds warn of an oncoming warm front. An eddy might sometimes represent a reversing oscillation, such as in how a stick is swept back and forth as a gentle wave passes by, or an irreversible transfer, as in how surf is swept in a breaking wave towards the shore.

Eddy variability is particularly pronounced on horizontal scales of several tens to a hundred kilometres in the ocean, referred to as the mesoscale, and on scales of a thousand kilometres in the atmosphere, referred to as the synoptic scale and linked to weather systems. Both these ocean eddies and atmospheric weather systems are generated through the instability of intense jets and narrow currents. For example, meanders in the Gulf Stream can intensify and break off from the current, forming mesoscale eddies, which have warm cores to the north or cold cores to the south of the current, respectively, as depicted in Figs. 9.1 and 9.2. Weather systems are likewise formed by meanders developing along the atmospheric Jet Stream, eventually leading to warm air swept poleward ahead of a low pressure and cold air swept equatorward behind the low.

In this chapter, we describe the eddy variability over the ocean and then explain the mechanism by which mesoscale eddies form, drawing on the

analogy between ocean eddies and atmospheric weather systems. The effect of eddies in transferring tracers is then discussed: for sea-surface temperature and dynamical tracers in the interior ocean, addressing how eddies provide advection and diffusion, and finally how there are competing effects from jets.

9.1 How does eddy variability alter over the globe?

The pattern of eddy variability over the globe is diagnosed here from the root-mean-square of eddy kinetic energy, as measured from satellite altimetry; the gradients in sea-surface height are interpreted as geostrophic flows (Section 4.2).

The eddy variability is concentrated along the western boundaries of ocean basins and along the Southern Ocean (Fig. 9.3a), coinciding with the position of intense boundary currents and zonal currents (Fig. 9.3b).

This eddy variability is often nearly as energetic as the intense currents which generate them. Once formed, intense eddies can disperse from their formation sites and spread into more quiescent parts of the ocean interior, where the eddy variability is often more energetic than the background time-averaged flow.

Variability in the northern hemisphere

The regions of eddy activity are mapped in the vicinity of intense currents. In the North Atlantic, there are local maxima in the eddy velocities

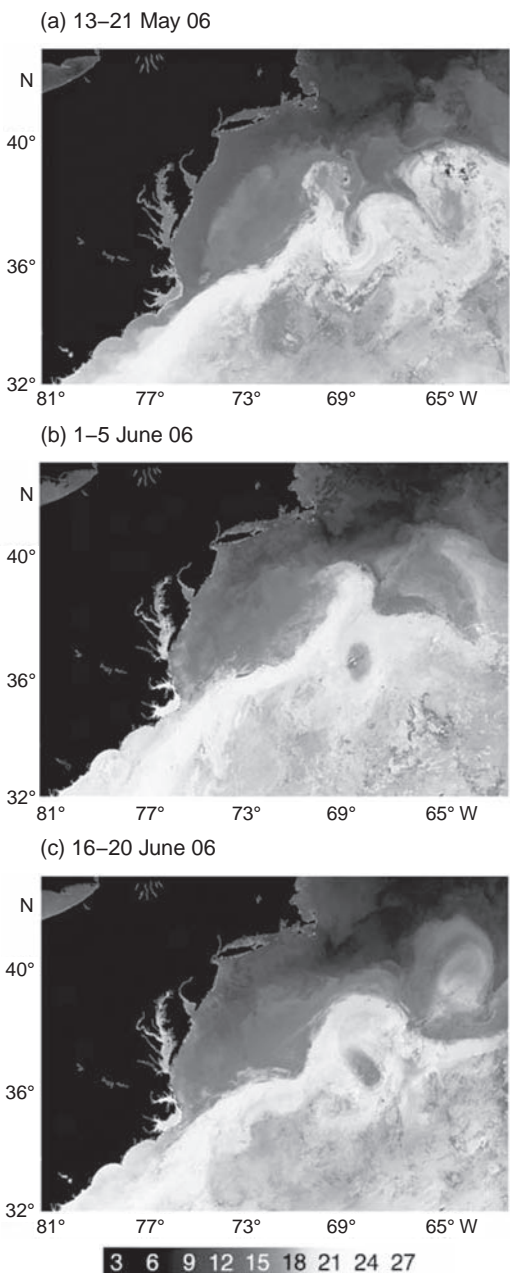


Figure 9.1 Sequence of remotely sensed sea-surface temperature images of the Gulf Stream revealing the formation of cold-core (dark) and warm-core (light) eddies; the cold-core eddy is formed in mid May at 36°N , 69°W , persisting for a month, while a warm-core eddy is formed in late June at 40°N , 64°W . The images are from a composite of cloud-free data from (a) 13 to 21 May 2006, (b) 1 to 5 June, and (c) 16 to 20 June 2006, and any remaining missing data are filled from a monthly composite; data from NASA Moderate-Resolution Imaging Spectroradiometer (MODIS), which were processed by Rhys Elsworth and Steve Groom, Plymouth Marine Laboratory.

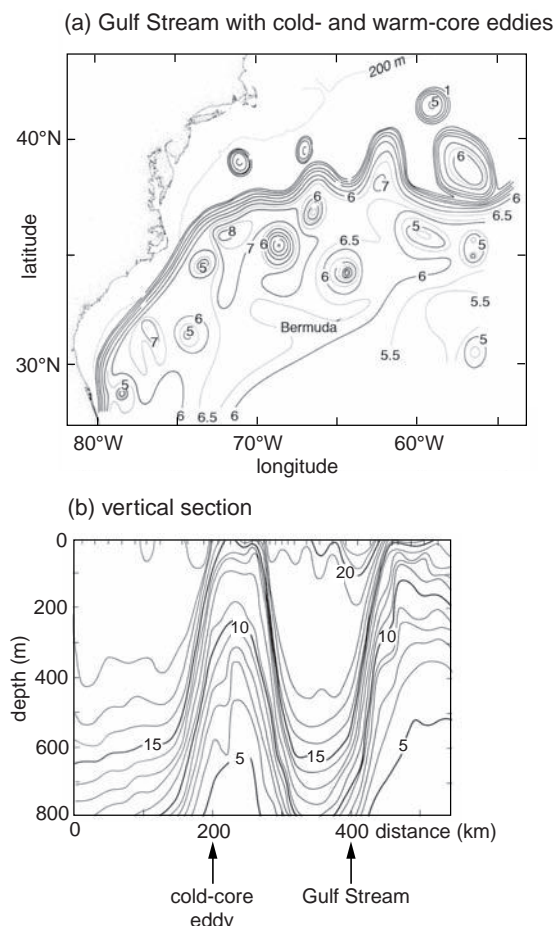
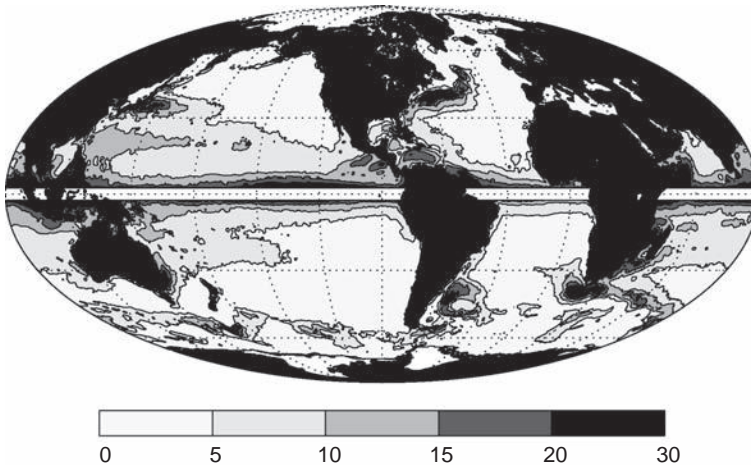


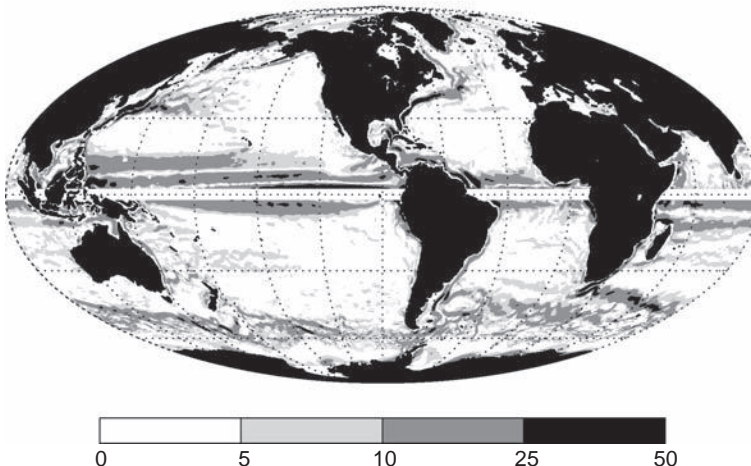
Figure 9.2 (a) Chart of the depth of the 15°C isotherm (in 100 m contours) revealing undulations of the thermocline and the Gulf Stream identified by the narrow band where the thermocline rapidly shoals northward. There are nine cold-core eddies with a raised thermocline to the south of the Gulf Stream, rotating cyclonically, and three warm-core eddies to the north with a deeper thermocline and rotating anticyclonically. The map is based on data from 16 March to 7 July 1975 and redrawn from Richardson *et al.* (1976). (b) A temperature section ($^{\circ}\text{C}$) through a cold-core eddy south of the Gulf Stream. There is a pronounced doming of the isotherms within the cold-core eddy reaching 500 m over a horizontal scale of 100 km. Courtesy of Phil Richardson.

reaching 30 cm s^{-1} following the path of the separated Gulf Stream (70°W , 35°N to 45°W , 45°N), where there is a tight spacing of dynamic height contours (Fig. 9.4a, shading and contours). The gyre interiors appear relatively quiescent, with eddy velocities less than 5 cm s^{-1} . Similarly, in the North Pacific, there is a local maximum in eddy

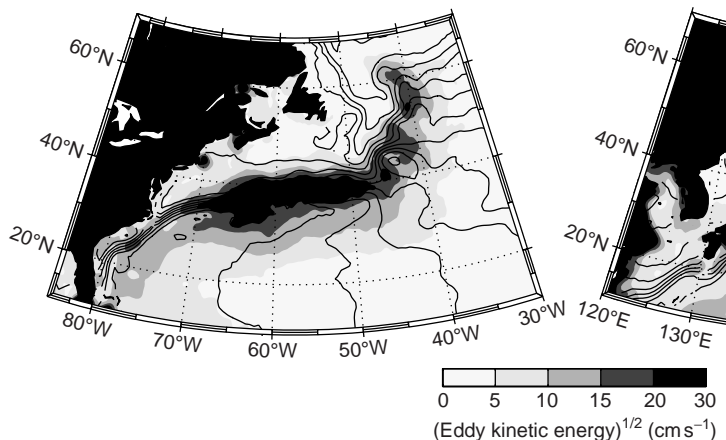
(a) (Eddy kinetic energy) $^{1/2}$ (cm s^{-1})



(b) surface speed (cm s^{-1})



(a) North Atlantic



(b) North Pacific

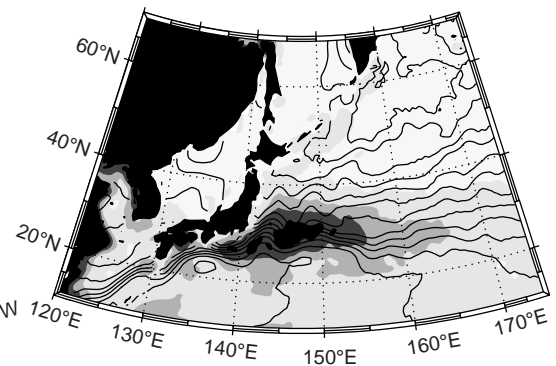


Figure 9.3 (a) Eddy velocity (cm s^{-1}) from the root-mean-square eddy kinetic energy, and (b) time-mean geostrophic speed (cm s^{-1}). The regions of high eddy kinetic energy are coincident with regions of intense flow, concentrated along the western boundaries within ocean basins or nearly zonal currents in the Southern Ocean and along the equator. The eddy kinetic energy is derived from combined TOPEX/Poseidon and ERS-1/2 data for 1992 to 2003 (data supplied by Chris Wilson) and the mean geostrophic speed is derived from mean dynamic topography of Maximenko and Niiler (2005); latitudes within 2° of the equator have been masked due to the vanishing of the Coriolis parameter.

Figure 9.4 Diagnostics of the eddy velocity (cm s^{-1}) from the square root of eddy kinetic energy from altimetry for (a) the Gulf Stream in the North Atlantic, and (b) the Kuroshio in the North Pacific. The mean dynamic topography from Maximenko and Niiler (2005) is given by thin contours (every 10 cm). Data supplied by Chris Wilson; further details in Williams et al. (2007).

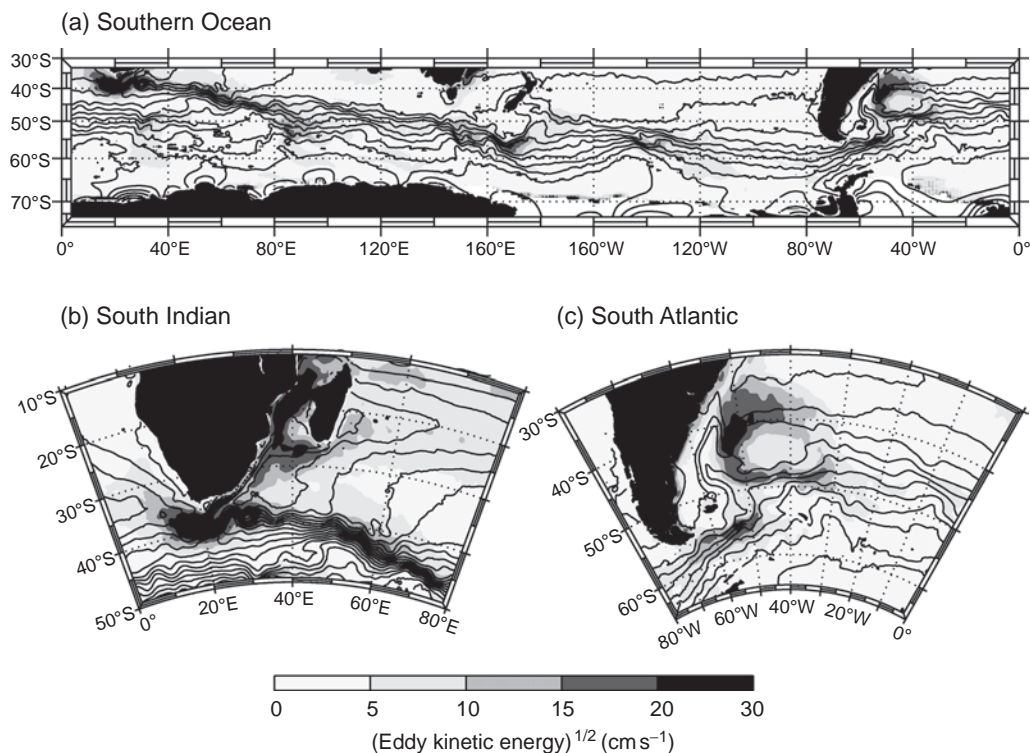


Figure 9.5 Diagnostics of the square root of eddy kinetic energy (shaded, cm s^{-1}) and the mean dynamic topography (contours every 20 cm) for (a) the Southern Ocean, together with (b) the South Indian, and (c) the South Atlantic sectors. Details as in Fig. 9.4.

velocity following the extension of the Kuroshio into the basin interior (140°E , 33°N to 155°E , 35°N ; Fig. 9.4b). Hence, maxima in eddy variability are directly linked with regions of strong flow in the separated jets leaving the western boundary.

These surface signatures of eddy variability extend below the surface and into the thermocline. For example, in the vicinity of the Gulf Stream, cold-core eddies are formed to the south and warm-core eddies to the north of the current (Fig. 9.2a). The cold-core eddies are associated with a doming of isotherms and a cyclonic circulation (Fig. 9.2b), while the warm-core eddies have a deeper thermocline and an anticyclonic circulation.

Variability in the southern hemisphere

Eddy variability increases along the near-zonal jets of the Antarctic Circumpolar Current, as well as along western boundary currents (Fig. 9.5a). Eddy velocities typically reach 20 cm s^{-1} , slightly weaker than the eddy signals associated with

the western boundary currents in the northern hemisphere.

In the South Indian sector, the eddy velocity is a maximum along the northern flank of the Antarctic Circumpolar Current (20°E , 40°S to 80°E , 48°S ; Fig. 9.5b), as well as along the western side of the Indian basin (40°E , 15°S to 30°E , 33°S). There is a particularly pronounced maximum in eddy activity close to the southern tip of South Africa (20°E , 38°S), where intense eddies are created, called Agulhas rings.

In the South Atlantic sector, the eddy velocity is again a maximum along the northern flank of the Antarctic Circumpolar Current (Fig. 9.5c), downstream of Drake Passage (65°W , 58°S to 50°W , 55°S) and along the Brazil Current in the subtropical gyre (40°S to 48°S along 50°W).

Summary

Eddies are ubiquitous phenomena occurring throughout the ocean. Enhanced eddy activity is associated with western boundary currents and

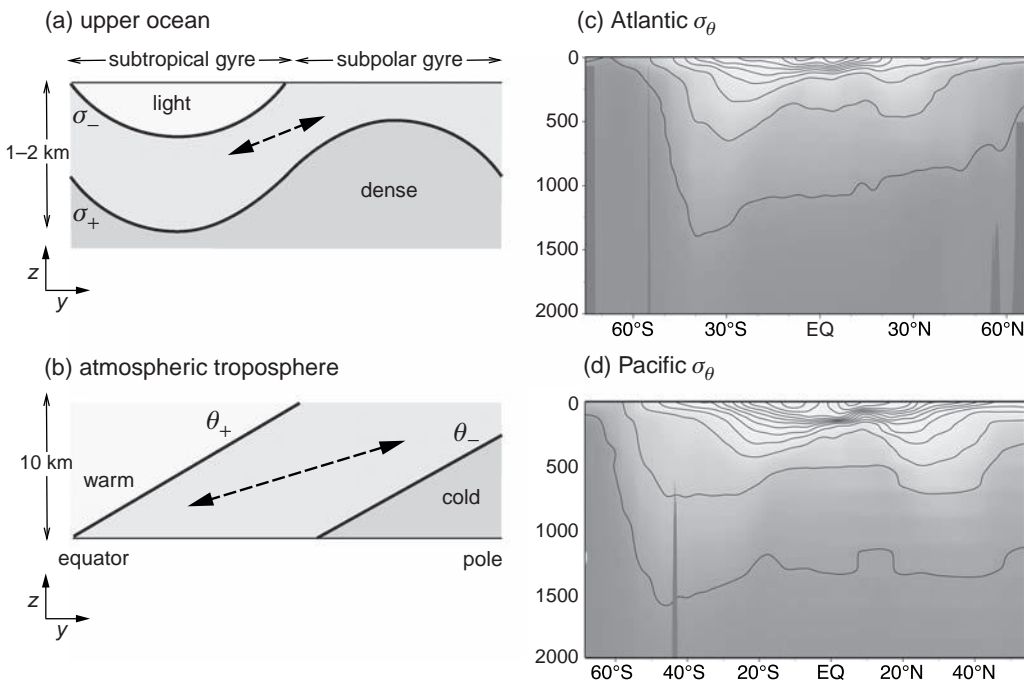


Figure 9.6 A schematic figure for (a) the upper ocean showing potential density surfaces, σ , undulating on a horizontal scale of several thousand kilometres within the main thermocline, and (b) the atmospheric troposphere showing sloping potential temperature surfaces, θ , both plotted over the northern hemisphere. Eddies are generated through a release of potential energy involving an exchange of fluid on sloping trajectories (dashed lines). In (c) and (d), meridional sections of σ_θ (kg m^{-3}) are shown through the entire Atlantic along 20°W and the Pacific along 170°W , revealing the undulations of the thermocline.

their extensions within ocean basins, and the near-zonal jets making up the Antarctic Circumpolar Current.

9.2 A theoretical view of ocean eddy variability

Ocean mesoscale eddies are now discussed from a more theoretical perspective, drawing upon their dynamical analogy with atmospheric, synoptic-scale weather systems, and focussing on their characteristic velocity, length and timescales.

9.2.1 Why is there intense eddy variability in the ocean?

The intense eddy variability in the ocean initially appears surprising. The external forcing of the ocean occurs on a much larger scale, winds induce undulations of the thermocline on a horizontal scale of several thousand kilometres (Fig. 9.6a,c–

d), while ocean mesoscale eddies only extend for a horizontal scale of tens to a hundred kilometres. In the atmosphere, the radiative forcing varies on a horizontal scale of ten thousand kilometres (Fig. 9.6b), much larger than atmospheric weather systems on a horizontal scale of a thousand kilometres. Rather than be generated directly by external forcing, both ocean mesoscale eddies and atmospheric synoptic-scale weather systems are formed by a dynamical instability of intense currents and jets, involving a flattening of sloping density surfaces, referred to as baroclinic instability.

Here, we provide a mechanistic view of this instability process, emphasising the energetics and the characteristic eddy structures following Green (1981).

9.2.2 How do eddies in the atmosphere and ocean acquire their energy?

In both the atmosphere and ocean, potential temperature and density surfaces sloping relative to

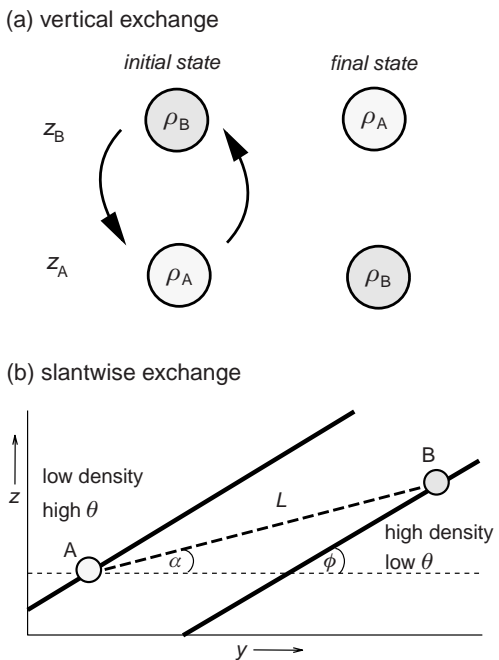


Figure 9.7 A schematic figure showing (a) a vertical exchange of two fluid parcels, A and B, where potential energy is released if a lighter fluid parcel rises and is replaced by a denser fluid parcel, and (b) a meridional section with sloping potential density surfaces (full lines), with lighter fluid immediately above the denser fluid. Potential energy is released when fluid parcels are exchanged on a sloping path, AB (dashed line), rather than along a purely horizontal path or along potential density surfaces. The optimal release of potential energy occurs for an exchange path at an angle, α , half the slope of the background potential density surfaces, ϕ ; L is the distance of AB. This slantwise exchange of fluid along this path also usually leads to heat being transferred poleward. Redrawn following Green (1981) and Vallis (2006).

the horizontal represent a reservoir of potential energy (Fig. 9.6a,b, full lines). Potential energy is converted into kinetic energy under certain circumstances; an everyday example is a ball rolling down a hill, where the ball acquires a speed, v , after a descent, h , due to potential energy being converted to kinetic energy:

$$\frac{1}{2}mv^2 = mgh. \quad (9.1)$$

In a similar manner, consider two fluid parcels exchanged vertically in the ocean or the atmosphere in Fig. 9.7a. Potential energy is only released and converted to kinetic energy if a denser fluid parcel sinks and is replaced by a

lighter fluid parcel (Box 9.1). On the other hand, if the denser fluid parcel is forced to rise and the lighter fluid parcel to sink, then work has to be done and potential energy increases.

How is the potential energy released from the background state? Outside the relatively thin, convective boundary layers, most of the atmosphere and ocean is *stably stratified*, with light fluid overlying dense fluid (Fig. 9.7a). Thus, a purely vertical exchange of two fluid parcels does not lead to a potential energy release.

Instead, potential energy can be released through a *slantwise exchange* involving both horizontal and vertical excursions (Fig. 9.7b, dashed line), such that parcels are exchanged along a sloping path lying between the background isopycnals and the horizontal. The maximum release of potential energy occurs when this exchange is at a slope half that of the isopycnals (Fig. 9.7b, dashed line). The implied potential energy release then can generate intense eddy velocities, even reaching magnitudes of typically 50 cm s^{-1} (see later Box 9.3).

9.2.3 What is the dynamical structure of the eddies?

In principle, slantwise exchange of fluid can release the necessary energy from the background state to excite eddy motions. However, there is a difficulty: only special forms of the eddy circulation are allowed. The problem is that the eddies are generated on a sufficiently long timescale, days in the atmosphere and weeks in the ocean, so that the rotation of the Earth becomes important in constraining the flow. The mechanism by which eddies satisfy this dynamical constraint and access this potential energy is called baroclinic instability; for a mathematical view of the instability process, see the original studies for the atmosphere by Charney (1947) and Eady (1949), and the ocean by Gill *et al.* (1974), and later reviews by Gill (1982) and Vallis (2006).

To understand the implications of these dynamical constraints, consider a zonal jet with the background temperature increasing equatorward (Fig. 9.8a).

The eddy circulations are associated with pressure perturbations, P' , developing along the axis

Box 9.1 | Energetics of slantwise exchange

Following Vallis (2006), consider the exchange of two fluid parcels of density ρ and height z labelled as A or B in Fig. 9.7a. The potential energy defined per unit volume (J m^{-3}), $PE = \int \rho g dz$, can either be increased or decreased through their exchange, such that the release in potential energy, ΔPE , the initial minus the final, is given by

$$\begin{aligned}\Delta PE &= g(\rho_A z_A + \rho_B z_B) - g(\rho_A z_B + \rho_B z_A) \\ &= g(\rho_A - \rho_B)(z_A - z_B) \equiv g \Delta \rho \Delta z.\end{aligned}\quad (9.2)$$

Potential energy is released if dense fluid sinks and light fluid rises, such that $\rho_B > \rho_A$ and $z_B > z_A$; otherwise work has to be done for an exchange and potential energy is increased.

The potential energy release depends on the slope of the parcel exchange, at an angle α to the horizontal, compared with the slope of the isopycnals, at an angle ϕ to the horizontal in Fig. 9.7b. Assuming that both these angles are small (so that $\sin \alpha \simeq \alpha$), the vertical displacement, Δz , is related to the displacement, L , of the parcels,

$$\Delta z = L \sin \alpha \simeq \alpha L,$$

and their density change, $\Delta \rho$, to the background density gradients by

$$\Delta \rho = \Delta y \frac{\partial \rho}{\partial y} + \Delta z \frac{\partial \rho}{\partial z} = L \cos \alpha \frac{\partial \rho}{\partial y} + L \sin \alpha \frac{\partial \rho}{\partial z} \simeq L \frac{\partial \rho}{\partial y} + L \alpha \frac{\partial \rho}{\partial z},$$

such that ΔPE can be expressed as

$$\Delta PE = g \Delta \rho \Delta z \simeq g \alpha L \left(L \frac{\partial \rho}{\partial y} + L \alpha \frac{\partial \rho}{\partial z} \right) = g \alpha L^2 \frac{\partial \rho}{\partial y} \left(1 - \frac{\alpha}{\phi} \right), \quad (9.3)$$

where $\phi = -\frac{\partial \rho}{\partial y}/\frac{\partial \rho}{\partial z}$. The change in potential energy, ΔPE , goes to zero when there is exchange in the horizontal, $\alpha = 0$, or along isopycnals, $\alpha = \phi$. The maximum release of potential energy occurs between these two limits when fluid particles are exchanged along half the slope of the isopycnals, $\alpha = \phi/2$, such that

$$\Delta PE \simeq \frac{g \alpha L^2}{2} \frac{\partial \rho}{\partial y}. \quad (9.4)$$

This released potential energy is then assumed to be converted to kinetic energy (see later Box 9.3).

of the jet relative to a time mean, \bar{P} , such that the eddy velocity is given from geostrophy by

$$v' = \frac{1}{\rho f} \frac{\partial P'}{\partial x}. \quad (9.5)$$

The eddy velocity is directed cyclonically around the low pressure, so that warmer fluid is advected poleward downstream of the low pressure and colder fluid advected equatorward upstream of the low pressure, which leads to the character-

istic pattern of a warm front swept ahead and a cold front behind a low pressure. The combination of velocity and temperature perturbations then leads to an eddy heat flux, $\rho C_p v' T' > 0$, directed down the temperature gradient (Fig. 9.8). Hence, the eddy heat flux is directed poleward, which is in accord with the slantwise exchange depicted in Fig. 9.7b.

In the vertical plane along the jet, lighter fluid rises downstream of the low pressure and denser

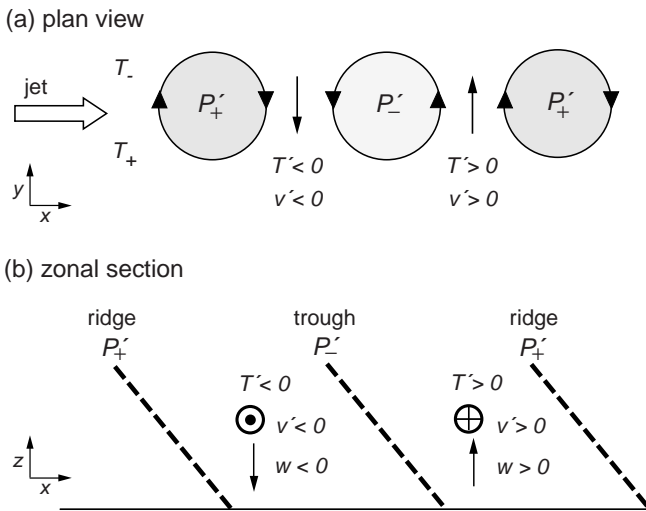


Figure 9.8 A schematic figure showing (a) the horizontal, and (b) vertical structure of eddies formed by baroclinic instability in the atmosphere or ocean. In (a), instability of a zonal jet leads to a sequence of low and high pressure anomalies P' . An eddy flow is directed cyclonically around the low pressure anomaly, leading to warmer fluid swept downstream of the low pressure and colder fluid swept upstream of the low pressure, resulting in a poleward eddy heat flux. In (b), in the warm sector ahead of the low pressure, light fluid is rising, while in the cold sector behind the low pressure, dense fluid is sinking. The denser fluid upstream of the low pressure leads to a stronger vertical decrease in pressure, compared with that in the lighter fluid downstream. This phase difference in temperature and pressure anomalies leads to the troughs (connecting low pressure anomalies with height) and ridges (connecting high pressure anomalies with height) tilting westward with height. Redrawn following Green (1981).

fluid sinks upstream of the low pressure (Fig. 9.8b), which is necessary for the slantwise convection to take place (Fig. 9.7). From hydrostatic balance,

$$\frac{\partial P}{\partial z} = -\rho g, \quad (9.6)$$

there is a larger pressure decrease with height within denser fluid than lighter fluid. As the denser fluid is upstream of the low pressure, then the ‘trough’ (linking low pressure anomalies with height) slopes westward with height (Fig. 9.8b). This westward tilt is a signature of how temperature and pressure disturbances are out of phase, a requirement for a poleward heat flux. Conversely, when the temperature and pressure disturbances become in phase, the energy conversion and poleward heat flux ceases, and ‘troughs’ and ‘ridges’ become vertical.

Hence, eddy motions can access the potential energy through slantwise convection, leading to a poleward eddy heat flux and a westward tilt of pressure anomalies with height, as illustrated in Figs. 9.7b and 9.8.

9.2.4 What is the characteristic horizontal scale for eddies?

The potential energy release from slantwise exchange can occur on a range of spatial scales, although if the horizontal scale becomes too small then the exchange does not involve significant

changes in potential temperature and density. In practice, energy release is most effective on a horizontal scale that reflects the competing effects of rotation and stratification (Box 9.2), called the internal baroclinic Rossby deformation radius,

$$L_d = \frac{NH}{f}, \quad (9.7)$$

where N is the buoyancy frequency, H is a thickness scale (typically the depth of the thermocline in the ocean or the thickness of the troposphere in the atmosphere) and f is the Coriolis parameter. This deformation radius, L_d , measures the length scale over which a dense perturbation spreads before being arrested by rotation (Fig. 9.9a).

For the ocean, assuming $H \sim 1$ km for the thickness of the thermocline, $N \sim 3 \times 10^{-3} \text{ s}^{-1}$ and $f \sim 10^{-4} \text{ s}^{-1}$ at mid latitudes, then typically $L_d \sim 30$ km. L_d increases as either stratification increases or as rotation weakens, such that L_d reaches 240 km close to the equator and decreases to less than 10 km at latitudes higher than 60° (Fig. 9.9b); over the mid latitudes, L_d increases westward, reflecting the stratification increase from the westward deepening of the base of the thermocline.

In comparison, L_d is much larger in the atmosphere, typically reaching 1000 km with larger values of $H \sim 10$ km and $N \sim 10^{-2} \text{ s}^{-1}$ in the troposphere.

Box 9.2 | How does the horizontal eddy scale relate to changes in the circulation and stratification?

The characteristic scale at which eddies emerge from baroclinic instability can be understood from the relative size of perturbations in a dynamic tracer; the potential vorticity, involving contributions from the circulation and stratification, $Q = (f + \zeta)/h$. Taking perturbations from a background mean state, f/\bar{h} , Q can be approximated as

$$Q = \frac{f + \zeta}{h + h'} = \frac{f}{\bar{h}} \left(\frac{1 + \zeta/f}{1 + h'/\bar{h}} \right) \approx \frac{f}{\bar{h}} \left(1 + \frac{\zeta}{f} - \frac{h'}{\bar{h}} + \dots \right), \quad (9.8)$$

where the perturbations are due to (i) circulation changes given by the ratio of relative and planetary vorticity, ζ/f , and (ii) stratification changes given by the relative size in layer thickness changes, h'/\bar{h} . The relative magnitude of these perturbations in circulation and stratification is given by

$$\left| \frac{\zeta}{f} \right| / \left| \frac{h'}{\bar{h}} \right|. \quad (9.9)$$

Now to estimate the magnitude of this ratio, assume that the magnitude of ζ is given by

$$\zeta \equiv \frac{\partial v}{\partial x} - \frac{\partial u}{\partial y} \sim \frac{U}{L}, \quad (9.10)$$

and use geostrophy to connect the velocity and thickness changes, such that

$$v = \frac{g'}{f} \frac{\partial h}{\partial x} \quad \text{implies} \quad U \sim \frac{g'}{f} \frac{h'}{L}, \quad (9.11)$$

where U and L are the characteristic eddy scales for the horizontal velocity and length, and $g' = g \Delta \rho / \rho$ is the reduced gravity. Substituting (9.10) and (9.11) leads to the ratio in (9.9) being given by

$$\left| \frac{\zeta}{f} \right| / \left| \frac{h'}{\bar{h}} \right| \sim \frac{g' \bar{h}}{(f L)^2} \equiv \left(\frac{L_d}{L} \right)^2, \quad (9.12)$$

where the deformation radius, $L_d \equiv (g' \bar{h})^{1/2} / f$ for a layer interface between two layers of moving fluid. Perturbations in Q are dominated by stratification for large horizontal scales, $L \gg L_d$, and instead by the circulation for small scales, $L \ll L_d$. Since eddies formed by baroclinic instability involve changes in both the circulation and stratification, they preferentially occur on the horizontal scale $L \sim L_d$ when these contributions to (9.8) are comparable.

If this scaling process is repeated for continuous stratification, $Q = -\frac{(f + \dot{q})}{\rho} \frac{\partial \sigma}{\partial z}$, then an internal deformation radius is obtained given by

$$L_d \equiv \frac{N H}{f},$$

where $N^2 \equiv -\frac{g}{\rho} \frac{\partial \sigma}{\partial z}$ and H is a vertical length scale. The same arguments apply for continuous stratification, with L_d being the preferred scale for baroclinic instability.

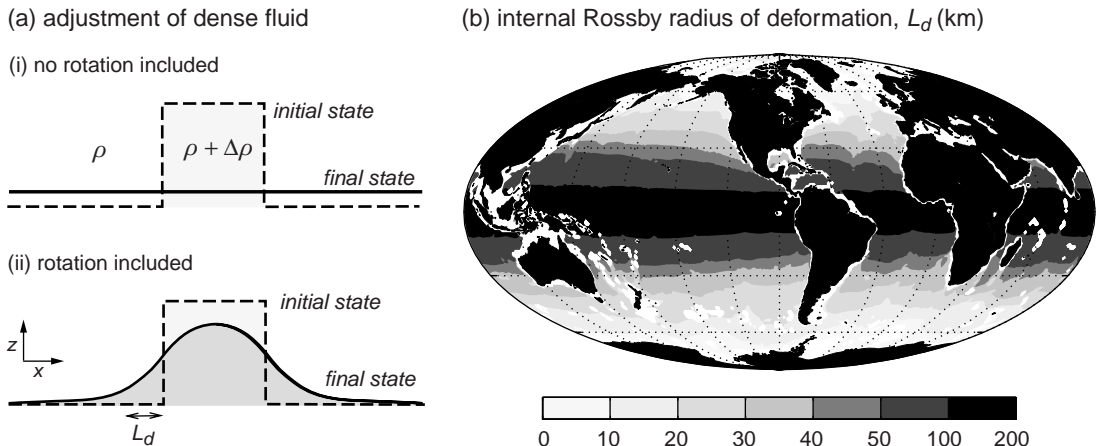


Figure 9.9 (a) A schematic figure showing an initial pulse of dense fluid (dashed line) and its subsequent spreading (full line) for two cases: (i) without rotation where the dense fluid spreads uniformly over the whole domain, and (ii) with rotation where the spreading is limited to a horizontal scale of typically L_d from the initial disturbance, where L_d is called the internal Rossby deformation radius. This limited spreading of the dense fluid leads to a horizontal circulation around the dense anomaly. (b) A global contour map of the baroclinic Rossby radius of deformation in the ocean, L_d (km), plotted from climatology; data from Dudley Chelton, for further details see Chelton *et al.* (1998).

9.2.5 What are the characteristic timescales for eddies to grow?

A characteristic growth rate for eddies is given by the ratio of their characteristic velocity and length scales,

$$\mathcal{T}^{-1} \simeq \frac{U_{\text{eddy}}}{L_{\text{eddy}}}.$$

Assuming that the horizontal length scale is given by L_d from (9.7) and the velocity scale is given from the available potential energy release for baroclinic instability from (9.21) in Box 9.3 where

$$U_{\text{eddy}} \sim \frac{H}{2} \left| \frac{\partial u}{\partial z} \right|,$$

then the growth rate for eddies is given approximately by

$$\mathcal{T}^{-1} \simeq \frac{1}{2} \frac{f}{N} \left| \frac{\partial u}{\partial z} \right|, \quad (9.13)$$

where N is the buoyancy frequency related to the vertical stratification and $\partial u / \partial z$ is the vertical shear in the horizontal velocity. For example, if $N \sim 3 \times 10^{-3} \text{ s}^{-1}$ and $f \sim 10^{-4} \text{ s}^{-1}$ with a velocity shear $\partial u / \partial z \sim (0.1 \text{ m s}^{-1}) (2000 \text{ m})^{-1}$, then this suggests the timescale for eddies to form, \mathcal{T} , is typically the order of 10 days. This scaling for

the eddy growth rate is now diagnosed over the ocean.

Eady growth period in the ocean

An eddy growth period, \mathcal{T} , based on linear instability theory is defined as

$$\mathcal{T}^{-1} = 0.31 \frac{f}{N} \left| \frac{\partial \mathbf{u}}{\partial z} \right|, \quad (9.14)$$

referred to as the Eady growth period, representing the fastest growing mode in baroclinic instability; here f is the Coriolis parameter, N is the buoyancy frequency and \mathbf{u} is the geostrophic velocity vector. This inverse timescale (9.14) is the same as that obtained from the scaling in (9.13) apart from the factor 0.5 being replaced by 0.31 (Lindzen and Farrell, 1980).

The Eady growth period is smallest in regions of strong jets and boundary currents where there are large isopycnal slopes and an associated large vertical shear in horizontal velocity. There are short Eady growth periods of 10 to 20 days along the path of the Gulf Stream, shortest close to where the current separates from the coast (Fig. 9.10a), compared with much longer periods of 100 days or more in the gyre interior. In a similar manner in the North Pacific, there is an Eady

Box 9.3 How large is the eddy velocity obtained from baroclinic instability?

Returning to the energetics of parcel exchange in Box 9.1, the potential energy release is given by

$$\Delta PE = g \Delta \rho \Delta z \simeq \frac{g \alpha L^2}{2} \frac{\partial \rho}{\partial y}, \quad (9.15)$$

where fluid is exchanged at an angle, α , half the slope of the background density surfaces (Fig. 9.7b),

$$\alpha = -\frac{1}{2} \frac{\partial \rho}{\partial y} / \frac{\partial \rho}{\partial z}. \quad (9.16)$$

The released potential energy is assumed to be converted to kinetic energy,

$$\Delta KE = \frac{1}{2} (\rho_A + \rho_B) \Delta v^2 \equiv \bar{\rho} \Delta v^2, \quad (9.17)$$

where Δv represents the change in velocity for the fluid parcels, $\bar{\rho}$ is the mean density of the fluid parcels and kinetic energy is defined per unit volume (J m^{-3}). Equating (9.15) and (9.17) implies that the change in velocity is

$$\Delta v^2 = \frac{g \alpha L^2}{2 \bar{\rho}} \frac{\partial \rho}{\partial y}. \quad (9.18)$$

Assuming thermal-wind balance,

$$\frac{\partial u}{\partial z} = \frac{g}{\bar{\rho} f} \frac{\partial \rho}{\partial y}, \quad (9.19)$$

a buoyancy frequency, $N^2 = -(g/\bar{\rho})\partial\rho/\partial z$, and the angle of the fluid particle exchange, α (9.16), allows (9.18) to be expressed as

$$\Delta v^2 = \left(\frac{L_f}{2N} \frac{\partial u}{\partial z} \right)^2. \quad (9.20)$$

Hence, the velocity change depends on the velocity shear weighted by the ratio of the Coriolis parameter and buoyancy frequency. Assuming that the horizontal scale for this exchange, L , is the same as the deformation radius, $L_d = NH/f$ in (9.7), and that the velocity magnitude for the eddy velocity $U_{\text{eddy}} \sim \Delta v$, then

$$U_{\text{eddy}} \sim \frac{H}{2} \left| \frac{\partial u}{\partial z} \right|. \quad (9.21)$$

Thus, the typical velocity for baroclinic eddies is given by half the background velocity change over their height scale, H . To test this scaling, see the Southern Ocean example in Q9.1.

growth period of less than 1 month (Fig. 9.10b), and in the Southern Ocean, a slightly longer Eady growth period from 1 to 2 months along the Antarctic Circumpolar Current (Fig. 9.10c).

The shortest Eady growth periods are slightly upstream of the maxima in eddy kinetic energy (compare Figs. 9.4 and 9.10a,b), suggesting that

eddy variability is initially generated and then either amplifies downstream or is advected downstream by the background flow.

9.2.6 Summary

Baroclinic instability generates eddy variability through a release of potential energy from

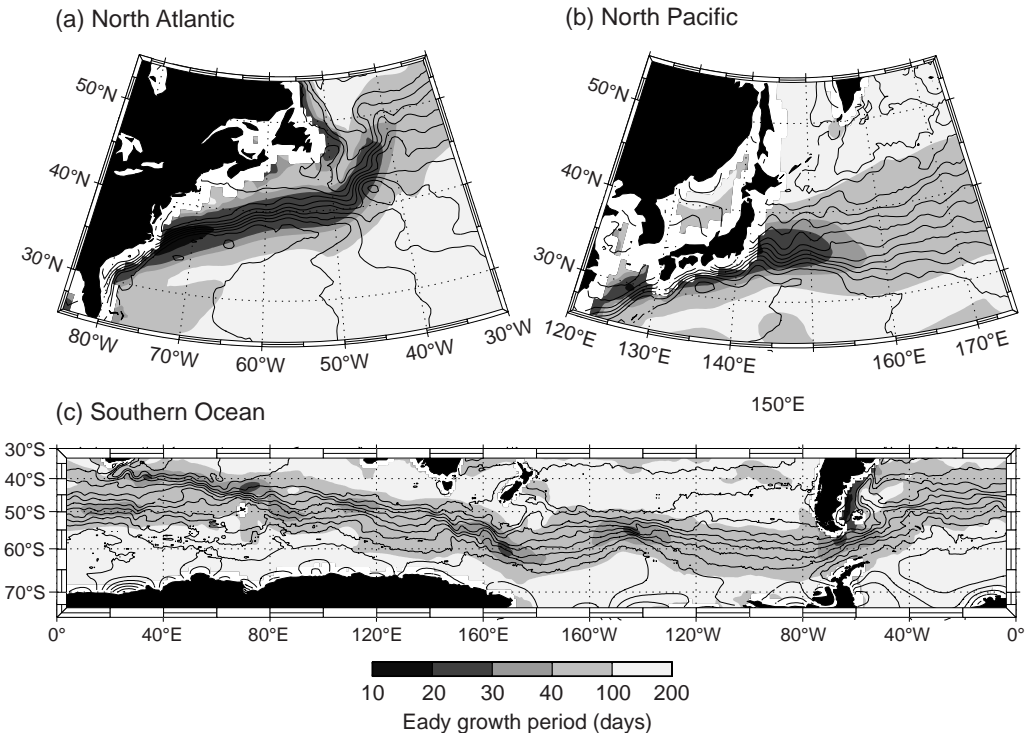


Figure 9.10 Diagnostics of the Eady growth period (days) for (a) the Gulf Stream in the North Atlantic, (b) the Kuroshio in the North Pacific, and (c) the Antarctic Circumpolar Current in the Southern Ocean. The Eady growth period is averaged over the upper 900 m and masked where depth is less than 1000 m, from climatology. The mean dynamic topography from Maximenko and Niiler (2005) is given by thin contours (every 10 cm). Data supplied by Chris Wilson; further details in Williams *et al.* (2007) and similar diagnostics in Smith (2007).

sloping potential density surfaces. This instability process preferentially occurs on a horizontal scale called the internal deformation radius, related to the Coriolis parameter and stratification. The distribution of eddy kinetic energy generally coincides with an enhancement in the poleward surface heat flux and the Eady growth rate.

Eddy kinetic energy can also be generated by other processes, involving the horizontal shear in the horizontal velocity, referred to as barotropic instability (see Vallis, 2006), as well as fine-scale fluctuations in wind forcing (Müller and Frankignoul, 1981) and flow interactions with bottom topography (Gille, 1997).

9.3 | Eddy fluxes of tracers

The presence of a vibrant eddy circulation means that the transfer of tracers over the ocean and

atmosphere cannot be understood simply in terms of the advection by the time-mean circulation plus a background diffusion.

To address how eddies transfer tracers, we first consider the effect of eddies in the atmosphere and then the ocean.

9.3.1 Atmospheric weather systems

In the atmosphere, weather systems are preferentially located where there are the fast-moving westerly jet streams in the mid latitude. There are relatively short growth periods of 1 to 2 days over the western side of the ocean basins in the northern hemisphere and over the Indian sector of the southern hemisphere (Fig. 9.11, shading).

In the same regions, there are pronounced poleward eddy heat fluxes (Fig. 9.11, thick contours), as well as increased variability in the height of a pressure surface (not shown). These regions are referred to as atmospheric storm tracks.

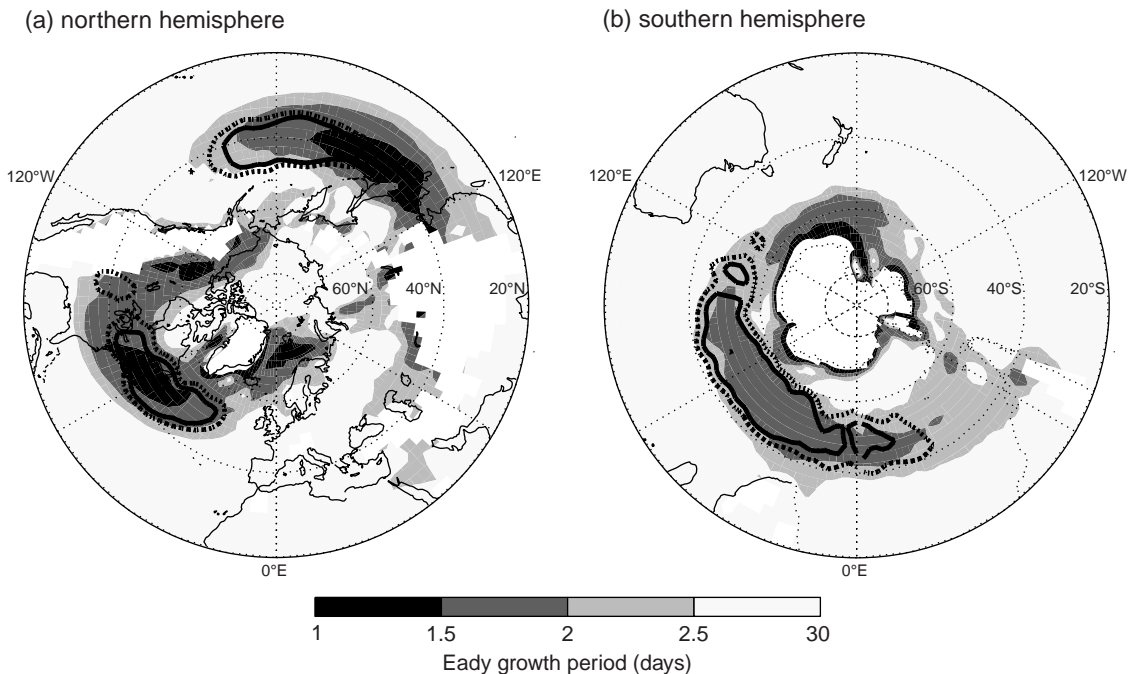


Figure 9.11 Diagnostics of atmospheric storm tracks in winter for eddy poleward heat flux $v' T'$, at 700 mbar (12 and $10 \text{ m s}^{-1} \text{ K}$ are thick solid and dashed contours) and Eady growth period at a height of 775 mbar (days, shaded) in (a) the northern hemisphere (DJF), and (b) the southern hemispheres (JJA). Regions where the mean height of the 775 mbar surface comes within 1 km of orography are masked. Figure supplied by Chris Wilson; further details in Williams *et al.* (2007).

One might expect that as an atmospheric storm is generated, the background temperature gradient is weakened and that subsequent atmospheric storms are formed elsewhere. In practice, the opposite appears to be the case: atmospheric weather systems are preferentially formed over the same region, the western side of the ocean basins in the northern hemisphere. There appears to be a characteristic life-cycle in the atmospheric storms: they initially form at the western start of the storm track, grow in time, then eventually decay over the eastern end of the storm track. During this life-cycle, the atmospheric eddies feed back on the mean flow: eddies provide an eastward acceleration to the mean flow over the start and core of the storm track, while as the eddies decay at the exit and downstream of the storm track, they instead provide a westward acceleration to the mean flow (Hoskins, 1983; Hoskins *et al.*, 1983).

The pattern of the atmospheric storm tracks and ocean variability appear to be partly connected. While the causal mechanism controlling this connection is unclear, Hoskins and Valdes

(1990) propose that the warm ocean feeds back on the atmosphere by providing a latent heat source that helps atmospheric weather systems intensify, while the long-term path of the atmospheric jet controls the position of the ocean gyre boundaries and affects the transport of warm water in the ocean boundary currents.

Now we return to consider how ocean eddies affect the transfer of heat and tracers.

9.3.2 Eddy sea-surface temperature fluxes

The eddy transfer of heat is now diagnosed through the use of remotely sensed altimetry and sea-surface temperature data, firstly for the northern basins and secondly for the southern hemisphere and the Antarctic Circumpolar Current (Figs. 9.12 and 9.13).

Variability in the northern hemisphere

In the northern hemisphere, there are maxima in the sea-surface temperature variance over the extension of the western boundary currents into

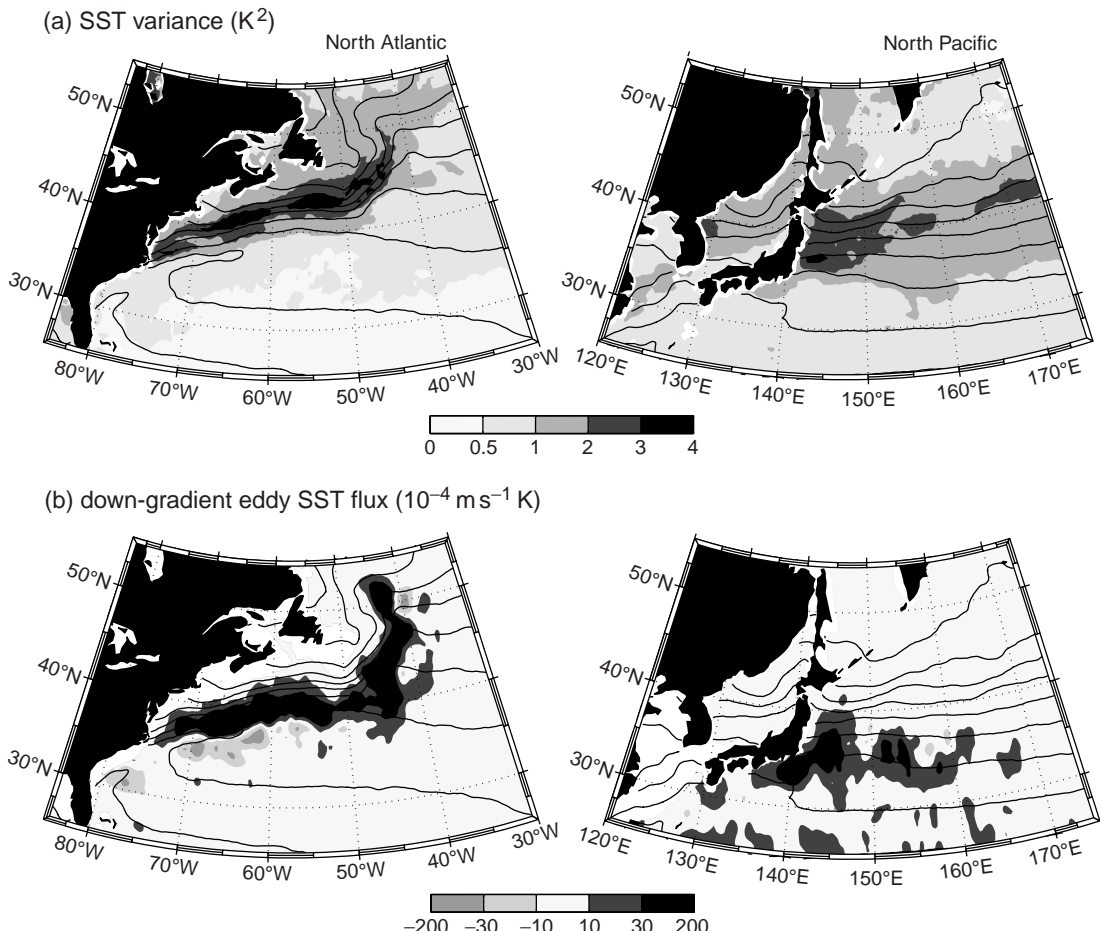


Figure 9.12 Diagnostics of (a) the variance in sea-surface temperature (SST) (K^2), and (b) the component of the eddy SST flux directed down the mean SST gradient, $-\bar{\mathbf{u}}' T' \cdot \nabla \bar{T} / |\nabla \bar{T}|$ (shaded, $10^{-4} \text{ m s}^{-1} \text{ K}$) for the North Atlantic (left panel) and North Pacific (right panel), together with the mean SST (thin contours every 2.5°C). The eddy flux is generally down gradient (plotted as positive) with a band of up-gradient SST flux on the southern edge of the Gulf Stream. The temperature variance is diagnosed from Advanced Very High Resolution Radiometer (AVHRR) on a 0.5° grid for the period 3 January 1990 to 26 March 2003 with a seasonal cycle removed. Diagnostics by Chris Wilson; further details in Williams et al. (2007).

the gyre interiors; temperature variance is defined by the square of the temperature deviations from the time-mean temperature. These maxima in temperature variance are coincident with a tightening of the sea-surface temperature contours (Fig. 9.12a), suggesting that the instability of these extended western boundary currents is responsible for the local maximum in temperature variance (Fig. 9.4a).

Eddy heat fluxes depend on the correlation of temporal variations in the circulation and sea surface temperature. The eddy heat flux is par-

ticularly pronounced along the separated jets of the Gulf Stream and Kuroshio, generally directed down gradient (Fig. 9.12b, dark shading), and acting to reduce surface temperature contrasts. This down-gradient transfer is consistent with baroclinic instability forming warm-core and cold-core eddies passing to the north and south of the Gulf Stream respectively (Fig. 9.2a).

An exception occurs on the southward flank of the Gulf Stream, where the eddies provide a narrow band of an up-gradient surface temperature flux (Fig. 9.12b, light shading), which is due

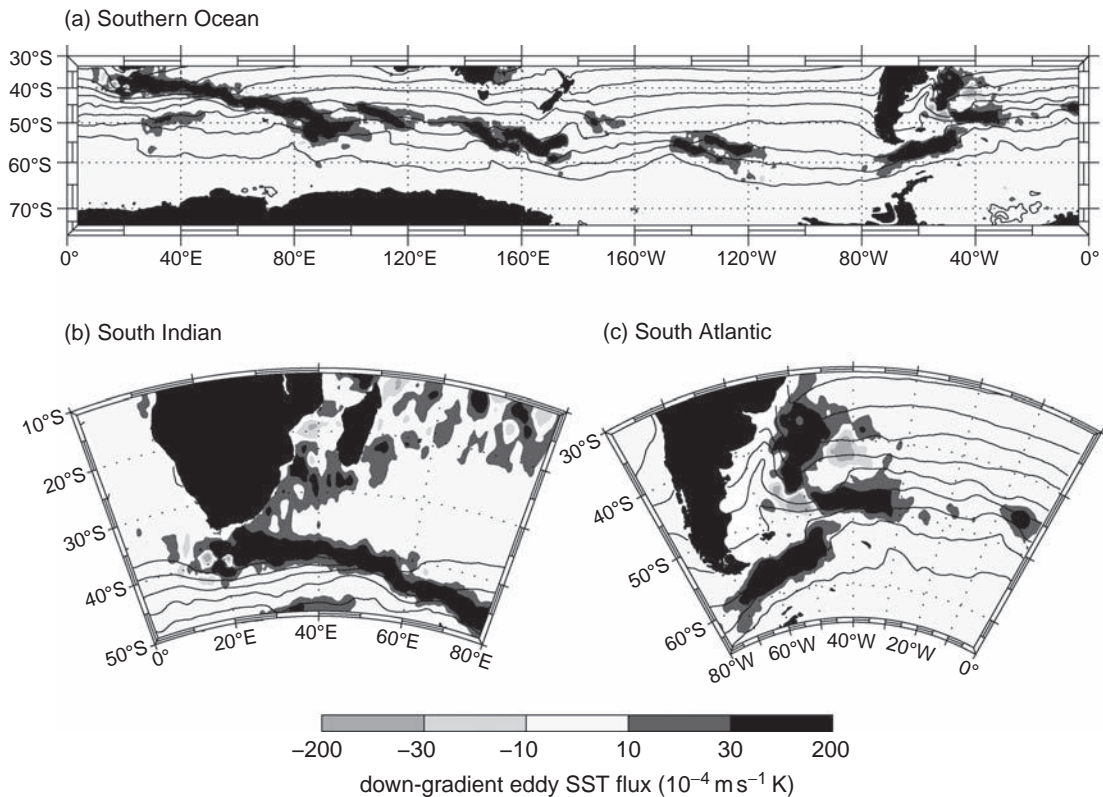


Figure 9.13 Diagnostics for the component of the eddy SST flux directed down the mean SST gradient, $-\bar{\mathbf{u}}' T' \cdot \nabla \bar{T} / |\nabla \bar{T}|$ (shaded, $10^{-4} \text{ m s}^{-1} \text{ K}$) with the mean SST (contours every 2.5°C) for (a) the Southern Ocean, together with (b) the South Indian, and (c) the South Atlantic sectors. Details as in Fig. 9.12.

to a narrow reversal in the northward gradient in surface temperature, $\partial T / \partial y > 0$, from advection of warm surface waters along the core of the current.

Variability in the southern hemisphere

In the southern hemisphere, there are pronounced eddy heat fluxes directed down gradient over the jets making up the Antarctic Circumpolar Current (Fig. 9.13a).

This eddy heat flux is particularly enhanced downstream of South Africa, south of Australia and through Drake Passage (Fig. 9.13a–c), where there is a tightening of surface temperature contours, probably associated with the underlying topography affecting the path of the current. In addition, there are enhanced down-gradient eddy fluxes of surface temperature in the vicinity of the Agulhas Current and Brazil Current (Fig. 9.13b,c).

This eddy transfer of heat within the Southern Ocean is directly analogous to the poleward heat

fluxes that atmospheric eddies provide across the mid-latitude jet stream (Fig. 9.11, thick contours).

9.3.3 Eddy stirring in the thermocline

Eddies transfer tracers throughout the ocean, including below the surface and within the thermocline. This transfer preferentially occurs along potential density surfaces within the ocean interior.

Eddy stirring is now illustrated using an eddy-resolving isopycnic model for a pair of wind-driven gyres in an idealised rectangular basin (Fig. 9.14). Advection by the mean circulation leads to tracer contours and streamlines becoming nearly coincident and closed over much of the interior domain. A dynamical tracer, the potential vorticity is stirred by the eddy circulation with a tight interleaving of tracer filaments after 1 year (Fig. 9.14a), which evolves to a nearly uniform distribution after 6 years (Fig. 9.14b).

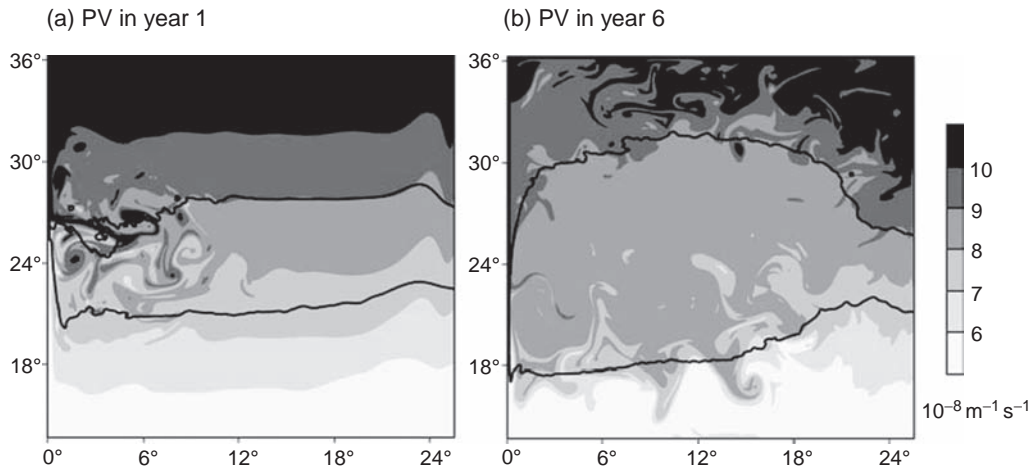


Figure 9.14 Potential vorticity (PV, $10^{-8} \text{ m}^{-1} \text{s}^{-1}$) in an eddy-resolving ($1/16^\circ$), 5 layer, model of idealised subtropical and subpolar gyres within a rectangular basin: instantaneous snapshots for (a) year 1, and (b) year 6, together with two time-averaged PV contours (thick lines) where the time-averaging is applied over a 600 day window. In this layer, there is no direct forcing by the wind or bottom friction, and the PV is only altered by the stirring from geostrophic eddies, as revealed by the fine filaments being drawn out. The eddy stirring leads to the contours of PV being gradually expelled from the central part of the basin. This nearly uniform PV distribution is reminiscent of the observations within the thermocline, as first argued by Rhines and Young (1982a,b). Model snapshots reproduced from Wilson and Williams (2004).

The effect of eddies in stirring tracers and leading to nearly uniform tracer distributions occurs for any tracers without strong sources or sinks lying within closed geostrophic streamlines, as first advocated by Rhines and Young (1982a,b); this eddy stirring can, though, be inhibited in the presence of jets (see later Section 9.3.6).

9.3.4 How do eddies advect and diffuse tracers?

Eddies lead to both a diffusive and advective transfer of tracers, as illustrated in Fig. 9.15. The diffusive transfer is easy to understand, eddies usually act to transfer tracers down gradient from high to low concentrations (Fig. 9.15a,b).

Eddies can also lead to an advective transfer which can transfer tracer either up or down gradient; for example, as depicted for the slumping of an interface in a two-layer fluid in Fig. 9.15a,c.

In order to understand this eddy advection, again consider the volume flux in an isopycnal layer (Section 3.3.3): the time-averaged thickness flux is made up by the advection by the time-mean flow and the eddy flux of thickness,

$$\bar{u}h = \bar{u}\bar{h} + \bar{u}'\bar{h}', \quad (9.22)$$

which can be written as

$$\bar{u}h = (\bar{u} + \bar{u}^*)\bar{h}, \quad (9.23)$$

where $\bar{u}^* \equiv \bar{u}'\bar{h}'/\bar{h}$. This additional eddy advection, \bar{u}^* , referred to as a bolus advection, can lead to tracers being advected up or down gradient. During baroclinic instability, the slumping of potential density surfaces is associated with the eddy bolus transport directed poleward in the upper layer and equatorward in the deeper layer, as depicted in Figs. 3.16 and 9.15c.

Idealised model illustration of eddy transport

The effect of this eddy transport is now illustrated in an idealised eddy-resolving model integration for a zonal channel, configured for the northern hemisphere (Fig. 9.16a). The channel is initialised with the density gradient sustained by cooling on the northern boundary and heating on the southern boundary. There is a zonal flow along the channel, which becomes unstable, generating an eddy circulation.

In this experiment, a tracer is released in the channel with low values to the south of the jet and high values to the north. After 5 days, the initial tracer front simply meanders with an eddy

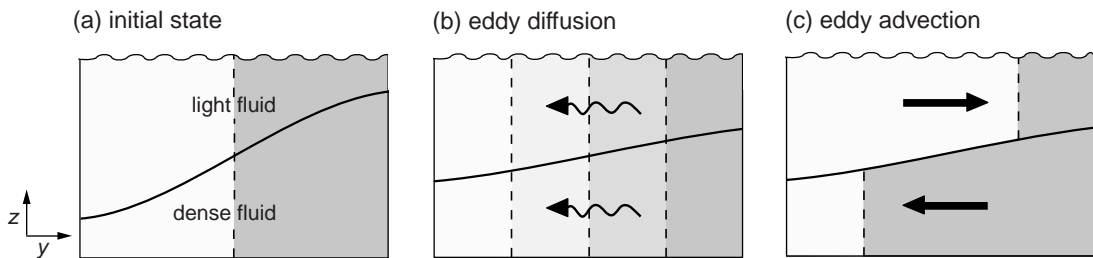


Figure 9.15 Schematic of eddy transfer of tracer. Eddies are generated through the slumping of the interface between light and dense fluid. In this thought experiment, an initial tracer contrast in (a) is modified through an eddy-induced diffusion in (b) and advection in (c). The eddy-induced advection arises from the slumping of the interface. This diffusion and advection can oppose or reinforce each other in spreading tracer, as illustrated in the upper and lower layers, respectively. Reproduced from Lee and Williams (2000), courtesy of J. Marine Res., Yale University.

developing along the jet (Fig. 9.16b). After a year, the initial tracer front has been smeared out, although there are still eddy undulations in the tracer contours (Fig. 9.16c). If there is a continual release of tracer (with low and high values on the southern and northern boundaries, respectively), then a surprising tracer distribution eventually emerges. After 18 years, the low tracer concentration from the south has preferentially spread northward over much of the top layer, while the high tracer concentration from the north has spread south over much of the bottom layer (Fig. 9.16d).

This tracer evolution can be understood in the following manner. The eddy circulation leads to a stirring and weakening of the initial tracer contrast, consistent with the expected down-gradient diffusion by eddies. However, there is also a systematic advection of the tracer by the eddies. The slumping of the isopycnal surfaces leads to a net northward transport and bolus velocity in the upper layer and a net southward transport and bolus velocity in the bottom layer. Consequently, the tracer from the southern boundary preferentially spreads further north in the top layer compared with the bottom layer, while the reverse occurs for the tracer from the northern boundary. In this experiment, the final tracer distribution is controlled by the location of tracer sources and the systematic advection by the eddies.

9.3.5 How to parameterise eddies?

Understanding how eddies affect the background state and developing parameterisations for them is challenging due to their myriad effects. Eddies

can either be parameterised in terms of their global effects or their local behaviour.

For global closures, there are two contrasting views:

- Eddy transfer can be represented by a down-gradient diffusion of any conserved tracer (Fig. 9.15b). This representation of eddies leads to homogenisation of potential vorticity within closed streamlines in shielded density layers (Rhines and Young, 1982a,b).
- Eddy transfer can be represented in terms of a down-gradient diffusion of thickness within a density layer (Fig. 9.15c), which mimics how baroclinic instability leads to a slumping of density layers and a release of potential energy from the background state. This eddy representation provides an additional eddy advection of tracers, as discussed in Section 3.3 and represented in Box 9.4; see Gent and McWilliams (1990) and Gent *et al.* (1995).

In practice, eddies can lead to both these global effects, as illustrated in the eddy-resolving model experiments shown in Figs. 9.14 and 9.16.

Alternatively, eddies can be viewed in terms of their life-cycle, in which case their effects vary according to whether the eddies are growing or decaying (see Q9.4). For example, atmospheric eddies transfer eastward momentum into the start of the storm tracks, sustaining and reinforcing the eastward flow there. At the exit of the storm track, atmospheric eddies dissipate and transfer westward momentum into the jet. Hence, there is an important feedback from the eddies to

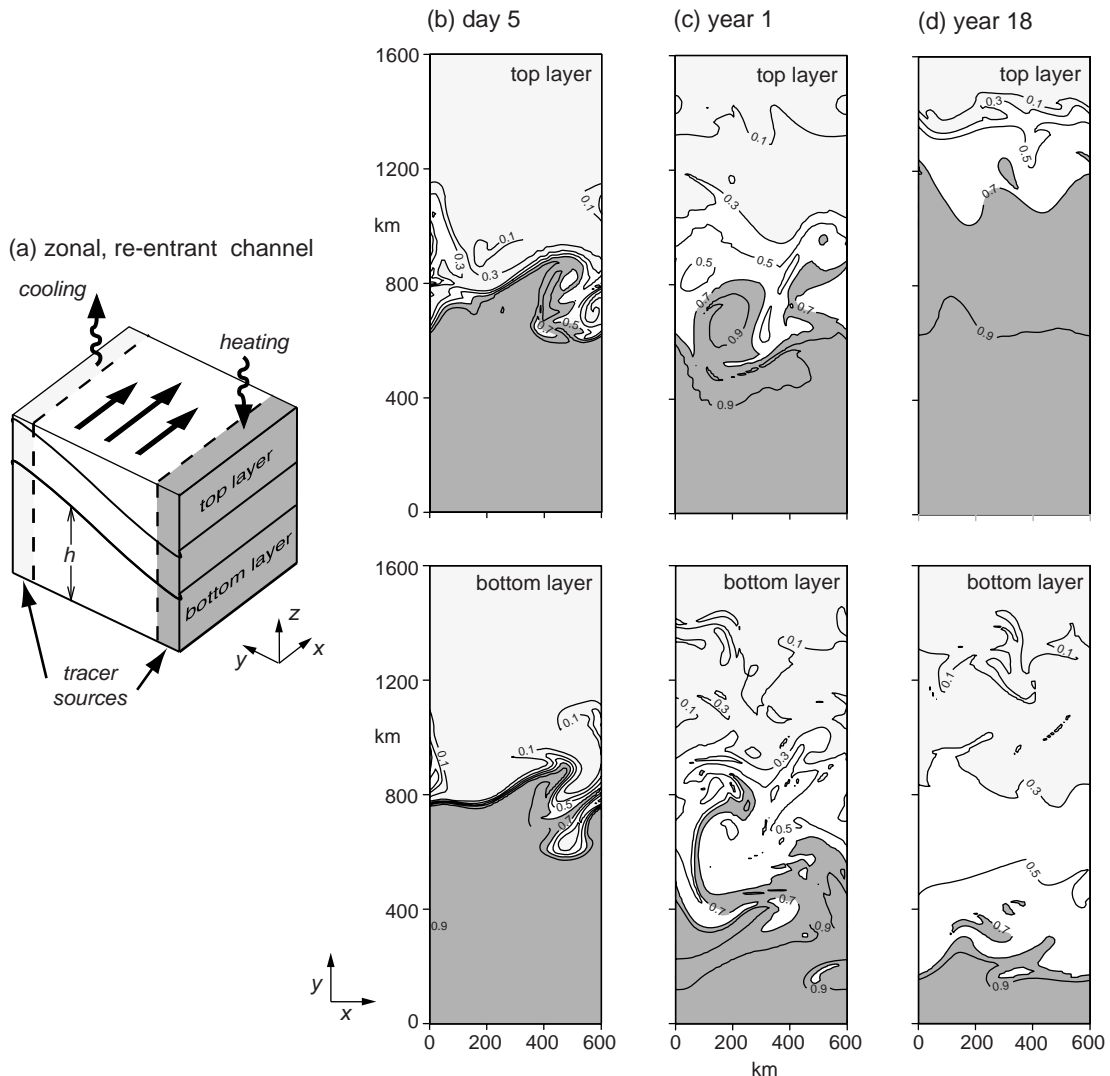


Figure 9.16 A model illustration of the eddy transport of tracer: (a) model domain consisting of a zonal, re-entrant channel in the northern hemisphere with three density layers, and (b) time series of tracer fields for the top and bottom layers after day 5 of year 0, (c) year 1, and (d) year 18. The model is forced by heating and cooling applied in relaxation zones on the southern and northern boundaries, leading to sloping isopycnals. There is a strong zonal flow, which is baroclinically unstable, forming meoscale eddies. Tracers are released in the relaxation zones and spread through the action of the eddy circulation. The asymmetrical tracer distribution at the final state is a result of the eddy bolus velocity being directed northward in the upper layer and southward in the bottom layer. Reproduced from Lee et al. (1997), courtesy of *J. Marine Res.*, Yale University.

the mean flow; see Hoskins (1983) and Hoskins *et al.* (1983).

9.3.6 The competing effects of jets and eddies

The role of eddies in transferring tracers cannot be understood in isolation of the background flow, particularly the presence of strong jets.

Jets provide a strong advective transfer, preferentially transferring tracers downstream along streamlines. If the streamlines originate from different regions, then the streamlines converging in a jet lead to a large tracer contrast forming across the width of the jet. Eddies locally stir tracers and, augmented by molecular diffusion, usually act to reduce tracer contrasts.

Box 9.4 How is eddy transport represented in the tracer equation?

Here, we present a derivation of the time-mean tracer equation for a zonal channel with no explicit source of tracer following Gent *et al.* (1995). The concentration of a tracer, C , within a density layer evolves through horizontal advection,

$$\frac{\partial C}{\partial t} + u \frac{\partial C}{\partial x} + v \frac{\partial C}{\partial y} = 0, \quad (9.24)$$

and similarly the thickness of the layer of fluid h varies as

$$\frac{\partial h}{\partial t} + \frac{\partial}{\partial x}(hu) + \frac{\partial}{\partial y}(hv) = 0. \quad (9.25)$$

Taking a combined time average over many eddy life-cycles and a zonal average over the width of the channel (which removes the $\partial/\partial x$ term) for (9.25) gives

$$\frac{\partial \bar{h}^{x,t}}{\partial t} + \frac{\partial}{\partial y}(\bar{h}^{x,t} \bar{v}^{x,t}) + \frac{\partial}{\partial y}(\bar{h}'v'^{x,t}) = 0, \quad (9.26)$$

where superscripts are henceforth dropped for simplicity. Multiply (9.24) by h and (9.25) by C , then combining gives the evolution of the thickness-weighted tracer:

$$\frac{\partial}{\partial t}(hC) + \frac{\partial}{\partial x}(uhC) + \frac{\partial}{\partial y}(vhC) = 0, \quad (9.27)$$

and again applying a time and zonal average gives

$$\frac{\partial}{\partial t}(\bar{h} \bar{C} + \bar{h}'\bar{C}') + \frac{\partial}{\partial y} \left\{ (\bar{h}\bar{v} + \bar{h}'\bar{v}')\bar{C}' \right\} = -\frac{\partial}{\partial y}(\bar{h}\bar{v}')\bar{C}'. \quad (9.28)$$

The time derivative of $\bar{h}'\bar{C}'$ is relatively small and can be neglected, then expanding the rate of change of each of the product terms, using

$$\frac{\partial}{\partial t}(\bar{h} \bar{C}) = \bar{h} \frac{\partial \bar{C}}{\partial t} + \bar{C} \frac{\partial \bar{h}}{\partial t},$$

and combining with (9.26), provides the time-mean tracer equation,

$$\frac{\partial \bar{C}}{\partial t} + (\bar{v} + v^*) \frac{\partial \bar{C}}{\partial y} \approx -\frac{1}{h} \frac{\partial}{\partial y}(\bar{h}\bar{v}')\bar{C}', \quad (9.29)$$

where $v^* = \bar{h}'\bar{v}'/\bar{h}$ is the bolus velocity. Hence, the effects of the eddies are included in the additional advection, v^* (third term on the left-hand side), and by the diffusive term (on the right-hand side). If there are no thickness variations, the advection in (9.29) reduces to the advection by the time-mean flow and the right-hand side reduces to the expected divergence of the eddy tracer fluxes, $-\frac{\partial}{\partial y}(\bar{v}')\bar{C}'$.

Hence, jets and eddies often compete with each other in either increasing or reducing local tracer gradients.

To understand these competing effects, we next consider observations of tracers and float signals along the Gulf Stream and, then, consider

a kinematic view of how particles are advected across a meandering jet.

Property contrasts across the Gulf Stream

The separated Gulf Stream, which is associated with a rapid northward shoaling of

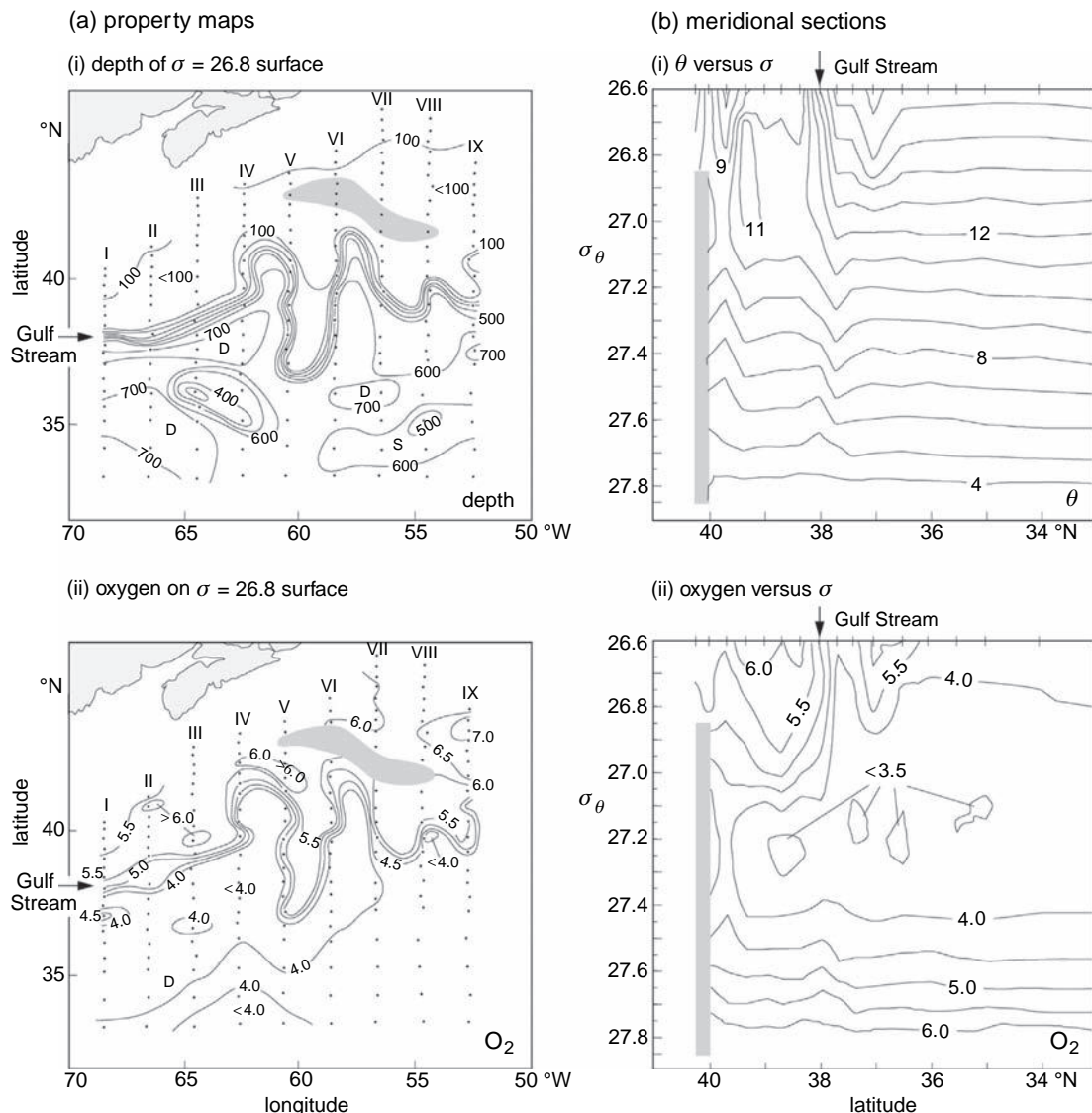


Figure 9.17 Property contrasts across the Gulf Stream: (a) maps of (i) depth (m) of $\sigma = 26.8$ surface and dissolved oxygen (ml l^{-1}) along the $\sigma = 26.8$ surface; and (b) meridional sections for (i) potential temperature, θ ($^{\circ}\text{C}$) versus σ and (ii) dissolved oxygen (ml l^{-1}) versus σ surfaces across the Gulf Stream along 68.5°W . The Gulf Stream is located between 37°N and 38°N at this longitude, associated with the sharp contrast in temperature and oxygen along σ surfaces lighter than 27.1. In contrast, properties are relatively uniform along denser σ surfaces. Redrawn from Bower *et al.* (1985).

potential density surfaces, meanders and extends for more than a thousand kilometres from the coast (Fig. 9.17a, i). Along light σ surfaces in the upper part of the thermocline, there is an undulating front in dissolved oxygen concentration, which resembles the movement of the front in the height of isopycnals (Fig. 9.17a, ii). However, this property contrast across the Gulf

Stream is not evident in the deeper thermocline, along denser σ surfaces greater than 27.1, where tracers have a more uniform concentration (Fig. 9.17b).

Consequently, the tracer contrasts across the Gulf Stream suggest that the jet acts as a barrier in the upper thermocline, while the combination of meanders and eddies act as a blender in the

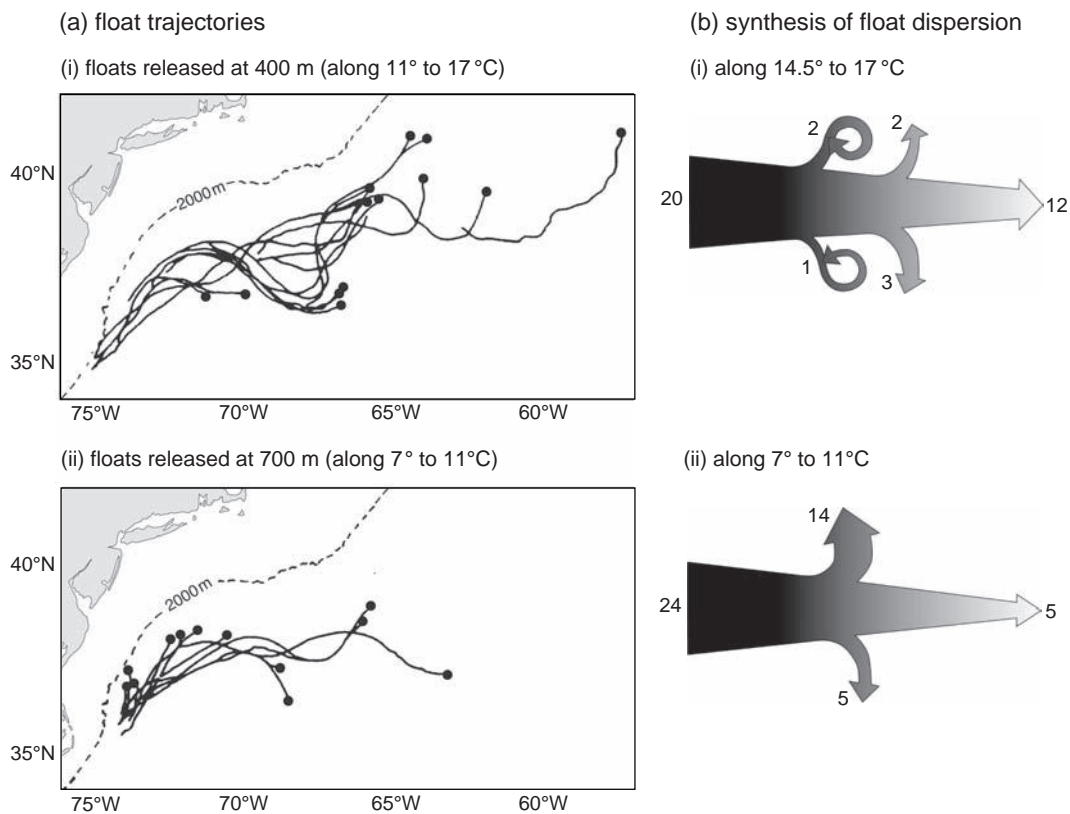


Figure 9.18 Float dispersion experiments. (a) Trajectories of floats up to the point of first escape from the Gulf Stream: (i) on temperature surfaces between 11° and 17 °C and (ii) between 7° and 11 °C, and (b) a schematic representation of float dispersion (i) 14.5°–17.0 °C and (ii) 7.0°–11.0 °C. In (a), 37 floats following isopycnals were released at depths of between 400 m and 700 m off Cape Hatteras and tracked for up to 45 days during 1984–85 from the SYNOP experiment, while in (b) float dispersion from both Pilot and SYNOP experiments, with the number of floats deployed in each layer shown on the left and the number of floats staying in the stream for more than 30 days shown on the right; the arrows shown leaving the main arrow shaft indicate floats that escaped from the stream via rings or other mechanisms. There was a greater loss of floats in the deep layer compared with the upper layer. Panels (a) redrawn from Bower and Rossby (1989) and (b) redrawn from Bower and Lozier (1994).

deeper thermocline; as originally set out by Bower *et al.* (1985).

Exchange of floats across the Gulf Stream

In order to assess the extent of the across-front transfer in the Gulf Stream, a series of observational programmes have been conducted: neutrally buoyant floats were released in the upper thermocline, the buoyancy of the floats adjusted to follow selected isopycnals and they were subsequently tracked to the point at which each float first left the stream.

Floats released in the Gulf Stream were more likely to be retained in the current within the upper thermocline (Fig. 9.18a), than within the

lower thermocline. Floats leaving the stream did not necessarily cross the stream and were usually involved in exchanges with meanders, and only a few of the floats were caught within intense eddies or rings (Fig. 9.18b).

Hence, observational studies suggest that exchange across the Gulf Stream is inhibited in the upper thermocline and enhanced in the lower thermocline.

Why does the Gulf Stream act both as a barrier and blender?

In order to understand the exchange across the Gulf Stream, we now consider how particles are advected by the time-varying flow. Assume that

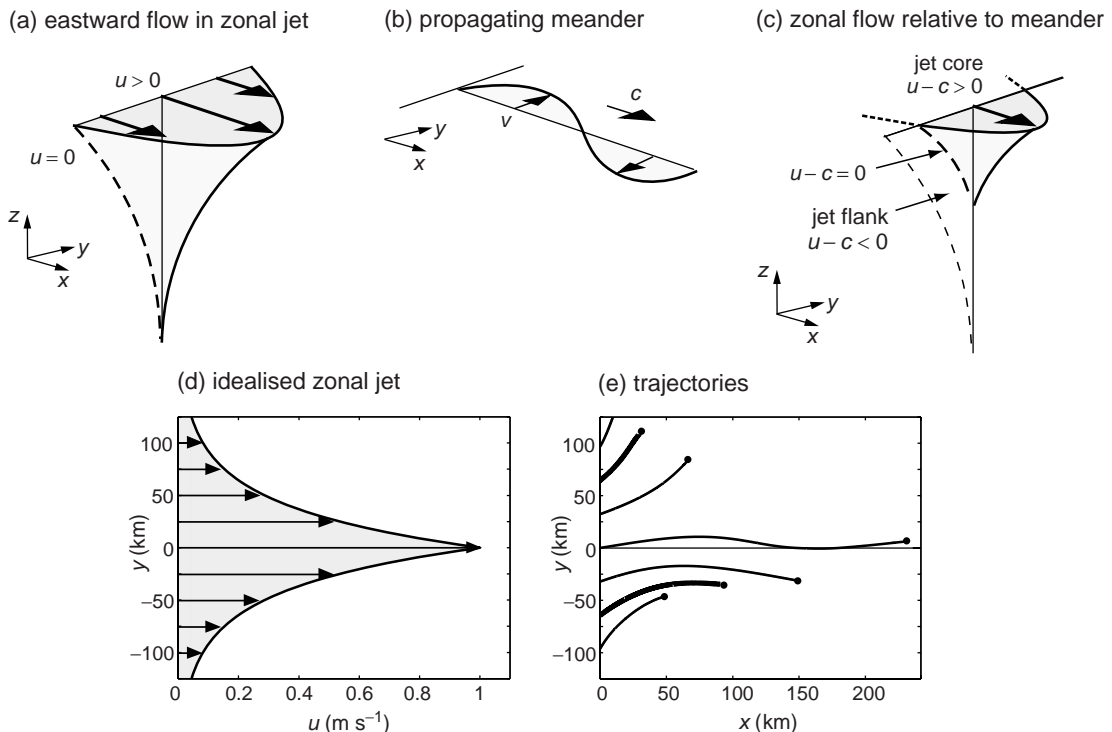


Figure 9.19 A schematic figure depicting where mixing is likely to occur across a jet: (a) a zonal jet with zonal velocity, $u(y, z)$; (b) cross-front flow, v , associated with a meander; propagating downstream with a wave speed, c (the speed of an individual crest or trough); and (c) the eastward flow relative to the meander, $u - c$ (with only positive values plotted). The flow relative to the meander, $u - c$, is positive in the core of the surface jet and negative on the outer flanks. At the interface, $u - c = 0$ (thick dashed line), fluid particles move eastward at the same speed as the meander propagation and so experience strong meridional exchange; this region of enhanced mixing moves into the core of the jet at depth and is called the steering level or critical layer. In (d) and (e), a model calculation reveals particles swept downstream in the core of the jet, but undergo more pronounced displacements on the flank of the jet (dots are at the end points of the trajectories and bold lines are along the steering level); the jet velocity, $u(y) = u_0 \exp(-y/(2y_{jet}))$, and the meander velocity, $v(x, t) = v_0 \cos(2\pi(x - ct)/\lambda)$, with maxima of $u_0 = 1 \text{ m s}^{-1}$ and $v_0 = 0.2 \text{ m s}^{-1}$, a wave speed $c = 0.2 \text{ m s}^{-1}$ and wavelength $\lambda = 200 \text{ km}$, and jet decay width, $y_{jet} = 20 \text{ km}$. For detailed trajectories in ocean jets, see Pratt et al. (1995).

the flow is made up of both an eastward, zonal jet and a meander propagating along the jet, and the only meridional flow is provided by the meander, as depicted in Fig. 9.19a,b. The meridional displacement of a particle moving along the jet depends on the relative speed of the particle to the propagation speed of the meander. There are two regimes:

- (i) If a particle is swept downstream along the jet at a much faster speed than the downstream speed of the meander, then the particle is swept in and out of the oscillating flows of the meander and so the particle effectively remains within the core of the current.

- (ii) If a particle is swept downstream along the jet at the same speed as the meander, then the particle experiences a strong displacement across the jet from the meridional flow of the meander.

These two regimes are reflected in the particle trajectories in Fig. 9.19e, either remaining along the centre of the jet or transferred meridionally along the flanks of the surface jet; also see Q9.3.

These contrasting regimes vary in depth, the region of enhanced displacement occurs along the flanks of the jet at the surface and moves towards the core of a jet at depth (Fig. 9.19c).

Summary

There are strong water-mass contrasts and limited particle exchange across the Gulf Stream within the upper part of the thermocline, but relatively uniform water-mass properties and enhanced particle exchange within the deeper part of the thermocline. The interaction of the background flow and propagating meanders suggests that enhanced horizontal exchange occurs along the flanks of a jet at the surface and along the centre of the jet at depth. Hence, the combination of the jet, meanders and eddies along the Gulf Stream leads to an effective barrier for tracer transfer in the upper thermocline and a blender for tracers in the deeper thermocline. This kinematic view for particle exchange carries over for other intense jets, such as the Antarctic Circumpolar Current in the Southern Ocean.

9.4 | Summary

Ocean mesoscale eddies and atmospheric synoptic-scale weather systems are dynamically analogous. These energetic eddies are not directly formed by the external forcing, but are instead predominantly formed from an instability of the background flow, referred to as baroclinic instability. This instability involves a slantwise exchange of fluid across a jet or frontal zone, where potential energy is released through a flattening of potential density surfaces: warm, light fluid rises and is replaced by colder, dense fluid. For a poleward decrease in temperature, this slantwise exchange leads to warm fluid rising and moving poleward, and cool fluid sinking and moving equatorward, such that there is a poleward eddy heat flux. In the growth phase of an eddy, meanders develop with the rising warm fluid occurring downstream of the trough (region of low pressure) and sinking cold fluid occurring downstream of the ridge (region of high pressure). This growth phase of the eddies is associated with a westward tilt of pressure anomalies with height.

In the ocean, enhanced eddy activity is seen wherever there are intense currents, associated with the western boundary currents within ocean basins and the near-zonal jets making up the

Antarctic Circumpolar Current. The meanders of the intense jets and currents amplify and may break off, forming eddies, such as the warm-core and cold-core eddies on either side of the Gulf Stream. Regions of increased eddy activity are evident in maxima in eddy kinetic energy and the down-gradient eddy heat flux, and minima in the Eady growth period.

In the atmosphere, weather systems are organised in storm tracks linked to the fast-moving eastward jets of air called jet streams. The storms are formed on timescales of one to two days and transfer heat poleward in their formation region. There is a characteristic life-cycle in the atmospheric storms: they initially form at the western start of the storm track, grow in time, then eventually decay over the eastern end of the storm track. Over the growth phase of the storm track, there is a poleward eddy heat flux and eddies provide eastward momentum to the zonal jet, while in the decay phase, the eddies return westward momentum to the jet.

Eddies affect the background state by transferring tracers, which can both be in a down-gradient diffusive manner and an advective manner, directed either up or down gradient. Eddy stirring can lead to homogenisation of conserved tracers within closed streamlines in shielded interior layers. Eddy thickness fluxes lead to an additional advection of tracers, which for a dynamically unstable jet is expected to be directed poleward in upper layers and equatorward in the deeper layers.

The role of eddies is taken forward in subsequent chapters exploring how ventilation occurs, how biological productivity is sustained and how the overturning operates in the Southern Ocean ([Chapters 10 to 12](#)).

9.5 | Questions

Q9.1. Energetics of slantwise exchange.

Slantwise convection involves the exchange of two fluid parcels where a light parcel rises and a dense parcel sinks.

- (a) Identify whether potential energy is released and converted to kinetic energy for the following

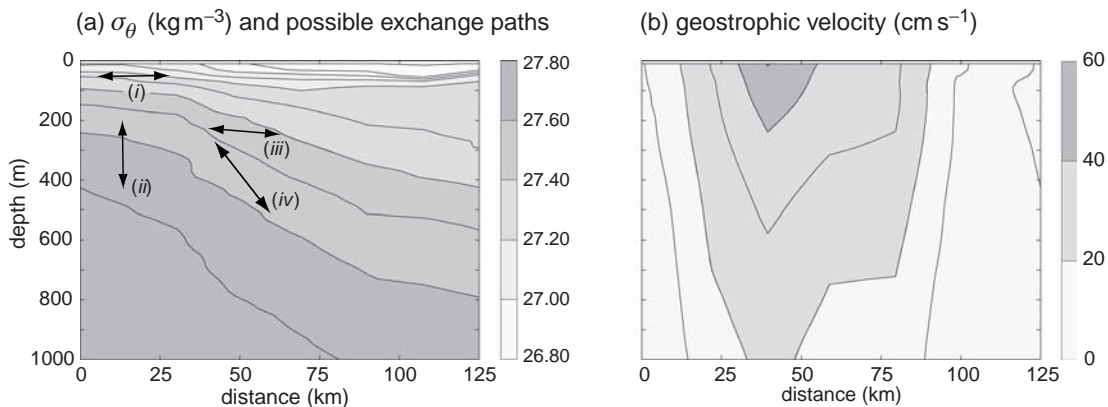


Figure 9.20 A meridional section crossing part of Drake Passage between South America and Antarctica in the Southern Ocean for (a) potential density (contours every 0.1 kg m^{-3} referenced to the sea surface minus 1000 kg m^{-3} , σ_θ), and (b) eastward geostrophic velocity (contours every 10 cm s^{-1}) versus depth. Possible exchange paths are marked as (i) to (iv) in (a). Data supplied by Brian King.

possible exchange paths marked as (i) to (iv) in Fig. 9.20a across part of Drake Passage in the Southern Ocean.

(b) For the case where there might be a release of potential energy, then estimate how large the velocity might be from the exchange of two fluid parcels, labelled A and B,

$$\bar{\rho}\Delta v^2 = g\Delta\sigma\Delta z = g(\sigma_A - \sigma_B)(z_A - z_B), \quad (9.30)$$

where σ_A and σ_B are the initial and final potential densities, and z_A and z_B are the initial and final vertical positions respectively (taken as negative depth); $g = 9.81 \text{ m s}^{-2}$ and $\bar{\rho}$ is the mean density of parcels A and B. Take your estimates from Fig. 9.20a and assume exchange on a horizontal scale of 25 km.

(c) How does your estimate for Δv compare with a scaling estimate of the eddy velocity U_{eddy} from the background velocity shear,

$$U_{\text{eddy}} \sim \frac{H}{2} \left| \frac{\partial u}{\partial z} \right|,$$

where the vertical scale $H \sim 1 \text{ km}$ and the velocity shear is estimated from the data in Fig. 9.20b?

Q9.2. Eddy heat flux.

Consider the direction of the poleward heat flux associated with a velocity and temperature perturbation given by $v'(x, t) = v_0 \sin(kx - \omega t)$ and either (i) $T'_1(x, t) = T_0 \cos(kx - \omega t)$ or

(ii) $T'_2(x, t) = T_0 \sin(kx - \omega t)$, where the wavenumber $k = 2\pi/\lambda$ and λ is the wavelength in the x direction.

(a) Sketch how the products $v' T'_1$ and $v' T'_2$ vary with x from 0 to λ for $t = 0$. Hence, speculate whether the eddy temperature flux, $v' T'$ averaged in x from 0 to λ , is positive, zero or negative.

(b) More formally, estimate the eddy temperature flux by integrating the expression,

$$\overline{v' T'} = \frac{1}{\lambda} \int_0^\lambda v'(x, t) T'(x, t) dx,$$

for cases (i) and (ii) at $t = 0$. Apply general trigonometric identities, $2 \sin \alpha \cos \alpha = \sin(2\alpha)$ and $2 \sin^2 \alpha = 1 - \cos(2\alpha)$, and integral relations, $\int_a^b \sin(\alpha x) dx = -\frac{1}{\alpha} [\cos(\alpha x)]_a^b$ and $\int_a^b \cos(\alpha x) dx = \frac{1}{\alpha} [\sin(\alpha x)]_a^b$.

Q9.3. Particle exchange across a jet.

Consider the movement of a particle in an eastward jet $u(y)$ when there is a propagating meander giving a northward flow, $v(x, t)$ (like that in Fig. 9.19).

Assume that the position of the particle is given by x_p, y_p , such that its northward position is given by

$$y_p(T) = \int_0^T v_0 \cos(k(x_p - ct)) dt, \quad (9.31)$$

where $v(x, t) = v_0 \cos(k(x_p - ct))$ and v_0 is the amplitude of the northward velocity in the

meander, $k = 2\pi/\lambda$ is the wavenumber, λ is the wavelength and c is the wave speed of the meander.

(a) Speculate on where the meridional displacement is likely to be greatest across the jet.

(b) If the eastward position of the particle is approximated by $x_p = ut$ (where for simplicity u is assumed constant for the particle), show that the northward position of the particle from (9.31) is given by

$$y_p(\mathcal{T}) = \frac{v_0 \sin(2\pi(u - c)/c)}{k(u - c)}, \quad (9.32)$$

note that the period $\mathcal{T} = 2\pi/(kc)$, since $c = \lambda/\mathcal{T}$.

(c) Roughly estimate the maximum value of $y_p(\mathcal{T})$ from (9.32) for three cases:

- (i) when the wave speed exceeds the eastward jet, $u \ll c$;
- (ii) when the wave speed is much less than the eastward jet, $u \gg c$; and
- (iii) when the wave speed is only slightly less than the eastward jet, $u = 5c/4$.

Compare your answers with your speculation in (a).

Q9.4. Direction of eddy tracer fluxes.

Consider how the direction of eddy tracer fluxes are controlled starting with the tracer equation for a generic tracer, c ,

$$\frac{\partial c}{\partial t} + \mathbf{u} \cdot \nabla c = F - D, \quad (9.33)$$

where \mathbf{u} is the advective velocity along an isopycnal and F and D represent a source and sink of the tracer respectively.

(a) Separate each of the variables into a time-mean and a time-varying component, such as $c = \bar{c} + c'$, and then apply a time average of (9.33) (where by definition $\bar{c}' \equiv 0$) to obtain an equation for the time-mean tracer, \bar{c} ,

$$\frac{\partial \bar{c}}{\partial t} + \bar{\mathbf{u}} \cdot \nabla \bar{c} + \overline{\mathbf{u}' \cdot \nabla c'} = \bar{F} - \bar{D}. \quad (9.34)$$

Then:

- (i) Obtain a similar equation for the temporal variation in the tracer from (9.33)–(9.34);
- (ii) Multiply your equation in (i) by c' and apply a time average to obtain an equation for tracer variance, $c'^2/2$,

$$\begin{aligned} \frac{\partial}{\partial t} \frac{\overline{c'^2}}{2} + \bar{\mathbf{u}} \cdot \nabla \frac{\overline{c'^2}}{2} + \overline{\mathbf{u}' \cdot \nabla \frac{c'^2}{2}} \\ + \overline{\mathbf{u}' c'} \cdot \nabla \bar{c} = \overline{F' c'} - \overline{D' c'}, \end{aligned} \quad (9.35)$$

which can be written more concisely by combining the first three terms as a time integral following the flow, $D/Dt = \partial/\partial t + \mathbf{u} \cdot \nabla$;

- (iii) Rearrange (9.35) so that the scalar product of the eddy tracer flux, $\overline{\mathbf{u}' c'}$, and the background tracer gradient, $\nabla \bar{c}$, is the only term on the left-hand side to obtain

$$\overline{\mathbf{u}' c'} \cdot \nabla \bar{c} = -\frac{\overline{D' c'^2}}{\overline{Dt}} + \overline{F' c'} - \overline{D' c'}. \quad (9.36)$$

- (b) Hence, using (9.36), identify when the eddy tracer flux, $\overline{\mathbf{u}' c'}$, is directed down the background tracer gradient. Assume that the forcing of tracer perturbations, $\overline{F' c'}$, is relatively small compared to the other terms. Conversely, when might the eddy tracer flux be directed up the background tracer gradient?

9.6 | Recommended reading

For an accessible and mechanistic view of how atmospheric weather systems form, see J. S. A. Green (1981). Trough-ridge systems as slant-wise convection. In *Dynamical Meteorology: An Introductory Selection*, ed. B. W. Atkinson. London: Methuen, pp. 176–194.

For a discussion of baroclinic instability including how potential energy can only be released in a certain manner, see A. E. Gill (1982). *Atmosphere-Ocean Dynamics*. New York: Academic Press, 692pp; particularly Chapter 13.

For a comprehensive assessment of how atmospheric and ocean eddies are formed, and their diffusive and advective transfer, see G. K. Vallis (2006). *Atmospheric and Oceanic Fluid Dynamics*. Cambridge: Cambridge University Press, 745pp.

Chapter 10

Ventilation

Tracers are transferred throughout the atmosphere and ocean, for example, as you see when watching black smoke billow out of a chimney stack and spread across the skyline, or in how a silt-laden river flows out to sea. In a similar manner, tracers are transferred from the surface mixed layer into the ocean interior, as depicted for the spreading of CFCs in Fig. 10.1; this process is generically referred to as ventilation. This ventilated transfer controls the physical properties of much of the ocean and the communication between the atmosphere and ocean interior.

Ventilation does not occur uniformly over the globe, like heat diffusing down a pipe, instead, some parts of the ocean are well ventilated and other parts are poorly ventilated. For example, the North Atlantic is well ventilated, with relatively high concentrations of CFCs spreading from the surface mixed layer, while the mid-depth and bottom waters of the North Pacific are poorly ventilated, with CFCs being absent (Fig. 10.1).

In this chapter, we describe the ventilation process by mapping how tracers spread over the globe, examining property distributions along potential density surfaces (with maps repeated in the colour plates 8 to 15). We then discuss the mechanisms by which fluid is transferred from the mixed layer, focussing on diagnostics for the North Atlantic, and include simple theoretical models for how the upper thermocline is formed.

10.1 How does ventilation vary over the globe?

To gain a conceptual view of ventilation, consider a water parcel, a small amount of fluid with constant mass, initially residing within the mixed layer. If the water parcel passes from the mixed layer into the interior, its salinity, potential temperature and potential density, σ_θ , are subsequently conserved, so that the water parcel spreads along σ_θ surfaces, as depicted in Fig. 10.2a,b. In a similar manner, water masses preferentially spread along these same σ_θ surfaces (or related neutral surfaces).

This picture of ventilation becomes more complicated for biogeochemical properties, such as nutrients, dissolved oxygen and dissolved inorganic carbon. There is still a ventilated transfer of biogeochemical properties from the mixed layer into the interior, but these biogeochemical properties are subsequently modified by interior sources and sinks, as illustrated schematically in Fig. 10.2c,d. For example, sinking organic matter is oxidised in the interior, reducing the interior oxygen concentrations, as well as returning the organic matter to dissolved inorganic forms. Whether the tracer distribution reflects the ventilated transfer from the mixed layer or the biogeochemical sources acting in the interior depends upon the particular biogeochemical property and region of the ocean. In general, biogeochemical

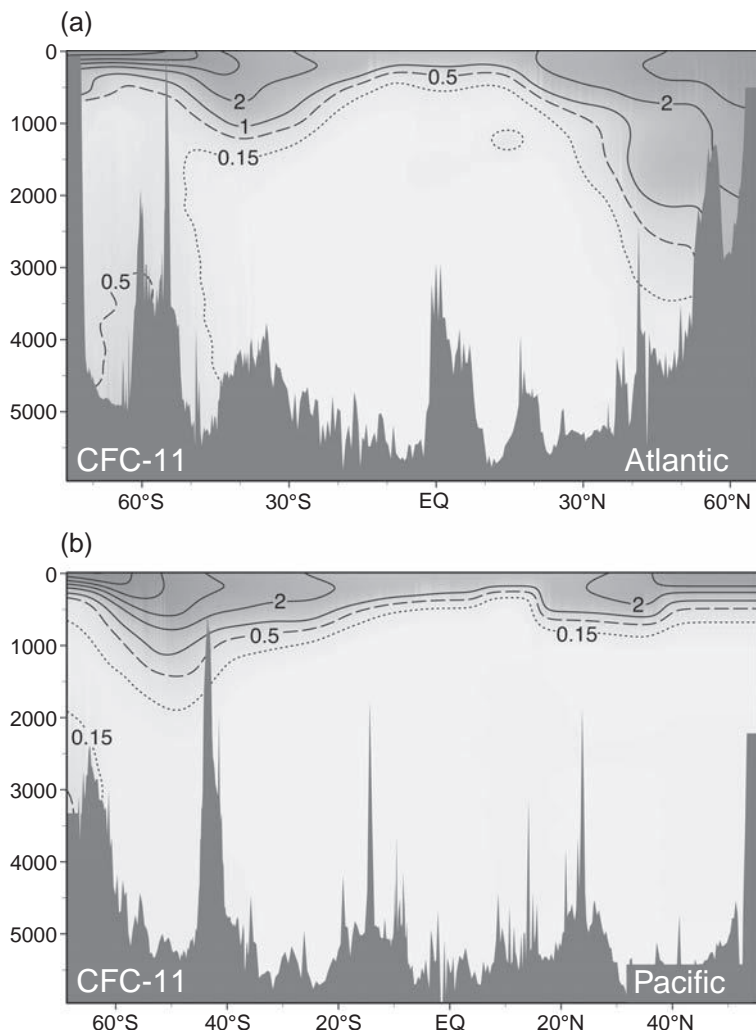


Figure 10.1 Transient tracers spreading into the ocean, as revealed by chlorofluorocarbons, CFC-11 (trichlorofluoromethane, CCl_3F ; $10^{-12} \text{ mol kg}^{-1}$), through a meridional section in (a) the Atlantic along 20°W , and (b) the Pacific along 170°W , based upon surveys in 1987 and 1988; see Plates 4a and 5a. CFC-11 has been released into the atmosphere since the 1950s, its atmospheric concentration peaking in the 1990s and has now started to decline. The CFC-11 concentration in the ocean has high concentrations in the upper waters, the mid-depth and deep waters of the North Atlantic, but has not yet spread into the deep waters of the Pacific.

properties along a σ surface are more influenced by ventilation close to the σ outcrop, but become increasingly affected by the accumulation of interior sources and sinks further downstream in the interior (represented by the dark shading in Fig. 10.2d).

To illustrate how ventilation varies, we now examine tracer distributions along a range of σ_θ surfaces spanning the upper thermocline, intermediate and deep waters: mode waters formed in the subtropical gyres are represented by the $\sigma_\theta = 26.2$ and 27.2 surfaces, an intermediate water mass by the $\sigma_2 = 36.9$ surface and a deep water mass by the $\sigma_4 = 45.87$ surface; for accompanying water-mass definitions, see Talley *et al.* (2011).

10.1.1 Ventilation tracers in the upper mode waters

Mode waters formed in the mid-latitude, subtropical gyres range in potential density from $\sigma_\theta = 26.2$ to 27.2 . The lighter mode waters along the $\sigma_\theta = 26.2$ surface extend to depths of 300 m over much of the globe, deepening over the subtropical gyres of the Pacific and reaching 600 m in the northern basin (Plate 8a).

There are high concentrations of CFC-12 and dissolved oxygen in the mid latitudes of each basin (Fig. 10.3a,b, dark shading), contrasting with low concentrations in the tropics. The highest concentrations of these dissolved gases are where the σ_θ surfaces shallow and outcrop into the mixed

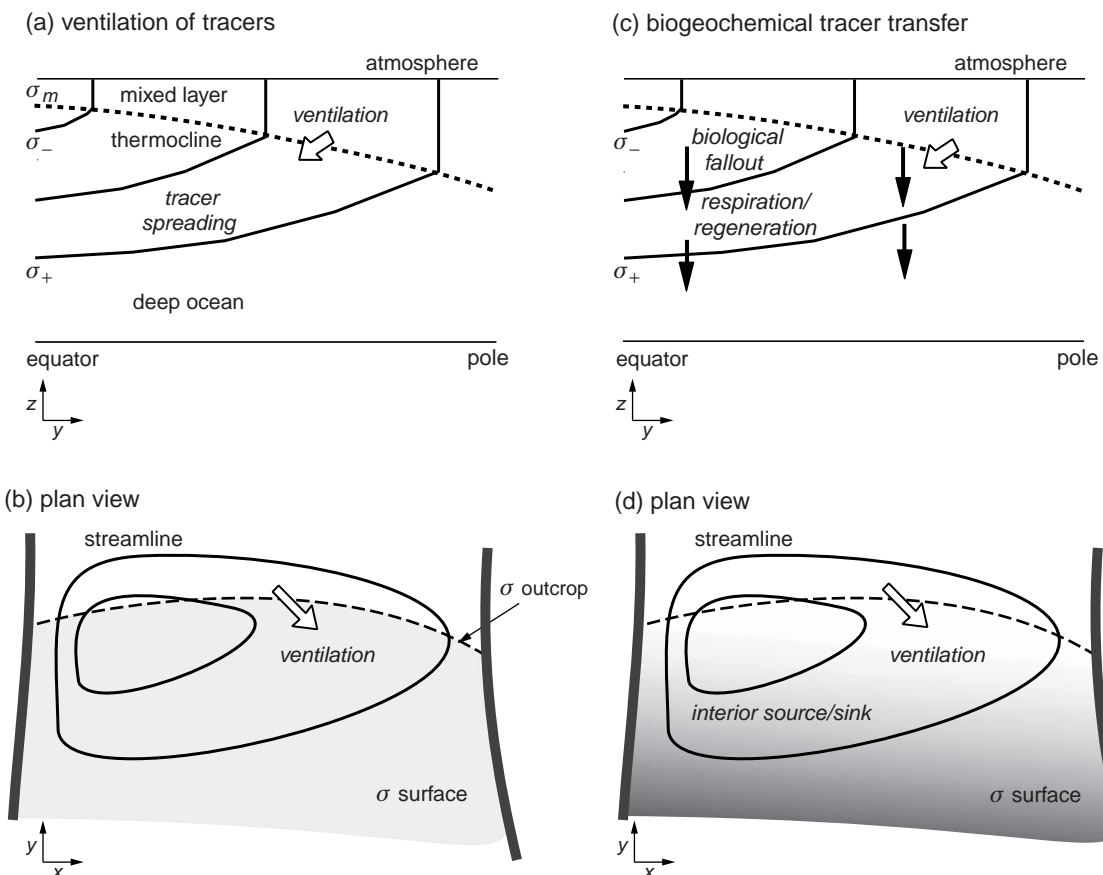


Figure 10.2 A schematic figure depicting an idealised view of the ventilation process for a subtropical gyre: (a) a meridional section of a mixed layer (dashed line for its base) overlying a thermocline and deep ocean, where σ surfaces in the interior outcrop into the mixed layer; (b) a map denoting a plan view of a σ surface (light shading), which outcrops into the mixed layer (dashed line), together with streamlines for a subtropical gyre (full lines). Ventilation (white arrow) represents the transfer of tracers from the mixed layer into the interior. Biogeochemical tracers are likewise transferred through ventilation, as well as modified by interior sources and sinks, such as biological fallout and respiration of organic matter (black arrows), and regeneration to inorganic nutrients as depicted in a meridional section in (c) and along a σ surface in (d).

layer; marked for the end of winter by the white contour in Fig. 10.3. The ventilation process then transfers these dissolved gases from the winter mixed layer into the interior along σ surfaces (Fig. 10.2b).

The denser mode waters along the $\sigma_\theta = 27.2$ surface extend to depths of 1 km, deeper on the western side of the subtropical gyres, and shallower in the tropics and high latitudes (Plate 10a). Along this σ_θ surface, there are high concentrations of CFC-12 and dissolved oxygen in the mid and high latitudes of the North Atlantic

and the high latitudes of the Southern Ocean (Fig. 10.4a,b), but very low concentrations over the tropical Atlantic and much of the Pacific and Indian basins. There is an asymmetric pattern, with recently ventilated waters in the northern North Atlantic and the Southern Ocean, but poorly ventilated waters extending over the North Pacific.

While there are broad similarities between the patterns of CFC-12 and dissolved oxygen, there are also subtle differences: CFC-12 is a transient tracer and there has been insufficient time for the

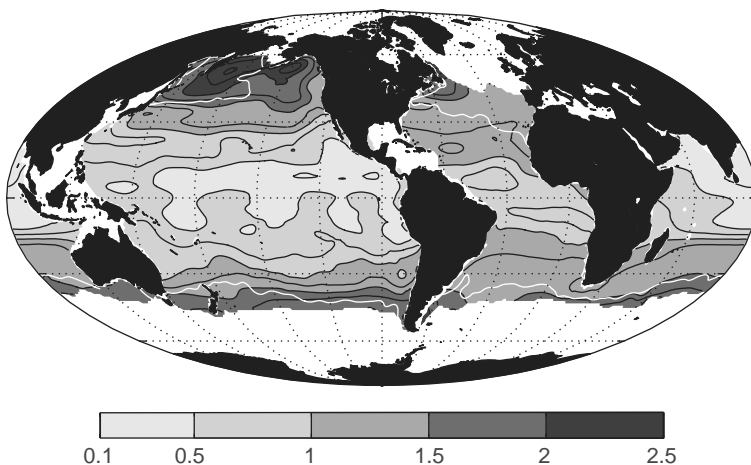
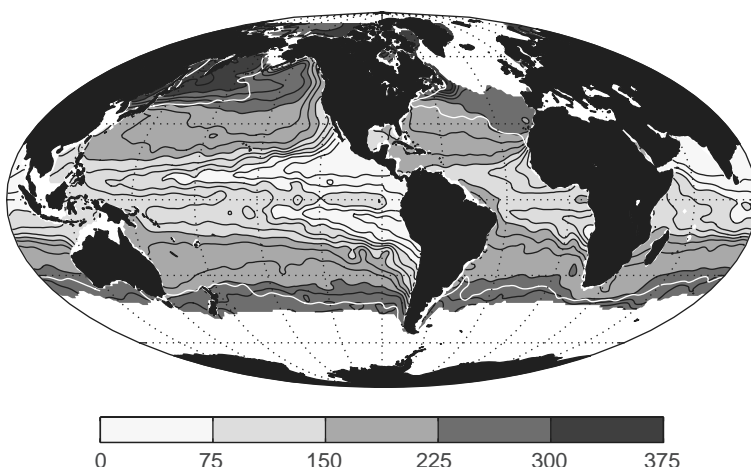
(a) CFC-12 (pmol kg^{-1}) along $\sigma_\theta = 26.2$ 

Figure 10.3 Global distributions for (a) CFC-12 (dichlorofluoromethane, CCl_2F_2 ; contours for 0.1 and every $0.25 \times 10^{-12} \text{ mol kg}^{-1}$), and (b) dissolved oxygen (contours every $25 \mu\text{mol kg}^{-1}$) along potential density surface, $\sigma_\theta = 26.2$; see Plates 8b and 9a. The outcrop of the σ_θ surface into the end of winter mixed layer is marked by the thick white contour.

(b) dissolved O₂ ($\mu\text{mol kg}^{-1}$) along $\sigma_\theta = 26.2$ 

CFC-12 to spread from the ventilation sites over the entire ocean, while the dissolved oxygen is closer to a steady state and has spread over the entire domain.

Now we consider the effect of this change in ventilation pattern for other water-mass and biogeochemical properties.

Salinity in the upper mode waters

Surface salinity varies strongly over the globe, with salty waters in the semi-enclosed Mediterranean and Red Seas, as well as in the mid latitudes of the North Atlantic, and fresher waters in the high latitudes of the Pacific basin and the

Southern Ocean. The ventilation process transfers this imprint of surface salinity from the mixed layer into the ocean interior. Along the $\sigma_\theta = 26.2$ surface, salty waters extend over the entire Atlantic, but along the $\sigma_\theta = 27.2$ surface, salty waters are confined to the North Atlantic and North Indian Oceans (Fig. 10.5a,b). Over the Pacific, there are salty waters in the tropics and fresher waters in the higher latitudes along the $\sigma_\theta = 26.2$ surface, while the entire Pacific is relatively fresh along the $\sigma_\theta = 27.2$ surface. Hence, on this denser σ_θ surface, salinity highlights the contrast in ventilation between the North Atlantic and Southern Ocean.

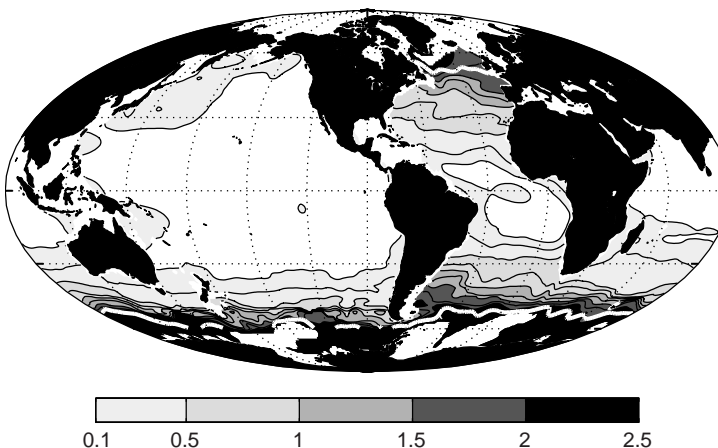
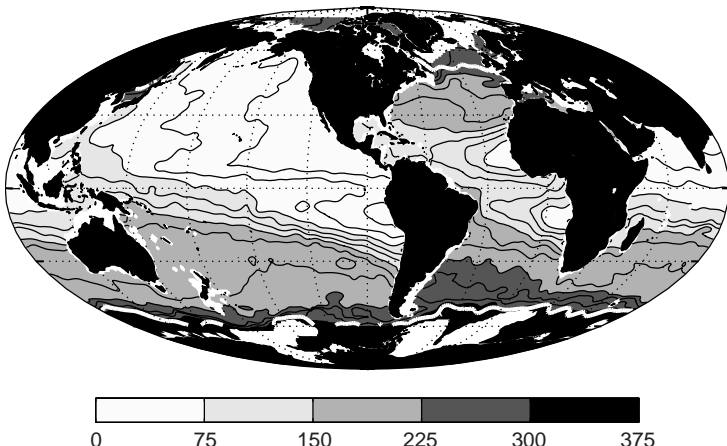
(a) CFC-12 (pmol kg^{-1}) along $\sigma_\theta = 27.2$ (b) dissolved O₂ ($\mu\text{mol kg}^{-1}$) along $\sigma_\theta = 27.2$ 

Figure 10.4 Global distributions for (a) CFC-12 (dichlorofluoromethane, CCl_2F_2 ; contours for 0.1 and every $0.25 \times 10^{-12} \text{ mol kg}^{-1}$, white represents no measurable CFC-12), and (b) dissolved oxygen (contours every $25 \mu\text{mol kg}^{-1}$) along potential density surface, $\sigma_\theta = 27.2$; see Plates 10b and 11a. The outcrop of the σ_θ surface into the end of winter mixed layer is marked by the thick white contour.

Phosphate in the upper mode waters

Surface phosphate concentrations are generally low over the subtropical gyres due to biological consumption. Consequently, any waters ventilated from these subtropical gyres carry low phosphate concentrations into the interior. Accordingly, along the $\sigma_\theta = 26.2$ surface, there are low phosphate concentrations over the mid latitudes of the Atlantic and Pacific basins (Fig. 10.6a), as well as along the $\sigma_\theta = 27.2$ surface in the North Atlantic (Fig. 10.6b). Hence, the phosphate distribution broadly resembles the inverse of the ventilation tracers in having low concentrations in well-ventilated waters rather than high concentrations. Again, there is a broadly symmetric phos-

phate distribution on the lighter σ_θ surface with well-ventilated signals in each basin, changing to an asymmetrical distribution on the denser σ_θ surface highlighting the enhanced ventilation in the North Atlantic.

An exception to this ventilated input of low phosphate occurs in the Southern Ocean, where there are relatively high concentrations in surface phosphate at high latitudes, probably reflecting iron limitation inhibiting biological consumption of phosphate in the euphotic zone.

The most phosphate-rich waters occur in the North Pacific and North Indian basins, reflecting the lack of recent ventilation, where phosphate concentrations increase in time through the

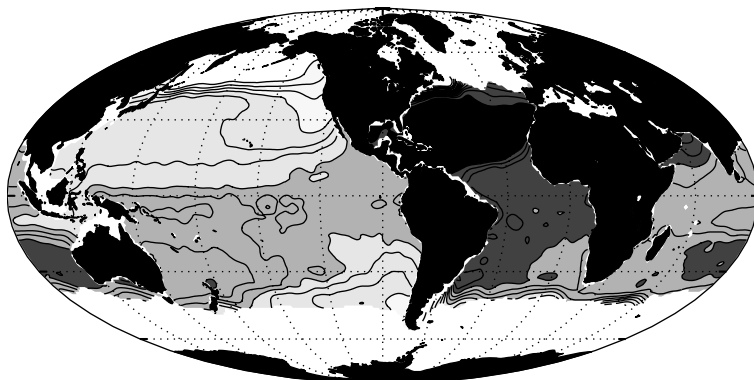
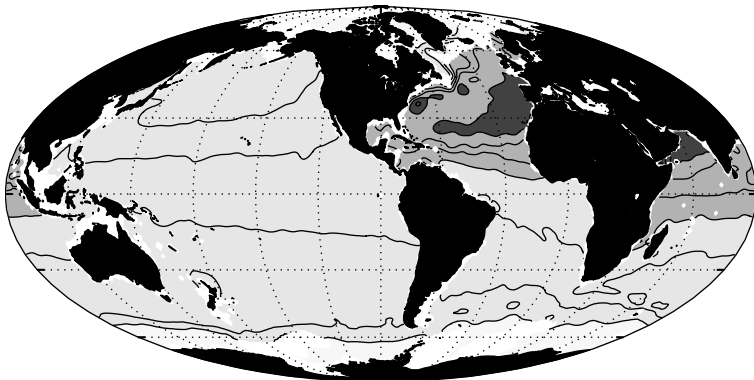
(a) salinity (g kg^{-1}) along $\sigma_\theta = 26.2$ (b) salinity (g kg^{-1}) along $\sigma_\theta = 27.2$ 

Figure 10.5 Global distributions for salinity (contours every 0.25 g kg^{-1}) along potential density surfaces (a) $\sigma_\theta = 26.2$, and (b) $\sigma_\theta = 27.2$.

accumulated effect of organic fallout, respiration and regeneration.

Dissolved inorganic carbon, DIC, in the upper mode waters

Surface DIC has high concentrations in the high latitudes and low concentrations in the tropics, reflecting the increased solubility in colder waters. However, this surface imprint of DIC does not simply convert to the DIC distribution seen along the σ_θ surfaces. Instead, there is the reverse pattern with generally higher concentrations of DIC in the tropics and poorly ventilated parts of the ocean (Fig. 10.7).

The DIC distribution alters in character between the $\sigma_\theta = 26.2$ and 27.2 surfaces. There is a relatively symmetric pattern of mid-latitude venti-

lation with a surface influx of relatively low DIC in each basin along the $\sigma_\theta = 26.2$ surface (Fig. 10.7a), which changes to an influx of low DIC restricted to the North Atlantic and Southern Ocean along the $\sigma_\theta = 27.2$ surface (Fig. 10.7b). Conversely, there are high concentrations of DIC in the poorly ventilated waters of the tropics along the $\sigma_\theta = 26.2$ surface and the North Pacific along $\sigma_\theta = 27.2$ surface.

Hence, the DIC distribution broadly resembles that of the phosphate distribution having high concentrations in the tropics and North Pacific, reflecting the accumulated effect of the respiration of organic fallout and regeneration of inorganic elements in older waters.

Now we consider the underlying intermediate and deep waters.

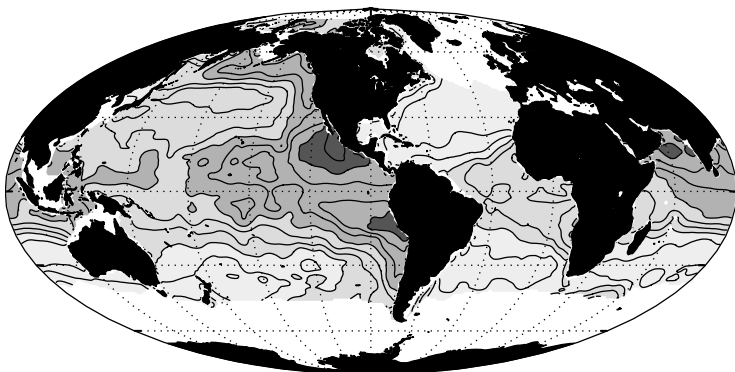
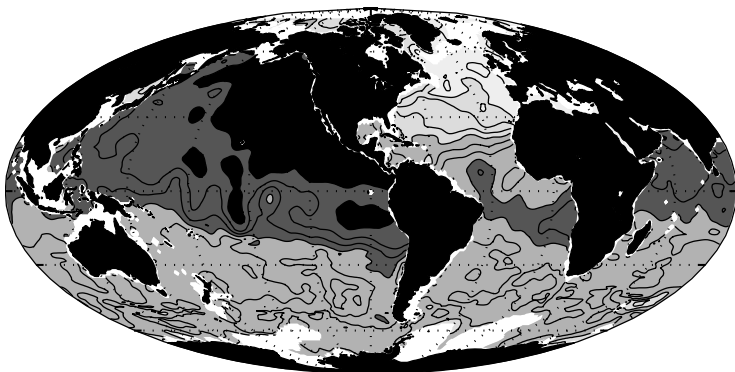
(a) phosphate ($\mu\text{mol kg}^{-1}$) along $\sigma_\theta = 26.2$ (b) phosphate ($\mu\text{mol kg}^{-1}$) along $\sigma_\theta = 27.2$ 

Figure 10.6 Global distributions for phosphate (PO_4^{3-} ; contours every $0.25 \mu\text{mol kg}^{-1}$) along potential density surfaces (a) $\sigma_\theta = 26.2$, and (b) $\sigma_\theta = 27.2$; see Plates 9b and 11b.

10.1.2 Intermediate water masses

Intermediate waters are formed in the mixed layer in the subpolar gyres of the northern basins, in the high latitudes of the Southern Ocean, or spread at intermediate depths of 1 to 2 km into a basin from neighbouring, semi-enclosed seas. The properties of the intermediate waters are shown here along the $\sigma_2 = 36.9$ surface, which varies in depth from 1500 m in the Atlantic to 2300 m in the Pacific (see colour plates 12 and 13). On this surface there are high concentrations of dissolved oxygen confined to the high latitudes of the North Atlantic and Southern Ocean (Plate 13a), indicating recent ventilation, contrasting with low concentrations over much of the Pacific and Indian basins, reflecting a lack of ventilation and the accumulated consumption by respiration. This ventilated imprint has a similar character to that of the overly-

ing denser subtropical mode water (Fig. 10.4). There is again the reverse pattern in inorganic nutrients and DIC, higher concentrations of dissolved inorganic matter over much of the Indian and Pacific basins (Fig. 10.8a), reflecting the ventilated imprint of relatively low DIC and the accumulated effect of organic fallout and respiration, as well as the fallout and dissolution of calcium carbonate (Section 6.4).

10.1.3 Deep and bottom waters

The deep and bottom waters are a composite of different water masses, combined at strong mixing sites, such as overflows, fracture zones and above rough topography.

The properties of the deep waters are shown here along the $\sigma_4 = 45.87$ surface, which extends to depths of 4.5 km in the central Pacific and

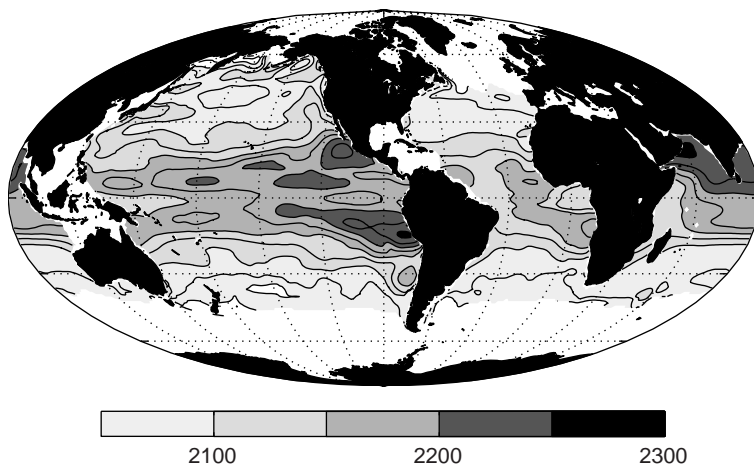
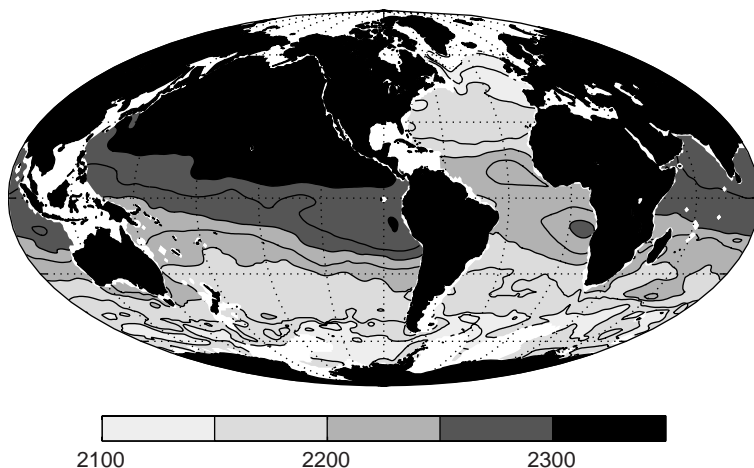
(a) DIC ($\mu\text{mol kg}^{-1}$) along $\sigma_\theta = 26.2$ (b) DIC ($\mu\text{mol kg}^{-1}$) along $\sigma_\theta = 27.2$ 

Figure 10.7 Global distributions for dissolved inorganic carbon, DIC (contours every $25 \mu\text{mol kg}^{-1}$), along potential density surfaces (a) $\sigma_\theta = 26.2$, and (b) $\sigma_\theta = 27.2$; note grey shades refer to higher concentrations in (b); see Plates 9c and 11c.

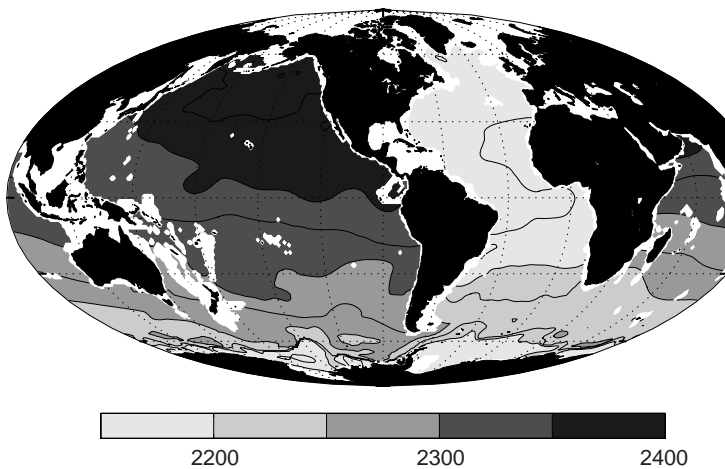
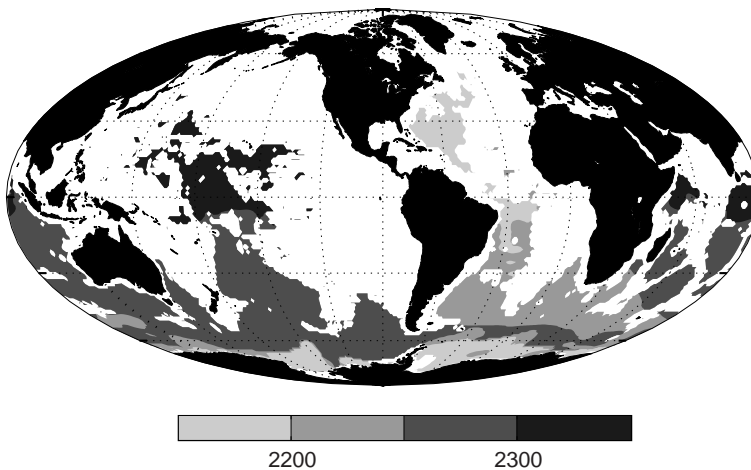
western Atlantic (see colour plates 14 and 15). There is again a ventilated input of oxygen-rich waters from confined parts of the high-latitude North Atlantic and Southern Ocean (Plate 15a), together with an influx of relatively low DIC (Fig. 10.8b). As the dense water spreads away from these ventilation sites, dissolved oxygen gradually becomes depleted and DIC increases in concentration following the respiration of organic fallout and dissolution of calcium carbonate, reaching highest concentrations in the central Pacific and Indian basins. There is, though, more oxygen in these deep waters in the central Pacific than in the overlying intermediate waters, reflecting

the greater ventilation of deep waters from the Southern Ocean.

Following this descriptive view of ventilation and resulting property distributions over the globe, we now consider the mechanisms by which ventilation occurs.

10.2 A mechanistic view of ventilation

Ventilation involves fluid in the mixed layer being transferred into the ocean interior to become part of the stratified thermocline or the weakly

(a) DIC ($\mu\text{mol kg}^{-1}$) along $\sigma_2 = 36.9$ (b) DIC ($\mu\text{mol kg}^{-1}$) along $\sigma_4 = 45.87$ 

stratified, deep ocean. Ventilation of the thermocline preferentially occurs in the mid-latitude, subtropical gyres and across frontal zones in the Southern Ocean; this process is referred to as subduction, drawing on the geological analogy of lithospheric plates being transferred into the upper mantle. Ventilation of the deep ocean instead occurs in higher-latitude, subpolar gyres, either involving deep convection sustained by surface heat loss or the overflow of dense waters formed along shallow shelves.

Ventilation does not occur in a uniform manner with the same volume in each temperature and salinity class. Instead there are large vol-

umes of water within particular temperature and salinity classes, referred to as 'mode waters'. For example, in the North Atlantic, there are three dominant mode waters, as revealed by a volumetric census, indicated by boxes in Fig. 10.9: a subtropical mode water formed in the Sargasso Sea; subpolar mode waters formed along the intergyre boundary and within the subpolar gyre; and Labrador Sea Water formed in the northwest corner of the subpolar gyre.

Our aim now is to provide a mechanistic view of thermocline ventilation, addressing how subtropical mode waters are formed, while ventilation of the deep ocean and formation of denser

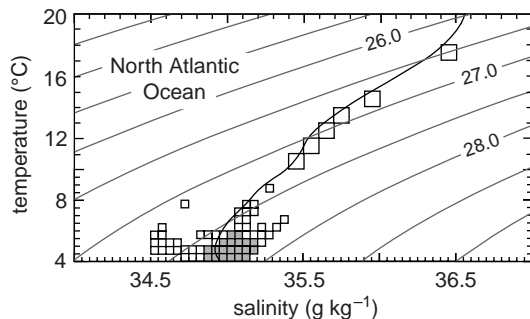


Figure 10.9 A volumetric census (boxes) of the temperature–salinity characteristics of the North Atlantic Ocean for warm waters ($T \geq 4^\circ\text{C}$), together with the average T – S relationship (thick line). The various T – S classes are ranked by their volume per 0.5°C and 0.05 g kg^{-1} . The highest ranked classes that collectively total 25% of the total warm water volume are represented by the shaded boxes, while those that collectively total 50% of the total warm water volume are together represented by the shaded and unshaded boxes. The volumetric census reveals subtropical mode water (top right box), subpolar mode waters (10 – 15°C) (middle boxes) and high volume, cold modes below 6°C , including Labrador Sea Water (bottom left boxes). Redrawn from McCartney and Talley (1982) and based upon original analysis by Worthington and Wright (1970).

subpolar mode waters is discussed later in Chapter 12. We next address the effects of the seasonal cycle of the mixed layer and the vertical and horizontal circulation.

10.2.1 How is ventilation affected by the seasonal cycle of the mixed layer?

The ventilation process involves the seasonal cycle of the mixed layer. We now, consider an idealised seasonal cycle following the movement of a water column (and only considering thermal forcing for simplicity). If there is no vertical velocity (Fig. 10.10a), the mixed layer shallows and warms in spring and summer, transferring fluid from the mixed layer into the thermocline, and thickens and cools during autumn and winter when the reverse transfer occurs. From the end of one winter to the next, if the mixed layer returns to its original maximum thickness and density, then there is no overall exchange of fluid between the mixed layer and thermocline (Fig. 10.10a).

If instead there is an annual heat input, then the mixed layer shallows and warms from the end of one winter to the next (Fig. 10.10b), leading

to fluid being permanently transferred into the main thermocline; a process referred to as subduction. For example, in the vicinity of the Gulf Stream, strong surface heat loss during winter forms 18°C mode water within the mixed layer (Fig. 2.4) and this mode water is transferred into the thermocline as the water column later warms, particularly when the water column moves south. This overall transfer from the mixed layer into the main thermocline can also occur through wind-induced downwelling (Fig. 10.10c) where the mixed layer warms and thins through an Ekman convergence of heat.

Conversely, if over an annual cycle, the mixed layer becomes cooler and thicker, then there is an overall transfer of fluid and water-mass properties from the main thermocline into the seasonal boundary layer (defined by the maximum thickness of the winter mixed layer); the reverse of the subduction process, sometimes referred to as obduction.

In general, whether fluid is subducted from the winter mixed layer or transferred from the thermocline into the seasonal boundary layer depends on the surface density changes (combining the effects of heat and freshwater fluxes) and the wind forcing experienced following a moving water column.

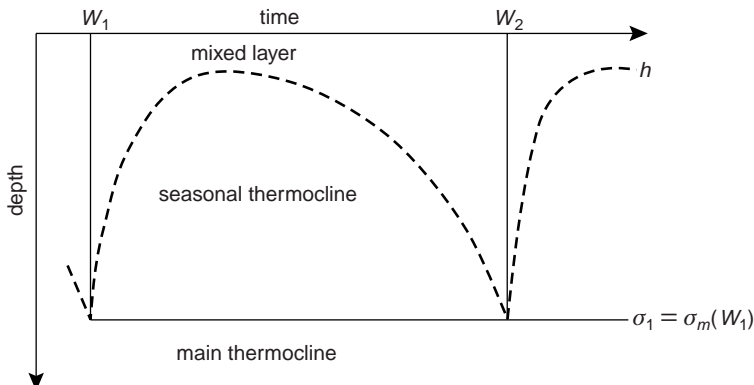
Next we consider the timing of this fluid transfer, the effect of the wind-induced downwelling and upwelling, and then the resulting patterns of subduction.

10.2.2 How is the timing of ventilation controlled?

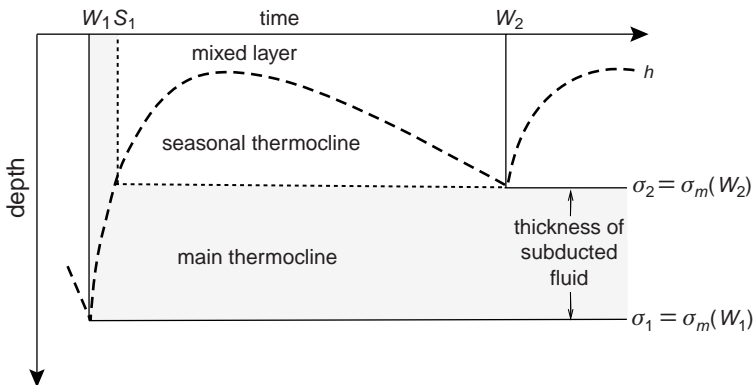
Density outcrops in the mixed layer migrate poleward during the heating seasons and retreat equatorward during the cooling seasons (Fig. 10.11a,b).

For example, in the North Atlantic, the $\sigma_\theta = 25.5$ outcrop migrates across the meridional extent of the subtropical gyre from March to August, while the $\sigma_\theta = 26.5$ outcrop moves from the northern flank of the subtropical gyre to the central part of the subpolar gyre (Fig. 10.11c,d). The seasonal displacement of these outcrops, reaching 1500 km to 2000 km, far exceeds the displacement of the actual fluid, which only typically reaches several hundred kilometres over the same period.

(a) mixed-layer cycle without annual heating or downwelling



(b) mixed-layer cycle with annual heating and no downwelling



(c) mixed-layer cycle with annual downwelling

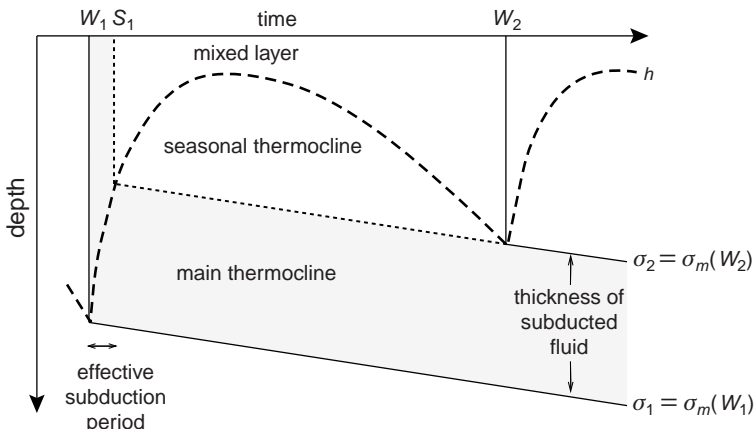


Figure 10.10 A schematic figure for the annual cycle of the mixed layer following the movement of a water column: (a) a repeating cycle when there is no annual heating or downwelling; a shoaling end of winter mixed layer in (b) and (c) when there is an overall warming of the water column without and with wind-induced downwelling, respectively. The mixed layer thickness is marked by the thick dashed line and σ_m denotes isopycnals (full lines) outcropping in the mixed layer at the end of winter, and the base of the seasonal thermocline is denoted by the short dashed line. Fluid is permanently subducted into the main thermocline during a short period after the end of winter W_1 until S_1 . Outside this subduction period (from S_1 until the end of winter W_2), fluid is transferred from the mixed layer into the seasonal thermocline, and then re-entrained into the mixed layer during the following autumn and winter. When there is downwelling, subducted isopycnals deepen after subduction. Modified from Marshall et al. (1993).

Consequently, fluid subducted from the mixed layer in summer is subsequently re-entrained back into the mixed layer a few months later during the equatorial migration of outcrops (Fig. 10.11a,b). Fluid only succeeds in being permanently

subducted into the main thermocline over a short period, one to two months long. This subduction period occurs at the end of winter when the density outcrops are at the equatorial end of their cycle (Fig. 10.11c,d) and the mixed layer rapidly

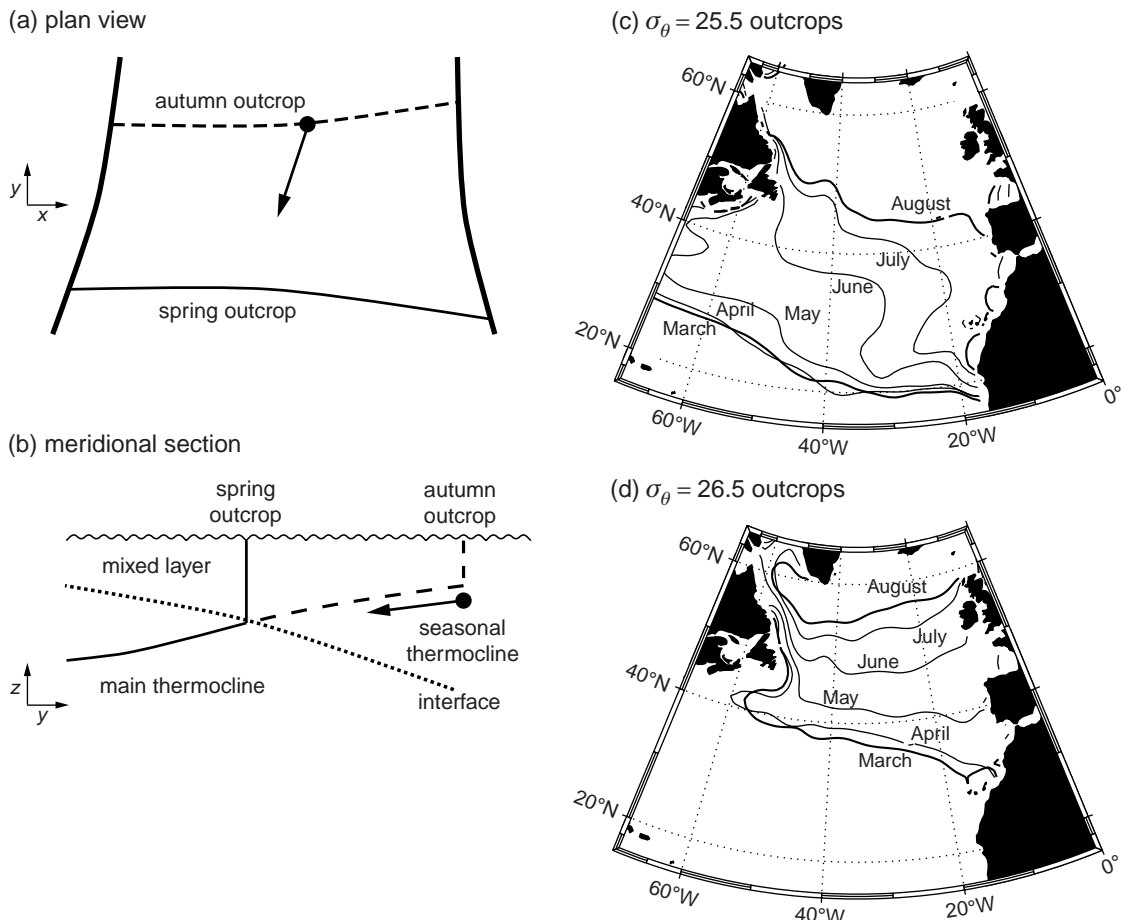


Figure 10.11 Schematic figure illustrating the seasonal migration of density outcrops for (a) a plan view at the sea surface, and (b) a meridional section of the mixed layer overlying a thermocline, together with, in (c) and (d), the observed position of density outcrops during the heating season for $\sigma = 25.5$ and $\sigma = 26.5$, respectively, diagnosed from World Ocean 2001 climatology (Conkright et al., 2002). In (a) and (b), over the cooling season, the outcrop of a density surface migrates equatorward from autumn to spring (denoted by dashed and full lines). Consider a fluid parcel (black dot) subducted from the mixed layer and advected equatorward along this density surface. If the fluid parcel is advected past the spring outcrop during the year, then the fluid parcel succeeds in being subducted into the main thermocline (the upper extent of which is shown by the dotted line), otherwise the fluid parcel is eventually entrained back into the mixed layer; as first explained by Stommel (1979). Panels (a) and (b) redrawn from Williams et al. (1995).

shoals; this response is also illustrated following a moving water column in Fig. 10.10b,c.

Hence, there is a biased coupling between the mixed layer and the thermocline over the seasonal cycle: the subduction of water masses at the end of winter makes the thermocline cooler than the annual-average temperature of the upstream mixed layer.

10.2.3 How is ventilation connected to the vertical velocity?

Ventilation is also affected by the vertical and horizontal circulation. Surface winds drive the gyre-scale circulation (Section 4.2), including horizontal Ekman volume fluxes, directed to the right of the wind in the northern hemisphere and to the left in the southern hemisphere.

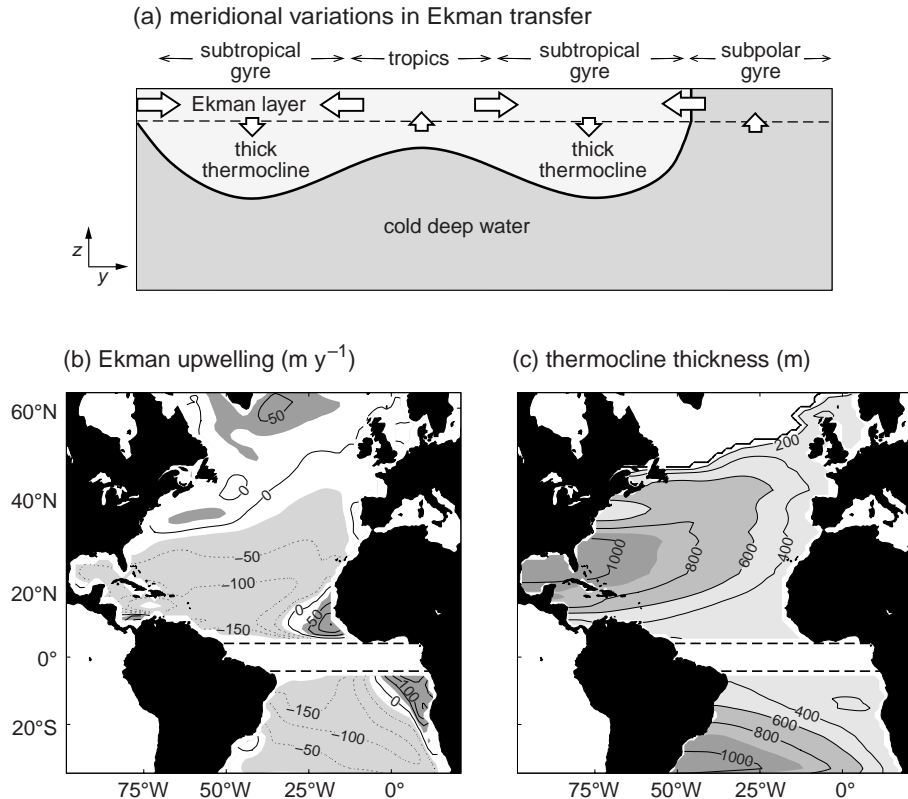


Figure 10.12 Ekman and idealised thermocline model diagnostics for the North Atlantic: (a) a schematic meridional section showing the general pattern of the horizontal Ekman volume flux (white horizontal arrows) and Ekman upwelling (white vertical arrows), together with the undulations of the thermocline (full line); (b) Ekman upwelling, w_{ek} (m y^{-1}); and (c) thickness of the thermocline (m) diagnosed from a one and a half layer model using (10.5) in Box 10.1. The diagnostics employ a wind stress from the European Weather Centre (ERA40) and assume a thermocline thickness on the eastern boundary of 300 m and a density jump across the thermocline of 0.5 kg m^{-3} ; values are not plotted along the equator due to the vanishing of f .

Their horizontal divergence leads to a vertical Ekman velocity at the base of the Ekman layer (Fig. 10.12a),

$$w_{ek} = \frac{\partial U_{ek}}{\partial x} + \frac{\partial V_{ek}}{\partial y} = \frac{1}{\rho} \left(\frac{\partial}{\partial x} \frac{\tau_y^s}{f} - \frac{\partial}{\partial y} \frac{\tau_x^s}{f} \right), \quad (10.1)$$

where $U_{ek} = \tau_y^s / (\rho f)$ and $V_{ek} = -\tau_x^s / (\rho f)$ are the eastward and northward Ekman horizontal volume fluxes per unit length ($\text{m}^2 \text{s}^{-1}$), and τ_x^s and τ_y^s are the corresponding wind stresses; see Q10.1. The wind forcing then leads to Ekman downwelling over much of the mid-latitude subtropical gyres, as well as opposing Ekman upwelling over

much of the high latitudes, some coastal boundaries and along the equator (Fig. 10.12b).

Effect of Ekman downwelling on the thermocline

The gyre-scale variations in Ekman downwelling and upwelling lead to the characteristic variations in the thermocline, thick over the subtropical gyres and thin over the tropics and high latitudes (Fig. 10.12a,b), as well as corresponding undulations in the depth of σ surfaces (Plate 8a and 10a). A simple model, representing the thermocline as a single moving layer, reveals that the westward deepening of the thermocline is connected to the zonal integral of the Ekman downwelling from the eastern boundary (Fig. 10.12c); see Box 10.1.

Box 10.1 | Wind-induced undulations of the thermocline

In order to illustrate how the Ekman downwelling and the thickness of the thermocline are connected, consider a single adiabatic layer of moving fluid of thickness h , representing the thermocline, overlying a stagnant abyss. The geostrophic velocity in the moving layer is simply given by the slope of the layer thickness, h ,

$$v = \frac{g'}{f} \frac{\partial h}{\partial x} \quad \text{and} \quad u = -\frac{g'}{f} \frac{\partial h}{\partial y}, \quad (10.2)$$

where u and v are the eastward and northward velocities, respectively, $g' = \frac{\Delta\rho}{\rho} g$ is the reduced gravity and $\Delta\rho$ is the density difference between the moving and stagnant layers.

Over the interior of the basin, the meridional transport, hv , within the thermocline is related to the Ekman upwelling, w_{ek} , at the base of the surface Ekman layer, assuming a Sverdrup balance for the geostrophic flow:

$$\beta vh = f w_{ek}. \quad (10.3)$$

Substituting (10.2) into (10.3) gives

$$\frac{\partial h^2}{\partial x} = \frac{2f^2}{\beta g'} w_{ek}, \quad (10.4)$$

and integrating (10.4) from the eastern boundary at x_e defines how the thickness of the thermocline varies,

$$h^2(x, y) = h_e^2 - \frac{2f^2}{\beta g'} \int_x^{x_e} w_{ek} dx, \quad (10.5)$$

where h_e is the layer thickness on the eastern boundary at x_e . In a subtropical gyre, $w_{ek} < 0$, the layer thickens westward, $h(x) \geq h_e$, while in a subpolar gyre, $w_{ek} > 0$, the layer thins westward, $h(x) \leq h_e$.

When this model (10.5) is applied with climatological winds over the Atlantic, the thermocline thickens westward from (10.5), reaching 1 km on the western boundary of the subtropical gyres (Fig. 10.12c); the model assumes that $h_e = 300$ m and the density jump across the thermocline is 0.5 kg m^{-3} . Conversely, the Ekman upwelling in the subpolar gyre leads to h vanishing westward, representing an outcropping of the thermocline. While this model is highly simplified, the modelled variation in thermocline thickness broadly resembles the westward deepening of σ surfaces observed in subtropical gyres (Plates 8a and 10a).

10.2.4 What is the rate of ventilation for the upper ocean?

The rate at which the upper ocean is ventilated depends on the seasonal changes in mixed-layer thickness, together with the subduction by the vertical and horizontal circulations. This ventilation rate can be evaluated in two ways: either following the mixed-layer cycle of a moving water column (as depicted in Fig. 10.10) or evaluating the volume flux passing through a control surface defined by the end of winter mixed layer (Fig. 10.13); see def-

itions in Box 10.2. Climatological estimates of the ventilation rate for the North Atlantic are now provided using the latter method.

For the North Atlantic, the surface heat loss to the atmosphere leads to the winter mixed layer thickening poleward (Fig. 10.14a), from typically 50 m in the subtropics to 500 m or more in the subpolar gyre. Fluid is transferred from the winter mixed layer to the thermocline through a combination of a vertical and horizontal transfer. Over much of the subtropical gyre,

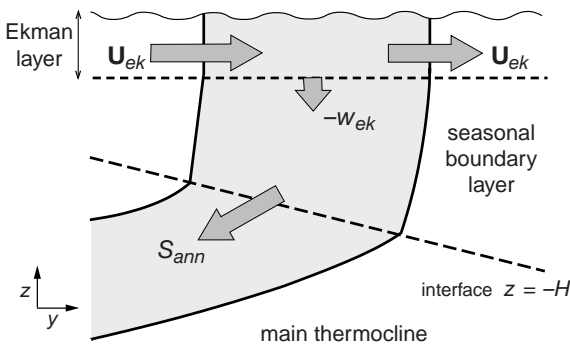
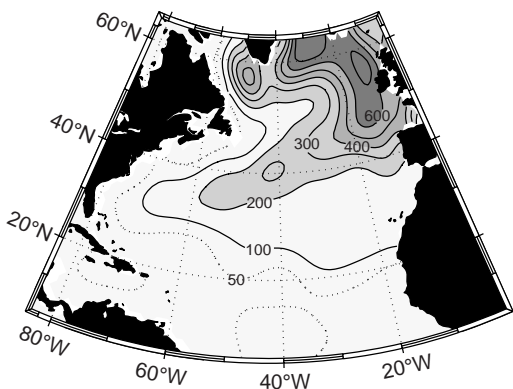
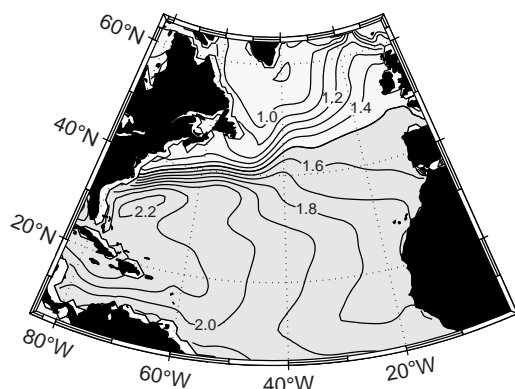


Figure 10.13 A schematic figure representing the annual subduction rate, S_{ann} , through a control surface defined by the interface between the main thermocline and the base of the seasonal boundary layer, $z = -H$, where the seasonal boundary layer is made up of the mixed layer and seasonal thermocline. The annual subduction is achieved by a vertical pumping of fluid through this interface, augmented by the horizontal transfer through the sloping interface. This annual subduction rate can be much greater than the vertical pumping, $-w_{ek}$, through the base of the Ekman layer, achieved by the convergence of the horizontal Ekman volume flux, \mathbf{U}_{ek} .

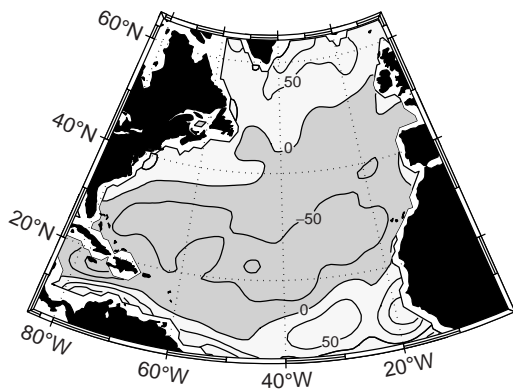
(a) March mixed-layer thickness (m)



(b) dynamic height (m)



(c) Ekman upwelling, w_{ek} ($m\text{y}^{-1}$)



(d) subduction rate, S_{ann} ($m\text{y}^{-1}$)

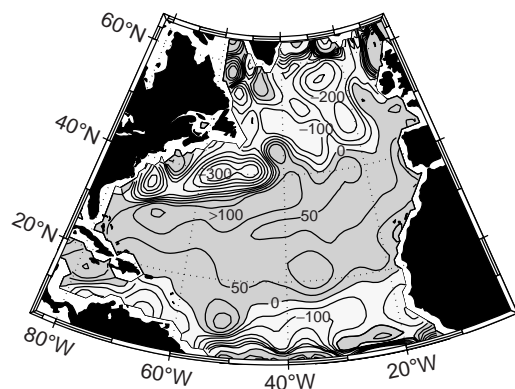


Figure 10.14 Ventilation over the North Atlantic based upon climatology from 5°N to 65°N : (a) March mixed-layer thickness, H (m), (smoothed); (b) dynamic height (m) diagnosed from the World Ocean Atlas 2001 (Conkright et al., 2002); (c) Ekman upwelling velocity, w_{ek} ($m\text{y}^{-1}$), defined as positive upwards; and (d) the annual subduction rate, $S_{ann} = -w_H - \mathbf{u}_H \cdot \nabla H$ in $m\text{y}^{-1}$, representing the volume flux per unit horizontal area transferred into the main thermocline, where w_H and \mathbf{u}_H are the vertical and horizontal velocities along the interface $z = -H$. In (c) and (d), shading highlights downwelling and subduction with contours every $100\text{ m}\text{y}^{-1}$ and $\pm 50\text{ m}\text{y}^{-1}$. Further details of calculation given in Marshall et al. (1993).

Box 10.2 | Evaluating the subduction rate

The subduction rate, measuring the rate at which fluid is transferred from the mixed layer into the thermocline, can be evaluated in two different ways: in a Lagrangian frame following a moving water column or an Eulerian frame at a fixed position.

Lagrangian viewpoint. Consider the seasonal cycle of the mixed layer following a moving water column, as depicted in Fig. 10.10. Following this water column, the instantaneous subduction rate, $S(t)$, is made up of two contributions:

$$S(t) = -\frac{Dh}{Dt} - w_b, \quad (10.6)$$

the rate at which the mixed-layer shoals following the moving water column, $-Dh/Dt$, and the rate of vertical downwelling at the base of the mixed layer, $-w_b$; the negative signs define $S(t)$ as positive whenever there is subduction. $S(t)$ measures a volume flux per unit horizontal area passing from the mixed layer; so is in units of $\text{m}^3 \text{s}^{-1} \text{m}^{-2} = \text{m s}^{-1}$.

The annual subduction rate, S_{ann} , into the main thermocline is given by the time integral of $S(t)$ from (10.6) over an annual cycle following a moving water column,

$$S_{ann} T_{year} = \int_{W_1}^{W_2} S(t) dt = -h(W_2) + h(W_1) - \int_{W_1}^{W_2} w_b dt, \quad (10.7)$$

where W_1 and W_2 mark the time of the end of winter 1 and winter 2 (as denoted in Fig. 10.10a) and T_{year} represents one year. The annual subduction is made up of contributions from the annual shoaling of the mixed layer between the end of winter 1 and 2, $h(W_1) - h(W_2)$, together with the annual pumping out of the base of the mixed layer, $\int_{W_1}^{W_2} w_b dt$; as marked by the vertical spacing between subducted isopycnals in Fig. 10.10b,c.

Eulerian viewpoint. The annual subduction rate, S_{ann} , can equivalently be defined at a fixed location by the volume flux per unit horizontal area passing through a control surface, $z = -H$, such that

$$S_{ann} = -w_H - \mathbf{u}_H \cdot \nabla H, \quad (10.8)$$

where the control surface is defined by the interface between the end of winter mixed layer and the main thermocline, as depicted in Fig. 10.13. S_{ann} now represents the sum of the vertical flux per unit area, w_H , and the horizontal flux per unit area passing through this control surface, $\mathbf{u}_H \cdot \nabla H$; where w_H and \mathbf{u}_H are the vertical velocity and horizontal velocity vector at the depth H .

The vertical velocity at the base of the winter mixed layer is related to the vertical velocity, w_{ek} , through the base of the Ekman layer (Fig. 10.13) via linear vorticity balance, $\beta v = f \partial w / \partial z$, to give

$$w_H = w_{ek} - \frac{\beta}{f} \int_{-H}^{-h_{ek}} v dz, \quad (10.9)$$

where h_{ek} is the thickness of the Ekman layer. The subduction rate, S_{ann} , can often exceed the Ekman pumping, although the sign of S_{ann} and w_{ek} are usually the same (Fig. 10.14c,d). For further details of the subduction process, see Cushman-Roisin (1987), Marshall et al. (1993) and Williams et al. (1995).

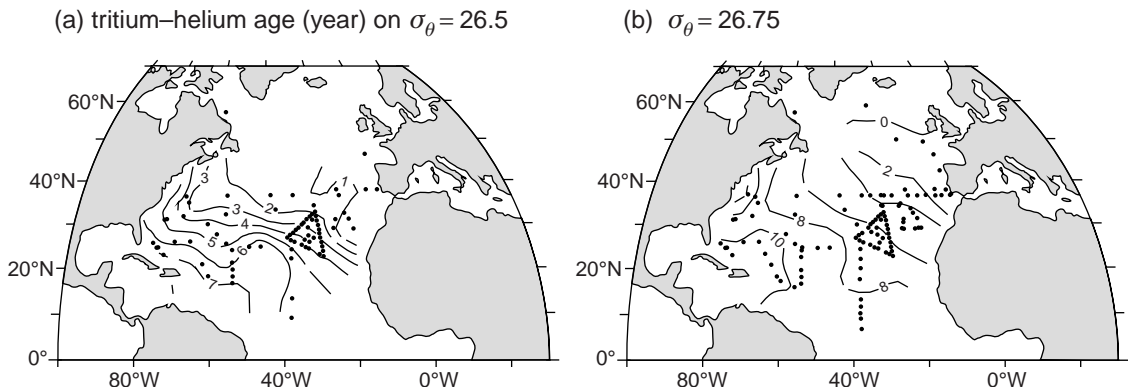


Figure 10.15 Observations of the tritium–helium age (years) on potential density surfaces (a) $\sigma_\theta = 26.5$, and (b) $\sigma_\theta = 26.75$, in the North Atlantic. These surfaces are ventilated from the northeast and the tritium–helium age increases following the anticyclonic circulation of the subtropical gyre. The implied ventilation age is typically 7 years and 10 years across the subtropical gyre along the $\sigma_\theta = 26.5$ and 26.75 surfaces. Original data points are marked by dots. Redrawn from Jenkins (1988a).

the anticyclonic circulation advects fluid horizontally from the winter mixed layer into the main thermocline (Fig. 10.14b). Ekman downwelling also transfers fluid vertically at a rate of -25 to -50 m y^{-1} (Fig. 10.14c). The resulting subduction rate, S_{ann} from (10.7), is positive and reaches between 50 m y^{-1} and 100 m y^{-1} (Fig. 10.14d). South of the Gulf Stream, there is a band of high subduction rates controlled by the horizontal transfer. Elsewhere, the subduction rates have a similar contribution from the vertical and horizontal transfers.

Over the subpolar gyre, the cyclonic circulation generally transfers fluid from the thermocline into the thickening mixed layer (Fig. 10.14b). Ekman upwelling also transfers fluid from the thermocline towards the surface (Fig. 10.14c). The resulting subduction rate, S_{ann} , is negative, directed from the thermocline into the winter mixed layer, reaching several -100 m y^{-1} (Fig. 10.14d). This fluid in the seasonal boundary layer eventually either returns to the thermocline via subduction along the western side of the subpolar gyre, or is swept into the subtropical gyre via the horizontal Ekman flux, or passes into the deep ocean through deep convection.

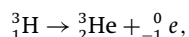
10.2.5 The effect of ventilation of the thermocline

The gyre-scale imprint of ventilation is seen in the distribution of tracers over the subtropical gyres, such as the input of high concentrations of CFC-

12 and dissolved oxygen, as well as low concentrations of phosphate (see earlier Figs. 10.3, 10.4 and 10.6). Now consider additional ventilation signals as revealed by a tritium–helium age and a dynamical tracer, potential vorticity.

Ventilation age

A ventilation age can be defined as the elapsed time since water was last in the mixed layer, which can be diagnosed from transient tracers with a known decay timescale or source function. For example, an isotope of hydrogen, tritium, decays to a daughter product, helium, with a half life of 12.3 years,



involving the conversion of a neutron to a proton and the emission of an electron, ${}_{-1}^0e$. Any helium formed in the mixed layer outgasses into the atmosphere, while any helium released below the mixed layer accumulates. Consequently, a ventilation age, T in years, can then be inferred from the ratio of the tritium and helium concentrations (see Q10.2),

$$T = 17.96 \ln \left(1 + \frac{[{}^3\text{He}]}{[{}^3\text{H}]} \right).$$

Over the North Atlantic, tritium–helium ages range from low values towards the northeast of the subtropical gyre, increasing to ages of 7 to 10 years in the southwest corner of the gyre (Fig. 10.15). Hence, fluid is youngest in the

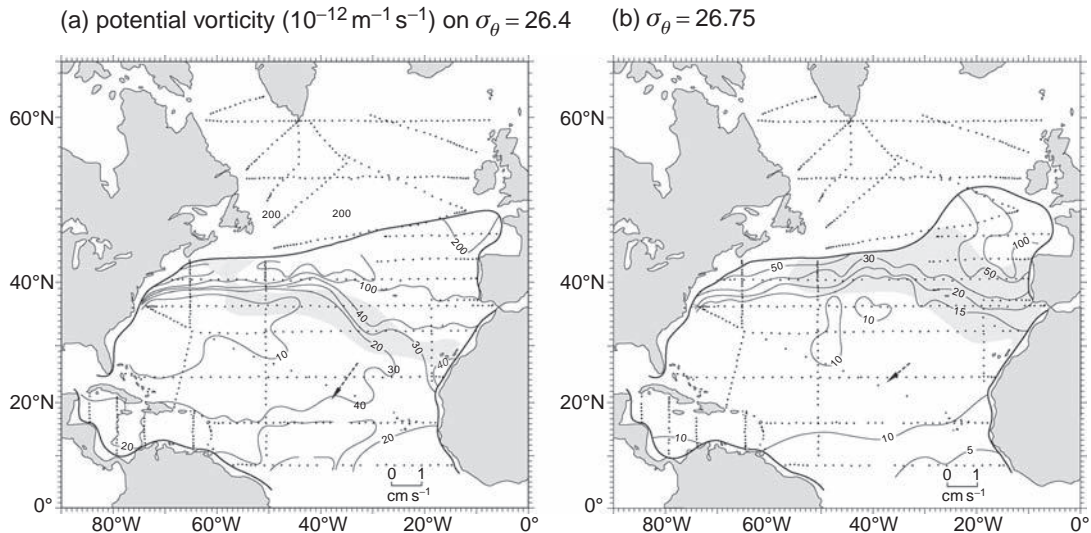


Figure 10.16 Diagnosed distribution of a dynamic tracer, potential vorticity, Q ($10^{-12} \text{ m}^{-1} \text{s}^{-1}$), over the North Atlantic: (a) between the potential density $\sigma_\theta = 26.3$ and 26.5 surfaces, the Q contours appear to be closed in the northwest Atlantic, or to be open in the northeast Atlantic and thread back to the winter outcrop (shaded area); and (b) between the $\sigma_\theta = 26.5$ and 27.0 surfaces, the Q field appears to be relatively homogeneous south of the winter outcrop over most of the subtropical gyre. There are also blocked Q contours running from coast to coast in the tropics, more clearly shown on other σ_θ surfaces. Original data points are marked by dots. Redrawn from McDowell *et al.* (1982).

northeast of the subtropical gyre and is probably subducted there, and then gradually ages following the anticyclonic circulation around the basin.

Dynamic tracer

Potential vorticity is a dynamic tracer, depending on the absolute spin of the fluid and the vertical stratification, which on the basin scale can be estimated from the product of the planetary vorticity, f , and stratification,

$$Q = -\frac{f}{\rho} \frac{\partial \sigma}{\partial z}, \quad (10.10)$$

where the contribution of relative vorticity ζ has been neglected. Climatological maps of potential vorticity reveal different regimes over the main thermocline as depicted in Fig. 10.16:

- (i) open Q contours extending from the mixed-layer outcrop at the end of winter (shading in Fig. 10.16a within the thermocline);
- (ii) closed Q contours containing nearly uniform Q within the thermocline, as evident in Fig. 10.16b; and

- (iii) blocked contours running zonally from coast to coast, usually associated with weak meridional flow unless directly forced, as hinted at in the tropics and along some denser surfaces.

Two different hypotheses have been invoked to explain these Q distributions.

Subduction view

Open Q contours are usually associated with gyre-scale subduction. Fluid is subducted from the end of winter mixed layer and Q is assumed to be subsequently conserved within the thermocline, taken to be adiabatic and inviscid.

Luyten, Pedlosky and Stommel (1983) constructed an idealised thermocline model to represent the subduction process over the interior of a subtropical gyre; see schematic views in Fig. 10.17 and model equations in Box 10.3. Their ventilation model suggests that the flow along each density layer consists of a ventilated region, where fluid passes from the mixed layer into the interior, bound by unventilated regions; to the west, fluid is swept in directly from the western boundary and to the east, fluid is assumed to

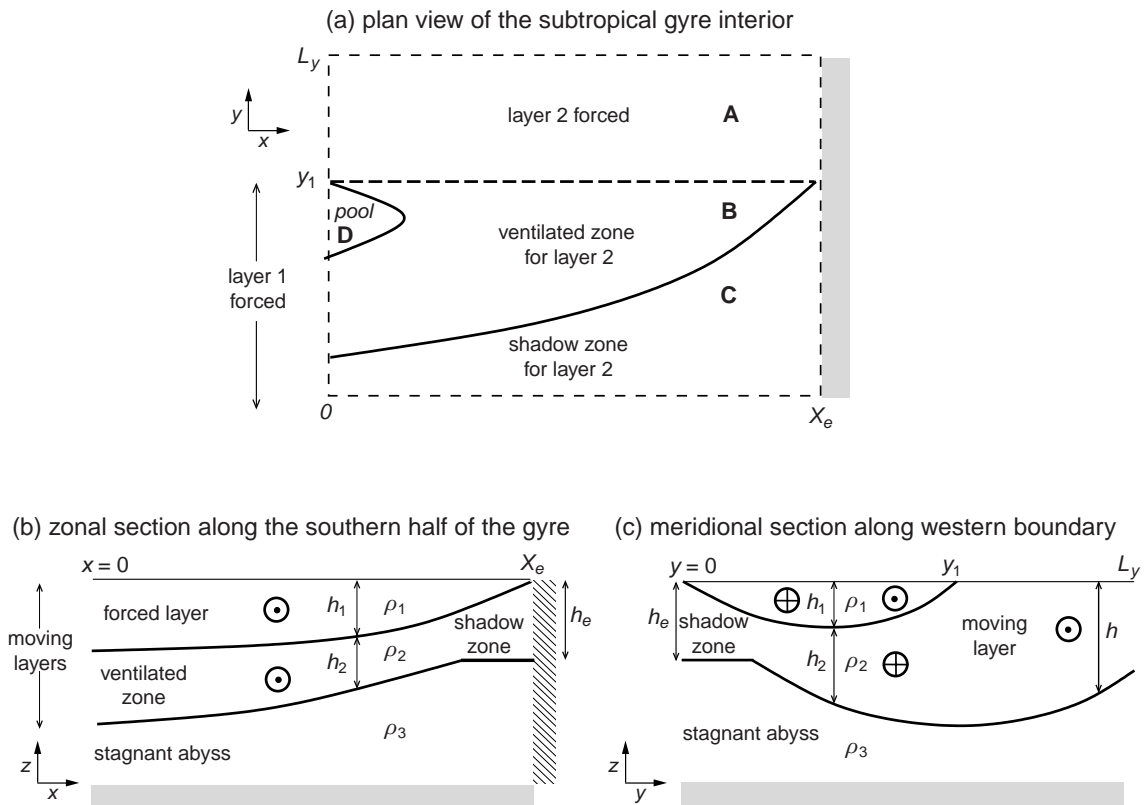


Figure 10.17 A schematic figure of the ventilated thermocline model of Luyten *et al.* (1983) for two moving layers: (a) a plan view of the interior of the subtropical gyre; (b) a zonal section in the southern half of the domain; and (c) a meridional section along the western side of model. The wind directly forces layers 2 and 1 north and south of y_1 , respectively. In regime A, only layer 2 is moving, and the layer thickens westward and southward due to the wind forcing. At y_1 , layer 2 is subducted beneath a lighter layer 1. The subducted fluid in layer 2 extends over the ventilated zone (region B), and is flanked by an eastern shadow zone (region C) and a western pool region (region D) where the potential vorticity in layer 2 is determined by the influx from the western boundary.

be motionless. The ventilated region extends over most of the subtropical gyre for light σ surfaces, but contracts eastward for denser surfaces.

Eddy stirring view

Extensive regions of nearly uniform Q , as evident in Fig. 10.16b, are instead usually associated with stirring by mesoscale eddies, which can homogenise tracers within closed geostrophic streamlines, as advocated by Rhines and Young (1982a,b) (see Fig. 9.14 in Section 9.3.3).

Gyre-scale subduction and eddy stirring can, however, occur simultaneously and modify each other. Ventilation helps control the tracers transferred along the winter outcrop of the potential density surface, while eddies act to smear out subducted mode waters and tracer contrasts in the ocean interior.

For example, a thermocline model using realistic end-of-winter mixed-layer variations (Fig. 10.18) can lead to regions of both open Q contours and nearly uniform Q within the thermocline, and plausible ideal ages, broadly resembling the observations (Figs. 10.16 and 10.15); see Q10.3 for how the mixed layer affects the link between subduction and potential vorticity. Likewise, eddy stirring along potential density surfaces might also provide a plausible age distribution, melding zero age at the surface outcrop and high age in the interior along potential density surfaces.

10.2.6 How is fluid exchanged across gyre boundaries?

Water masses formed in the subtropical gyre through the ventilation process do not necessarily remain within the subtropical gyre. Fluid

Box 10.3 | A thermocline model of subduction

Luyten *et al.* (1983) provided an elegant analytical model of the subduction process, representing the upper ocean as several moving layers of constant density overlying a dense, motionless abyss; schematically set out in Fig. 10.17. For two moving layers, the geostrophic velocity is given by the slope of the layer interfaces (10.2),

$$v_2 = \frac{g'}{f} \frac{\partial h}{\partial x} \quad \text{and} \quad v_1 = v_2 + \frac{g'}{f} \frac{\partial h_1}{\partial x} = \frac{g'}{f} \frac{\partial}{\partial x} (h + h_1), \quad (10.11)$$

where $g' = g \Delta \rho / \rho_0$ is a reduced gravity and $\Delta \rho$ is the density difference between each layer. The depth-integrated meridional transport is related to the Ekman upwelling, w_{ek} , by Sverdrup balance (8.5),

$$\beta(v_2 h_2 + v_1 h_1) = f w_{ek}, \quad (10.12)$$

which combining with (10.11) gives a forcing relationship,

$$\frac{\partial}{\partial x} (h^2 + h_1^2) = \frac{2f^2}{\beta g'} w_{ek}. \quad (10.13)$$

Assuming that the moving water has a constant thickness on the eastern boundary, h_e , and the light layer vanishes there, $h_1(x_e) = 0$, then integrating (10.13) between x and the eastern wall, x_e , relates the thickness of the interior layers to the zonally integrated Ekman pumping,

$$h^2 + h_1^2 = h_e^2 - \frac{2f^2}{\beta g'} \int_x^{x_e} w_{ek} dx, \quad (10.14)$$

which can be solved given w_{ek} , h_e , imposed density outcrops and subject to knowing how the layer thickness, $h_2 = h - h_1$, varies. There are several different regimes over the subtropical gyre (Fig. 10.17a):

(a) A single moving layer (region A, $y > y_1$) where only layer 2 is directly forced: $h_1 = 0$ and $h = h_2$, such that (10.14) can be solved as in the previous one and a half layer model (Fig. 10.12c).

(b) Two moving layers (region B, $y < y_1$) where layer 1 is directly forced by the wind, while layer 2 is subducted beneath layer 1 and is now shielded from direct wind forcing. Along this shielded layer 2, the large-scale potential vorticity is assumed to be conserved along a streamline, such that contours of h and Q_2 are coincident; the downstream Q_2 is defined by the value of Q_2 subducted at the outcrop y_1 , such that

$$Q_2(x, y) = \frac{f(y)}{h_2(x, y)} = \frac{f_1}{h_2(x, y_1)}, \quad (10.15)$$

which then relates the layer thicknesses, such that $h_2(x, y) = (f/f_1)h_2(x, y_1) = (f/f_1)h$ and $h_1(x, y) = (1 - f/f_1)h$, and allows h to be solved in (10.14).

(c) There are regions in layer 2 where fluid is not subducted and (10.15) cannot be applied. To the east, there is a 'shadow zone' (region C) where fluid is assumed to be unventilated and stagnant in layer 2, while to the west, there is a 'pool zone' (region D) where fluid enters the domain from the western boundary and its potential vorticity has to be assumed.

In the solutions, fluid moves equatorward over the interior of the subtropical gyre (Fig. 10.17b), and is swept eastward from the western boundary into each moving layer along its northern flank and returned westward along its southern flank (Fig. 10.17c).

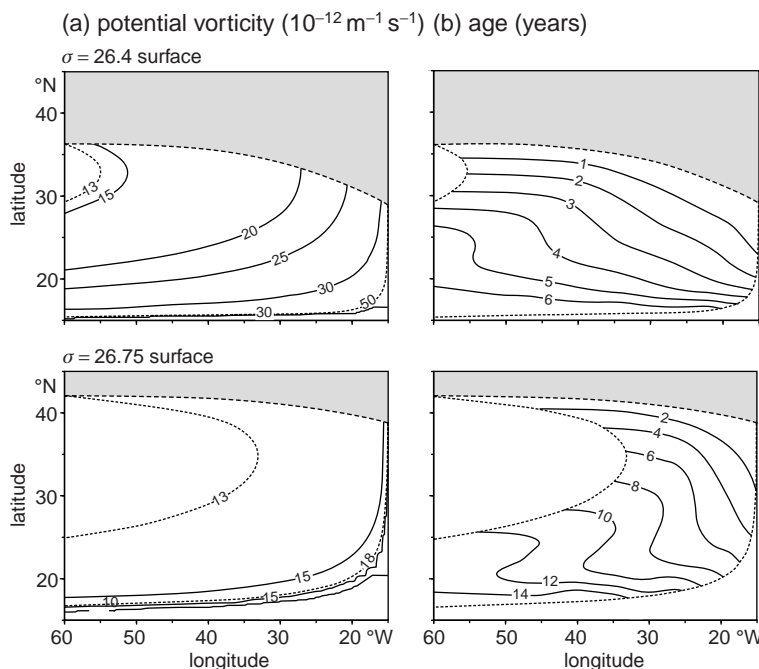


Figure 10.18 Thermocline model solutions for (a) the dynamic tracer, potential vorticity Q ($10^{-12} \text{ m}^{-1} \text{ s}^{-1}$), and (b) the ideal age (years), measuring the time since fluid was last in the surface mixed layer along $\sigma_\theta = 26.4$ and 26.75 surfaces. Fluid is subducted across the density outcrop in the mixed layer (long dashed line) into the thermocline (within a ventilated zone between the short dashed lines). For a mixed layer thickening to the north and becoming denser to the northeast, the subducted Q becomes nearly uniform, as obtained along the denser surface (lower panel); model solutions compare favourably with the observations in Figs. 10.15 and 10.16. Redrawn from Williams (1991).

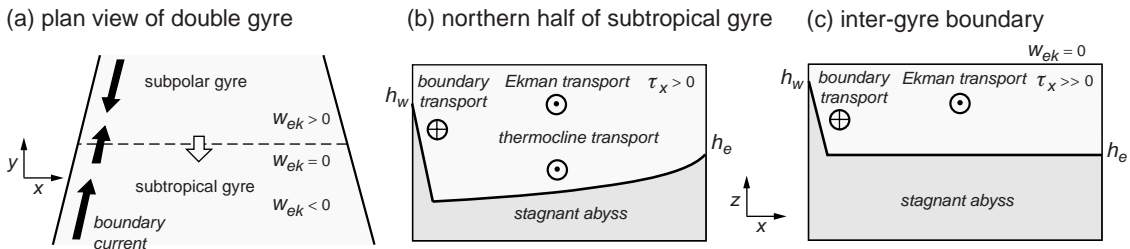


Figure 10.19 A schematic figure depicting how fluid is transported between a subtropical and subpolar gyre: (a) plan view showing the southward horizontal Ekman transport (white arrow) across the inter-gyre boundary, which is offset by the northward boundary transport (black arrow); zonal sections showing the transports and thickness of the thermocline across the subtropical gyre along (b) its northern flank and (c) along its northern boundary, where there is no Ekman pumping, $w_{ek} = 0$; the thickness of the thermocline is h_w and h_e on the western and eastern sides of the basin.

is exchanged between the subtropical gyre, the tropics and the subpolar gyre.

To understand these exchanges, consider a simplified model of the upper ocean consisting of a single layer of moving fluid, representing the thermocline, over a motionless abyss. The transport in this upper moving layer can be separated into that carried by the surface Ekman layer, and the geostrophic flow within the thermocline either in the basin interior or the western boundary (Box 10.4).

In the northern half of the subtropical gyre (Fig. 10.19a,b), there is a southward Ekman trans-

port induced by the eastward wind stress, a southward geostrophic transport over the gyre interior associated with a westward thickening of the thermocline, and a northward geostrophic transport in the western boundary current associated with a westward shoaling of the thermocline.

Assuming that the volume of warm water transported northward remains constant, the western boundary transport adjusts to accommodate the wind-driven changes in the Ekman transport and interior thermocline transport. At the inter-gyre boundary, there is no interior geostrophic transport, so there has to be a

Box 10.4 A simple model of the transport between the subtropical and subpolar gyres

In order to understand how the gyre circulation transports fluid between the subtropical and subpolar gyres, consider again a single adiabatic layer of moving fluid overlying a stagnant abyss as depicted in Fig. 10.19a; following Parsons (1969) and Veronis (1970). For simplicity, assume that the layer is forced by a surface wind stress, τ_x , which varies only with latitude, and that the layer has a constant thickness, h_e , along the eastern boundary.

The surface Ekman transport directed northward across the basin is given by

$$-\int_0^{x_e} \frac{\tau_x}{\rho f} dx = -\frac{x_e \bar{\tau}_x}{\rho f}, \quad (10.16)$$

where $\bar{\tau}_x$ is the zonally averaged, eastward wind stress and x_e is the width of the basin.

The geostrophic transport directed northward across the basin is given by

$$\int_0^{x_e} h v dx = \frac{g'}{2f} (h_e^2 - h_w^2), \quad (10.17)$$

assuming a geostrophic balance for the moving layer (10.2), where h represents the thickness of the moving layer, and h_e and h_w are the values on the eastern and western boundaries, respectively. This geostrophic transport is made up of two contributions, the transport within the basin interior and within the western boundary. The overall northward transport is then given by the sum of the Ekman and geostrophic transports, (10.16) and (10.17),

$$-\frac{x_e \bar{\tau}_x}{\rho f} + \frac{g'}{2f} (h_e^2 - h_w^2). \quad (10.18)$$

If this northward transport of warm water is conserved, then the boundary current transport has to adjust with latitude to accommodate the wind-driven changes in the Ekman transport and the thermocline transport over the basin interior (Fig. 10.19b).

At the inter-gyre boundary, defined by $w_{ek} = 0$, the thermocline is flat over the interior (10.5) and the western boundary current then provides a northward transport of warm water given by

$$\frac{g'}{2f} (h_e^2 - h_w^2)$$

from the subtropical to subpolar gyre (Fig. 10.19c). If the wind stress becomes sufficiently large, then the layer of warm water eventually outcrops on the western boundary, $h_w = 0$, and the boundary current then separates from the coast, leading to the warm water becoming confined towards the eastern side of the basin; see Q10.4.

northward geostrophic transport in the western boundary to offset the southward Ekman transport (Fig. 10.19c). Hence, the western boundary current transports fluid from the subtropical to the subpolar gyre, as well as redistributing fluid within each gyre.

10.3 | Summary

The ventilation process helps determine the distribution of physical tracers and the stratification over the global ocean. Ventilation forms

mode waters with large volumes of a particular temperature–salinity class. Light subtropical mode waters are formed throughout the subtropical gyres over the global ocean, as highlighted by the input of transient tracers, like CFCs and dissolved oxygen. Ventilation is more active over the North Atlantic and Southern Ocean for denser subtropical mode waters, as well as intermediate and denser water masses. Consequently, there are relatively older waters in the Pacific and Indian Oceans with higher concentrations of nutrients and carbon.

The ventilation of the upper ocean is controlled by a combination of the seasonal cycle of the mixed layer and the fluid transfer by the vertical and horizontal circulation. The seasonal cycle leads to fluid being preferentially transferred into the main thermocline in late winter and early spring, rather than throughout the year. Following the movement of a moving water column, fluid is transferred into the main thermocline through a combination of shoaling of the mixed layer from one winter to the next, together with a vertical downwelling of fluid. This transfer into the main thermocline occurs preferentially over the interior of the subtropical gyres.

This ventilated transfer of fluid into the permanent thermocline helps determine the relatively long memory of the ocean interior, compared with that of the surface mixed layer. Conversely, the reverse of the ventilation process is also important, the transfer of thermocline fluid into the seasonal boundary layer affects the downstream water-mass properties of the mixed layer. This transfer of fluid from the thermocline occurs preferentially over the interior of the subpolar gyres.

Ventilation affects the cycling and transport of nutrients and carbon, which in turn modify the patterns of biological productivity and the transfer of carbon into the ocean; this biogeochemical theme is taken forward in [Chapter 11](#) and an integrated diagnostic view is provided in [Chapter 13](#).

10.4 | Questions

Q10.1. Ekman upwelling velocity.

The Ekman upwelling velocity at the base of the

Ekman layer is related to the wind stress by

$$w_{ek} = \frac{1}{\rho_0} \left(\frac{\partial \tau_y^s}{\partial x} f - \frac{\partial \tau_x^s}{\partial y} f \right). \quad (10.19)$$

(a) For the following cases, identify whether the wind forcing denotes a subtropical gyre with $w_{ek} < 0$ or a subpolar gyre with $w_{ek} > 0$:

- (i) the eastward wind stress decreases northward in the northern hemisphere;
- (ii) the eastward wind stress increases northward in the northern hemisphere;
- (iii) the eastward wind stress decreases northward in the southern hemisphere; and
- (iv) the eastward wind stress increases northward in the southern hemisphere.

In each case, ignore any changes in the northward wind stress.

(b) Derive the relationship for Ekman upwelling ([10.19](#)) based upon continuity of volume,

$$\frac{\partial u_{ek}}{\partial x} + \frac{\partial v_{ek}}{\partial y} + \frac{\partial w}{\partial z} = 0,$$

and the definition of the horizontal Ekman velocities,

$$\int_{-h_{ek}}^0 u_{ek} dz = \frac{\tau_y^s}{\rho_0 f} \quad \text{and} \quad \int_{-h_{ek}}^0 v_{ek} dz = -\frac{\tau_x^s}{\rho_0 f}. \quad (10.20)$$

Q10.2. Tritium–helium age.

Tritium decays to helium with a half life of 12.3 years. The helium outgasses to the atmosphere within the surface mixed layer, but accumulates within the ocean interior. Consequently, a ventilation age, defined by the time since fluid was in the surface mixed layer, can be estimated from the ratio of the tritium and helium concentrations,

$$T(\text{years}) = 17.96 \ln \left(1 + \frac{{}^3\text{He}}{{}^3\text{H}} \right). \quad (10.21)$$

(a) Evaluate the ventilation age assuming (i) a tritium concentration, ${}^3\text{H}$, of 2.5 TU and a helium concentration, ${}^3\text{He}$, of 1.5 TU; and (ii) a tritium concentration of 0.5 TU and a helium concentration of 1 TU (1 tritium unit TU equals 1 tritium atom in 10^{18} hydrogen atoms).

(b) Assuming that tritium decays as

$$\frac{d}{dt} {}^3\text{H} = -\alpha {}^3\text{H}, \quad (10.22)$$

show that the tritium concentration decays as ${}^3\text{H}(t) = {}^3\text{H}(0) \exp(-\alpha t)$, where $\alpha = 1/(17.96 \text{ years})$.

(c) Given that tritium decays to helium, show that helium accumulates in the interior as ${}^3\text{He}(t) = {}^3\text{H}(0)(1 - \exp(-\alpha t))$. Assume that there is initially no helium present in the mixed layer.

(d) Hence, derive the ventilation age given in (10.21).

Q10.3. Potential vorticity and the mixed layer.

The potential vorticity of fluid subducted beneath the mixed layer (as in Fig. 10.10) is defined by

$$Q = -\frac{f}{\rho S(t)} \frac{D\sigma_m}{Dt} = \frac{f}{\rho(w_b + \frac{Dh}{Dt})} \frac{D\sigma_m}{Dt}, \quad (10.23)$$

where $D\sigma_m/Dt$ represents the rate of change of mixed-layer density following the flow, $S(t)$ is the instantaneous subduction rate (10.6), w_b is the vertical velocity at the base of the mixed layer and Dh/Dt is the rate of change of mixed-layer thickness following the flow (Williams, 1991); this relationship ignores any contribution from relative vorticity.

(a) For there to be subduction, $S(t) > 0$, how does the mixed-layer density have to vary in time?

(b) What are the criteria for low values of Q , such as that occurring in mode waters?

(c) Derive the relationship for potential vorticity (10.23). Consider a particle initially within the mixed layer, which is then subducted into the thermocline and conserves its density. Derive (i) how the density difference between the particle and the overlying mixed layer, $\Delta\sigma$, increases with the time t since subduction; (ii) how the vertical spacing between the particle and the overlying mixed layer, Δz , increases with t ; and then (iii) combine with the definition for potential vorticity, $Q = -(f/\rho)\Delta\sigma/\Delta z$, on the basin scale.

Q10.4. Transport of warm water and the separation of the boundary current.

Consider a single layer of moving fluid, representing the thermocline, overlying a dense abyss

within a wind-forced, subtropical gyre (as in Fig. 10.19 and Box 10.4). The overall northward transport of warm water in this model, T_{north} , is given by the sum of the Ekman transport, $-\frac{x_e \bar{\tau}_x}{\rho f}$, and geostrophic transport, $\frac{g'}{2f} (h_e^2 - h_w^2)$,

$$T_{north} = -\frac{x_e \bar{\tau}_x}{\rho f} + \frac{g'}{2f} (h_e^2 - h_w^2). \quad (10.24)$$

(a) Calculate the Ekman transport and the geostrophic transport in Sv, assuming $x_e = 5000 \text{ km}$, $\bar{\tau}_x = 0.1 \text{ N m}^{-2}$, $\rho = 10^3 \text{ kg m}^{-3}$, $f = 10^{-4} \text{ s}^{-1}$, $g' = 0.01 \text{ m s}^{-2}$, $h_w = 200 \text{ m}$ and $h_e = 600 \text{ m}$.

(b) For the same northward transport, T_{north} , how does the layer thickness on the western boundary, h_w , vary if the wind stress increases? What value has the wind stress to reach if the layer thickness on the western boundary vanishes, $h_w = 0$?

(c) When $h_w = 0$, the transport of warm water is instead given by

$$T_{north} = -(x_e - X_p(y)) \frac{\bar{\tau}_x}{f} + \frac{g'}{2f} h_e^2, \quad (10.25)$$

where $X_p(y)$ defines the western outcrop of the warm water. If the northward transport of warm water remains conserved and the wind stress increases further north, how does the western outcrop of the warm water vary in position?

10.5 | Recommended reading

Accessible reviews of ventilation and the subduction process are provided in the WOCE book by K. Hanawa and L. D. Talley (2001), Mode waters, and J.F. Price (2001), Subduction. In *Ocean Circulation and Climate: Observing and Modelling the Global Ocean*, ed. G. Siedler, J. Church and J. Gould. San Diego, CA: Academic Press, pp. 373–386 and 357–372.

A discussion of how the mixed layer affects the stratification of the ocean interior is provided by J. D. Woods (1985). The physics of thermocline ventilation. In *Coupled Ocean-Atmosphere Models*, ed. J. C. J. Nihoul. Kiel: Elsevier, pp. 543–590.

A theoretical view of ventilation models is provided by J. Pedlosky (1996). *Ocean Circulation Theory*. Berlin: Springer, 453pp.

Cycling and transport of nutrients and carbon

Phytoplankton require sunlight and nutrients to grow in the surface ocean. Sustaining phytoplankton growth is difficult in the open ocean because organic particles fall through gravity out of the sunlit, surface ocean into the dark interior, taking essential nutrient elements with them. Without ocean circulation the surface ocean would become a marine desert lacking the nutrients to support photosynthesis. Instead, physical processes continually resupply nutrients to the surface ocean, leading to some interesting consequences: phytoplankton are most abundant at high latitudes and least in the mid latitudes of the open ocean, reflecting the effect of the circulation and mixing of nutrients, rather than the pattern of insolation.

In the dark interior below the sunlit surface layer, inorganic nutrient and carbon distributions are controlled by a combination of physical transport and mixing processes, as well as biologically achieved respiration of organic matter and regeneration of inorganic form, as depicted in Fig. 11.1. Physical transport leads to a layered structure in the inorganic nutrient and carbon distributions over the globe, while respiration increases inorganic concentrations in the waters which have resided at depth for the longest time.

In this chapter, we start in the surface waters and discuss how the growth of phytoplankton is maintained, focussing on the physical transport of nutrients over the North Atlantic. We address the role of boundary currents, physical transfers between the mixed layer and interior, and con-

vection within the surface mixed layer. We discuss how phytoplankton growth is sustained over the mid-latitude subtropical gyres, where wind-induced downwelling inhibits the surface supply of nutrients. We then move below the surface ocean and consider how the global-scale inorganic nutrient and carbon distributions are controlled in the dark interior. The inorganic nutrients are separated into components due to physical transport and biologically mediated transfer. Similarly, dissolved inorganic carbon is separated into components related to physical and biological transfers, as well as the efficiency of air-sea exchange.

11.1 How are basin-scale contrasts in biological productivity maintained?

Phytoplankton growth occurs in the surface ocean whenever there is enough sunlight and sufficient supply of nutrients and trace metals. This connection between biological productivity and surface nutrients is highlighted over the North Atlantic, where enhanced productivity in the high latitudes and the tropics coincides with increased nutrient concentrations at the base of the euphotic zone, while much weaker productivity over the mid latitudes coincides with lower concentrations of nutrients (Fig. 11.2a,b). Elsewhere in the Southern Ocean and parts of the Pacific Ocean, this connection becomes more complicated, since biological

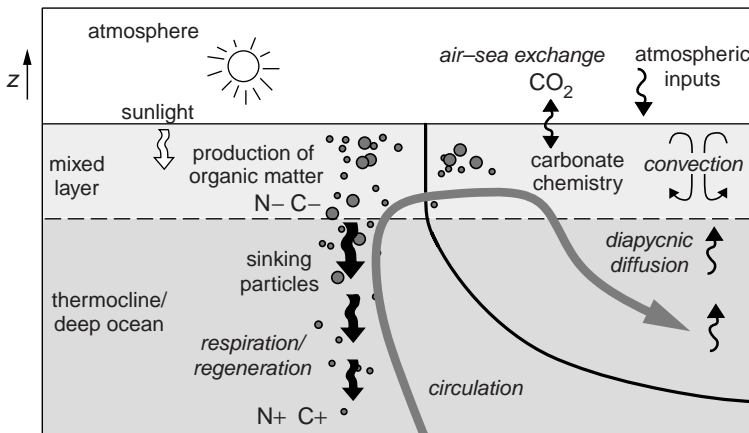


Figure 11.1 Schematic view of the processes affecting nutrient and carbon cycling. In the vertical, there is phytoplankton growth within the euphotic zone, formation of organic matter, sinking of particles together with respiration and regeneration at depth. This biological productivity is partly maintained through the physical transfer of nutrients within the ocean involving the circulation, diapycnic diffusion and convection. The cycling of carbon is also affected by air-sea exchange, mediated by carbonate chemistry.

productivity instead becomes limited by the availability of trace metals, so there can be low productivity even if there are high concentrations of the macro-nutrients, nitrate, phosphate and silica.

While this connection between biological productivity and surface concentrations of nutrients and trace metals is to be expected (Fig. 11.2), a more profound question is, how are these patterns sustained? Phytoplankton growth converts inorganic nutrients into organic matter, a fraction of which escapes from the sunlit ocean through gravitational sinking and transport. A return supply of inorganic nutrients is needed to oppose this export and sustain productivity. While sources of nutrients from atmospheric deposition and river run-off are important close to the coast, they are weak over the open ocean. There, surface nutrients are maintained by the physical redistribution of nutrients from the ocean interior.

Nutrients are redistributed through a range of physical transport and mixing processes (as illustrated in Fig. 11.2c), involving the following phenomena: gyre and overturning circulations, convection in the surface mixed layer, exchange between the mixed layer and thermocline, time-dependent eddy and frontal-scale transfers, and diapycnal mixing within the thermocline. We now consider how each of these physical phenomena maintain the production of organic matter in the surface ocean. While we use examples from the North Atlantic, these phenomena are generic and occur throughout the global ocean.

11.1.1 Boundary current transfer

To understand how productivity is sustained, we start by considering how nutrient-rich waters are redistributed over the upper ocean. As part of the gyre and overturning circulations, the strongest basin flows are the western boundary currents, such as the Gulf Stream, revealed by a surface front in chlorophyll (Fig. 1.7b), separating productive, nutrient-rich water on its northern edge and less productive, nutrient-depleted waters to the south.

More important than this surface signature, the Gulf Stream provides a flux of nutrients directed along its path (Fig. 11.3a) defined by the product of its along-stream velocity and nitrate concentration. This flux reaches a subsurface maximum of more than $10 \text{ mmol N m}^{-2} \text{ s}^{-1}$, within a depth range from 250 m to 750 m (Fig. 11.3b). There is no surface signature of this flux as the surface nitrate concentrations are extremely depleted.

The intense nitrate flux provided by the Gulf Stream is referred to as a 'nutrient stream' (Pelegrí and Csanady, 1991) and provides a conduit of nutrients which pass mainly into the subpolar gyre, but also partly recirculate in the subtropical gyre (Fig. 11.4a). There are accompanying streams for other tracers, such as dissolved organic nitrogen (DON); DON is preferentially swept around the subtropical gyre (Fig. 11.4b) since DON is more surface intensified than nitrate.

Nutrient streams are important in redistributing essential elements on the basin scale, as depicted in Fig. 11.4c. They connect the

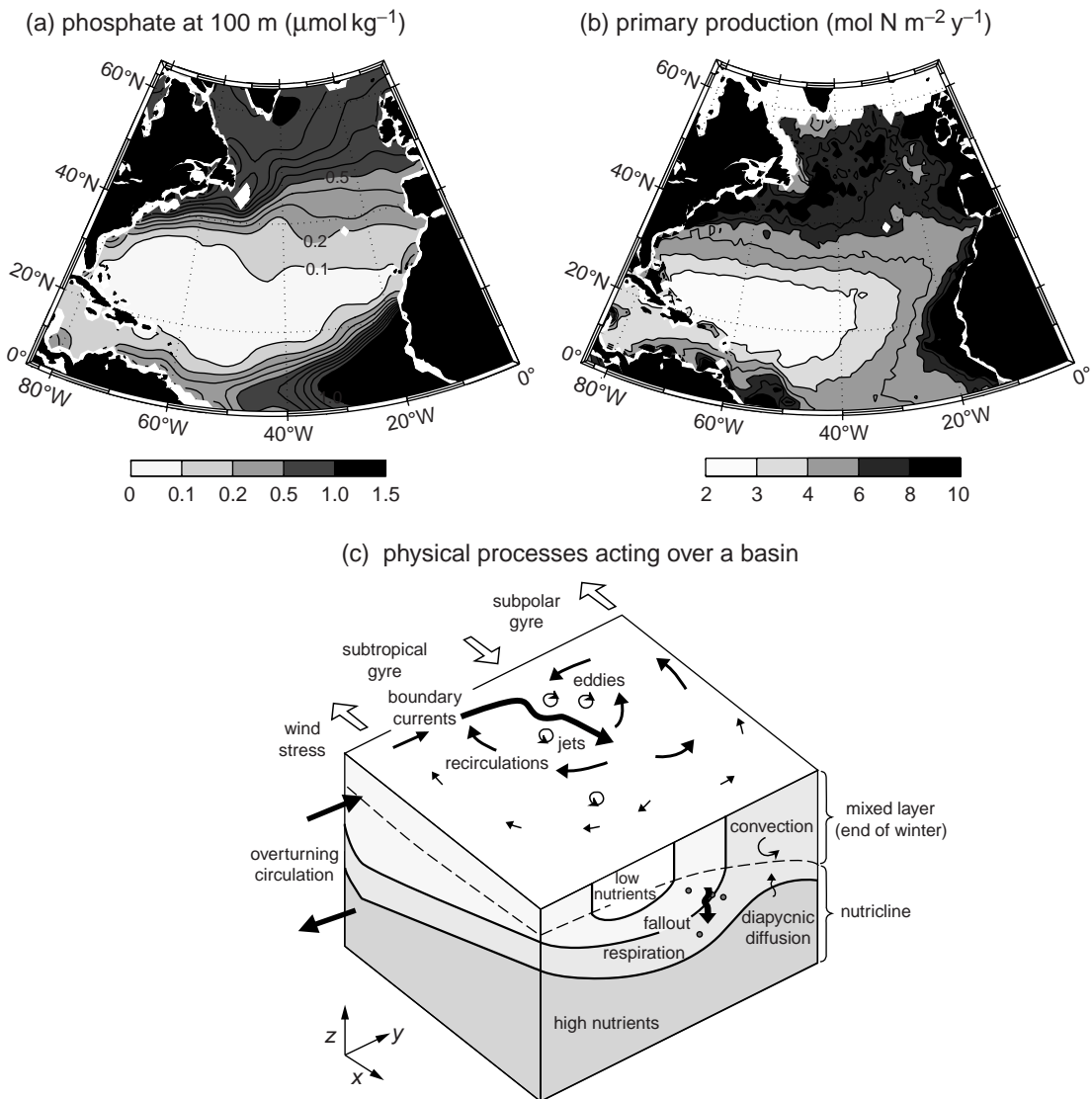


Figure 11.2 (a) Phosphate concentration ($\mu\text{mol kg}^{-1}$) at the base of the euphotic zone, taken to be at a depth of 100 m. (b) Primary production ($\text{mol N m}^{-2} \text{y}^{-1}$), the rate of production of organic matter by photosynthesis over the North Atlantic, as inferred from remote-sensing-based estimates of surface chlorophyll and temperature for 2005 (Behrenfeld and Falkowski, 1997a), assuming a C : N ratio of 106 : 16. (c) A schematic view of the physical processes acting to maintain biological productivity involving the three-dimensional circulation consisting of boundary currents, separated jets, interior flows, eddy and frontal circulations, as well as spatial variations in convection and diapycnic diffusion.

nutrient depleted surface waters of the northern basins with the Southern Ocean. In the Southern Ocean, macro-nutrient concentrations are relatively high in the surface mixed layer, because biological consumption is inhibited by lack of iron and/or light, and is unable to consume all the upwelled nutrients. These water masses, rich

in macro nutrients, are subducted into the thermocline and spread northward in each basin, transported via the gyre and overturning circulations; they can be identified by their freshness and are made up of a combination of Sub-Antarctic Mode Water and Antarctic Intermediate Water. In the tropics, the local nutrient concentrations

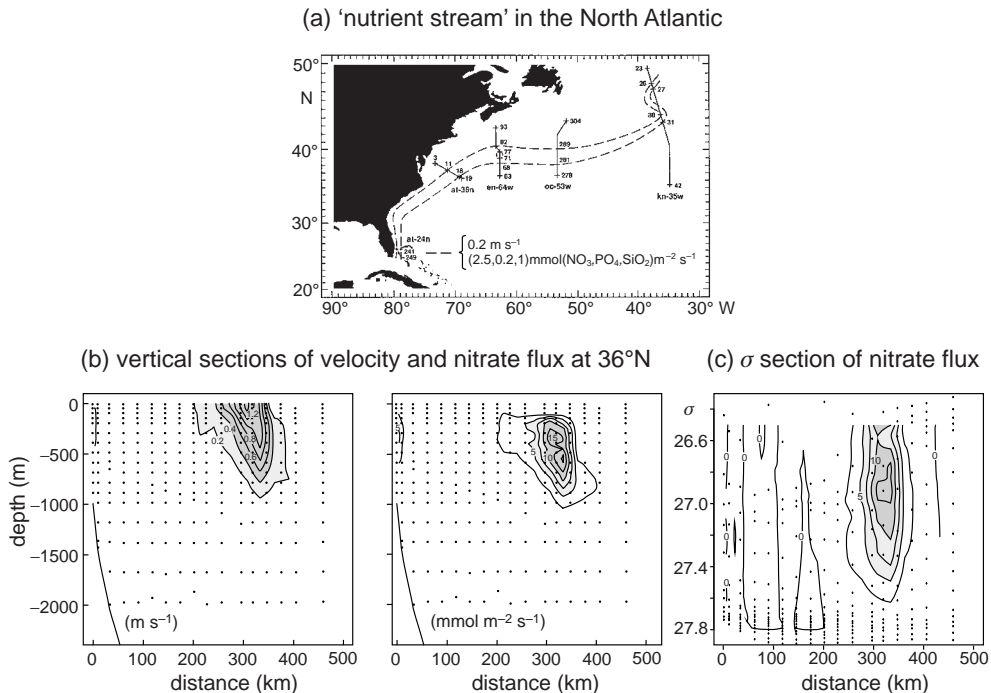


Figure 11.3 Diagnostics revealing how the Gulf Stream acts as a ‘nutrient stream’: (a) dashed lines depict the boundaries of the ‘nutrient stream’ and full lines depict hydrographic sections; (b) along-stream velocity (m s^{-1}) and nitrate flux ($\text{mmol m}^{-2} \text{s}^{-1}$) versus depth along 36°N ; and (c) nitrate flux ($\text{mmol m}^{-2} \text{s}^{-1}$) versus σ along 36°N . Redrawn from Pelegri and Csanady (1991) and Pelegri et al. (1996).

increase through a local cycle of upwelling, fallout and regeneration. The nutrient-enriched waters then continue into the northern basins via the western boundary current and separated jet. What is the fate of these nutrient-rich waters?

11.1.2 Advection of nutrients into the mixed layer

Below the surface in the Gulf Stream, nutrients are transferred along potential density layers which eventually outcrop into the downstream mixed layer, as illustrated in Fig. 11.5a. Close to where the Gulf Stream separates from the coast, the nutrient flux is greatest in the density layers from $\sigma = 26.7$ to 27.4 (Fig. 11.3c). These layers outcrop into the mixed layer at the end of winter over both the northern flank of the subtropical gyre and much of the subpolar gyre (Fig. 11.5b). This advective influx of nutrients then maintains high surface

concentrations of macro nutrients and vigorous productivity over the subpolar gyre (Fig. 11.5c).

The advection of fluid into the downstream mixed layer is achieved through the reverse of the subduction process: fluid is transferred by a combination of vertical upwelling and horizontal advection into a thickening mixed layer, as depicted in Fig. 11.6a. The associated advective flux of nutrients into the downstream mixed layer at the end of winter is given by

$$N_H (w_H + \mathbf{u}_H \cdot \nabla H) \equiv -N_H S_{ann}, \quad (11.1)$$

where N_H is the nutrient concentration, \mathbf{u}_H and w_H are the horizontal and vertical velocities at the base of the end of winter mixed layer, $z = -H$, and S_{ann} is the subduction rate.

This advective transfer of nutrients into the end of winter mixed layer defines two separate biological regimes:

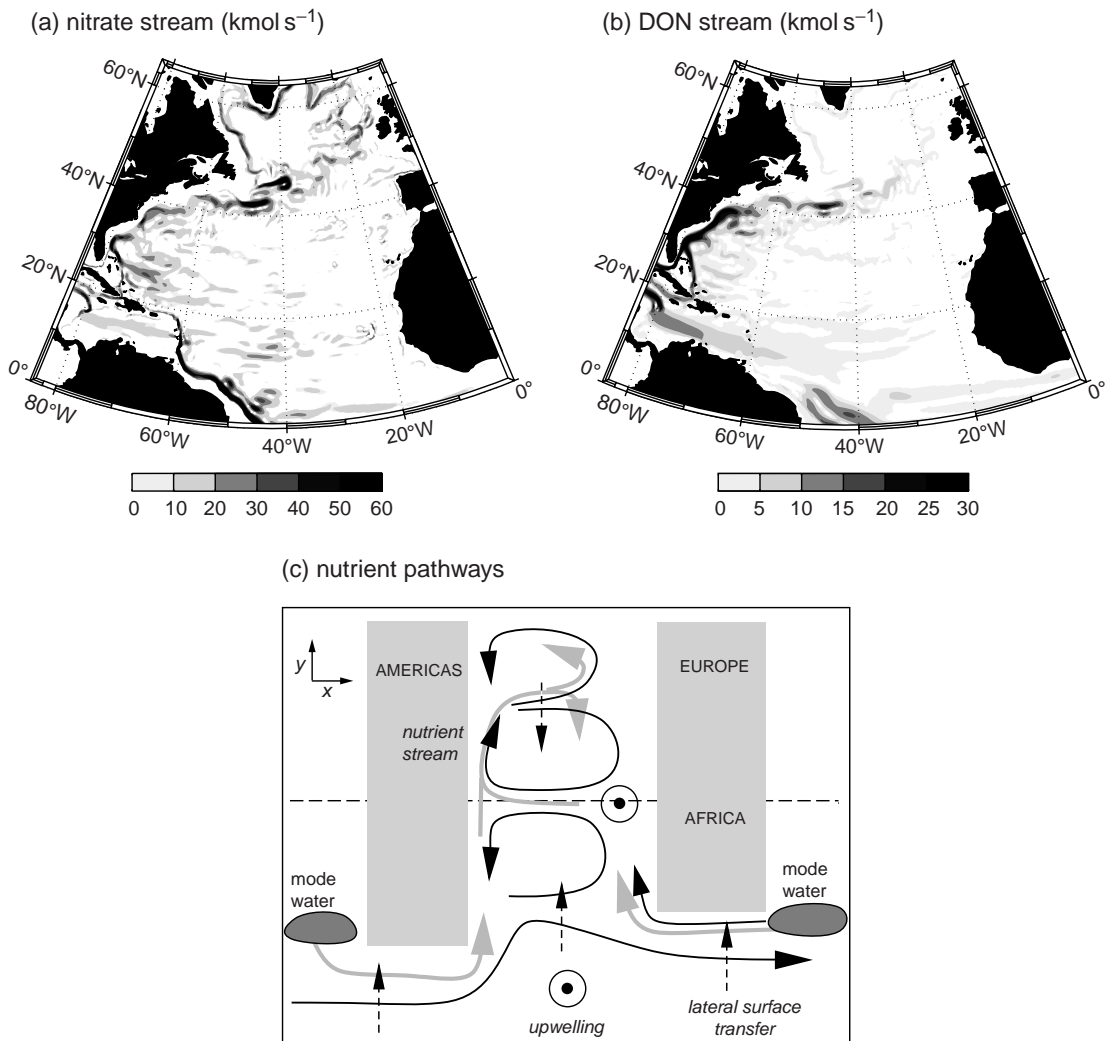


Figure 11.4 Nutrient pathways over the Atlantic. In (a) nitrate (kmol s^{-1}), and (b) dissolved organic nitrogen (DON) transport (kmol s^{-1}), displayed as the magnitude of a depth integral of $v N$, where v is the horizontal velocity and N is the nutrient concentration from a numerical isopycnic circulation model at 0.23° , integrated in (a) between σ_θ surfaces 26.5 and 27.5, and in (b) between the sea surface and $\sigma_\theta = 26.5$. In (c), a schematic view of the nutrient pathways in the Atlantic; Sub-Antarctic Mode Waters (dark grey shaded) are formed in the southern hemisphere, transferred northward, and eventually subducted into the downstream mixed layer; the transport involves a combination of the horizontal Ekman (dashed line), gyre (black) and intermediate (grey) circulations. Panels (a) and (b) from Williams *et al.* (2011) and panel (c) from Williams *et al.* (2006).

- Productive, subpolar gyres where nutrient-rich water is transferred from the thermocline into the winter mixed layer, as marked by positive transfer in Fig. 11.6b.
- Oligotrophic subtropical gyres where nutrient-depleted water is instead subducted from the

mixed layer into the thermocline, as marked by negative transfer in Fig. 11.6b.

The sign of this advective transfer broadly reflects the sign of the wind-induced Ekman upwelling (Fig. 11.6c), since Ekman pumping determines the

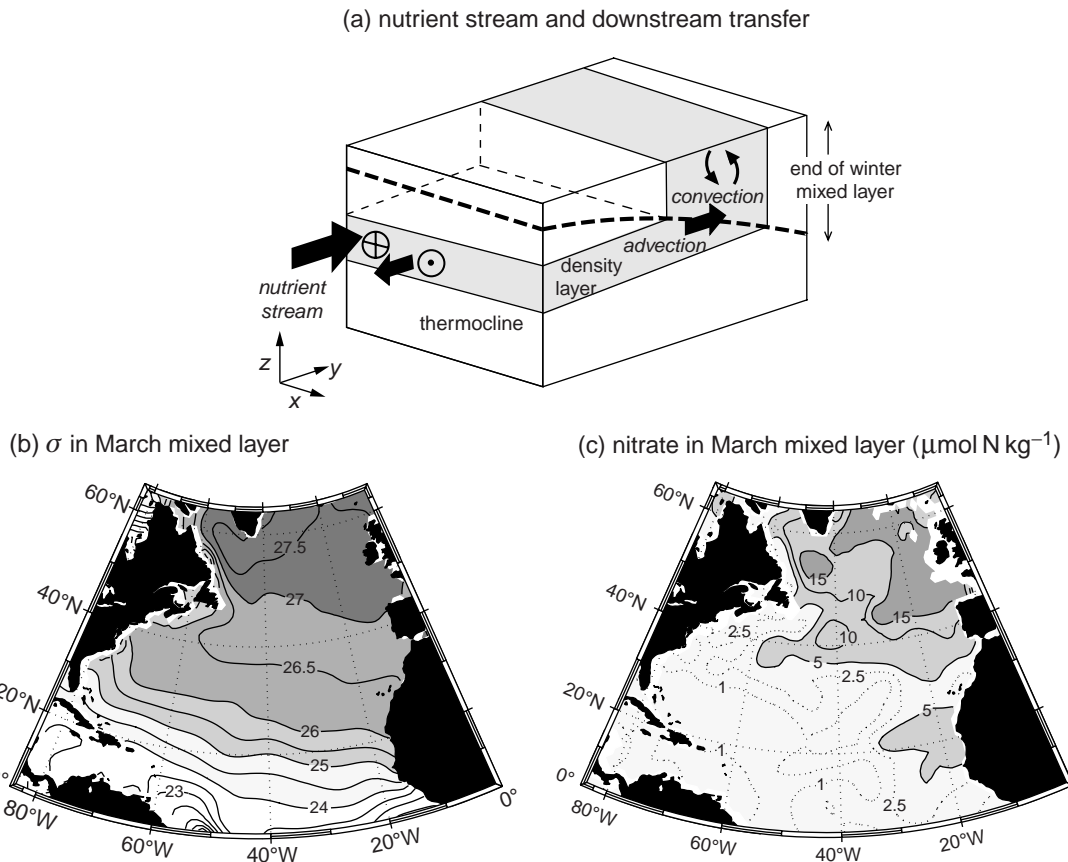


Figure 11.5 The surface density and nutrient distributions at the end of winter reflect the effect of the underlying circulation: (a) a schematic view of how a nutrient stream (black arrow) associated with the western boundary current transfers nutrients along an isopycnal layer (shading) into the downstream mixed layer (dashed line) at the end of winter; and the nutrients are then vertically redistributed through convection (curved arrows); diagnostics of (b) mixed-layer density, σ (kg m^{-3}), and (c) nitrate ($\mu\text{mol kg}^{-1}$) for March from climatology over the North Atlantic (Conkright et al., 2002; Conkright et al., 1994).

sign of the gyre rotation. However, the actual magnitude of the transfer over the subpolar gyre is primarily determined by the horizontal advection into the winter mixed layer.

Hence, nutrients are supplied by advection to the thick, winter mixed layer. How does this transfer then sustain phytoplankton growth in the euphotic zone?

11.1.3 Convective transfer of nutrients

Primary production is confined to the euphotic layer, where the photon flux is sufficient to sustain photosynthesis. The euphotic layer varies in thickness from a few metres in very turbid waters to as much as even 200 m in clear waters.

Whenever the mixed layer is thicker than the euphotic zone, then the nutrient profile is affected by the interplay of biological consumption and convection (Fig. 11.7a). Over each 24-hour period, the mixed layer thickens through surface cooling during the night, entraining nutrient-enriched thermocline waters. The enhanced turbulence homogenises the nutrient profile vertically over the mixed layer. Over the following daytime, sunlight enables photosynthesis which drives the consumption of nutrients within the euphotic layer.

In a similar manner, the seasonal cycle of the mixed layer causes the nutrients advected into the seasonal boundary layer to be vertically

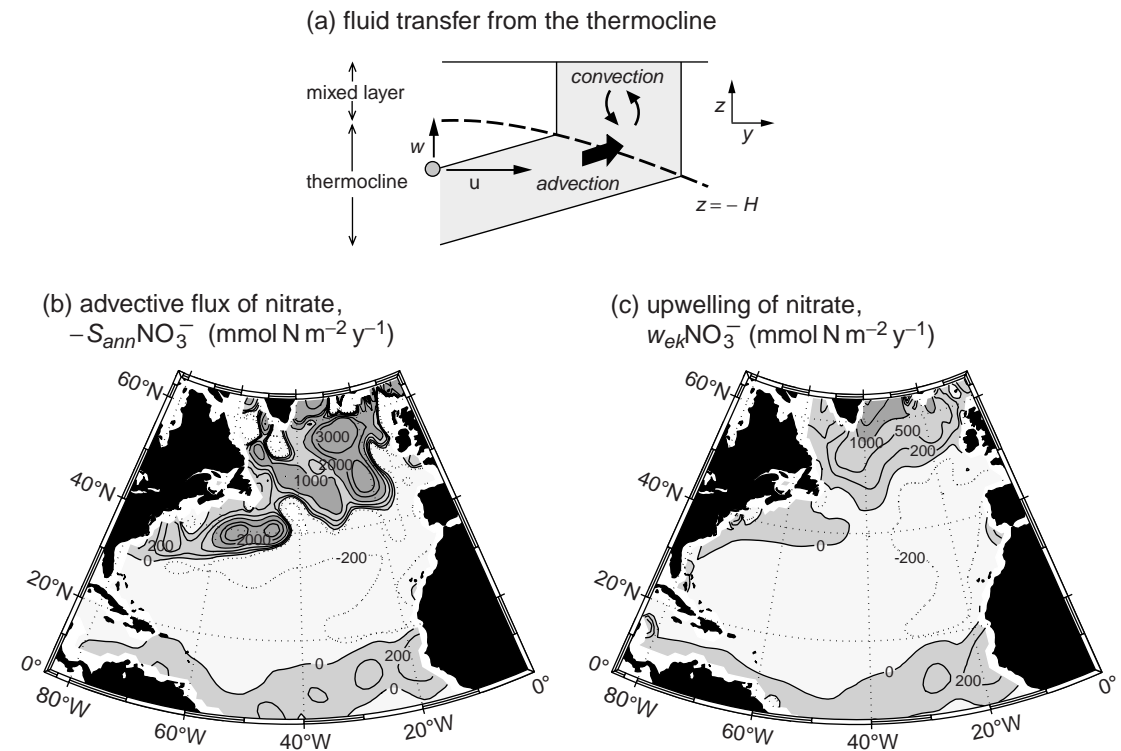


Figure 11.6 (a) A schematic view of a density layer (shaded) outcropping into the mixed layer at the end of winter. Fluid is transferred from the thermocline across the base of the sloping mixed layer (dashed line, $z = -H$) through the advective transfer by horizontal velocity u and vertical velocity, w ; (b) advective transfer of nitrate into the winter mixed layer, $-S_{ann}\text{NO}_3^-$ (mmol N m $^{-2}$ y $^{-1}$), where S_{ann} is the subduction rate, and (c) Ekman upwelling of nitrate, $w_{ek}\text{NO}_3^-$ (mmol N m $^{-2}$ y $^{-1}$), defined as positive as upwards. There are two regimes: nitrate transferred into the mixed layer, $-S_{ann}\text{NO}_3^- > 0$, or nitrate transferred into the thermocline, $-S_{ann}\text{NO}_3^- < 0$; further details in Williams *et al.* (2006).

redistributed within the thick mixed layer at the end of winter, entraining them into the euphotic zone. This seasonal supply of nutrients from convection then sustains production over the euphotic zone in the following spring and, through recycling, the summer. For example, over the North Atlantic, the winter mixed layer is thicker than 300 m over the northern flank of the subpolar gyre. This winter-time thickening leads to a convective entrainment of nitrate to the euphotic zone of up to 600 mmol N m $^{-2}$ y $^{-1}$ (Fig. 11.7b,c).

Phytoplankton growth is then sustained over much of the open ocean through a two-stage process:

- Nutrients are advected into the seasonal boundary layer through a combination of the horizontal and vertical circulations (as suggested on the gyre scale by Fig. 11.6b).

- Convection redistributes the nutrients vertically within the mixed layer, which then supplies them to the euphotic zone (Fig. 11.7c).

If convection were to occur in isolation from the large-scale advective transfer, then productivity would gradually diminish: the nutrient inventory of the seasonal boundary layer would progressively decline as organic particles sink into deeper waters.

In the simpler case where the mixed layer is shallower than the euphotic zone, such as in the tropics and low latitudes, convection does not provide a source of nutrients. Biological productivity is instead sustained by the direct physical transfer of nutrients into the euphotic zone. This supply is probably achieved here mostly by vertical upwelling and diapycnic diffusion, with a contribution from horizontal transfer across the sloping base of the euphotic zone.

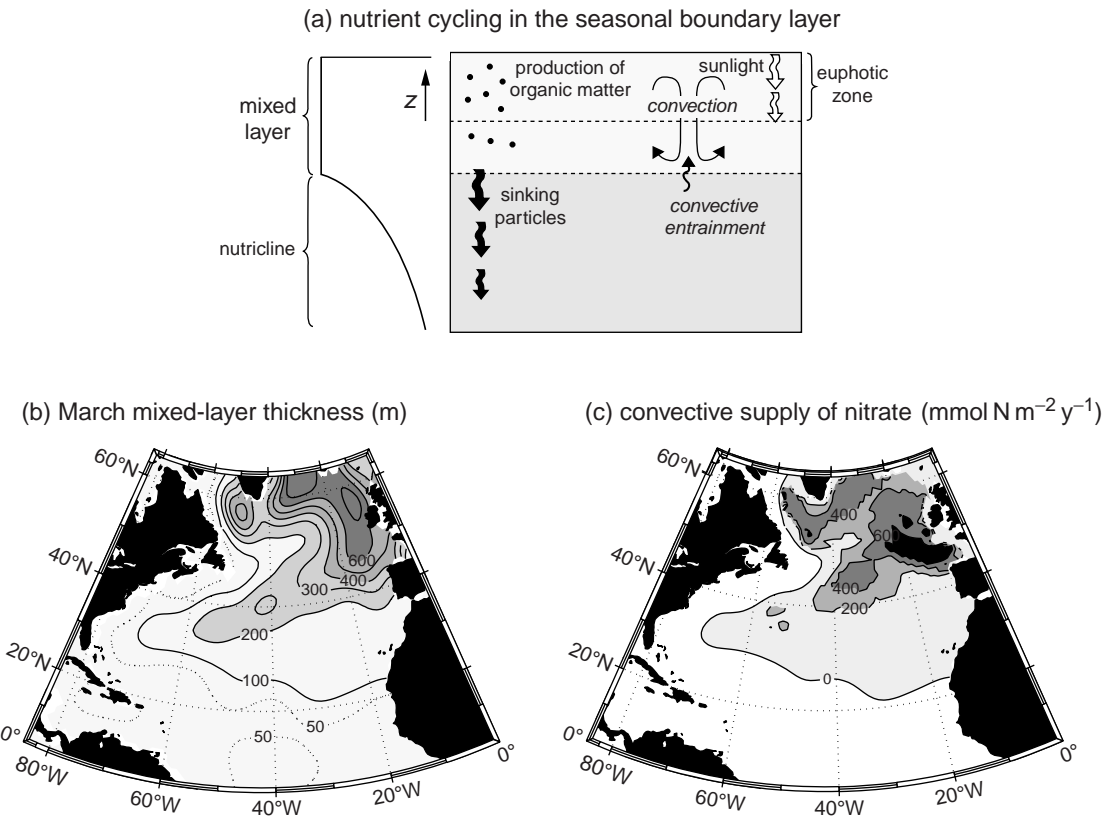


Figure 11.7 (a) A schematic view of a convective, mixed layer overlying a nutricline. Organic matter is produced in the sunlit, euphotic zone and a small fraction is exported through sinking particles and transport of dissolved organic matter. Convection provides an entrainment flux of nutrients into the euphotic zone (whenever the euphotic zone is shallower than the mixed layer). Climatological estimates of (b) the thickness (m) of the mixed layer in March, and (c) the convective supply of nitrate ($\text{mmol N m}^{-2} \text{y}^{-1}$) to the euphotic zone, assumed a thickness of 100 m. The convective supply is estimated from the depth-integrated change between the end of winter and summer nitrate profiles, which is greatest when there are thick mixed layers with a strong seasonal nitrate contrast and vanishes whenever the euphotic zone is thicker than the winter mixed layer.

11.2 How is biological productivity sustained in ocean deserts?

Given the view that biological productivity is ultimately sustained by nutrient transfer from the thermocline into the mixed layer, how can we explain the maintenance of photosynthesis in the subtropical gyres where the winds induce widespread downwelling? The subtropical gyres are sometimes viewed as oceanic deserts due to the low rate that nutrients are supplied to the surface. However, primary production does still occur

there, albeit at weaker rates than at high latitudes or the tropics. Despite the lower rates of primary production, the extensive area of the subtropical gyres means that they account for up to half of the global export of organic matter.

A range of hypotheses have been set out to explain how the productivity of the subtropical oceans is sustained. At the simplest level, the question is how are nutrients supplied to the euphotic zone from the underlying nutrient-rich waters? This supply is probably achieved primarily via vertical exchanges involving convection, diapycnic mixing and time-varying upwelling (Fig. 11.8). However, for these processes to continue to act

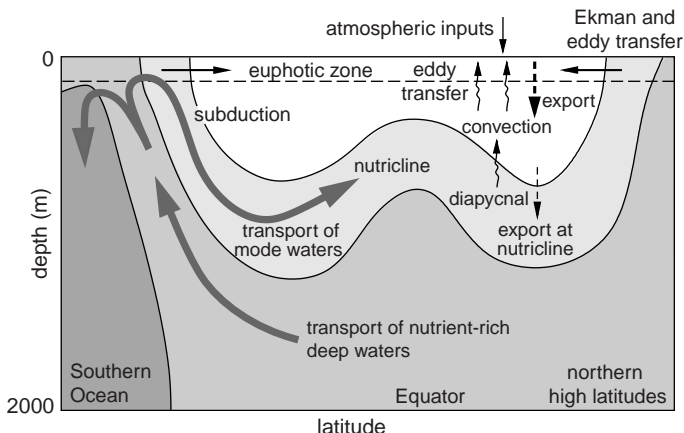


Figure 11.8 A schematic view of a meridional section with nutrient-depleted waters (white) in the subtropical gyre overlying nutrient-rich waters in the nutricline and deep waters (shaded). The export of organic matter from the euphotic zone (horizontal dashed line) reaches typically $0.5 \text{ mol N m}^{-2} \text{ y}^{-1}$, which is sustained by a combination of vertical processes involving diapycnic diffusion, convection, eddy upwelling and nitrogen fixation. There are also horizontal transfers of nutrients across the inter-gyre boundaries involving the surface Ekman and eddy flows, and boundary current flows.

as a nutrient source, the nutrient concentrations in the waters underlying the euphotic zone need to be maintained, otherwise the vertical supply of nutrients into the euphotic zone gradually weakens over time. The greater penetration of light over the clearer waters of the subtropical gyres leads to production occurring well below the mixed layer, making the nutricline deeper than the thermocline. The supply of nutrients to the upper thermocline of the subtropical gyre involves vertical exchanges with waters in the underlying nutricline and horizontal exchanges with the neighbouring subpolar gyres, the tropics and ultimately the Southern Ocean (Fig. 11.8).

11.2.1 Case study of biological export in the North Atlantic subtropical gyre

Quantifying the rate at which organic matter is exported from the euphotic zone is very difficult. The sinking flux of organic particles can be directly measured via sediment traps, although their accuracy near the surface becomes questionable due to the strong horizontal flows. Export production can also be indirectly inferred from the rate at which oxygen accumulates within the euphotic zone (but below the mixed layer) during summer, or the rate at which oxygen is utilised by the respiration of exported material below the euphotic zone.

In the Sargasso Sea, these indirect estimates suggest that export production reaches $0.47 \pm 0.12 \text{ mol N m}^{-2} \text{ y}^{-1}$; three different methods have

been applied, all remarkably consistent with each other within error bars; see Table 11.1 for references. To maintain a steady state, this export of organic matter needs to be compensated by sources of nutrients to the euphotic zone. However, the obvious nutrient sources seem to be too weak: for example, for nitrogen, atmospheric deposition only reaches $0.03 \text{ mol N m}^{-2} \text{ y}^{-1}$ and the convective supply of nitrate is about $0.13 \pm 0.05 \text{ mol N m}^{-2} \text{ y}^{-1}$. Hence, there is a shortfall, an additional $0.31 \text{ mol N m}^{-2} \text{ y}^{-1}$ is needed to sustain the estimated export production (Table 11.1).

We now consider physical processes which might enhance the supply of nutrients to the subtropical gyre, discussed first in terms of vertical transfer and then horizontal transfer. We then consider other alternative, biologically mediated sources.

Over the subtropical gyres, large-scale downwelling acts to transfer nutrients from the mixed layer to the thermocline, and inhibit biological production. This large-scale descent is partially opposed by diffusive transfers and time-dependent upwelling.

11.2.2 Diffusive transfer

Vertical transport by turbulent mixing processes, such as the breaking of internal waves, leads to a vertical nutrient flux, described by $-\kappa \partial N / \partial z$, where κ is the effective diffusivity and $\partial N / \partial z$ is the vertical gradient of nutrient. This diffusive transfer is usually associated with a transfer across density surfaces, referred to as diapycnic transfer.

Table 11.1 Geochemical estimates of export production in the Sargasso Sea and nitrogen sources, based upon McGillicuddy *et al.* (1998) and more recent updates

Export production	Method	Value (mol N m ⁻² y ⁻¹)	Reference
	O ₂ utilisation	0.48 ± 0.10	Jenkins and Wallace (1992)
		0.42 ± 0.09	Jenkins and Goldman (1985)
	O ₂ production	0.46 ± 0.09	" "
		0.39 ± 0.16	Spitzer and Jenkins (1989)
		0.51 ± 0.14	" "
	³ He flux gauge	0.56 ± 0.16	Jenkins (1988b)
Nitrogen demand	mean	0.47 ± 0.12	
Nitrogen sources	Method	Value (mol N m ⁻² y ⁻¹)	Reference
Atmospheric deposition		0.03	Knap <i>et al.</i> (1986)
Winter convection	O ₂ production	0.17 ± 0.05	Michaels <i>et al.</i> (1994)
	NO ₃ removal	0.09 ± 0.04	" "
Diapycnic diffusion	Microstructure	0.05 ± 0.01	Lewis <i>et al.</i> (1986)
	NO ₃ ⁻ and velocity	0.05 to 0.15	Dietze <i>et al.</i> (2004)
Salt fingering	Model assessment	0.03	Oschlies <i>et al.</i> (2003)
Ekman flow	Climatology	0.03 ± 0.01	Williams and Follows (1998)
Eddy upwelling	Model simulation	0.35 ± 0.10	McGillicuddy and Robinson (1997)
	Satellite data and model	0.19 ± 0.10	McGillicuddy <i>et al.</i> (1998)
	Model simulation	<0.05	Oschlies (2002)
Nitrogen fixation	N*	0.07	Gruber and Sarmiento (1997)
	Excess nitrate	0.02 to 0.08	Hansell <i>et al.</i> (2004)
Supply of DON	Model and <i>in situ</i> data	0.05 ± 0.02	Roussenov <i>et al.</i> (2006)
Nitrate supply	mean using low or high estimates of eddy upwelling	0.43 to 0.65	

In regions of strong mechanical forcing, such as in shallow shelf waters, above the shelf break or above rough topography, the effective diffusivity, κ , can exceed 10^{-4} m² s⁻¹. However, over much of the interior of the open ocean, the mechanical forcing is relatively weak and the diffusivity is much smaller; typically, reaching 10^{-5} m² s⁻¹ in the upper thermocline. The nutrient flux estimated by $-\kappa \partial N / \partial z$ is then generally too small to sustain the observed biological productivity; for example, diapycnic mixing is estimated to supply only 0.05 ± 0.01 mol N m⁻² y⁻¹ in the Sargasso Sea (Table 11.1).

11.2.3 Time-dependent upwelling

While the winds induce a large-scale downwelling over the subtropical gyre, there can be more intense vertical velocities (both downward and upward) on finer horizontal scales. One might expect that a transient vertical velocity, reversing in sign, might have a limited effect, since tracer surfaces will be both lifted up and pushed down. However, this turns out not to be the case when there is active photosynthesis. When an isopycnal surface is lifted into the euphotic zone, it can stimulate phytoplankton growth by creating conditions where there is both sufficient sunlight and

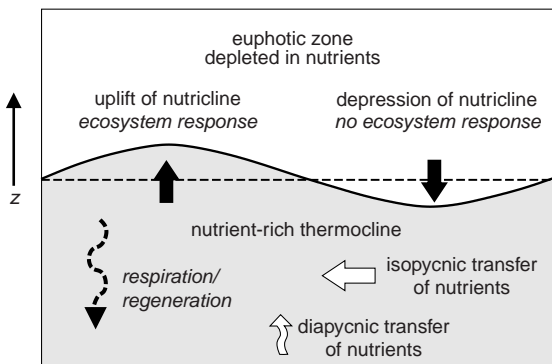
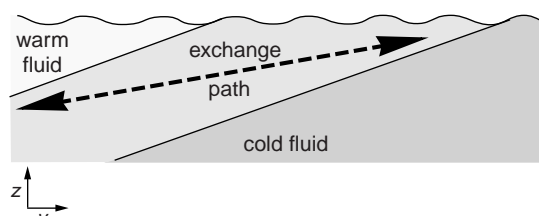


Figure 11.9 A schematic depiction of the ecosystem response to an uplift and depression of the nutricline. When nutrient-rich isopycnals are raised into the euphotic zone, there is biological production. Conversely, when the nutrient-rich isopycnals are pushed into the dark interior, there is no biological response. In order for the transient upwelling to persist, there needs to be a process maintaining the nutrient concentrations in the thermocline, which might be achieved by respiration of organic fallout and regeneration of inorganic nutrients, diapycnal transfer or a lateral influx of nutrients from the time-mean or time-varying circulations. Adapted from McGillicuddy and Robinson (1997); from Williams and Follows (2003).

nutrients (Fig. 11.9). Conversely, when the isopycnal surface is pushed down out of the euphotic zone, nutrients are not consumed as there is insufficient sunlight for photosynthesis. Thus, in principle, a rectified effect occurs where organisms exploit the upwelling phase of the reversing vertical velocity, leading to a consumption of nutrients and an additional contribution to export production.

There is a caveat to this mechanism; nutrients in the upwelled waters must be continually replenished in order for this transient upwelling to sustain phytoplankton growth over the long term. There are different views as to the importance of time-varying upwelling: several studies argue that eddy-scale upwelling can provide up to $0.35 \text{ mol N m}^{-2} \text{ y}^{-1}$ over the Sargasso Sea, sufficiently large to be the primary term sustaining export production. Other studies argue that, after an initial transient peak, the eddy upwelling provides only $0.05 \text{ mol N m}^{-2} \text{ y}^{-1}$ in the long-term average (Table 11.1). This discrepancy is mainly due to different assumptions in how rapidly nutrients are resupplied in the upper thermocline.

(a) slantwise exchange of fluid



(b) plan view of meandering jet

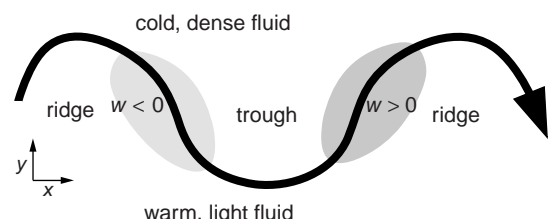


Figure 11.10 Schematic view of how eddies form through baroclinic instability: in (a), there is a slantwise exchange of fluid (dashed line) leading to a flattening of isotherms (full lines), while in (b), this slantwise exchange is achieved in a meandering jet by warm fluid rising and moving poleward (downstream between the low-pressure trough and high-pressure ridge) and cold fluid sinking and moving equatorward (downstream between the ridge and trough). Meanders may develop and form cold-core, cyclonic eddies on the warm, light flank of the jet and warm-core, anticyclonic eddies on its cold, dense flank. From Williams and Follows (2003).

The most important time-varying vertical velocities are probably associated with time-dependent mesoscale eddies, on horizontal scale of several tens of kilometres, analogous to the atmospheric weather systems, and with finer-scale frontal features on a scale of several kilometres.

Upwelling signals of eddies and fronts

Most mesoscale eddies are formed by baroclinic instability involving a slantwise exchange of cold water and warm water across a meandering jet (Fig. 11.10a,b). The shallower thermocline and nutricline seen in a cold-core, cyclonic eddy is not due to a simple vertical transfer, since cold fluid sinks and warm fluid rises in slantwise exchange. Instead, cold-core cyclones bring these characteristics with them as they move horizontally across a jet, which has a shallower thermocline and nutricline on its colder side. Likewise, warm-core anticyclones bring a deeper

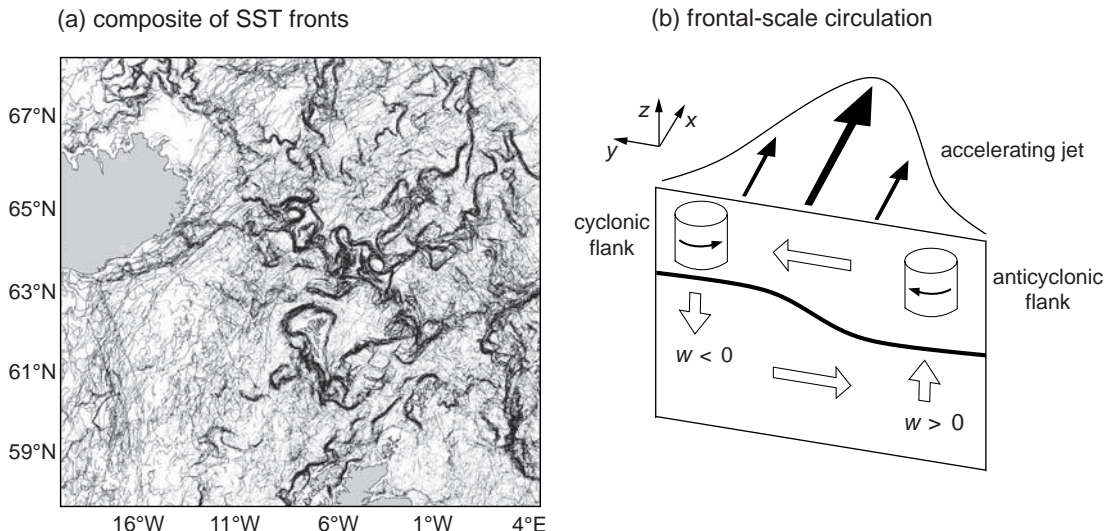


Figure 11.11 Fronts occur throughout the ocean. In (a) composite map of sea-surface temperature fronts for 14–20 April 2003, and in (b) a schematic view of frontal-scale circulations. When a jet accelerates, a secondary circulation is excited across the jet with upwelling occurring on the anticyclonic side and downwelling on the cyclonic side. Panel (a), courtesy of Peter Miller; further details, see Miller (2009). Aspects of this frontal structure were reproduced in a map, the *Carta Marina*, published in 1539, and may have been known earlier by Vikings travelling to Iceland; see historical discussion by Rossby and Miller (2003).

thermocline and nutricline as they move horizontally into a colder environment. If instead of baroclinic instability, the cyclones are generated by the interaction of the large-scale flow and topographic features, then a vertical uplift of the nutricline should provide enhanced production (Fig. 11.9). There are also eddy–eddy interactions, distortions of the nutricline as eddies come into close proximity, which might intensify features and lead to a local uplift of the nutricline.

In addition to the mesoscale eddy circulation, there are embedded frontal circulations, with horizontal scales of several kilometres to tens of kilometres. They are associated with strong horizontal contrasts in sea-surface temperature (Fig. 11.11a). Frontal-scale circulations are associated with upwelling on the anticyclonic side and downwelling on the cyclonic side of an accelerating jet (Fig. 11.11b). The opposing circulation occurs in the decelerating region. In an analogy of the eddy-scale uplifting of isopycnals and nutricline, frontal-scale upwelling can drive a rectified transfer of nutrients into the euphotic zone, sustaining productivity on a frontal scale (in accord with Fig. 11.9).

Frontal circulations appear to play an important role in idealised numerical model studies (Lèvy *et al.*, 2001). Observational support is presently rather tentative due to the intermittent nature and fine horizontal scales. Maxima in surface chlorophyll have, though, been observed on the anticyclonic side of fronts and plumes of short-lived chlorophyll have been observed penetrating into the stratified thermocline on a horizontal scale of several tens of kilometres.

In summary, time-varying upwelling by baroclinic eddies and frontal-scale circulations augment the time-mean, gyre-scale circulation in providing an additional transfer of nutrients into the euphotic zone. However, the magnitude of this contribution is not clearly constrained, and this supply is only effective as long as there is a mechanism by which nutrients are replenished in the upper thermocline.

Accordingly, we now move on to mechanisms that transfer nutrients horizontally (some of which have already been touched upon), considering their effect on both the surface nutrients and the nutrient reservoir within the upper thermocline (Fig. 11.8).

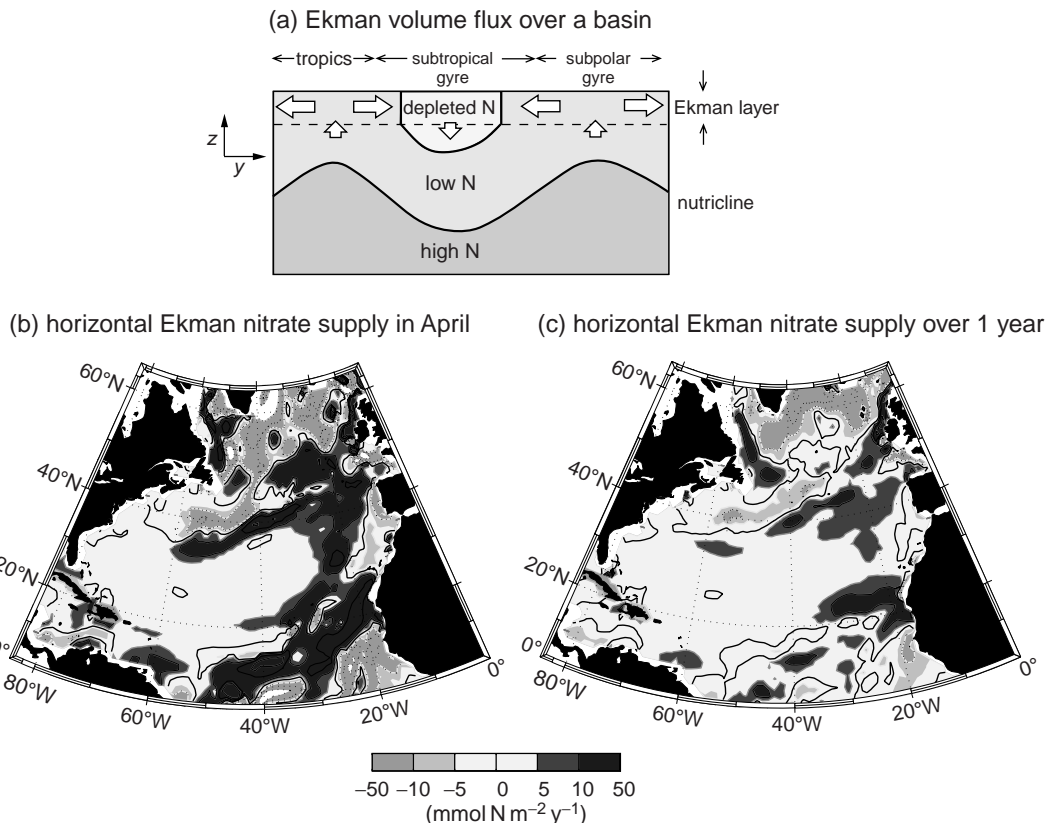


Figure 11.12 (a) A schematic view of the Ekman volume flux (white arrows) across the tropics, subtropical and subpolar gyres. The Ekman pumping in the subtropical gyre is achieved by a horizontal convergence of the horizontal Ekman flux, which also transfers nutrients. Estimates of the convergence of Ekman nitrate flux ($\text{mmol N m}^{-2} \text{y}^{-1}$) over the North Atlantic in (b) April, and (c) an annual average. Replotted from Williams and Follows (1998).

11.2.4 Horizontal transfers of nutrients into the subtropical gyre

The subtropical gyre is defined by the pattern of the overlying winds, inducing an anticyclonic circulation. At the northern and southern edges of the subtropical gyre, the time-averaged geostrophic flow is generally directed along the inter-gyre boundaries rather than across them. Any transfer between the gyres is achieved by departures from the time-averaged geostrophic flow. These cross-gyre flows include the boundary currents and separated jets (Figs. 11.3 to 11.4), surface Ekman transport and transient eddy exchanges.

Surface Ekman transfer

Downwelling over the subtropical gyre is achieved by a convergence of the horizontal Ekman vol-

ume flux. These horizontal Ekman fluxes likewise transfer nutrients into the subtropical gyre from the neighbouring nutrient-rich waters in the tropics and subpolar gyre (Fig. 11.12a). The nutrient supply associated with the Ekman flow across the inter-gyre boundaries reaches 10 to 50 $\text{mmol N m}^{-2} \text{y}^{-1}$ (Fig. 11.12b,c), strongest on the flanks of the gyre and weakest towards the centre of the gyre. This Ekman supply is much smaller than that needed to sustain local, annual productivity in the euphotic zone (Table 11.1), but it is comparable to the downward flux of organic matter across the thermocline at a few hundred metres. Hence, this lateral trickle of nutrients into the subtropical gyre is probably important in sustaining the integrated inventory of nutrients within the thermocline (Fig. 11.8).

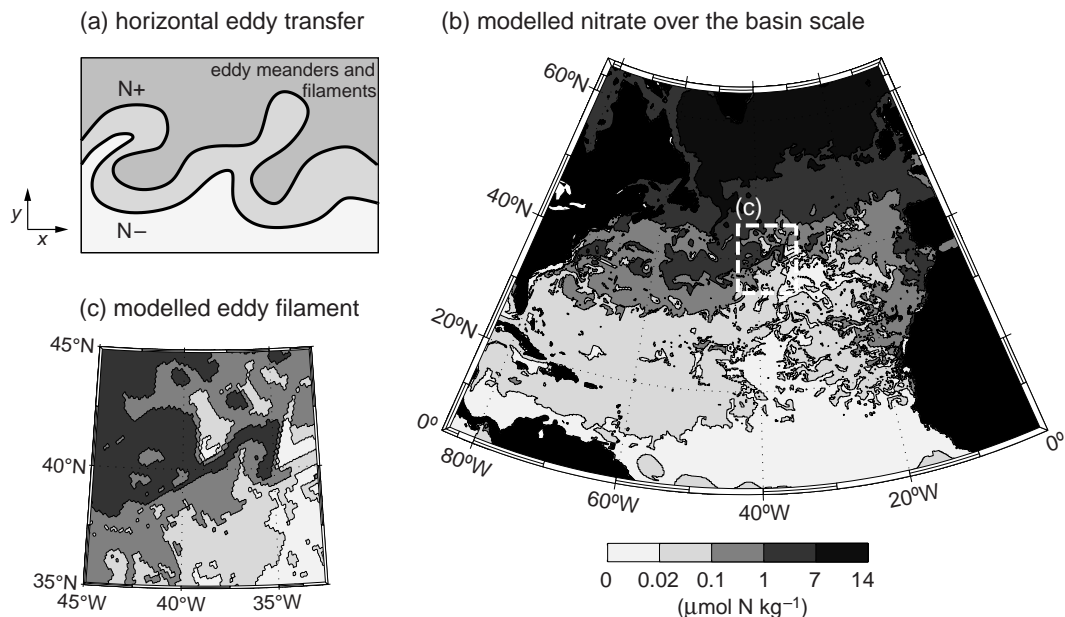


Figure 11.13 The eddy circulation transfers nitrate and other tracers, as illustrated schematically in (a), as well as revealed in the fine-scale horizontal variations in surface nitrate ($\mu\text{mol kg}^{-1}$) for model simulations (b) over the North Atlantic, and in (c) a blow-up around 40°N , 40°W . This snapshot is in the month of February in a simulation using a fine-resolution ($\sim 1/6^\circ$) configuration of the MIT ocean model. Model output provided by O. Jahn.

Surface eddy lateral transfer

Geostrophic eddies on scales of several tens of kilometres transfer properties horizontally, as well as vertically, redistributing heat, nutrients and other tracers over the ocean (Fig. 11.13a). Eddies stir tracers, drawing out filaments, which are eventually dissipated by finer-scale mixing, leading to an eddy flux of tracers, usually directed down the tracer gradient. Eddies provide an influx of nutrients into the subtropical gyre, laterally transferring nutrient-rich surface waters from the subpolar gyre and from regions of coastal upwelling (Fig. 11.13b,c).

The magnitude of this eddy transfer is difficult to quantify from observations given their transient nature and scale, but this view is supported by eddy-resolving model simulations.

11.2.5 Other nutrient sources

In addition to the physical transfer of inorganic compounds, there are other sources of nutrients to the surface oceans. Some organisms can fix dissolved nitrogen gas into organic form, relieving nitrogen limitation and providing a source of

nitrogen to the ocean. Dissolved organic forms of nutrients are also transported by the ocean circulation and may be remineralised by heterotrophs to supply inorganic forms, or utilised directly by some phytoplankton. In particular, dissolved organic phosphorus may be a significant source for primary producers in the subtropical oceans.

Nitrogen fixation

The waters of the subtropics can be extremely nutrient depleted, limiting production. Some types of cyanobacteria, referred to as diazotrophs, have exploited the niche where inorganic nitrogen is particularly limited and are able to utilise nitrogen gas to form ammonia and amino acids. There is a price for this flexibility, though: diazotrophs must produce the iron-rich enzyme nitrogenase and expend energy breaking the triple bond of nitrogen gas molecules. Thus they have a higher iron demand, relative to other elements, and slower growth rates relative to other phytoplankton. These trade-offs enable diazotrophs to flourish in nutrient-starved waters where there are sufficiently high iron

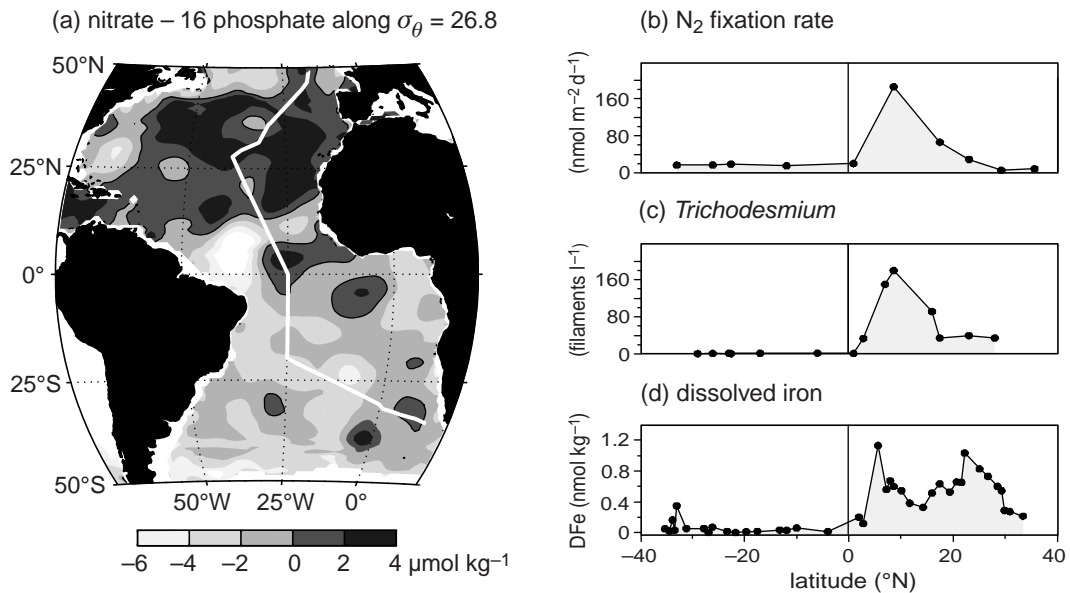


Figure 11.14 Signatures of nitrogen fixation: (a) map of excess nitrate versus phosphate on $\sigma_\theta = 26.8$, $\text{NO}_3^- - 16\text{PO}_4^{3-}$ ($\mu\text{mol kg}^{-1}$), together with transect data, for (b) total integrated water column rates of N_2 fixation rate ($\text{nmol m}^{-2} \text{d}^{-1}$), (c) surface concentration of *Trichodesmium* (filaments l^{-1}), and (d) dissolved iron concentration (nmol kg^{-1}) along the AMT-17 (marked on the map). The enhanced nitrogen fixation rates are coincident with the increase in dissolved iron concentration. The iron distribution mirrors that of aluminium, suggesting that the iron is supplied from airborne dust. Panels (b) to (d) from Moore *et al.* (2009).

sources, such as the tropical and subtropical North Atlantic. A meridional transect reveals enhanced rates of nitrogen fixation, reaching a peak of $70 \text{ mmol N m}^{-2} \text{y}^{-1}$ (converted from the daily to a maximum annual rate) and increased abundances of a key diazotroph, *Trichodesmium*, coincident with enhanced surface concentrations in dissolved iron (Fig. 11.14). The iron supply is significantly enhanced here by atmospheric dust deposition, as indicated by the associated, elevated concentrations of aluminium.

A consequence of production sustained by nitrogen fixation is that the resulting organic matter has a higher than normal proportion of nitrogen relative to phosphorus. The subsequent export and remineralisation of this organic matter increases the concentration of nitrate relative to phosphate in thermocline waters. A signal of elevated nitrate to phosphate concentrations extends over much of the North Atlantic, indicated by excess nitrate, $\text{DIN}_{xs} = \text{NO}_3^- - 16\text{PO}_4^{3-}$, with values greater than $2.5 \mu\text{mol kg}^{-1}$ in the upper thermocline, as illustrated in Fig. 11.14a.

The contribution of nitrogen fixation to the maintenance of productivity in the subtropical gyres is still uncertain with direct measurements over a year ranging from 0.02 to $0.08 \text{ mol N m}^{-2} \text{y}^{-1}$ (Mahaffey *et al.*, 2005). While nitrogen fixation plays a role in closing the nitrogen budget of the subtropical North Atlantic, it demands a corresponding supply of phosphorus, which has no analogous source.

Dissolved organic nutrients

Over much of the ocean, the dissolved inorganic pools of nitrogen and phosphorus are much greater in concentration than the dissolved organic pools of nitrogen (DON) and phosphorus (DOP). However, in the surface waters of the subtropical gyres, where biological consumption draws down the concentrations of inorganic nutrients, surface concentrations of DON and DOP significantly exceed those of nitrate and phosphate, as seen over the North Atlantic in Fig. 11.15a,b.

Dissolved organic matter (DOM) represents a spectrum of molecules with different properties. A fraction of the dissolved organic matter can be

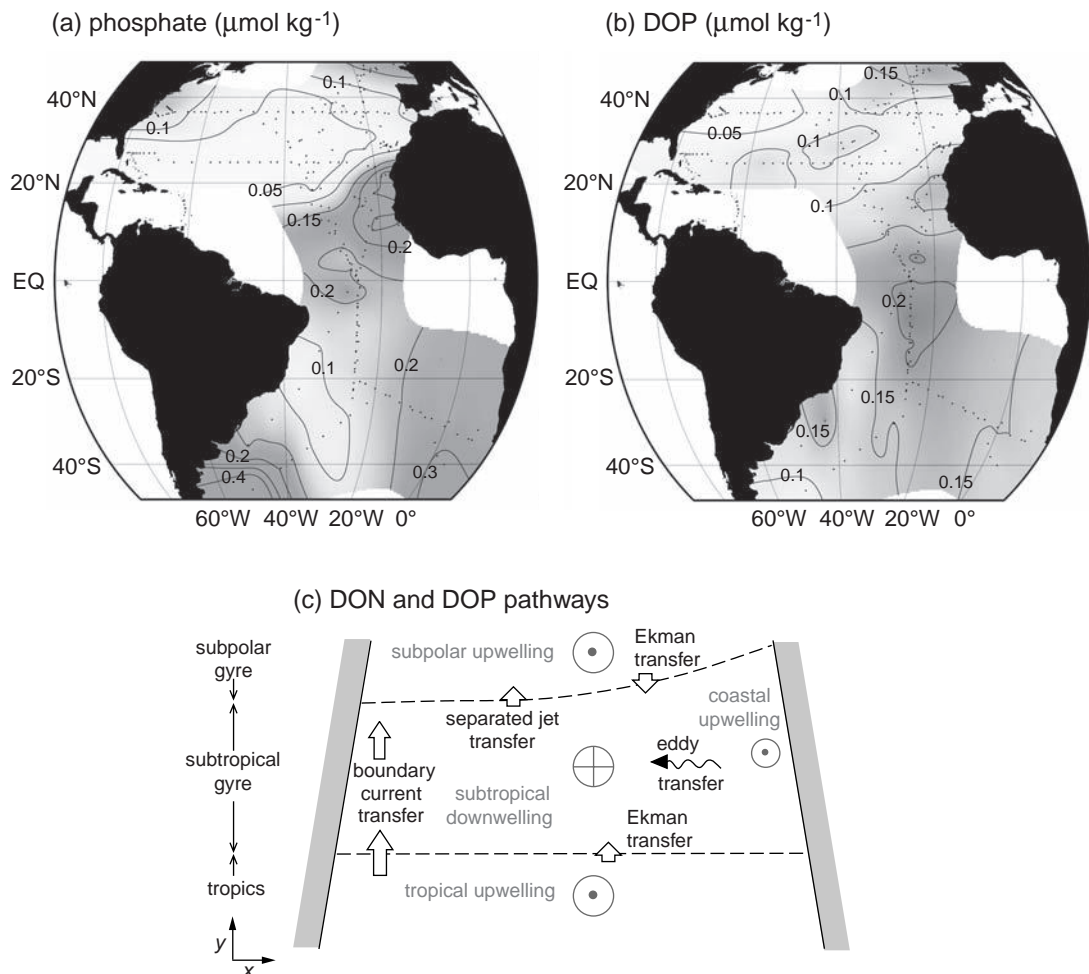


Figure 11.15 Composite maps of (a) phosphate ($\mu\text{mol kg}^{-1}$), and (b) DOP ($\mu\text{mol kg}^{-1}$), over the upper 100 m (original data marked by dots). In (c), a schematic figure denoting pathways for DON and DOP, which are preferentially produced in productive upwelling zones, then transferred by the flow over the basin, involving gyre circulation, Ekman, eddy and boundary flows. Panels (a) and (b) from Sinhue Torres-Valdes; see Torres-Valdes *et al.* (2009) for further details.

utilised by bacteria on relatively short timescales of up to a few days or months; typically referred to as labile and semi-labile DOM respectively. Other components are not so easily utilised and are referred to as refractory. A larger fraction of the DON is refractory, perhaps originating from structural proteins, while DOP is generally more labile, originally associated with genetic material or lipids in the cell. DOM, by definition, is the fraction of organic detritus which is transported by the circulation, convection and mixing, and does not sink gravitationally. The transport and remineralisation, or utilisation, of the semi-labile components of DON and DOP are potentially

important for the maintenance of productivity in oligotrophic regimes which are bounded by productive regions.

DON and DOP are formed in productive upwelling zones in the tropics or by the coast and transferred by the circulation of the subtropical gyre (Fig. 11.15c); as illustrated in the case of boundary currents and separated jets in Fig. 11.4b. The gradients of DON in the subtropical gyres suggest that its transport and recycling might provide an additional nitrogen source of up to $0.05 \text{ mol N m}^{-2} \text{ y}^{-1}$ in the subtropical North Atlantic; a relatively small contribution to annual production in terms of nitrogen. In contrast, the

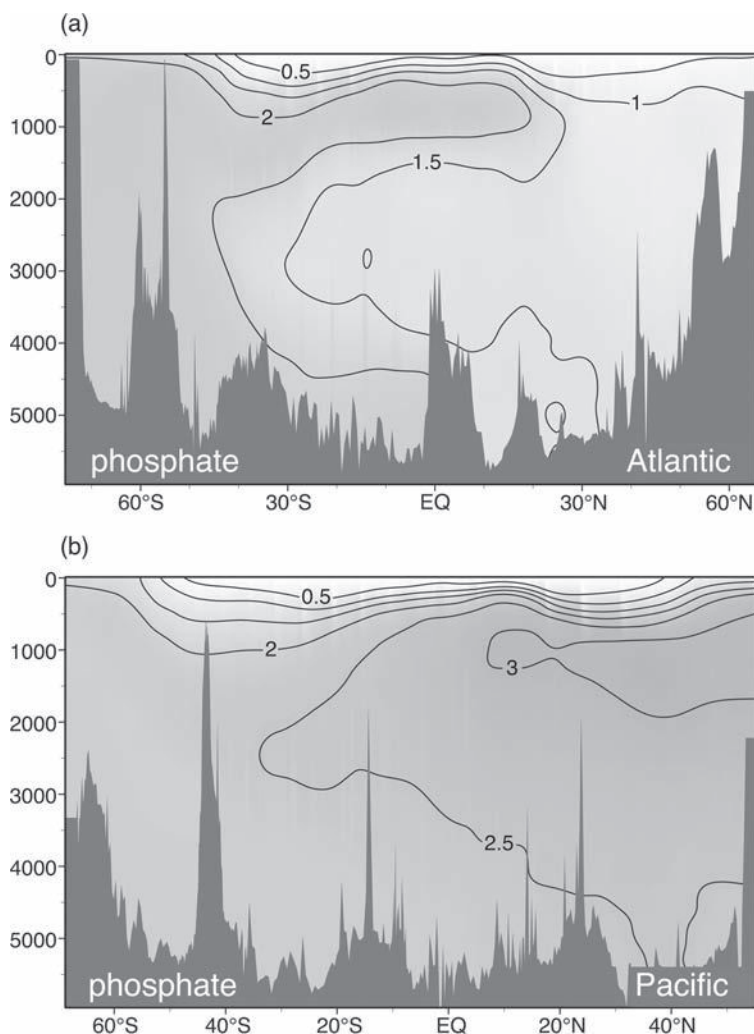


Figure 11.16 Observed meridional sections of phosphate, PO_4^{3-} ($\mu\text{mol kg}^{-1}$) in (a) the Atlantic along 20°W , and (b) the Pacific along 170°W ; see Plates 6b and 7b.

transport and cycling of DOP is probably more important for the phosphorus budget since DOP is more reactive and there is no equivalent of nitrogen fixation. Numerical model studies suggest that as much as half of the biological export of phosphorus in the region might be sustained by recycling of DOP (Roussenov *et al.*, 2006).

In summary, production over the subtropical gyres is sustained by a range of physically and biologically mediated processes which provide the necessary nitrogen, phosphorus and trace metals. There is still considerable debate as to the relative importance of the different sources for the whole gyre, possibly reflecting uncertainties in the estimates, but also their real spatial variations. For example, eddy transfers are likely to be important near the intense boundary currents where

there are strongly sloping density surfaces, nitrogen fixation is locally significant where there is atmospheric dust deposition and the transport of dissolved organic matter might be important near tropical and coastal upwelling sites.

11.3 What sets the nutrient distributions in the ocean interior?

We now consider how macro-nutrients are returned to the dark interior of the ocean by both transport and the export and respiration of organic detritus, setting the basin-scale distributions illustrated in Fig. 11.16.

Some of the nutrients in the euphotic layer are subducted back into deeper waters in inorganic form, without being consumed by living organisms or having been consumed and quickly regenerated. The remaining nutrient transfer is in organic form, either as gravitationally sinking particles or subducted dissolved organic matter. Almost all of the exported organic matter is returned to inorganic form by respiration before arriving at the sea floor. In the following sections, we set out a framework for mapping and interpreting the contributions of subduction and biological export to the ocean's nutrient and carbon reservoirs.

11.3.1 Preformed and regenerated nutrients

The concentration of an inorganic nutrient, such as phosphate PO_4^{3-} , below the euphotic layer may be separated into two components (Redfield *et al.*, 1963):

$$\text{PO}_4^{3-} = \text{PO}_4^{\text{pre}} + \text{PO}_4^{\text{reg}}, \quad (11.2)$$

the preformed contribution, PO_4^{pre} , that which the water parcel had at the time of subduction, and the regenerated contribution, PO_4^{reg} , the result of the accumulated regeneration from organic matter in the water parcel since the time of subduction, as depicted in Fig. 11.17. Nutrient utilisation, \mathcal{P}^* , is defined as the relative magnitude of the regenerated and total phosphate concentrations in a water parcel below the mixed layer and euphotic zone (Ito and Follows, 2005),

$$\mathcal{P}^* = \frac{\text{PO}_4^{\text{reg}}}{\text{PO}_4^{3-}}. \quad (11.3)$$

The limit $\mathcal{P}^* = 0$ indicates that all of the phosphate in the water parcel was present at the time of subduction, while the limit $\mathcal{P}^* = 1$ indicates that all of the phosphate in the water parcel is due to the respiration of organic detritus.

11.3.2 Estimating the regenerated contribution using oxygen observations

The regeneration of inorganic nutrients is accompanied by the consumption of dissolved oxygen through respiration. The dissolved oxygen concen-

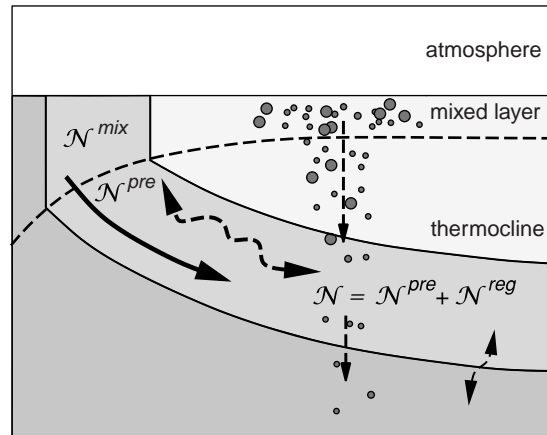


Figure 11.17 A schematic view of the nutrient distribution in an ocean section. Below the mixed layer, the concentration of a generic nutrient tracer, \mathcal{N} , is defined to be the sum of preformed and regenerated contributions: the preformed concentration is the nutrient concentration at the time of subduction, while the regenerated concentration is the subsequent accumulation of inorganic nutrient regenerated through the respiration of organic detritus.

tration may also be separated into a preformed and a regenerated component (which will have a negative value),

$$\text{O}_2 = \text{O}_2^{\text{pre}} + \text{O}_2^{\text{reg}}. \quad (11.4)$$

In the surface ocean, oxygen is observed to be very close to its saturated concentration due to the relatively short air-sea equilibration timescale, so we assume that

$$\text{O}_2^{\text{pre}} \approx \text{O}_2^{\text{sat}}(T, S). \quad (11.5)$$

Since the mixing ratio of oxygen in the atmosphere is effectively unchanging, the saturation concentration may be described simply in terms of its solubility, varying as a function of temperature, and salinity (Garcia and Gordon, 1992). Potential temperature, θ , and salinity are conserved below the surface mixed layer so, for an isolated water parcel, their interior values are the same as their surface values at the time of subduction. Assuming fixed elemental ratios, the oxygen consumed in respiration, O_2^{reg} , is related to the regenerated phosphate by

$$\text{O}_2^{\text{reg}} = R_{\text{OP}} \text{PO}_4^{\text{reg}}. \quad (11.6)$$

Using Redfield ratios, $\text{C:N:P:O}_2 = 106 : 16 : 1 : -170$ (Takahashi *et al.*, 1985), the ratio of oxygen

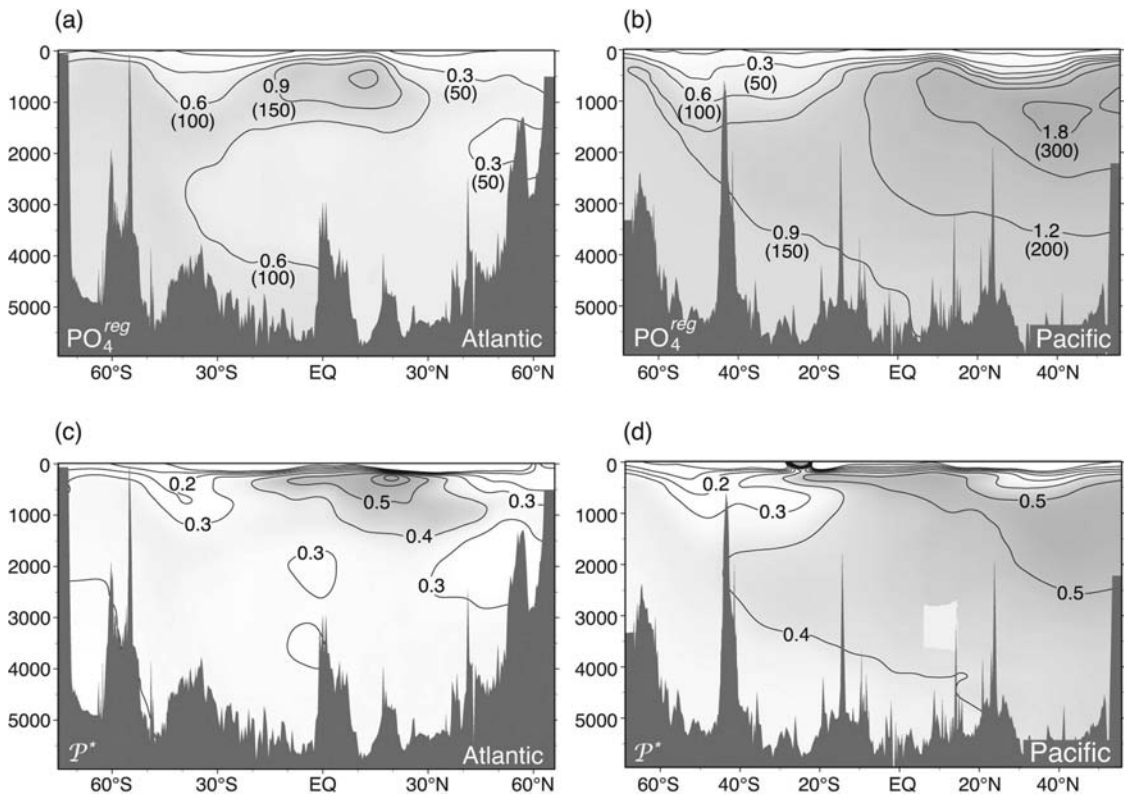


Figure 11.18 Meridional sections of regenerated biological phosphate, $\text{PO}_4^{\text{reg}} = -\text{AOU}/R_{\text{OP}}$, ($\mu\text{mol kg}^{-1}$) in (a) and (b), diagnosed from apparent oxygen utilisation, AOU (magnitude of AOU in brackets, $\mu\text{mol kg}^{-1}$) assuming $R_{\text{OP}} = -170$; and local nutrient utilisation, $\mathcal{P}^* = \text{PO}_4^{\text{reg}}/\text{PO}_4^{3-}$, in (c) and (d) for the Atlantic and Pacific.

consumption to phosphate regeneration, R_{OP} , is taken to be -170 . Combining (11.4) to (11.6), allows the regenerated phosphate concentration to be expressed in terms of measured properties (O_2 , θ and S),

$$\text{PO}_4^{\text{reg}} \simeq \frac{(\text{O}_2 - \text{O}_2^{\text{sat}}(\theta, S))}{R_{\text{OP}}} = \frac{-\text{AOU}}{R_{\text{OP}}}, \quad (11.7)$$

where Apparent Oxygen Utilisation, AOU, is defined as the difference between the saturated and measured oxygen concentrations,

$$\text{AOU} \equiv \text{O}_2^{\text{sat}}(\theta, S) - \text{O}_2. \quad (11.8)$$

The efficiency of nutrient utilisation, \mathcal{P}^* is likewise diagnosed as

$$\mathcal{P}^* = \frac{\text{PO}_4^{\text{reg}}}{\text{PO}_4^{3-}} \simeq \frac{-\text{AOU}}{R_{\text{OP}}\text{PO}_4^{3-}}. \quad (11.9)$$

We now consider diagnostics of PO_4^{reg} and \mathcal{P}^* over the Atlantic and Pacific, while accepting there are

some significant uncertainties; deep waters are probably undersaturated in oxygen at the time of subduction (Körtzinger *et al.*, 2004) causing \mathcal{P}^* to be over-estimated by as much as 0.2 in some dense water masses (Ito *et al.*, 2004).

11.3.3 Nutrient utilisation in the Atlantic and Pacific basins

The regenerated phosphate, PO_4^{reg} , distributions of the Atlantic and Pacific contrast strongly, as depicted in Fig. 11.18a,b. In the Atlantic basin, the regenerated phosphate, PO_4^{reg} , ranging in value between 0.3 to $0.9 \mu\text{mol P kg}^{-1}$, broadly resembles the distribution of water masses. There is elevated PO_4^{reg} in the intermediate and bottom waters originating from the Southern Ocean, and lower PO_4^{reg} in the deep waters of the North Atlantic, mimicking the interleaving of fresh and salty waters, respectively. PO_4^{reg} is particularly elevated over the upper few hundred metres in the

Box 11.1 | Nutrient utilisation

The regenerated nutrients in the deep ocean are controlled by the efficiency of *nutrient utilisation* in the euphotic layer: the fraction of upwelled nutrients that is returned to depth in organic form (Francois et al., 1992; Ito and Follows, 2005). This balance is illustrated in a simple model, where w is a vertical exchange velocity (m s^{-1}) and E is the biological export ($\text{mol N m}^{-3} \text{s}^{-1}$).

The nutrient concentration in the deep ocean is the sum of preformed and regenerated contributions, $\{\mathcal{N}\} = \{\mathcal{N}^{\text{pre}}\} + \{\mathcal{N}^{\text{reg}}\}$. The rate of change of surface nutrient concentration, $\{\mathcal{N}^{\text{pre}}\}$ (mol N m^{-3}) is determined by the balance between the physical nutrient supply, from upwelling of nutrient-rich deep waters minus the subduction of surface waters, and the biological consumption and export, E ,

$$hA \frac{d\{\mathcal{N}^{\text{pre}}\}}{dt} = Aw(\{\mathcal{N}\} - \{\mathcal{N}^{\text{pre}}\}) - hAE, \quad (11.10)$$

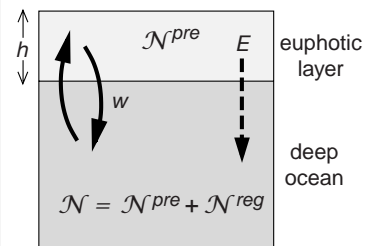
where A is the surface area (m^2) and h the thickness of the euphotic layer (m). Assuming a steady state, $d/dt = 0$, (11.10) can be manipulated to provide equilibrium solutions for the regenerated nutrient,

$$\{\mathcal{N}^{\text{reg}}\} = \frac{Eh}{w}, \quad (11.11)$$

and the extent of nutrient utilisation,

$$\mathcal{P}^* = \frac{\mathcal{N}^{\text{reg}}}{\mathcal{N}} = \frac{Eh}{w\{\mathcal{N}\}}. \quad (11.12)$$

The efficiency of nutrient utilisation is thus set by the competition between the biologically driven downward flux of phosphorus Eh , versus the physical supply of nutrients to the surface, $w\{\mathcal{N}\}$ (both $\text{mol m}^{-2} \text{s}^{-1}$). The regenerated store of phosphate (and carbon) in the ocean interior is proportional to the nutrient utilisation, \mathcal{P}^* .



tropics, enhanced due to high tropical productivity and regeneration from sinking organic particles. The relatively weak signature of PO_4^{reg} in the deep waters of the North Atlantic, and the dominance of transport-related water mass patterns, reflects the relatively young age and rapid ventilation of these waters. In addition, regenerated phosphate accumulates relatively slowly at depth because most of the exported organic matter is respired higher in the water column.

In contrast, in the Pacific basin, PO_4^{reg} is much larger, varying from 0.9 to 1.8 $\mu\text{mol P kg}^{-1}$, in the deep and mid-depth waters, (Fig. 11.18b), and there is a greater vertical contrast than seen in salinity. The deep waters of the Pacific are filled by the northward transport, upwelling and mixing of bottom waters originating in Antarctica. During

this slow transit, the waters acquire PO_4^{reg} from the regeneration of exported organic matter. The 'oldest' waters in the ocean, those which have spent the longest time since last at the surface, are at the mid depths in the North Pacific, coincident with the highest values of PO_4^{reg} .

The higher values of PO_4^{reg} in the deep Pacific compared with the Southern Ocean or Atlantic are consistent with less vigorous physical exchanges of nutrients (see Box 11.1 for a simple model description).

The efficiency of nutrient utilisation, \mathcal{P}^* , typically reaches 0.3 over the Atlantic basin, only enhanced to 0.5 in the tropical thermocline, but is generally larger over the Pacific basin, ranging from 0.4 to 0.5 (Fig. 11.18c,d). Hence, nutrient utilisation, \mathcal{P}^* , averaged over the globe is less than

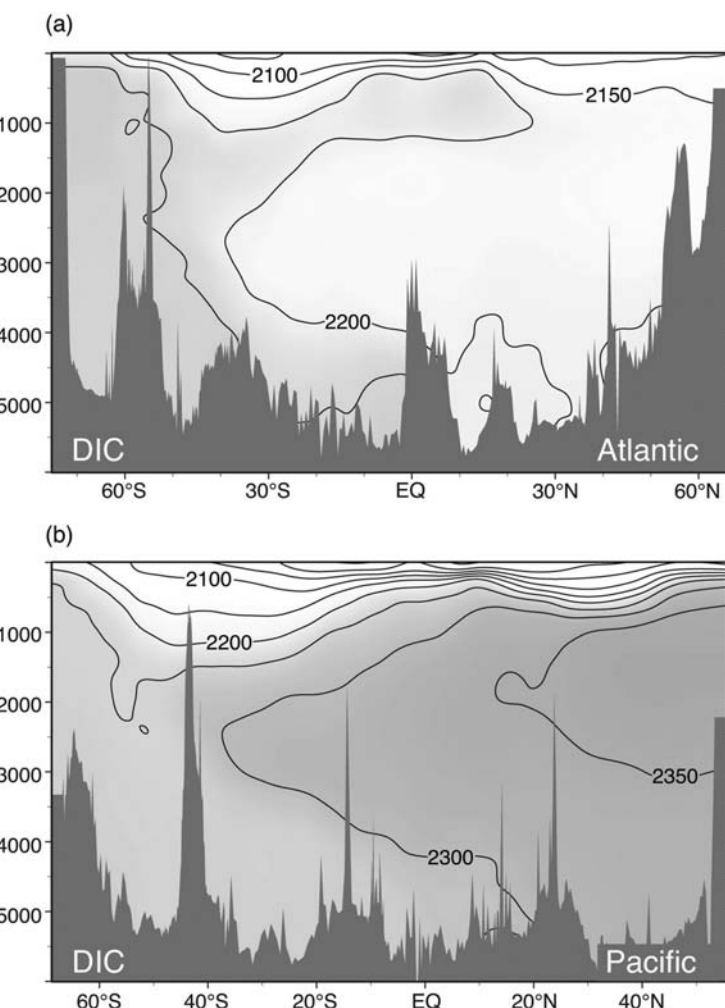


Figure 11.19 Observed meridional sections of dissolved inorganic carbon DIC ($\mu\text{mol kg}^{-1}$) in (a) the Atlantic along 20°W , and (b) the Pacific along 170°W ; see Plates 6a and 7a. Data from Key *et al.* (2004).

0.5, so the efficiency with which living organisms are consuming and exporting available phosphorus is less than 50% of its full potential. If each mole of exported organic phosphorus brings with it about 106 moles of organic carbon (the Redfield ratio), there is a corresponding store of carbon in the deep ocean, proportional to PO_4^{reg} . Apparently this store of carbon is less than half of its possible upper limit. If the efficiency of nutrient utilisation were to increase, the biological storage of carbon in the deep ocean could be enhanced, as it might have been in other periods of Earth's history. How large is this biologically mediated reservoir of carbon in the ocean and how does it relate to other reservoirs of carbon in the ocean? These questions are addressed in the next section.

11.4 Quantifying the ocean's carbon reservoirs

The observed distribution of DIC reveals a background concentration of about $2200 \mu\text{mol kg}^{-1}$ with variations on the order of $\pm 10\%$. The Atlantic basin has lower concentrations than the Pacific, and DIC decreases towards the surface, as depicted in Fig. 11.19. What are the relative contributions of solubility and biologically mediated processes that set these patterns? To answer this question, we extend the preformed and regenerated framework to the carbon system (Fig. 11.17), broadly following the approach taken by Brewer (1978), Chen and Millero (1979) and Gruber *et al.* (1996).

11.4.1 Surface ocean

In the surface mixed layer, there is active exchange of dissolved gases with the atmosphere, so that the dissolved inorganic carbon, DIC, may be separated into the sum of two components: C^{sat} , the concentration the water parcel would have at equilibrium with the partial pressure of carbon dioxide in the overlying atmosphere, and ΔC , the remaining *disequilibrium* contribution,

$$DIC = C^{sat} + \Delta C. \quad (11.13)$$

The saturated contribution, $C^{sat}(pCO_2^{at}, \theta, S, A_T)$, in the surface ocean may be evaluated from the water parcel's potential temperature, salinity, alkalinity, and partial pressure of CO₂ in the atmosphere (see Section 6.6.4). The magnitude of ΔC reflects the effect of physical, biological and chemical processes which continually drive the surface waters away from local equilibrium, in competition with the damping effect of air-sea gas exchange. ΔC , the disequilibrium of carbon, is significant due to the slow equilibration timescale, about one year (whereas the disequilibrium of oxygen is usually neglected due to the faster equilibration timescale of a few weeks, see Section 6.6.5).

11.4.2 Subsurface ocean

Below the surface mixed layer, DIC may again be separated into two contributions: the preformed carbon C^{pre} , the DIC that the water parcel had at the time of subduction, and the regenerated carbon, C^{reg} , accumulated since subduction due to biologically mediated processes:

$$DIC = C^{pre} + C^{reg}. \quad (11.14)$$

Preformed carbon

Preformed carbon, C^{pre} may be further separated into saturation and disequilibrium components of the mixed layer at the time of subduction, following (11.13),

$$C^{pre} = C^{sat} + \Delta C. \quad (11.15)$$

$C^{sat}(pCO_2, \theta, S, A_T^{pre})$ may be evaluated for a water parcel in the interior of the ocean: using the local potential temperature θ and S , since they are assumed to be conserved in the interior; and the preformed alkalinity, A_T^{pre} , estimated from S

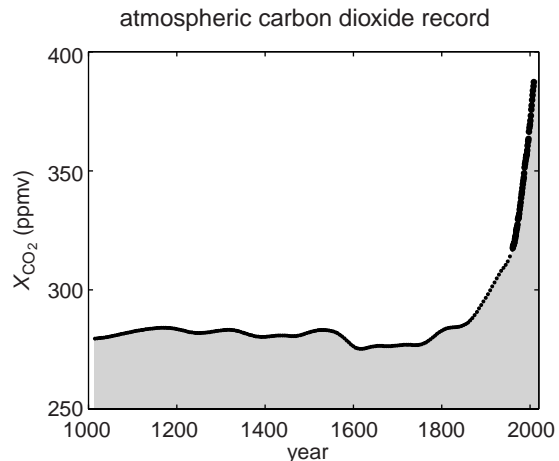


Figure 11.20 Mixing ratio of atmospheric carbon dioxide, X_{CO_2} (ppmv) over the past millennium from ice-core measurements from Law Dome, Antarctica (data from Etheridge et al., 1998) and direct observations at Mauna Loa, Hawaii since 1958 (Keeling et al., 1976; data from Dr. Pieter Tans, NOAA/ESRL). The ice-core record, pre-1958, was derived from a spline fit with a 75-year cut-off. Annual averages are displayed for the post-1958 Mauna Loa record.

taking advantage of the tight linear relationship between the two variables in the surface ocean. The reference pCO_2^{at} , related to the mixing ratio X_{CO_2} , needs to be chosen in order to estimate the equilibrium C^{sat} .

While atmospheric pCO₂ exhibits only small variations with latitude and season, anthropogenic emissions have led to an extremely rapid rise in X_{CO_2} relative to the preceding millennium, as illustrated in Fig. 11.20. During the pre-industrial period, the atmospheric mixing ratio of CO₂ was very stable, with a time-mean surface value of 278 ppmv evaluated from air-bubbles trapped in Antarctic and Arctic ice sheets (Fig. 11.20). Assuming that during the millennia preceding the industrial revolution, the whole ocean approached equilibrium with the stable pCO_2^{at} , then C^{sat} may be separated into C_{pre}^{sat} , the saturation concentration for the pre-industrial era (where $X_{CO_2} = 278$ ppmv) and C_{ant}^{sat} representing the anthropogenic contribution due to the increase in pCO_2^{at} since the 1750s.

$$C^{sat} = C_{pre}^{sat} + C_{ant}^{sat}. \quad (11.16)$$

C_{pre}^{sat} may be evaluated in the modern ocean using measured θ and S , along with estimated A_T^{pre}

Box 11.2 | Regenerated alkalinity

The regenerated alkalinity A_T^{reg} may be related to contributions from the dissolution of calcium carbonate and the respiration of organic matter to nitrate. Start with the definition of alkalinity as the sum of charge concentration associated with conservative ions,

$$\begin{aligned} A_T = & [\text{Na}^+] + 2[\text{Mg}^{2+}] + 2[\text{Ca}^{2+}] + \dots - [\text{Cl}^-] - 2[\text{SO}_4^{2-}] - [\text{Br}^-] \\ & - [\text{F}^-] - [\text{NO}_3^-] - \dots \end{aligned} \quad (11.17)$$

Calcium carbonate dissolution and the respiration of organic matter alters $[\text{Ca}^{2+}]$ and $[\text{NO}_3^-]$, while all other concentrations remain constant, so that the changes in alkalinity may be described as

$$\delta A_T = 2\delta[\text{Ca}^{2+}] - \delta[\text{NO}_3^-], \quad (11.18)$$

so the regenerated alkalinity, A_T^{reg} , may be diagnosed from δA_T . Each mole of calcium released from dissolving calcium carbonate is accompanied by a mole of carbon released into the dissolved inorganic pool, so $C^{\text{carb}} = \delta[\text{Ca}^{2+}]$. Assuming fixed Redfield ratios, for each mole of oxygen consumed in the respiration of organic matter, $R_{\text{NO}} = -16/170$ moles of nitrate are regenerated, so $\delta[\text{NO}_3^-] = -R_{\text{NO}} \text{AOU}$, and then the regenerated alkalinity may be expressed in terms of C^{carb} as

$$A_T^{\text{reg}} = 2C^{\text{carb}} + R_{\text{NO}} \text{AOU}. \quad (11.19)$$

and X_{CO_2} , assuming that temperature, salinity and alkalinity have not significantly changed since the pre-industrial era.

Regenerated carbon

The regenerated carbon, C^{reg} , may be further separated into contributions due to the respiration of organic matter, C^{soft} (often termed the *soft-tissue pump*), and the dissolution of calcium carbonate, C^{carb} (the *carbonate pump*),

$$C^{\text{reg}} = C^{\text{soft}} + C^{\text{carb}}. \quad (11.20)$$

Assuming fixed elemental ratios in biologically mediated transformations between inorganic and organic forms, the *soft-tissue contribution*, C^{soft} , is simply related to the regenerated phosphate, PO_4^{reg} , by $C^{\text{soft}} = R_{\text{CP}} \text{PO}_4^{\text{reg}}$ and evaluated from AOU ,

$$C^{\text{soft}} = -R_{\text{CO}} \text{AOU}, \quad (11.21)$$

where $R_{\text{CO}} = -106/170$.

The *carbonate contribution*, C^{carb} , may be estimated from the change in alkalinity, A_T , which

is also separated into preformed and regenerated components:

$$A_T = A_T^{\text{pre}} + A_T^{\text{reg}}. \quad (11.22)$$

A_T^{pre} , the alkalinity that the water parcel had when last in the mixed layer, may be estimated from the measured salinity since it has a relatively tight, linear relationship to A_T in the surface ocean (Section 6.3). Regenerated alkalinity, A_T^{reg} , is related to C^{carb} , the source of carbonate ions from the dissolution of CaCO_3 , and AOU due to the regeneration of nitrate from organic matter (see Box 11.2). Combining (11.19) and (11.22), the carbonate pump, C^{carb} , is then defined by the change in alkalinity due to the production of calcium ions since subduction and any changes associated with the regeneration of nitrate,

$$C^{\text{carb}} = \frac{1}{2} (A_T - A_T^{\text{pre}} - R_{\text{NO}} \text{AOU}), \quad (11.23)$$

where $R_{\text{NO}} = -16/170$. C^{carb} can then be evaluated from the measured properties of a water parcel

and the empirical relationship between surface salinity and alkalinity.

11.4.3 Mapping the carbon reservoirs of the ocean

DIC is thus described as the sum of the saturation, soft-tissue, carbonate and disequilibrium components:

$$\text{DIC} = C_{\text{pre}}^{\text{sat}} + C^{\text{soft}} + C^{\text{carb}} + C_{\text{ant}}^{\text{sat}} + \Delta C. \quad (11.24)$$

Both ΔC and $C_{\text{ant}}^{\text{sat}}$ are very difficult to evaluate from observations. Here we simply combine the two components into a ‘residual’ reservoir, $C^{\text{res}} = \Delta C + C_{\text{ant}}^{\text{sat}}$. The subsurface DIC concentration, DIC, is then defined as the sum of four contributions,

$$\text{DIC} = C_{\text{pre}}^{\text{sat}} + C^{\text{soft}} + C^{\text{carb}} + C^{\text{res}}. \quad (11.25)$$

Here we evaluate the components C^{sat} , C^{soft} and C^{carb} using measurements of DIC, together with concurrent observations of salinity, temperature, alkalinity and oxygen, as described above. Then C^{res} is inferred as the residual, subtracting the sum of $C_{\text{pre}}^{\text{sat}}$, C^{soft} and C^{carb} from DIC.

Again, there are several sources of uncertainty. Firstly, the assumption of fixed elemental ratios in all transformations to and from organic matter. Secondly, seawater samples represent a mixture of contributions which have multiple origins and different pathways through the ocean. If the solubility of a gas is not a strictly linear function of temperature and salinity, an error is introduced by inferring saturation from local θ and S . Thirdly, it is assumed that water parcels were at equilibrium with respect to oxygen at the time of subduction, but oxygen disequilibrium in subducted dense waters may lead to errors of up to $40 \mu\text{mol kg}^{-1}$ in the corresponding C^{soft} (Ito *et al.*, 2004). Accepting these caveats, we can gain some insight into the ocean’s carbon reservoirs from this framework.

11.4.4 How are the carbon reservoirs distributed in the ocean?

The components of ocean DIC are diagnosed from observations along sections through the Atlantic and Pacific Oceans and displayed in Figs. 11.21 and 11.22.

Saturated DIC contribution

The saturated contribution referenced to the pre-industrial atmosphere, $C_{\text{pre}}^{\text{sat}}$, accounts for about 90% of DIC over the globe, typically exceeding $2000 \mu\text{mol kg}^{-1}$ (Figs. 11.21a and 11.22a). Cooler, denser waters have a higher saturation DIC and there is a strong decrease in $C_{\text{pre}}^{\text{sat}}$ towards the surface in the thermocline. While surface $C_{\text{pre}}^{\text{sat}}$ is modulated by both temperature and alkalinity, the increase in $C_{\text{pre}}^{\text{sat}}$ with depth indicates that temperature is the dominant control. There is very little contrast between the Atlantic and Pacific basins and the deep and bottom waters have nearly uniform values. This enhancement of C^{sat} with depth in the ocean is often referred to as the *solubility pump*.

Soft-tissue contribution

The soft-tissue pump, C^{soft} , is the second largest contribution, ranging between 50 and $100 \mu\text{mol kg}^{-1}$ over most of the Atlantic and Southern Oceans, reaching $150 \mu\text{mol kg}^{-1}$ in the tropical Atlantic thermocline, and greater than $100 \mu\text{mol kg}^{-1}$ over most of the Pacific, reaching $200 \mu\text{mol kg}^{-1}$ in the northern basin (Figs. 11.21b and 11.22b). While C^{sat} accounts for the largest fraction of DIC globally, C^{soft} contributes much of the large-scale structure in the distribution (Fig. 11.19).

C^{soft} is proportional to the regenerated phosphate, PO_4^{reg} (Fig. 11.18), with the lowest values at mid depths in the Atlantic where there are recently ventilated waters and low regeneration rates below the thermocline. The older waters of the Pacific have the largest accumulation of C^{soft} from the carbon regenerated from sinking organic particles. Other than a sharp, near-surface gradient, the waters around Antarctica are relatively homogeneous with respect to C^{soft} , reflecting the relatively rapid communication by the Antarctic Circumpolar Current around the Southern Ocean.

Carbonate contribution

C^{carb} measures the direct contribution of the formation and dissolution of sinking calcium carbonate particles to the distribution of DIC. C^{carb} is relatively small in the Atlantic, only reaching $20 \mu\text{mol kg}^{-1}$ in the Southern Ocean, but increases

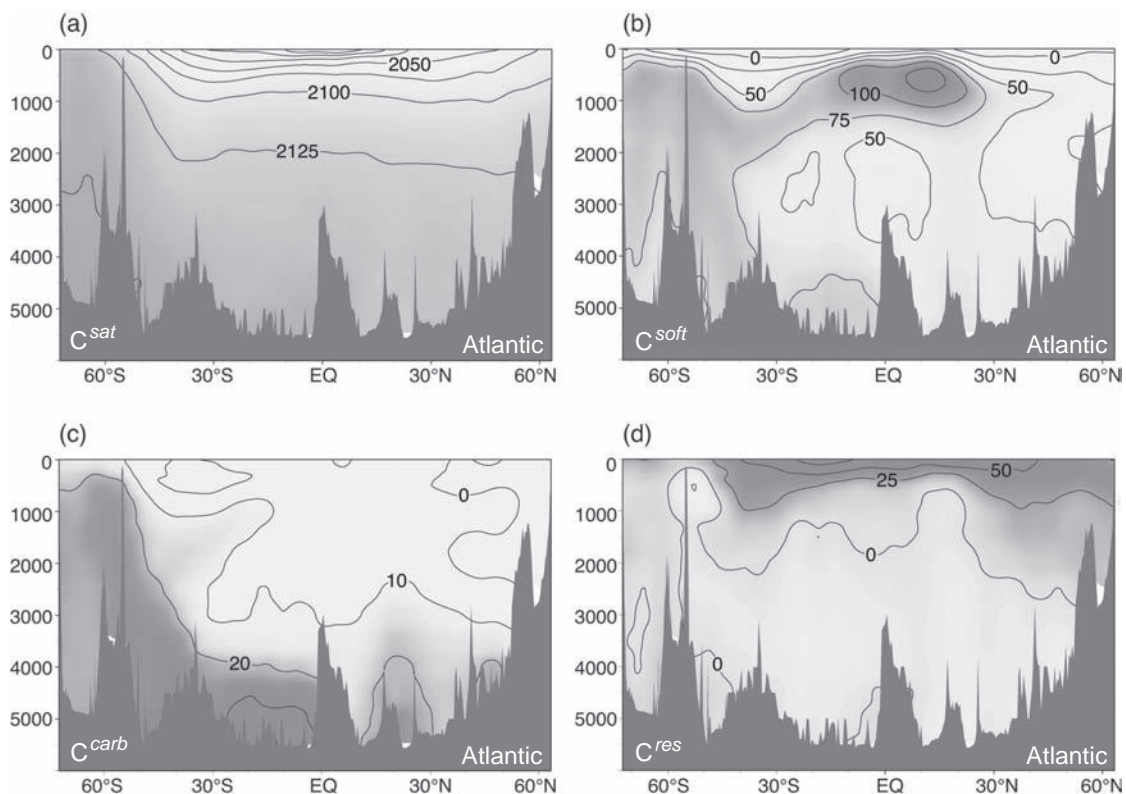


Figure 11.21 Meridional diagnostics of Atlantic carbon pumps: (a) saturated carbon concentration, $C_{\text{pre}}^{\text{sat}}$ ($\mu\text{mol kg}^{-1}$), with respect to the pre-industrial atmosphere ($\text{pCO}_{2,\text{pre}}^{\text{at}} = 278 \mu\text{atm}$); (b) soft-tissue pump of carbon, C^{soft} ($\mu\text{mol kg}^{-1}$); (c) carbonate pump, C^{carb} ($\mu\text{mol kg}^{-1}$); (d) residual carbon concentration, C^{res} ($\mu\text{mol kg}^{-1}$), which includes contributions from anthropogenic carbon, the disequilibrium component of preformed carbon, and errors introduced through approximations made in the estimation of other terms.

to $60 \mu\text{mol kg}^{-1}$ in the deep waters of the Pacific (Figs. 11.21c and 11.22c). Both carbonate and soft-tissue pumps are associated with sinking particles. The organic matter in sinking particles is mostly regenerated at shallower depths, while the dissolution of calcium carbonate occurs at greater depths. Consequently, the carbonate pump affects waters deeper than the soft-tissue pump.

The carbonate pump contribution is of greater magnitude in the Pacific and extends significantly higher within the water column (Figs. 11.21c and 11.22c). The basin-to-basin contrast reflects the reduced $[\text{CO}_3^{2-}]$ in the thermocline and deep waters of the Pacific, relative to the Atlantic (Fig. 11.23). This contrast is due to the accumulated DIC from the soft-tissue pump in the older waters of the deep Pacific Ocean decreasing the pH and moving the speciation of the carbon-

ate system towards CO_2^* and away from CO_3^{2-} (Fig. 6.11b).

The lower carbonate ion concentration in the Pacific then leads to a shallower saturation horizon and an enhanced C^{carb} . At the same time, less calcium carbonate arrives at the sea floor in the Pacific, witnessed by the smaller percentage of calcium carbonate in North Pacific core-top sediments (Archer, 1996).

Residual contribution from anthropogenic and disequilibrium components

The residual contribution, C^{res} , combines ΔC , the disequilibrium between the surface ocean and atmosphere at the time of subduction, and $C_{\text{ant}}^{\text{sat}}$, the enhancement of C^{sat} due to the increase in atmospheric pCO_2 since pre-industrial times. C^{res} varies from about $75 \mu\text{mol kg}^{-1}$ in the upper

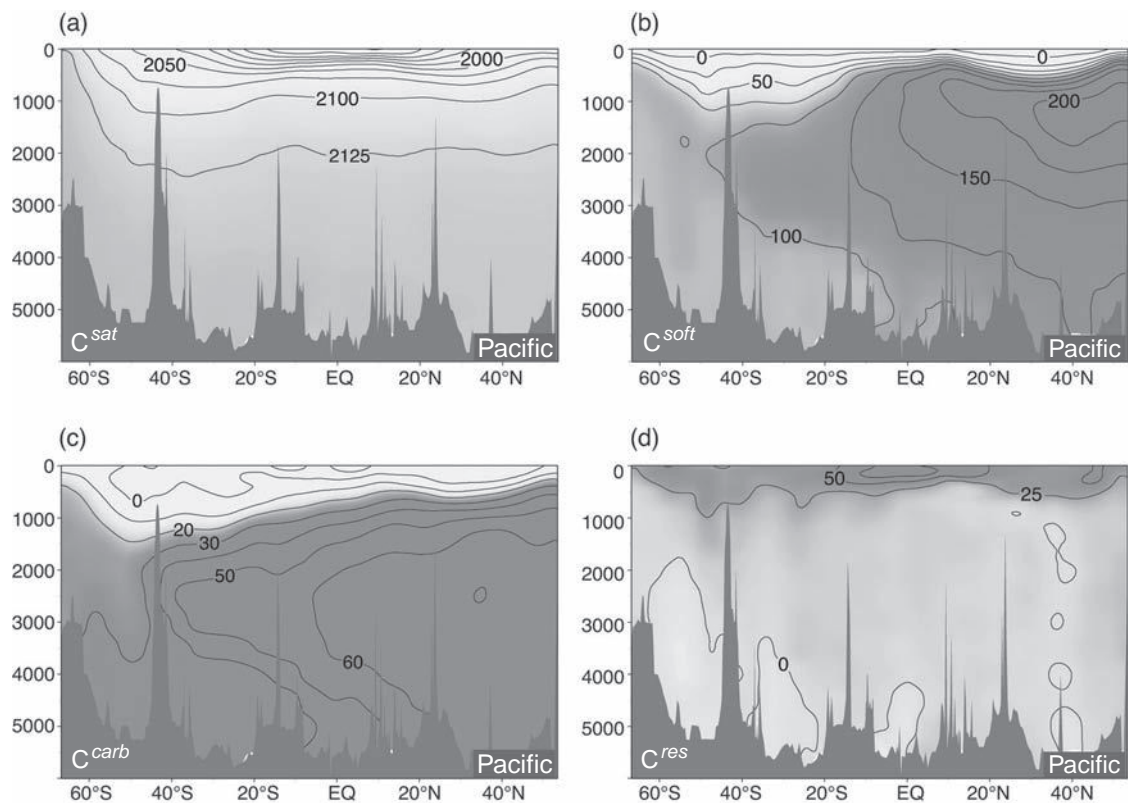


Figure 11.22 Meridional diagnostics of Pacific carbon pumps: (a) saturated carbon concentration, C_{pre}^{sat} ($\mu\text{mol kg}^{-1}$), with respect to the pre-industrial atmosphere ($p\text{CO}_{2,pre}^{at} = 278 \mu\text{atm}$); (b) soft-tissue pump of carbon, C^{soft} ($\mu\text{mol kg}^{-1}$); (c) carbonate pump, C^{carb} ($\mu\text{mol kg}^{-1}$); (d) residual carbon concentration, C^{res} ($\mu\text{mol kg}^{-1}$), which includes contributions from anthropogenic carbon, the disequilibrium component of preformed carbon, and errors introduced through approximations made in the estimation of other terms.

carbonate ion at 2000 m ($\mu\text{mol kg}^{-1}$)

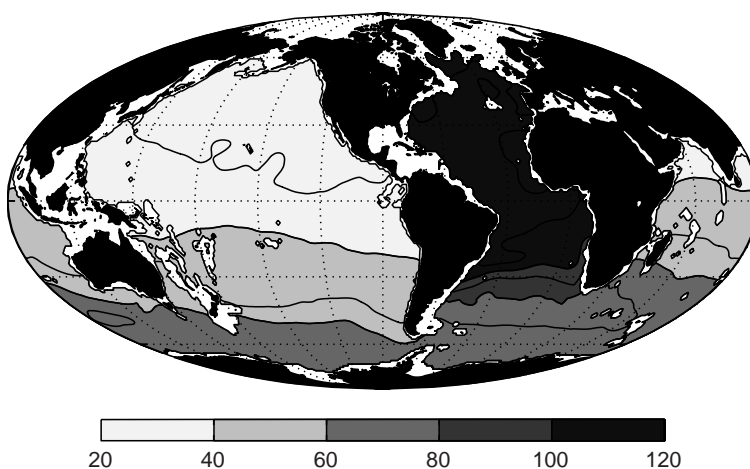


Figure 11.23 Distribution of the carbonate ion, $[\text{CO}_3^{2-}]$ ($\mu\text{mol kg}^{-1}$) at 2000 m depth in the global ocean. Evaluated using data from Conkright et al. (2002) and Key et al. (2004).

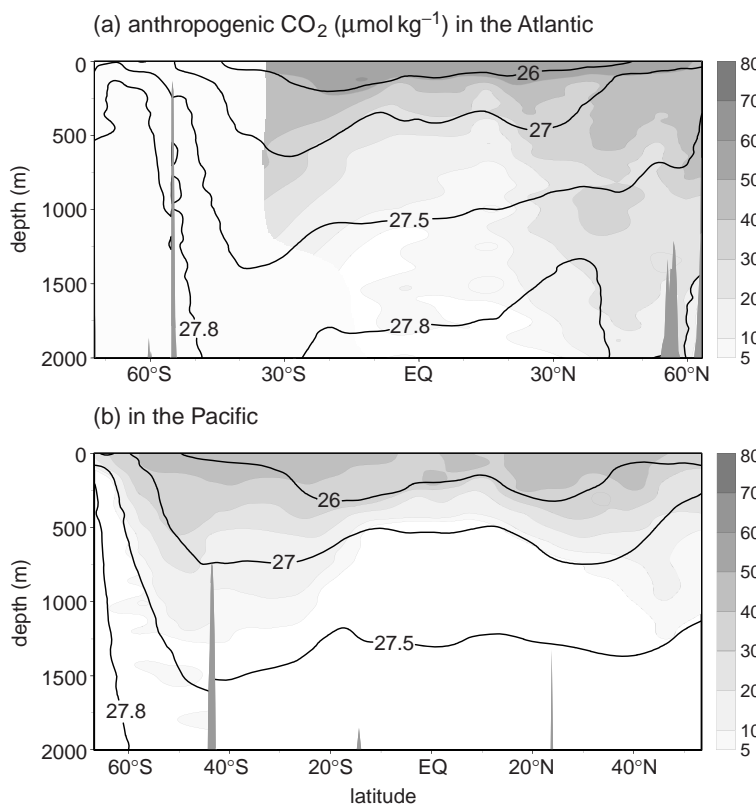


Figure 11.24 An estimate of C_{ant}^{sat} ($\mu\text{mol kg}^{-1}$, shading), the contribution to DIC due to the anthropogenic increase in atmospheric pCO_2 since the pre-industrial period, in (a) the Atlantic Ocean, and (b) the Pacific Ocean, together with σ_θ (kg m^{-3} , contours). The estimate is based on observations from the 1990s, as described by Sabine *et al.* (2004). Data from Key *et al.* (2004).

thermocline of both basins to slightly negative concentrations over much of the Atlantic basin below the thermocline (Figs. 11.21d and 11.22d). The pattern of the deep C^{res} is plausible, although its magnitude is comparable to the uncertainties in the analysis.

The positive value for residual contribution, C^{res} , over much of the upper ocean is consistent with a dominant contribution from C_{ant}^{sat} , the influx of anthropogenic carbon over the past century or so, as atmospheric carbon dioxide levels have rapidly increased. The anthropogenic component C_{ant}^{sat} has been estimated using the record of atmospheric pCO_2 and estimates of ventilation age (the time since subduction) and transport pathways evaluated using other ocean tracers (e.g., Gruber *et al.*, 1996). This anthropogenic signal reveals an influx of carbon over the upper thermocline of both basins (Fig. 11.24), consistent with the thermocline having a ventilation timescale of several decades. There is more anthropogenic carbon being transferred into the deeper waters of the northern North Atlantic, reflecting the more vig-

orous ventilation there. Most of the deeper waters are still largely unaffected by the anthropogenic CO_2 .

In the deep waters of the Atlantic, C^{res} is slightly negative (Fig. 11.21d), probably because these dense waters are cooling at the time of subduction. Cooling increases the solubility of CO_2 , driving down pCO_2 and leading to undersaturation and a negative ΔC . Due to the long air-sea equilibration timescale (~ 1 year), air-sea exchange is unable to eradicate this surface disequilibrium, ΔC , and the negative ΔC signal is subducted into the interior.

In contrast, in the deep waters of the Southern Ocean and Pacific, C^{res} is slightly positive (Fig. 11.22d). This signal can be attributed to the upwelling of waters rich in regenerated carbon, C^{soft} , in the Southern Ocean. On reaching the surface layer, the regenerated carbon increases both pCO_2 and ΔC . The positive anomaly of ΔC might be reduced by cooling, biological consumption and gas exchange. However, if the water parcel remains in the mixed layer for only a short time,

relative to air-sea equilibration, the remaining positive anomaly of ΔC can be subducted into deep waters and propagated over the deep Southern Ocean and Pacific basin (Fig. 11.22d).

11.5 | Summary

The patterns of biological production and nutrient transport processes are linked over a broad spectrum of space and timescales. On a daily to seasonal timescale, biological productivity in the euphotic zone is mainly sustained by the convective, vertical redistribution of nutrients within the seasonal boundary layer. Time-varying circulations may locally enhance biological production through a rectified transfer of nutrients across the base of the euphotic zone.

On longer timescales, nutrients must be supplied to the seasonal boundary layer to maintain biological productivity and offset the loss due to the export of organic matter to the ocean interior. This supply involves both horizontal and vertical redistributions of nutrients by a range of physical phenomena. Nutrients are transported via the gyre and overturning circulations, including advection along western boundary currents and separated jets. Nutrients are transferred along isopycnals in the upper thermocline and are eventually swept downstream into deep mixed layers at the end of winter. This advective influx of nutrients then sustains the convective, vertical transfer of nutrients into the euphotic zone. The imprint of this advective transfer into the mixed layer enhances surface nutrient concentrations in the subpolar gyres and reduces them in the subtropical gyres. There are also transfers of nutrients across gyre boundaries in the upper ocean through boundary currents, surface Ekman flows and time-varying eddies.

The interior nutrient distributions are principally determined by a combination of subduction from the surface mixed layer and regeneration from organic detritus. Subduction is the dominant process in the Atlantic, while the two contributions are comparable in the Pacific. Globally, less than half the nutrients in the deep

ocean arrived there through the fallout of organic matter.

The carbon distribution may be understood in terms of contributions from saturation with the atmosphere, regeneration from organic carbon and calcium carbonate, disequilibrium in the surface, and the uptake of anthropogenic CO_2 . The vast majority of carbon in the ocean is attributable to near saturation with the atmosphere. The next largest contribution is from the soft-tissue pump, notably a large biologically driven store in the deep Pacific. The carbonate pump provides a smaller contribution, and is modulated by the variations in DIC and pH caused by the other pumps. There is a clear signal of the invasion of anthropogenic carbon in the upper thermocline.

11.6 | Questions

Q11.1. Global export production over the oligotrophic, subtropical gyres.

Export production has been estimated to reach $2 \text{ mol C m}^{-2} \text{ y}^{-1}$ close to Hawaii in the North Pacific subtropical gyre (Emerson *et al.*, 1997). Assuming that this export is representative of other subtropical oceans and that their collective surface area makes up 60% of the global ocean (with the ocean making 71% of the surface area of the Earth), then estimate the following:

- the surface area of the subtropical gyres over the globe (assume the Earth's radius of 6400 km);
- the area-integrated export production over the subtropical gyres (note that 1 mole of carbon is equivalent to 12 g of carbon); and
- what proportion of the global export estimated as 10 Pg C y^{-1} is provided by export from the oligotrophic subtropical gyres.

Q11.2. Nutrient transport in boundary currents.

Consider the nutrient transport in a western boundary current and their likely downstream fate.

(a) If a boundary current has an along-stream velocity of 1 m s^{-1} and a nitrate concentration of 10 mmol N m^{-3} over a width of 100 km and a vertical scale of 500 m, then what is the along-stream transport from the area integral of the product of velocity and concentration? Give your answer in units of mol N y^{-1} .

(b) If this nutrient transport directed along a boundary current is eventually transferred onto density surfaces outcropping in the downstream, winter mixed layer in the subpolar gyre, then what is the effective nutrient flux per unit horizontal area passing into the winter mixed layer? Assume the surface horizontal area of the winter mixed layer in the subpolar gyre is given by 4000 km by 3000 km. Give your answer in units of $\text{mol N m}^{-2} \text{y}^{-1}$ and compare your answer to the nutrient transfer estimates in Section 11.1.

Q11.3. Scale analysis of the nitrate budget for the mixed layer.

Consider a simplified nitrate budget over a mixed layer of thickness, h , given by

$$h \frac{\partial \mathcal{N}_m}{\partial t} = \mathcal{F}_{\mathcal{N}} + \Lambda(\mathcal{N}_{th} - \mathcal{N}_m) \frac{\partial h}{\partial t} - K_v \left. \frac{\partial \mathcal{N}}{\partial z} \right|_{z=-h} - \mathbf{U}_e \cdot \nabla \mathcal{N}_m - h \lambda \mathcal{N}_m \quad (11.26)$$

where \mathcal{N}_m represents here, $\mathcal{F}_{\mathcal{N}}$ is the air-sea flux into the mixed layer, $\Lambda(\mathcal{N}_{th} - \mathcal{N}_m) \frac{\partial h}{\partial t}$ is the entrainment flux, $-K_v \left(\frac{\partial \mathcal{N}}{\partial z} \right)_{z=-h}$ is the vertical diffusive input at the base of the mixed layer, and $-\mathbf{U}_e \cdot \nabla \mathcal{N}_m$ is the Ekman advective supply, and $-h \lambda \mathcal{N}_m$ represents biological consumption.

Identify (a) the dominant balances for the winter versus the summer, and (b) identify the relative importance of advection over a year. Make the following assumptions:

- (i) The air-sea flux from deposition, $\mathcal{F}_{\mathcal{N}}$, typically reaches $0.01 \text{ mol N m}^{-2} \text{y}^{-1}$;
- (ii) The entrainment flux, $\Lambda(\mathcal{N}_{th} - \mathcal{N}_m) \frac{\partial h}{\partial t}$, only occurs when the mixed layer thickens (represented by $\Lambda = 1$ when $\partial h / \partial t > 0$ and otherwise 0) and $\mathcal{N}_{th} - \mathcal{N}_m$ represents the difference in nutrient concentration between the thermocline and mixed layer. Estimate this entrainment flux by

$$-\Lambda h \frac{\partial \mathcal{N}}{\partial z} \frac{\partial h}{\partial t},$$

where $h \sim 50 \text{ m}$ in summer and $h \sim 200 \text{ m}$ in winter with the deepening occurring over 6 months, and the vertical nutrient profile is assumed to be $\partial \mathcal{N} / \partial z \sim -10^{-5} \text{ mol N m}^{-4}$;

- (iii) Assume that the diffusive supply of nutrients has a vertical diffusivity of $K_v = 2 \times 10^{-5} \text{ m}^{-2} \text{s}^{-1}$;
- (iv) The Ekman advective transfer is simply taken from the meridional transfer,

$$-\mathbf{U}_e \cdot \nabla \mathcal{N}_m \sim -V_e \frac{\partial \mathcal{N}_m}{\partial y},$$

where the Ekman volume flux per unit length $V_e \sim 1 \text{ m}^2 \text{s}^{-1}$ (equivalent to an Ekman velocity of $\pm 1 \text{ cm s}^{-1}$ over a thickness of 100 m) and $\partial \mathcal{N}_m / \partial y \sim 10^{-9} \text{ mol N m}^{-4}$.

- (v) The biological consumption of nitrogen is simply represented here by an exponential decay of the mixed-layer nitrate with a decay timescale of $(1/\lambda)$. Assume that the decay timescale is typically the order of 15 days in summer, but there is no consumption in winter due to light limitation, and the mixed-layer nutrient concentration is typically, $\mathcal{N}_m \sim 0.5 \times 10^{-3} \text{ mol N m}^{-3}$.

11.7 Recommended reading

An accessible, descriptive view of ocean biogeochemical cycles is provided by S. R. Emerson and J. I. Hedges (2009). *Chemical Oceanography and the Marine Carbon Cycle*. Cambridge: Cambridge University Press.

A mechanistic view of how nutrients are transported is given by R. G. Williams and M. J. Follows (2003). Physical transport of nutrients and the maintenance of biological production. In *Ocean Biogeochemistry: The Role of the Ocean Carbon Cycle in Global Change*. ed. M. Fasham. Berlin: Springer-Verlag, pp. 19–51.

A review of the effects of mesoscale and frontal circulations on biological productivity is provided by M. Lévy (2008). The modulation of biological production by mesoscale turbulence, *Lect. Notes Phys.*, 744, 219–261. In *Transport in Geophysical Flow: Ten Years After*, ed., J. B. Weiss and A. Provenzale. Heidelberg: Springer.

A comprehensive and high-level review of biogeochemical cycling with an in-depth assessment of organic matter production, remineralisation and the carbon cycle is provided by J. L. Sarmiento and N. Gruber (2006). *Ocean Biogeochemical Dynamics*. Princeton, NJ: Princeton University Press, 526pp.

The deep ocean and overturning

The deep ocean is puzzling and intriguing, a vast expanse of cold water below the thermocline, slowly moving around the globe. For much of the time, these deep waters are isolated from the atmosphere and only reach the surface in a few remote regions. Most deep waters are very old, many years have elapsed since these waters were last in contact with the atmosphere, so their properties provide a memory of the past atmosphere. Up to now, only a small fraction of the deep waters carry any signal of anthropogenic CFCs or fossil-fuel derived carbon dioxide.

At the simplest level, the deep circulation is connected to dense waters forming in the high latitudes through interactions with the atmosphere or overlying ice, which eventually sink and spread beneath lighter waters. The effect of the surface forcing is not the entire story. The vertical ordering of dense waters is affected by intense mixing at overflows, where dense waters plunge down sloping topography and are blended and diluted with the background waters. These composite water masses then spread far over a basin and even the globe. Dense waters eventually return to the sea surface, preferentially over the Southern Ocean.

In this chapter, we firstly provide a descriptive overview of the deep ocean and why the overturning is so different in the northern basins. Secondly, we provide a mechanistic view of the processes affecting dense water, focussing on examples in the North Atlantic, including convection, cascading, overflows, mixing in fracture zones and overturning. Thirdly, we provide a theoretical view of how dense waters circulate over a basin, taking on

board constraints from rotation and topography. Finally, we address how dense waters return to the surface through a combination of upwelling and mixing, focussing on the Southern Ocean, and discuss the sources of energy which sustain these circulations.

12.1 Why is the deep ocean important?

We start with an overview: discussing the properties of the deep ocean and tracer signals of the overturning, and then addressing why the overturning is different in the North Atlantic and North Pacific, and how this difference might affect the overlying atmosphere.

12.1.1 Properties of the deep ocean

The properties of the deep ocean dominate any volumetric census of the global ocean. The global-mean temperature is less than 4 °C, even though surface waters are much warmer over most of the globe (Fig. 12.1). These low temperatures of the deep waters reflect how cold, dense waters are formed at high latitudes, then sink and spread over the global ocean. Tracer distributions by themselves do not reveal the separate contributions of advection and mixing, so plausible spreading pathways are marked by the arrows in Figs. 12.1–12.3 (in the same spirit as Wüst, 1935). The temperature contrasts in these deep and bottom waters are very small, reflecting how there

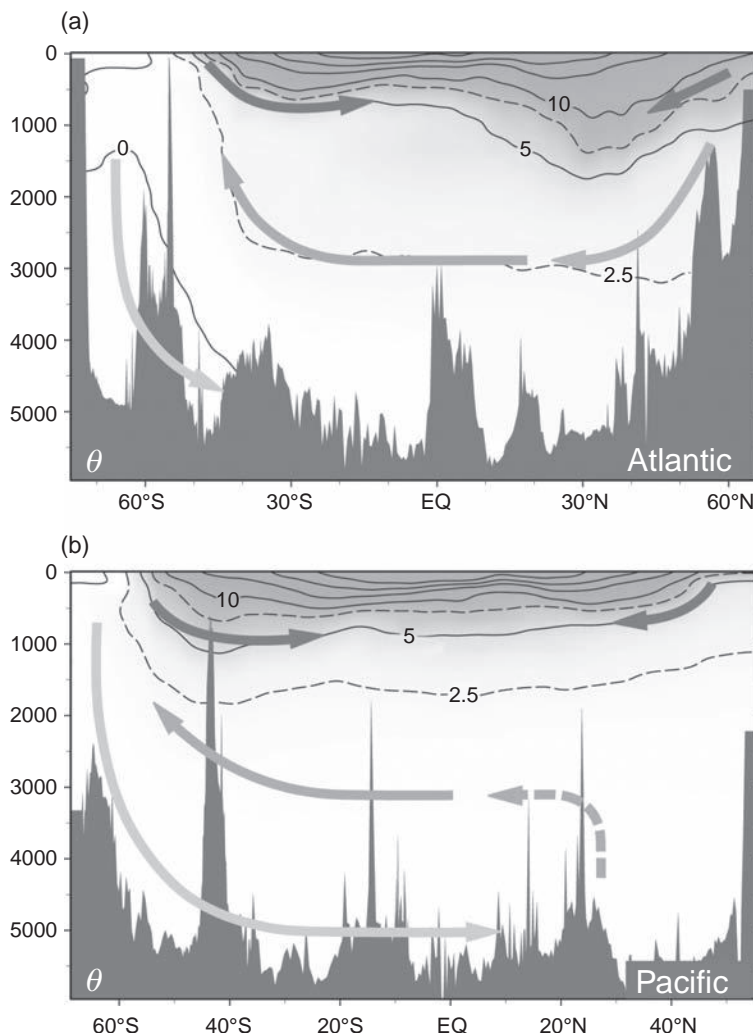


Figure 12.1 Observed meridional sections, latitude versus depth (m), of potential temperature, θ ($^{\circ}$ C) for (a) the Atlantic along 20° W, and (b) the Pacific along 170° W; see Plates 2a and 3a. There is cold water below the thermocline, extending over nearly all the global ocean. The cold waters connect to the surface over the Southern Ocean. Physical spreading pathways are superimposed for intermediate, deep and bottom waters (dark, mid and light grey arrows, respectively) based upon the salinity distribution (Plates 2b and 3b), as well as the assumed lightening and return of bottom water in the North Pacific (dashed arrow).

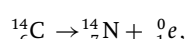
are only a few major sources of deep water and how the geothermal sources of heat are relatively weak along the sea floor.

The biogeochemical contrasts are much larger in the deep and bottom waters: there are relatively low concentrations of inorganic nutrients and carbon in the deep waters of the North Atlantic and high concentrations in the North Pacific as illustrated for silica in Fig. 12.2. These contrasting patterns reflect differences in the ventilation pathways and regeneration of organic matter in each basin.

The deep waters account for more than 80% of carbon in the ocean, about 50 times the atmospheric inventory. Any changes in the temperature of these deep waters significantly impacts

ocean solubility and the partitioning of carbon between the atmosphere and ocean.

The nutrient and carbon contrast between the basins reflects the age of the water, younger deep waters in the North Atlantic and older deep waters in the North Pacific. This age difference can be inferred from the transient tracer, radiocarbon. This heavy isotope of carbon ^{14}C decays to nitrogen through beta decay,



with a half life of 5370 years. There are about 10^{12} stable ^{12}C atoms for each atom of ^{14}C in the atmosphere and ocean. $\Delta^{14}\text{C}$ is a measure of the difference in the ratio of radioactive ^{14}C and stable ^{12}C in natural samples relative to a

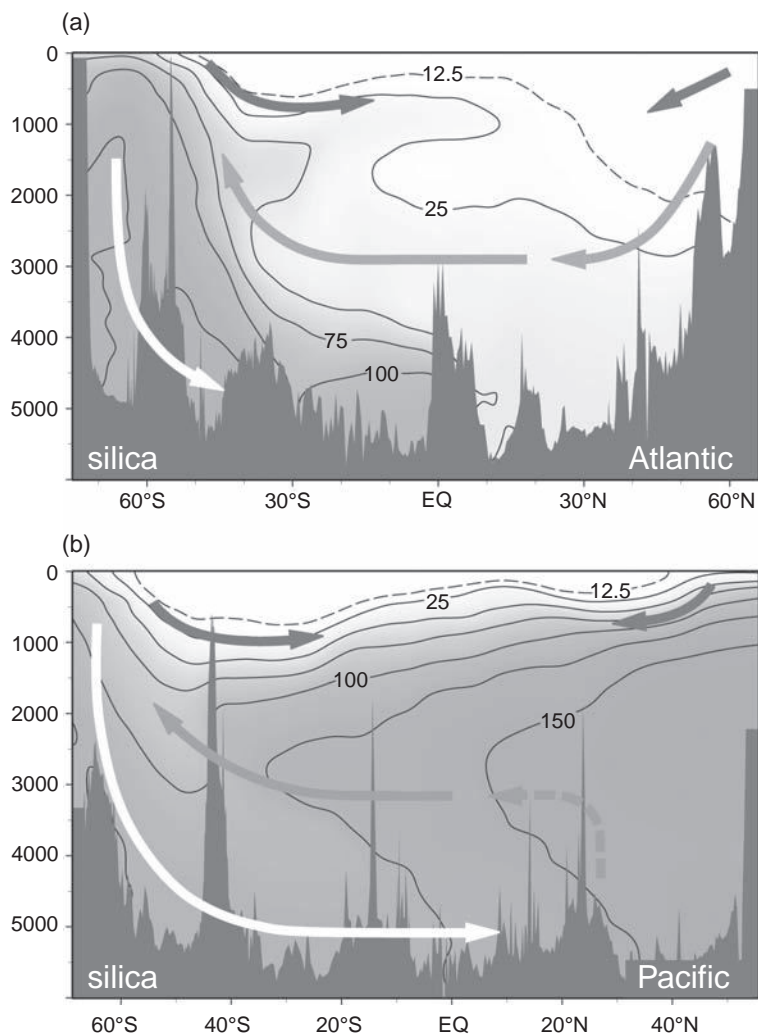


Figure 12.2 Observed meridional sections, latitude versus depth (m), of silica ($\mu\text{mol kg}^{-1}$) for (a) the Atlantic along 20°W , and (b) the Pacific along 170°W ; see Plates 6c and 7c. There are relatively low concentrations of silica in the upper waters of the Atlantic and Pacific, together with higher concentrations over the Southern Ocean, the deep waters of the South Atlantic and the entire Pacific basin. Physical spreading pathways are superimposed for intermediate, deep and bottom waters (dark, mid and light grey arrows, respectively) based upon the salinity distribution, as well as the assumed lightening and return of bottom water in the North Pacific (dashed arrow).

standard (with some correction for biological transformation). As time passes, radiocarbon decays and the value of $\Delta^{14}\text{C}$ in a water parcel decreases. The distribution of $\Delta^{14}\text{C}$ in the ocean, illustrated in Fig. 12.3, provides a view and timescale of transport pathways. In the surface mixed layer, $\Delta^{14}\text{C}$ equilibrates with the atmospheric value, which was close to zero in pre-industrial times and had a sharp positive spike in the 1960s due to atmospheric bomb testing leading to $\Delta^{14}\text{C}$ reaching $\sim 50\text{‰}$ in near-surface waters (Fig. 12.3). $\Delta^{14}\text{C}$ becomes increasingly negative in deep waters reaching -100 to -150‰ in the deep Atlantic and less than -200‰ in the northern Pacific. These negative values are due to the bomb signal having not penetrated in the deep waters

and the decay of ^{14}C since subduction. Knowing the decay rate of ^{14}C , these deep values imply approximate ventilation ages of greater than 400 years in the deep North Atlantic and 1600 years in the deep North Pacific; for detailed discussion of carbon isotopes and their interpretation, see Broecker and Peng (1982).

12.1.2 Overturning cells

The spreading of water masses over the globe can be viewed in terms of a series of overturning cells, such as presented in the synthesis in Fig. 12.4. This schematic view presents a zonally averaged view for each basin and most flows are concentrated along the western margin of the basins.

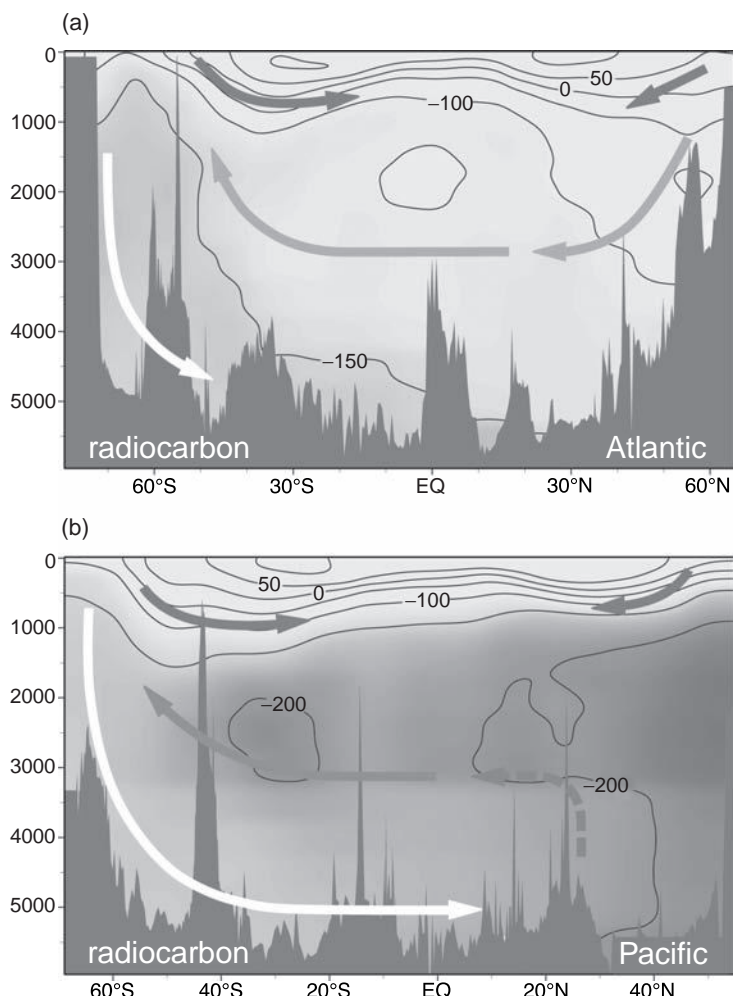


Figure 12.3 Observed meridional sections, latitude versus depth (m), of the radiocarbon, normalised anomaly, $\Delta^{14}\text{C}$ (‰), for (a) the Atlantic along 20°W, and (b) the Pacific along 170°W; see Plates 4c and 5c. The more positive values represent younger waters, more recently in contact with the atmosphere, while more negative values represent older waters. Physical spreading pathways are superimposed for intermediate, deep and bottom waters (dark, mid and light grey arrows, respectively) based upon the salinity distribution, as well as the assumed lightening and return of bottom water in the North Pacific (dashed arrow).

The spreading pathways vary from overturning cells confined with a sub-basin or basin, and extending to overturning cells connecting the separate northern basins with the Southern Ocean.

While the overturning cells are generic, their imprint on the tracer distributions depends on the particular tracer and timescale of interest:

- Some tracers, such as CFCs or oxygen, are quickly reset within the mixed layer as they equilibrate across the sea surface in about a month (see Section 6.6.5). The distribution of these tracers reflects the pattern of recent ventilation. There are ventilated inputs from both the North Atlantic and Southern Ocean, as well as along the lightest surfaces from the North Pacific (see Plates 8 to 11).

- Other tracers equilibrate the mixed layer with the atmosphere much more slowly. Carbon dioxide takes about one year, and radiocarbon takes a decade. If a water parcel stays in the mixed layer for only a year or so, as is likely the case in the Southern Ocean, radiocarbon will not have time to come back into equilibrium and this relatively brief stay in the mixed layer will not significantly modify its distribution. Hence, tracers that are modified slowly by air-sea interactions in the mixed layer have simpler interior distributions than more reactive tracers.

The ocean overturning has often been characterised by a single cell ‘conveyor belt’, where dense water is formed in the North Atlantic and spreads

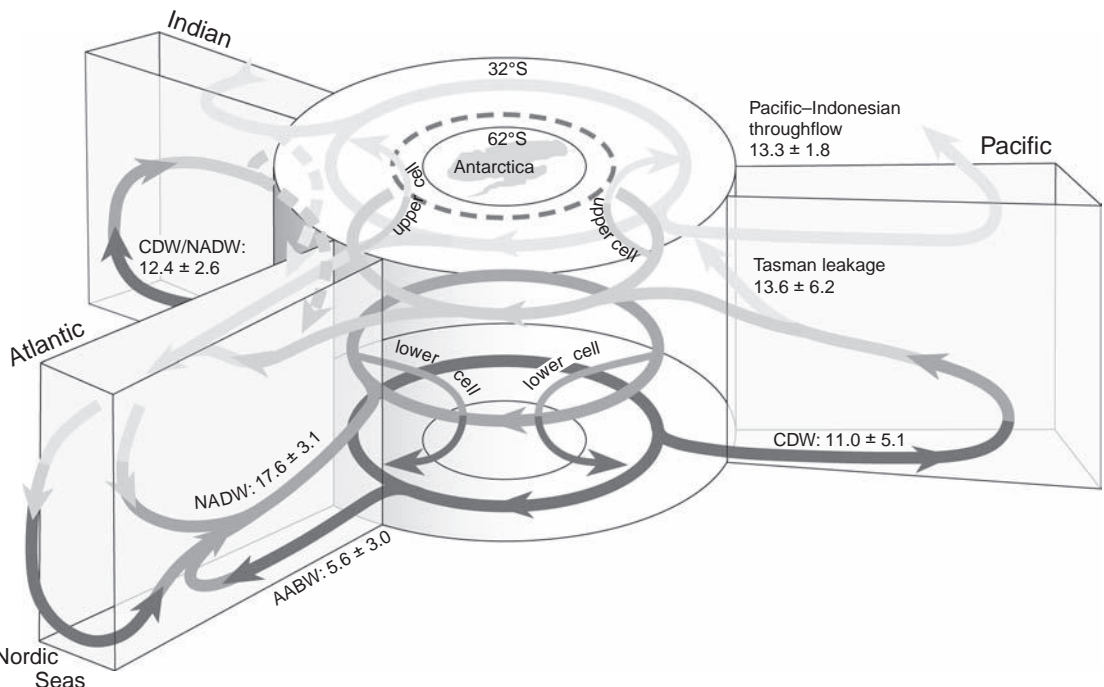


Figure 12.4 A schematic view of the global overturning circulation, including dominant pathways within the Atlantic, Pacific and Indian basins, and their horizontal connections with the Southern Ocean and the Indonesian Passages; grey shades become darker for denser waters. The dominant dense water masses marked are North Atlantic Deep Water (NADW), Circumpolar Deep Water (CDW) and Antarctic Bottom Water (AABW). In the Atlantic basin, there is 5.6 ± 3.0 Sv of AABW spreading northward and 17.6 ± 3.1 Sv of NADW spreading southward; in the Pacific basin, 11.0 ± 5.1 Sv of CDW spreading northward into the Pacific; and 12.4 ± 2.6 Sv of CDW/NADW passing into the Indian basin. Dashed arrows represent Indian to Atlantic westward exchange and thin arrows represent conversions involving the upper or lower cells; the dashed circle represents the surface outcrop of neutral surface $\gamma = 27.6$, which separates these upper and lower cells. Shallow subtropical cells not included. Figure redrawn from Lumpkin and Speer (2007), including transport estimates and uncertainties from their model inversion, with format adapted from Schmitz (1996).

over the entire globe (Broecker, 1991). While the global overturning cell might be invoked to explain the radiocarbon distribution, this view is inappropriate for tracers that are more rapidly reset in the mixed layer. These tracers support a view in which separate overturning cells in each basin connect with the Southern Ocean, as depicted schematically in Fig. 12.4.

12.1.3 Why is the overturning different in the Atlantic and Pacific?

The overturning pattern is fundamentally different in the Atlantic and Pacific: dense water is formed in the mixed layer in the high latitudes of the North Atlantic, sinking to depths of several kilometres, then spreading southward over the rest of the basin, while dense water only

sinks to intermediate depths of typically less than 1 kilometre in the high latitudes of the North Pacific. In both basins, intermediate and dense bottom waters spread northward from the Southern Ocean.

Why is there a different overturning response in these northern basins? To answer this question, we consider first the surface properties and, second, the air-sea exchange for each basin.

Surface properties

In the high latitudes, there are similar surface temperatures in the North Atlantic and North Pacific at the end of winter; surface waters approach freezing close to the land on the north-western sides of both basins (Fig. 12.5a). The surface waters of the North Atlantic are much saltier

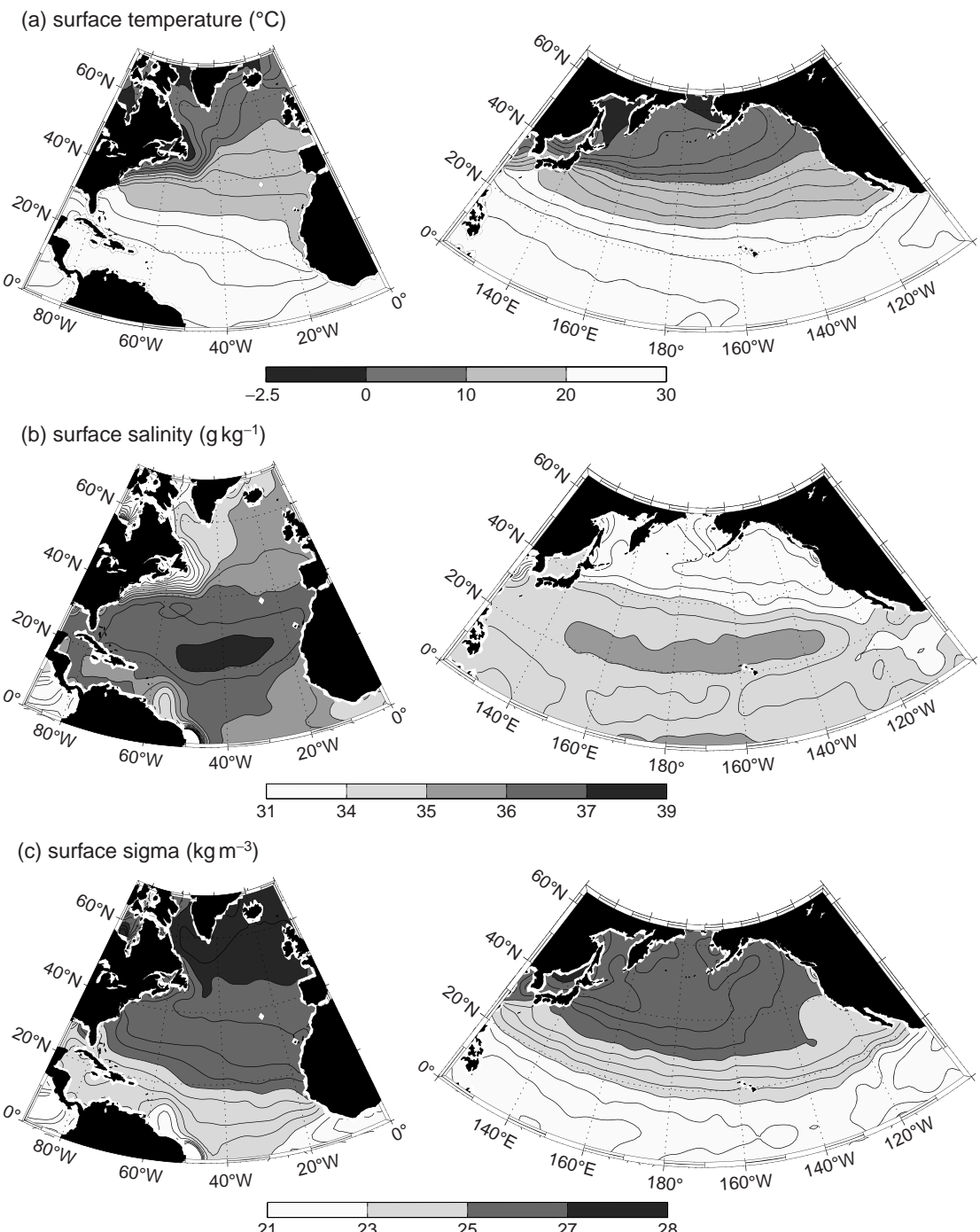


Figure I2.5 Surface maps of (a) temperature (contours every 2.5°C), (b) salinity (contours every 0.5 g kg^{-1}), and (c) σ (contours every 0.25 kg m^{-3}) at the end of winter in March for the North Atlantic (left panel) and the North Pacific (right panel) diagnosed from climatology.

than those of the North Pacific (Fig. 12.5b), even though more major rivers flow into the Atlantic than the Pacific. Consequently, the surface waters of the Atlantic are the denser of the two (Fig. 12.5c).

The high surface density in the North Atlantic drives a sinking and southward transport of dense water at depth, as well as a northward influx of lighter water near the surface. In contrast, in the North Pacific, surface waters sink only to intermediate depths of less than a kilometre depth and the overturning is dominated by an invasion of deeper, denser waters from the Southern Ocean.

Surface freshwater exchange

Why does surface density and salinity differ so much between the North Atlantic and North Pacific? This question was first addressed by Warren (1983). Consider the patterns of air-sea freshwater exchange and surface circulation of the two basins. While there is a broadly similar pattern of freshwater exchange, with net precipitation in the tropics and high latitudes and net evaporation in the subtropics, there are some important, though subtle, differences:

- Precipitation occurs at a greater rate in the tropics and over the western side of the subtropics in the Pacific compared with the Atlantic (Fig. 12.6a, dark shading). This freshening is either associated with a westward moisture flux from the Atlantic to the Pacific carried by the easterly Trade winds or a northward moisture flux to the northern Pacific associated with the Asian monsoon (Emile-Geay *et al.*, 2003). Elsewhere, precipitation is broadly comparable. Most river run-off actually enters the North Atlantic and Arctic, rather than the North Pacific.
- Evaporation occurs over a larger fraction of the subtropics in the North Atlantic compared with the North Pacific (Fig. 12.6b, dark shading), which is a consequence of a greater extent of warmer, surface waters in the North Atlantic (Fig. 12.5a). The highest evaporation rates are over the extensions of both western boundary currents.
- Fluid parcels circulating the subtropical gyre experience a greater freshwater loss to the atmosphere in the North Atlantic compared with the

North Pacific (Fig. 12.6c, thick black line; also see Czaja, 2009), such that there is a greater gain in salinity following a fluid parcel within the mixed layer,

$$\frac{DS}{Dt} = \frac{S(\mathcal{E} - \mathcal{P})}{h},$$

where $\mathcal{E} - \mathcal{P}$ (ms^{-1}) is the net freshwater flux into the ocean and h (m) is the mixed-layer thickness (ignoring entrainment and diffusion for simplicity). Accordingly, surface waters become saltier while recirculating around the subtropical North Atlantic (Fig. 12.5b).

- The influence of net freshwater loss over the North Atlantic is not confined to the subtropics. The Gulf Stream and inter-gyre boundary are orientated from the southwest to the northeast (Fig. 12.6, thin contours), leading to warm, salty water from the subtropical gyre being transferred into the subpolar gyre along its eastern side and to higher latitudes. In contrast, the Kuroshio and the inter-gyre boundary are orientated more zonally in the North Pacific (Fig. 12.6, thin contours), so that the subtropical waters remain more confined to the mid latitudes.

Warren (1983) argued that a positive feedback operates connecting together the ocean overturning and air-sea exchange of fresh water: the vigorous overturning in the North Atlantic leads to warmer, surface waters being transported northward, which in turn leads to greater evaporation; conversely, the weaker overturning in the North Pacific reduces the northward transport of warm, salty water, which then reduces the evaporation.

While this positive feedback might operate, some perturbation must initiate the stronger overturning and evaporation in the North Atlantic basin. There are a range of possible ways to perturb the system:

- The most likely candidate is the pattern of atmospheric forcing. The path of the atmospheric Jet Stream, itself affected by the position of the mountain ranges and land-sea contrasts, leads to the inter-gyre boundary tilting from the southwest to the northeast in the North Atlantic, but is more zonal over the Pacific. This tilt enhances the northward spreading of warm water in the North Atlantic.

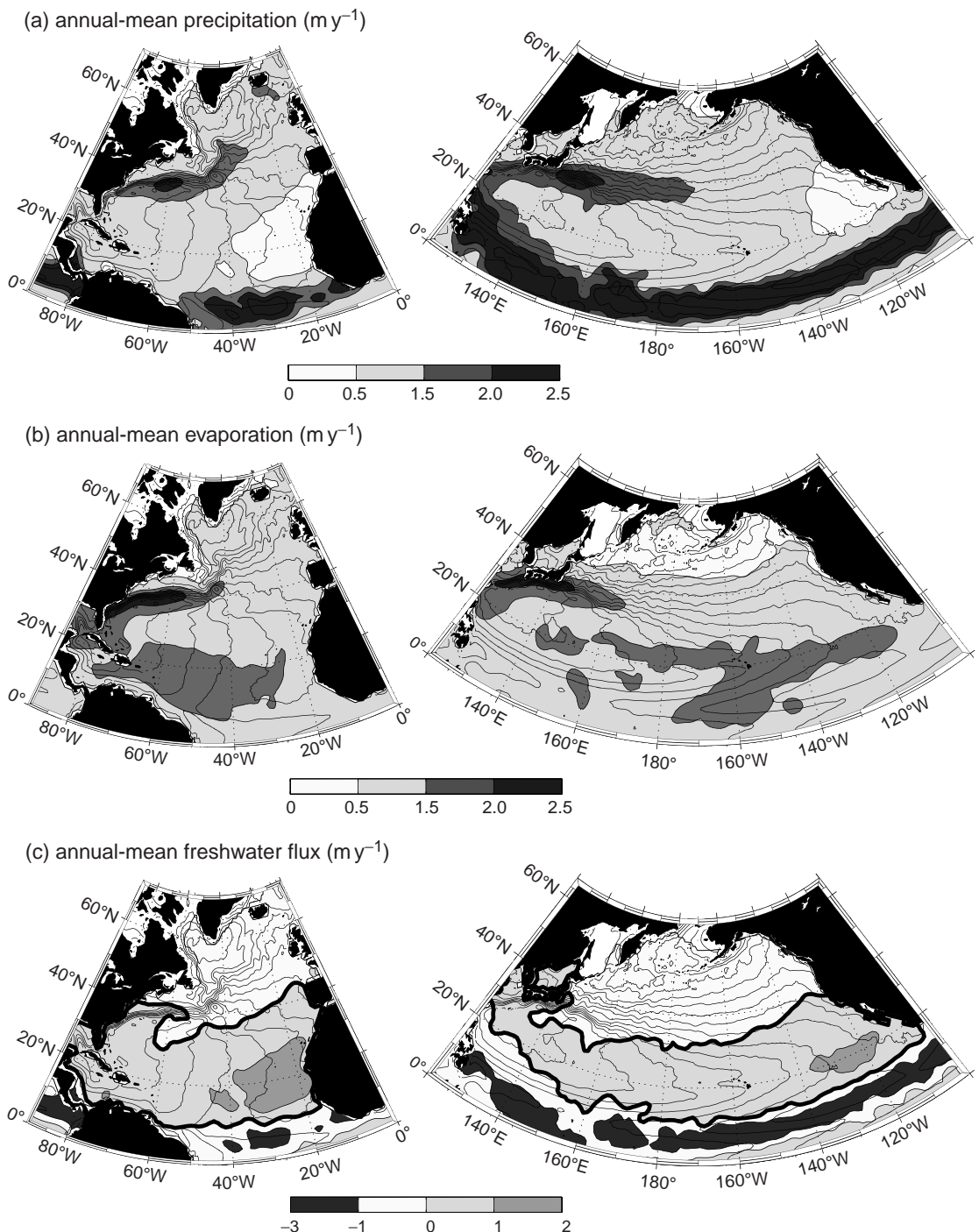


Figure 12.6 Air-sea freshwater exchange (shading, very thin contours every 0.5 m y^{-1}) over the North Atlantic (left panel) and the North Pacific (right panel): (a) precipitation, P , and (b) evaporation, E , and (c) net freshwater flux, $E - P$, into the ocean (thick contour is zero line); data from the NOCS climatology (Josey et al., 1999) together with dynamic height (thin contours every 10 cm) (Niiler et al., 2003; Maximenko and Niiler, 2005). There are significant uncertainties in this freshwater flux, perhaps ranging from 10% to 20% for each component.

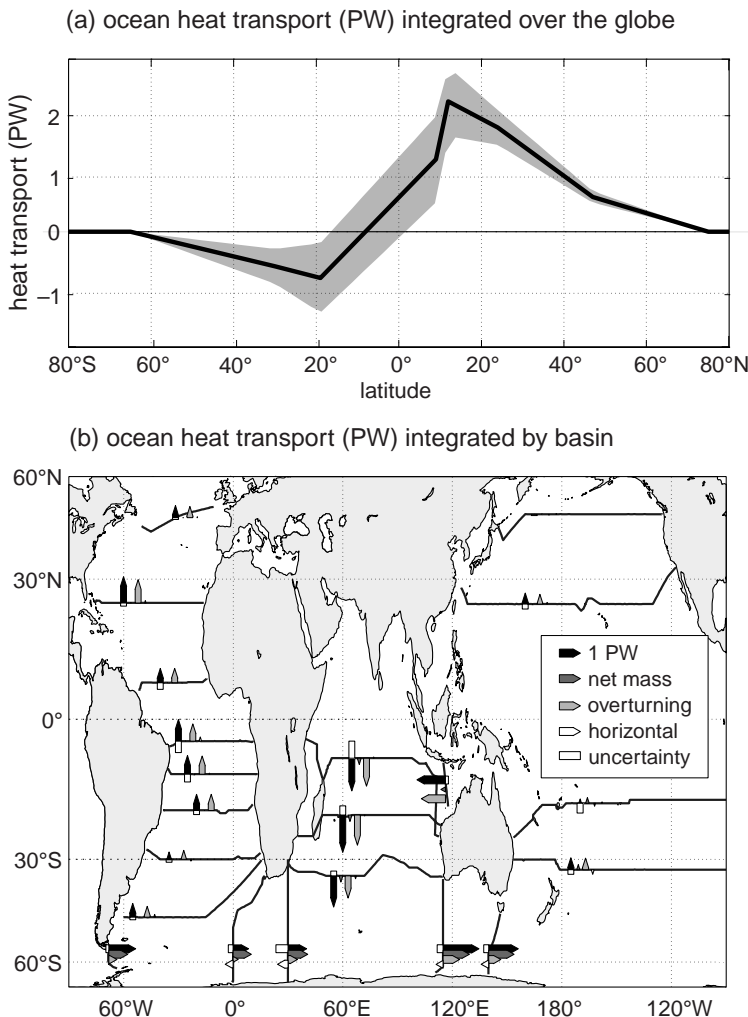


Figure 12.7 Inverse model estimates of ocean heat transport ($PW \equiv 10^{15}$ watts): (a) integrated over the globe versus latitude (black line) with error range (shading), and (b) integrated across ocean sections, separated into the total transport (black arrow) with contributions from the net mass transport (dark grey arrow), vertical overturning (grey arrow) and the horizontal correlations for temperature and velocity (white arrow). The global inverse model is based upon hydrographic sections from 1985 to 1996. Panels (a) and (b) courtesy of Carl Wunsch and Alex Ganachaud; further details, see Wunsch (2005) and Ganachaud and Wunsch (2003).

- The water-mass exchange with the semi-enclosed Mediterranean makes the Atlantic basin saltier, possibly enhancing the overturning (Reid, 1979), although this injection of salt occurs at a depth of 1 km rather than at the surface.
- The geometry of the basins might also play a role through the narrower width and greater latitudinal extent of the Atlantic versus the Pacific. Moisture is preferentially transported from a narrow basin into a wider basin via the atmosphere, as demonstrated by idealised coupled ocean-atmosphere model studies (Ferreira *et al.*, 2010). Hence, the analogue of the Atlantic

basin is likely to be saltier and more prone to overturning.

12.1.4 Heat transfer

The ocean provides a poleward heat transport reaching 2 PW in the northern hemisphere and 1 PW in the southern hemisphere (Fig. 12.7a), compared with a larger heat transport in the atmosphere reaching 4 to 5 PW in the mid latitudes (Section 2.2.2). The ocean heat transfer occurs through a combination of overturning cells and horizontal circulations. In the overturning cells, warm water moves meridionally in the upper ocean and cold water moves in the opposite direction at depth.

In the horizontal circulations, water flows meridionally in a western boundary current and moves in the opposite direction with a different temperature in the basin interior, but at the same depth.

For the Atlantic, the ocean heat transport is dominated by the overturning, directed northward at all latitudes, while in the Indian and Pacific basins there is a much weaker overturning and the horizontal circulation is more important in transferring heat poleward (Fig. 12.7b).

Is the ocean heat transport important?

There is an ongoing debate as to how important the ocean heat transport is for the wider climate system. There is a widespread popular view that the heat transport involving the Gulf Stream and the overturning circulation leads to the mild winter climate over Europe. Seager *et al.* (2002) have challenged this view and emphasised how (i) the heat transport by the atmosphere is much greater than that of the ocean in the mid latitudes and (ii) most of the heat released by the ocean in winter has been locally provided by heat gain in the preceding summer. Hence, most of the heat warming Europe has either been carried across the Atlantic basin by the atmosphere or been released to the atmosphere from the heat locally stored in the ocean. Now we consider whether the ocean circulation provides any additional role.

The ocean releases heat and moisture to the atmosphere most vigorously over the western boundary currents (Figs. 12.8a and 12.6b). In these same regions, atmospheric storms and weather systems preferentially form (Section 9.3.1) and then develop as they move downstream, usually eastward across the basin, linked to the path of the upper air Jet Stream. Hence, the Gulf Stream does play an indirect role (albeit more limited than popular conception) in maintaining the mild climate over Europe: the Gulf Stream transports heat from the tropics to the mid latitudes along the western side of the basin; warming the surface waters and overlying atmosphere; and then the warmer and moister air is transported across the basin by the prevailing atmospheric circulation.

The more subtle question is whether the difference in overturning circulations affects the maritime climates for the North Atlantic and North Pacific. To highlight this effect, following Rhines *et al.* (2008), we now consider the thermal effect of the ocean on the overlying atmosphere: the ocean supplies heat to the atmosphere through the sum of latent and sensible heat, and the net infrared radiation (Fig. 12.8b). This ocean heat supply to the overlying atmosphere is again largest over the western boundary currents, reaching more than 250 W m^{-2} , as well as being large over the tropics and subtropics in both basins (Fig. 12.8b). In the mid and high latitudes, there is, though, a striking difference between each basin: the heat supply to the atmosphere ranges from 100 to 200 W m^{-2} over parts of the North Atlantic, but is less than 100 W m^{-2} over the North Pacific (Fig. 12.8b). Hence, the stronger ocean overturning in the North Atlantic enables an increased heating of the overlying atmosphere by 50 to 100 W m^{-2} over much of the mid and high latitudes, ultimately enhancing the warming of the downstream European climate.

12.1.5 Summary

The properties of the deep ocean dominate any volumetric census, so the global ocean averages are low for temperature and high for concentrations of inorganic nutrients and carbon, relative to typical surface values. Dense water is preferentially formed in the high latitudes of the North Atlantic and the Southern Ocean. The sinking of dense waters leads to a range of overturning cells extending over the globe, each basin separately connected to the Southern Ocean. The stronger overturning in the North Atlantic compared with the North Pacific reflects how high-latitude waters are saltier and denser in the North Atlantic, a consequence of their greater freshwater loss to the atmosphere. The overturning affects the climate system by transporting heat from the tropics to the mid latitudes and warming the overlying atmosphere. The overturning also affects the carbon cycle by altering the air-sea exchange of carbon and the redistribution of nutrients and carbon over the global ocean.

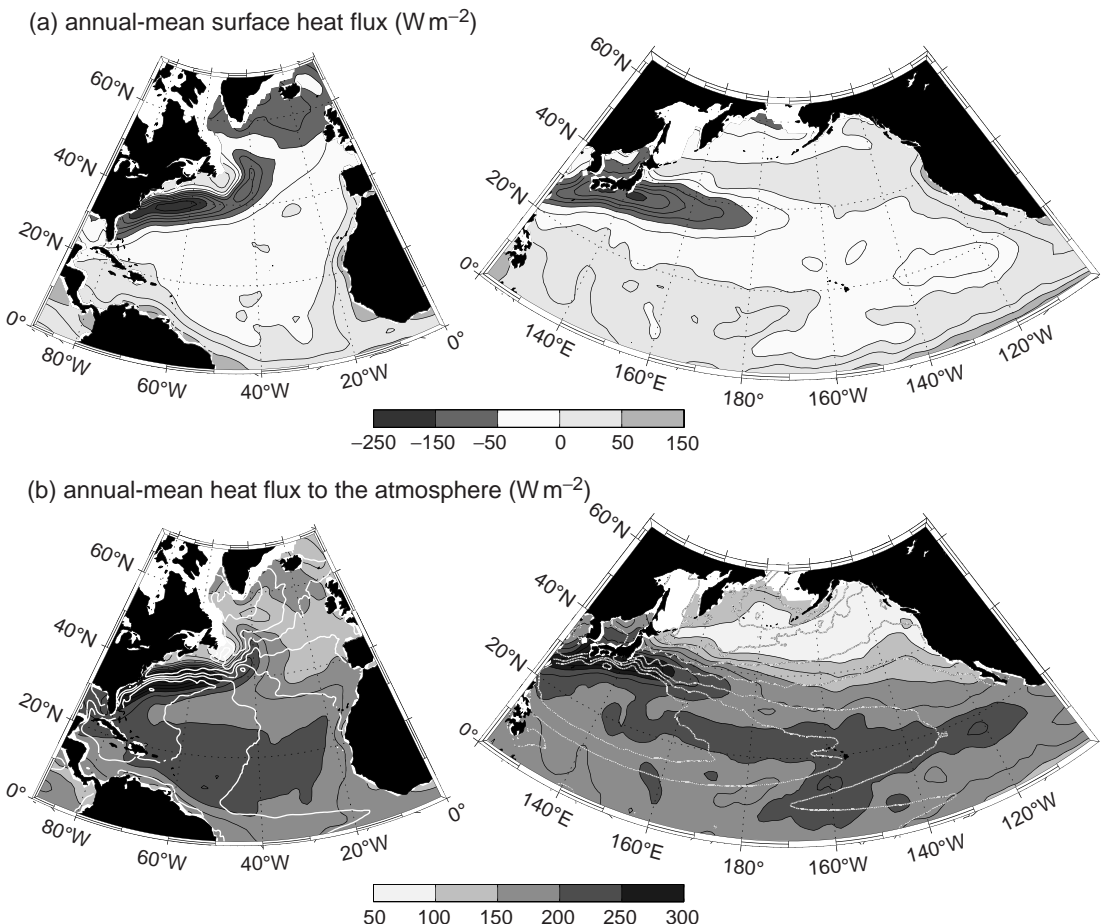


Figure 12.8 Air–sea heat exchange over the North Atlantic (left panel) and the North Pacific (right panel): (a) net heat flux into the ocean, and (b) heat flux from the ocean to the atmosphere (grey shading and black contours every 25 W m^{-2}) diagnosed from the NOCS climatology (Josey et al., 1999) together with dynamic height (white/light grey contours every 20 cm) (Niiler et al., 2003; Maximenko and Niiler, 2005). There are significant uncertainties in this air–sea flux, perhaps ranging from 10% to 20% for each component making up the net flux (see components in Section 4.4).

Next we consider the mechanisms by which dense waters are formed and modified, followed by a theoretical view of how dense waters circulate and, finally, how dense waters return to the sea surface.

12.2 How does dense water form, mix and spread?

Now we consider the mechanisms by which dense waters form, locally mix and spread, focussing on observational examples for the North Atlantic.

12.2.1 Surface exchange of density

In the high latitudes, surface waters become denser through air–sea exchanges of heat and moisture (Figs. 12.8a and 12.6c; Section 4.4) and, in polar regions, also through cooling in ice leads and beneath ice, and salt gain when ice freezes. Air–sea exchange becomes locally enhanced whenever there are strong contrasts between the sea and land or ice, such as when cold, dry air blows from the continent over the warmer ocean, leading to intense surface heat loss and evaporation.

Maxima in surface density do not, however, simply reflect the pattern of surface heat and

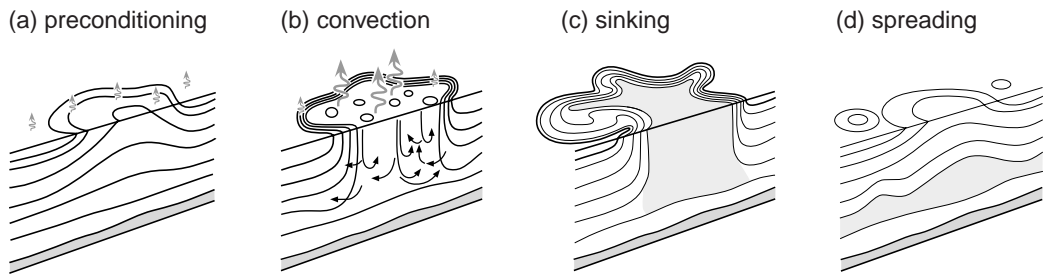


Figure 12.9 Schematic figure of the three phases of open ocean convection (depicted in three dimensions): (a) preconditioning with uplifted isopycnals (continuous lines); (b) convection and vertical overturning following surface heat loss (curly arrows); (c) sinking and (d) lateral spreading of the convected waters (shaded). Redrawn from Marshall and Schott (1999).

freshwater fluxes, but also depend on the past history of surface forcing for a water parcel following the circulation. For example, in the North Atlantic, surface waters gradually increase in density as they move cyclonically around a subpolar gyre, which in the North Atlantic culminates in dense waters forming in the Labrador Sea or Irminger Sea.

Next we consider the processes which subsequently affect dense water after being formed within the mixed layer.

12.2.2 Convection

Whenever surface waters become denser than the underlying water column, convection occurs, redistributing properties in the vertical. There are several phases of deep convection, as depicted in Fig. 12.9 (Marshall and Schott, 1999):

- Initially, there is a preconditioning phase where density surfaces are uplifted (Fig. 12.9a), associated either with wind-induced upwelling or a larger-scale cyclonic circulation.
- Surface heat loss to the atmosphere erodes the heat stored within a thin thermocline, eventually leading to fluid overturning in a series of narrow convective plumes (Fig. 12.9b); the whole convective region is referred to as a convective chimney.
- After the surface heat loss has ceased, convected waters within the chimney (Fig. 12.9c, shading) are denser than in the surrounding waters at a similar depth, inducing a cyclonic surface circulation around the dense water. This density contrast leads to a slantwise eddy exchange, where dense, cold waters spread away from

the convective site at depth and are replaced by lighter, warmer waters near the surface (Fig. 12.9d).

Next we consider examples of convection along the shelf and open ocean.

Cascading

In the shelf seas, the vertical extent of winter convection is restricted by the thickness of the water column. Surface heat loss leads to a larger density anomaly being formed over the shallower water column in the shelf seas, whereas a smaller density anomaly is formed in the open ocean where convection extends to a greater depth in the open ocean. The dense anomalies formed over the shallow shelf can eventually overflow down the slope (Fig. 12.10a), a process referred to as cascading.

Signatures of cascading have been identified in the Barents Sea in the Arctic Ocean (Fig. 12.10b). Dense water is formed along the shelf through the release of salt during ice freezing and becomes well mixed during winter (Fig. 12.10c). The cold dense water subsequently spreads along the slope into the interior (Fig. 12.10d), as detected during summer.

Deep convection

Convection extends to depths of several hundred metres over much of the North Atlantic in the mid and high latitudes (Section 7.1.4). Winter convection can extend to greater depths over scales of a few hundred kilometres whenever there is pronounced surface heat loss in a region of cyclonic flow. For example, over the Labrador Sea, profiling floats reveal convection reaching depths of more than 500 m and even greater than 800 m

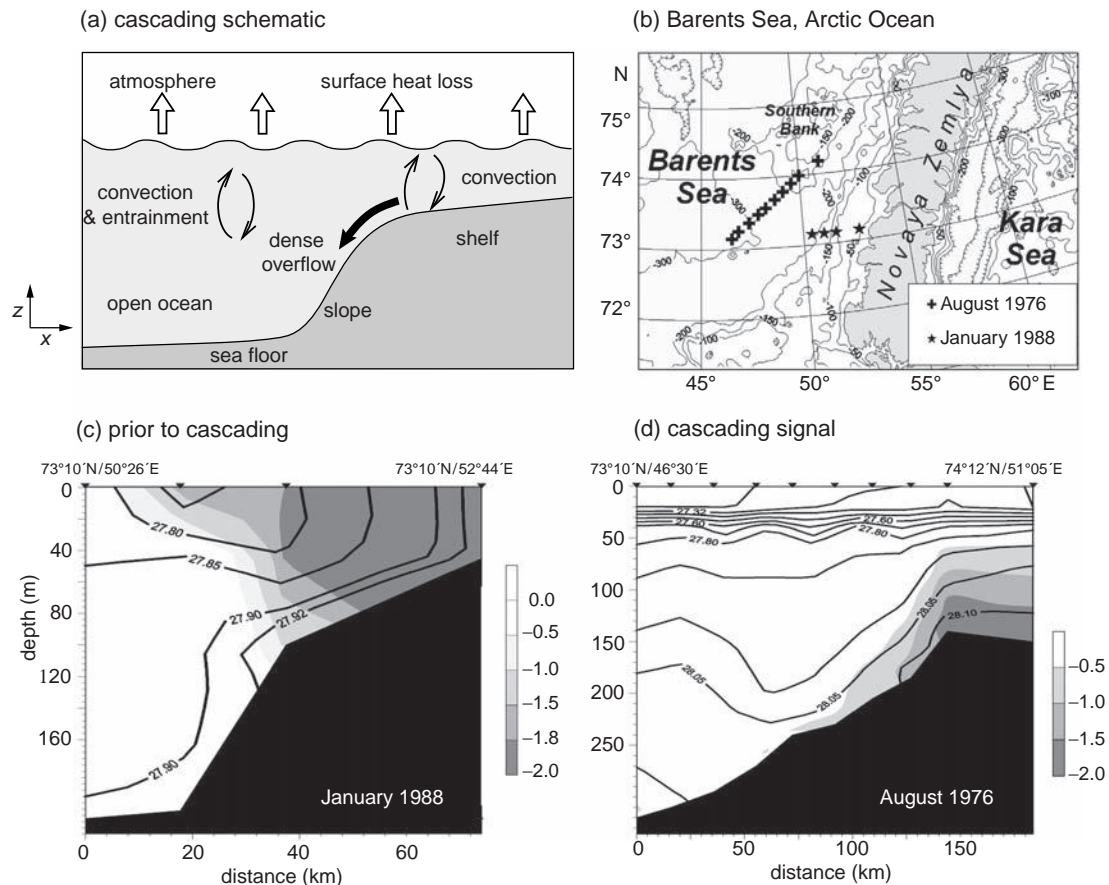


Figure 12.10 (a) A schematic figure of cascading and a case study in the Barents Sea in the Arctic Ocean; (b) map of the topography and two ship sections for January 1998, and August 1976; (c) density sections (cold water shaded) prior to cascading in January 1998, and (d) after cascading in August 1976. In (c), cascading is in its early stage, there is a pool of vertically nearly homogeneous water on the shallow shelf leading to a temperature front. In (d), cascading of dense water has occurred, driven by both temperature and salinity anomalies from the shelf, where the salinity is increased through brine release during ice formation. Courtesy of Grisha Shapiro; full details in Ivanov *et al.* (2004).

over its southwestern flank (Fig. 12.11a, circles and stars).

Deep convection forms a pool of nearly uniform properties with weak stratification, referred to as a mode water. The extent of the convection and the temperature of the convected waters (and resulting mode water) vary year on year according to the surface winter loss and the strength of the background stratification; see variations in θ for the mode waters in Fig. 12.11b,c.

How does dense water spread away from deep convection sites?

While deep convection is important in determining the properties of the local dense waters, there

is only a wider impact if these dense waters are able to disperse and spread over the rest of the basin.

Rotation inhibits the spreading of dense water in the open ocean after a day or so, since a cyclonic circulation is formed around the dense water (as in Fig. 12.11a, low pressure L). For dense water to spread away from the formation site requires this symmetry to be broken either by

- dense water spreading along topography via a boundary current; or
- the cyclonic circulation being disrupted by geostrophic eddies transferring dense water away from the formation site (Fig. 12.9c). A

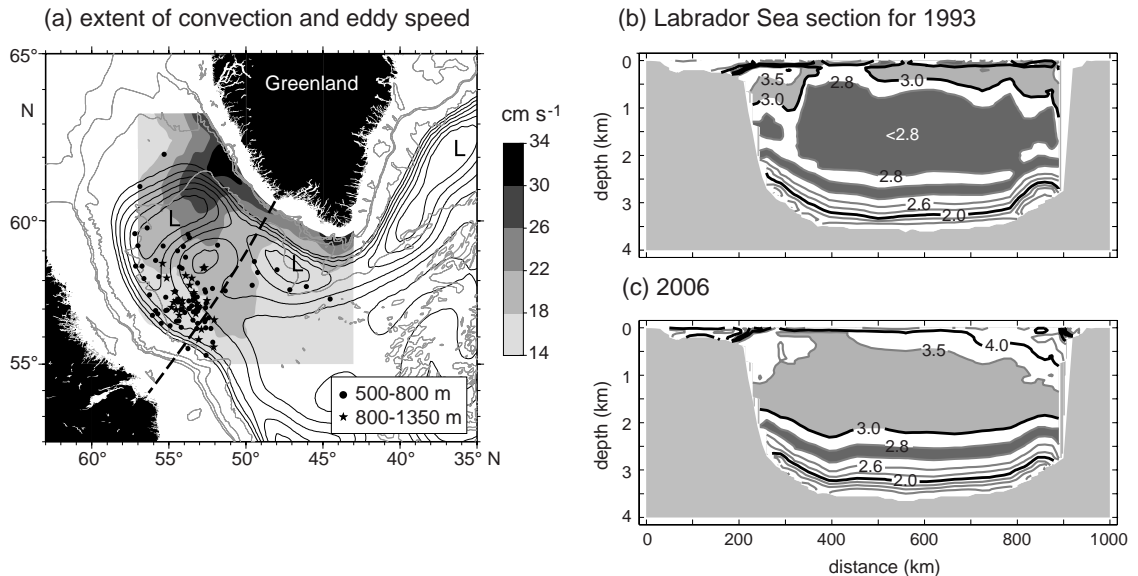


Figure 12.11 Deep convection in the Labrador Sea: (a) the extent of convection measured by profiling floats in winter 1997, circles for 500 to 800 m and stars for 800 to 1350 m, together with streamlines for the geostrophic flow at 700 m (contours, every 1 cm; low pressure indicated by L) and the distribution of surface eddy speed (cm s^{-1} , grey shade), and isobaths (1000 m, 2000 m and 3000 m); see Lavender et al. (2002) and Lilly et al. (2003), respectively. Sections of potential temperature (θ , $^{\circ}\text{C}$) through the Labrador Sea for (b) 1993, and (c) 2006 (along the dashed line in (a)). In (b), convection in the Labrador Sea extends to depths of 2000 m, forming a mode water with θ from $2.6\text{ }^{\circ}\text{C}$ to $2.8\text{ }^{\circ}\text{C}$ (dark shading) in 1993. In (c), following a series of mild winters, the mode water is instead formed with warmer properties with θ from $3.3\text{ }^{\circ}\text{C}$ to $3.5\text{ }^{\circ}\text{C}$ (light shading) in 2006; see Lazier et al. (2002) and Labrador Sea Monitoring Group (2007). Panel (a) courtesy of Bob Pickart and panels (b) and (c), courtesy of Ross Hendry.

possible signature of this eddy transfer is seen in the Labrador Sea, where the presence of eddies (Fig. 12.11a, dark shading) is possibly associated with a reduction in deep convection (Fig. 12.11a, circles, rather than stars), due to the eddy lateral transfer of heat partly offsetting the surface heat loss.

Signals of deep convection have often been assumed to be concomitant with a vigorous larger-scale overturning. However, this connection need not automatically hold, since overturning is probably associated with sinking of dense water along topographical boundaries, rather than within sites of deep convection; see idealised model investigations emphasising this distinction by Marotzke and Scott (1999) and Pickart and Spall (2007).

12.2.3 Mixing of dense water

Even when dense waters succeed in spreading from their formation sites, their wider impact

is affected by the mixing experienced during their journey. Next we consider two examples of enhanced mixing at an overflow across a submerged sill and a fracture zone in a topographical ridge.

Mixing at overflows

If dense water is supplied to a sub-basin with a submerged sill, then dense water accumulates behind this barrier until it spills over the edge; in much the same manner as water sloshes over the edge of a filled bath with a continually dripping tap. This spilling of dense water over a submerged sill is referred to as an overflow.

In the North Atlantic, dense waters form in the Nordic Seas, spread southward over the northern part of the basin, meeting a ridge running from Greenland to Iceland to Scotland, and then overflow at two sills; the Denmark Strait and the Faroe–Shetland Strait. Consider observations for the latter overflow in more detail: cold, dense water enters the Faroe–Shetland channel from the

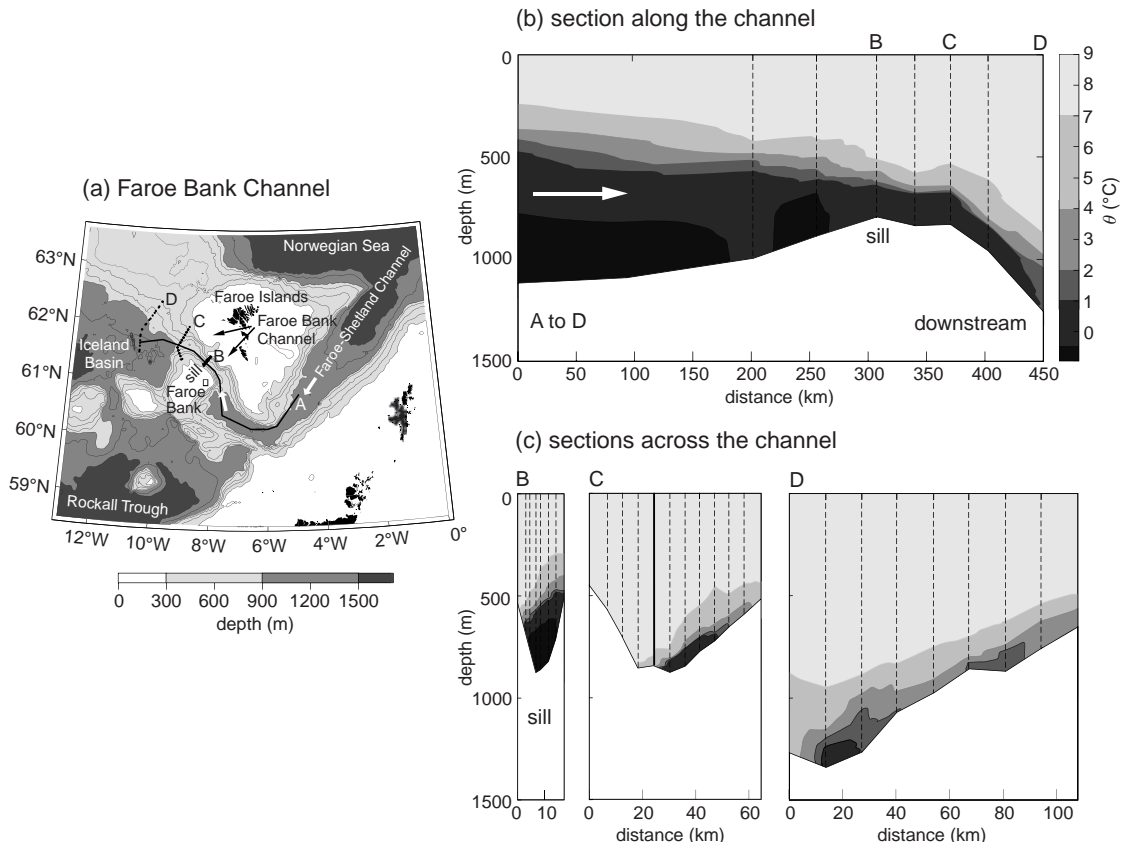


Figure 12.12 Faroe Bank Channel Overflow between Iceland and Scotland in the North Atlantic: (a) map of the sea-floor depth (m) and position of sections, and (b) potential temperature sections ($^{\circ}$ C) running along the channel (A to D) from the Nordic Seas (left) to the North Atlantic (right), and (c) sections across the channel at (B) the main sill, (C) and (D) downstream of the sill; dashed lines show position of stations. Note how there is a plume of cold water entering the channel from the Nordic Seas, which is present at the main sill, but has become diluted downstream of the overflow. Courtesy of Jim Price; further details, see Mauritzen *et al.* (2005).

north, spreads along the channel and overflows at the sill (Fig. 12.12a,b). At the narrow sill, very cold waters plunge down the slope and experience strong mixing. These overflow waters are progressively diluted with the background environment and become warmer and lighter (Fig. 12.12c, B to D).

Mixing in these overflow sites leads to a strong reordering of density classes. For example, at the Gibraltar Strait, the density of the salty water flowing out of the Mediterranean, $\sigma_{\theta} = 28.95 \text{ kg m}^{-3}$, greatly exceeds the density of bottom water in the North Atlantic, $\sigma_{\theta} = 27.95 \text{ kg m}^{-3}$, but mixing and dilution along the overflow leads to the salty water acquiring a more modest, intermediate density, $\sigma_{\theta} = 27.6 \text{ kg m}^{-3}$ (Price *et al.*, 1993). The modified warm, salty outflow from the Mediterranean then

spreads out at a depth of 1100 m over the North Atlantic.

Hence, bottom waters are not usually formed by surface waters with the maximum density, as might initially be expected, due to intense mixing experienced at overflows. Instead, bottom waters are made up of slightly less dense surface waters which experience less mixing and dilution as they pass from the surface to the sea floor (Price, 1992).

Mixing at fracture zones

Mixing is particularly pronounced in regions of rough topography, such as in fracture zones within topographical ridges.

For example, consider the northward spreading of fresh, cold bottom water originating from

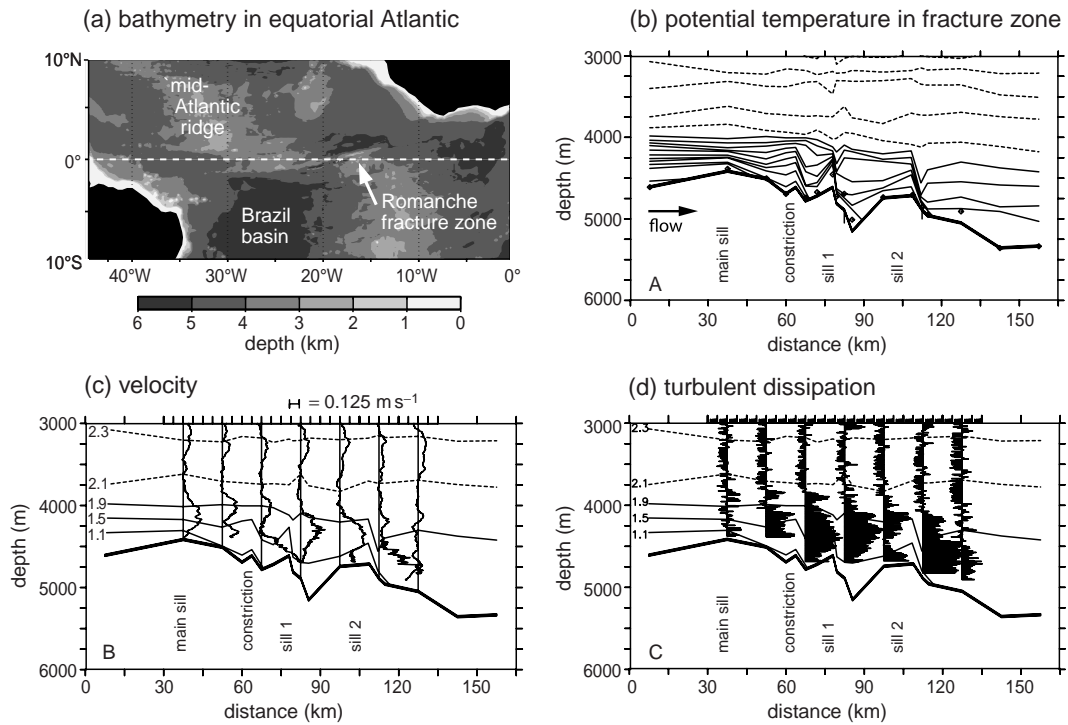


Figure 12.13 Mixing in the equatorial Atlantic: (a) map of bathymetry (shading in km) identifying the Romanche fracture zone just north of the equator (0.78°N , 13.42°W) and along channel sections through this fracture zone for (b) contours of potential temperature, θ (contours every 0.1°C , solid contours for $\leq 1.9^{\circ}\text{C}$ denoting Antarctic Bottom Water), (c) velocity profiles (m s^{-1}), and (d) turbulent kinetic energy dissipation (reference value of $10^{-10} \text{ W kg}^{-1}$ with a log profile). There is enhanced mixing and grounding of θ contours downstream of the sills and constrictions in the fracture zone. Courtesy of Kurt Polzin; further details, see Polzin et al. (1996).

the Southern Ocean, the Antarctic Bottom Water, into the Atlantic basin. Bottom waters warmer than $\sim 0.9^{\circ}\text{C}$ pass through a narrow fracture zone in the mid-Atlantic ridge close to the equator (Fig. 12.13a), while colder waters remain blocked by the ridge. The bottom waters passing through the fracture zone experience pronounced mixing (Fig. 12.13b-d). Turbulence mixes the bottom water over a layer 500 m above the sea floor (Fig. 12.13b). The mixing with the overlying, slightly warmer and lighter waters warms the bottom waters by $\sim 0.6^{\circ}\text{C}$ as they pass through the fracture zone.

Hence, fracture zones in topographical barriers effectively select which deep and bottom waters pass from one basin to another. The localised mixing acts to warm and lighten the bottom waters, creating sharp contrasts in properties upstream and downstream of the mixing site.

12.2.4 Spreading of dense water

Following this view of how dense waters are formed and partially mixed, we now consider observational signals of two different dense waters spreading southward over the North Atlantic: an intermediate water mass, the Labrador Sea Water, formed in a region of deep convection (Fig. 12.11); and a deep water mass, the Denmark Strait Overflow Water, formed through mixing at an overflow. Based on compilations of observations in the late twentieth century, vertically integrated inventories of the transient tracer CFC-11 have been estimated for water masses at different depths in the Atlantic (Smethie and Fine, 2001). For both these dense waters, there are higher concentrations of CFC-11 running along the western side of the basin and extending to the equator (Fig. 12.14a,b). This enhanced spreading of water masses along the western boundary is

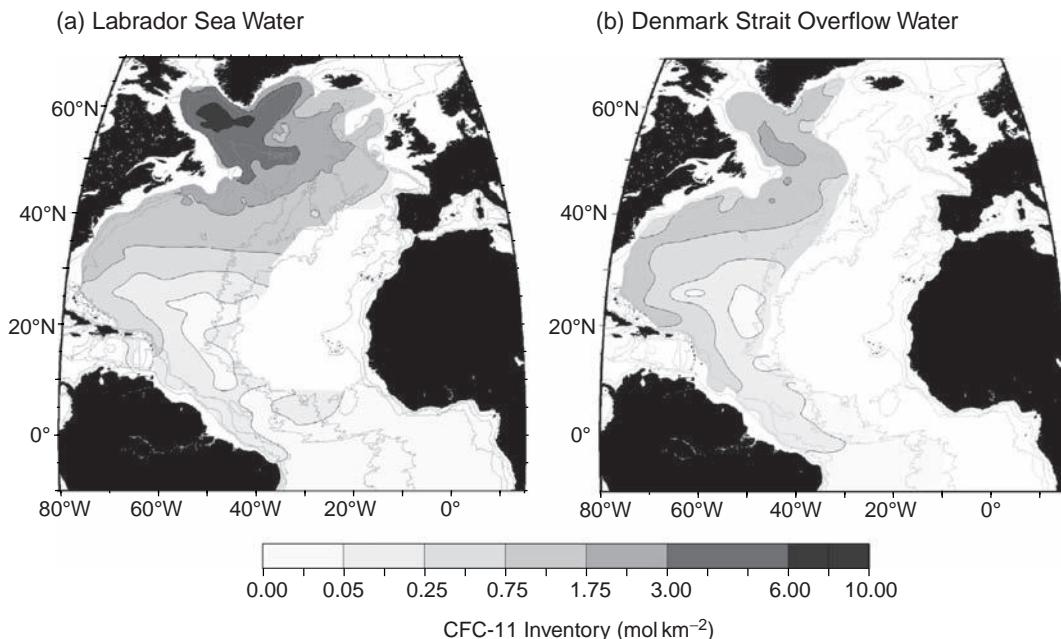


Figure 12.14 Map of CFC-11 inventory (mol km^{-2}) integrated over the thickness of a water-mass layer in the subtropical western North Atlantic for (a) central Labrador Sea Water, and (b) Denmark Strait Overflow Water. In the Labrador Sea, the central Labrador Sea Water extends to depths of from 1 to 2 km, while the Denmark Strait Overflow Water lies typically 3 to 3.5 km. Redrawn from Smethie and Fine (2001).

also revealed in earlier tracer maps, such as first provided by Wušt (1935).

Hence, transient tracers and water masses preferentially spread meridionally along the western side of the basin, rather than being confined to their formation sites. How might this spreading be achieved? Now we consider two of the possible mechanisms.

Deep western boundary currents

There is a deep western boundary current running alongside the continental slope, ranging in depth from typically 1500 m to 4000 m. The deep boundary current flows southward with speeds reaching 20 cm s^{-1} (Fig. 12.15, black arrows), passing beneath the Gulf Stream flowing in the opposite direction off Cape Hatteras with speeds of more than 1 m s^{-1} (Fig. 12.15, grey arrows).

The deep boundary current can then partly account for the southward tongue of CFC-11 running along the western side of the basin.

Over the globe, there is a network of deep western boundary currents, each providing a conduit of dense waters and accompanying tracers.

The deep western boundary currents do not vary in strength in a systematic manner according to their high-latitude sources: their transport can strengthen or weaken downstream according to whether there are local recirculations connecting the boundary current with the local interior (Hogg, 2001).

Tracer spreading by eddy stirring and local recirculations

The presence of deep boundary currents might not be the whole story. For example, at 40°N , the highest CFC-11 concentrations within the intermediate water, Labrador Sea Water, occur offshore around 50°W (Fig. 12.14a), rather than along the western boundary, suggesting that other transport processes also play a role in transferring the tracer.

To reveal the dominant transport pathways, subsurface floats have been released in the deep western boundary current in the Labrador Sea at depths of 700 m and 1500 m (Fig. 12.16; Bower *et al.*, 2009), which led to a surprising result. Most of these floats spread either southward into

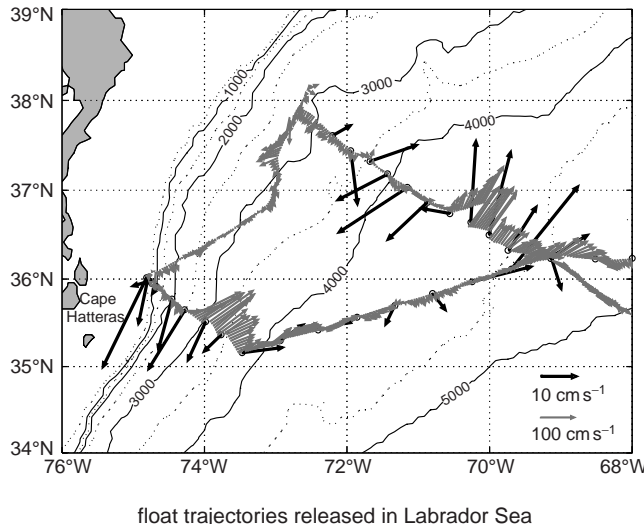


Figure 12.15 Velocity vectors at the near surface at 130 m (grey, 100 cm s^{-1}) and just off the sea floor (black, 10 cm s^{-1}) in the northwest Atlantic along sections at 35.5°N and 37°N , together with bathymetry (contours in m). The deep western boundary current flows southwestward and passes beneath the Gulf Stream off Cape Hatteras. Redrawn from Williams *et al.* (2011); further details see McDonagh *et al.* (2010).

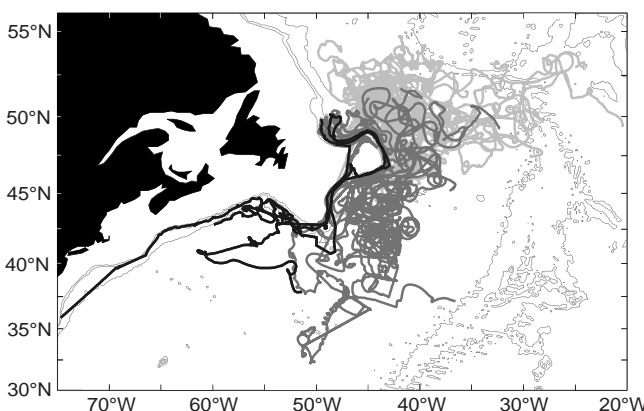


Figure 12.16 Spreading of Lagrangian floats released in the deep western boundary current in the Labrador Sea. 32 floats were launched near Orphan Knoll ($49.5^\circ\text{W}, 49.8^\circ\text{N}$ to $47.8^\circ\text{W}, 50.4^\circ\text{N}$) from July 2003 to July 2007: 14 of the floats were launched near 1500 m depth and 18 of the floats were launched near 700 m depth. Only one of these floats was swept south in the deep western boundary current (black). Instead most floats either spread southward to the east of the continental slope (dark grey) or recirculated over the subpolar gyre (light grey). Courtesy of Susan Lozier; further details see Bower *et al.* (2009) and wider discussion, see Lozier (2010).

the interior of the western basin or recirculated within the subpolar gyre (Fig. 12.16, light and dark grey), rather than being swept southward within the deep western boundary current running along the continental slope (Fig. 12.16, black trajectory). The float trajectories were complex and interwoven, suggesting that they spread predominantly by eddy flows and local recirculations. Dense water masses and tracers are assumed to spread in a similar manner to the floats, so that their spreading over an entire basin (as in Fig. 12.14) involves a combination of deep boundary transport, eddy stirring and local recirculations.

The relative importance of these different transport pathways probably varies with the domain, sometimes the imprint of the deep western boundary current dominates, while in other regions, eddy stirring and local recirculations hold sway.

12.2.5 Meridional overturning and its variability

The spreading of dense water can collectively be viewed in terms of a meridional overturning represented by a transport streamfunction, ψ ($\text{m}^3 \text{s}^{-1}$), defined by the northward velocity $v(x, y, z, t)$ integrated with longitude and depth across the basin,

$$\psi(y, z, t) = \int_z^0 \int_{x_w}^{x_e} v(x, y, z, t) dx dz, \quad (12.1)$$

where the integration limits, x_w and x_e , denote the western and eastern boundaries. For the Atlantic, the overturning transport varies from 12 to 18 Sv based upon hydrographic data and inverse calculations (Lumpkin and Speer, 2007). There is a northward transport of light waters extending to a depth of 1300 m and a southward return transport of dense water typically between 1300 m and 4000 m; for example, see ψ in Fig. 12.17a

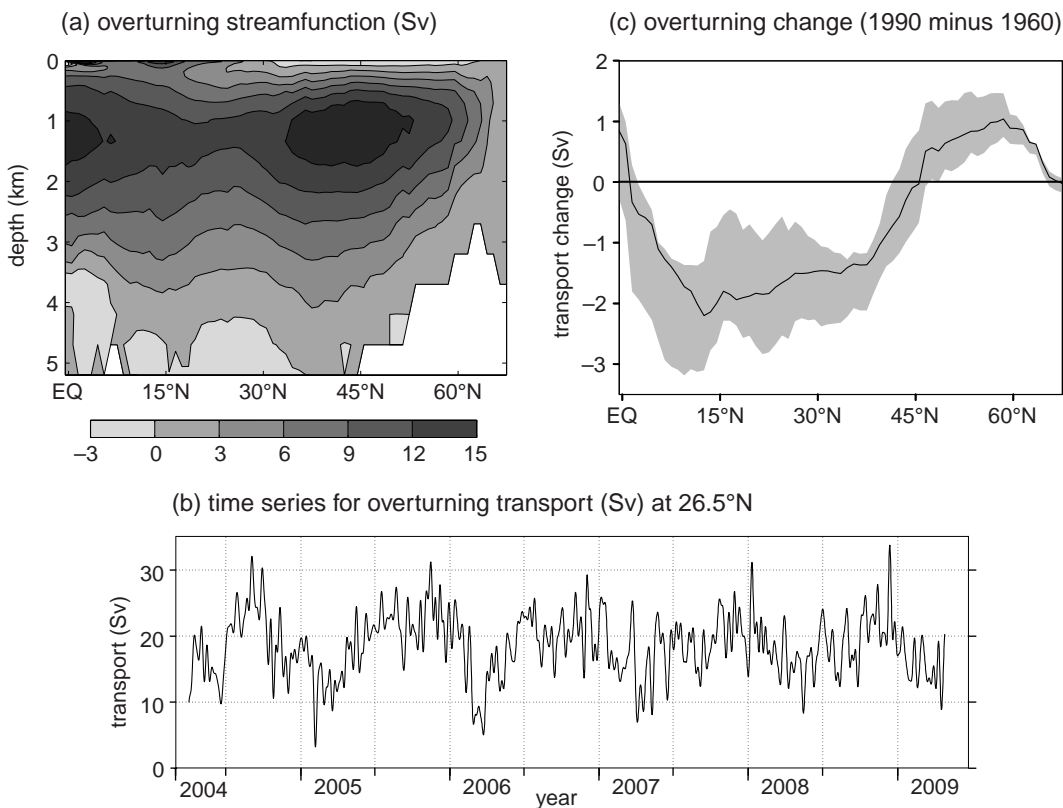


Figure 12.17 Meridional overturning in the North Atlantic: (a) overturning streamfunction (Sv) versus latitude, light water moving northward and dense water moving southward, diagnosed from a 50-year average of temperature and salinity data combined with a circulation model; (b) measurements of the overturning (Sv) across 26.5°N from 5 years of data from the RAPID array; (c) change in the overturning transport (Sv) between two 20-year periods, 1980 to 2000 minus 1950 to 1970, versus latitude, diagnosed as in (a) with shading representing uncertainty from ensemble calculations. Panels (a) and (c) from Lozier *et al.* (2010), and panel (b) courtesy of Stuart Cunningham from Kanzow *et al.* (2010).

diagnosed from historical data. Associated with the meridional overturning, there is a northward ocean heat flux reaching 1.24 ± 0.25 PW at 24°N over the Atlantic.

An intense monitoring programme at 26.5°N has revealed significant variability in the meridional overturning in Fig. 12.17b: the mean over 48 months is 18.7 ± 2.1 Sv with root-mean-square fluctuations reaching 4.8 Sv (Cunningham *et al.*, 2007; Kanzow *et al.*, 2010). There is a pronounced seasonality, reaching 6.7 Sv with a maximum strength in autumn and a minimum in spring.

At the same time, the overturning changes need not extend over the entire basin, but can be gyre specific; the meridional overturning diagnosed between two 20-year periods, 1980–2000

and 1950–1970, reveals a slight weakening of -1.5 ± 1 Sv over the subtropical gyre and a slight strengthening of $+0.8 \pm 0.5$ Sv over the subpolar gyre (Fig. 12.17c; Lozier *et al.*, 2010). These overturning changes are probably reversing in time, rather than reflecting any longer-term signal of climate change.

Longer-term possible overturning changes

Given that so much of the heat transport is associated with the overturning in the North Atlantic, there is widespread interest in whether the overturning has altered in the past, especially during glacial periods. Any inferences of the past overturning have to be made via proxy data and caution needs to be applied as to the robustness of the reconstructions. While noting this

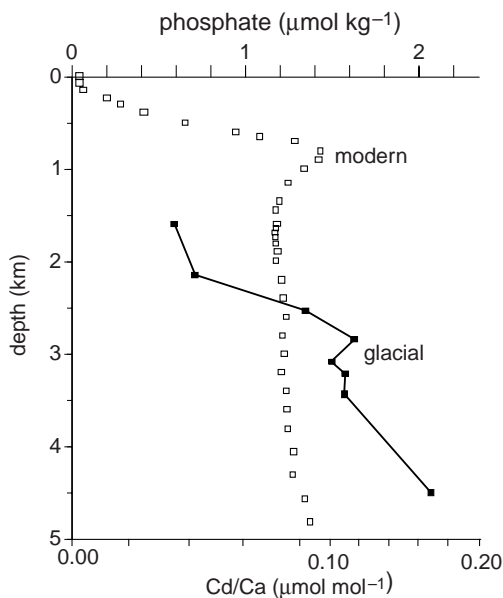


Figure 12.18 A phosphate profile representative of the present-day, western North Atlantic compared with a glacial profile reconstructed from Cd/Ca ratios of benthic foraminifera in sediment cores (from Boyle and Keigwin, 1987). The glacial reconstruction assumes that the Cd–P relationship of the glacial oceans was similar to the present day. The reconstruction suggests a significant increase in the vertical gradient in phosphate over the North Atlantic during the last glacial period.

caveat, the phosphate profile inferred for the last glacial maximum has a much larger vertical gradient with higher concentrations in bottom waters (Fig. 12.18; Boyle and Keigwin, 1987). These changes might plausibly be due to an expansion of dense, nutrient-rich waters from the Southern Ocean and a reduction or lightening in the dense, nutrient-poor waters spreading from the North Atlantic during the last glacial.

How this possible change in water-mass distribution and overturning is controlled is unclear. Based on simple box models, we expect that a key factor is the surface density contrasts between the high latitudes of the North Atlantic and Southern Ocean; see Box 12.1 and the review of Marotzke (2000).

12.2.6 Why is the formation of deep water important for the carbon cycle?

The deep and bottom waters of the ocean form very large reservoirs of carbon and nutrients. The

nature and scale of the deep water formation processes are very important in setting the concentrations of carbon and nutrients in the deep waters and the partitioning of carbon between the atmosphere and ocean.

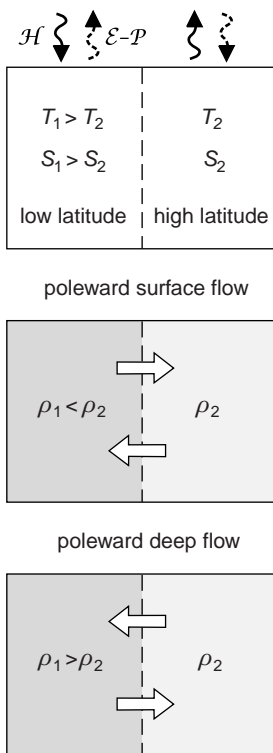
The physical transfer of carbon in dense waters

Carbon is more soluble in cold waters. As high latitude waters cool and become more dense, the solubility of carbon dioxide increases, promoting uptake from the atmosphere. The equilibration of mixed-layer carbon with the atmosphere takes more than year or so in regions of vigorous convection; recently cooled waters are likely to be subducted before fully equilibrating at the new, higher solubility. Thus the preformed carbon concentration which is physically transferred from the surface to the deep ocean depends on the extent of equilibration which, in turn, reflects the small physical and short temporal scales of processes involved in dense water formation.

The biological transfer of carbon and extent of nutrient utilisation

The biologically driven storage of carbon in the ocean is affected by the extent that nutrients are biologically utilised and exported in surface waters during the conversion to dense waters. Nutrient concentrations in the deep waters have preformed and regenerated contributions (Section 11.3). The preformed nutrients were physically transferred from the surface to the deep ocean, while the regenerated nutrients were transferred as sinking or advected organic matter, which was subsequently respiration back to inorganic form. The regenerated nutrients are associated with regenerated carbon, also transferred in organic form, which enhances the ocean's total storage of carbon. Presently, a little less than half of the deep nutrients in the ocean are regenerated. To enhance the regenerated carbon inventory in the ocean requires an enhancement of the regenerated nutrient inventory which, in turn, demands a reduction in the preformed nutrient concentration.

During winter, deep convection vertically homogenises the water column, forming a mode water, and mixes nutrients to the surface. During



Box 12.1 | Box-model solutions for overturning

In principle, the sign of the overturning can vary according to the contrasts in surface temperature and freshwater forcing. Following Stommel (1961), consider the ocean as made up of two well-mixed boxes of equal volume, a low-latitude box with temperature T_1 and salinity S_1 , and a high-latitude box with T_2 and S_2 , such that $T_1 > T_2$ and $S_1 > S_2$ from a surface heat flux, \mathcal{H} , and freshwater flux, $\mathcal{E} - \mathcal{P}$. Assume that both boxes are simply connected by a surface flow and an opposing deep flow, and the flow direction is determined by their density differences.

If the temperature contrast determines the sign of the density contrast, then there are denser waters at high latitudes, $\rho_1 < \rho_2$, implying a poleward surface flow and an opposing equatorward deep flow, consistent with the present-day Atlantic.

On the other hand, if the salinity contrast determines the sign of the density contrast, the opposite response occurs: the low-latitude box becomes denser than the high-latitude box, $\rho_1 > \rho_2$, implying an equatorward surface flow and a poleward deep flow. Hence, there are two stable solutions: a thermally dominated poleward near-surface flow or a salinity-dominated equatorward near-surface flow. Aspects of this two-box solution are implausible, though: the lack of any gyre dynamics and the deep ocean filling up with warm water in the salinity mode.

Following Rooth (1982), now consider a three-box model that arguably has more relevance. At the surface, assume that a tropical box is separately connected to two boxes, northern and southern high-latitude boxes, while at depth, these northern and southern boxes are directly connected. If temperature is assumed to be symmetric about the equator, then the bottom flow is determined by which high-latitude box is saltier: a saltier northern box implies a southward bottom flow, while a saltier southern box implies a northward bottom flow; see Marotzke (2000) for details of the solutions. Again there are two stable solutions: a bottom flow spreading either from the northern box or the southern box. Proxy data suggests that the strength of dense water spreading from the North Atlantic and Southern Ocean has varied in the past, as implied by Fig. 12.18, possibly in accord with the arguments of the three-box model.

the spring, these surface waters become lighter and the water column restratifies through surface heating and eddy transfers. When convection is inhibited, light limitation is relieved and biological consumption of surface nutrients proceeds rapidly. However, most of the nutrients held in the mode water remain beneath the euphotic zone, so that they are not consumed during the following summer and may be transported directly into the ocean interior. Hence, by its nature, deep convection at high latitudes tends to favour high concentrations of preformed nutrients and low nutrient

utilisation, preventing the biological sequestration of carbon in the ocean from achieving its theoretical maximum.

Less clear is the extent of nutrient utilisation in regions where dense waters are formed by cascading along the shelf seas and continental margins. Observations of nutrient concentrations in regions of cascades are still very sparse indeed. Perhaps in shallow margins, light limitation is less of an issue, apart from in the polar night, so more efficient nutrient utilisation may be possible compared with deep convection sites.

12.2.7 Summary

Dense waters are formed at the surface through cooling by the overlying atmosphere or, in polar regions, by cooling from ice or an increase in salinity during freezing of ice. Dense waters are redistributed vertically through convection and then spread away from their formation sites by western boundary currents running alongside topography, as well as by local recirculations and transfers by the time-varying eddy circulation.

Mixing strongly modifies the properties of the dense water, particularly at overflows and fracture zones, affecting the vertical ordering of dense waters and the communication of bottom waters between sub-basins separated by topographical ridges.

The global ocean storage of carbon is strongly affected by how carbon-rich surface waters are physically transferred into the deep ocean and the efficiency of the biological utilisation of surface nutrients during dense water formation.

Following this observational view of the mechanisms affecting the spreading of dense water, we now turn to theoretical views of how dense water circulates.

12.3 How does the deep ocean circulate?

We now consider a theoretical model of the abyssal circulation as first proposed by Stommel (1958), emphasising how the deep flow is affected by the Earth's rotation, and then consider the modifying role of topography.

12.3.1 Idealised abyssal model

Stommel set out a conceptual view of the abyssal circulation based on the following assumptions:

- Cold, dense water is formed in a few localised, high-latitude sites, including the northern North Atlantic and Southern Ocean, then sinks and spreads at depth over the globe.
- Away from these formation sites, cold water is gradually heated and converted to warmer water. This heating is assumed to occur uniformly over the domain, a downward diffusion

of heat locally balancing an upwelling of cold water (Fig. 12.19a),

$$w \frac{\partial T}{\partial z} = \frac{\partial}{\partial z} \left(\kappa \frac{\partial T}{\partial z} \right), \quad (12.2)$$

where κ is the vertical diffusivity of heat ($\text{m}^2 \text{s}^{-1}$) and $\kappa \partial T / \partial z$ a vertical diffusive flux of temperature ($\text{m s}^{-1} \text{K}$).

- To infer the circulation, Stommel then assumed a linear vorticity balance (8.10), where a stretching of a water column leads to a poleward flow,

$$\beta v = f \frac{\partial w}{\partial z}, \quad (12.3)$$

where $\beta = df/dy > 0$; the units of each side are $(\text{m}^{-1} \text{s}^{-1}) (\text{m s}^{-1})$ and $(\text{s}^{-1}) (\text{m s}^{-1}) (\text{m}^{-1})$, so s^{-2} . Over the layer of cold water, there is a vertical upwelling, $w > 0$, at the top of the layer and taking $w = 0$ for a flat sea floor leads to a vertical divergence, $\partial w / \partial z > 0$, which implies a poleward flow, $v > 0$, from (12.3). At first sight, this result is counterintuitive: cold water is predicted to move away from the equator and towards the sources of cold water in the high latitudes (Fig. 12.19b).

- Rather than discard the solution as implausible, Stommel made a brilliant intuitive leap to assume that the interior circulation was sustained by a network of deep boundary currents (Fig. 12.19b,c). He chose the boundary currents to be on the western side of the basin based upon the vorticity arguments applied previously for the gyre circulations (Section 8.3).

This theoretical prediction of a deep boundary current was originally taken as being vindicated by subsurface floats spreading southward along the western boundary; in hindsight, this agreement was rather fortuitous given the eddy stirring seen in Fig. 12.16. All the same, a range of hydrographic and tracer measurements have subsequently confirmed the presence of the deep western boundary currents (such as illustrated in Fig. 12.15).

These model predictions were applied over the global ocean (Stommel and Arons, 1960) and supported by rotating tank, laboratory experiments (Stommel *et al.*, 1958). Given this conceptual

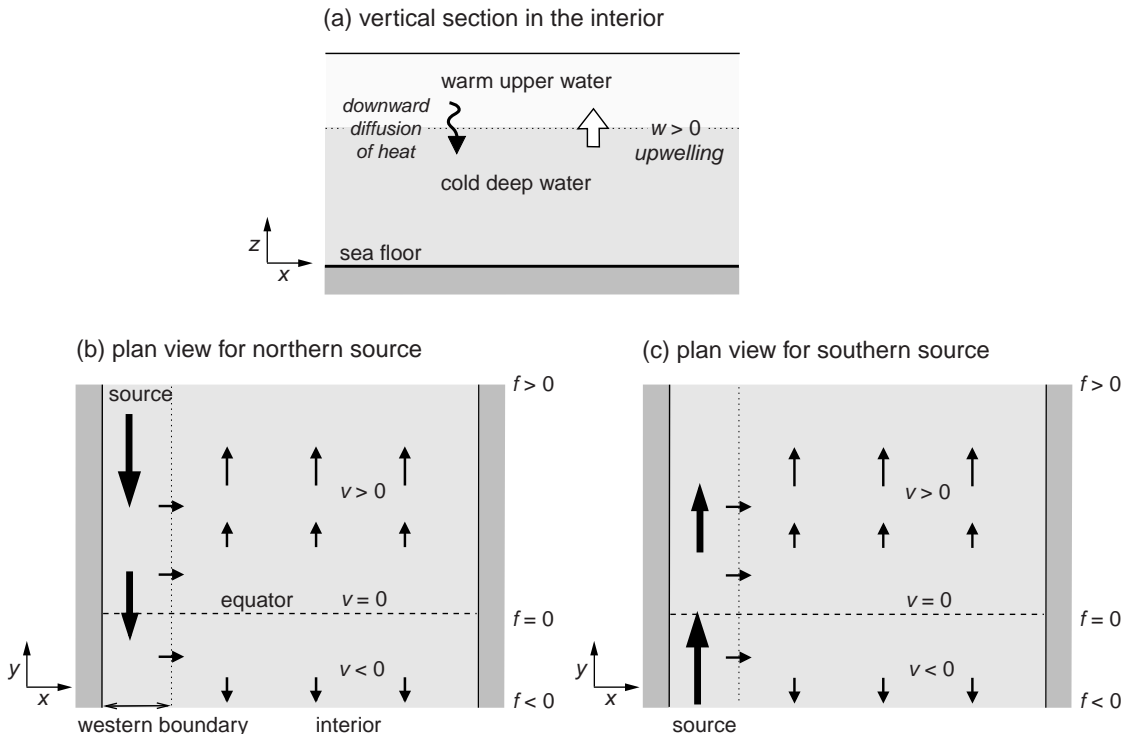


Figure 12.19 A schematic figure for the Stommel and Arons (1960) model of the deep circulation: (a) a vertical section depicting a layer of warm water overlying a layer of cold water. A downward diffusion of heat is assumed to balance an upwelling of cold water, which leads to $\partial w / \partial z > 0$ over the layer of cold water; plan view for the deep circulation of cold water with either (b) a northern or (c) a southern source of cold, dense water. The large-scale vorticity balance, $\beta v = f \partial w / \partial z$, implies that there is a poleward interior flow, which strengthens with f . The poleward flow is assumed to be supplied via a deep western boundary current, which gradually weakens from its source region.

breakthrough, next we consider the strengths and weaknesses of the model.

Strengths and weaknesses of the abyssal model

The Stommel model provided an inspired prediction of deep western boundary currents, theory preceding observational confirmation. However, beyond this conceptual advance, the model has turned out to have limitations. There has not been any observational support for the predicted interior flows, directed poleward on either side of the equator; when float studies were applied in the interior, the float trajectories revealed the mesoscale eddy field. The strength of the deep western boundary currents were also not reliably predicted, in that their strength does not progressively weaken from the high-latitude source

regions, but instead is strongly affected by local recirculations (Hogg, 2001).

So what are the limitations of the Stommel model?

- At first sight, representing the deep ocean by a single moving layer of fluid of uniform thickness is implausible, where the velocity variations are not connected to the thickness of the layer. This weakness can easily be overcome by considering a single moving deep layer of constant density with variable thickness, as applied by Speer and McCartney (1992).
- The deep ocean contains water masses spreading in opposing directions with depth, rather than a single uniform layer. However, the Stommel model could still be viewed as being relevant for the depth-integrated movement of these combined layers.

- More significantly, the mixing is not spatially uniform and instead is much more intense in overflows (Fig. 12.12), in fracture zones (Fig. 12.13) and where flow goes over rough topography (see later Fig. 12.24).
- Probably most importantly of all, the sea floor cannot be assumed to be flat and variations in topography strongly affect the pattern of the deep circulation.

Given these reservations, we next consider the effect of topography in modifying the path of the circulation.

12.3.2 Effect of topography

To understand how the flow pattern is affected by topography, we now consider the flow in an idealised laboratory experiment, then the effect of the continental slope and, finally, revisit the problem of how dense water spreads within a basin.

Steering by topography

When flow encounters a bump, the fluid can either go around or over the bump. While both options occur in everyday situations, rotation constrains the response for flows lasting a day or longer; see Box 12.2.

To illustrate this rotational control, consider a laboratory experiment where a submerged obstacle is placed in a spinning tank of water (Fig. 12.20a). The water is circulating relative to the obstacle and the water can either flow around or over it. To see which response occurs, small pieces of paper were placed on the surface and tracked (Fig. 12.20b): the particles were first aligned in a formation where their paths were expected to pass over the obstacle; instead most particles moved aside of the submerged obstacle (although one particle just passed over the edge of the obstacle). Hence, the submerged obstacle acted as a barrier to the overlying flow (Fig. 12.20c).

Now we consider how relevant this laboratory example and the accompanying theory (Box 12.2) is for the ocean: we first consider the effect of the topographical slope in shallow water and, second, a numerical experiment for the deep Pacific.

Coastal example of topographical control: the slope current

In the coastal ocean, there is a strong current running along bathymetric contours, referred to as a slope current, separating the shallow shelf and open ocean (Fig. 12.21a). For example, warm surface waters spreading northeastward (as part of the North Atlantic Drift current) do not pass onto the shallow shelf around the UK, but instead are deflected along the continental slope (Fig. 12.21b). The slope current is observed to be preferentially directed along the bathymetric contours (Fig. 12.21c). The presence of this slope current is in accord with the prediction that currents preferentially move around submerged obstacles, rather than over them when there is weak stratification (Box 12.2).

Abyssal model with topography

Now we return to the deep ocean and the balances used in the Stommel model, but include variations in topography. The interior flow again satisfies the linear vorticity balance (12.3): a vertical stretching is linked to a poleward flow. Integrating over the thickness of the cold layer relates the meridional flow to the relative size of the upwelling velocity at the top of the layer, w_t , and the sea floor, w_b (Fig. 12.22a; see Box 12.3):

$$\beta v = f(w_t - w_b)/h, \quad (12.4)$$

where h is the thickness of the layer. The flow is directed poleward when there is vertical stretching, $w_t > w_b$, and equatorward when there is vertical convergence, $w_t < w_b$.

Now consider the spreading of bottom water in two idealised basin experiments: either for a flat sea floor or using topography for the North Pacific. For the basin with a flat sea floor, a deep western boundary current sustains a poleward flow over the basin interior (Fig. 12.22b), in accord with the Stommel model.

For the basin with realistic topography, the bottom flow is strongly steered by the topography moving around submerged obstacles (Fig. 12.22c) and there is hardly any resemblance with the idealised flat-bottom case.

Hence, the inclusion of topography fundamentally alters the deep circulation, the topography

Box 12.2 | Does fluid move over or around a bump?

Assume that ocean currents lasting a few days are geostrophic, where the flow is directed along pressure contours,

$$u = -\frac{1}{\rho_0 f} \frac{\partial P}{\partial y} \quad \text{and} \quad v = \frac{1}{\rho_0 f} \frac{\partial P}{\partial x}, \quad (12.5)$$

and volume conservation applies, such that

$$\frac{\partial u}{\partial x} + \frac{\partial v}{\partial y} + \frac{\partial w}{\partial z} = 0. \quad (12.6)$$

Substituting (12.5) into (12.6) gives

$$\frac{1}{\rho_0} \left(\frac{\partial}{\partial x} \left(-\frac{1}{f} \frac{\partial P}{\partial y} \right) + \frac{\partial}{\partial y} \left(\frac{1}{f} \frac{\partial P}{\partial x} \right) \right) + \frac{\partial w}{\partial z} = 0. \quad (12.7)$$

For relatively small horizontal scales where f does not significantly vary, the first two terms in (12.7) cancel and the geostrophic flow becomes horizontally non-divergent,

$$\frac{\partial u}{\partial x} + \frac{\partial v}{\partial y} \approx 0, \quad (12.8)$$

implying that the vertical velocity satisfies,

$$\frac{\partial w}{\partial z} \approx 0, \quad (12.9)$$

referred to as the Taylor-Proudman constraint, named after Geoffrey Taylor (1886–1975) and Joseph Proudman (1888–1975).

To understand the importance of (12.9), consider the effect of a bump on the flow: when a horizontal flow hits a bump, fluid is upwelled with a vertical velocity given by

$$w_b = - \left(u_b \frac{\partial H}{\partial x} + v_b \frac{\partial H}{\partial y} \right), \quad (12.10)$$

where subscript b denotes a velocity on the bottom and H is the thickness of the water column. If, at the same time, w is close to zero at the sea surface, then the constraint (12.9) requires that w_b along the sea floor is likewise close to zero, which in turn requires either (i) the bottom horizontal velocity is zero ($\mathbf{u}_b = 0$), or (ii) the bottom flow is parallel to bathymetry ($\mathbf{u}_b \cdot \nabla H = 0$) from (12.10).

Therefore, if there is weak stratification and the flow only weakly varies with depth, then any surface flow is required to go around a bump rather than over it. However, if there is strong stratification and the flow strongly varies with depth, then the surface flow can pass over the bump (as the bottom flow can vanish and $w_b = 0$).

acting to steer the flow around submerged obstacles (as in Box 12.2).

12.3.3 Effect of eddy stirring

While the effects of topography are the primary limitation of the Stommel model, there are other

difficulties. The interior circulation at depth is dominated by eddies, which mask any weak background flow.

The eddies can also have a systematic effect on the deep flow: eddies transfer momentum from the surface to the deep ocean during baroclinic

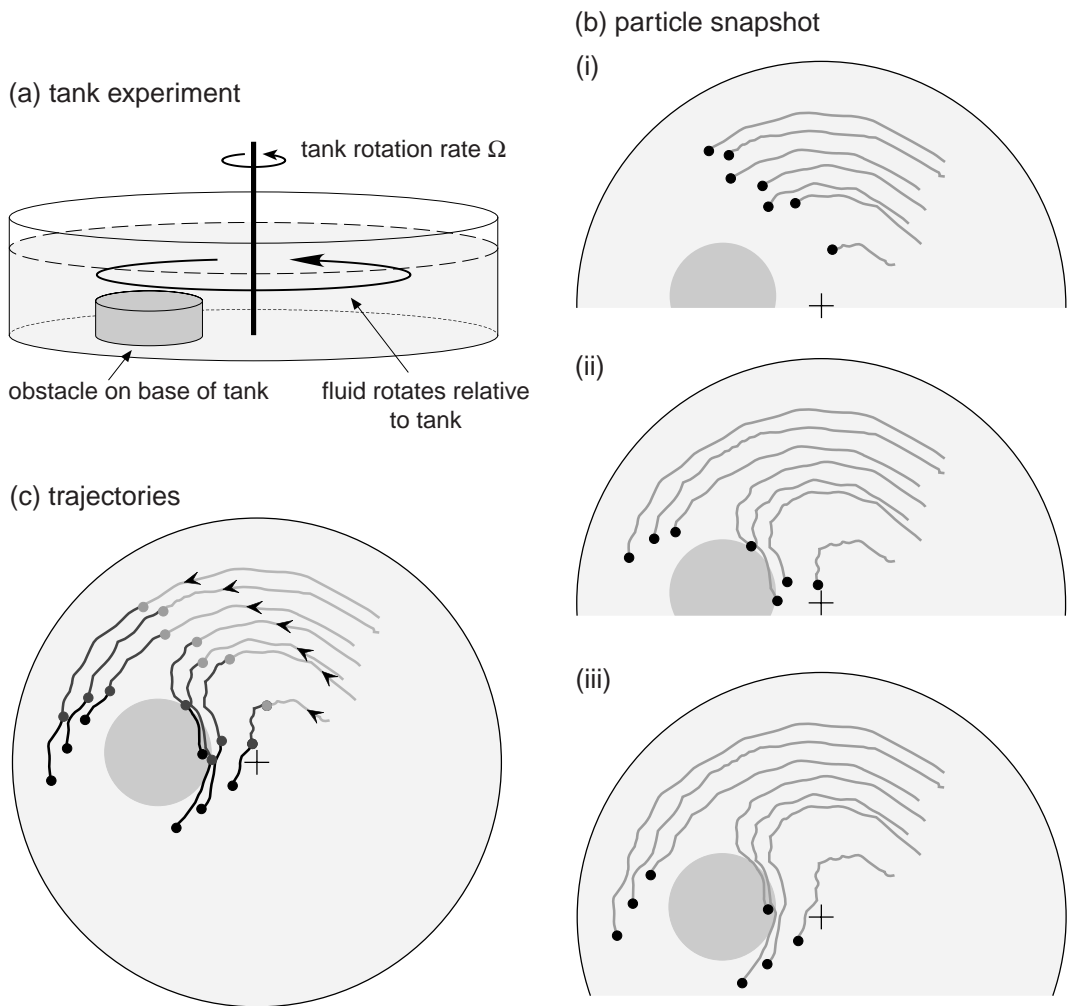


Figure 12.20 A laboratory experiment illustrating the effect of a submerged obstacle on the rotating flow: (a) a schematic view of the apparatus; (b) three snapshots of the position of particles (black) together with their past trajectories (grey lines) and the submerged obstacle (grey); and (c) a composite view of the trajectories (figure drawn by K. Lancaster). Experiment conducted with John Marshall at MIT; for an explanation of ocean dynamics drawing on laboratory experiments and theory, see Marshall and Plumb (2007).

instability. This transfer can help spin up deep recirculations, as seen in idealised eddy-resolving model experiments (Holland and Rhines, 1980).

In partial support of this view, neutrally buoyant floats released in the Labrador Sea spread southward via an interior pathway with spiralling trajectories (Fig. 12.16). This float-spreading pattern is coincident with observations of nearly uniform potential vorticity in intermediate waters (Lozier, 1997), a signal expected from eddy stirring of tracers within closed geostrophic streamlines; see Section 9.3.3.

12.3.4 Summary

The deep circulation is constrained by both rotation and topography. Stommel constructed a model predicting the existence of deep western boundary currents, based upon a background diapycnal mixing sustaining an upwelling of cold water and leading to a poleward interior flow. While there are these deep western boundary currents, there is also a much more complicated response: deep currents are also strongly steered by the topography; there are strong spatial variations in mixing affecting the flow; and

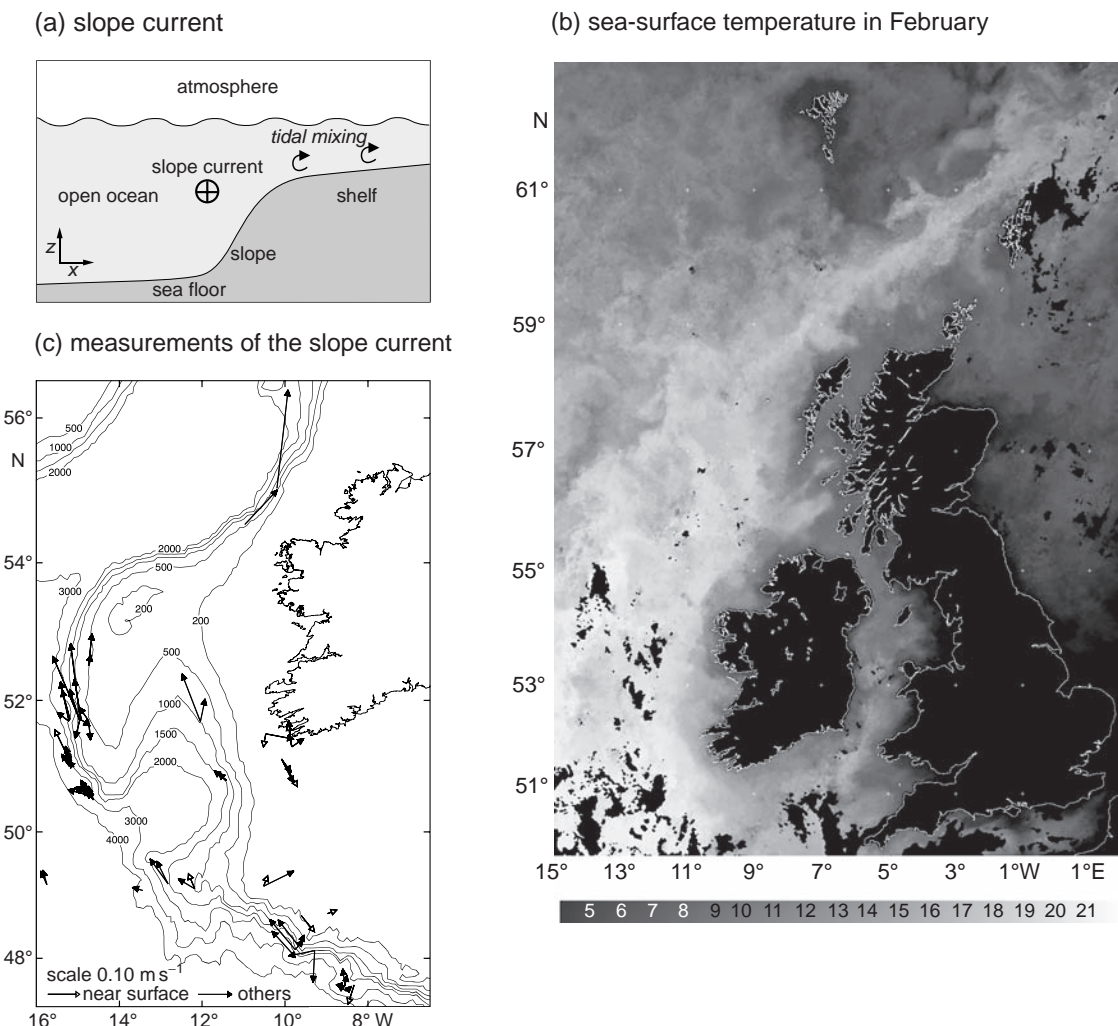


Figure 12.21 (a) A schematic figure of the slope current; (b) a remotely sensed sea-surface temperature composite picture for 16–22 February 2006, revealing the slope current as a plume of warmer water running along the shelf break around the UK (courtesy of Steve Groom, NEODASS, Plymouth); (c) a synthesis of current-meter estimates along the continental slope off Ireland, which reveals a poleward flowing slope current reaching typically speeds of 0.1 m s^{-1} (courtesy of John Huthnance; see Huthnance *et al.*, 2001).

eddy stirring is important in redistributing tracers, as well as in possibly spinning up deep recirculations.

12.4 How is dense water returned to the surface?

Dense water is formed in the high latitudes and spreads below the thermocline over the global

ocean. If there is a continuous source of dense water, the ocean will eventually fill up with dense water unless there are opposing processes acting to lighten it. There are two main ways by which dense water can lighten:

- Winds induce upwelling over the subpolar gyres, the tropics, near coastal boundaries and over the Southern Ocean. The upwelling lifts dense water and leads to dense surfaces outcropping in the surface mixed layer, which can

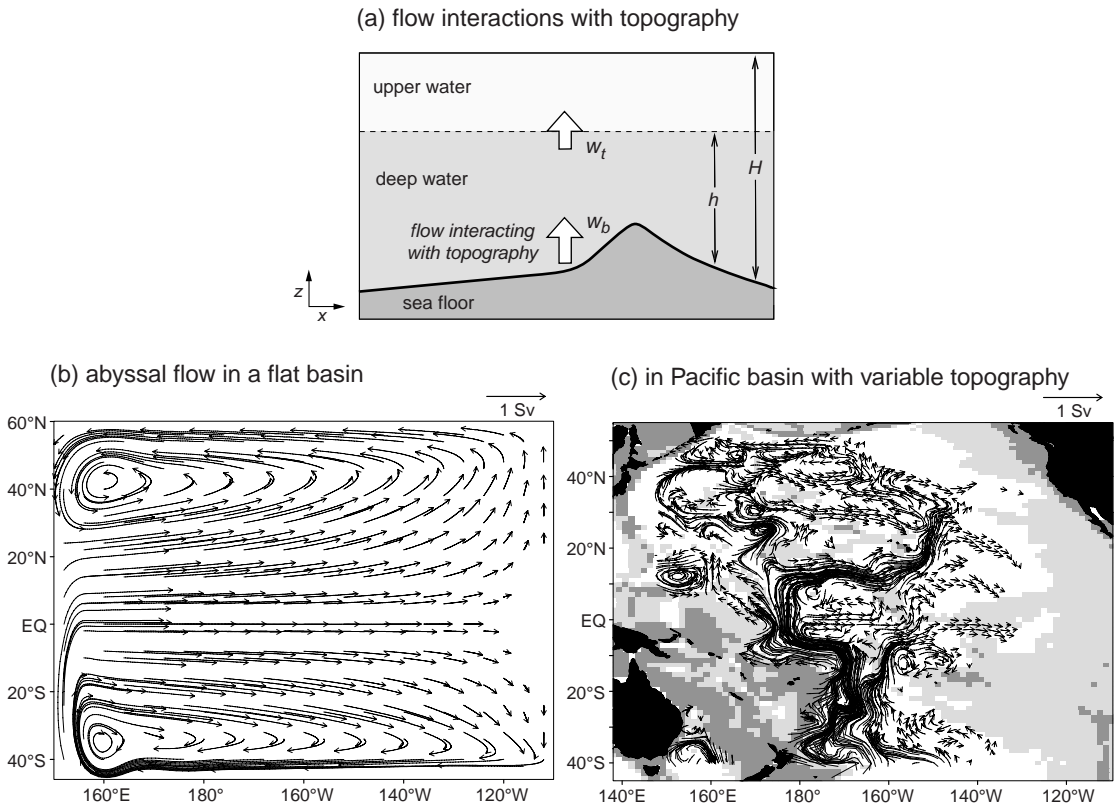


Figure 12.22 (a) A schematic view of the deep circulation including topography: an upwelling of cold water, $w_t > 0$, and a vertical velocity at the bottom of the layer, given by $w_b = -\mathbf{u}_b \cdot \nabla H$. Model solutions for the deep circulation (vectors are bottom transport vector in Sv) in (b) for an idealised flat basin with a southern source of dense water and (c) for a Pacific domain with realistic bottom topography (depths less than 3000 m and 4500 m denoted by dark and light shading). Note how the inclusion of topography fundamentally changes the pattern of the deep circulation. Panels (b) and (c) courtesy of Vassil Roussetov; further details see Roussetov et al. (2004).

subsequently lighten through surface warming and freshening.

- Turbulence within the water column reduces vertical density contrasts and makes the water column more vertically uniform; dense, deep waters become lighter, while light, surface waters become denser.

In practice, both mechanisms play a role over different parts of the ocean. To understand their effect, we consider more carefully the overturning and mixing in the Southern Ocean, which is probably the most important region over the globe in modifying and returning dense water to the surface.

12.4.1 How does the meridional overturning operate across the Southern Ocean?

The meridional overturning represents a secondary circulation crossing the path of the much stronger, eastward flowing Antarctic Circumpolar Current. The meridional overturning is composed of two cells providing a northward flux of surface and bottom waters, and an opposing southward flux of dense waters (Fig. 12.23, thick arrows).

Upper cell

In the upper cell, eastward winds drive a northward surface Ekman current, evident both in the northward spreading of icebergs and a

Box 12.3 | Stommel model with bottom topography

Consider again the problem of how the flow goes over a bump (Box 12.2), but now include variations in f with latitude, such that $\beta = df/dy \neq 0$. Combining geostrophic flow (12.5) and continuity of volume (12.6) leads to a linear vorticity balance,

$$\beta v = f \frac{\partial w}{\partial z}, \quad (12.11)$$

rather than the flow being horizontally non-divergent on relatively small horizontal scales (12.8) as in Box 12.2. Integrating (12.11) over the thickness of the moving layer, h , leads to the meridional flow depending on the difference between the vertical velocity at the top of the cold layer, w_t , and on the sea floor, w_b ,

$$\beta v = f (w_t - w_b)/h. \quad (12.12)$$

Combining with the relationship between the vertical velocity on the sea floor and the horizontal flow intersecting topography (12.10) leads to

$$\beta v - \frac{f}{h} \left(u_b \frac{\partial H}{\partial x} + v_b \frac{\partial H}{\partial y} \right) = f w_t/h. \quad (12.13)$$

In this special case, where the upper interface of the cold water is flat, gradients in the thickness of cold water are the same as that of the fluid depth, $\partial h / \partial x = \partial H / \partial x$, and assuming a uniform deep flow with $v = v_b$, then (12.13) can be rearranged to

$$u_b \frac{\partial}{\partial x} \left(\frac{f}{h} \right) + v_b \frac{\partial}{\partial y} \left(\frac{f}{h} \right) = f \frac{w_t}{h^2}. \quad (12.14)$$

Hence, upwelling of cold water drives an interior flow across f/h contours, directed from low to high f/h . Conversely, whenever mixing is negligible, the flow of dense waters is expected to be aligned along f/h contours (with $w_t = 0$ in (12.14)); for example, as illustrated in idealised experiments for the spreading of Antarctic Bottom Water (Stephens and Marshall, 2000).

surface layer of fresh water from Antarctica (Fig. 8.21d). The horizontal variation in the northward Ekman flux (between the latitude of the maximum westerly wind and the Antarctic continent) leads to widespread upwelling, bringing dense waters from the deep ocean up to the surface. These dense waters are swept northward within the surface mixed layer and are made lighter through a combination of surface heating and precipitation.

This northward Ekman flux is partly opposed by an eddy-driven circulation across the Antarctic Circumpolar Current, where the eddies are formed through an instability of the intense current. There is a competition between the winds acting to increase the meridional tilt of density

surfaces and eddies acting to flatten the density surfaces.

Which process dominates at the surface depends on the sign of the surface density flux. Climatologies of the air-sea fluxes, while containing large errors, suggest that there is an overall lightening of these surface waters, implying that the wind-driven, northward Ekman flux dominates over the eddy flux; the sum of these two opposing circulations is referred to as the residual circulation.

Deeper cell

In the deeper cell, dense waters are formed over the Antarctic shelves, spilling over the topography and forming bottom waters. This dense water is

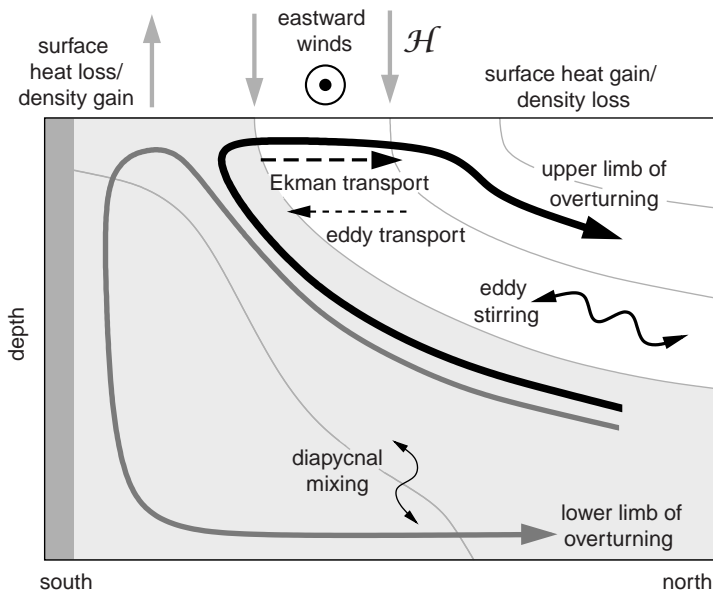


Figure 12.23 Schematic figure of the overturning in the Southern Ocean, which consists of two limbs; the upper limb (dark thick arrow) is directed northward and associated with a surface density loss involving a northward Ekman transport and southward eddy transport. The lower limb (light thick arrow) is associated with a density gain driving dense water formation over Antarctic shelves and an eventual northward transport of bottom water; density surfaces marked by thin grey contours.

marked by its low temperature acquired either by atmospheric cooling in open shelf waters or ice-free leads, or by cooling at depth from underneath the actual ice sheet. This bottom water spreads northward away from the formation sites into the basins connected to the Southern Ocean.

12.4.2 Mixing in the Southern Ocean

Turbulent mixing is highly inhomogeneous, very weak over much of the open ocean, with a diffusivity of typically $10^{-5} \text{ m}^2 \text{ s}^{-1}$, but the diffusivity increases by two to three orders of magnitude over regions of rough topography or near coastal boundaries.

One of the most spectacular examples of enhanced mixing is in the Southern Ocean, following the path of the Antarctic Circumpolar Current over a series of sills in the vicinity of Drake Passage (Fig. 12.24a). There is enhanced mixing over the Scotia Sea ridge, the diffusivity reaching $10^{-3} \text{ m}^2 \text{ s}^{-1}$ or higher, which affects most of the water column and extends to within the upper 500 m of the surface (Fig. 12.24b, middle panel). This mixing reduces the vertical contrasts in water-mass properties and weakens the stratification.

Global energetics of mixing

Turbulent mixing causes dense waters to be lifted and mixed with overlying lighter waters, which raises the centre of mass for the water column and increases its potential energy. This increase in potential energy requires an input of potential energy or a conversion of kinetic to potential energy; like a football kicked up a hill that gradually comes to a rest at a greater height and its initial kinetic energy has been converted to potential energy.

While thermal forcing is central in controlling surface temperatures and the ocean heat store, thermal forcing turns out to be very inefficient in either increasing potential energy or kinetic energy in the ocean. This inefficiency is in contrast with how heating water in a steam engine can power its forward motion through the expansion of water into steam. There are two reasons why thermal forcing is particularly inefficient in the ocean. Firstly, seawater is only slightly compressible, so temperature changes only induce small density changes relative to the background density. Secondly, thermal forcing from the atmosphere is concentrated within the surface mixed layer, which is relatively thin over most of the ocean (Fig. 7.5).

Instead, the mechanical forcing from the winds and the gravitational forcing of the tides

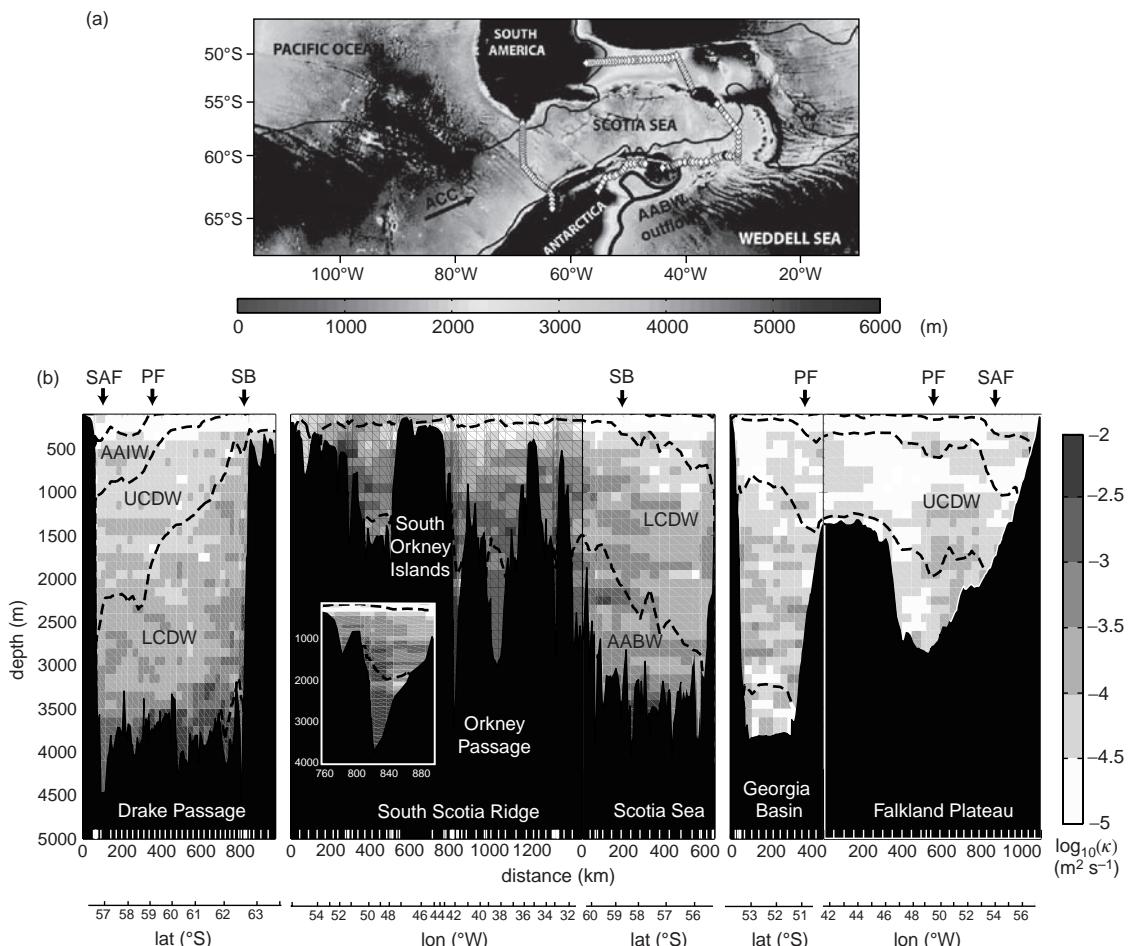


Figure 12.24 Variation of mixing in the Scotia Sea: (a) map of the sea-floor depth (m) and data sections (white dots), and (b) vertical distribution of the diffusivity, κ (as \log_{10} in $\text{m}^2 \text{s}^{-1}$, shading) following an anticlockwise path along the rim of the Scotia Sea spanning (left to right) the Drake Passage, the South Scotia ridge, the Scotia Sea and the Falkland Plateau (latitudes and longitudes marked below). There is a dramatic increase in diffusivity (dark shading) over the Scotia Sea ridge (middle panel) where the Antarctic Circumpolar Current (ACC) passes over rough topography. Crossings of the two main frontal jets of the ACC (SAF, the Sub-Antarctic Front, the northern boundary of the ACC; PF, Polar Front) and its southern boundary (SB) are marked in the upper axis. Density surfaces separating the main water masses are shown by the thick dashed lines: AAIW, Antarctic Intermediate Water; UCDW and LCDW, Upper and Lower Circumpolar Deep Water; AABW, Antarctic Bottom Water. Figure kindly provided by Alberto Naveira Garabato; further details, see Naveira Garabato *et al.* (2004), reprinted with permission from AAAS.

turn out to be important sources of kinetic energy and increasing the potential energy of the ocean. Hence, the continual circulation of the ocean, involving both the overturning and formation of baroclinic eddies, is sustained through energy inputs associated with the winds and tides; see Box 12.4 and the discussion of energy pathways and conversions in Wunsch and Ferrari (2004) and Huang (2004).

12.4.3 Summary

Most dense water probably returns to the surface around the Southern Ocean. The meridional overturning in the Southern Ocean involves an interplay of partly opposing Ekman and eddy transfers across the Antarctic Circumpolar Current, together with diapycnic mixing above rough topography. The relative importance of these different pathways is unclear: probably a

Box 12.4 | Energetics, overturning and eddies

Overturning involves dense waters sinking, spreading at depth, and being replaced by lighter waters at the surface. This rearrangement of the fluid leads to a lowering of the centre of mass and a release of potential energy; like a ball rolling down a hill and converting potential to kinetic energy. In a similar manner, the formation of baroclinic eddies involves a flattening of potential density surfaces and a reduction in potential energy (Gill *et al.*, 1974). Their combined loss of potential energy over the globe is estimated to reach typically 2 to 3×10^{12} W (Wunsch and Ferrari, 2004).

For a steady state, to sustain the ocean circulation including the formation of eddies, there needs to be an opposing input of potential energy or kinetic energy. Following Wunsch and Ferrari (2004), consider the following possible forcing mechanisms:

- Winds blowing over the ocean transfer kinetic energy from the atmosphere to kinetic energy and potential energy in the ocean. The work done by the wind, estimated from the product of the wind stress and the ocean's geostrophic velocity, $\tau \cdot \mathbf{u}_g$, reaches typically $\approx 1 \times 10^{12}$ W (Wunsch, 1998), with the majority of this kinetic energy input occurring over the Southern Ocean; see Q12.4.
- Variations in gravitational forcing from the Moon and Sun provide an input of potential energy over the water column, converted to kinetic energy through the motion of the tides, estimated to reach 3.5×10^{12} W over the globe (Munk and Wunsch, 1998). Most of the energy associated with the tides is dissipated over the shelf seas, leaving perhaps an upper bound of 1×10^{12} W to be dissipated over the open ocean.
- Surface heating and cooling are confined to a relatively thin mixed layer. Warming leads to expansion, a rise in the centre of mass and a gain in potential energy, while cooling leads to contraction, a lowering in the centre of mass and a loss in potential energy. The effect of the cooling is greater than the warming, since the cooling extends over a thicker mixed layer due to convection. Averaged over the globe, the effect of surface heating and cooling is relatively small in terms of potential energy changes, estimated as $\approx -0.2 \times 10^{12}$ W, representing a sink of potential energy rather than a source (Huang and Wang, 2003).
- Geothermal heating along the sea floor is relatively weak, providing a potential energy input of 0.05×10^{12} W (Huang, 2004).

Consequently, the ocean circulation, including the overturning and formation of baroclinic eddies, requires a source of potential and kinetic energy, which is sustained by the mechanical forcing from the winds and gravitational forcing from the Moon and Sun.

combination of the Ekman and eddy transfers dominate for the upper waters, while diapycnic mixing dominates in the deep waters.

The overturning involves density changes from surface heat and freshwater fluxes, and mechanical forcing by the winds and gravitational forc-

ing from the Moon and Sun: the density forcing leads to surface density contrasts being formed, inducing sinking and spreading of dense water; and ultimately the combination of the mechanical and gravitational forcing enables the return of dense water to the surface.

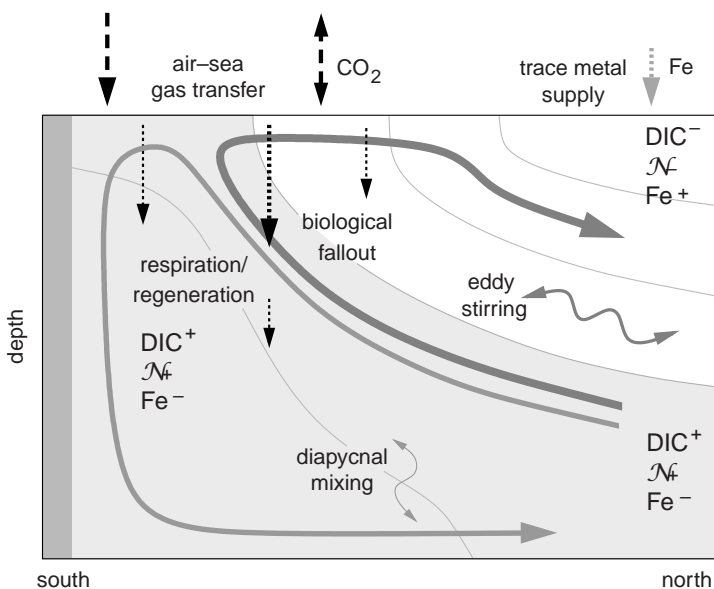


Figure 12.25 Schematic figure of the biogeochemical cycling and overturning in the Southern Ocean (extending the physical view in Fig. 12.23). There is an air-sea transfer of CO_2 driven by a combination of surface heating, biological transfers and an outgassing from the mixing of carbon-rich deep waters. Biological fallout and subsequent respiration leads to deep waters being nutrient and carbon rich. A combination of the physical circulation and mixing eventually returns these nutrient- and carbon-rich waters to the surface. There are surface inputs of iron near the land, but much of the waters are depleted in iron over the Southern Ocean.

Next we consider the effect of the overturning on how nutrients and carbon are transported and cycled over the Southern Ocean.

12.4.4 Southern Ocean nutrient and carbon cycling

The Southern Ocean is a very important region for marine carbon and nutrient cycles, since overturning returns a large fraction of the deep and bottom waters to the surface here (grey arrows in Fig. 12.25). These carbon- and nutrient-enriched waters may then once again communicate with the atmosphere and fuel biological production. The surface waters may subsequently be subducted into the ocean interior as part of the overturning circulation (Fig. 12.25, arrows on right-hand side). For example, subduction leads to a tongue of high concentrations of dissolved oxygen being transported downward and northward along $\sigma_\theta = 27.2$ in the Southern Ocean (Fig. 12.26a), accompanied by low, but non-zero, nitrate concentrations (Fig. 12.26b). At the same time, old deep waters are very low in oxygen and rich in nitrate are transported northward and upward on σ_θ surfaces between 27.5 and 27.8.

What are the implications for biological productivity?

The upwelling over the Southern Ocean transfers macro-nutrient-rich waters to the surface,

although the same waters are depleted in iron (due to the long-term exposure to scavenging by particles) (Fig. 12.25). Primary production is higher than in the oligotrophic subtropical waters due to the availability of macro-nutrients, but constrained by the shortfall in upwelled iron. Primary production is also inhibited through light limitation due to the relatively thick mixed layers which occur over much of the year (Hiscock *et al.*, 2003, and Section 7.1.4).

As one moves northward away from Antarctica, silicic acid is stripped from the surface quickly by blooms of opportunistic diatoms (Fig. 12.27a), but nitrate and phosphate maintain relatively high concentrations towards the subtropics (Fig. 12.27b), until eventually atmospheric inputs of iron allow the macro-nutrients to be completely utilised. Due to their limited utilisation, nitrate and phosphate concentrations still remain relatively high in the regions of mode water formation to the north of the Antarctic Circumpolar Current where they are subducted. This signature of nitrate- and phosphate-rich waters, together with low silica, is seen within mode waters spreading from the Southern Ocean (Fig. 12.27, white arrows). The northward transfer of nitrate and phosphate within these mode waters helps sustain the productivity of the northern basins (Sarmiento *et al.*, 2004; also see Section 11.1.1).

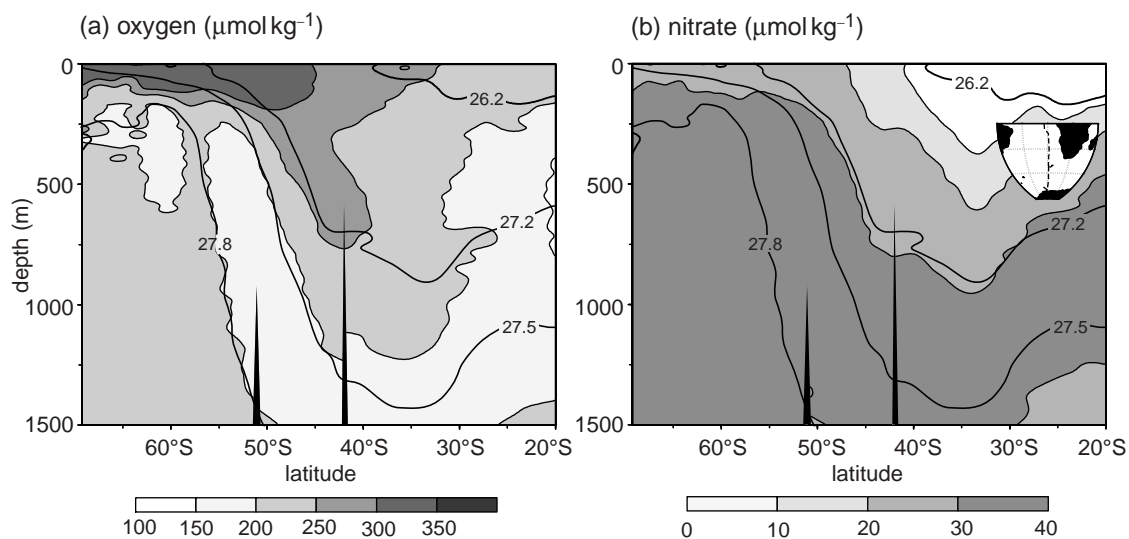


Figure 12.26 Meridional sections of (a) dissolved oxygen (shaded, $\mu\text{mol kg}^{-1}$), and (b) nitrate (shaded, $\mu\text{mol kg}^{-1}$), together with σ_0 surfaces over the upper 1500 m in the Southern Ocean along the Greenwich meridian. Note how closely the tracer and σ_0 surfaces are aligned together, indicating largely isopycnal transport.

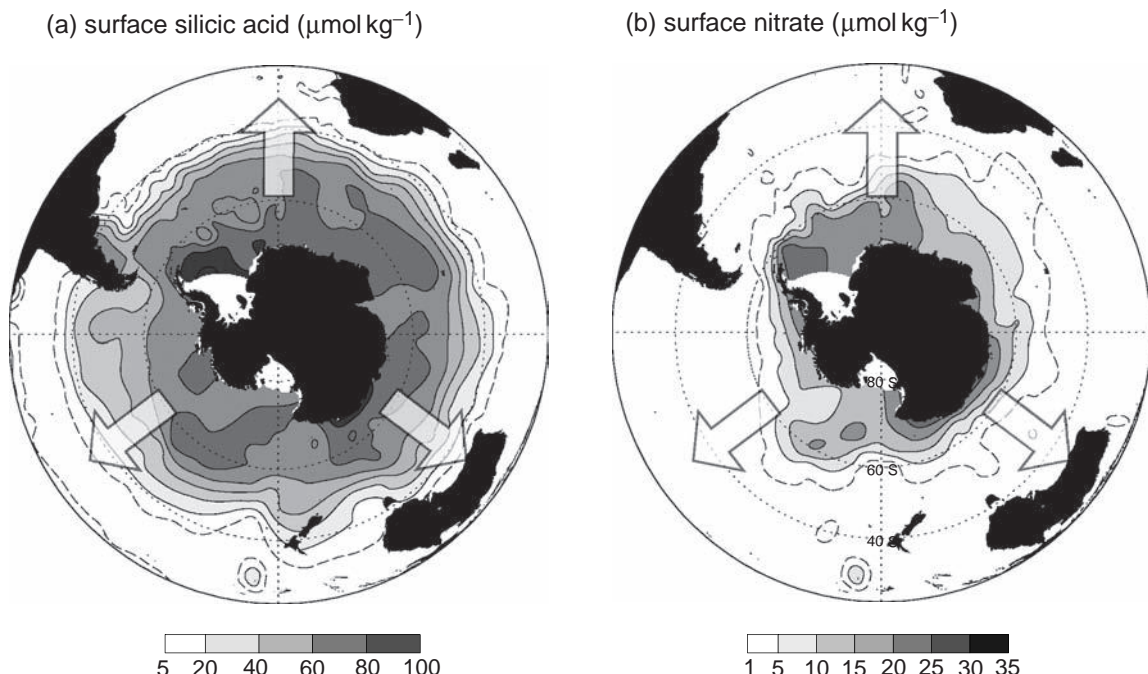


Figure 12.27 Surface distributions of (a) silicic acid ($5 \mu\text{mol kg}^{-1}$ dashed contour) and (b) nitrate ($1 \mu\text{mol kg}^{-1}$ dashed contour) over the southern hemisphere (latitude circles marked at 20°S and 40°S). The nitrate-rich waters extend further north over the Southern Ocean than for silica. The surface imprint of nitrate-rich, but silica-depleted waters, is carried within the mode waters spreading northward along density surfaces into the northern basins (arrows denote spreading direction); see discussion of the implications of this transfer by Sarmiento *et al.* (2004).

What are the implications for carbon?

The upwelling waters return regenerated carbon in the deep ocean to the surface, which in turn leads to an excess carbon anomaly in the surface and a super-saturation of carbon dioxide. There are three possible fates for this excess carbon: outgassing to the atmosphere, transport and eventual subduction following the upper or lower limbs of the overturning circulation (Figs. 12.23 and 12.25, thick arrows), or consumption by primary producers fuelled by the nutrient-rich environment.

This balance turns out to be complicated in the Southern Ocean: models suggest that the residence time for CO₂ in the surface is about one year before reventilation, the timescale for equilibration with the atmosphere by air-sea exchange is comparable and, perhaps due to iron or light limitation, the timescale for nutrient utilisation is of the same order. The net exchange of CO₂ across the sea surface in this region is difficult to anticipate, controlled by this complex interplay of processes all acting on similar timescales. In the present day, anthropogenically increasing atmospheric pCO₂ acts to drive an influx of CO₂ over much of the region, but this signal is difficult to confirm with spatially and temporally sparse observations.

12.5 | Summary

Dense water is formed by the surface exchange of heat and moisture with the atmosphere or in polar regions by interactions with the overlying ice. Dense water spreads away from the formation sites in the mixed layer through a combination of the large-scale interior circulation, boundary currents running alongside topography and by transfers by the time-varying eddy circulation. Mixing strongly modifies the properties of the dense water and determines the vertical ordering of dense waters, as well as affecting the downstream properties of bottom waters.

Dense water is preferentially formed in the high latitudes of the North Atlantic and the Southern Ocean. The overturning in each basin is connected to the Southern Ocean. The stronger overturning in the North Atlantic relative to the North Pacific is due to high latitude waters being saltier and denser, which is a consequence of greater

freshwater loss to the atmosphere over the North Atlantic. The overturning circulation contributes to the poleward heat transport and leads to an enhanced warming of the atmosphere in the mid and high latitudes.

Dense waters are returned to the sea surface through a combination of wind-induced upwelling and a lightening of dense water through mixing. This return of dense waters mainly occurs over the Southern Ocean, where there is strong wind-induced upwelling, partly opposed by eddy transfers, as well as intense mixing as the Antarctic Circumpolar Current passes over regions of rough topography.

The overturning involves surface density changes from surface thermal and freshwater fluxes, mechanical forcing by the winds and gravitational forcing by the Moon and Sun. The surface density contrasts lead to sinking and spreading of dense water. The combination of mechanical and gravitational forcing provides the energy for dense water to return to the surface, as well as maintaining other ocean circulations.

The deep waters provide the largest store of carbon in the global ocean and this is maintained by both physical and biological transfers of carbon. The size and efficiency of this carbon store is modulated by the relatively small-scale processes of deep and bottom water formation, which affect the equilibration of carbon dioxide and the efficiency of nutrient utilisation. The Southern Ocean provides the main conduit for the return of the nutrient- and carbon-rich dense waters to the sea surface to communicate with the atmosphere and fuel primary production once again. Subsequent transport over the globe affects the patterns of biological productivity and air-sea exchange of carbon dioxide.

Integrated frameworks to understand how carbon is cycled and how the overturning connects to surface density forcing are next provided in Chapter 13.

12.6 | Questions

Q12.1. Heat transport by the ocean.

Consider the relative importance of the heat transport by the ocean from the horizontal gyres and

the vertical overturning using

$$\rho C_p \Delta\theta \psi / T, \quad (12.15)$$

where $\Delta\theta$ is a potential temperature difference, ψ/T is a volume transport ($\text{m}^3 \text{s}^{-1}$), $\rho \sim 10^3 \text{ kg m}^{-3}$ and $C_p \sim 4 \times 10^3 \text{ J kg}^{-1} \text{ K}^{-1}$. Estimate the heat transport using (12.15) with typical values for the North Atlantic:

- (a) The gyre circulation with a west–east temperature contrast, $\Delta\theta \sim 2 \text{ K}$ across the basin and the volume transport, $\psi/T \sim 30 \times 10^6 \text{ m}^3 \text{s}^{-1}$. Check the units of your answer.
- (b) The overturning circulation with a vertical temperature contrast, $\Delta\theta \sim 15 \text{ K}$ and a volume transport, $\psi/T \sim 15 \times 10^6 \text{ m}^3 \text{s}^{-1}$.
- (c) What fraction of the total ocean heat transport is carried by the overturning?

Q12.2. Overturning and pressure contrasts.

Consider the meridional transport by the geostrophic flow within a basin, which is defined by a west–east integral of the velocity across the basin and a depth integral from the surface to a level of no motion, $z = -d_{ref}$,

$$\int_{-d_{ref}}^{z=0} \int_{x_w}^{x_e} v_g dx dz, \quad (12.16)$$

where x_w and x_e define the western and eastern sides of the basin.

- (a) By assuming geostrophic flow, $v_g = (1/(\rho_0 f)) \partial P / \partial x$, show that (12.16) can be expressed as a pressure contrast across the basin,

$$\frac{1}{\rho_0 f} \int_{-d_{ref}}^{z=0} (P(x_e) - P(x_w)) dz. \quad (12.17)$$

- (b) For a poleward transport above the level of no motion, how does the pressure on each boundary compare with each other?

- (c) How might the height of the sea surface η then vary across the basin? Assume that greater pressure at depth is achieved by a thicker water column with a nearly uniform density.

- (d) Assume that the pressure distribution remains unchanged along the eastern boundary. If the overturning strengthens with a greater poleward upper transport, then does sea level rise or fall on

the western boundary? For an application of this balance to relate overturning and sea level along the North American eastern coast, see Bingham and Hughes (2009).

Q12.3. Stommel–Arons model of the deep ocean.

Assume that the cold, deep water is slowly upwelling and balancing a downward diffusion of heat:

$$w \frac{\partial T}{\partial z} = \kappa \frac{\partial^2 T}{\partial z^2}. \quad (12.18)$$

- (a) Use scale analysis to relate w (m s^{-1}) and the diffusivity of heat, κ ($\text{m}^2 \text{s}^{-1}$), and the depth scale, H (m).
- (b) Relate v , w and κ by assuming linear vorticity balance, $\beta v = f \partial w / \partial z$, where β is in units of $\text{m}^{-1} \text{s}^{-1}$ and f in s^{-1} .
- (c) Estimate the magnitude of w , v , and the poleward volume transport, $v H L_x$, for $\kappa \sim 10^{-4} \text{ m}^2 \text{s}^{-1}$, $H \sim 3 \text{ km}$ and $L_x \sim 5000 \text{ km}$. Quote the volume transport in sverdrups ($10^6 \text{ m}^3 \text{s}^{-1}$).
- (d) Sketch a plan view of the horizontal flow in the deep waters over the North Pacific, which is implied by the Stommel and Arons model.
- (e) Observations suggest that $\kappa \sim 10^{-5} \text{ m}^2 \text{s}^{-1}$ is very small in the interior of the ocean from tracer-release experiments, but is enhanced near topography. Given your relations between v and κ , speculate on how the Stommel and Arons solution changes if there is a larger κ running along the eastern boundary of the Pacific and a zero value elsewhere.
- (f) What are the strengths and weaknesses of the Stommel–Arons model?

Q12.4. Consider the work done by the wind on the ocean.

- (a) Over subtropical gyres, the winds provide an Ekman pumping, pushing down density surfaces and deforming the thermocline, which increases the potential energy. Gill *et al.* (1974) argued that this work done by the wind provides an increase in potential energy per unit horizontal area of 10^{-3} W m^{-2} over the subtropical gyres, which is assumed to sustain the formation of ocean eddies. Estimate the work done by the wind averaged over

the area of the subtropical gyres; assume subtropical gyres make up 60% of the global ocean and the ocean makes up 71% of the surface area of the Earth; take the Earth's radius as 6400 km.

(b) Over the Southern Ocean, the winds are strongly aligned with the Antarctic Circumpolar Current. Estimate the work done by the wind on the ocean per unit horizontal area from the product of the wind stress and geostrophic current in the ocean, $\tau \cdot \mathbf{u}_g$, assuming the magnitudes of the wind stress $\tau \sim 0.15 \text{ N m}^{-2}$ and surface geostrophic flow are $\mathbf{u}_g \sim 0.1 \text{ m s}^{-1}$; check your units (remember $J \equiv \text{N m} \equiv \text{kg m}^2 \text{ s}^{-2}$).

(c) Estimate the work done by the wind averaged over the Southern Ocean, assuming that the latitudinal extent of the Antarctic Circumpolar Current is 20° and the current encircles the globe at a latitude of typically 50°S .

(d) Estimate the work done by the wind over the globe from the sum of your answers to (a) and (c), and the fraction of the global work done by the wind occurring over the Southern Ocean.

12.7 | Recommended reading

For a historical account of theoretical views of the deep ocean, see B. A. Warren (1981). Deep circulation of

the World Ocean. In *Evolution of Physical Oceanography*. Cambridge, MA: The MIT Press, pp. 6–41.

To understand how deep western boundary currents vary, see N. G. Hogg (2001). Quantification of the deep circulation. In *Ocean Circulation and Climate: Observing and Modelling the Global Ocean*, ed. G. Siedler, J. Church and J. Gould. San Diego, CA: Academic Press, pp. 259–270.

To review how dense water circulates, see M. S. Lozier (2010). Deconstructing the Conveyor Belt. *Science*, 328, 1507, doi:10.1126/science.1189250.

To explore how ocean overturning affects the climate system, see P. B. Rhines, S. Häkkinen and S. A. Josey (2008). Is oceanic heat transport significant in the climate system? In *Arctic-Subarctic Ocean Fluxes: Defining the Role of the Northern Seas in Climate*, ed. R. R. Dickson, J. Meincke and P. B. Rhines. New York: Springer, pp. 265–279.

To address the role of the Southern Ocean and its part in the deep circulation, see S. C. Rintoul, W. Hughes and D. Olbers (2001). The Antarctic Circumpolar Current System. In *Ocean Circulation and Climate: Observing and Modelling the Global Ocean*, ed. G. Siedler, J. Church and J. Gould, San Diego, CA: Academic Press, pp. 271–302.

To understand the energetics of the ocean, see C. Wunsch and R. Ferrari (2004). Vertical mixing, energy, and the general circulation of the oceans. *Annu. Rev. Fluid. Mech.*, 36, 281–314, and R. X. Huang (2004). Energy Flows in the Ocean. In *Encyclopedia of Energy*, ed. C. J. Cleveland. Amsterdam: Elsevier, pp. 497–509.

Part IV

Synthesis

Integral frameworks

It is a challenge to understand the role of the ocean in the climate system due to the complex interplay of physical, chemical and biological processes, and their range in spatial scales from diffusion on the molecular scale to overturning on the global scale. While there is widespread interest in the role of the ocean in climate change, it is unclear how the ocean has behaved in the geological past and how the ocean might respond in the future to changes in climate forcing.

In order to gain insight into how the ocean behaves, we now consider two simplifying diagnostic frameworks. The first framework addresses the global carbon cycle, considering the atmosphere and ocean as a container of air overlying water and examines their long-term equilibrium between them. The partitioning of carbon between the air and water depends on the properties of the water (temperature, alkalinity and biological activity), as well as the external inputs and outputs of carbon and minerals. This model is useful for understanding how atmospheric carbon dioxide has varied on millennial timescales in the past, such as during glacial periods, and how it might change in the future with continuing anthropogenic emissions.

The second framework addresses how water masses form, relating the area-integrated density forcing at the sea surface, the interior mixing and the rate at which water masses are transformed between density classes. Patterns of surface density forcing reveal the asymmetry between the overturning in the Atlantic and Pacific, and provide clues as to how the overturning operates in the Southern Ocean.

First we set out the carbon cycle framework and then describe the physics framework.

13.1 Variations in the ocean–atmosphere carbon cycle

We now draw on the understanding of the carbon cycle processes discussed in earlier chapters to construct a simple integral framework, which is employed to address two central questions: what will the fate of anthropogenic carbon dioxide be over the next 100 000 years and what controlled the variations in atmospheric carbon dioxide over glacial–interglacial cycles?

13.1.1 Global integral constraints

Our aim is to develop simple models of the carbon system, employing globally integrated mass conservation statements and parameterisations of key chemical and biological processes. We begin with a statement of global conservation of carbon in the surface Earth system, as depicted in Fig. 13.1. The total inventory of carbon, I_C (moles), is assumed to be conserved and to be made up of contributions from the ocean–atmosphere system, I_{oa} , terrestrial biomass and organic carbon in soils, I_{terr} , carbon in accessible fossil fuels, I_{ff} , and inorganic and organic carbon in sedimentary rocks, I_{geo} :

$$I_C = I_{oa} + I_{terr} + I_{ff} + I_{geo}. \quad (13.1)$$

Table 13.1 Global ocean integrals for dissolved inorganic carbon, DIC, separated into different components: saturated carbon, C^{sat} , soft-tissue carbon, C^{soft} , carbonate, C^{carb} , and disequilibrium ΔC . Evaluated from the datasets of Key *et al.* (2004) and Conkright *et al.* (2002). The DIC and A_T datasets cover about 95% of ocean volume, so the integrals are slight underestimates for the global ocean.

C reservoir units	Global integral 10^{18} moles C	Global integral Pg C	mean concentration $\mu\text{mol kg}^{-1}$
DIC	2.961	35 538	2253
C^{sat}	2.777	33 330	2113
C^{soft}	0.139	1672	105
C^{carb}	0.042	502	33
ΔC	0.003	38	2

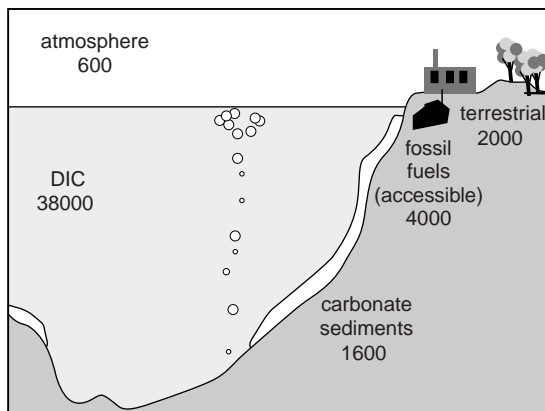


Figure 13.1 A schematic view of the global carbon cycle indicating the size of the carbon reservoirs (Pg C), based on pre-industrial estimates (IPCC, 2007) and an estimate of accessible carbonate sediments (Archer, 1996).

13.1.2 Carbon in the ocean–atmosphere system

The total amount of carbon in the ocean and atmosphere is defined by the ocean–atmosphere carbon inventory, I_{oa} (moles C), made up of atmospheric CO_2 and dissolved inorganic carbon in the oceans, neglecting organic forms,

$$I_{oa} = \underbrace{MX_{\text{CO}_2}}_{\text{atmosphere}} + \underbrace{V_0\rho_0 \overline{\text{DIC}}}_{\text{ocean}}, \quad (13.2)$$

where M is the total abundance of gas molecules in the atmosphere (moles), X_{CO_2} is the atmospheric mixing ratio of CO_2 (mol mol^{-1} , typically expressed for convenience in ppmv) and $V_0\rho_0$ is the mass of the ocean (kg). $\overline{\text{DIC}}$ is the mean con-

centration of dissolved inorganic carbon in the global ocean (mol kg^{-1}), defined by

$$\overline{\text{DIC}} = \frac{\int \text{DIC } dV}{\int dV} = \frac{1}{V_0} \int \text{DIC } dV,$$

where $V_0 = \int dV$ is the volume of the ocean (m^3). The ocean inventory of dissolved inorganic carbon is the sum of contributions from saturated ($\overline{C^{sat}}$), biogenic regenerated ($\overline{C^{reg}}$) and disequilibrium ($\overline{\Delta C}$) contributions (Section 11.4), so that (13.2) is expressed as

$$I_{oa} = \underbrace{MX_{\text{CO}_2}}_{\text{atmosphere}} + \underbrace{V_0\rho_0 (\overline{C^{sat}} + \overline{C^{reg}} + \overline{\Delta C})}_{\text{ocean}}. \quad (13.3)$$

The atmospheric inventory of carbon dioxide is currently about 600 Pg C. The ocean dissolved inorganic carbon inventory of 38 000 Pg C is largely accounted for by the saturated carbon, C^{sat} (93.8%). There are smaller contributions from the soft-tissue pump, C^{soft} (4.7%), and the carbonate pump, C^{carb} (1.4%), which together make up the regenerated components, C^{reg} . There is also a small residual or disequilibrium component, ΔC (0.1%); percentages based on Table 13.1.

13.1.3 Variations in the ocean–atmosphere carbon system

If the total amount of carbon in the Earth's crust and fluid environments is conserved, then changes in any of the reservoirs are compensated by changes in the other reservoirs, such that $\delta I_C = 0$ from (13.1). Hence, changes in the

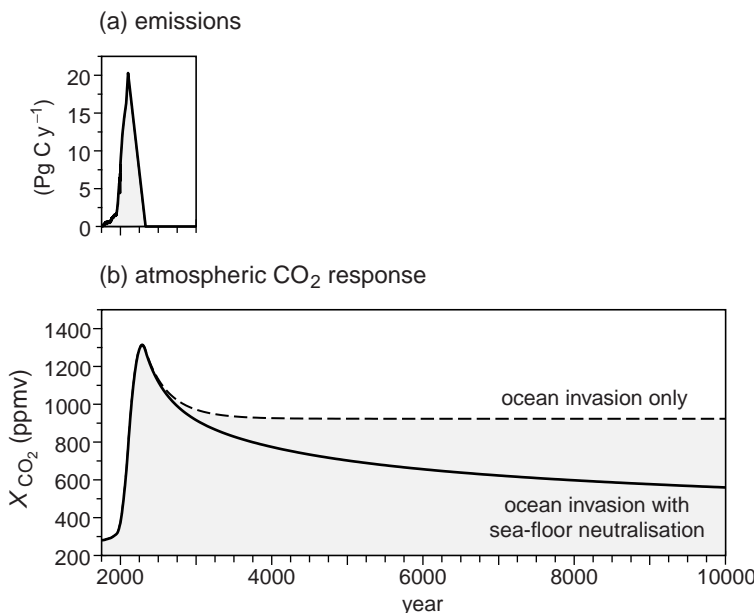


Figure 13.2 A study of the fate of fossil fuel carbon dioxide in an Earth system model: (a) carbon emissions totalling 4000 Pg C are emitted into the atmosphere over a period of 400 years; (b) the corresponding history of atmospheric mixing ratio for carbon dioxide X_{CO_2} (ppmv) for ocean invasion alone (dashed line) and ocean invasion with subsequent neutralisation by interaction with calcium carbonate sediments (black line). In this model, ocean uptake is assumed to occur with an e-folding timescale of 300 years, while equilibration with the sedimentary calcium carbonate reservoir takes tens of thousands of years. Adapted from Ridgwell and Hargreaves (2007).

ocean-atmosphere carbon, δI_{oa} , are related to the sum of variations in each of the other reservoirs,

$$\delta I_{oa} = -(\delta I_{terr} + \delta I_{ff} + \delta I_{geo}), \quad (13.4)$$

where a change in reservoir I is denoted by δI . At the same time, the change in the ocean carbon inventory is the sum of variations in its components from (13.3), so that

$$\delta I_{oa} = M \delta X_{CO_2} + V_0 \rho_0 (\delta \bar{C}^{sat} + \delta \bar{C}^{reg} + \delta \bar{\Delta C}). \quad (13.5)$$

Next we exploit this simple model, (13.4) and (13.5), to examine the effect of a variety of perturbations on the combined atmosphere-ocean system.

13.2 What is the fate of fossil-fuel carbon dioxide?

How does the ocean-atmosphere system respond to an external input of carbon dioxide, such as from the burning of fossil fuels? Over the industrial era, humans have emitted about 250 Pg C (IPCC, 2007), which is equivalent to more than a third of the pre-industrial atmosphere's carbon inventory. A further 4000 Pg C of fossil fuels are potentially extractable and, at present rates of consumption, could be released to the atmosphere in

just a few hundred more years. Leaving aside the terrestrial and soil carbon reservoirs, what will the fate of this carbon dioxide be over the course of time?

13.2.1 Transient response to carbon emissions

The carbon system is likely to respond in the following manner to carbon emissions, as illustrated in Fig. 13.2a,b from a numerical model study of the coupled atmosphere, ocean and sediments:

- Initially, there is a transient increase in the amount of carbon dioxide held in the atmosphere and the dissolved inorganic carbon within the surface mixed layer of the ocean (Fig. 13.2b). The atmosphere and ocean mixed layer communicate rapidly and come close to equilibrium on timescales of a few years, as can be seen at Hawaii, where surface ocean pCO_2 closely tracks the increase in atmospheric pCO_2 (Fig. 6.1). Indeed, one third of the annual, anthropogenic emissions of carbon dioxide are absorbed in the surface ocean within a year.
- On timescales of several decades, surface waters in the mixed layer pass into the thermocline, so that the dissolved inorganic carbon within the upper 1000 m or so comes into equilibrium with the atmosphere. The deep waters

take much longer to equilibrate. In some well-ventilated regions, like the North Atlantic, deep waters are ventilated on timescales of a few hundreds of years; while in poorly ventilated regions, like the North Pacific, the deep waters are instead ventilated on timescales of more than a thousand years (as suggested by analyses of carbon isotopes). The uptake of carbon by the thermocline and deep ocean leads to the gradual decline in atmospheric carbon dioxide following the exhaustion of fossil fuels and the end of emissions, as shown in Fig. 13.2a,b.

3. Assuming that ocean alkalinity, biological cycling and climate remain constant, the ocean and atmospheric reservoirs of carbon then come into equilibrium after one to two thousand years, as shown in Fig. 13.2b, dashed line.
4. The increase in DIC and ocean acidity gives rise to further changes on timescales of several thousand years. A decrease in pH at fixed alkalinity decreases $[CO_3^{2-}]$, so that previously deposited calcium carbonate dissolves (and the saturation horizon for $CaCO_3$ shoals). While this dissolution further increases DIC, it also leads to an increase in alkalinity at twice the rate, driving a net increase in the ability of the ocean to absorb carbon dioxide from the atmosphere. Hence, the atmospheric inventory of carbon dioxide slowly declines over tens of thousands of years, as illustrated in Fig. 13.2b, solid line. This gradual reduction is the result of the interaction of the marine carbon cycle and carbonate sediments and is referred to as carbonate compensation (Archer, 2005).

Next we recall some key features of ocean carbonate chemistry which, along with the basic mass conservation statements (13.4) and (13.5), allow us to construct some simple, but informative, models of the global carbon system.

13.2.2 Carbonate chemistry

To make more quantitative assessments, we need to introduce some additional tools.

How do changes in the saturated ocean carbon relate to environmental factors?

The bulk of the carbon in the ocean is in the form of saturated dissolved inorganic carbon con-

centration, $\overline{C^{sat}}$, the concentration at equilibrium with an overlying mixing ratio, X_{CO_2} , at the given temperature and alkalinity. If there are small perturbations, changes in $\overline{C^{sat}}$ may be written in terms of the sum of changes in atmospheric mixing ratio, δX_{CO_2} , potential temperature, $\delta\theta$, and alkalinity, $\delta\overline{A_T}$, with linear dependencies,

$$\begin{aligned}\delta\overline{C^{sat}} &= \frac{\partial\overline{C^{sat}}}{\partial X_{CO_2}} \delta X_{CO_2} + \frac{\partial\overline{C^{sat}}}{\partial\theta} \delta\theta + \frac{\partial\overline{C^{sat}}}{\partial\overline{A_T}} \delta\overline{A_T} \\ &= \frac{\partial\overline{C^{sat}}}{\partial X_{CO_2}} \delta X_{CO_2} + \gamma_T \delta\theta + \gamma_A \delta\overline{A_T}.\end{aligned}\quad (13.6)$$

$\overline{C^{sat}}$ decreases almost linearly with potential temperature for fixed alkalinity and X_{CO_2} , as illustrated in Fig. 13.3a, so that $\gamma_T = \partial\overline{C^{sat}}/\partial\theta$ is nearly constant. $\overline{C^{sat}}$ increases almost linearly with alkalinity for fixed temperature and X_{CO_2} in Fig. 13.3b, so that $\gamma_A = \partial\overline{C^{sat}}/\partial\overline{A_T}$ is nearly constant. In contrast, the relationship between $\overline{C^{sat}}$ and X_{CO_2} (or pCO_2) is non-linear, but can be described by invoking the Revelle buffer factor,

$$B = \frac{\partial pCO_2}{\partial\overline{C^{sat}}} \frac{\overline{C^{sat}}}{pCO_2} \simeq \frac{\partial X_{CO_2}}{\partial\overline{C^{sat}}} \frac{\overline{C^{sat}}}{X_{CO_2}}, \quad (13.7)$$

which, when reinterpreted in terms of small, finite changes, describes the relationship between X_{CO_2} and $\overline{C^{sat}}$ in terms of B :

$$\frac{\partial\overline{C^{sat}}}{\partial X_{CO_2}} \simeq \frac{\delta\overline{C^{sat}}}{\delta X_{CO_2}} = \frac{\overline{C^{sat}}}{BX_{CO_2}}. \quad (13.8)$$

Note that B has not been assumed constant in deriving (13.8).

The buffered carbon inventory

To understand how atmosphere and ocean inventories respond to perturbations, consider a simple case where there is an external source of carbon to the ocean-atmosphere system, for example, from anthropogenic emissions or a net respiration of terrestrial vegetation and organic carbon. At the simplest level, there is unlikely to be a direct impact on the biological and disequilibrium reservoirs of carbon in the ocean. The former is regulated by light and nutrient limitation, while the latter is sensitive to the residence time of water parcels in the surface relative to biological and physical forcing. In such a case, changes in

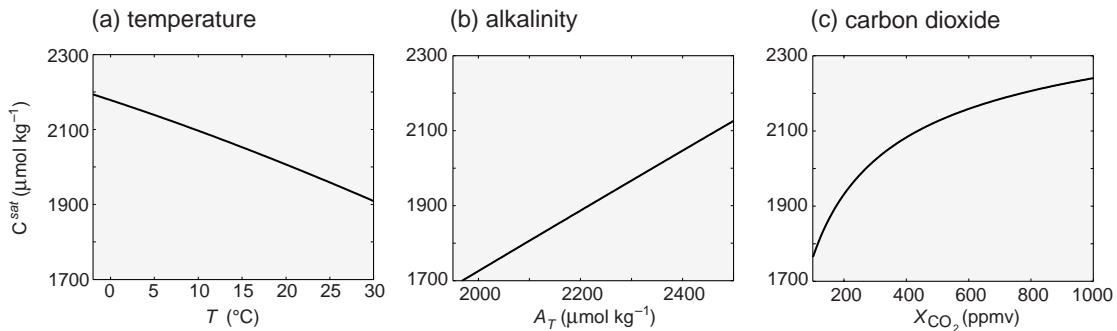


Figure 13.3 Change in saturation (equilibrium) dissolved inorganic carbon concentration C^{sat} ($\mu\text{mol kg}^{-1}$) with (a) temperature for a water parcel in equilibrium with a fixed atmospheric X_{CO_2} of 278 ppmv and alkalinity of $2350 \mu\text{mol kg}^{-1}$; (b) alkalinity for a water parcel in equilibrium with a fixed atmospheric X_{CO_2} of 278 ppmv and temperature of $20 \text{ }^\circ\text{C}$; and (c) atmospheric X_{CO_2} with fixed temperature of $20 \text{ }^\circ\text{C}$ and alkalinity of $2350 \mu\text{mol kg}^{-1}$.

regenerated and disequilibrium carbon are neglected ($\delta C^{reg} = \delta \Delta C = 0$), and the perturbation to the ocean–atmosphere carbon inventory is assumed to be split between the atmosphere and saturated carbon reservoir.

$$\delta I_{oa} = M \delta X_{CO_2} + V_0 \rho_0 \delta \overline{C^{sat}}. \quad (13.9)$$

Substituting for $\delta \overline{C^{sat}}$ from (13.6) and (13.8), assuming that alkalinity and temperature do not change, then the carbon perturbation in (13.9) is related to changes in the atmospheric mixing ratio X_{CO_2} by

$$\delta I_{oa} = \left(M + V_0 \rho_0 \frac{\overline{C^{sat}}}{B X_{CO_2}} \right) \delta X_{CO_2}, \quad (13.10)$$

which can be rearranged to give the sensitivity of atmospheric X_{CO_2} to the external carbon source for a long-term equilibrium,

$$\frac{\partial X_{CO_2}}{\partial I_{oa}} \simeq \frac{\delta X_{CO_2}}{\delta I_{oa}} = \frac{X_{CO_2}}{M X_{CO_2} + \frac{V_0 \rho_0 \overline{C^{sat}}}{B}}. \quad (13.11)$$

The denominator of (13.11) is referred to as the buffered carbon inventory, I_B (Goodwin *et al.*, 2007),

$$I_B \equiv M X_{CO_2} + \frac{V_0 \rho_0 \overline{C^{sat}}}{B}, \quad (13.12)$$

where $M X_{CO_2}$ is the amount of carbon in the atmosphere and $V_0 \rho_0 \overline{C^{sat}}/B$ is the amount of the ocean's dissolved inorganic carbon in the ocean that can effectively interact with the atmosphere due to buffering. I_B is less than 10% of the ocean's total carbon inventory ($\sim 3100 \text{ Pg C}$; Goodwin

et al., 2007); typical values of the variables assumed in this chapter are listed in Table 13.2. I_B remains relatively constant over a wide range of conditions in the ocean–atmosphere carbonate system, compared with larger relative changes in the Revelle buffer factor, B , as illustrated in Fig. 13.4 and explained in Box 13.1. Hence, for a wide range of perturbations, we can assume I_B is constant so that (13.11) becomes

$$\frac{\partial X_{CO_2}}{\partial I_{oa}} = \frac{X_{CO_2}}{I_B}, \quad (13.13)$$

which when integrated provides a simple exponential relationship between the atmospheric mixing ratio, X_{CO_2} , and the change in the ocean–atmosphere carbon inventory at a long-term equilibrium (Goodwin *et al.*, 2007):

$$X_{CO_2}(I_{oa}) = X_{CO_2}(I_{oa}^{ref}) e^{\Delta I_{oa}/I_B}, \quad (13.14)$$

where ΔI_{oa} is the change in the ocean–atmosphere inventory of carbon (Pg C) relative to a reference value, I_{oa}^{ref} , and I_B is the buffered carbon inventory (Pg C).

Hence, adding carbon to the ocean–atmosphere system (without changes in alkalinity, climate or other factors) leads to an exponential increase in atmospheric X_{CO_2} when a new equilibrium has been reached. The exponential relationship in (13.14) reveals that the rate of increase in atmospheric X_{CO_2} progressively accelerates as cumulative emissions grow. As more carbon is emitted, the buffer factor increases and the ocean becomes less effective at sequestering additional CO₂. Hence, a larger

Table 13.2 Constants and parameter values used in the simple carbon model. The Revelle buffer factor of close to 14 reflects the surface value at high latitudes where deep waters are formed. Buffered carbon inventory, I_B , estimated using a global ocean model in Goodwin *et al.* (2007).

Parameter	Symbol	Value	Units
Moles of gas in the atmosphere	M	1.8×10^{20}	mol
Volume of the ocean	V_0	1.4×10^{18}	m^3
Buffer factor (high latitude)	B	~ 14	dimensionless
Solubility of CO_2 (20°C)	K_0	0.033	$\text{mol kg}^{-1} \text{ atm}^{-1}$
Atmospheric X_{CO_2} (pre-industrial)	X_{CO_2}	278	ppmv
$C^{\text{sat}}(\text{modern})$	C^{sat}	~ 2000	$\mu\text{mol kg}^{-1}$
dC^{sat}/dT	γ_T	-9.0	$\mu\text{mol kg}^{-1} \text{ K}^{-1}$
dC^{sat}/dA_T	γ_A	0.80	dimensionless
Reference density	ρ_0	1024.5	kg m^{-3}
Buffered carbon inventory	I_B	~ 3100	Pg C

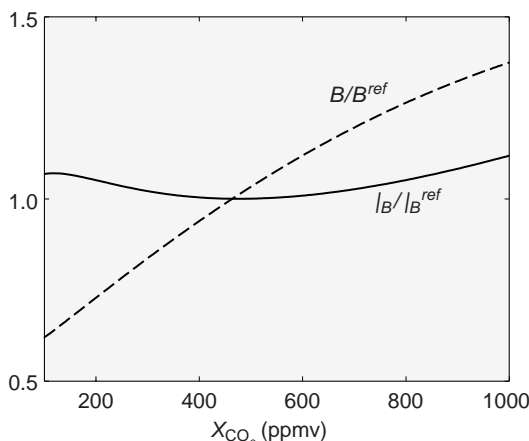


Figure 13.4 Relative changes in the Revelle buffer factor, B (dashed line), and buffered carbon inventory, I_B (solid line), in a system where a parcel of seawater is brought into equilibrium with a range of atmospheric mixing ratios of CO_2 . Each has been normalised by the value when $X_{\text{CO}_2} = 450$ ppmv. Over this range, the Revelle buffer factor varies by a factor of more than two, while I_B varies by only 10%; see Box 13.1.

fraction of the emitted carbon remains in the atmosphere at equilibrium. The resulting effect on radiative heating is explored in Q13.1.

13.2.3 How much carbon dioxide will remain in the atmosphere after 1000 years?

How much carbon dioxide will then remain in the atmosphere following the cessation of fossil-fuel burning, but prior to significant interaction with

the carbonate sediments? The choice of emission scenario alters the amplitude of the transient peak in X_{CO_2} , as depicted in the two model examples in Fig. 13.5a,b. However, the long-term equilibrium is the same in each case, depending only on the integrated amount of carbon emitted (Fig. 13.5b). Based upon the equilibrium predicted from (13.14), if the known fossil-fuel reservoirs of 4000 Pg C are emitted to the atmosphere without any compensating carbon capture, then atmospheric X_{CO_2} would stabilise at about 1000 ppmv in a thousand years, as illustrated in Fig. 13.6.

Over the subsequent tens of thousands of years, atmospheric carbon dioxide is further eroded by interaction of the ocean-atmosphere system with the carbonate sediments (see previous Fig. 13.2b), as discussed next.

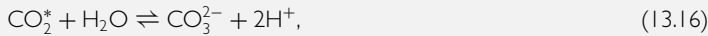
13.2.4 How does the carbonate system vary over 10 000 years?

Now consider a thousand years or so after fossil-fuel burning has ceased, carbon dioxide has invaded the ocean and a quasi-equilibrium has been reached. Initially there is little effect on alkalinity, but eventually the reduction in deep ocean pH and $[\text{CO}_3^{2-}]$ causes dissolution of calcium carbonate deposits (reflected in the shoaling of the carbonate compensation depth and lysocline in Fig. 13.7a). This dissolution of mineral calcium carbonate produces calcium ions, represented simply as



Box 13.1 Why does the buffered carbon inventory, I_B , vary so little?

To understand why I_B is relatively constant, consider again the buffering of the ocean. The net effect of the reactions of carbonate species in seawater from the sum of (6.2) and (6.3) is that



working through the intermediary HCO_3^- (Section 6.3.6). A change in surface ocean $[\text{CO}_2^*]$ (and pCO_2) requires a compensating change in carbonate ion concentration, $[\text{CO}_3^{2-}]$. The DIC in the global ocean is largely attributable to the saturated component and the Revelle buffer factor (derived in Section 6.5 and Box 6.4) may be approximated by

$$B \sim \frac{\text{DIC}}{[\text{CO}_3^{2-}]/\beta_c + [\text{CO}_2^*]} \sim \frac{\overline{C^{sat}}}{[\text{CO}_3^{2-}] + [\text{CO}_2^*]}, \quad (13.17)$$

assuming that $\beta_c \sim 1$. Substituting into the definition of the buffered carbon inventory (13.12),

$$I_B = M X_{\text{CO}_2} + \frac{V_0 \rho_0 \overline{C^{sat}}}{B}, \quad (13.18)$$

and, noting that the surface atmospheric pressure, X_{CO_2} in ppmv, is approximately the same value as pCO_2 in μatm , so that $X_{\text{CO}_2} \simeq [\text{CO}_2^*]/K_0$, with K_0 in $\text{mol kg}^{-1} \text{ppmv}^{-1}$, then I_B can be re-expressed as

$$I_B \sim \left(\frac{M}{K_0} + V_0 \rho_0 \right) [\text{CO}_2^*] + V_0 \rho_0 [\text{CO}_3^{2-}]. \quad (13.19)$$

Thus, I_B is approximately equivalent to the sum of the atmospheric and dissolved oceanic reservoirs of CO_2 , plus the oceanic reservoir of $[\text{CO}_3^{2-}]$. When there are carbon perturbations, changes in $[\text{CO}_2^*]$ and $[\text{CO}_3^{2-}]$ play off each other, while the intermediary HCO_3^- remains approximately constant at present-day pH (Fig. 6.7), so that I_B remains relatively invariant, as illustrated in Fig. 13.4.

which then increases alkalinity. Next, we explore a simple equilibrium relationship between the change in global ocean alkalinity due to changes in calcium carbonate reservoirs and atmospheric X_{CO_2} .

Solving for the relationship of X_{CO_2} and changes in alkalinity

Returning to the changes in the globally integrated carbon reservoirs (13.5),

$$\delta I_{oa} = M \delta X_{\text{CO}_2} + V_0 \rho_0 \left(\delta \overline{C^{sat}} + \delta \overline{C^{reg}} + \delta \overline{\Delta C} \right),$$

and assuming that there are no changes in the soft-tissue and disequilibrium reservoirs, $\delta \overline{C^{reg}} =$

$\delta \overline{\Delta C} = 0$, then

$$\delta I_{oa} = M \delta X_{\text{CO}_2} + V_0 \rho_0 \delta \overline{C^{sat}},$$

as in (13.9). Now consider perturbations to the saturated DIC reservoir from changes in both atmospheric X_{CO_2} and alkalinity in (13.6), such that

$$\delta \overline{C^{sat}} = \frac{\overline{C^{sat}}}{X_{\text{CO}_2} B} \delta X_{\text{CO}_2} + \gamma_A \delta \overline{A_T}, \quad (13.20)$$

and so (13.9) can be expressed as

$$\begin{aligned} \delta I_{oa} &= M \delta X_{\text{CO}_2} \\ &+ V_0 \rho_0 \left(\frac{\overline{C^{sat}}}{X_{\text{CO}_2} B} \delta X_{\text{CO}_2} + \gamma_A \delta \overline{A_T} \right). \end{aligned} \quad (13.21)$$

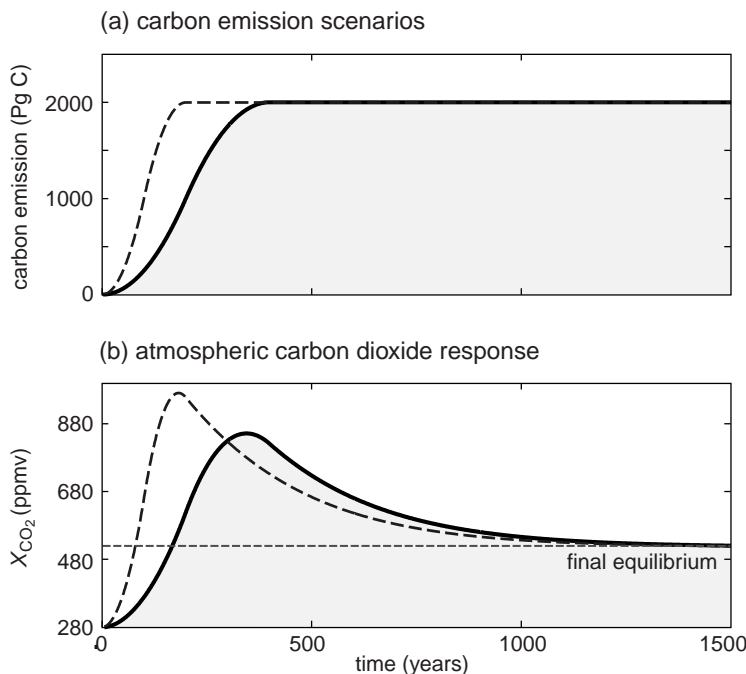


Figure 13.5 An idealised ocean-atmosphere box-model solution for two different imposed emission scenarios (full and dotted lines) for a total emission of 1000 Pg C spread over several hundred years: (a) accumulated carbon emissions ($Pg\text{ C} = 10^{15}\text{ g C}$), and (b) atmospheric mixing ratio of CO_2 (ppmv) versus time (years). In the two model cases, the same total amount of carbon is emitted but spread out over different lengths of time. The transient atmospheric response is different. As expected, the peak atmospheric mixing ratio of CO_2 is higher in a more rapid emission scenario (long dashed line) but the long-term equilibrium is the same in both cases (short dashed line) in (b). These model solutions do not account for the further neutralisation of carbon dioxide by sediments, which occurs on timescales of tens of thousands of years. (Courtesy P. Goodwin.)

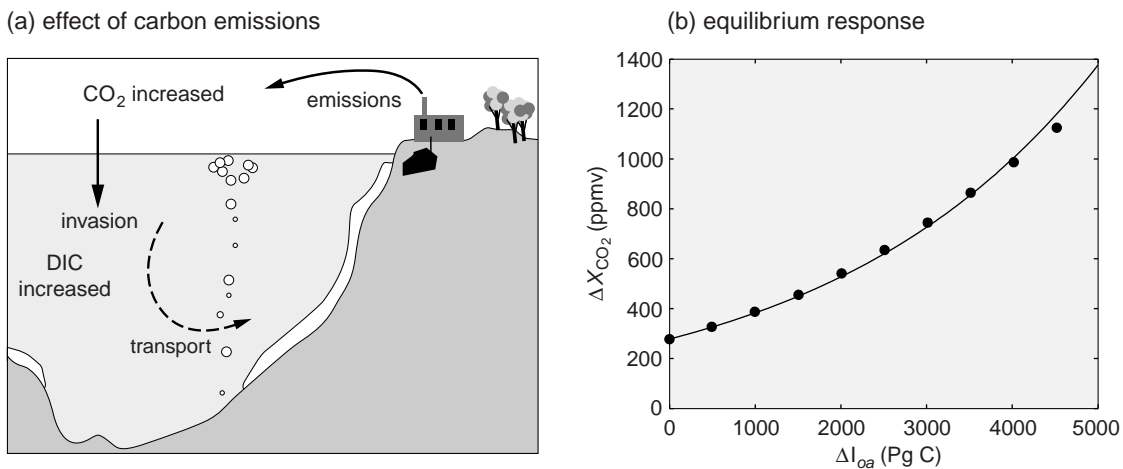


Figure 13.6 Effect of carbon emissions on the ocean and atmosphere: (a) schematic view of the processes and (b) the equilibrium response of atmospheric X_{CO_2} (ppmv) to total emissions from the combustion of fossil fuel as estimated using (13.14). Here we have assumed equilibrium partitioning between atmosphere and ocean reservoirs but not yet any significant interaction with calcium carbonate, so this might represent the state of the system a few thousand years after emissions have ended. I_B is assumed constant at 3180 Pg C, assuming an effective global value of the Revelle buffer factor of 14.1, appropriate for high-latitude surface waters (Goodwin *et al.*, 2007).

From the schematic reaction in (13.15), we see that the formation of calcium carbonate removes two units of A_T (from the double charge of Ca^{2+}) from seawater for every unit of DIC. Thus, pro-

vided there are no other sources and sinks of these properties, we can relate the changes in ocean-atmosphere inventory of carbon, ΔI_{oa} , to changes in global-mean ocean alkalinity, which in turn are

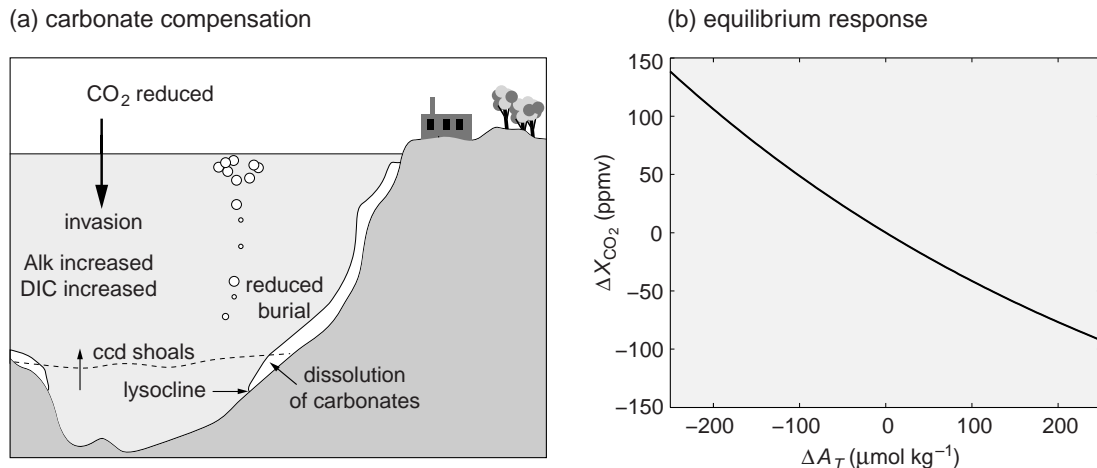


Figure 13.7 (a) A schematic view of carbonate compensation of anthropogenic CO₂. After about a millennium, emitted fossil fuels have invaded the ocean, initially reducing deep ocean pH and [CO₃²⁻], causing the carbonate compensation depth (ccd, dashed line) and lysocline to shoal. The rate of burial of exported carbonate is then reduced below the source of carbon and alkalinity from continental weathering, increasing global ocean alkalinity, the capacity of the oceans to hold DIC and the deep CO₃²⁻ concentration. Burial increases again until the weathering supply is balanced again. (b) Equilibrium relationship between changes in global ocean alkalinity and atmospheric XCO₂, as expressed in the exponential relation (13.23).

related to changes in global-mean calcium ion concentration,

$$2\delta I_{oa} = V_0 \rho_0 \delta \bar{A}_T. \quad (13.22)$$

Combining (13.21) and (13.22), rearranging to eliminate δI_{oa} and assuming that I_B is constant leads again to an exponential relationship between X_{CO_2} and the alkalinity change, $\Delta \bar{A}_T = \bar{A}_T - \bar{A}_T^{\text{ref}}$,

$$X_{CO_2}(\bar{A}_T) = X_{CO_2}(\bar{A}_T^{\text{ref}}) e^{V_0 \rho_0 (0.5 - \gamma_A) \Delta \bar{A}_T / I_B}, \quad (13.23)$$

which is illustrated in Fig. 13.7b. Since $\gamma_A \sim 0.8$ then $(0.5 - \gamma_A) \sim -0.3$ and an increase in global alkalinity, \bar{A}_T , due to CaCO₃ dissolution or weathering drives a decline in X_{CO_2} , and vice versa.

Hence, injection of fossil fuel CO₂ drives a dissolution of calcium carbonate and increases the concentration of calcium ions and alkalinity.

Carbonate compensation

The reduced burial drives an imbalance in the calcium cycle. If the rate of burial of calcium carbonate falls below the riverine input of calcium ions from weathering, there is an increase in global-mean alkalinity. Hence the capacity of the oceans

to hold DIC increases, which leads to an eventual reduction in the atmospheric XCO₂, as illustrated from (13.23) in Fig. 13.7b.

The resulting increase in alkalinity increases deep CO₃²⁻ concentrations and enhances the burial of calcium carbonate until the weathering supply is once more balanced. This process is referred to as carbonate compensation and probably takes tens to hundred of thousand years to come to completion; as suggested in the transient response in Fig. 13.2 (also see Q13.2). After carbonate compensation is completed, only about 10% of the total emissions of carbon dioxide remains in the atmosphere and the extra carbon has been transferred to the deep ocean and sediments (Goodwin and Ridgwell, 2010).

13.2.5 Summary

Carbon emissions are driving a transient increase in atmospheric CO₂ and DIC over much of the upper ocean (Fig. 11.24). On timescales of many hundreds of years, the deeper ocean will gradually equilibrate with the atmosphere. The response of the ocean is not straightforward: the lowering of pH causes dissolved CO₂* to increase at a greater rate than DIC and the ocean takes

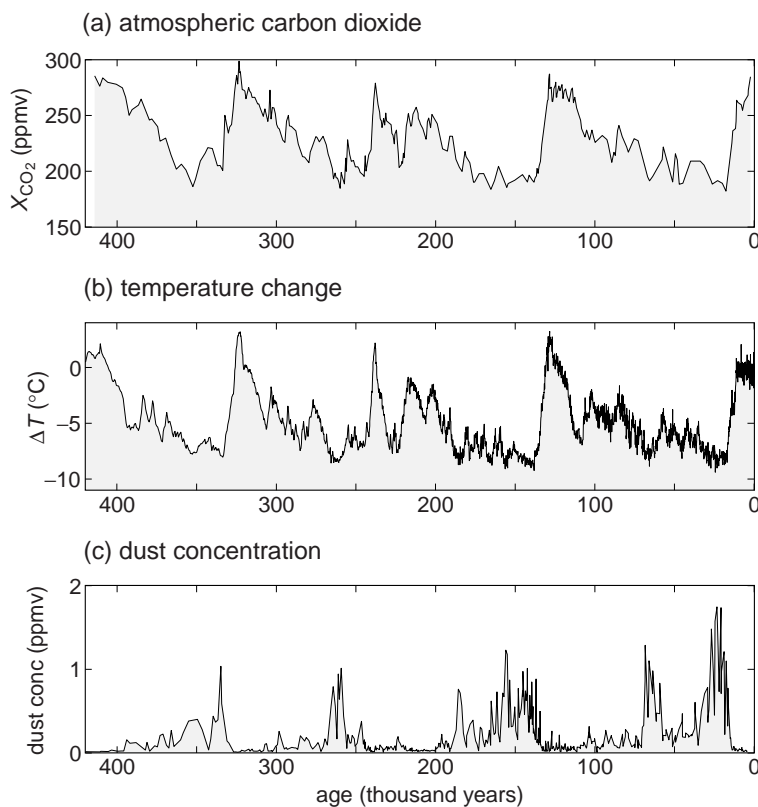


Figure 13.8 Changes associated with glacial–interglacial variations as recorded in the Vostok ice core from Antarctica over the last 400 000 years. Each year, snow accumulates and is eventually packed down into ice; the bubbles of air trapped in the ice provide information about long-term changes in the planet: (a) atmospheric mixing ratio X_{CO_2} (ppmv) measured in bubbles of gas trapped in the ice, which can be viewed as representing a global change, since carbon dioxide is well mixed in the atmosphere; (b) local temperature change ($^{\circ}\text{C}$) as indicated by the isotopic composition of the water in the ice; and (c) concentration of windborne dust deposited in the ice; higher dust concentrations might reflect stronger continental sources or changes in wind strength and circulation, which is likely to be similar for the delivery of dustborne iron to the remote Southern Ocean. Data from Petit *et al.* (1999).

up less of the emitted carbon. After the ocean and atmosphere have equilibrated, but prior to sediment interactions, there is an exponential relationship between atmospheric CO_2 and the integrated amount of carbon being emitted. This simple balance suggests that if the known fossil-fuel reservoirs of 4000 Pg C are consumed (without any compensating carbon capture), then atmospheric X_{CO_2} increases to 1000 ppmv on a millennial timescale (after a larger transient peak). Over the subsequent tens of thousands of years, atmospheric carbon dioxide is eventually reduced by interaction of the ocean–atmosphere system with the carbonate sediments.

Next we consider some possible drivers of past glacial–interglacial cycles using the same simplified model framework.

13.3 Glacial–interglacial changes in atmospheric CO_2

There have been striking glacial–interglacial variations in atmospheric carbon dioxide over nearly

the last million years, as revealed by analysis of ice cores from Greenland and Antarctica (illustrated in Fig. 13.8a). Prior to the industrial era, atmospheric carbon dioxide consistently reached a maximum of 280 to 300 ppmv during interglacial periods and declined to a minimum of about 180 ppmv during glacial periods. These changes in atmospheric carbon dioxide are positively correlated with variations in Antarctic temperatures (Fig. 13.8b).

For the transition at 240 000 years ago, the Antarctic temperature changes lead the atmospheric carbon dioxide changes by 800 ± 200 years and are followed by deglaciation in the northern hemisphere over the subsequent ~ 4200 years (Caillon *et al.*, 2003). For the changes at 130 000 years, the Antarctic temperature and atmospheric carbon dioxide changes are closely coupled, both increasing over 8000 years, again the changes preceding melting of the northern hemisphere ice sheets and any reorganisation of nutrients in the North Atlantic (Broecker and Henderson, 1998). Hence, glacial–interglacial changes might be initiated by physical changes

in the Southern Ocean, which are then amplified by the carbon cycle and subsequent changes in ocean chemistry (Peacock *et al.*, 2006).

These glacial-interglacial cycles pose profound challenges to our understanding of climate and the carbon cycle: which mechanisms determine the upper and lower bounds for atmospheric CO₂, what is the extent that climate change drives the CO₂ variations and how important is the climate feedback from atmospheric CO₂? There are many hypotheses as to the controlling mechanisms, but few widely accepted answers. Next we discuss some potentially significant mechanisms in determining the magnitude of the atmospheric CO₂ changes; more comprehensive reviews are provided in Section 13.7.

13.3.1 Why is the ocean implicated in glacial-interglacial changes of CO₂?

The glacial-interglacial swings in atmospheric CO₂ are large, transferring hundreds of Pg C between the carbon reservoirs (Fig. 13.1). Some of the carbon changes are relatively rapid, moving into the interglacials, atmospheric CO₂ increases in just a few thousand years, as illustrated in Fig. 13.8a. Now we consider which carbon reservoirs might play a role in taking up carbon from the atmosphere during the glacials and returning carbon during the interglacials.

The atmosphere and ocean are connected to the very large, geological inventories of carbon via weathering and sedimentation, but these processes act on relatively slow timescales of tens of thousands to millions of years. The atmosphere can also exchange carbon relatively rapidly with the terrestrial reservoirs, including carbon stored in soils and vegetation. However, the terrestrial store of carbon is expected to decrease during glacial periods due to the drier, windier, ice-covered continents, which would act to release carbon to the atmosphere, rather than take up carbon as is required. Since neither geological and terrestrial changes appear likely to explain glacial-interglacial cycles, we are left with ocean changes as the remaining plausible option. The carbon reservoirs in the ocean can re-equilibrate with the atmosphere in a few thousand years and the ocean inventory is large enough that small

perturbations can drive significant changes in atmospheric carbon dioxide.

Next we consider in turn some of the possible ocean mechanisms that may play an important role in glacial-interglacial changes.

13.3.2 Temperature and solubility changes

Measurements of the properties of pore waters in sediments suggest that the deep waters of the ocean might have been as much as 4 °C colder at the Last Glacial Maximum (Adkins *et al.*, 2003). Cooler deep waters mean higher solubility and enhance the ocean uptake of carbon from the atmosphere. How much of the recorded 80–100 ppmv decrease in X_{CO₂} during glacial periods might be simply due to ocean cooling?

How does X_{CO₂} vary with global ocean temperature?

The largest contribution to the ocean's dissolved inorganic carbon is the saturated carbon, $\overline{C^{sat}}$, due to the abiotic equilibration of the ocean and atmospheric reservoirs (Section 11.4). The vast majority of the ocean is made up of deep and bottom waters, so that $\overline{C^{sat}}$ is very dependent on their temperature and alkalinity.

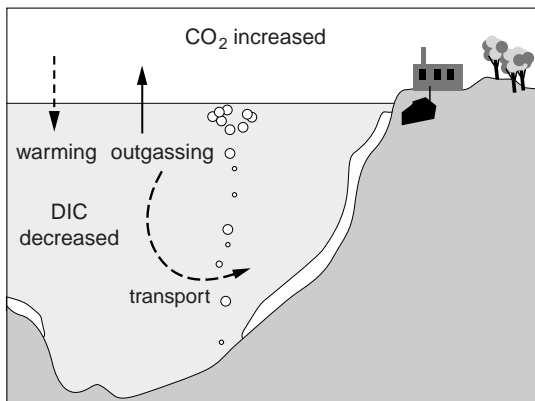
$\overline{C^{sat}}$ decreases almost linearly with increasing temperature at fixed X_{CO₂} (Fig. 13.3a), so a decrease in the global-mean temperature should lead to an increase in $\overline{C^{sat}}$ and a decrease in atmospheric X_{CO₂}. This decline in X_{CO₂} partly compensates for the temperature-driven increase in $\overline{C^{sat}}$, and this feedback needs to be accounted for. We can use the simple carbon inventory framework (provided by (13.5)–(13.8)) to evaluate this relationship between global-mean ocean temperature and atmospheric X_{CO₂}.

Assuming that the total ocean-atmosphere carbon inventory remains fixed ($\delta I_{oa} = 0$) and that there is no change in the magnitude of the biological and disequilibrium carbon reservoirs ($\delta \overline{C^{reg}} = \delta \overline{\Delta C} = 0$), then changes in the atmospheric inventory are equal and opposite to the change in the saturated carbon inventory, such that (13.5) reduces to

$$0 = M \delta X_{CO_2} + V_0 \rho_0 \delta \overline{C^{sat}}. \quad (13.24)$$

Since we are assuming no change in ocean alkalinity ($\delta \overline{A_T} = 0$), combining with (13.6) and (13.8)

(a) effect of warming



(b) equilibrium response

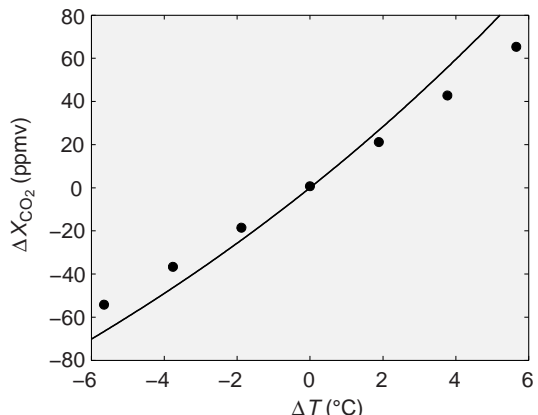


Figure 13.9 (a) A schematic view of the role of global-mean ocean temperature in regulating atmospheric carbon dioxide. (b) The equilibrium response of atmospheric X_{CO_2} (ppmv) to changes in global-mean ocean temperature according to the simple relationship in (13.25). Points indicate corresponding values from sensitivity studies with a numerical ocean model (Omta *et al.*, 2011). Model results provided by A. W. Omta.

we describe the system by

$$0 = M \delta X_{CO_2} + V_0 \rho_0 \left(\gamma_T \delta \bar{\theta} + \frac{\bar{C}^{sat}}{B X_{CO_2}} \delta X_{CO_2} \right), \quad (13.25)$$

where the first term on the right indicates the change in the atmospheric inventory of carbon and the second indicates the direct change on \bar{C}^{sat} and the ocean carbon inventory due to a change in potential temperature. The last term on the right accounts for the buffering feedback induced by changing X_{CO_2} : as the ocean cools and carbon dioxide is absorbed, X_{CO_2} is reduced, which in turn partly reduces \bar{C}^{sat} .

Rearranging (13.25) provides an estimate of the sensitivity of atmospheric carbon dioxide to changes in global-mean ocean potential temperature,

$$\begin{aligned} \frac{\partial X_{CO_2}}{\partial \bar{\theta}} &= -\frac{V_0 \rho_0 X_{CO_2} \gamma_T}{M X_{CO_2} + \frac{V_0 \rho_0 \bar{C}^{sat}}{B}} \\ &= -V_0 \rho_0 X_{CO_2} \frac{\gamma_T}{I_B}. \end{aligned} \quad (13.26)$$

This expression accounts only for the direct effect of temperature on the seawater carbonate chemistry and neglects any indirect changes, for example, those due to a response in the biological

carbon pumps. The change in atmospheric X_{CO_2} is then exponentially related to the change in potential temperature, $\Delta\theta = \theta - \bar{\theta}^{ref}$, for a long-term equilibrium,

$$X_{CO_2}(\bar{\theta}) = X_{CO_2}(\bar{\theta}^{ref}) e^{-\Delta\bar{\theta}} V_0 \rho_0 \gamma_T / I_B. \quad (13.27)$$

Since γ_T is negative, this response is consistent with atmospheric X_{CO_2} increasing as climate warms due to the decrease in solubility and net outgassing from the ocean. While (13.27) is an exponential expression, for realistic parameters (Table 13.2), the equilibrium X_{CO_2} varies in a relatively linear fashion with a 10 ppmv increase in X_{CO_2} for each degree increase in ocean temperature, as illustrated in Fig. 13.9.

This response can be complicated by other feedbacks. An increase in deep ocean DIC due to a decrease in temperature, for example, acidifies the deep waters, reduces burial of calcium carbonate and increases global alkalinity. In this case, the alkalinity increase and subsequent carbonate compensation further enhances ocean storage of carbon and amplifies the initial decline in X_{CO_2} due to temperature (e.g., Brovkin *et al.*, 2007).

Implications for glacial-interglacial change

During the glacial intervals of the past half million years or so of Earth's history, the waters of

the deep ocean were almost certainly cooler: measurements of pore waters in marine sediments suggest that water masses were as much as 4 °C cooler during the Last Glacial Maximum than today in the North Atlantic, and 2 °C cooler in the Southern Ocean and Pacific basin (Adkins *et al.*, 2003). Might this cooling of the oceans, and the associated increase in the solubility of CO₂ and C^{sat}, account for the 100 ppmv reduction of atmospheric CO₂ in glacial periods? The simple carbon relationship (13.27) suggests that a global change in ocean temperature, ΔT, of ±4 °C leads to a change in the atmospheric mixing ratio of CO₂ by ±40 ppmv (Fig. 13.9b), all other factors remaining constant. Hence, temperature changes can make an important contribution to the observed glacial-interglacial changes in CO₂, but by themselves cannot explain the entire signal. Next we consider the effect of other contributing factors.

13.3.3 Changes in alkalinity and calcium carbonate cycling

There might be alkalinity changes during glacial periods from a reduction in suitable habitat for corals (Berger, 1982) or a shift from calcifying primary producers to diatoms (Brzezinski *et al.*, 2002), assuming no change in continental weathering rates. The initial response to a shift from calcification in the surface ocean is to increase surface alkalinity, enhancing the capacity of surface waters to hold DIC, and increasing preformed DIC in the deep ocean at the expense of atmospheric CO₂.

Over many thousands of years, the deficit in burial (relative to the weathering source) leads to an increase in global-average alkalinity, further increasing DIC and further reducing atmospheric CO₂ (Sigman and Boyle, 2000). The decline in burial increases global alkalinity at twice the rate that it delivers DIC, which increases pH and [CO₃²⁻] in the deep ocean and increases the burial rate of CaCO₃ (and deepens the carbonate-compensation horizon). Over tens to hundreds of thousands of years, a balance between weathering and burial is restored, and ocean alkalinity is returned to the pre-perturbation value.

On what timescale does calcium carbonate export significantly alter ocean alkalinity?

On timescales of less than hundreds of thousands of years, there can be an imbalance between the input of calcium ions to the ocean from weathering of calcium carbonate, and the burial of calcium carbonate in marine sediments. If burial of calcium carbonate decreased by 10%, perhaps from an ecologically driven change in the ratio between organic and inorganic carbon in sinking particles, while the rate of weathering remained constant with a river supply of 10¹³ moles Ca²⁺ to the ocean each year, global-average alkalinity would increase at a rate of about 14 μmol kg⁻¹ every 10 000 years, with an associated decrease in atmospheric X_{CO₂} of about 8 ppmv using (13.23); see Q13.2 for details. Viewed simply, if this rate of change persists over 100 000 years then ocean alkalinity increases by 140 μmol kg⁻¹ and, using (13.23) and Fig. 13.7b atmospheric X_{CO₂} decreases by 80 ppmv.

Implications for glacial-interglacial change

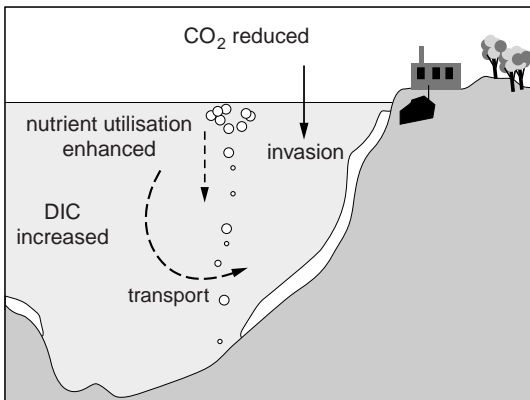
While such a change in calcium carbonate burial and global ocean alkalinity provides a potentially appealing explanation for glacial decline in X_{CO₂}, the reduction in the export of CaCO₃ to the sea floor would also lead to an increase in deep ocean [CO₃²⁻]. In turn, the lysocline would deepen by more than 1 km as the system moved towards a new equilibrium (Sigman and Boyle, 2000). However, such a change in the lysocline is not supported by sedimentary evidence and so global alkalinity changes are not thought to account for the majority of the glacial reduction in X_{CO₂}, although they may be a contributing factor.

Next we consider how a change in ocean productivity and nutrient utilisation might influence atmospheric carbon dioxide, X_{CO₂}.

13.3.4 Changes in the export of organic carbon

An increase in the export of organic carbon to the deep ocean might have occurred in glacial periods, either through an increase in the abundance of a limiting nutrient and/or an increase in the efficiency of nutrient utilisation. An increase in the atmospheric transport of iron-rich dust to

(a) effect of soft-tissue biological cycling



(b) equilibrium response

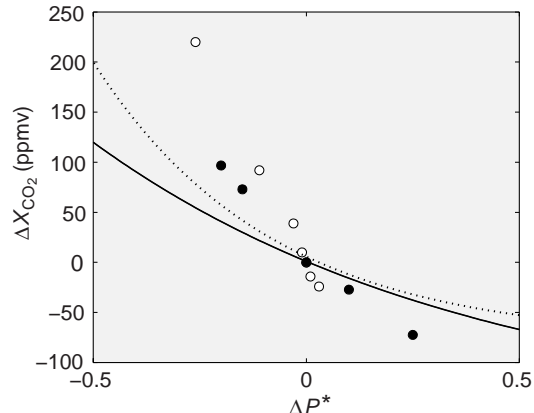


Figure 13.10 (a) A schematic view of the regulation of atmospheric X_{CO_2} by the ocean's soft-tissue pump. (b) The equilibrium response of atmospheric X_{CO_2} (ppmv) to changes in global-mean nutrient utilisation, assuming that ocean-atmosphere inventory of carbon, disequilibrium carbon reservoir and ocean temperature are unchanging. Solid line indicates the simple analysis of (13.32), while the points indicate numerical model results from Ito and Follows (2005; filled circles) and Parekh *et al.* (2006; open circles) which have a steeper gradient. The steeper dotted line indicates the modified relationship when accounting for the coupling between the soft-tissue ($\overline{C^{\text{reg}}}$) and disequilibrium ($\Delta\overline{C}$) pumps; in this case, upwelled waters are resubducted rapidly relative to outgassing or biological uptake of the entrained nutrients and carbon; this regime is explored in Q13.3.

the remote oceans (Fig. 13.8) might have relieved iron limitation of export in high nitrate, low chlorophyll regimes (as proposed by Martin and Fitzwater, 1988) or led to an increase in the abundance of nitrogen-fixing organisms and relieved nitrogen limitation over the oligotrophic gyres (Falkowski, 1997). If changes in ocean circulation led to an increased availability of silicic acid in the surface ocean, a shift towards diatom production and away from coccolithophorids might also have enhanced export efficiency (Brzezinski *et al.*, 2002).

How does X_{CO_2} vary with changes in the soft-tissue pump?

The vast majority of DIC in the ocean reflects an abiotic equilibration with the atmosphere, the soft-tissue pump enhances the ocean's DIC inventory by nearly 1700 Pg C (Table 13.1), almost half the magnitude of the buffered carbon inventory (Fig. 13.10a). Starting again from the statement of conservation of carbon in the ocean-atmosphere system (13.5),

$$\delta I_{oa} = M \delta X_{\text{CO}_2} + V_0 \rho_0 (\delta \overline{C^{\text{sat}}} + \delta \overline{C^{\text{reg}}} + \delta \Delta \overline{C}),$$

we assume that total ocean-atmosphere carbon inventory is conserved, $\delta I_{oa} \sim 0$, on the timescale

of several thousand years, over which the ocean and atmosphere inventories approach equilibrium (not considering the longer timescale adjustment and equilibration with the carbonate sediments). We also assume that the disequilibrium reservoir does not change, $\delta \Delta \overline{C} \sim 0$, leading to the relationship:

$$0 = \frac{M}{V_0 \rho_0} \delta X_{\text{CO}_2} + \delta \overline{C^{\text{sat}}} + \delta \overline{C^{\text{reg}}}. \quad (13.28)$$

Substituting for $\delta \overline{C^{\text{sat}}}$ from (13.6) and (13.8) and assuming that alkalinity and temperature do not change, $\delta A_T = \delta \theta = 0$, (13.28) leads to

$$0 \simeq \left(M + V_0 \rho_0 \frac{\overline{C^{\text{sat}}}}{B X_{\text{CO}_2}} \right) \delta X_{\text{CO}_2} + V_0 \rho_0 \delta \overline{C^{\text{reg}}}. \quad (13.29)$$

Changes in the globally integrated soft-tissue pump, $V_0 \rho_0 \delta \overline{C^{\text{reg}}}$, the global ocean inventory of DIC that is attributable to the formation and export of organic compounds, are related to the integrated regenerated phosphorus pool and the global-mean efficiency of nutrient utilisation, \overline{P}^* (see Sections 11.3 and 11.4):

$$\overline{C^{\text{reg}}} = R_{\text{CP}} \text{PO}_4^{\text{reg}} = R_{\text{CP}} \overline{\text{PO}_4^{3-}} \overline{P}^*. \quad (13.30)$$

$\overline{\mathcal{P}}^*$ lies between 0 and 1. If $\overline{\mathcal{P}}^*$ is 1, all of the phosphate present in the subsurface ocean arrived there through the export and regeneration of organic matter. This limit represents the maximum efficiency of the biological utilisation of available nutrient and $\overline{C^{reg}} \sim R_{CP} \overline{PO_4^{3-}}$. On the other hand, if $\overline{\mathcal{P}}^*$ is 0, all of the phosphate in the subsurface ocean arrived there through subduction from the surface waters. In this limit, the ocean is effectively dead and $\overline{C^{reg}} \sim 0$.

Combining (13.29) and (13.30), utilising the definition of I_B (13.12), and rearranging, leads to an expression describing the sensitivity of atmospheric X_{CO_2} to the global efficiency of nutrient utilisation $\overline{\mathcal{P}}^*$:

$$\frac{\delta X_{CO_2}}{X_{CO_2}} \simeq -\frac{V_0 \rho_0 R_{CP} \overline{PO_4^{3-}}}{I_B} \delta \overline{\mathcal{P}}^*, \quad (13.31)$$

which, when integrated provides a simple exponential relationship between atmospheric carbon dioxide and the efficiency of nutrient utilisation,

$$X_{CO_2}(\overline{\mathcal{P}}^*) = X_{CO_2}(\overline{\mathcal{P}}_{ref}^*) e^{-V_0 \rho_0 R_{CP} \overline{PO_4^{3-}} \Delta \overline{\mathcal{P}}^*/I_B}, \quad (13.32)$$

where $\overline{\mathcal{P}}^* = \overline{\mathcal{P}}_{ref}^* + \Delta \overline{\mathcal{P}}^*$. This relationship reflects how the storage of carbon increases in the deep ocean due to the formation and export of soft-tissue organic matter, which in turn reduces the atmospheric carbon dioxide at equilibrium; this relationship is illustrated in Fig. 13.10, considering changes in $\overline{\mathcal{P}}^*$ relative to a typical present-day value of about 0.4 and using values from Table 13.2. The relationship is non-linear, with stronger sensitivity to nutrient utilisation efficiency as the soft-tissue pump weakens; over the whole range of $\overline{\mathcal{P}}^*$, from a dead ocean to maximum efficiency, this simple model suggests a decrease of atmospheric X_{CO_2} of almost 200 ppmv.

Implications for glacial-interglacial change

In the global ocean, changes to iron, nitrogen and light availability are likely candidates for the regulation of productivity and phosphorus utilisation. The availability of iron has been demonstrated experimentally in the Southern Ocean, tropical Pacific and Sub-Arctic Pacific. Examination of ice cores from Antarctica have revealed

that in the cold, dry, windy glacial climates, the atmospheric transport of iron-bearing terrestrial dust to the remote Southern Ocean increased (Fig. 13.8c; Petit *et al.*, 1999). Could the increased atmospheric deposition of dust in the remote Southern Ocean have relieved iron limitation, enhanced macro-nutrient utilisation and reduced atmospheric X_{CO_2} by as much as 100 ppmv?

The simple equilibrium relationship between X_{CO_2} and $\overline{\mathcal{P}}^*$ in (13.32) suggests that a drawdown of 100 ppmv in atmospheric X_{CO_2} might be possible (Fig. 13.10b). Currently, nutrient utilisation, $\overline{\mathcal{P}}^* \sim 0.4$, so the soft-tissue pump is acting considerably below its maximum efficiency. Increasing nutrient utilisation significantly so that $\overline{\mathcal{P}}^* \sim 1$ could reduce atmospheric X_{CO_2} by about 100 ppmv, all other factors being equal, according to this simple model.

However, more complex and more realistic numerical models of the three-dimensional global ocean circulation and carbon cycle suggest that it is difficult to increase nutrient utilisation efficiency by enhancing the iron supply. Increasing the source of iron to the remote oceans by a factor of five in such models, in accord with glacial levels of dust deposition, increases nutrient utilisation only marginally ($\Delta \overline{\mathcal{P}}^* \leq +0.1$) and reduces X_{CO_2} by only 10 or 20 ppmv (e.g., Parekh *et al.*, 2006). These models suggest that iron fertilisation is not the single cause of glacial-interglacial X_{CO_2} changes, although it might play a contributing role.

What controls the efficiency of global ocean nutrient utilisation?

Why is iron fertilisation unlikely to enhance global-mean nutrient utilisation? The total abundance of phosphate in the ocean is the sum of preformed and regenerated components, $\overline{PO_4^{3-}} = \overline{PO_4^{pre}} + \overline{PO_4^{reg}}$. The biologically (soft-tissue) mediated storage of carbon in the deep ocean is proportional to $\overline{PO_4^{reg}}$. If the total inventory of phosphorus, $V_0 \rho_0 \overline{PO_4^{3-}}$, is constant, then the regenerated component (and nutrient utilisation) can only be increased if the preformed component can be simultaneously reduced.

For complete nutrient utilisation, any phosphate brought into the surface mixed layer

by physical transport must be consumed by phytoplankton and returned to depth in organic form. At higher latitudes, nutrients are brought to the surface by the physical transport and convection. During winter, when convection is active, the Sun is low in the sky, the mixed layer is thick and consumption of nutrients is usually light limited. When light limitation is relieved in the spring, the shoaling of the mixed layer leads to the subduction of nutrient-rich waters into the thermocline prior to the onset of significant biological uptake. Adding iron to the surface waters may enhance the utilisation of macronutrients during the summer, but will be ineffective during the light-limited period. Hence, the timing of wintertime convection and light limitation place strong constraints on the efficiency of nutrient utilisation. Likewise the timing of dense, cold bottom waters formed by cascading from high latitude, shallow shelves occurs during winter or spring, probably prior to any phytoplankton bloom.

How the preformed nutrients in deep waters might vary with climate change is still an open question. For obvious, practical reasons we have few direct observations of deep and bottom water formed in convective chimneys or shelf overflows, nor an understanding of the extent of nutrient utilisation during these events. Yet these processes critically affect the long-term partitioning of carbon between the atmosphere and ocean.

13.3.5 Reorganisation of water masses in glacial–interglacial change

Large scale rearrangements of the deep water masses might significantly affect how much carbon is stored in the ocean on glacial–interglacial timescales (e.g., Toggweiler *et al.*, 2003). During the last glacial, there is thought to have been an increase in the volume of bottom waters emanating from Antarctica, and a reduction of the volume of deep waters originating in the northern North Atlantic, based upon inferred paleoceanographic data, such as the reconstructed phosphate profile for the last glacial in Fig. 12.18.

The effect of change in the relative proportions of bottom and deep waters from the Antarctica and the northern North Atlantic, as well as the other factors already discussed, have been inves-

tigated in an Earth system model (Brovkin *et al.*, 2007). The reorganisation of deep water masses leads to a global ocean cooling of 3 °C, increases the volume of high DIC bottom waters, and bathes the deep Atlantic sediments in more acidic waters, reducing carbonate burial. A combination of these processes leads to an overall reduction in X_{CO_2} of nearly 90 ppmv during a glacial (summarised in Table 13.3), which is comparable to the observed change. While this agreement is encouraging, there are large inherent uncertainties in this and any other model estimate for glacial–interglacial changes.

13.3.6 Carbon summary

Despite the complexity in the carbon system, simple models can be developed, which reveal the essential response of the carbon cycle to natural and anthropogenic perturbations on timescales of thousands of years and longer. For the anthropogenic future, the ocean will take up an increasingly smaller fraction of carbon emissions due to changes in ocean chemistry, and so reduce its effect in ameliorating climate forcing.

Oceanic processes are strongly implicated as drivers of glacial–interglacial changes in atmospheric carbon dioxide. While no single mechanism is likely to account for the whole change, a combination of mechanisms may contribute (Peacock *et al.*, 2006; Brovkin *et al.*, 2007), including temperature and solubility changes, modification of ocean ecosystems and the biological pumps, and interactions with sedimentary calcium carbonate reservoirs; for more detailed discussion, see the reviews in Section 13.7.

13.4 Water-mass formation and transformation

The physical circulation involves a wide range of phenomena: seasonal mixing in the surface ocean, basin circulations involving gyres and boundary currents, near-zonal flows in the tropics and Southern Ocean, eddy stirring, enhanced turbulent mixing near rough topography and overturning circulations. Due to the importance of many of these processes acting on relatively fine horizontal

Table 13.3 Contributions to the glacial reduction of atmospheric CO₂ in the Earth system model of Brovkin *et al.* (2007). This coupled model of atmospheric and oceanic circulation and biogeochemical cycles included explicit representation of calcium carbonate burial and dissolution in sediments. In a series of sensitivity studies, various potentially significant mechanisms were switched on and off in the model. In all cases, the response of the ocean system included the response of carbonate compensation, which occurs over tens of thousands of years. These estimates have large inherent uncertainties.

Process	Glacial reduction in X _{CO₂} with carbonate compensation (ppmv)	Note
Circulation and temperature change	-43	Global ocean ΔT = -3°C
Complete Sub-Antarctic, Atlantic and Indian	-37	Complete utilisation not supported by explicit iron cycle models
Ocean phosphate utilisation		
Complete Sub-Arctic Pacific phosphate utilisation	-7	
Shallow-water carbonate sedimentation	-12	
20% decrease in rain ratio	-15	
Terrestrial carbon change	+15	
Sea level change	+12	
Sum	-87	

scales, it is easy to lose sight of the global connections between how the ocean is forced at the surface and how water masses spread and overturn over the globe. To highlight this connection, we now consider an integrated physical view of the global ocean, addressing how water masses form and their transformation from light to dense water, following an isopycnal framework developed by Walin (1982).

13.4.1 Walin isopycnal view

Consider a volume element, ΔV , bound by two potential density surfaces, ρ and $\rho + \Delta\rho$, which outcrop over the sea surface and exit the domain through an open boundary, as depicted in Fig. 13.11a; henceforth ρ is taken as potential density in this chapter.

The volume between the bounding potential density surfaces can increase in time through the net volume flux out of the domain, $\Delta\Psi$, and the difference in the diapycnal volume fluxes passing into the layer, $G(\rho)$, and out of the layer $G(\rho + \Delta\rho)$ (Fig. 13.11a); here the volume fluxes, G and $\Delta\Psi$, have units of m³ s⁻¹ and see Box 13.2 for accompanying volume and density budgets.

Water-mass formation

The water-mass formation rate, $M\Delta\rho$, is defined as the rate of accumulation of water between the two potential density surfaces, ρ and $\rho + \Delta\rho$, given by the rate at which the volume element increases in time, $\partial\Delta V/\partial t$, plus the net volume flux leaving the domain, $\Delta\Psi$,

$$M\Delta\rho \equiv \left(\frac{\partial\Delta V}{\partial t} + \Delta\Psi \right) = -\Delta\rho \frac{\partial G}{\partial\rho}, \quad (13.33)$$

which balances the convergence of the diapycnal volume fluxes, $-\Delta\rho\partial G/\partial\rho$.

Diapycnal volume flux and transformation

The density budget of the control volume between the bounding surfaces, ρ and $\rho + \Delta\rho$, involves a balance between advective and diffusive density fluxes, as depicted in Fig. 13.11b.

The volume flux directed across the density surfaces, G , represents a diapycnal volume flux, defined as positive when directed towards increasing density. G is also referred to as transformation, since positive G represents the transfer of volume across a density surface, which is equivalent to light water being transformed to dense water. G

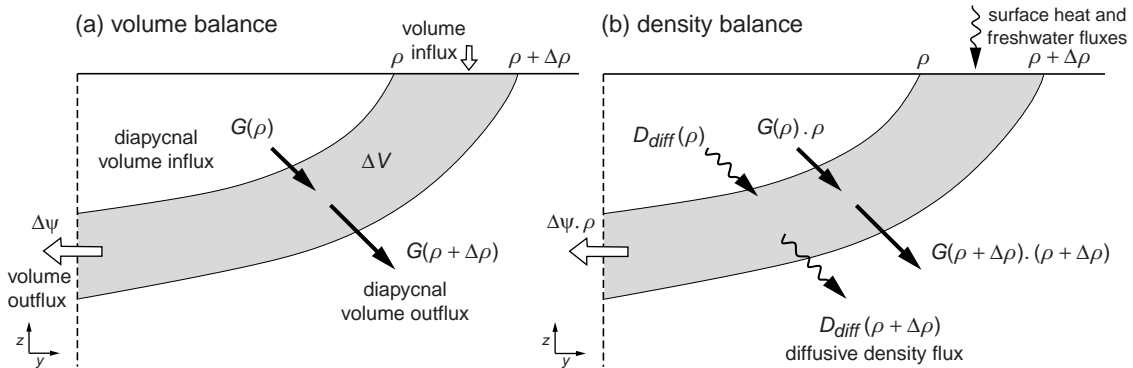


Figure 13.11 Schematic vertical sections showing the volume and the density balances for a volume element bounded by the potential density surfaces ρ and $\rho + \Delta\rho$ that outcrop at the sea surface: (a) the volume of the layer depends on the difference in the diapycnal volume fluxes, $G(\rho)$ and $G(\rho + \Delta\rho)$, crossing the density surfaces, the volume flux leaving the domain minus the volume flux passing through the sea surface, $\Delta\Psi$; (b) density content of the layer depends on the advective change from the diapycnal volume flux, ρG , the mass exiting the domain, $\rho \Delta\Psi$, as well as the difference in the diffusive density fluxes across the layer, D_{diff} and the density gained from the atmosphere from the surface heat and freshwater fluxes over the surface outcrop, $\int_{\text{outcrop}} D_{\text{in}} dA$. Redrawn from Nurser et al. (1999).

depends on the gradients in the surface and diffusive fluxes in density space,

$$G = -\frac{\partial D_{\text{diff}}}{\partial \rho} + \frac{1}{\Delta\rho} \int_{\text{outcrop}} D_{\text{in}} dA, \quad (13.34)$$

such that a diapycnal volume flux directed from light to dense water, $G(\rho) > 0$, requires a density supply either from a convergence of diffusive density fluxes, $-\partial D_{\text{diff}}/\partial \rho > 0$, or from the effective surface density flux, $\int_{\text{outcrop}} D_{\text{in}} dA > 0$. Here, the effective surface density flux depends upon the surface heat and freshwater fluxes given by $D_{\text{in}} = -\frac{\alpha_T}{C_p} H + \rho \beta_S S(\mathcal{E} - \mathcal{P})$ and has units of mass per unit area and unit time, $\text{kg m}^{-2} \text{s}^{-1}$, and the diffusive density flux integrated along the density surface, D_{diff} , is in units of mass per unit time, kg s^{-1} .

The transformation is now estimated over the globe for seasonal changes in the air-sea heat and freshwater fluxes, ignoring the contribution of diffusive mixing; this limit has been applied in diagnosing mode-water formation in the North Atlantic by Speer and Tziperman (1992).

Seasonal transformation from air-sea fluxes

Surface density forcing leads to an overall reduction in surface density in the tropics and gain in surface density over the western boundary currents and the high latitudes (Fig. 13.12, light and dark shading, respectively).

The diapycnal volume flux or transformation, G , in density space depends on the surface density flux for a particular month, integrated along the same density outcrop over the globe. The density outcrop migrates seasonally, reaching its most equatorward position at the end of winter and most poleward position at the end of summer (Fig. 13.12, full and dashed lines, respectively).

G is evaluated over the globe using the surface heat and freshwater fluxes for each month along each density outcrop, then each monthly contribution summed for either the cooling or heating seasons. In the northern hemisphere, G reaches 150 Sv in the cooling period, representing water being transformed from light to dense water (Fig. 13.13a, dotted line). While in the warming period, G reverses to -100 Sv, representing water being transformed from dense to light water (Fig. 13.13a, dashed line).

A similar balance occurs over the southern hemisphere with slightly larger seasonal changes (Fig. 13.13b), reflecting the larger fractional area of the ocean.

Annual transformation from air-sea fluxes

For these monthly transformations summed over the entire year, G is positive for $\sigma > 23.5$, representing an overall transformation to dense water,

Box 13.2 | Water-mass transformation and formation

Consider the volume bound by the ρ and $\rho + \Delta\rho$ surfaces, which outcrop over the sea surface, over a limited part of the ocean with an open boundary (Fig. 13.11a).

The *volume budget* is given by a balance between the temporal increase in the volume element, ΔV , the volume flux out of the domain through the open boundary minus the volume flux entering the domain through the sea surface, $\Delta\Psi$, and the difference in the diapycnal volume fluxes passing into the layer; $G(\rho)$, and out of the layer $G(\rho + \Delta\rho)$:

$$\left(\frac{\partial \Delta V}{\partial t} + \Delta\Psi \right) = G(\rho) - G(\rho + \Delta\rho) = -\Delta\rho \frac{\partial G}{\partial \rho}. \quad (13.35)$$

The *density budget* of the control volume between the ρ and $\rho + \Delta\rho$ surfaces is a balance between advective and diffusive density fluxes (Fig. 13.11b):

$$\begin{aligned} & \underbrace{\left(\frac{\partial(\Delta V)}{\partial t} + \Delta\Psi \right) \rho + (\rho + \Delta\rho)G(\rho + \Delta\rho) - \rho G(\rho)}_{\text{density gain}} \\ &= -\underbrace{(D_{\text{diff}}(\rho + \Delta\rho) - D_{\text{diff}}(\rho))}_{\text{diffusive fluxes}} + \underbrace{\int_{\text{outcrop}} \mathcal{D}_{\text{in}} dA}_{\text{surface flux}}, \end{aligned} \quad (13.36)$$

which can be written more concisely as

$$\left(\frac{\partial(\Delta V)}{\partial t} + \Delta\Psi \right) \rho + \Delta\rho \frac{\partial}{\partial \rho} (\rho G) = -\Delta\rho \frac{\partial D_{\text{diff}}}{\partial \rho} + \int_{\text{outcrop}} \mathcal{D}_{\text{in}} dA, \quad (13.37)$$

where the surface density forcing is given by $\mathcal{D}_{\text{in}} = -\frac{\alpha_T}{C_p} \mathcal{H} + \rho \beta_S S (\mathcal{E} - \mathcal{P})$ in units of $\text{kg m}^{-2} \text{s}^{-1}$.

The *diapycnal volume flux*, G , can be defined by combining the volume and tracer budgets, (13.35) and (13.37), and dividing by $\Delta\rho$,

$$G = -\frac{\partial D_{\text{diff}}}{\partial \rho} + \frac{1}{\Delta\rho} \int_{\text{outcrop}} \mathcal{D}_{\text{in}} dA,$$

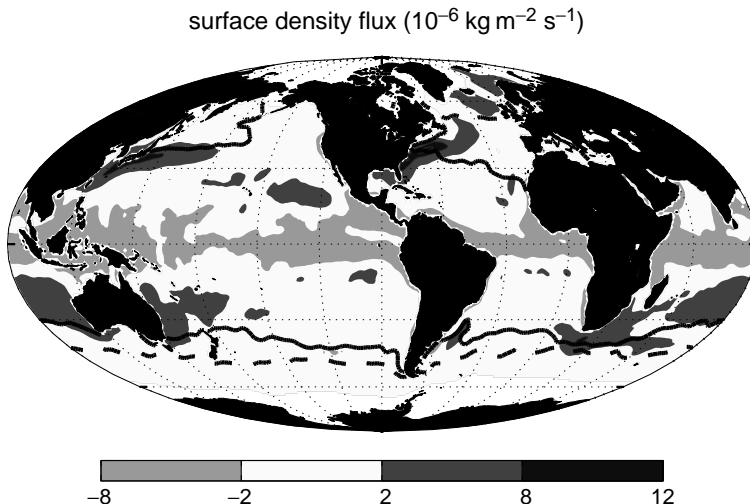
where $\partial(\rho G)/\partial\rho$ is expanded as $\rho \partial G / \partial \rho + G$.

but is negative for lighter σ , representing an overall transformation to lighter water (Fig. 13.13a, full line). Hence, the air-sea fluxes act to enhance the density contrasts across the ocean, increasing the volume of dense and light water.

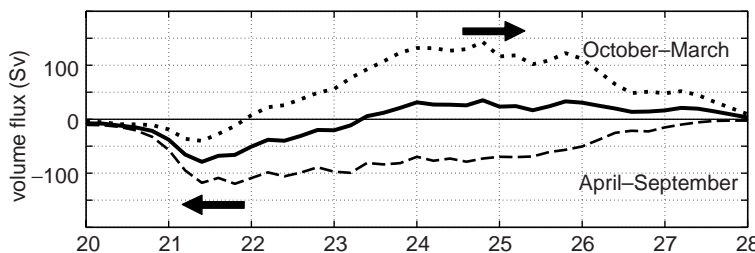
For a steady state, this transformation over the entire globe into a particular density class has to be opposed by diapycnal mixing, as otherwise there would be a continual increase or loss in volume; for a rough scaling see Q13.4, and more detailed discussion in Walin (1982), Speer (1997) and Nurser *et al.* (1999).

Regional transformation from air-sea fluxes

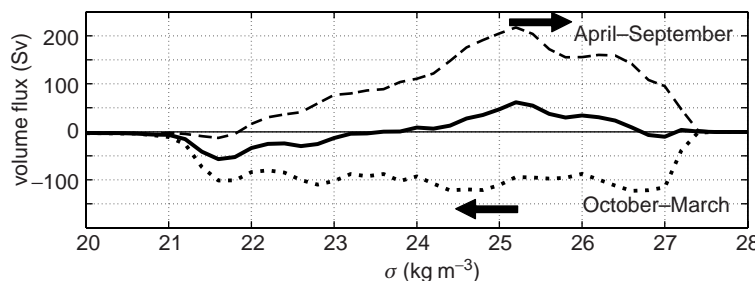
Now consider the annual transformation rates separated into different domains. For a semi-enclosed basin, the transformation integrated over the basin need not be balanced by mixing within the basin. Instead, the convergence of the transformation relates to the volume flux within a density layer exiting the domain, $\Delta\Psi$ in (13.35), and, hence, provides an estimate of the overturning circulation in density space; for a discussion of this link to subduction, see Marshall (1997) and Marshall *et al.* (1999), as well as cautionary notes



(a) seasonal transformation for northern hemisphere



(b) seasonal transformation for southern hemisphere



about its applicability in light tropical waters by Large and Nurser (2001).

For the North Atlantic, the annual transformation reaches a positive peak of 25 ± 5 Sv at $\sigma = 26$, directed toward denser waters, decreasing to a secondary peak of 17 ± 2 Sv at $\sigma = 27.2$, then vanishing by $\sigma = 28$ (Fig. 13.14a). The convergence of this transformation then represents a formation of dense waters between $\sigma = 26$ and 28 within the northern North Atlantic (Fig. 13.15, dark shading).

Figure 13.12 Map of the climatological, surface density flux ($10^{-6} \text{ kg m}^{-2} \text{ s}^{-1}$) from the effect of air-sea fluxes of heat and fresh water,
 $\mathcal{D} = -\frac{\alpha T}{C_p} \mathcal{H} + \rho \beta S (\mathcal{E} - \mathcal{P})$, together with the outcrop of $\sigma_\theta = 26.2$ in the spring (full line) and autumn (dashed line), where spring and autumn are taken as either March or September according to the hemisphere. The surface density flux is evaluated monthly using air-sea fluxes from NOCS (Josey et al., 1999) and temperature and salinity from the World Ocean Atlas 2001 (Conkright et al., 2002).

Figure 13.13 Diapycnal volume flux or transformation, G (Sv) versus σ (kg m^{-3}) in (a) the northern and (b) the southern hemisphere for the warming and cooling halves of the year, together with the annual mean (thick full line); arrows denote the direction of the transformation maxima, positive towards denser waters separately evaluated for October to March (dotted line) and April to September (dashed line). The transformation is evaluated using air-sea heat and freshwater fluxes calculated from the NOCS monthly climatology and the NODC monthly density climatology using a σ bin of 0.2 kg m^{-3} . Fluid is transformed into denser classes in winter and into lighter classes in summer.

For the North Pacific, the annual transformation reaches a positive peak of 22 ± 7 Sv at $\sigma = 24$ decreasing to a secondary peak of 13 ± 3 Sv at $\sigma = 25.8$, then vanishing by $\sigma = 26.8$ (Fig. 13.14b). The density over which there is water-mass formation is much lighter than in the North Atlantic. The convergence of the transformation accordingly represents a formation of intermediate waters between $\sigma = 24$ and 26.8 within the northern North Pacific (Fig. 13.15, light shading).

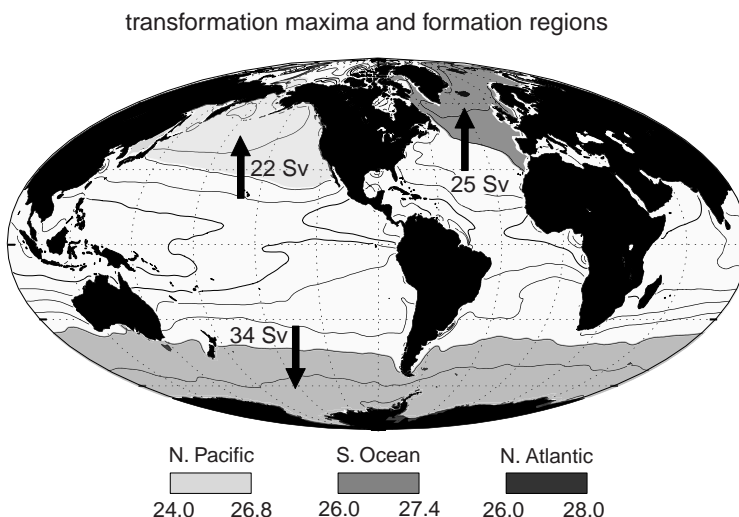
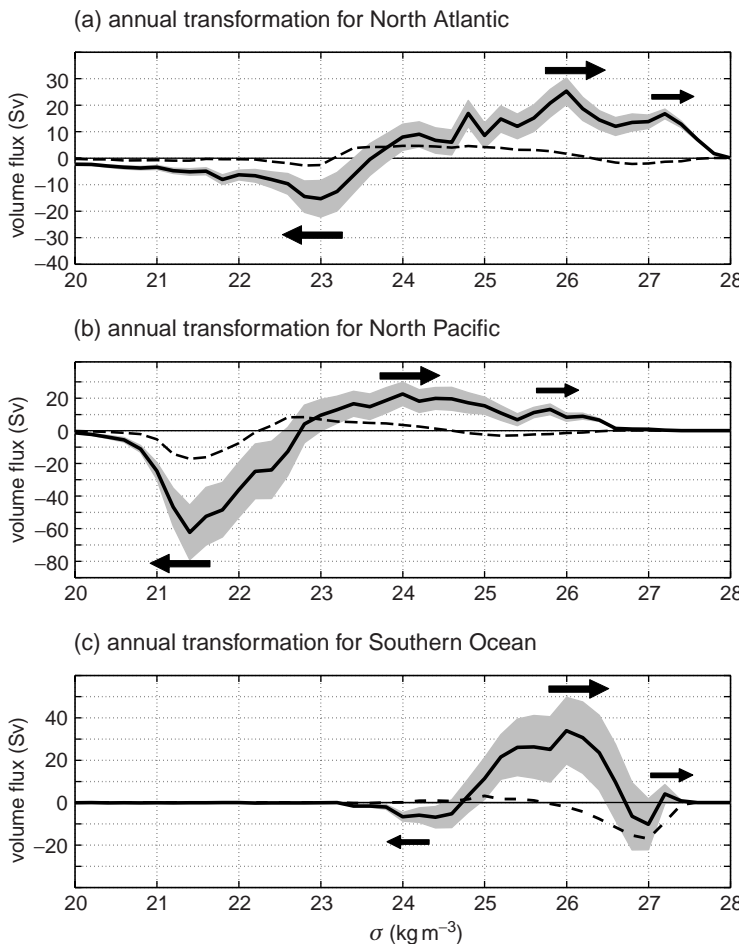


Figure 13.14 Diapycnal volume flux or transformation into denser water, G (Sv), versus σ (kg m^{-3}) over an annual cycle for (a) the North Atlantic (0° – 85° N, 90° W– 0°), (b) North Pacific (0° – 85° N, 100° E– 100° W) and (c) Southern Ocean (30° S– 85° S); arrows denote the direction of transformation maxima, positive towards denser waters. Calculation as in Fig. 13.13 uses NOCS surface heat and freshwater fluxes. The annual estimate (solid line) is subject to significant possible error, so a confidence range is denoted by applying a systematic offset of $\pm 10 \text{ W m}^{-2}$ to the air-sea heat flux (shading). In the North Atlantic (a), the annual-mean transformation reaches a local maximum of $25 \pm 5 \text{ Sv}$ at $\sigma = 26$ and the freshwater contribution is relatively unimportant (dashed line). In the North Pacific (b), the maximum transformation is $22 \pm 7 \text{ Sv}$ in lighter water at $\sigma = 24$. In the Southern Ocean (c), the maximum transformation is $34 \pm 16 \text{ Sv}$ at $\sigma = 26$ and the transformation changes sign, directed into lighter waters, at $\sigma = 27$, implying formation and subduction of intermediate water between these σ values; for estimates with different choices of air-sea fluxes, see Badin and Williams (2010).

Figure 13.15 Maxima for the transformation to denser waters (arrows, Sv) with shading for the σ range where there is overall formation in spring (together with contours (every 0.5 kg m^{-3}) of annual-mean σ diagnosed from climatology).

For the Southern Ocean, there is a more complex response and large uncertainties. The annual transformation reaches a positive peak of 34 ± 16 Sv at $\sigma = 26$ and vanishes by $\sigma = 27.4$ (Fig. 13.14c), which implies an overall formation of denser waters further south (Fig. 13.15, medium shading). However, there is also probably a negative peak of about -10 ± 20 Sv at $\sigma = 27.0$, directed towards lighter densities, suggesting a formation of an intermediate water between $\sigma = 26.0$ and $\sigma = 27.0$.

A note of caution is required; there are significant errors in the air-sea fluxes, particularly over the Southern Ocean, and the contribution of diapycnal mixing has been ignored. All the same, these transformation diagnostics are broadly consistent with our picture of how intermediate and denser waters are formed over the globe (Fig. 13.15).

13.4.2 Water-mass formation summary

The physical transformation of light to dense water integrated over a basin depends on the surface heat and freshwater fluxes applied over surface density outcrops and diapycnal mixing in the ocean interior. The transformation rates for an individual basin can often be reasonably estimated from surface fluxes alone. Assuming that mixing is not locally important, then the convergence of the transformation is equivalent to estimating the volume flux exiting the domain within a particular density class, so providing an estimate of the overturning in density space; for an application to the Southern Ocean, see Marshall (1997), Speer *et al.* (2000) and Marshall and Radko (2003).

Over the entire globe, the transformation driven by surface fluxes has to be opposed by diapycnal mixing, as otherwise there would be a continual increase or loss in volume, which then allows bulk estimates of the diapycnal mixing to be inferred; see Q13.4 and Walin (1982), Speer (1997) and Nurser *et al.* (1999).

13.5 | Summary

The ocean contains a range of physical, chemical and biological processes, which operate on a range

of space and timescales. Integral frameworks provide a useful diagnostic way of understanding how the ocean behaves.

Carbon emissions are driving a transient increase in atmospheric CO₂ and DIC over much of the upper ocean, which over many hundreds of years will be communicated to the deep ocean. The carbon framework can be used to understand how the deep ocean eventually affects atmospheric CO₂. The ocean response is not straightforward, the increasing acidity causes the ocean to gradually take up a smaller and smaller fraction of the annual carbon emissions. For a long-term equilibrium between the atmosphere and ocean, the simple carbon balances suggest that atmospheric CO₂ increases exponentially with the integrated carbon emissions; if the known fossil-fuel reservoirs of 4000 Pg C are consumed (without any compensating carbon capture), then after about a millennium, atmospheric X_{CO₂} is likely to be about 1000 ppmv, having passed through an even larger transient spike. Over the subsequent tens of thousands of years, atmospheric CO₂ is eventually reduced by interaction with carbonate sediments.

The ocean is probably a very important driver of glacial-interglacial changes in atmospheric carbon dioxide: the ocean taking up carbon from the atmosphere during the glacials and returning carbon during the interglacials. No single mechanism explains all of the observed change, but a combination of contributions from temperature and solubility changes, modification of ocean ecosystems and the biological pumps, reorganisation of the deep ocean by circulation changes, and interactions with sedimentary calcium carbonate reservoirs, might account for much of the 100 ppmv reduction in atmospheric CO₂ during glacial periods. Balancing the glacial-interglacial carbon budget is still an open challenge.

A physical framework can be used to understand how water masses are formed across the global ocean. Surface heat and freshwater fluxes increase the density contrasts across the basin and the transformation of light to dense water is related to the formation of dense waters in the mid to high latitudes. Climatological diagnostics reveal the greater transformation of dense water in the North Atlantic compared with the North

Pacific, consistent with the lack of dense-water formation in the North Pacific. In the Southern Ocean, the surface density fluxes induce a convergence of the transformation fluxes, consistent with the formation of intermediate mode waters, which are part of the upper limb of the overturning or residual circulation. For a steady state, this transformation over the entire globe into a particular density class has to be opposed by diapycnal mixing, as otherwise there would be a continual increase or loss in volume. This Walin (1982) framework has been applied in density space, but is valid for any tracer budget, so long as the appropriate tracer surfaces, sources and sinks are identified.

13.6 Questions

Q13.1. Radiative heating and carbon emissions.

The extra radiative heating from carbon dioxide, $\Delta\mathcal{H}$ (in W m^{-2}), increases logarithmically with the mixing ratio of atmospheric carbon dioxide, X_{CO_2} , where

$$\Delta\mathcal{H} = \alpha_r \ln(X_{\text{CO}_2}(t)/X_{\text{CO}_2}(t_0)), \quad (13.38)$$

with X_{CO_2} increasing from times t_0 to t , and $\alpha_r = 5.4 \text{ W m}^{-2}$ depends on the chemical composition of the atmosphere.

(a) Why does the radiative heating vary logarithmically with increasing atmospheric carbon dioxide, rather than increase linearly? Provide a mechanistic explanation.

(b) On a millennial timescale, atmospheric carbon dioxide increases exponentially with carbon emissions, ΔI (this long-term equilibrium state is depicted in Fig. 13.5),

$$X_{\text{CO}_2}(t) = X_{\text{CO}_2}(t_0) \exp(\Delta I/I_B), \quad (13.39)$$

with the buffered carbon inventory for the atmosphere and ocean, I_B , being typically 3500 Pg C.

Estimate the atmospheric carbon dioxide $X_{\text{CO}_2}(t)$ at equilibrium for carbon emissions of $\Delta I = 1000, 2000, 3000$ and 4000 Pg C . Plot $X_{\text{CO}_2}(t)$ versus ΔI . Assume X_{CO_2} is a pre-industrial value of 280 ppmv.

(c) Why does the atmospheric carbon dioxide vary exponentially with carbon emissions in (13.39)? Provide a mechanistic explanation.

(d) For a long-term equilibrium, show how extra radiative heating from carbon dioxide, $\Delta\mathcal{H}$, varies linearly with carbon emissions, ΔI , such that

$$\Delta\mathcal{H} = \frac{\alpha_r}{I_B} \Delta I. \quad (13.40)$$

Check the units of your expression; see Goodwin *et al.* (2009) for a discussion of this relationship.

(e) Estimate how the extra radiative heating from carbon dioxide, $\Delta\mathcal{H}$, varies with carbon emissions of $\Delta I = 1000, 2000, 3000$ and 4000 Pg C in (13.40). Plot $\Delta\mathcal{H}$ versus ΔI .

(f) The conventional carbon reserves are estimated to reach up to typically 5000 Pg C (Rogner, 1997). What then are the implications for the radiative heating of the planet if all the conventional carbon reserves are utilised (without carbon capture from the atmosphere)? What further processes might eventually lead to a reduction of the atmospheric carbon dioxide?

Q13.2. Cycling of calcium ions.

The average calcium ion concentration in rivers due to weathering is about $370 \mu\text{mol kg}^{-1}$ (Langmuir, 1997) and the riverine flux of fresh waters to the ocean about 1 Sv ($1 \text{ Sv} = 10^6 \text{ m}^3 \text{ s}^{-1}$).

(a) How many moles of calcium ions are delivered to the ocean each year?

(b) The average concentration of calcium ions in the global ocean is about 10 mmol kg^{-1} . What is the total inventory of calcium ions in the ocean? Assume that the volume of ocean is $1.4 \times 10^{18} \text{ m}^3$.

(c) What is the average lifetime of calcium ions in the ocean?

(d) If the burial rate is perturbed and decreases by 10%, but the delivery through weathering remains steady, how long would it take for ocean alkalinity to increase by $10 \mu\text{mol kg}^{-1}$?

(e) What would be the effect on atmospheric X_{CO_2} ?

Q13.3. Soft-tissue pump.

Upwelling of deep ocean DIC usually leads to a super-saturation in the mixed layer and outgassing of carbon dioxide. This disequilibrium DIC in the mixed layer is represented by ΔC . Assume that a fraction ϵ_C of the ΔC anomaly is then subducted back into the thermocline and the remainder, $1 - \epsilon_C$, is either outgassed to the atmosphere or consumed by phytoplankton.

- (a) What is the meaning of $\epsilon_C = 0$ and $\epsilon_C = 1$?
- (b) Assuming that the initial disequilibrium ΔC is due to the soft-tissue pump, C^{soft} , increasing the deep ocean DIC, then starting from (13.5) and substituting $\delta\Delta C = \epsilon_C \delta C^{\text{soft}}$, derive an expression for the relationship of atmospheric X_{CO_2} and P^* which accounts for this process.
- (c) How does the sensitivity to P^* change as ϵ_C increases from 0 to 1?

Q13.4. What are the typical rates of density forcing and transformation?

The rate at which water masses are transformed from one density class to another can be estimated, given knowledge of the surface heat and freshwater fluxes.

- (a) Estimate the effect of a surface cooling on the density gain over the North Atlantic. Assume the surface heat flux, $\mathcal{H} \sim -40 \text{ W m}^{-2}$, then estimate the effective surface density flux, $D_{\text{in}} = -\alpha_T \mathcal{H}/C_p$ for $\alpha_T = 2 \times 10^{-4} \text{ K}^{-1}$ and $C_p = 4 \times 10^3 \text{ J kg}^{-1} \text{ K}^{-1}$. Check your units.

- (b) Roughly estimate the implied transformation rate, G , using a differenced form of (13.34) (and ignoring the contribution of any diffusive fluxes, D_{diff}),

$$G \sim \frac{1}{\Delta\rho} D_{\text{in}} A_{\text{outcrop}},$$

where the density interval, $\Delta\rho = 0.2 \text{ kg m}^{-3}$, the effective surface density flux D_{in} is taken from (a), and is assumed to apply uniformly over a density outcrop with a surface area, A_{outcrop} , of $4000 \text{ km} \times 500 \text{ km}$. Compare your estimate to Fig. 13.14a.

- (c) For a steady state, ultimately this transformation of light to dense water needs to be off-

set by an opposing transformation of dense to light water, which can either be achieved by surface forcing for the density outcrop over another part of the globe, or by a diffusive flux across the isopycnal.

Now assume that diapycnal mixing is important: the surface density flux into dense waters is assumed to be balanced by the diffusive flux across the isopycnal (based upon the two terms on the right-hand side of (13.34) balancing when integrated from the densest ρ at the surface to the ρ at the outcrop), such that

$$D_{\text{in}} A_{\text{surface}} \sim -\kappa \frac{\partial \rho}{\partial z} A_{\text{therm}},$$

where A_{surface} is the horizontal extent of waters denser than ρ at the sea surface, the diffusive flux into denser water is written as $\kappa \frac{\partial \rho}{\partial z}$, integrated over the horizontal area of the isopycnal in the thermocline and deep water, A_{therm} ; see Walin (1982), Speer (1997) and Nurser *et al.* (1999) for a careful evaluation. Rearrange to solve for the diapycnal diffusivity, κ . Assume that the vertical gradient in potential density is $\partial\rho/\partial z \sim (1026.4 - 1028) \text{ kg m}^{-3}/2 \times 10^3 \text{ m}$, A_{surface} is $4000 \text{ km} \times 1000 \text{ km}$ and the horizontal area of the isopycnal in the thermocline, A_{therm} is $4000 \text{ km} \times 20000 \text{ km}$.

- (d) *In situ* measurements of diapycnal mixing in the thermocline suggest that κ is often only $2 \times 10^{-5} \text{ m}^2 \text{ s}^{-1}$. Compare with your answer in (c) and speculate on the implications.

13.7 Recommended reading

For in-depth discussions of the sequence of events in glacial–interglacial cycles, and the mechanisms regulating the cycles of atmospheric CO₂, see:

W. S. Broecker and G. M. Henderson (1998). The sequence of events surrounding Termination II and their implications for the cause of glacial–interglacial CO₂ changes. *Paleoceanogr.*, 13(4), 352–364;

N. Caillon, J. P. Severinghaus, J. Jouzel *et al.* (2003). Timing of atmospheric CO₂ and Antarctic temperature changes across Termination III. *Science*, 299, 1728–1731;

S. Peacock, E. Lane and J. M. Restrepo (2006). A possible sequence of events for the generalized

glacial-interglacial cycle. *Global Biogeochem. Cycles*, **20**, GB2010, doi:10.1029/2005GB002448; and

D. M. Sigman and E. A. Boyle (2000). Glacial/interglacial variations in atmospheric carbon dioxide. *Nature*, **407**, 859–869.

For a comprehensive overview of the long-term fate of anthropogenic carbon dioxide, see D. Archer, M. Eby, V. Brovkin *et al.* (2009). Atmospheric lifetime of

fossil-fuel carbon dioxide. *Ann. Rev. Earth Planet. Sci.*, **37**, 117–134, doi:10.1146/annurev.earth.031208.100206.

For a description of water-mass transformation, see W. G. Large and A. J. G. Nurser (2001). Ocean surface water mass transformation. In *Ocean Circulation and Climate: Observing and Modelling the Global Ocean*, ed. G. Siedler, J. Church and J. Gould. San Diego, CA: Academic Press, pp. 317–336.

Chapter 14

Overview and further challenges

At the simplest level, the role of the ocean on the Earth is relatively easy to understand. The ocean stores and redistributes heat, makes the atmosphere moist and the Earth's climate more equitable. The ocean contains dissolved nutrients and gases, and provides an environment for a vast diversity of living creatures. Phytoplankton grow in the sunlit, surface ocean, performing half of the photosynthesis over the globe, creating organic matter which sustains almost all of the living creatures in the sea. The ocean holds more than sixty times as much carbon as in the atmosphere due to the reactivity of carbon dioxide in seawater.

To gain a deeper understanding of the ocean, we must adopt a holistic approach and understand the interplay of physical, chemical and biological processes, as illustrated in Fig. 14.1a,b. Next we discuss these connections.

14.1 Interconnections between the physics, chemistry and biology

To develop a more complete view, we must first understand a set of fundamental concepts: how tracers are transported; how the ocean circulates in response to atmospheric forcing; how phytoplankton cells turn inorganic nutrients into organic matter; and how carbon dioxide reacts in seawater and is exchanged with the atmosphere. Drawing on these concepts, the interconnections within the ocean become much clearer; many of the physical phenomena leave a characteristic

imprint on the distributions and cycles of nutrients and carbon, in turn affecting life in the ocean.

Mixed layers

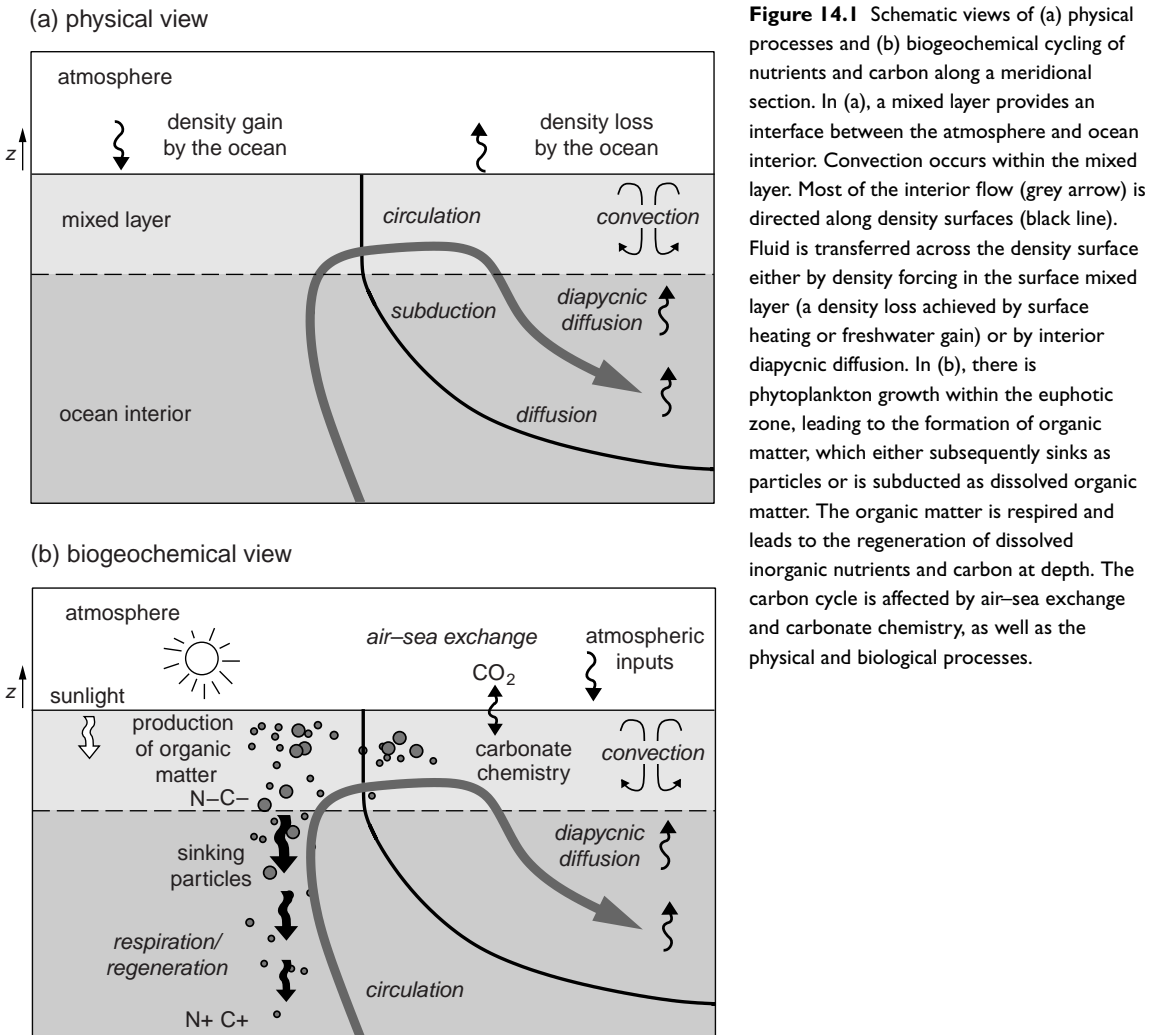
Surface mixed layers are turbulent regions in contact with the atmosphere (Fig. 14.1a); during periods of heating, the mixed layer thins due to warming and thickens due to mechanical mixing, while during cooling periods, the mixed layer thickens and entrains underlying stratified waters. The seasonality of the mixed layer modulates the rate and timing of the production of organic matter, affecting light and nutrient availability, which then alters the structure of the ecosystem. In turn, seasonal and vertical patterns in phytoplankton pigments modify the profile of solar heating in the water column. The timescale for the air-sea equilibration of dissolved gases is affected by the depth of the surface boundary layer, proceeding more rapidly in the shallow summer mixed layer.

Thermocline

The thermocline is a region of strong stratification in the upper ocean, relatively thick in the subtropics and thin in the tropics and subpolar latitudes. This undulating structure is reflected in the vertical distributions of nutrients and carbon over the upper ocean. In the subtropics, the winds induce a downwelling over the subtropics, creating a thick layer of nutrient-depleted waters, reducing biological productivity.

Gyres

The winds drive large-scale recirculations, the ocean gyres, between continental barriers: subtropical gyres rotate anticyclonically and subpolar



gyres cyclonically. Surface waters are relatively green and productive over the subpolar gyres and higher latitudes, usually sustaining a seasonal succession of larger phytoplankton, some investing in internal nutrient stores to enhance growth or in protective material to inhibit predation. Conversely, surface waters are relatively clear and less productive over the subtropical gyres, populated by tiny phytoplankton whose small size leads to efficient, diffusive uptake of scarce nutrients; see the ecosystem model illustration in colour Plate 16.

Western boundary currents

Intense boundary currents provide the return flow of the gyre circulations, which are con-

fined to the western boundary due to the Earth being a rapidly rotating sphere. These intense flows induce enhanced fluxes of heat, nutrients and carbon directed along isopycnals, which help determine the downstream properties within the mixed layer. There are sharp tracer contrasts across the separated boundary currents, associated with a poleward shoaling of the thermocline. The swift currents connect and intermingle populations of plankton from widely separated regions.

Zonal currents in the Southern Ocean

Over the Southern Ocean, the westerly winds drive the Antarctic Circumpolar Current encircling the globe. The momentum imparted by the wind is

ultimately taken out of the water column by pressure differences across ridges along the sea floor. The upwelling on the poleward side of the Antarctic Circumpolar Current brings high concentrations of nutrients to the surface, sustaining seasonal blooms of large phytoplankton. However, not all of the surface macro-nutrients are utilised by plankton, probably due to the very low availability of trace metals and/or lack of sunlight to sustain growth in thick mixed layers. There are particularly low concentrations of iron, which is depleted in upwelling waters and though there is some compensation from atmospheric transport, this supply is weak due to the remoteness from land.

Eddies and fronts

Eddies are formed through instabilities of the intense jets and the extension of western boundary currents. The eddies and embedded finer-scale fronts have strong vertical velocities, which can enhance biological productivity by increasing the nutrient supply to the sunlit, surface ocean. Possibly more significantly, eddies affect the larger-scale environment by flattening density surfaces and transferring tracers, including nutrients, along them; this transfer involves an additional advection, as well as an effective down-gradient diffusion. In the atmosphere, weather systems are crucial in transferring heat poleward across the fast-moving westerly jet stream at mid latitudes. In the ocean, mesoscale eddies perform a similar role across the Antarctic Circumpolar Current.

Dense water formation, sinking and spreading

Dense waters are formed in the surface mixed layer at high latitudes, particularly in the North Atlantic and Southern Ocean. These dense waters with their accompanying nutrient and carbon concentrations sink and spread over the abyssal ocean through a combination of deep boundary currents, recirculations and eddies. The deep flows are strongly steered by topography, avoiding bumps and ridges, and experience enhanced mixing in regions of rough topography. Dense waters return to the sea surface through the work done by the winds and the effect of tidal forcing. Differences in air-sea exchange of fresh water cause

dense waters preferentially to form in the high latitudes of the North Atlantic, rather than the North Pacific.

Nutrient and carbon distributions reflect ventilation pathways: relatively low concentrations within younger waters more recently formed in the mixed layer and relatively high concentrations in older water reflecting the accumulated effect of biological fallout, respiration and regeneration (Fig. 14.1b).

Most of the carbon reservoir is in deep waters, screened for much of the time from the atmosphere, and physically transferred there as cold waters sink at high latitudes and spread throughout the abyss, all the time being enhanced by the respiration of sinking organic particles. This biologically mediated store of carbon only reaches half of its possible magnitude in the present day; variations in this efficiency could be important in determining atmospheric carbon dioxide and influencing climate.

Effects on air-sea exchange of carbon dioxide

The exchange of carbon dioxide across the air-sea interface is modulated by these physical phenomena, the underlying processes sometimes opposing or reinforcing each other (Fig. 14.1b). The ocean outgasses carbon dioxide in regions of warming or where carbon-rich waters return to the surface from the deep ocean, such as the tropics. The ocean absorbs carbon dioxide in regions of cooling or vigorous biological productivity, particularly in the high latitudes. In the Southern Ocean, there are opposing contributions from cooling and warming, and upwelling of carbon-rich waters and biological consumption, such that the sign and magnitude of the air-sea exchange is difficult to quantify. The anthropogenic increase in atmospheric carbon dioxide superimposes a net flux of carbon dioxide into the ocean as a whole, although this flux is small compared with natural exchanges.

14.2 | Research approaches

We believe that progress is made by adopting an integrated approach, involving an interplay of data, models and theory.

14.2.1 Observations

Much of the book has drawn upon carefully collected physical and biogeochemical data gathered on research cruises, including the observations from the World Ocean Circulation Experiment and Joint Global Ocean Flux Study, which have provided views of the variation of physical and chemical properties over the global ocean. These views are now being extended and challenged through the application of new observation technologies, including autonomous drifters, gliders and satellite remote sensing which are providing high-resolution data with unprecedented coverage.

Unravelling the ocean's biogeochemical cycles is particularly challenging because of the difficulty in making some of the measurements, including those of key trace metals, such as iron, which is abundant in the terrestrial world and on ships, but has very low concentrations in the ocean. Insight into biogeochemical cycles and the circulation of the past ocean can be obtained by analysing isotopic signatures of nutrients, oxygen and carbon, as well as molecular biomarkers, neither of which are discussed in this book. Our perspectives of the living marine world are also being transformed by new techniques from molecular biology, including the characterisation of the abundance and expression of genes.

14.2.2 Modelling

Frequently in this book we have dealt with simple mathematical models. Models can be used to synthesise understanding of complex systems, test hypotheses, interpret patterns and signals in observations, or make predictions. For predictions to be useful, models require adequate initial conditions, forcing functions and closures, as well as some means to assess whether the output has any skill. The appropriate degree of complexity of a model is not absolute, but depends upon the question being addressed.

Conceptual models

While details of the phenomena in the ocean are highly complicated, it is often useful to cut to the heart of a problem, making appropriate

simplifications to gain insight. To that end, we have presented a set of conceptual models (often described mathematically in the more technical boxes), which emphasise particular mechanisms, drawing on important advances in the literature. These conceptual models can be used as idealised reference points, either to interpret data or to understand the response in a more complicated model. We feel that without such idealised models, one is left struggling to understand the ocean, since descriptive or statistical views by themselves only provide limited insight and complex numerical simulations can be very difficult to interpret.

Frameworks

We have also discussed two synthesising frameworks: a model of coupled global carbon reservoirs and an isopycnal perspective of how water masses are transformed. While both frameworks are largely diagnostic, they offer insight into the integrated effect of many finer-scale phenomena. For example, the carbon reservoir framework can be used to understand the long-term response of the ocean to rising carbon emissions or warming, while the isopycnal framework can be used to understand how overturning is connected to surface heat and freshwater fluxes, and the effect of mixing.

14.3 Challenges

The quest to understand the workings of the oceans and their role in the coupled biogeochemical and climate systems of the Earth offers many challenges to the research community. By discussing the ocean in terms of fundamental principles, conceptual models and frameworks that describe underlying mechanisms, we hope that this book provides a useful perspective for readers and a springboard in taking forward their own studies and research.

Research is organic and continually changing. New questions emerge, and new observations and new perspectives challenge prevailing views,

including those set out in this book. Next we set out some key research challenges.

14.3.1 How do small-scale processes affect the larger-scale environment?

From a physical perspective, there is an increasing awareness of the importance of turbulence and transport which can occur on very fine scales, for example, mixing in the vicinity of rough topography and eddy or frontal circulations leading to the transport and stirring of tracers. Yet their large-scale, integrated impact is still unclear. Likewise, the overturning of the ocean extends over entire basins, but many of the key processes occur on very fine scales involving the formation, spreading and mixing of dense water. How can we connect these contrasting scales and understand how they work in concert and how short-lived intermittent events affect a longer-term state?

For marine microbes and biogeochemical cycles, there is a strikingly similar conundrum. At the individual cellular level, energy and mass conservation apply, constraining trade-offs at the metabolic and cellular scale and the response to environmental factors. In turn, the response of individuals, when integrated over large populations, regulates regional community structure (illustrated from an ecosystem model in Plate 16) and affects the biogeochemical environment over the entire global ocean. It is a challenge to connect these phenomena which are tightly connected, yet occur at extremely disparate scales.

14.3.2 How does the ocean work as part of the coupled Earth system?

It is a major challenge to understand the ocean as a fully coupled part of the Earth system, particularly on long timescales. While research has typically been rather discipline-oriented in recent decades, the fully interconnected nature of the Earth system demands that these are complemented strongly with interdisciplinary studies.

The ocean and atmosphere are clearly tightly interconnected as fluid environments, rapidly exchanging heat, momentum and water. While the atmosphere drives ocean circulation, the

ocean can provide an important feedback; for example, in how the mid-latitude storm belts are energised when cold, dry air passes from the continents over a warmer ocean. The El-Niño Southern Oscillation also reveals a two-way coupling between the extent of warm water over the tropical Pacific and strength of the Trade winds. Ice forms the third part of this triumvirate, reflecting sunlight leading to a positive climate feedback. Freezing of seawater also expels brine, forming dense waters and affecting the circulation in the polar ocean.

The global carbon cycle is the end result of a complicated interplay of physical, chemical and biological phenomena, which couple the fluid environments with the terrestrial biosphere and solid Earth. The atmosphere and ocean share their carbon inventories relatively rapidly, along with the terrestrial biosphere. All are modulated on longer timescales by interactions with sediments and, ultimately, via plate tectonics with the Earth's interior. The continents provide the source of essential windborne nutrients to the distant oceans. Understanding this system is a truly interdisciplinary effort and we have not yet fully understood how the carbon cycle operates in the climate system. For example, it is unclear as to how glacial-interglacial variations in carbon dioxide are controlled.

14.3.3 What does the future hold?

Increasing carbon dioxide in the atmosphere is leading to a persistent radiative heating, evident on timescales of several decades in the warming of the global ocean and accompanying rise in sea level. However, there can be much larger regional variability in the atmosphere and ocean, including changes in winds which dramatically alter the ocean's heat storage above the thermocline. How marine ecosystems respond to climate change is very unclear. Perhaps different phytoplankton species might flourish in a warmer or more acidic environment? How different might these organisms be in other regards? Natural variability in the ecosystem is likely to dominate for the foreseeable future and probably mask any clear signals of climate-driven change. The impact on the

carbon cycle is difficult to predict, particularly in important regions like the Southern Ocean, where there is a delicate balance between competing processes. What is clear, though, is that rising atmospheric carbon dioxide increases the acidity of the

oceans, which in turn reduces the ocean uptake of carbon. Hence, more of the emitted carbon is likely to remain in the atmosphere, reinforcing concerns about how the climate system is being perturbed.

Appendix

The first part of this appendix summarises the mathematical notation employed in the book, the second part derives the momentum equations used to understand how fluid circulates on a rotating planet and the third part describes how to solve the set of carbonate chemistry equations.

A.I Mathematical definitions

Here we define the mathematical notation used in the book.

A.I.1 Vector operators

The partial derivative operator, ∇ , referred to as del, is defined by

$$\nabla = \mathbf{i} \frac{\partial}{\partial x} + \mathbf{j} \frac{\partial}{\partial y} + \mathbf{k} \frac{\partial}{\partial z}, \quad (\text{A.1})$$

where \mathbf{i} , \mathbf{j} and \mathbf{k} are unit vectors pointing in the x , y and z directions.

Consider the effect of this operator on a scalar field $\phi(x, y, z)$ and a vector field $\mathbf{V}(x, y, z) = iV_x + jV_y + kV_z$.

Gradient of a scalar

The gradient of a scalar is represented by

$$\text{grad } \phi = \nabla \phi = \mathbf{i} \frac{\partial \phi}{\partial x} + \mathbf{j} \frac{\partial \phi}{\partial y} + \mathbf{k} \frac{\partial \phi}{\partial z}, \quad (\text{A.2})$$

providing a vector directed from low to high ϕ . For example, if the scalar represents height on a map, such as the elliptical dashed contours in Fig. A.1a, the gradient is given by the arrows directed from low to high.

The del operator can be applied in two different ways to a vector.

Divergence of a vector

The divergence is provided by the scalar product of the ∇ operator and a vector, \mathbf{V} , such that

$$\text{div } \mathbf{V} = \nabla \cdot \mathbf{V} = \frac{\partial V_x}{\partial x} + \frac{\partial V_y}{\partial y} + \frac{\partial V_z}{\partial z}, \quad (\text{A.3})$$

providing a scalar result. Positive divergence represents more vectors leaving the domain

than entering, while negative divergence or convergence represents more vectors entering the domain than leaving. For example, there is a positive divergence associated with the vectors depicted in Fig. A.1b. For a fluid, there is usually no divergence, such that $\nabla \cdot \mathbf{u} = 0$, such that the same amount of fluid enters a domain as leaves it.

Curl of a vector

The curl is provided by a cross product between the ∇ operator and a vector, \mathbf{V} , such that

$$\text{curl } \mathbf{V} = \nabla \times \mathbf{V}, \quad (\text{A.4})$$

providing a vector result directed normal to the vector \mathbf{V} , which is a measure of the rotation of the vector field and this vector result is normal to vector field. For example, there is a positive curl associated with the anticlockwise rotation of the vectors depicted in Fig. A.1c. For a fluid, there is usually a curl, $\nabla \times \mathbf{u} = \boldsymbol{\zeta}$, which is called the vorticity, providing a measure of the spin of the fluid. The vorticity can be visualised by imagining placing a paddle wheel in the flow and seeing which way the paddle wheel rotates.

A.I.2 Material derivative

It is often useful to consider the rate of change following a fluid parcel, rather than at a fixed location. Consider a fluid parcel, such as an untethered balloon or float, moving with the flow in a background environment. Assume that there is a scalar property, ϕ , such as temperature or a tracer, varying in space and time. For small time intervals, the change in ϕ following the fluid parcel can be related to the background variations in ϕ in time and space,

$$\delta\phi_{\text{parcel}} = \delta t \left. \frac{\partial \phi}{\partial t} \right|_{x,y,z} + \delta x \left. \frac{\partial \phi}{\partial x} \right|_{t,y,z} + \delta y \left. \frac{\partial \phi}{\partial y} \right|_{t,x,z} + \delta z \left. \frac{\partial \phi}{\partial z} \right|_{t,x,y}, \quad (\text{A.5})$$

where the subscripts denote the variables that are kept constant for the differentiation. Dividing by the time interval, δt , and defining the velocity

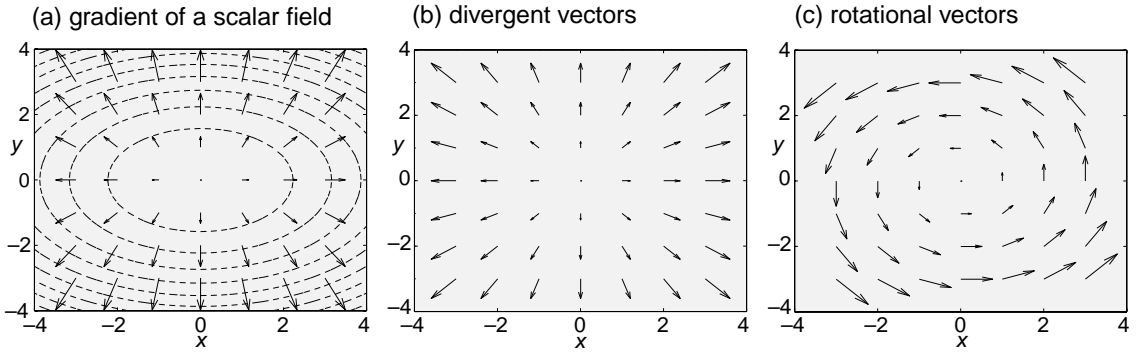


Figure A.1 A schematic figure denoting (a) the gradient (arrows) of a scalar field (dashed contours), (b) divergent vectors, and (c) rotational vectors.

components by $u \equiv \frac{\delta x}{\delta t}$, $v \equiv \frac{\delta y}{\delta t}$ and $w \equiv \frac{\delta z}{\delta t}$, leads to

$$\begin{aligned} \frac{\delta \phi}{\delta t}_{\text{parcel}} &= \left. \frac{\partial \phi}{\partial t} \right|_{x,y,z} + u \left. \frac{\partial \phi}{\partial x} \right|_{t,y,z} \\ &\quad + v \left. \frac{\partial \phi}{\partial y} \right|_{t,x,z} + w \left. \frac{\partial \phi}{\partial z} \right|_{t,x,y}. \end{aligned} \quad (\text{A.6})$$

This rate of change of a property following the moving fluid parcel is expressed in terms of a material derivative, sometimes also referred to as a substantial derivative, given by

$$\begin{aligned} \frac{D}{Dt} &\equiv \frac{\partial}{\partial t} + u \frac{\partial}{\partial x} + v \frac{\partial}{\partial y} + w \frac{\partial}{\partial z} \\ &= \frac{\partial}{\partial t} + \mathbf{u} \cdot \nabla, \end{aligned} \quad (\text{A.7})$$

with the subscripts henceforth dropped for brevity. This material derivative includes the contribution from the rate of change at a fixed point and horizontal and vertical advection.

A.I.3 Taylor expansion

It is often useful to evaluate gradients either from data or model variables, or to represent mathematical expressions numerically. Consider a general variable, ϕ , that varies with x , so that the changes in ϕ with a small change in Δx can be expressed in terms of a general Taylor expansion,

$$\begin{aligned} \phi(x + \Delta x) &= \phi(x) + \Delta x \frac{\partial \phi}{\partial x} + \frac{\Delta x^2}{2} \frac{\partial^2 \phi}{\partial x^2} \\ &\quad + \frac{\Delta x^3}{3!} \frac{\partial^3 \phi}{\partial x^3} + \dots + \frac{\Delta x^n}{n!} \frac{\partial^n \phi}{\partial x^n}. \end{aligned} \quad (\text{A.8})$$

Based on this Taylor expansion, a horizontal gradient can be expressed to an accuracy of Δx by

$$\frac{\partial \phi}{\partial x} = \frac{\phi(x + \Delta x) - \phi(x)}{\Delta x} + \frac{\Delta x}{2} \frac{\partial^2 \phi}{\partial x^2} + \dots \quad (\text{A.9})$$

A more accurate estimate of the gradient can be obtained by repeating (A.8) for a negative perturbation $-\Delta x$ to give

$$\begin{aligned} \phi(x - \Delta x) &= \phi(x) - \Delta x \frac{\partial \phi}{\partial x} + \frac{\Delta x^2}{2} \frac{\partial^2 \phi}{\partial x^2} \\ &\quad - \frac{\Delta x^3}{3!} \frac{\partial^3 \phi}{\partial x^3} + \dots + (-1)^n \frac{\Delta x^n}{n!} \frac{\partial^n \phi}{\partial x^n}, \end{aligned} \quad (\text{A.10})$$

then combining (A.8) minus (A.10) gives to an accuracy of Δx^2

$$\frac{\partial \phi}{\partial x} = \frac{\phi(x + \Delta x) - \phi(x - \Delta x)}{2\Delta x} + \frac{\Delta x^2}{3!} \frac{\partial^3 \phi}{\partial x^3} + \dots \quad (\text{A.11})$$

In a similar manner, a second differential of ϕ in x can be defined in terms of

$$\begin{aligned} \frac{\partial^2 \phi}{\partial x^2} &= \frac{\phi(x + \Delta x) - 2\phi(x) + \phi(x - \Delta x)}{\Delta x^2} \\ &\quad + \frac{2\Delta x^2}{4!} \frac{\partial^4 \phi}{\partial x^4} + \dots \end{aligned} \quad (\text{A.12})$$

These differenced relations for $\partial \phi / \partial x$ and $\partial^2 \phi / \partial x^2$ can be used to evaluate differentials and form the basis for a numerical representation of the equations of motion on a spatial grid.

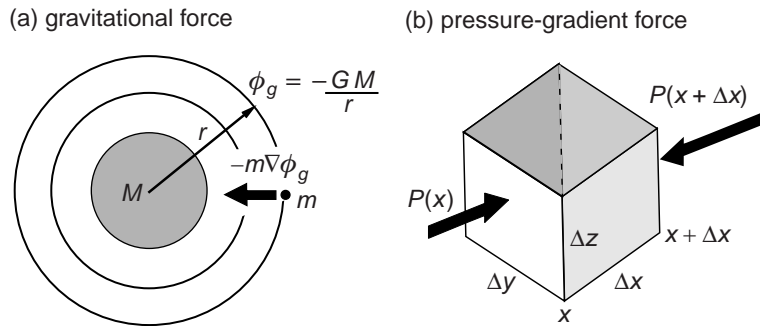


Figure A.2 A schematic figure denoting (a) how the gravitational force (thick black arrow) on a unit mass, m , is directed towards the centre of the Earth, down the gradient of gravitational potential, $-m\nabla\phi_g$, where the potential becomes less negative with increasing distance r from the centre of Earth, $\phi_g = -GM/r$; and (b) how the pressure force (black arrow) is directed inwards on a cube with a force of $P(x)\Delta y\Delta z$ on the x face and $-P(x+\Delta x)\Delta y\Delta z$ on the $x+\Delta x$ face, with the net force directed down the pressure gradient.

A.2 | Derivation of the momentum equations

To understand how the atmosphere and ocean circulate, start with Newton's second law expressing how a fluid particle is accelerated by an external force,

$$\mathbf{F} = m\mathbf{a}, \quad (\text{A.13})$$

where \mathbf{F} is the external force (in units of $\text{N} \equiv \text{kg m s}^{-2}$), m is a unit mass (kg) and \mathbf{a} is the acceleration (m s^{-2}); bold represents a vector with both a magnitude and a direction. The acceleration is given by the rate of change in velocity, which is written following the fluid particle by

$$\mathbf{a} = \frac{D\mathbf{u}}{Dt}.$$

Our aim is now to represent mathematically the external forces acting on the fluid particle and to take into account the effects of the Earth's rotation.

A.2.1 What are the external forces?

For a fluid motion measured in a non-rotating frame, the principal external forces involve gravity, pressure gradients and friction. Their effects are intuitively easy to understand.

Gravitational force

The gravitational force accelerates masses towards each other. This force is represented by a mass, m ,

being accelerated from high to low gravitational potential (Fig. A.2a),

$$-m\nabla\phi_g, \quad (\text{A.14})$$

where the gravitational potential ϕ_g is defined for the Earth as $\phi_g = -\frac{GM}{r}$; G is the gravitational constant ($\text{N m}^2 \text{ kg}^{-2}$), M is the mass of the Earth (kg) and r is the distance (m) from the centre of the Earth. The gravitational force is directed towards the centre of the Earth, $-GMm/r^2$, varying inversely with the square of the distance.

Pressure-gradient force

Pressure represents the force acting normal to a cross-sectional area (Nm^{-2}). In a fluid, pressure depends on the weight of overlying fluid. The pressure-gradient force accelerates fluid from high to low pressure. Consider the pressure acting on a cube (Fig. A.2b): the force acting in the positive x direction is given by $P(x)\Delta y\Delta z$ at x and $-P(x+\Delta x)\Delta y\Delta z$ at $x+\Delta x$, where the change in sign reflects how the pressure acts to compress the cube. The overall force acting in the x -direction is given by

$$(-P(x+\Delta x) + P(x))\Delta y\Delta z,$$

which is equivalent to

$$-\Delta V \frac{\partial P}{\partial x},$$

where the volume of the cube is given by $\Delta V = \Delta x\Delta y\Delta z$; the pressure gradient is in N m^{-3} and the volume in m^3 , so their product provides a force in N . A net force is exerted by the contrast in the

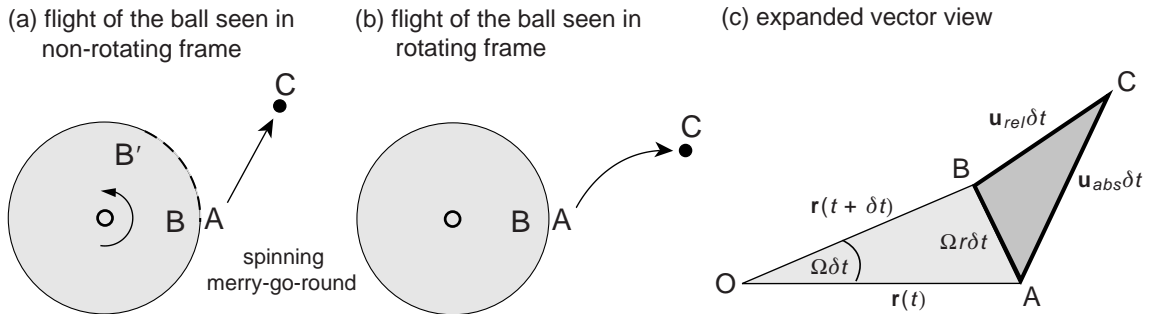


Figure A.3 A schematic view of the flight of a ball seen in (a) a non-rotating frame by A and C, and in (b) a rotating frame, as seen by B, such as on a spinning merry-go-round. In (a), the ball moves in a straight line, while in (b) the ball appears to move in a curved path. In (c), the displacements of the ball are represented by vectors, where the displacement in the non-rotating frame, **AC**, equals the displacement from the rotation of the frame, **AB**, plus the displacement in the rotating frame, **BC**. The displacements **AC** and **BC** can be related to the velocity vectors, \mathbf{u}_{abs} and \mathbf{u}_{rel} , viewed in the non-rotating and rotating frames, respectively. The effect of the rotation of the frame is denoted by $|\mathbf{AB}| = |\Omega \mathbf{r} \delta t|$, where r defines positions A and B at time t and rotates to a new position for B at $t + \delta t$; the angle and distance between $\mathbf{r}(t)$ and $\mathbf{r}(t + \delta t)$ is given by $\Omega \delta t$ and $\Omega r \delta t$, respectively (where $\Omega = 2\pi/\text{period}$).

pressure and is directed down the pressure gradient. Repeating the process for each face gives an overall pressure-gradient force on the cube as

$$-\Delta V \left(\mathbf{i} \frac{\partial P}{\partial x} + \mathbf{j} \frac{\partial P}{\partial y} + \mathbf{k} \frac{\partial P}{\partial z} \right),$$

where \mathbf{i} , \mathbf{j} and \mathbf{k} represent unit vectors in the x , y and z directions. This pressure-gradient force can be more concisely written in terms of a gradient operator (Section A.1),

$$-\frac{m}{\rho} \nabla P, \quad (\text{A.15})$$

where the density $\rho = m/\Delta V$ relates the mass and volume of the cube.

Frictional force

The frictional force can act either to decelerate the flow, such as friction acting to reduce the speed of a moving ball, or to accelerate the flow, such as the wind blowing over a calm ocean. The frictional force is simply defined here as

$$m \mathcal{F}. \quad (\text{A.16})$$

The frictional acceleration \mathcal{F} (m s^{-2}) is often represented by the vertical gradient in a frictional stress, τ (N m^{-2}),

$$\mathcal{F} = \frac{1}{\rho} \frac{\partial \tau}{\partial z}.$$

Combining Newton's second law (A.13) with these external forces (A.14), (A.15) and (A.16), and

dividing by the mass m , leads to

$$\frac{D\mathbf{u}}{Dt} = -\nabla \phi_g - \frac{1}{\rho} \nabla P + \mathcal{F}, \quad (\text{A.17})$$

representing how a fluid parcel is accelerated (i) towards a large mass, (ii) from high to low pressure, and (iii) in the direction of a frictional acceleration.

This form of Newton's second law is only valid when the velocities are measured in a non-accelerating reference frame, such as a frame where the stars do not appear to rotate. The momentum equation needs to be modified whenever velocities are measured in a frame fixed on the spinning Earth.

A.2.2 What is the effect of rotation?

Consider how a moving object appears when viewed from a rotating frame. Return to the example of a spinning merry-go-round (Fig. A.3a, discussed in Section 4.1): child A throws a ball to a child C, both standing on the ground, while the other child B watches from a spinning merry-go-round. For the two children standing on the ground, the ball appears to move in a straight line from A to C (Fig. A.3a). However, child B on the spinning merry-go-round sees a different trajectory, the ball appears to move in a curved path and be accelerated (Fig. A.3b). This apparent acceleration is a consequence of the rotation of the reference frame.

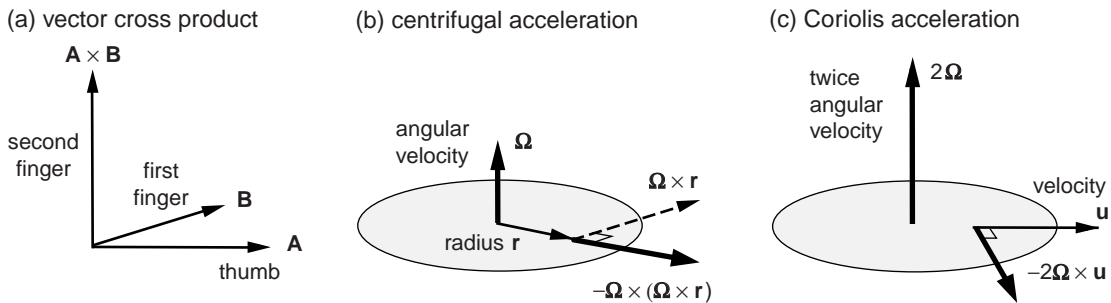


Figure A.4 A schematic figure denoting (a) how to diagnose the directions for a vector cross product from the right-hand rule, where the thumb points in the direction of vector \mathbf{A} , the first finger in the direction of vector \mathbf{B} and the second finger points in the direction of the cross product, $\mathbf{A} \times \mathbf{B}$; (b) for a spinning disc with angular velocity $\boldsymbol{\Omega}$, the direction of the centrifugal acceleration, $-\boldsymbol{\Omega} \times (\boldsymbol{\Omega} \times \mathbf{r})$, at a radius \mathbf{r} ; and (c) for a velocity \mathbf{u} viewed from the spinning disc, the direction of the Coriolis acceleration, $-2\boldsymbol{\Omega} \times \mathbf{u}$.

Vector representation for a rotating frame

For this merry-go-round example, now consider the displacements of the ball in terms of vectors, as depicted in Fig. A.3c, where

$$\mathbf{AC} = \mathbf{AB} + \mathbf{BC}, \quad (\text{A.18})$$

with \mathbf{AC} the displacement of the ball as seen in the non-rotating frame, which is equivalent to the displacement \mathbf{BC} in the rotating frame plus \mathbf{AB} , the rotation of the frame.

Each of these vectors can be represented by velocities: the displacement of the ball in the non-rotating frame, $\mathbf{AC} = \mathbf{u}_{abs}\delta t$, and the displacement in the rotating frame, $\mathbf{BC} = \mathbf{u}_{rel}\delta t$, where \mathbf{u}_{abs} and \mathbf{u}_{rel} are the velocities of the ball as measured in the non-rotating and rotating frames, respectively.

The more tricky vector to define is \mathbf{AB} , representing the rotation of the frame given by the movement of B on the merry-go-round. Let the position of B be defined by a position $\mathbf{r}(t)$ that rotates to $\mathbf{r}(t + \delta t)$ in a time δt (Fig. A.3c), with an angle between these position vectors given by $\Omega\delta t$. The displacement between the end points of these vectors, $\mathbf{r}(t)$ and $\mathbf{r}(t + \delta t)$, is given by the vector \mathbf{AB} of magnitude $|\Omega\mathbf{r}\delta t|$, where $\Omega = 2\pi/\tau$ and τ is the period of rotation (seconds); if one sums over many small time-steps over a rotational period, then this angle of rotation is 2π and the distance along the arc is $2\pi r$ as expected. Replacing the vectors in (A.18) by their velocities and dividing by δt gives

$$\mathbf{u}_{abs} = \mathbf{u}_{rel} + \boldsymbol{\Omega} \times \mathbf{r}, \quad (\text{A.19})$$

where the absolute velocity, \mathbf{u}_{abs} , depends on the relative velocity, \mathbf{u}_{rel} , plus a vector cross-product

term, $\boldsymbol{\Omega} \times \mathbf{r}$, measuring the effect of the frame rotation; this term has a magnitude given by $\Omega r \sin \phi$, where ϕ is the angle between $\boldsymbol{\Omega}$ and \mathbf{r} (which is 90° if $\boldsymbol{\Omega}$ is vertical and \mathbf{r} is horizontal as depicted in Fig. A.4b).

General coordinate transformations for a rotating frame

There is a general coordinate transformation where the rate of change in a non-rotating frame, D/Dt_{abs} , is given by the rate of change measured in a rotating frame, D/Dt_{rel} , plus a term measuring the rate at which the frame rotates, $\boldsymbol{\Omega} \times$, which, when applied to the position vector \mathbf{r} , gives

$$\frac{D\mathbf{r}}{Dt_{abs}} = \frac{D\mathbf{r}}{Dt_{rel}} + \boldsymbol{\Omega} \times \mathbf{r}, \quad (\text{A.20})$$

which is equivalent to (A.19) with $\mathbf{u}_{abs} \equiv \frac{D\mathbf{r}}{Dt_{abs}}$ and $\mathbf{u}_{rel} \equiv \frac{D\mathbf{r}}{Dt_{rel}}$.

If this coordinate transformation (A.20) is applied now to the velocity vector, \mathbf{u}_{abs} , then

$$\frac{D\mathbf{u}_{abs}}{Dt_{abs}} = \frac{D\mathbf{u}_{abs}}{Dt_{rel}} + \boldsymbol{\Omega} \times \mathbf{u}_{abs}, \quad (\text{A.21})$$

and substituting (A.19) and $\mathbf{u}_{rel} \equiv D\mathbf{r}/Dt_{rel}$ leads to

$$\frac{D\mathbf{u}_{abs}}{Dt_{abs}} = \frac{D\mathbf{u}_{rel}}{Dt_{rel}} + 2\boldsymbol{\Omega} \times \mathbf{u}_{rel} + \boldsymbol{\Omega} \times (\boldsymbol{\Omega} \times \mathbf{r}). \quad (\text{A.22})$$

Hence, in a rotating frame, an observer only understands the acceleration of a moving particle by including two apparent accelerations, $-2\boldsymbol{\Omega} \times \mathbf{u}_{rel}$ and $-\boldsymbol{\Omega} \times (\boldsymbol{\Omega} \times \mathbf{r})$,

$$\frac{D\mathbf{u}_{rel}}{Dt_{rel}} = \frac{D\mathbf{u}_{abs}}{Dt_{abs}} - 2\boldsymbol{\Omega} \times \mathbf{u}_{rel} - \boldsymbol{\Omega} \times (\boldsymbol{\Omega} \times \mathbf{r}), \quad (\text{A.23})$$

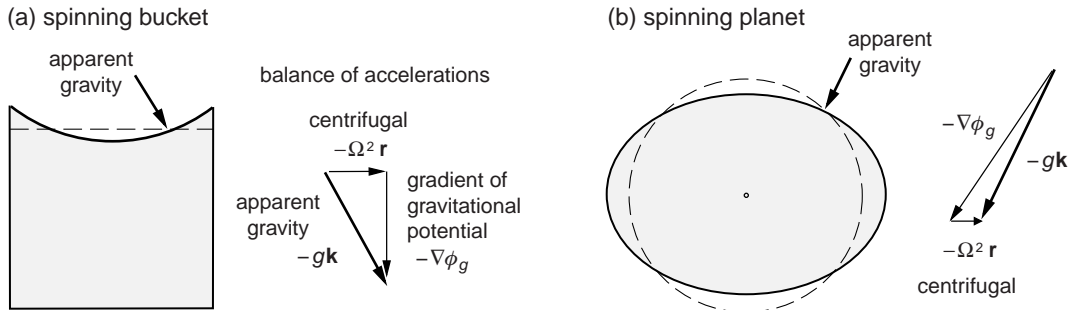


Figure A.5 A schematic figure denoting the direction of the apparent gravity $-g\mathbf{k}$ and the directions of the gradient of the gravitational potential $-\nabla\phi_g$ and the centrifugal acceleration $-\Omega^2\mathbf{r}$ as viewed for a rotating frame for (a) a spinning bucket of water, and (b) the rotating Earth.

which are referred to as the Coriolis and centrifugal accelerations (m s^{-2}), respectively.

Centrifugal and Coriolis accelerations

The centrifugal acceleration, $-\boldsymbol{\Omega} \times (\boldsymbol{\Omega} \times \mathbf{r})$, provides an outward acceleration away from the rotational axis (Fig. A.4b). This acceleration is independent of the motion of the fluid.

The Coriolis acceleration, $-2\boldsymbol{\Omega} \times \mathbf{u}_{\text{rel}}$, provides an acceleration deflecting a particle perpendicular to its motion (Fig. A.4c). If there is a cyclonic circulation of the reference frame ($\boldsymbol{\Omega}$ is positive), the Coriolis acceleration is directed to the right of the particle motion. Conversely, if there is an anticyclonic circulation of the frame, the Coriolis acceleration is to the left of the motion. If the particle is not moving in the reference frame, there is no Coriolis acceleration.

Apparent gravity and the centrifugal acceleration

The persistence of the centrifugal acceleration means that a rotating fluid has to change its mass distribution to offset this acceleration. For example, consider a bucket of water: at rest, the water surface is flat, while if the bucket is spun around, mass moves from the centre to the outer edges of the bucket (Fig. A.5a). From the viewpoint of the rotating frame, there is an outward centrifugal acceleration and a downward acceleration from the gradient of the gravitational potential. The sum of these two persistent accelerations is repre-

sented by an apparent gravity, defined by

$$-g\mathbf{k} = -\nabla\phi_g - \boldsymbol{\Omega} \times (\boldsymbol{\Omega} \times \mathbf{r}), \quad (\text{A.24})$$

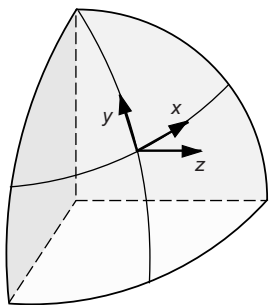
where \mathbf{k} is a unit vector pointing normal to the fluid surface or the ground for the Earth. At equilibrium, the water is aligned so that the net force from the apparent gravity is normal to the surface and there is no sideways acceleration. In a similar manner, for the spinning Earth, the mass adjusts, such that the sum of the gradient of the gravitational potential (directed towards the centre of mass) and centrifugal acceleration (directed outward away from the rotational axis) acts normal to the surface of the Earth (Fig. A.5b). This balance leads to the equatorial radius being slightly greater than the polar radius.

A.2.3 Vector components of the momentum equation

Combining the accelerations acting in a non-rotating frame (A.17) and the coordinate transformation to a rotating frame (A.23) leads to the momentum equation,

$$\frac{D\mathbf{u}}{Dt} = -\nabla\phi_g - \frac{1}{\rho}\nabla P - 2\boldsymbol{\Omega} \times \mathbf{u} - \boldsymbol{\Omega} \times (\boldsymbol{\Omega} \times \mathbf{r}) + \mathcal{F}, \quad (\text{A.25})$$

where all variables are now assumed to be measured in the rotating frame (and subscripts rel for velocity are now omitted). The vector form of the momentum equation is mathematically complete, but is not very accessible. Separating the single vector equation into three separate equations

(a) x , y and z coordinates

(b) twice angular velocity

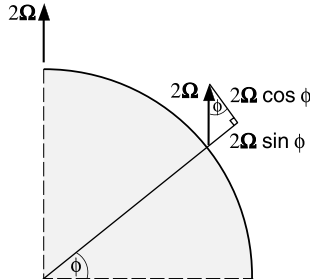


Figure A.6 A schematic figure denoting (a) the definition of the position vectors, and (b) how the vector, 2Ω , is separated into a normal component, $2\Omega \sin \phi$, and a tangential, northwards component, $2\Omega \cos \phi$, where ϕ is the latitude and Ω is the angular velocity with a magnitude of $2\pi/1$ day.

for its components in the x , y and z directions, then the velocity vector is

$$\mathbf{u} = u\mathbf{i} + v\mathbf{j} + w\mathbf{k}, \quad (\text{A.26})$$

where \mathbf{i} , \mathbf{j} and \mathbf{k} denote unit vectors pointing in the x , y and z directions, and the acceleration is

$$\frac{D\mathbf{u}}{Dt} = \frac{Du}{Dt}\mathbf{i} + \frac{Dv}{Dt}\mathbf{j} + \frac{Dw}{Dt}\mathbf{k}. \quad (\text{A.27})$$

The pressure-gradient force is then written as

$$\nabla P = \frac{\partial P}{\partial x}\mathbf{i} + \frac{\partial P}{\partial y}\mathbf{j} + \frac{\partial P}{\partial z}\mathbf{k}, \quad (\text{A.28})$$

and the frictional acceleration as

$$\mathcal{F} = \mathcal{F}_x\mathbf{i} + \mathcal{F}_y\mathbf{j} + \mathcal{F}_z\mathbf{k}. \quad (\text{A.29})$$

The vector 2Ω is separated into two components, $2\Omega \sin \phi$, normal to the surface of the planet and $2\Omega \cos \phi$ directed northward along the tangent parallel to the surface of the planet (Fig. A.6b), such that

$$2\Omega = 2\Omega \cos \phi \mathbf{j} + 2\Omega \sin \phi \mathbf{k}. \quad (\text{A.30})$$

The Coriolis acceleration given by the vector cross product, $-2\Omega \times \mathbf{u}$, is then

$$\begin{aligned} -2\Omega \times \mathbf{u} &= (-2\Omega w \cos \phi + 2\Omega v \sin \phi)\mathbf{i} \\ &\quad - 2\Omega u \sin \phi \mathbf{j} + 2\Omega u \cos \phi \mathbf{k}. \end{aligned} \quad (\text{A.31})$$

Collecting the different terms (A.24), (A.27), (A.28), (A.29) and (A.31) then leads to the momentum equation (A.25) for the separate x , y and z com-

ponents being written as

$$\frac{Du}{Dt} + 2\Omega w \cos \phi - 2\Omega v \sin \phi + \frac{1}{\rho} \frac{\partial P}{\partial x} = \mathcal{F}_x, \quad (\text{A.32})$$

$$\frac{Dv}{Dt} + 2\Omega u \sin \phi + \frac{1}{\rho} \frac{\partial P}{\partial y} = \mathcal{F}_y, \quad (\text{A.33})$$

$$\frac{Dw}{Dt} - 2\Omega u \cos \phi + g + \frac{1}{\rho} \frac{\partial P}{\partial z} = \mathcal{F}_z. \quad (\text{A.34})$$

While this derivation of the momentum equation is exact, this form of the momentum equation is rather complicated and non-intuitive to understand. Next consider an approach to reveal the controlling terms.

A.2.4 Scale analysis of the momentum equation

The dominant balances in the momentum equation, (A.32) to (A.34), usually depend on the characteristic time and space scales of the problem. To gain insight about these balances, consider the relative size of the different terms for a horizontal flow with a typical speed U , a vertical velocity W , horizontal length scale L and vertical length scale H . For an order of magnitude scaling, the horizontal velocity components are assumed to have a typical magnitude given by $u \sim v \sim U$, and a vertical velocity a magnitude by $w \sim W$. Any horizontal gradients are simply taken by the reciprocal of the horizontal length scale, $\partial/\partial x \sim \partial/\partial y \sim 1/L$, and any vertical gradients similarly by $\partial/\partial z \sim 1/H$. Finally, a typical advective timescale for the flow

is given by the ratio of the horizontal length and velocity scales,

$$T \sim \frac{L}{U}. \quad (\text{A.35})$$

Applying this crude scaling to each term in the unforced momentum equations (apart from the pressure gradients),

$$\underbrace{\frac{Du}{Dt}}_{\frac{U^2}{L}} + \underbrace{2\Omega w \cos \phi - 2\Omega v \sin \phi}_{2\Omega W \cos \phi} + \underbrace{\frac{1}{\rho} \frac{\partial P}{\partial x}}_{2\Omega U \sin \phi} = 0, \quad (\text{A.36})$$

$$\underbrace{\frac{Dv}{Dt}}_{\frac{U^2}{L}} + \underbrace{2\Omega u \sin \phi}_{2\Omega U \sin \phi} + \underbrace{\frac{1}{\rho} \frac{\partial P}{\partial y}}_{2\Omega U \sin \phi} = 0, \quad (\text{A.37})$$

$$\underbrace{\frac{Dw}{Dt}}_{\frac{UW}{L}} - \underbrace{2\Omega u \cos \phi}_{2\Omega U \cos \phi} + \underbrace{g}_{g} + \underbrace{\frac{1}{\rho} \frac{\partial P}{\partial z}}_{\frac{1}{\rho} \frac{\partial P}{\partial z}} = 0 \quad (\text{A.38})$$

The relative size of each term varies with the particular problem. Now consider two special characteristics of large-scale flow: (i) the dominance of horizontal flow over vertical flow; and (ii) the slowness of the motion relative to the Earth's rotational period.

Smallness of the vertical velocity and the hydrostatic balance

To understand why the horizontal flow is much larger than the vertical flow, crudely estimate the size of the terms in continuity of volume,

$$\underbrace{\frac{\partial u}{\partial x} + \frac{\partial v}{\partial y} + \frac{\partial w}{\partial z}}_{\frac{U}{L}} = 0. \quad (\text{A.39})$$

Note that the purpose is solely to find a typical magnitude, so that the scales for $\frac{\partial u}{\partial x}$ and $\frac{\partial v}{\partial y}$ are not added together to have a factor 2, since each of these terms might oppose each other. Rearranging (A.39) suggests that a typical magnitude for the vertical velocity is given by

$$w \sim U \frac{H}{L}. \quad (\text{A.40})$$

In practice, this estimate is often an upper bound due to the flow usually being close to horizon-

tal non-divergence. This ratio H/L is called the aspect ratio and is usually very small for large-scale motion in the ocean or atmosphere. For example, an ocean gyre circulation typically has a depth scale of 1 km and a horizontal scale of 1000 km, so that the aspect ratio is 1 : 1000, similar to that for a sheet of paper. The smallness of the aspect ratio then implies that $W \ll U$ for large-scale flows in the ocean.

Applying this scaling for the smallness of the vertical velocity and assuming a typical magnitude for a horizontal flow in the ocean leads to the first two terms, Dw/Dt and $-2\Omega U \cos \phi$, being much smaller than g in (A.38), so that a hydrostatic balance is obtained

$$\frac{\partial P}{\partial z} = -\rho g, \quad (\text{A.41})$$

where the vertical changes in pressure only depend on the density of the fluid and do not depend on the vertical motion.

Likewise, the vertical velocity terms are relatively unimportant in the horizontal components of the momentum equation. In addition, a Boussinesq approximation is often applied where density variations are assumed to be small, with terms involving ρ replaced by a reference density ρ_0 (apart from when density is multiplied by gravity). Applying both the smallness of w and the Boussinesq approximation, leads to (A.36) and (A.37) reducing to

$$\frac{Du}{Dt} - fv + \frac{1}{\rho_0} \frac{\partial P}{\partial x} = 0 \quad (\text{A.42})$$

$$\frac{Dv}{Dt} + fu + \frac{1}{\rho_0} \frac{\partial P}{\partial y} = 0, \quad (\text{A.43})$$

where the Coriolis parameter is $f \equiv 2\Omega \sin \phi$; note that this approximated form of the momentum equation only retains the Coriolis component normal to the surface of the Earth.

Slowness of the motion and geostrophic balance

The strength of rotational control in the momentum equation is measured by the non-dimensional Rossby number given by the ratio of the local

accelerations and the Coriolis acceleration, which for the x -component of (A.42) is given by

$$Ro = \left(\frac{Du}{Dt} \right) \left(\frac{1}{fv} \right),$$

and more generally defined as

$$Ro = \frac{U}{fL}. \quad (\text{A.44})$$

The large-scale motion in the ocean is usually very slow, with an advective timescale comparable or longer than the Earth's rotational period of a day. For an ocean eddy at mid latitudes, the horizontal flow is typically of a magnitude $U \sim 0.1 \text{ m s}^{-1}$ over a horizontal scale of $L \sim 50 \text{ km}$ and a depth scale of $H \sim 1 \text{ km}$, which implies an advective timescale, $T \sim \frac{L}{U} \sim 5 \times 10^5 \text{ s}$ and the Rossby number is $(0.1 \text{ m s}^{-1})(10^{-4} \text{ s}^{-1} 5 \times 10^4 \text{ m})^{-1} \sim 0.02 \ll 1$, where $f \sim 10^{-4} \text{ s}^{-1}$ for mid latitudes. Thus, the rotational control and the Coriolis acceleration become very important in controlling the motion. The unforced horizontal momentum equations, (A.42) and (A.43), then reduce to a geostrophic balance,

$$-fv + \frac{1}{\rho_0} \frac{\partial P}{\partial x} \simeq 0, \quad (\text{A.45})$$

$$fu + \frac{1}{\rho_0} \frac{\partial P}{\partial y} \simeq 0. \quad (\text{A.46})$$

This geostrophic flow is along P contours (high P to right of motion where $f > 0$), rather than directed across the P contours.

If the frictional acceleration is retained, as is relevant in the surface layer, then on timescales longer than a day, there is a three-way balance between the Coriolis acceleration, pressure gradient and frictional accelerations.

A.2.5 The equation set

A closed set of equations with the same number of unknown variables (u, v, w, P, ρ, T and S) and equations is obtained from:

- the horizontal component of the momentum equation (with the Boussinesq approximation applied),

$$\frac{Du}{Dt} - fv + \frac{1}{\rho_0} \frac{\partial P}{\partial x} = \frac{1}{\rho_0} \frac{\partial \tau_x}{\partial z},$$

$$\frac{Dv}{Dt} + fu + \frac{1}{\rho_0} \frac{\partial P}{\partial y} = \frac{1}{\rho_0} \frac{\partial \tau_y}{\partial z},$$

with a frictional forcing from the vertical gradient in frictional stress, τ ,

- the hydrostatic equation,

$$\frac{\partial P}{\partial z} = -\rho g,$$

- conservation equations for volume,

$$\nabla \cdot \mathbf{u} = \frac{\partial u}{\partial x} + \frac{\partial v}{\partial y} + \frac{\partial w}{\partial z} = 0,$$

- temperature equation with a heat source Q ,

$$\frac{DT}{Dt} = \frac{\partial T}{\partial t} + \mathbf{u} \cdot \nabla T = Q,$$

- salinity equation,

$$\frac{\partial S}{\partial t} + \mathbf{u} \cdot \nabla S = 0,$$

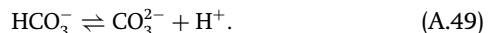
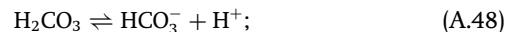
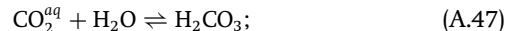
- an equation of state for density,

$$\rho = \rho(P, S, T).$$

This set of equations form the basis of most numerical models of the ocean circulation and can be solved when there are appropriate forcing functions (for the frictional stress and heat source) and appropriate boundary conditions for the exchange of momentum, heat, salt and fresh water.

A.3 Solving the carbonate chemistry system

In the aqueous system, carbon dioxide dissolves, forming aqueous carbon dioxide, CO_2^{aq} , and carbonic acid, H_2CO_3 , which dissociates into negatively charged bicarbonate, HCO_3^- , and carbonate, CO_3^{2-} , ions:



Since CO_2^{aq} and H_2CO_3 are difficult to distinguish it is customary to refer to their combined dissolved concentration, which we represent here by $[\text{CO}_2^*]$, and refer to as dissolved carbon dioxide. We define dissolved inorganic carbon, DIC, as the sum of carbonate species in a water parcel:

$$\text{DIC} = [\text{CO}_2^*] + [\text{HCO}_3^-] + [\text{CO}_3^{2-}]. \quad (\text{A.50})$$

It is conservative with respect to advection and mixing: The air-sea flux of CO₂ is often evaluated as a function of the difference between atmospheric and surface ocean pCO₂, which is related to [CO₂^{*}] by

$$p\text{CO}_2 = \frac{[\text{CO}_2^*]}{K_0(T, S)}, \quad (\text{A.51})$$

where K₀ is an empirically determined function of temperature, salinity and pressure (Weiss, 1974). We must solve for the partitioning of DIC to find [CO₂^{*}].

Reactions (A.47)–(A.49) proceed to equilibrium on timescales of minutes, so we assume equilibrium partitioning of the carbonate species within DIC. The relative abundances can be quantified using empirically determined (temperature, salinity and pressure dependent) equilibrium coefficients (e.g., DOE, 1994; Millero, 1995; Zeebe and Wolf-Gladrow, 2001):

$$K'_1 = \frac{[\text{HCO}_3^-][\text{H}^+]}{[\text{CO}_2^*]}, \quad (\text{A.52})$$

$$K'_2 = \frac{[\text{CO}_3^{2-}][\text{H}^+]}{[\text{HCO}_3^-]}. \quad (\text{A.53})$$

We now have four relations: (A.50), (A.51), (A.52) and (A.53), and five unknowns ([HCO₃⁻], [CO₃²⁻], [CO₂^{*}], [H⁺], pCO₂). We can find the relationship between pCO₂ and hydrogen ion concentration,

$$p\text{CO}_2 = \frac{\text{DIC}}{K_0} \left[1 + \frac{K'_1}{[\text{H}^+]} + \frac{K'_1 K'_2}{[\text{H}^+]^2} \right]^{-1}, \quad (\text{A.54})$$

but further constraints are required to solve for both [H⁺] and pCO₂. An expression for alkalinity provides the additional constraint of charge balance. Here we define the titration alkalinity, A_T (following Dickson, 1981; DOE, 1994):

$$\begin{aligned} A_T &= [\text{HCO}_3^-] + 2[\text{CO}_3^{2-}] + [\text{B(OH)}_4^-] + [\text{OH}^-] \\ &\quad + [\text{HPO}_4^{2-}] + 2[\text{PO}_4^{3-}] + [\text{SiO(OH)}_3^-] \\ &\quad - [\text{H}^+] - [\text{H}_3\text{PO}_4]. \end{aligned} \quad (\text{A.55})$$

We have neglected further contributions from ammonium, sulphur, fluorine and other minor species. In analogy to the equilibrium description of the carbonate species, laboratory-determined,

T and S dependent equilibrium coefficients, K_B, K_{Si}, K_{P1}, K_{P2}, K_{P3} (DOE, 1994; Millero, 1995; Zeebe and Wolf-Gladrow, 2001) define the relationship of the boron, silicon, and phosphorus species to total dissolved inorganic boron, B_T, dissolved inorganic silicon, Si_T, and dissolved inorganic phosphorus, P_T, respectively.

If DIC, A_T, P_T, B_T, and Si_T can be specified, the system of 10 relationships below (A.56–A.65) can be solved iteratively for the remaining 10 unknowns, including [CO₂^{*}] (see, for example, Follows *et al.*, 2006, for a method of solution):

$$\text{DIC} = [\text{CO}_2^*] + [\text{HCO}_3^-] + [\text{CO}_3^{2-}], \quad (\text{A.56})$$

$$\begin{aligned} A_T &= [\text{HCO}_3^-] + 2[\text{CO}_3^{2-}] + [\text{B(OH)}_4^-] \\ &\quad + [\text{OH}^-] + [\text{HPO}_4^{2-}] + 2[\text{PO}_4^{3-}] \\ &\quad + [\text{SiO(OH)}_3^-] - [\text{H}^+] - [\text{H}_3\text{PO}_4], \end{aligned} \quad (\text{A.57})$$

$$K'_1 = \frac{[\text{HCO}_3^-][\text{H}^+]}{[\text{CO}_2^*]}, \quad (\text{A.58})$$

$$K'_2 = \frac{[\text{CO}_3^{2-}][\text{H}^+]}{[\text{HCO}_3^-]}, \quad (\text{A.59})$$

$$K_w = [\text{H}^+] [\text{OH}^-], \quad (\text{A.60})$$

$$[\text{B(OH)}_4^-] = \frac{K_B B_T}{K_B + [\text{H}^+]}, \quad (\text{A.61})$$

$$[\text{SiO(OH)}_3^-] = \frac{K_{\text{Si}} S_i T}{K_{\text{Si}} + [\text{H}^+]}, \quad (\text{A.62})$$

$$\begin{aligned} [\text{H}_3\text{PO}_4] &= \frac{P_T [\text{H}^+]^3}{[\text{H}^+]^3 + K_{\text{P1}}[\text{H}^+]^2 + K_{\text{P1}}K_{\text{P2}}[\text{H}^+] + K_{\text{P1}}K_{\text{P2}}K_{\text{P3}}}, \\ &\quad (\text{A.63}) \end{aligned}$$

$$\begin{aligned} [\text{HPO}_4^{2-}] &= \frac{P_T K_{\text{P1}} K_{\text{P2}} [\text{H}^+]}{[\text{H}^+]^3 + K_{\text{P1}}[\text{H}^+]^2 + K_{\text{P1}}K_{\text{P2}}[\text{H}^+] + K_{\text{P1}}K_{\text{P2}}K_{\text{P3}}}, \\ &\quad (\text{A.64}) \end{aligned}$$

$$\begin{aligned} [\text{PO}_4^{3-}] &= \frac{P_T K_{\text{P1}} K_{\text{P2}} K_{\text{P3}}}{[\text{H}^+]^3 + K_{\text{P1}}[\text{H}^+]^2 + K_{\text{P1}}K_{\text{P2}}[\text{H}^+] + K_{\text{P1}}K_{\text{P2}}K_{\text{P3}}}. \\ &\quad (\text{A.65}) \end{aligned}$$

Symbols and definitions

Biological and chemical symbols

Chemical definition	Name	Units
A_C	carbonate alkalinity	$\mu\text{mol kg}^{-1}$
$A_T, A_T^{\text{pre}}, A_T^{\text{reg}}$	total alkalinity, preformed and regenerated	" "
AOU	apparent oxygen utilisation	" "
B	Revelle buffer factor $B = (\delta[\text{CO}_2^*]/[\text{CO}_2^*]) / (\delta\text{DIC}/\text{DIC})$	dimensionless
B_N	biomass	mol m^{-3} or mol kg^{-1}
c	dissolved concentration of gas, c	mol m^{-3} or mol kg^{-1}
$C^{\text{pre}}, C^{\text{reg}}$	preformed and regenerated DIC	$\mu\text{mol kg}^{-1}$
C^{sat}	saturated DIC	" "
C^{soft}	soft-tissue component of C^{reg}	" "
C^{carb}	carbonate component of C^{reg}	" "
C^{res}	residual component of DIC	" "
CaCO_3	calcium carbonate	" "
Ca^{2+}	calcium ions	" "
CO_2^{aq}	aqueous carbon dioxide	" "
CO_2^*	dissolved carbon dioxide, $[\text{CO}_2^*] = [\text{CO}_2^{\text{aq}}] + [\text{H}_2\text{CO}_3]$	" "
CO_3^{2-}	carbonate	" "
DIC	dissolved inorganic carbon, $\text{DIC} = [\text{CO}_2^*] + [\text{HCO}_3^-] + [\text{CO}_3^{2-}]$	" "
DOC, POC	dissolved and particulate organic carbon	" "
DON, PON	dissolved and particulate organic nitrogen	" "
DOP, POP	dissolved and particulate organic phosphorus	" "
\mathcal{F}	air-sea flux of a gas, c	$\text{mol cm}^{-2} \text{s}^{-1}$ or $\text{mol c kg}^{-1} \text{m s}^{-1}$
\mathcal{F}_C	air-sea flux of CO_2	$\text{mol C m}^{-2} \text{s}^{-1}$
$\mathcal{F}_C^{\text{pot}}$	potential air-sea flux of CO_2	$\text{mol C m}^{-2} \text{s}^{-1}$
H^+	hydrogen ions	$\mu\text{mol kg}^{-1}$
HCO_3^-	bicarbonate	" "
H_2CO_3	carbonic acid	$\mu\text{mol kg}^{-1}$
I, I_{oa}	carbon inventory, for the combined atmosphere and ocean	gC or mol C
I_B	buffered carbon inventory of the atmosphere and ocean	gC or mol C
K_g	air-sea gas exchange coefficient or exchange velocity	m s^{-1}
K_0, K_0^c	solubility of carbon dioxide and a general gas, c	$\mu\text{mol kg}^{-1} \mu\text{atm}^{-1}$
K'_1, K'_2	thermodynamic equilibria	mol kg^{-1}
K_{sat}	half saturation	mol m^{-3} or mol kg^{-1}
m	mortality	s^{-1}

Biological and chemical symbols (cont.)

Chemical definition	Name	Units
M	number of moles	mol
\mathcal{N}	generalised nutrient	mol m^{-3} or mol kg^{-1}
NH_4^+	ammonium	$\mu\text{mol kg}^{-1}$
NO_3^-	nitrate	" "
NO_2^-	nitrite	" "
$\text{O}_2, \text{O}_2^{\text{pre}}, \text{O}_2^{\text{reg}}$	oxygen, preformed and regenerated	" "
p	atmospheric pressure	atm or N m^{-2}
P^{at}	atmospheric pressure	atm
p_c	partial pressure for a gas c	μatm
$p\text{CO}_2, p\text{CO}_2^{\text{at}}$	partial pressure for carbon dioxide, in the atmosphere	μatm
\mathcal{P}^*	ratio of regenerated and total phosphate	dimensionless
pH	$\text{pH} = -\log_{10}[\text{H}^+]$	
$\text{PO}_4^{3-}, \text{PO}_4^{\text{pre}}, \text{PO}_4^{\text{reg}}$	phosphate, preformed and regenerated	$\mu\text{mol kg}^{-1}$
Q_N	nutrient quota	mol cell^{-1}
R	Redfield ratio of elements in marine phytoplankton	dimensionless
V_{\max}	maximum uptake rate	$\text{mol m}^{-3} \text{s}^{-1}$ or $\text{mol kg}^{-1} \text{s}^{-1}$
X	cell number density	cells ml^{-1}
X_c	mixing ratio for a gas c	ppmv
X_{CO_2}	mixing ratio for carbon dioxide	ppmv
μ	population growth rate	s^{-1}
τ	gas exchange timescale, h/K_g	s

Physical symbols

Variable	Description	Units
a	acceleration (vector)	m s^{-2}
A	area	m^2
A_v	eddy viscosity	$\text{m}^2 \text{s}^{-1}$
c	generic tracer concentration	tracer units (mol m^{-3} or mol kg^{-1})
$\{c\}$	tracer concentration per unit volume	mol m^{-3}
$[c]$	tracer concentration per unit mass	mol kg^{-1}
c	wave speed	m s^{-1}
C_p	heat capacity for seawater at constant pressure	$\text{J kg}^{-1} \text{K}^{-1}$
d	thickness of boundary layer	m
D	depth of water column	m
\mathcal{D}	surface density flux into the ocean	$\text{kg m}^{-2} \text{s}^{-1}$
\mathcal{E}	evaporation rate	m y^{-1}

(cont.)

Physical symbols (cont.)

Variable	Description	Units
f	Coriolis parameter = $2\Omega \sin \phi$, and vertical component of planetary vorticity	s^{-1}
F	flux of tracer, $c u$	(tracer unit) m s^{-1}
\mathbf{F}	external force (vector)	N
\mathcal{F}	frictional acceleration	m s^{-2}
g	gravitational acceleration	m s^{-2}
g'	reduced gravity, $g' = g\Delta\rho/\rho$ where $\Delta\rho$ is the density difference between two density layers.	m s^{-2}
G	gravitational constant	$\text{N m}^2 \text{kg}^{-2}$
G	diapycnal volume flux or transformation	$\text{m}^3 \text{s}^{-1}$
h	thickness of mixed layer	m
H	vertical length scale	m
\mathcal{H}	heat flux into the ocean	$\text{J m}^{-2} \text{s}^{-1} = \text{W m}^{-2}$
$\mathcal{H}_{\text{latent}}, \mathcal{H}_{\text{sens}}$	latent and sensible heat flux	W m^{-2}
$\mathcal{H}_{\text{long}}, \mathcal{H}_{\text{solar}}$	long-wave and solar radiative heat flux	W m^{-2}
$\mathbf{i}, \mathbf{j}, \mathbf{k}$	unit vectors in the x , y and z directions	
k	wavenumber of a wave, $2\pi\lambda^{-1}$	m^{-1}
K	eddy transfer coefficient	$\text{m}^2 \text{s}^{-1}$
L	horizontal length scale	m
L_{ang}	angular momentum per unit mass	$\text{m}^2 \text{s}^{-1}$
m	mass	kg
$M\Delta\rho$	water-mass formation in a density interval, $\Delta\rho$	$\text{m}^3 \text{s}^{-1}$
N	buoyancy frequency	s^{-1}
P	pressure	$\text{N m}^{-2} = \text{kg m}^{-1} \text{s}^{-2}$
\mathcal{P}	precipitation rate	m y^{-1}
Pe	Peclet number, $\frac{UL}{\kappa}$	
PW	petawatt	10^{15}W
Q	internal temperature source	K s^{-1}
Q	dynamic tracer, potential vorticity	$\text{m}^{-1} \text{s}^{-1}$
r, R	radius or distance	m
\mathbf{r}	position vector	m
Ro	Rossby number, $\frac{U}{fL}$	dimensionless
S	salinity, concentration of dissolved mass	g kg^{-1}
S_c	solar constant	W m^{-2}
S_c	tracer source	(tracer unit) s^{-1}
$S(t), S_{\text{ann}}$	instantaneous subduction rate, annual subduction rate,	$\text{m}^3 \text{s}^{-1} \text{m}^{-2}$
Sv	sverdrup, unit for volume transport	$10^6 \text{ m}^3 \text{s}^{-1}$
t	time	s
T	advection timescale, $\frac{L}{U}$	s
T	period	s
T	temperature	K or $^{\circ}\text{C}$
TW	terawatt	10^{12}W
u, v, w	velocities in the x , y and z directions	m s^{-1}
\mathbf{u}	velocity (vector)	m s^{-1}

Physical symbols (*cont.*)

Variable	Description	Units
u^*	friction velocity, $\tau = \rho u_*^2$	m s^{-1}
U	typical magnitude of horizontal velocity	m s^{-1}
u_{ag}, v_{ag}	ageostrophic velocities	m s^{-1}
u_{ek}, v_{ek}	Ekman velocities	m s^{-1}
U_{ek}, V_{ek}	Ekman volume fluxes per unit length	$\text{m}^2 \text{s}^{-1}$
u_g, v_g	geostrophic velocities	m s^{-1}
$v^* = \frac{1}{h} h' v'$	bolus velocity, where h is layer thickness and v is the velocity in the layer	m s^{-1}
$v_{Stokes} = v_0^2/(2c)$	Stokes' velocity, where v_0 is amplitude of oscillating velocity and c is wave speed	m s^{-1}
$\bar{v} + v^*$	meridional transport velocity	m s^{-1}
V	scaling for meridional velocity	ms^{-1}
V, V_0	volume, volume of the ocean	kg m^3
w_{ek}	Ekman upwelling velocity	m s^{-1}
W	typical magnitude of vertical velocity	m s^{-1}
x, y, z	Cartesian coordinates: position in eastward, northward and vertical directions	m
α_r	radiative heating constant	W m^{-2}
α_T	density expansion coefficient for temperature, $-\frac{1}{\rho} \frac{\partial \rho}{\partial T}$	K^{-1}
β	planetary vorticity gradient, df/dy	$\text{m}^{-1} \text{s}^{-1}$
β_S	density contraction coefficient for salinity, $\frac{1}{\rho} \frac{\partial \rho}{\partial S}$	$(\text{g kg}^{-1})^{-1}$
γ	neutral density surface	kg m^{-3}
γ_s	strain rate	s^{-1}
ζ	vertical component of relative vorticity, $\frac{\partial v}{\partial x} - \frac{\partial u}{\partial y}$	s^{-1}
η	dynamic height	m
θ	potential temperature	$^{\circ}\text{C}$
κ	molecular diffusivity	$\text{m}^2 \text{s}^{-1}$
λ	wavelength	m
ρ	density	kg m^{-3}
ρ_0	constant reference density	kg m^{-3}
ρ_θ	potential density	kg m^{-3}
σ_{sb}	Stefan–Boltzmann constant	$\text{W m}^{-2} \text{K}^{-4}$
σ_T	sigma, $\rho - 1000 \text{ kg m}^{-3}$	kg m^{-3}
σ_θ	sigma theta, $\rho_\theta - 1000 \text{ kg m}^{-3}$	kg m^{-3}
τ_x, τ_y	frictional stresses directed eastward and northward	N m^{-2}
τ_x^b, τ_y^b	bottom stress	N m^{-2}
τ_x^s, τ_y^s	surface wind stress	N m^{-2}
ϕ	latitude	degrees or radians
ϕ_g	gravitational potential for the Earth	$\text{m}^2 \text{s}^{-2}$
ψ	streamfunction for velocity or transport	$\text{m}^2 \text{s}^{-1}, \text{m}^3 \text{s}^{-1}$
ω	angular frequency of a wave, 2π period $^{-1}$	s^{-1}
Ω	angular velocity of a rotating frame, 2π period $^{-1}$, angular velocity of the Earth, 2π day $^{-1}$	s^{-1}

Mathematical definitions

Vector relations	Description	Units
$\text{grad } c$	gradient of a scalar, c $\nabla c = \mathbf{i} \frac{\partial c}{\partial x} + \mathbf{j} \frac{\partial c}{\partial y} + \mathbf{k} \frac{\partial c}{\partial z}$	(unit of c) m^{-1}
$\text{div } \mathbf{V}$	divergence of a vector, \mathbf{V} $\nabla \cdot \mathbf{V} = \frac{\partial V_x}{\partial x} + \frac{\partial V_y}{\partial y} + \frac{\partial V_z}{\partial z}$	(unit of \mathbf{V}) m^{-1}
$\text{curl } \mathbf{V}$	curl of a vector \mathbf{V} , $\nabla \times \mathbf{V}$	(unit of \mathbf{V}) m^{-1}
D/Dt	rate of change following the flow $\frac{\partial}{\partial t} + \mathbf{u} \cdot \nabla = \frac{\partial}{\partial t} + u \frac{\partial}{\partial x} + v \frac{\partial}{\partial y} + w \frac{\partial}{\partial z}$	s^{-1}

Glossary

The glossary is separated into biological, chemical and physical terms, so that readers can more easily work through terms from a particular discipline.

Biological glossary

Ballast: dense mineral components of marine particles which provide negative buoyancy and drive sinking.

Biomass: the concentration of element N in seawater in the form of living organic matter (B_N , mol N kg $^{-1}$).

Chlorophyll a: a pigment common to all phytoplankton which is used to harvest photons.

Coccolithophores: phytoplankton which create mineral calcium carbonate components.

Complexation: the formation of a weak inter-molecular bond between a ligand, an organic molecule with an appropriate binding site, and a substrate or reactant.

Diatoms: phytoplankton which create mineral silica structural components.

Diazotrophs: organisms which can break the triple bond and fix nitrogen gas, relieving the need to take up dissolved inorganic nitrogen.

DNA: deoxyribonucleic acid; the molecules which record the genetic blueprint of living organisms.

Enzymes: proteins which facilitate biochemical reactions which would otherwise proceed slowly or not at all.

Euphotic layer: the uppermost waters of the ocean where a significant flux of visible solar radiation is present. Depending upon the absorption properties of the water and the incident irradiance, this layer can extend to depths of only several metres to more than two hundred metres.

Export production: the fraction of primary production which is transported from the euphotic layer into the dark, deeper waters, either as gravitationally sinking organic particles, or dissolved organic matter transported by ocean circulation and mixing processes.

Flagellates, dinoflagellates: phytoplankton with flagella or protrusions which can be whipped, propelling the cells through the water.

Dinoflagellates have dual flagella and most are mixotrophic.

Heterotrophy: the strategy of harvesting energy by ingesting and respiring existing organic matter.

Lipids: biochemical components of cells which perform membrane functions or act as a chemical store of energy.

Michaelis-Menten kinetics: the mathematical description of enzymatic reactions. Many biological phenomena exhibit similar saturating relationships.

Mixotrophy: the ability of some organisms to practise both phototrophy and heterotrophy.

New production: the fraction of primary production which is fuelled by inorganic nutrients that have not been incorporated into organic matter since their arrival in the euphotic layer.

Nutrient quota: the cellular content of a particular nutrient element (Q_N , mol N cell $^{-1}$).

Nutrient streams: regions of enhanced nutrient flux carried along isopycnals, coinciding with boundary currents or separated jets.

Nutrient utilisation: the relative magnitude of the biogenic and total phosphate concentrations.

Organic matter: molecules or material originating in living cells. Dissolved organic matter (DOM) is defined as material passing through a 0.45 µm filter, while particulate organic matter (POM) does not pass through.

Organic molecules: the molecules produced by living creatures and which contain carbon-hydrogen bonds.

Photosynthesis: the production of organic matter from inorganic nutrients, fuelled by energy from captured photons.

Phototrophy: the strategy of using light as an energy source to fuel the creation of organic matter from inorganic nutrients. Photo-autotrophy is when this strategy is used exclusively.

Preformed nutrient: the concentration of nutrients in a water parcel at the time of subduction.

Primary production: the creation of organic matter from inorganic nutrients by photosynthesis.

Prochlorococcus: the smallest, micron-scale phytoplankton which dominate the biomass of the surface subtropical oceans.

Proteins: organic compounds in all living organisms which perform special functions, for example, acting as enzymes, and provide structure.

Recycled production: the fraction of primary production which is fuelled by nutrients that have previously been incorporated into organic matter and respired while still within the euphotic layer.

- Redfield ratio:** the bulk average ratio of elements in marine plankton: C : N : P : O₂ = 106 : 16 : 1 : -170.
- Regenerated nutrient:** the accumulation of nutrients in a water parcel since subduction from the respiration of sinking particulate or dissolved organic matter.
- Respiration:** the oxidation of organic matter to release energy, typically consuming oxygen.
- RNA:** ribonucleic acid; organic molecules which are used to translate the blueprint from DNA into new proteins.
- Substrate:** a reaction which takes part in a biochemical reaction.
- Synechococcus:** micron-scale phytoplankton common in subtropical and coastal oceans; slightly larger than Prochlorococcus.
- Zooplankton:** heterotrophic plankton which make a living by grazing on other living cells.

Chemical glossary

- Acids:** substances which, when dissolved in water, increase the concentration of hydrogen ions, [H⁺]. A *strong acid* is one which completely ionises in water. A *weak acid* is one which exists in partially ionised form in water. An alternative definition of an acid is a substance which donates a proton to another in a proton transfer reaction.
- Alkalinity:** see *total alkalinity* and *carbonate alkalinity*.
- Anions:** ions with a negative charge, i.e., more electrons than protons.
- Apparent oxygen utilisation, AOU:** the difference in local oxygen concentration from the local saturation value.
- Bases:** substances which, when dissolved in water, increase the concentration of hydroxide ions, [OH⁻]. A *strong base* is one which completely ionises in water. A *weak base* is one which exists in partially ionised form in water. An alternative definition of a base is a substance which consumes a proton from another in a proton transfer reaction.
- Buffer factor:** the Revelle buffer factor measures the fractional changes in the partial pressure of carbon dioxide, pCO₂, divided by the fractional changes in dissolved inorganic carbon:
- $$B = \frac{\delta p\text{CO}_2/\text{pCO}_2}{\delta \text{DIC}/\text{DIC}} = \frac{\delta[\text{CO}_2^*]/[\text{CO}_2^*]}{\delta \text{DIC}/\text{DIC}}$$
- Buffering:** a buffered property is one for which changes due to external perturbations are damped by negative feedbacks.

- Bicarbonate:** HCO₃⁻.
- Carbon pumps:** how the store of carbon in the deep ocean is enhanced by physical and biological transfers of carbon from the surface ocean; the solubility pump refers to how physical processes enhance the store of carbon, while the biological pump refers to how biological processes enhance the store of carbon.
- Carbonate:** CO₃²⁻.
- Carbonate alkalinity, A_C:** the contribution of the carbonate species to the total alkalinity:
- $$A_C = [\text{HCO}_3^-] + 2[\text{CO}_3^{2-}]$$
- Carbonate system:** the compounds and reactions between CO₂^{*}, HCO₃⁻, and CO₃²⁻ in water.
- Cations:** ions with a positive charge, i.e., more protons than electrons.
- Conservative ions:** compounds which are always completely ionised in seawater, independent of temperature, salinity, and pH. They include [Na⁺], [Mg²⁺], and [Cl⁻].
- Dissolved carbon dioxide:** [CO₂^{*}] = [CO₂^{aq}] + [H₂CO₃], the sum of the aqueous CO₂ and carbonic acid in seawater.
- Dissolved inorganic carbon:**
- $$\text{DIC} = [\text{CO}_2^*] + [\text{HCO}_3^-] + [\text{CO}_3^{2-}],$$
- the sum of the concentrations of the carbonate species in water.
- Electrolytes:** molecules that dissolve in water to form ions, creating a conductive solution. *Strong electrolytes* are those that dissociate completely in water and exist in solution almost completely as ions. *Weak electrolytes* are those which remain mostly as molecules in solution, with only a small fraction in ionic form.
- Hydrogen ions:** the ionic form of hydrogen in water, denoted as the concentration of hydrogen ions [H⁺]. However, in water, hydrogen ions are associated with water molecules in the form of hydronium, H₃O⁺, from 2H₂O = OH⁻ + H₃O⁺.
- Inorganic molecules:** all compounds which are not organic; see *organic molecules*.
- Mixing ratio of carbon dioxide, X_{CO₂}:** the number of moles of carbon dioxide per mole of air (expressed as parts per million by volume, ppmv).
- Partial pressure of carbon dioxide, pCO₂^{at}:** the contribution of carbon dioxide to the total atmospheric pressure, P^{at}, defined by the product of the mixing ratio and total atmospheric pressure, pCO₂^{at} = X_{CO₂} P^{at} (expressed as μatm).
- pH:** measures the concentration of hydrogen ions, [H⁺], in water, pH = -log₁₀[H⁺]. A decrease in pH

corresponds to an increase in hydrogen ion concentration.

Solubility: the solubility of a gas c , K_0^c , quantifies the ratio of the concentration of the dissolved gas in seawater, $[c]$, and the partial pressure in the air, p_c , when there is an equilibrium (i.e., no net flux of c) across the air–water interface: $K_0 \equiv [c]/p_c$ in units of $\text{mol kg}^{-1} \mu\text{atm}^{-1}$.

Solubility of carbon dioxide, K_{CO_2} ($\text{mol kg}^{-1} \mu\text{atm}^{-1}$): measures the capacity for carbon dioxide to dissolve in seawater. The solubility decreases with temperature and, to a lesser extent, salinity.

Total alkalinity: total alkalinity, A_T , is the concentration of charge associated with the conservative ions:

$$\begin{aligned} A_T \equiv & [\text{Na}^+] + 2[\text{Mg}^{2+}] + 2[\text{Ca}^{2+}] + [\text{K}^+] + 2[\text{Sr}^{2+}] \\ & - [\text{Cl}^-] - 2[\text{SO}_4^{2-}] - [\text{Br}^-] - [\text{F}^-] - [\text{NO}_3^-] \\ & + \dots = [\text{HCO}_3^-] + 2[\text{CO}_3^{2-}] + [\text{B(OH)}_4^-] \\ & + [\text{OH}^-] - [\text{H}^+] + \dots, \end{aligned}$$

which, for overall charge conservation, must equal the total charge concentration associated with all the other ions; see also *carbonate alkalinity*.

Physical glossary

Advection: the transfer of tracer and displacement of fluid particles by the background circulation.

Angular velocity (s^{-1}): the rate at which an object rotates, defined as 2π divided by the period.

Baroclinic instability: generates eddy variability through a release of potential energy from a slumping of sloping potential density surfaces, associated with a strong vertical shear in horizontal velocity. This process forms most of the eddy variability on the ocean mesoscale and atmospheric synoptic scale.

Barotropic instability: generates eddy variability through a release of kinetic energy from the mean flow, associated with a strong horizontal shear in the horizontal velocity.

Beta effect: $\beta = df/dy$, represents how the planetary vorticity, f , increases northward over the spherical Earth. This beta effect turns out to be crucial in the formation of western boundary currents and weak interior gyre flows.

Bolus velocity: the additional eddy advection due to correlations in perturbations in velocity and thickness, $\mathbf{u}^* = \bar{\mathbf{u}}' \bar{h}' / \bar{h}$. For an eastward jet (with poleward shoaling isopycnals), a slumping of

isopycnals leads to a poleward bolus velocity in the upper waters and an equatorward bolus velocity in deeper waters.

Cascading: the formation of dense water on the shallow shelf, which overflows into the neighbouring open ocean.

Centrifugal acceleration: an apparent acceleration when viewing any object from a rotating reference frame. The centrifugal acceleration is always directed outward and occurs even if objects are not moving. The centrifugal acceleration can be seen in how water moves outward in a spinning bucket and in how the spinning Earth is deformed from a sphere to an ellipsoid with an equatorial radius greater than the polar radius.

Coriolis acceleration: an apparent acceleration when viewing any moving object from a rotating reference frame. If the reference frame rotates in an anticlockwise sense, then a moving object viewed in that frame appears to be deflected in a clockwise sense. When viewing objects from the rotating Earth, objects appear to be deflected to the right of the motion in the northern hemisphere and to the left of the motion in the southern hemisphere.

Diffusion: the systematic transfer of tracer from high to low concentration, achieved through correlations in the fine-scale fluctuations in velocity and tracer concentration, provided on the smallest scale by the random motion of molecules.

Dispersion: how particles spread away from their centre of mass. In a wave context, dispersion also refers to how waves of different wavelengths have a different wave speed, such as in how the fastest surface waves propagating from a storm over the ocean have the longest wavelength.

Dynamic height: the vertical displacement of a pressure surface from a reference surface, called the geoid (a surface of constant gravitational acceleration). The surface geostrophic flow follows contours of dynamic height, in the same way as winds follow pressure contours on a weather map.

Eady growth period: the timescale for eddies to form through baroclinic instability given by $T^{-1} = 0.31(f/N) |\partial \mathbf{u}/\partial z|$, where f is the Coriolis parameter, N is the buoyancy frequency, and $\partial \mathbf{u}/\partial z$ is the vertical shear in the horizontal velocity.

Eddy: a deviation in the flow from a background state. An eddy can be defined in terms of a temporal deviation from a time-mean flow or a spatial deviation from a spatially averaged flow.

Eddy diffusivity, K , or eddy transfer coefficient: measures the correlation of an eddy velocity and

eddy length scale ($\text{m}^2 \text{s}^{-1}$). The tracer flux is often parameterised in terms of a product of the eddy transfer coefficient and the tracer gradient, such that the flux is transferred down gradient.

Ekman flow: the frictionally driven flow close to surface or bottom boundaries. The Ekman flow involves a dynamical balance between the Coriolis acceleration and the vertical change in frictional stress. The Ekman flow integrated over the surface or bottom boundary layer is related to the frictional stress acting at the boundary: for a surface wind stress, the Ekman transport is directed to the right of the stress in the northern hemisphere and to the left in the southern hemisphere.

El Niño–Southern Oscillation (ENSO): represents a coupled mode involving changes in the atmosphere and ocean over the tropical Pacific, typically varying on timescales of 3 to 7 years. The El Niño and La Niña phases are associated with surface waters in the eastern Pacific being warmer or cooler, respectively.

Energy: measured in joules ($1 \text{ J} = \text{N m} = \text{kg m}^2 \text{s}^{-2}$). Energy cannot be created or destroyed, it can only change form. Internal energy is the sum of all forms of energy of a system: the change in internal energy depends on the heat added to the system and the mechanical work done on the system. The internal energy can be held in many different forms: thermal energy linked to the temperature, potential energy linked to the static constituents and distribution of mass, and kinetic energy linked to the motion. An object can efficiently exchange energy between the different forms, apart from thermal energy where there are limits to the efficiency in converting to other forms of energy.

Eulerian velocity: the velocity measured at a fixed position.

Flux: flux of a property is given by the amount of a property passing through a fixed area per unit time. The units of a volume flux is in $\text{m}^3 \text{s}^{-1} \text{m}^{-2} = \text{m s}^{-1}$, heat flux in $\text{J s}^{-1} \text{m}^{-2} = \text{W m}^{-2}$ and nutrient flux in $\text{mol N s}^{-1} \text{m}^{-2}$.

Force: measured in newtons ($1 \text{ N} = \text{kg m s}^{-2}$). Force equals the rate of change of momentum, usually expressed as mass multiplied by acceleration.

Form drag: the pressure difference occurring across topographical bumps. This form drag acts to decelerate ocean currents by transferring momentum from the water column to the solid Earth.

Geoid: the surface of constant gravitational acceleration, which the sea surface would follow if

the ocean was not moving. The geoid undulates by several hundred metres over the globe due to variations in the gravitational field induced by changes in the Earth's density from magma, mountain ranges and deep-sea trenches.

Geostrophic flow: the flow directed along pressure contours with high pressure to the right of the motion in the northern hemisphere and to the left in the southern hemisphere. The geostrophic flow involves a dynamical balance between the Coriolis acceleration and the horizontal pressure gradient.

Gyre: the horizontal patterns of ocean circulation confined within a basin. A subtropical gyre occurs at mid latitudes and circulates anticyclonically, which is clockwise in the northern hemisphere and anticlockwise in the southern hemisphere. A subpolar gyre occurs at higher latitudes and circulates in the opposite sense.

Hydrostatic balance: the vertical gradient in pressure balances the density multiplied by downward gravitational acceleration, such the pressure increases with the weight of overlying fluid per unit horizontal area.

Lagrangian velocity: the velocity measured following a moving particle. This velocity usually differs from the Eulerian velocity at a fixed point. The Lagrangian velocity can be approximated by the Eulerian velocity plus a contribution from the time-varying velocity, this latter contribution is called a Stokes' drift correction.

Mechanical: mechanical work is the amount of energy transferred by a force acting over a distance. The power supplied is the force multiplied by velocity, so that the winds provide a power to the ocean per unit area given by the product of the wind stress multiplied by the surface velocity.

Mesoscale eddies: ocean eddies with a characteristic length scale from ten to a hundred kilometres. Dynamically analogous to atmospheric weather systems,

Mixed layer: the region where properties are nearly uniform in the vertical, occurring at the surface and the bottom of the ocean.

Mixing: the irreversible transfer of fluid across a tracer contrast. This irreversible transfer is ultimately achieved on a molecular scale through diffusion, although mixing is often taken to refer to any irreversible transfer process.

North Atlantic Oscillation (NAO): atmospheric mode, empirically defined by the pressure contrast between the Icelandic low and Azores high pressure systems.

The NAO effectively provides a measure of the strength and direction of the jet stream and storm tracks across the North Atlantic.

Ocean overturning: the transfer of fluid meridionally from one latitude to another. In the Atlantic basin, the overturning circulation leads to a northward transfer of warm, upper water and southward transfer of cold, deeper water.

Overflows: the spreading of dense water over a topographical sill, leading to the dense water plunging down the topographical slope. The intense mixing at overflows leads to the original density anomaly being diluted by mixing with the background environment.

Potential density: the density that water would have if it moved adiabatically to the sea surface.

Potential temperature, θ in °C: the temperature a water parcel would have at the sea surface if the parcel moved from its depth to the surface without any external heat input or heat exchange with adjacent water. If there is not this heat exchange, the motion is referred to as being adiabatic.

Potential vorticity: a dynamic tracer related to the stratification and rotation of the fluid. Potential vorticity is defined for a layer of moving fluid by $Q = (\zeta + f)/h$, where the absolute vorticity, $\zeta + f$, is divided by a thickness scale, h ; the thickness scale in an unstratified fluid is simply the thickness of the water column, while in a stratified fluid, h is a vertical spacing between two potential density surfaces. In the absence of any frictional twisting accelerations and diabatic forcing, Q is conserved, such that if a water column vertically stretches and h increases, then $\zeta + f$ increases.

Pressure, P : normal force per unit horizontal area measured in N m^{-2} . Pressure is a scalar. Fluid is accelerated from high to low pressure. See *geostrophic flow* and *hydrostatic balance* for the different horizontal and vertical balances.

Residual circulation: a combination of a mean advection and an eddy advection, where the mean represents a combined zonal and time average and an eddy represents a deviation from this mean. Often the mean and eddy contributions oppose each other, hence the use of the term ‘residual’.

Rossby deformation radius: the preferred scale for eddies to form by baroclinic instability given by $L_d = NH/f$, where N is the buoyancy frequency, H is a thickness scale and f is the Coriolis parameter. This deformation radius, L_d , also measures the length scale over which a dense perturbation spreads before being arrested by rotation.

Rossby waves or planetary waves: wave motions with a restoring force due to the change in planetary vorticity with latitude. The phase speed of Rossby waves propagates westward relative to the background flow. The group velocity and energy propagation is directed westward relative to the background flow for waves with a long west–east horizontal length scale and, conversely, directed eastward for waves with a short west–east horizontal length scale.

Salinity: salinity, S , is traditionally measuring the concentration of salt in water, the number of grams of salt in a kilogram of seawater, in units of g kg^{-1} ; practical salinity is also defined by the conductivity of seawater. Absolute salinity is now the recommended choice, defined by the concentration of dissolved mass in seawater in g kg^{-1} (so also including the contribution of nutrients), which is more exactly related to the thermodynamic properties of seawater (McDougall *et al.*, 2009).

Seasonal boundary layer: a region over which seasonal changes occur involving changes in the mixed layer and seasonal thermocline. The base of the seasonal boundary layer is defined by the maximum thickness of the mixed layer at the end of winter.

Slantwise exchange: the exchange of fluid parcels along sloping trajectories, which can lead to the conversion of potential energy to kinetic energy in baroclinic instability. The optimal release of potential energy occurs for particle exchange at half the slope of the background potential density surfaces.

Steering level: the position where the zonal velocity, u , is the same as the wave speed, c , which can lead to enhanced lateral exchange.

Stirring: how patches of tracer are drawn into narrow filaments through contrasts in advection, which increase tracer gradients. In principle, stirring of a tracer is reversible, but in practice there is irreversible transfer of tracer when stirring is combined with mixing.

Stokes’ drift: the systematic displacement of particles from a time-varying circulation due to correlations in the horizontal and temporal changes in velocity. The Lagrangian velocity (following a particle) can be approximated by the Eulerian velocity (at a fixed point) plus the Stokes’ drift velocity.

Strain rate: the deformation of the velocity field; the strain rate is largest when the velocity field acts to stretch tracer contours apart in one direction and compress them in a perpendicular direction. The

effective strain rate measures the rate at which particles spread away from each other.

Stress, τ : tangential force per unit horizontal area measured in N m^{-2} . Stress is a vector, so has a direction. The ocean is accelerated by frictional stresses acting at the sea surface and sea floor; see *Ekman flow*.

Subduction: the transfer of fluid from the mixed layer into the stratified thermocline. Subduction rate is the volume flux per unit horizontal area passing from the mixed layer into the stratified thermocline.

Sverdrup balance: connects the meridional volume flux ($\text{m}^2 \text{s}^{-1}$) to the twisting acceleration from the surface winds; cyclonic winds provide a vorticity input leading to a water column moving northward and increasing its planetary vorticity.

Thermocline: the region of strong vertical gradients of temperature, usually coincident with strong vertical gradients of density, salinity and nutrients, which are referred to as pycnocline, halocline and nutricline, respectively.

Tracer concentration, c : the amount of substance defined either in terms of unit mass, $[c]$ (mol kg^{-1}), or unit volume, $\{c\}$ (mol m^{-3}).

Tracer flux: a flux given by the product of velocity and tracer concentration; if the tracer concentration is in mol m^{-3} , then the tracer flux is in $\text{mol m}^{-2} \text{s}^{-1}$.

Tracer variance: defined by the square of the tracer deviation from the time-mean tracer concentration.

Tracers: properties that are conserved following the movement of fluid. Examples include salt concentration, defined as salinity, and a pressure-corrected temperature, called potential temperature.

Transformation: the diapycnal volume flux directed across a density surface. A positive value leads to light water being transformed to dense water.

Transport: the transfer of tracers involving both advection, following the large-scale movement of the

fluid, and diffusion within the fluid. Time-averaged transport involves a contribution from the time-averaged velocity at a fixed point plus a contribution from the time-varying velocity, referred to as the Stokes' drift. The units for transport are given by the area integrated flux of the property, so volume transport is in $\text{m}^3 \text{s}^{-1}$, heat transport in $\text{J s}^{-1} = \text{W}$ and nutrient transport in mol N s^{-1} .

Ventilation: the transfer of fluid from the mixed layer into the ocean interior.

Vorticity (s^{-1}): the rate at which an object or a fluid rotates. The vorticity of a rotating solid object is twice the angular velocity. The vorticity of fluid on the Earth is separated into the planetary vorticity and the relative vorticity, where the planetary vorticity measures how rapidly the solid Earth rotates and the relative vorticity measures how the fluid rotates relative to the solid Earth. Often the vertical component of the vorticity is focussed on, which is normal to the Earth's surface.

Water masses: collections of fluid defined by characteristic properties of potential temperature, salinity, oxygen and nutrient concentrations. Water masses are formed in the surface mixed layer and then spread via ventilation over the rest of the ocean.

Water-mass formation: is the rate of accumulation of water between two density surfaces, equivalent to the convergence of the transformation in density space.

Weather systems: atmospheric eddies containing warm and cold fronts, and which have a characteristic length scale of several thousand kilometres; this scale is often referred to as the synoptic scale.

Western boundary currents: intense flows along the western boundaries of ocean basins, providing the return flow of gyres and the primary pathway for ocean overturning.

Answers

The exercises are designed to reinforce the more quantitative material in the book and introduce high-level topics. Answers and brief solutions are provided here; more detailed working is also provided at www.cambridge.org/williamsandfollows.

Chapter 2

Q2.1. 2.5 m of ocean holds as much heat as the overlying atmosphere (10^7 J for the parameters given).

Q2.2. (a) (i) The solar radiation absorbed by a planet is given by $S_c \pi R^2 (1 - \alpha)$; (ii) the outgoing long-wave radiation is given by $4\pi R^2 \sigma_{sb} T^4$; the factor 4 is due to the long-wave radiation being emitted over an entire sphere with area $4\pi R^2$, whereas the solar radiation is only absorbed over a circular disc of area, πR^2 ; equate (i) and (ii) for a steady state, and rearrange.

(b) The estimated equilibrium temperatures are lower than the observed surface temperatures. The actual surface temperature is warmer due to the extra surface heating from the absorption and radiation of long-wave radiation in the atmosphere. There is only a slight warming for Mars due to its thin atmosphere, a warming of typically 30 K for the Earth and a very large warming for Venus due to the high CO₂ content of its atmosphere (despite its extensive cloud cover and high albedo).

(c) A local radiative heat balance implies a pole-equator temperature contrast more than twice as large as the observed contrast.

Q2.3. (a) $\Delta H \sim 1.1 \text{ W m}^{-2}$, and (b) Use $\overline{\Delta H}$ as half the answer in (a), as an average, so that $\Delta T \sim 0.4^\circ\text{C}$ after 50 years for a thickness of 500 m.

Q2.4. (a) Assume that angular momentum is conserved, so that the value at the equator, $L_{ang} = \Omega R^2$, is the same as at higher latitudes, $L_{ang} = (u + \Omega R \cos \phi) R \cos \phi$, which then leads to a prediction for the zonal velocity, $u = \Omega R \sin^2 \phi / \cos \phi$.

(b) Obtain a prediction of high zonal velocities, 133 m s⁻¹ at 30°N, with very fast, westerly jets of air formed. In practice, these zonal jets go unstable, leading to a poleward eddy transfer of heat.

Chapter 3

Q3.1. (a) In the non-rotating case, the dye spreads out from the point source in a relatively uniform manner. In the rotating case, the dye is stretched out horizontally in narrow filaments.

(b) (i) $\gamma_e = \frac{1}{9 \text{ days}} \ln \left(\frac{30 \text{ km}}{7 \text{ km}} \right)$ and (ii) $\frac{1}{33 \text{ days}} \ln \left(\frac{150 \text{ km}}{30 \text{ km}} \right)$. How the strain rate varies depends on the scales of the underlying eddies; as the patch expands above the scale of the eddies, the strain rate is likely to decrease.

Q3.2. Any flow can be considered as being made up of contributions from rotation and pure strain. When vorticity dominates over the strain rate, tracer contours remain relatively confined and there is hardly any stirring. In contrast, when the strain rate dominates over the vorticity, chaotic stirring occurs and the horizontal spacing between tracer contours increases at a rate proportional to $\exp(\pm(\gamma^2 - \zeta^2)^{1/2} t)$.

In (i), the rotational case, the strain rate is given by $\gamma = 0$ and the vorticity by $\zeta = 2a$, so that $\gamma^2 - \zeta^2 < 0$, implying that the tracer patch remains confined by the rotational flow in Fig. 3.20b, since $\exp(\pm i 2at)$ gives oscillatory solutions in time. Conversely, in (ii), the pure strain case, the strain rate is given by $\gamma = 2a$ and vorticity by $\zeta = 0$, so that $\gamma^2 - \zeta^2 > 0$, implying that filaments are drawn out by the flow in Fig. 3.20c, since $\exp(\pm 2at)$ gives solutions amplifying or decaying in time. Hence, tracers are expected either to be confined in blobs or drawn out in filaments according to the relative size of the strain rate and vorticity.

Q3.3. $\overline{u(t) c(t)} = \bar{u} \bar{c} + \overline{u'(t) c'(t)}$ with $\overline{u'(t) \bar{c}} = 0$ and $\overline{\bar{u} c'(t)} = 0$. Thus, the time-averaged flux of tracer depends on the time-mean advection of the time-mean tracer, $\bar{u} \bar{c}$, plus the time-averaged contribution from the time-varying correlations between the velocity and tracer, $\overline{u'(t) c'(t)}$.

Q3.4. (a) Substituting (3.36) and (3.37) into (3.35) leads to consistent relationships as long as $v_0 \equiv gh_0/c$.

(b) The eddy volume flux, $v_0 h_0/2$, is in the same direction as the wave speed so there is a greater volume flux, v_h , carried beneath the crest of the wave, than returned in the trough.

(c) For this special case of shallow-water waves approaching the shore, the eddy bolus velocity, v^* , and Stokes' drift velocity, $v_{\text{Stokes}} = v_0^2/(2c)$ are equivalent; as obtained by combining the definition $v^* = \frac{v_0 h_0}{2\bar{h}}$, and relations for the shallow-water waves, $c = (gh)^{1/2}$ and $v_0 \equiv gh_0/c$.

Chapter 4

Q4.1. Larger Coriolis acceleration for faster velocity in case (i). However, the larger displacement to the right of the motion and greater angle of deflection occurs for case (ii) with the longer timescale. Thus, Coriolis acceleration is important when the timescale of motion is comparable or longer than a rotational period. Deflection to the left of the motion in the southern hemisphere.

Q4.2. (a) Starting with geostrophic balance (4.4a), apply a vertical differential to each side, assume that the vertical variations of ρ are relatively small compared with the vertical variation of P , so take ρ outside the differential. Reorder the differentials using the general rule for second partial differentials, $\frac{\partial^2}{\partial z \partial y} \equiv \frac{\partial^2}{\partial y \partial z}$, and substitute for $\partial P / \partial z$ using hydrostatic balance (4.2), such that

$$\frac{\partial u}{\partial z} = -\frac{1}{\rho f} \frac{\partial}{\partial z} \left(\frac{\partial P}{\partial y} \right) = -\frac{1}{\rho f} \frac{\partial}{\partial y} \left(\frac{\partial P}{\partial z} \right) = \frac{g}{\rho f} \frac{\partial \rho}{\partial y}.$$

(b) Assuming a horizontal density contrast, $\Delta\rho \sim -0.3 \text{ kg m}^{-3}$ over a north-south distance $\Delta y \sim 200 \text{ km}$ and a depth change $\Delta z \sim 2 \text{ km}$ implies a velocity change over this depth scale of typically

$$\begin{aligned} \Delta u_g &\sim -\frac{(10 \text{ m s}^{-2})(-0.3 \text{ kg m}^{-3})(2 \times 10^3 \text{ m})}{(10^3 \text{ kg m}^{-3})(-10^{-4} \text{ s}^{-1})(2 \times 10^5 \text{ m})} \\ &\sim 0.3 \text{ m s}^{-1}, \end{aligned}$$

where $f \sim -10^{-4} \text{ s}^{-1}$. This estimate of the eastward velocity is in accord with the diagnosed geostrophic flow assuming no flow along the sea floor (Fig. 4.21); in practice, there is a flow along the sea floor which increases the eastward velocities and transport through the Drake Passage.

Q4.3. (a) For the ocean ring, a plausible horizontal length scale $L \sim 100 \text{ km}$ implies (i) an advective timescale given by $L/U \sim (10^5 \text{ m})(0.5 \text{ m s}^{-1})^{-1} \sim 2 \times 10^5 \text{ s} \sim 2 \text{ days}$ and (ii) an upper bound for the vertical velocity is given by $W < UH/L \sim (0.5 \text{ m s}^{-1})(0.5 \text{ km})(100 \text{ km})^{-1} \sim 2.5 \times 10^{-3} \text{ m s}^{-1}$.

(b) The typical magnitude of the different terms in the momentum equation are given by $\frac{Du}{Dt} \sim \frac{U^2}{L} \sim (0.5)^2(10^5)^{-1} = 2.5 \times 10^{-6} \text{ m s}^{-2}$; $2\Omega w \cos \phi \sim$

$2\Omega W \cos \phi \sim (2.5 \times 10^{-3}) \times (1.1 \times 10^{-4}) \sim 3 \times 10^{-7} \text{ m s}^{-2}$; and $-fv \sim 2\Omega U \sin \phi \sim (0.5) \times (0.8 \times 10^{-4}) \sim 4 \times 10^{-5} \text{ m s}^{-2}$. Hence, the largest of these terms in the x -component of the momentum equation is $-fv$, which is typically one order of magnitude larger than the local acceleration, Du/Dt .

(c) $(Du/Dt)/(fv) \sim (U^2/L)/(fL) = U/(fL)$, which is the same as the Rossby number. For the Gulf Stream ring, $Ro = U/(fL) \sim (0.5 \text{ m s}^{-1})(8 \times 10^{-5} \text{ s}^{-1} 10^5 \text{ m})^{-1} \sim 0.06 \ll 1$. Thus, the horizontal components of the momentum equation reduce to geostrophic balance with an accuracy of typically 10% or better.

Q4.4. (a) (i) For the circulating flow, the horizontal velocity converges towards the centre and so there is negative divergence. A paddle wheel placed in the flow will rotate in a negative sense (clockwise). (ii) For the reversing jet, the horizontal flow does not converge and so is non-divergent. A paddle wheel placed in the flow rotates in a positive sense (anticlockwise) for positive y and a negative sense for negative y on either side of the jet.

(b) The horizontal divergence, $\frac{\partial u}{\partial x} + \frac{\partial v}{\partial y}$ in (i) -2 , and (ii) 0 . The relative vorticity, $\zeta = \frac{\partial v}{\partial x} - \frac{\partial u}{\partial y}$, in (i) -2 , and (ii) y , so changes in sign across the jet. The signs of these answers are consistent with (a).

Chapter 5

Q5.1. Number of bacteria cells in the ocean \sim (a) $(1.4 \times 10^{18} \text{ m}^3)(10^5 \text{ cells ml}^{-1})(10^6 \text{ ml m}^{-3}) = 1.4 \times 10^{29}$ cells $\sim 10^{29}$ cells.

If *Prochlorococcus* occupy half the surface area of ocean to a depth of about 250 m, with the full depth being 5000 m, then the ocean volume occupied $\sim (1.4 \times 10^{18} \text{ m}^3)(0.5)(250 \text{ m}/5000 \text{ m}) = 3.5 \times 10^{16} \text{ m}^3$. Number of *Prochlorococcus* cells in the ocean $\sim (3.5 \times 10^{16} \text{ m}^3)(10^5 \text{ cells ml}^{-1})(10^6 \text{ ml m}^{-3}) = 3.5 \times 10^{16} \text{ cells} \sim 10^{27}$ cells.

(b) Global biomass (standing stock) of bacteria $\sim (1.4 \times 10^{29} \text{ cells})(50 \times 10^{-15} \text{ g C cell}^{-1}) = 7 \text{ Pg C}$. Global biomass (standing stock) of *Prochlorococcus* $\sim (3.5 \times 10^{27} \text{ cells})(50 \times 10^{-15} \text{ g C cell}^{-1}) = 0.18 \times 10^{15} \text{ g C} = 0.18 \text{ Pg C}$.

(c) If each *Prochlorococcus* cell is reproduced once a day, annual primary production by *Prochlorococcus* $\sim (365 \text{ days})(0.18 \text{ Pg C day}^{-1}) = 66 \text{ Pg C}$.

Q5.2 (a) If the number of children carrying a marble is unchanging, then the magnitude of the sink and source have to be equal in (5.38) and (5.39), $k_{\text{find}} MS =$

$M \cdot S / T_{drop}$, then combining with the total number of school children (5.37) allows (5.39) to be rewritten.

(b) The rate-limiting process is the time for a child to find a marble, then the rate of increase of marbles in the bucket is given by $S_T k_{\text{find}} M$.

(c) The rate-limiting process is the time for a child to carry the marble to the bucket and drop it in, then the rate of increase of marbles in the bucket is S_T / T_{drop} . These relationships and limit cases are exactly analogous to the Michaelis–Menten description of an enzymatic reaction (5.11).

Q5.3. (a) Rearrange (5.41), so all the factors involving r are on the left-hand side, then integrate from radius R to infinity, using the boundary conditions $\mathcal{N}(r = R) = \mathcal{N}_0$ and $\mathcal{N}(r = \infty) = \mathcal{N}_\infty$ to find the cell uptake of nutrients is $4\pi\kappa R(\mathcal{N}_\infty - \mathcal{N}_0)$.

(b) When cell wall transporters provide a larger transfer flux than diffusion can support.

$$(c) \mu = \int F(R)dA/Q_N \text{ s}^{-1}.$$

(d) The smaller cells: the diffusive uptake scales with the cell radius, R , but the cell quota scales with cell volume or R^3 , so the population growth rate, μ , scales as $R/R^3 = R^{-2}$.

Q5.4. (a) Assume steady state, $d/dt = 0$, from (5.42) and (5.44), find $\rho = Q_N D$, and substitute into (5.43) to obtain $Q_N = (\mathcal{N}_{\text{in}} - \mathcal{N})/X$.

(b) Steady state of (5.45) gives $\mu = D$. Change dilution rate to manipulate μ .

(c) Cell needs a finite, minimum amount of \mathcal{N} to be viable.

(d) More large cells with many just about to divide and high RNA content when reproducing (phosphorus only). Cell quota provides internal store of \mathcal{N} , which can be accessed rapidly.

(e) Stable upwelling region in the tropics. Upwelling drives phytoplankton growth and lateral flow removes phytoplankton.

Chapter 6

Q6.1. (a) $S_{\text{Na}^+} = [\text{Na}^+]_R \psi_R \delta_0 = 9.0 \times 10^{12} \text{ mol}^{-1}$.

(b) $I_{\text{Na}^+} = [\text{Na}^+] V_0 \delta_0 = 6.7 \times 10^{20} \text{ moles}$.

(c) The inventory has dimensions of moles, the source has dimensions moles time $^{-1}$. Thus dividing the inven-

tory by the source reveals a timescale (the residence time). $\tau_{\text{Na}^+} = I_{\text{Na}^+}/S_{\text{Na}^+} \sim 75 \text{ million years}$. This is an approximate estimate.

(d) If the inventory is unchanging, then the rate of loss must balance the source rate.

$$\text{Q6.2. (a)} \text{DIC} = [\text{CO}_2^*] \left(1 + \frac{K'_1}{[\text{H}^+]} + \frac{K'_1 K'_2}{[\text{H}^+]^2} \right).$$

(b) Assume surface ocean DIC is close to equilibrium with pCO_2^{at} in regions where deep waters are formed, $[\text{CO}_2^*] = K_0 \text{pCO}_2^{\text{at}} = 15.1 \times 10^{-6} \text{ mol kg}^{-1}$, $[\text{H}^+] = 10^{-\text{pH}} = 6.66 \times 10^{-9} \text{ mol kg}^{-1}$, and using the solution from (i), evaluate $\text{DIC} = 2120 \times 10^{-6} \text{ mol kg}^{-1}$. Global inventory of dissolved inorganic carbon = $\text{DIC} \rho_0 V_0 M_C = 36\,500 \text{ Pg C}$, where $M_C = 12 \text{ g mole}^{-1}$ is the atomic mass of carbon.

(c) Does not account for biological pumps, fossil-fuel CO_2 , or disequilibria in the surface ocean.

Q6.3. There are four equations and four unknowns. Use the thermodynamic equilibrium expressions to eliminate $[\text{HCO}_3^-]$ and $[\text{CO}_3^{2-}]$ from the definitions of DIC and A_C , then divide the two expressions to find an equation for DIC/A_C in terms of K'_1 , K'_2 and $[\text{H}^+]$. Rearrange to find a quadratic in $[\text{H}^+]$ and solve to find

$$[\text{H}^+] = \frac{1}{2} \left((\gamma - 1) K'_1 + \left\{ (1 - \gamma)^2 K'_1^2 - 4 K'_1 K'_2 (1 - 2\gamma) \right\}^{\frac{1}{2}} \right),$$

where $\gamma = \text{DIC}/A_C$. Other variables can then be expressed in terms of $[\text{H}^+]$.

Q6.4. (a) From equation (4.13)

$$\frac{DT}{Dt} = \frac{1}{\rho C_p} \frac{\mathcal{H}}{h}.$$

(b) The rate of change in DIC is described by the vertical flux divergence of carbon.

$$\frac{D}{Dt} \text{DIC} = \frac{D}{Dt} \text{DIC}_{\text{sat}} + \frac{D}{Dt} \Delta \text{DIC} = \frac{\mathcal{F}_C}{\rho h}.$$

(c) Assuming a linear relationship between DIC_{sat} and T ,

$$\frac{D}{Dt} \text{DIC}_{\text{sat}} = \gamma_T \frac{DT}{Dt},$$

then combining with (b) gives

$$\gamma_T \frac{DT}{Dt} + \frac{D}{Dt} \Delta \text{DIC} = \frac{\mathcal{F}_C}{\rho h}.$$

(d) Combining (a) and (c) when the disequilibrium is unchanging, $D(\Delta DIC)/Dt = 0$, the potential carbon flux is then given by

$$\mathcal{F}_C^{pot} = \gamma_T \frac{\mathcal{H}}{C_p}.$$

(e) (i) Tropical potential carbon flux: the surface heat flux in the tropics, $\mathcal{H} \sim 100 \text{ W m}^{-2}$ (i.e. into the ocean), so that $\mathcal{F}_C^{pot} = (-9 \times 10^{-6} \text{ mol kg}^{-1} \text{ K}^{-1})(100 \text{ W m}^{-2})(4000 \text{ J kg}^{-1} \text{ K}^{-1})^{-1} = -0.23 \times 10^{-6} \text{ mol m}^{-2} \text{ s}^{-1}$ or $-7 \text{ mol m}^{-2} \text{ y}^{-1}$ (out of the ocean).

Gulf Stream potential carbon flux: the surface heat flux over the Gulf Stream, $\mathcal{H} \sim -200 \text{ W m}^{-2}$ (i.e. out of the ocean), so that $\mathcal{F}_C^{pot} = 0.45 \times 10^{-6} \text{ mol m}^{-2} \text{ s}^{-1}$ or $14 \text{ mol m}^{-2} \text{ y}^{-1}$ (into the ocean).

(f) Local carbon fluxes are not exactly described by the potential carbon flux because lateral and vertical mixing, biological processes and freshwater fluxes may also be significant. In addition, the long timescale for equilibration of carbon across the sea surface (on the order of one year) means that water parcels may be swept along way down stream before an air-sea carbon flux fully equilibrates in response to a surface heat flux.

Chapter 7

Q7.1. (a) $\partial T / \partial t$ is most positive at $t = \mathcal{T}/2$, the summer solstice, and most negative at $t = \mathcal{T}$, the winter solstice.

(b) T is largest at $t = 3\mathcal{T}/4$, the autumn equinox after the surface heat input ceases and is smallest at $t = \mathcal{T}/4$, the spring equinox after the surface cooling ceases.

(c) Integrate (7.5) using $\int_0^t \cos(at) dt = \frac{1}{a} \sin(at)$.

(d) The typical seasonal temperature range is 2.5 K for this shallow sea. Units of $(\mathcal{H}_0 \mathcal{T})/(\rho C_p D)$ are $(\text{J s}^{-1} \text{ m}^{-2})(\text{s})/(\text{kg m}^{-3})(\text{J kg}^{-1} \text{ K}^{-1})(\text{m}))^{-1} \equiv \text{K}$.

Q7.2. (a) h in m and $2mu_*^3$ in $(\text{m s}^{-1})^3$, and $g\alpha_T \mathcal{H}$ in $(\text{m s}^{-2})(\text{K}^{-1})(\text{J s}^{-1} \text{ m}^{-2})$ and ρC_p in $(\text{kg m}^{-3})(\text{J kg}^{-1} \text{ K}^{-1})$, which combine together to give units of m on both sides of the equation.

(b) $\tau = 0.14 \text{ N m}^{-2}$, $u_* = 0.012 \text{ m s}^{-1}$.

(c) $h = 42 \text{ m}$ and $m = 1.28$; and

(d) (i) $2^3 = 8$, (ii) 0.5.

Q7.3. (a) Rate of input of mechanical energy available for mixing given by $m\rho u_*^3 + m_b c_b \rho u_b^3$, can be written as $m_e c_d \rho_a u_a^3 + m_b c_b \rho u_b^3$ (from Q7.2).

(b) Ratio of tidal input/wind input of mechanical energy available for mixing is (i) ~ 5 and (ii) $\sim 5 \times 10^{-3}$, thus, tidal mixing dominates for strong currents and wind mixing for weak currents.

(c) Hence, combination of tidal and wind mixing versus surface heating leads to the water column being well mixed over a depth of (i) 246 m and (ii) 42 m, leading to the tidally mixed front being located at this depth.

Q7.4. (a) A warming trend of 0.5°C per decade over this period.

(b) A surface heat flux of 0.4 W m^{-2} .

(c) There is much larger inter-annual variability, a warming of 2°C in 4 years between 1986 and 1990 or a cooling of -1°C in 2 years between 1998 and 2000. Need a record of at least several decades to detect a robust signal of climate warming.

Chapter 8

Q8.1. (a) The meridional velocity in the boundary current has a typical magnitude v_{bdry} and a width L_{bdry} , then implies $\partial v / \partial x \sim |v_{bdry}/L_{bdry}|$ to give $\beta v_{bdry} \sim r v_{bdry} / L_{bdry}$ from (8.25). Hence, $L_{bdry} \sim r/\beta$, which is 100 km for $\beta = 10^{-11} \text{ m}^{-1} \text{ s}^{-1}$ and a spin-down timescale for the currents of $r^{-1} \sim 10$ days.

(b) $v_{bdry} = -(v_{int} H L_{int})/(H L_{bdry})$, then as $v_{int} H L_{int} = -50 \times 10^6 \text{ m}^3 \text{ s}^{-1}$, $H \sim 10^3 \text{ m}$ and $L_{bdry} \sim 10^5 \text{ m}$, then $v_{bdry} \sim 0.3 \text{ m s}^{-1}$.

Q8.2. Scaling as in Q8.1 gives $L_{bdry} \sim (K_h/\beta)^{1/3}$, which is 46 km for $\beta = 10^{-11} \text{ m}^{-1} \text{ s}^{-1}$ and $K_h = 10^3 \text{ m}^2 \text{ s}^{-1}$.

Q8.3. (i) When taking $\partial/\partial x(8.29) - \partial/\partial y(8.28)$, terms involving h gradients cancel; (ii) $\partial/\partial x(fu) = f\partial u/\partial x$ as f does not vary with x , while $\partial/\partial y(fv) = f\partial v/\partial y + v\partial f/\partial y$ as f varies with y ; (iii) the order of two differentials can be reordered, such that $\partial/\partial x(\partial/\partial z) \equiv \partial/\partial z(\partial/\partial x)$.

Q8.4. (a) Particle B has to acquire negative relative vorticity, $\zeta < 0$, in order to conserve $q = \zeta + f$. This secondary circulation around particle B then displaces particle C northward and particle A southward. In turn, particle C has to acquire $\zeta < 0$, which then deflects particle D northward and returns particle B southward. This process continues to repeat itself with the northward displacement propagating westward as a wave motion.

(b) The thickness h increases for particle B in order for f/h to be conserved. If there is increased layer thickness, then from geostrophy, $v = \frac{g}{f} \partial h / \partial x$, there is a northward flow to the west of B and a southward flow to the east. This induced circulation displaces C northward and A southward. Consequently, a thickness anomaly propagates from B to C and further to the west. In both cases, the Rossby waves have a phase (linking lines of crests or troughs) which propagate westward. To understand the energy transferred by Rossby waves and how they might account for the spin up of western boundary currents, see Gill (1982).

Chapter 9

Q9.1. (a) In (i) $\Delta z = 0$, so $\Delta v^2 = 0$; in (ii) and (iv), lighter fluid overlies denser fluid along the exchange paths, so $\Delta v^2 < 0$; in (iii) denser fluid overlies lighter fluid along the exchange path, so $\Delta v^2 > 0$.

(b) For path (iii), fluid parcels chosen to have values $\sigma_A = 27.45$ at $z = -200$ m and $\sigma_B = 27.4$ at $z = -250$ m, which implies $\Delta v = 0.15$ m s $^{-1}$.

(c) $\partial u / \partial z \sim (0.3 \text{ m s}^{-1})(1000 \text{ m})^{-1}$ implying $U_{\text{eddy}} \sim 0.15 \text{ m s}^{-1}$, in accord with the rough estimate in (b), rather fortuitously the same given the approximations made.

Q9.2. (a) In (i) v' and T' are out of phase, so expect either their product is small or vanishes, while in (ii) v' and T' are in phase, so that their product is positive.

(b) at $t = 0$,

$$\begin{aligned}\overline{v' T'_1} &= \frac{v_0 T_0}{\lambda} \int_0^\lambda \cos(kx) \sin(kx) dx \\ &= \frac{v_0 T_0}{2\lambda} \int_0^\lambda \sin(2kx) dx = 0, \\ \overline{v' T'_2} &= \frac{v_0 T_0}{\lambda} \int_0^\lambda \sin(kx) \sin(kx) dx \\ &= \frac{v_0 T_0}{2\lambda} \int_0^\lambda (1 - \cos(2kx)) dx = \frac{v_0 T_0}{2},\end{aligned}$$

using $k = 2\pi/\lambda$.

Q9.3. (a) Expect little meridional displacement in the core of the jet, but enhanced meridional displacement on the flanks of the jet where the zonal velocity is comparable to the wave speed, such that the particle moves downstream at a comparable speed as the propagating meander.

(b) Integrate the definition of the meridional velocity (9.31) and substitute $x_p = ut$, then use general integral relation, $\int_0^T \cos(\alpha t) dt = (1/\alpha)[\sin(\alpha t)]_0^T = (1/\alpha)\sin(\alpha T)$, where α in this case is $k(u - c)$.

(c) $y_p(T)$ from (9.32) becomes (i) 0 for $u \ll c$, (ii) $(v_0/(ku))\sin(2\pi u/c) < v_0/(ku)$ for $u \gg c$ and (iii) $5v_0/(ku)$ for $u = 5c/4$. Thus, the greatest meridional displacement on the flank of the jet is where jet speed is comparable to the wave speed.

Q9.4. (a) The equation for the temporal variation in tracer is

$$\begin{aligned}\frac{\partial c'}{\partial t} + \bar{\mathbf{u}} \cdot \nabla c' + \mathbf{u}' \cdot \nabla \bar{c} + \mathbf{u}' \cdot \nabla c' - \bar{\mathbf{u}}' \cdot \nabla c' \\ = F' - D'.\end{aligned}$$

(b) The direction of the eddy tracer flux, $\overline{\mathbf{u}' c'}$, relative to the gradient in the time-mean tracer is given by the scalar product $\overline{\mathbf{u}' c'} \cdot \nabla \bar{c}$, the eddy flux is directed down the gradient of the time-mean tracer when the scalar product is negative and directed up the gradient when it is positive. Using the simplified version of (9.36),

$$\overline{\mathbf{u}' c'} \cdot \nabla \bar{c} \simeq -\frac{\overline{D' c'^2}}{\overline{D t}} - \frac{\overline{D' c'}}{2},$$

the eddy flux is directed down gradient when either there is (i) strong eddy dissipation of tracer perturbations, $\overline{D' c'} \gg 0$, such as for surface temperature damped by air-sea heat fluxes or surface nitrate damped by the biology, or (ii) a Lagrangian increase in tracer variance, $\overline{\frac{D' c'^2}{D t}} \gg 0$, following the flow.

Chapter 10

Q10.1. (a) (i) Subpolar gyre, (ii) subtropical gyre, (iii) subtropical gyre, (iv) subpolar gyre;

(b) Integrate continuity with depth over the surface Ekman layer, assume w at the sea surface is zero, then $w_{ek} = \int_{-h_{ek}}^0 \left(\frac{\partial u_{ek}}{\partial x} + \frac{\partial v_{ek}}{\partial y} \right) dz$, swap the order of the depth integral and horizontal differentials, then substitute definitions of horizontal Ekman velocities (10.20).

Q10.2. (a) (i) 8.4 years, (ii) 19.7 years.

(b) Integrate (10.22) with respect to time, $\int_0^t \frac{d^3H}{dt} = -\int_0^t \alpha dt$ giving ${}^3H(t) = {}^3H(0) \exp(-\alpha t)$.

(c) Total amount of helium and tritium is conserved in the interior, so that ${}^3H(t) + {}^3He(t) = {}^3H(0) + {}^3He(0)$, with ${}^3He(0) = 0$ due to degassing, so that ${}^3He(t) = {}^3H(0) - {}^3H(t) = {}^3H(0)(1 - \exp(-\alpha t))$.

(d) Find ratio ${}^3\text{He}(t)/{}^3\text{H}(t) = \exp(\alpha t) - 1$, then rearrange to obtain $t = \alpha^{-1} \ln(1 + {}^3\text{He}(t)/{}^3\text{H}(t))$.

Q10.3. (a) The mixed layer has to become lighter, $\frac{D\sigma_m}{Dt} < 0$, for subduction.

(b) Q is low whenever there is only a small downstream lightening of the mixed layer, $D\sigma_m/Dt < 0$, a large downward velocity at the base of the mixed layer, $w_b \ll 0$, or there is a pronounced shoaling of the mixed layer, $Dh/Dt \ll 0$.

(c) (i) $\Delta\sigma = -t D\sigma_m/Dt$, and (ii) $\Delta z = -t S$ where S is the instantaneous subduction rate, then combine together to obtain (10.23).

Q10.4. (a) Ekman transport $= -5 \text{ Sv}$ and geostrophic transport $= 16 \text{ Sv}$.

(b) h_w decreases with increasing wind stress; $\tau_x = 0.14 \text{ N m}^{-2}$ for $h_w = 0$.

(c) The width of the warm water, $x_e - X_p(y)$, decreases with an increasing wind stress, leading to the western boundary current moving eastward.

Chapter 11

Q11.1. (a) Surface area of the Earth given by $4\pi r^2$ with $r = 6400 \text{ km}$, then surface area of subtropical gyres over the globe $\sim (0.71)(0.6)(4\pi(6.4 \times 10^6)^2 \text{ m}^2) = 2.2 \times 10^{14} \text{ m}^2$;

(b) Mean export over subtropical gyres $\sim (2 \text{ mol C m}^{-2} \text{ y}^{-1})(12 \text{ g mol}^{-1})(2.2 \times 10^{14} \text{ m}^2) = 5.3 \times 10^{15} \text{ g C m}^{-2} \text{ y}^{-1} \sim 5 \text{ Pg C m}^{-2} \text{ y}^{-1}$;

(c) Typically 1/2 of global export of carbon occurs over subtropical gyres.

Q11.2. (a) Along-stream transport is $(1 \text{ m s}^{-1})(10 \text{ mmol N m}^{-3})(10^5 \text{ m})(5 \times 10^2 \text{ m}) \sim 1.6 \times 10^{13} \text{ mol N y}^{-1}$;

(b) Flux into the winter mixed layer is given by $(1.6 \times 10^{13} \text{ mol N y}^{-1})(12 \times 10^{12} \text{ m}^2)^{-1} \sim 1 \text{ mol N m}^{-2} \text{ y}^{-1}$.

Q11.3. Seasonal nutrient balances.

$$\begin{aligned} h \frac{\partial \mathcal{N}_m}{\partial t} &= \mathcal{F}_{\mathcal{N}} + \Lambda h \frac{\partial \mathcal{N}}{\partial z} \frac{\partial h}{\partial t} \\ &\quad - K_v \frac{\partial \mathcal{N}}{\partial z} \Big|_{z=-h} - V_e \frac{\partial \mathcal{N}_m}{\partial y} - h \lambda \mathcal{N}_m, \end{aligned}$$

Winter : 0.01 0.6 0.01 ± 0.03 0,
Summer : 0.01 0 0.01 ± 0.03 -0.6 ,
values in units of $\text{mol N m}^{-2} \text{ y}^{-1}$.

(a) On a seasonal basis, the mixed-layer nitrate budget is dominated by entrainment during winter, and biological export during summer.

(b) Advection in each season is an order of magnitude smaller than the leading processes. However, integrating over the entire year, the biological export and entrainment terms largely oppose each other leaving advection with a more significant role in setting the annual nitrate distribution.

Chapter 12

Q12.1. (a) Units $\text{W} = \text{J s}^{-1}$, $2.4 \times 10^{14} \text{ W}$.

(b) $9 \times 10^{14} \text{ W}$.

(c) $9/(9 + 2.4) = 0.79$.

Q12.2. (a) $\int_{x_w}^{x_e} \partial P / \partial x dx = P(x_e) - P(x_w)$.

(b) Poleward upper flow is associated with greater pressure on the eastern boundary, x_e , relative to reduced pressure on the western boundary, x_w .

(c) Greater pressure on x_e is associated with a thicker water column and, conversely, a reduced pressure on x_w with a thinner water column, so sea level is higher at x_e compared with x_w .

(d) Increased overturning with a poleward upper transport flux is associated with a fall in sea level on the western boundary.

Q12.3. The typical magnitudes of the polewards velocity V and the vertical velocity W from scaling are given by (a) $W \sim \kappa/H$; (b) $V \sim fW/(\beta H) \sim f\kappa/(\beta H^2)$.

(c) The vertical velocity $W \sim 1 \text{ my}^{-1}$, the horizontal velocity, $V \sim 10^{-4} \text{ m s}^{-1}$ in the interior, and the poleward volume transport $\sim 1.7 \text{ Sv}$.

(d) Stommel–Arons picture always has a poleward interior flow (increasing with larger f) and vanishing at the equator. In the North Pacific, dense bottom water is not supplied at the northern boundary, but instead from the Southern Ocean via a predicted deep western boundary current.

(e) If mixing is enhanced on the eastern boundary, then the poleward interior flow will be concentrated there, rather than over the middle parts of the basin. Then expect zonal flows over the mid basin.

(f) Strengths of Stommel–Arons model: first prediction of deep western boundary currents. Weaknesses of the Stommel–Arons model: no account of topographical steering, assumption of uniform mixing, no variations in deep flows with depth, and flows can be masked by eddies.

$$\text{Q12.4. (a)} \quad (10^{-3} \text{ W m}^{-2}) \quad (0.6)(0.71)(4\pi)(6.4 \times 10^6 \text{ m})^2 = 0.22 \times 10^{12} \text{ W} = 0.22 \text{ TW.}$$

$$(b) (0.15 \text{ N m}^{-2})(0.1 \text{ m s}^{-1}) = 15 \times 10^{-3} \text{ W m}^{-2}.$$

$$(c) (15 \times 10^{-3} \text{ W m}^{-2})(20 \times 110 \times 10^3 \text{ m})(2\pi \cos 50^\circ) \times 6.4 \times 10^6 \text{ m} = 0.85 \times 10^{12} \text{ W} = 0.85 \text{ TW.}$$

(d) Total is 1.07 TW with ~80% provided from the Southern Ocean; compare with altimetric diagnostics by Wunsch (1998).

$$(b) [\text{Ca}^{2+}] \rho_0 V_0 \sim (10 \text{ mmol kg}^{-1})(10^3 \text{ kg m}^{-3})(4 \times 10^{18} \text{ m}^3) \sim 1.4 \times 10^{19} \text{ mol Ca}^{2+}.$$

$$(c) \text{Lifetime} = \text{inventory/source} \sim (1.4 \times 10^{19} \text{ mol Ca}^{2+}) / (10^{13} \text{ mol Ca}^{2+} \text{ y}^{-1})^{-1} \sim 1.4 \text{ million years.}$$

(d) Net rate of increase in ocean calcium ion concentration = $0.1 \times 10^{13} \text{ mol Ca}^{2+} \text{ y}^{-1} = 0.2 \times 10^{13} \text{ mol A}_T \text{ y}^{-1}$. Alkalinity increases at twice the rate of the calcium ions because calcium ions are doubly charged. Timescale = change in A_T net rate of increase in alkalinity $\sim (10 \times 10^{-6} \text{ mol A}_T \text{ kg}^{-1})(10^3 \text{ kg m}^{-3})(1.4 \times 10^{18} \text{ m}^3) / (0.2 \times 10^{13} \text{ mol A}_T \text{ y}^{-1}) \sim 7000 \text{ years.}$

(e) From Fig. 13.8, we expect about 5 ppmv decrease in X_{CO_2} for a $10 \mu\text{mol kg}^{-1}$ increase in alkalinity derived from calcium carbonate weathering.

Q13.3. (a) $\epsilon_C = 0$, all soft-tissue pump contribution to upwelled DIC is either outgassed or biologically utilised before resubduction. $\epsilon_C = 1$, none of soft-tissue pump contribution is outgassed or biologically utilised.

(b) Start with $\delta \Delta C = \epsilon_C \delta C^{\text{soft}}$, follow steps (13.28) to (13.32), to obtain $X_{\text{CO}_2}(\overline{\mathcal{P}}^*) = X_{\text{CO}_2}(\overline{\mathcal{P}}_{\text{ref}}^*) \exp(-V_0 \rho_0 R_{\text{CP}} \text{PO}_4^{3-} (1 + \epsilon_C) \Delta \overline{\mathcal{P}}^* / I_B)$.

(c) Exponential decay rate of X_{CO_2} with \mathcal{P}^* increases by a factor of two as ϵ_C increases from 0 to 1.

Q13.4. (a) $\mathcal{D}_{\text{in}} \sim -(2 \times 10^{-4} \text{ K}^{-1})(-40 \text{ W m}^{-2})(4 \times 10^3 \text{ J kg}^{-1} \text{ K}^{-1})^{-1} \sim 2 \times 10^{-6} \text{ kg m}^{-2} \text{ s}^{-1}$.

(b) Transformation $G \sim \frac{1}{\Delta \rho} \mathcal{D}_{\text{in}} \Delta A \sim (0.2 \text{ kg m}^{-3})^{-1} (2 \times 10^{-6} \text{ kg m}^{-2} \text{ s}^{-1})(2 \times 10^{12} \text{ m}^2) \sim 20 \times 10^6 \text{ m}^3 \text{ s}^{-1}$.

(c) Diapycnic diffusivity $\kappa \sim -\mathcal{D}_{\text{in}} A_{\text{surface}} / (\partial \rho A_{\text{therm}}) \sim -(2 \times 10^6 \text{ kg m}^{-2} \text{ s}^{-1})(4 \times 10^{12} \text{ m}^2)((-8 \times 10^{-4} \text{ kg m}^{-4}) (8 \times 10^{13} \text{ m}^2))^{-1}$, which implies $\kappa \sim 2.5 \times 10^{-4} \text{ m}^2 \text{ s}^{-1}$.

(d) *In situ* measurements of κ are an order of magnitude smaller. Either (i) the mixing might be occurring in localised regions and so *in situ* measurements of κ are not representative of the bulk estimate of κ from (c), or (ii) the surface density flux is not offset by diffusion in the thermocline, but instead by an opposing surface density flux in another region, such as the Southern Ocean.

Chapter 13

Q13.1. (a) The effect of CO_2 on the absorption and emission of long-wave radiation gradually saturates.

(b) For an emission of $\Delta I = 1000 \text{ Pg C}$, $X_{\text{CO}_2} = (280 \text{ ppmv}) \exp(1000 \text{ PgC}/3500 \text{ PgC}) = 373 \text{ ppmv}$; increasing for higher emissions to 496, 660 and 878 ppmv.

(c) Increasing atmospheric carbon dioxide affects the partitioning of carbon in the ocean, increasing the amount of dissolved CO_2 at the expense of carbonate ions, which inhibits the further ocean uptake of carbon dioxide. Hence, an increasing fraction of the carbon emitted remains in the atmosphere.

(d) Substitute (13.39) into (13.38). $\Delta \mathcal{H}$ in W m^{-2} and $\alpha_r \Delta I / I_B$ in $(\text{W m}^{-2})(\text{Pg C})/(\text{Pg C})^{-1}$ on either side of (13.40), so the units balance.

(e) For an emission of $\Delta I = 1000 \text{ Pg C}$, the extra heating $\Delta \mathcal{H} = (5.4 \text{ W m}^{-2})(1000 \text{ Pg C})(3500 \text{ Pg C}) = 1.5 \text{ W m}^{-2}$; increasing for higher emissions to 3.1, 4.6 and 6.2 W m^{-2} .

(f) Increase in heat flux of 7 to 8 W m^{-2} lasting for millennia, until sediment interactions and weathering lead to a reduction in atmospheric carbon dioxide.

Q13.2. (a) $(370 \mu\text{mol Ca}^{2+} \text{ kg}^{-1})(10^3 \text{ kg m}^{-3})(10^6 \text{ m}^3 \text{ s}^{-1}) = 3.7 \times 10^5 \text{ mol Ca}^{2+} \text{ s}^{-1} \sim 10^{13} \text{ mol Ca}^{2+} \text{ y}^{-1}$.

References

- Abraham, E. R., C. S. Law, P. W. Boyd, et al. (2000). Importance of stirring in the development of an iron-fertilized phytoplankton bloom. *Nature*, **407**, 727–730.
- Adkins, J. F. and D. P. Schrag (2003). Reconstructing Last Glacial Maximum bottom water salinities from deep-sea sediment pore fluid profiles. *EPSL*, **216**, 109–123.
- Aiken, J., N. Rees, S. B. Hooker, et al. (2000). The Atlantic Meridional Transect: overview and synthesis of data. *Prog. Oceanogr.*, **45**(3–4), 257–312.
- Allegre, C. J. and S. H. Schneider (2005). The evolution of Earth. *Sci. Am. (Spec. Edn.)*, 4–13.
- Anderson, L. A. (1995). On the hydrogen and oxygen content of marine phytoplankton. *Deep-Sea Res. I*, **42**, 1675–1680.
- Anderson, L. A. and J. L. Sarmiento (1994). Redfield ratios of remineralization determined by nutrient data analysis. *Global Biogeochem. Cycles*, **8**, 65–80.
- Andrews, D. G., J. R. Holton, and C. B. Leovy (1987). *Middle Atmosphere Dynamics*. Orlando, FL: Academic Press, 489pp.
- Archer, D. (1996). An atlas of the distribution of calcium carbonate in sediments of the deep sea. *Global Biogeochem. Cycles*, **10**, 159–174.
- Archer, D. (2007). *Global Warming: Understanding the Forecast*. Malden, MA: Blackwell Publishing, 208pp.
- Archer, D. A. (2005). The fate of fossil fuel CO₂ in geologic time. *J. Geophys. Res.*, **110**, C09S05, doi:10.1029/2004JC002625.
- Archer, D., M. Eby, V. Brovkin, et al. (2009). Atmospheric lifetime of fossil-fuel carbon dioxide. *Ann. Rev. Earth Planet. Sci.*, **37**, 117–134.
- Armstrong, R. (2008). Nutrient uptake as a function of cell-size and surface transporter density: a Michaelis-like approximation to the model of Pasciak and Gavis. *Deep-Sea Res. I*, **55**, 1311–1317.
- Armstrong, R. A., C. Lee, J. I. Hedges, S. Honjo, and S. G. Wakeham (2002). A new, mechanistic model for organic carbon fluxes in the ocean based on the quantitative association of POC with ballast minerals. *Deep-Sea Res. II*, **49**, 219–236.
- Badin, G. and R. G. Williams (2010). On the buoyancy forcing and residual circulation in the Southern Ocean: the feedback from Ekman and eddy transfer. *J. Phys. Oceanogr.*, **40**, 295–310.
- Barnola, J.-M., P. Pimienta, D. Raynaud, and Y. S. Korotkevich (1991). CO₂-climate relationship as deduced from the Vostok ice core: a re-examination based on new measurements and on a re-evaluation of the air dating. *Tellus*, **43**(B), 83–90.
- Bates, N. R. (2001). Interannual changes of oceanic CO₂ and biogeochemical properties in the western North Atlantic subtropical gyre. *Deep-Sea Res. II*, **48**(8–9), 1507–1528.
- Bates, N. R., A. H. Knap, and A. F. Michaels (1998). The effect of hurricanes on the local to global air-sea exchange of CO₂. *Nature*, **395**, 58–61.
- Bates, N. R., A. F. Michaels, and A. H. Knap (1996). Seasonal and interannual variability of the oceanic carbon dioxide system at the U.S. JGOFS Bermuda Atlantic Time-series Site. *Deep-Sea Res. II*, **43**(2–3), 347–383.
- Behrenfeld, M. J. and P. G. Falkowski (1997a). Photosynthetic rates derived from satellite-based chlorophyll concentration. *Limnol. Oceanogr.*, **42**(1), 1–20.
- Behrenfeld, M. J. and P. G. Falkowski (1997b). A consumer's guide to phytoplankton primary productivity models. *Limnol. Oceanogr.*, **42**, 1479–1491.
- Berge, T., P. J. Hansen, and O. Moestrup (2008). Prey size spectrum and bioenergetics of the mixotrophic dinoflagellate *Karlodinium armiger*. *Aquat. Microb. Ecol.*, **50**, 289–299, doi: 10.3354/ame01166.
- Berger, W. H. (1982). The increase of carbon dioxide in the atmosphere during deglaciation: the coral reef hypothesis. *Naturwissenschaften*, **69**, 87–88.
- Berner, R. A. (1999). A new look at the long-term carbon cycle. *GSA Today*, **9**(11), 1–6.
- Bertilsson, S., O. Berglund, D. M. Karl, and S. W. Chisholm (2003). Elemental composition of marine *Prochlorococcus* and *Synechococcus*: implications for the ecological stoichiometry of the sea. *Limnol. Oceanogr.*, **48**(5), 1721–1731.
- Bingham, R. J. and C. W. Hughes (2009). Signature of the Atlantic meridional overturning circulation in sea level along the east coast of North America. *Geophys. Res. Lett.*, **36**, L02603.
- Bissinger, J. E., D. J. S. Montagnes, J. Sharples, and D. Atkinson (2008). Predicting marine phytoplankton maximum growth rates from temperature: improving on the Eppley curve using quantile regression. *Limnol. Oceanogr.*, **53**, 487–493.
- Bolin, B. and E. Eriksson (1958). Changes in the carbon content of the atmosphere and sea due to fossil fuel combustion. In *The Atmosphere and the Sea in Motion*:

- Scientific Contributions to the Rossby Memorial Volume*, ed. B. Bolin. New York: Rockefeller Institute Press, pp. 130–142.
- Bower, A. S. and M. S. Lozier (1994). A closer look at particle exchange in the Gulf Stream. *J. Phys. Oceanogr.*, **24**, 1399–1418.
- Bower, A. S. and T. Rossby (1989). Evidence of cross-frontal exchange processes in the Gulf Stream based on isopycnal RAFOS float data. *J. Phys. Oceanogr.*, **19**, 1177–1190.
- Bower, A. S., M. S. Lozier, S. F. Gary, and C. Boening (2009). Interior pathways of the Atlantic meridional overturning circulation. *Nature*, **459**, 243–247.
- Bower, A. S., H. T. Rossby, and J. L. Lillibridge (1985). The Gulf Stream: barrier or blender? *J. Phys. Oceanogr.*, **15**, 24–32.
- Boyd, P. W., T. Jickells, C. S. Law, et al. (2007). A synthesis of mesoscale iron-enrichment experiments 1993–2005: key findings and implications for ocean biogeochemistry. *Science*, **315**, 612–617, doi:10.1126/science.1131669.
- Boyle, E. A. and L. Keigwin (1987). North Atlantic thermohaline circulation during the past 20,000 years linked to high-latitude surface temperature. *Nature*, **330**, 35–40.
- Brewer, P. G. (1978). Direct observation of the oceanic CO₂ increase. *Geophys. Res. Lett.*, **5**, 997–1000, doi:10.1029/GL005i012p00997.
- Broecker, W. S. (1991). The great ocean conveyor. *Oceanogr.*, **4**, 79–89.
- Broecker, W. S. and G. M. Henderson (1998). The sequence of events surrounding Termination II and their implications for the cause of glacial–interglacial CO₂ changes. *Paleoceanography*, **13**(4), 352–364.
- Broecker, W. S. and T.-H. Peng (1982). *Tracers in the Sea*. New York: Eldigio Press, 690pp.
- Brovkin, V., A. Ganopolski, D. Archer, and S. Rahmstorf (2007). Lowering of glacial pCO₂ in response to changes in oceanic circulation and marine biogeochemistry. *Paleoceanogr.*, **22**, PA4202, doi:10.1029/2006PA001380.
- Bruland, K. W., K. J. Orians, and J. P. Cowen (1994). Reactive trace metals in the stratified central North Pacific. *Geochem. Cosmochim. Acta*, **58**, 3171–3182.
- Brzezinski, M. A., C. J. Pride, D. M. Sigman, et al. (2002). A switch from Si(OH)₄ to NO₃⁻ depletion in the glacial Southern Ocean. *Geophys. Res. Lett.*, **29**, doi:10.1029/2001GL014349.
- Burd, A. B., G. A. Jackson, R. S. Lampitt, and M. Follows (2002). Shining a light on the ocean's twilight zone. *EOS*, **83**, 49.
- Burmaster, D. E. (1979). The unsteady continuous culture of phosphate-limited *Monochrysis lutheri* Droop: experiments and theoretical analysis. *J. Exp. Mar. Biol. Ecol.*, **39**, 167–186.
- Caillon, N., J. P. Severinghaus, J. Jouzel, et al. (2003). Timing of atmospheric CO₂ and Antarctic temperature changes across Termination III. *Science*, **299**, 1728–1731.
- Caperon, J. (1968). Population growth response of *Isochrysis galbana* to nitrate variation at limiting concentrations. *Ecology*, **49**, 866–872.
- Carr, M-E., M. A. Friedrichs, M. Schmeltz, et al. (2006). A comparison of global estimates of marine primary production from ocean color. *Deep-Sea Res.*, **53**, 741–770.
- Charney, J. G. (1947). The dynamics of long waves in a baroclinic westerly current. *J. Meteor.*, **4**, 135–162.
- Chelton, D. B., R. A. deSzoeke, M. G. Schlax, K. El Naggar, and N. Siwertz (1998). Geographical variability of the first-baroclinic Rossby radius of deformation. *J. Phys. Oceanogr.*, **28**, 433–460.
- Chen, G.-T. and F. J. Millero (1979). Gradual increase of oceanic carbon dioxide. *Nature*, **277**, 205–206.
- Civitarese, G., M. Gacic, V. Cardin, and V. Ibello (2005). Winter convection continues in the warming southern Adriatic. *EOS*, **86**, 45.
- Conkright, M. E., H. E. Garcia, T. D. O'Brien, et al. (2002). *World Ocean Atlas 2001*. Volume 4: Nutrients, ed. S. Levitus, NOAA Atlas NESDIS 52. Washington, D.C.: U.S. Government Printing Office, 392pp., CD-ROMs.
- Conkright, M. E., S. Levitus and T. P. Boyer (1994). *World Ocean Atlas 1994*. Volume 1: Nutrients, NOAA Atlas NESDIS 1. Washington D.C.: U.S. Dept. of Commerce, 150pp.
- Cunningham, S. A., S. G. Alderson, M. A. Brandon, and B. A. King (2003). Transport and variability of the Antarctic Circumpolar Current. *J. Geophys. Res.*, **108**, doi:10.1029/2001JC001147.
- Cunningham, S. A., T. O. Kanzow, D. Rayner, et al. (2007). Temporal variability of the Atlantic Meridional Overturning Circulation at 26.5°N. *Science*, **317**, 935–938.
- Cushman-Roisin, B. (1987). 'Subduction'. Dynamics of the oceanic surface mixed layer. In *Proceedings of Hawaiian Winter Workshop*, University of Hawaii at Manoa, HI, pp. 181–196.
- Cushman-Roisin, B. (1994). *Introduction to Geophysical Fluid Dynamics*. Englewood Cliffs, NJ: Prentice Hall, 320pp.
- Czaja, A. (2009). Atmospheric control on the thermohaline circulation. *J. Phys. Oceanogr.*, **39**, 234–247.

- Dale, T., F. Rey, and B. R. Heimdal (1999). Seasonal development of phytoplankton at a high latitude oceanic site. *SARISA*, **84**, 419–435.
- Davidson, K., G. Wood, E. H. John, and K. J. Flynn (1999). An investigation of non steady state algal growth: I. An experimental model ecosystem. *J. Plankton Res.*, **21**, 811–837.
- Dickson, A. G. (1981). An exact definition of total alkalinity, and a procedure for the estimation of alkalinity and total inorganic carbon from titration data. *Deep-Sea Res.*, **28**, 609–623.
- Dickson, A. G. (1992). The development of the alkalinity concept in Marine chemistry. *Mar. Chem.* **40**, 49–63.
- Dickson, R., J. Lazier, J. Meinke, P. Rhines, and J. Swift (1996). Long-term coordinated changes in convective activity of the North Atlantic. *Prog. Oceanogr.*, **38**, 241–295.
- Dietze, H., A. Oschlies, and P. Kähler (2004). Internal-wave-induced and double-diffusive nutrient fluxes to the nutrient-consuming surface layer in the oligotrophic subtropical North Atlantic. *Ocean Dyn.*, **54**, 1–7.
- DOE (Department of Energy) (1994). *Handbook of Methods for the Analysis of the Various Parameters of the Carbon Dioxide System in Sea Water*, Version 2, ed. A. G. Dickson and C. Goyet. ORNL/CDIAC-74.
- Dore, J. E. (2009). Hawaii Ocean Time-series surface CO₂ system data product, 1988–2008. SOEST, University of Hawaii, Honolulu, HI. <http://hahana.soest.hawaii.edu/hot/products/products.html>.
- Droop, M. R. (1968). Vitamin B12 and marine ecology: IV. The kinetics of uptake, growth and inhibition in *Monochrysis lutheri*. *J. Mar. Biol. Assoc. UK*, **48**, 689–733.
- Eady, E. T. (1949). Long waves and cyclone waves. *Tellus*, **1**, 33–57.
- Eckart, C. (1948). An analysis of the stirring and mixing process in incompressible fluids. *J. Mar. Res.*, **7**, 265–275.
- Emerson, S. and J. Hedges (2008). *Chemical Oceanography and the Marine Carbon Cycle*. Cambridge: Cambridge University Press, 468pp.
- Emerson, S., P. Quay, D. Karl, et al. (1997). Experimental determination of the organic carbon flux from open-ocean surface waters. *Nature*, **389**, 951–954.
- Emile-Geay, J., M. A. Cane, N. Naik, et al. (2003). Warren revisited: atmospheric freshwater fluxes and ‘why is no deep water formed in the North Pacific?’ *J. Geophys. Res.*, **108**, 3178.
- Eppley, R. W. (1972). Temperature and phytoplankton growth in the sea. *Fish. Bull.*, **70**, 1063–1085.
- Etheridge, D. M., L. P. Steele, R. L. Langenfelds, et al. (1998). Historical CO₂ records from the Law Dome DE08, DE08-2, and DSS ice cores. In *Trends: A Compendium of Data on Global Change*. Oak Ridge, TN: U.S. Department of Energy.
- Falkowski, P. G. (1997). Evolution of the nitrogen cycle and its influence on the biological sequestration of CO₂ in the ocean. *Nature*, **327**, 242–244.
- Falkowski, P. and J. Raven (1997). *Aquatic Photosynthesis*. Princeton, NJ: Princeton University Press.
- Falkowski, P. G. and Y. Isozaki (2008). Geology. The story of O₂. *Science*, **322**(5901), 540–554.
- Falkowski, P. G., Z. Dubinsky, and K. Wyman (1985). Growth-irradiance relationships in phytoplankton. *Limnol. Oceanogr.*, **30**(2), 311–321.
- Ferreira, D., J. Marshall, and J.-M. Campin (2010). Localization of deep water formation: role of atmospheric moisture transport and geometrical constraints on ocean circulation. *J. Clim.*, **23**, 1456–1476.
- Follows, M. J. and S. W. Dutkiewicz (2002). Meteorological modulation of the North Atlantic spring bloom. *Deep-Sea Res. II*, **49**, 321–344.
- Follows, M. J., S. Dutkiewicz, S. Grant, and S. W. Chisholm (2007). Emergent biogeography of microbial communities in a model ocean. *Science*, **315**, 1843–1846, doi:10.1126/science.1138544.
- Follows, M. J., S. Dutkiewicz, and T. Ito (2006). On the solution of the carbonate system in ocean biogeochemistry models. *Ocean Model.*, **12**, 290–301.
- Francois, R., M. A. Altabet, and L. H. Burckle (1992). Glacial to interglacial changes in surface nitrate utilization in the Indian sector of the Southern Ocean as recorded by sediment δ¹⁵N. *Paleoceanogr.*, **7**, 589–606.
- Ganachaud, A. and C. Wunsch (2003). Large scale ocean heat and freshwater transports during the World Ocean Circulation Experiment. *J. Clim.*, **16**, 696–705.
- Garcia, H. E. and L. I. Gordon (1992). Oxygen solubility in seawater: better fitting equations. *Limnol. Oceanogr.*, **37**, 1307–1312.
- Geider, R. J., H. L. MacIntyre, and T. M. Kana (1997). Dynamic model of phytoplankton growth and acclimation: responses of the balanced growth rate and the chlorophyll-a:carbon ratio to light, nutrient-limitation and temperature. *Mar. Ecol. Prog. Ser.*, **148**, 187–200.
- Gent, P. R. and J. C. McWilliams (1990). Isopycnal mixing in ocean circulation models. *J. Phys. Oceanogr.*, **20**, 150–155.
- Gent, P. R., J. Willebrand, T. J. McDougall, and J. C. McWilliams (1995). Parameterising eddy-induced

- tracer transports in ocean circulation models. *J. Phys. Oceanogr.*, **25**, 463–474.
- Gill, A. E. (1982). *Atmosphere-Ocean Dynamics*. New York: Academic Press, 692pp.
- Gill, A. E., J. S. A. Green, and A. J. Simmons (1974). Energy partition in the large-scale ocean circulation and the production of mid-ocean eddies. *Deep-Sea Res.*, **21**, 499–528.
- Gille, S. T. (1997). The Southern Ocean momentum balance: evidence for topographic effects from numerical model output and altimeter data. *J. Phys. Oceanogr.*, **27**, 2219–2232.
- Gledhill, M. and C. van den Berg (1994). Determination of complexation of iron (III) with natural organic complexing ligands in seawater using cathodic stripping voltammetry. *Mar. Chem.*, **47**, 41–54.
- GLOBALVIEW-CO₂ (2009). Cooperative Atmospheric Data Integration Project – Carbon Dioxide. CD-ROM, NOAA ESRL, Boulder, CO. Also available on Internet via anonymous FTP to ftp.cmdl.noaa.gov, Path: ccg/co2/GLOBALVIEW.
- Godfrey, J. S., G. C. Johnson, M. J. McPhaden, G. Reverdin, and S. E. Wijffels (2001). The tropical ocean circulation. In *Ocean Circulation and Climate*, ed. G. Siedler, J. Church and J. Gould. San Diego, CA: Academic Press, pp. 215–246.
- Goodwin, P. and A. Ridgwell (2010). Ocean-atmosphere partitioning of anthropogenic carbon dioxide on multimillennial timescales. *Global Biogeochem. Cycles*, **24**, GB2014, doi:10.1029/2008GB003449.
- Goodwin, P., R. G. Williams, M. J. Follows, and S. Dutkiewicz (2007). The ocean-atmosphere partitioning of anthropogenic carbon dioxide on centennial timescales. *Global Biogeochem. Cycles*, **21**, GB1014, doi:10.1029/2006GB002810.
- Goodwin, P., R. G. Williams, A. Ridgewell, and M. J. Follows (2009). Climate sensitivity to the carbon cycle modulated by past and future changes in ocean chemistry. *Nat. Geosc.*, doi:10.1038/ngeo416.
- Goody, R. M. and Y. L. Yung (1989). *Atmospheric Radiation: Theoretical Basis*. 2nd edition. New York: Oxford University Press.
- Green, J. S. A. (1981). Trough-ridge systems as slant-wise convection. In *Dynamical Meteorology: An Introductory Selection*, ed. B. W. Atkinson. London: Methuen & Co., pp. 176–194.
- Gruber, N. (2004). The dynamics of the marine nitrogen cycle and its influence on atmospheric CO₂ variations. In *The Ocean Carbon Cycle and Climate*, NATO Science Series IV, Vol. 40, ed. M. Follows and T. Oguz. Dordrecht: Kluwer Academic, pp. 97–148.
- Gruber, N. and J. L. Sarmiento (1997). Global patterns of marine nitrogen fixation and denitrification. *Global Biogeochem. Cycles*, **11**, 235–266.
- Gruber, N., J. L. Sarmiento, and T. F. Stocker (1996). An improved method for detecting anthropogenic CO₂ in the ocean. *Global Biogeochem. Cycles*, **10**, 809–837.
- Halkin, D. and T. Rossby (1985). The structure and transport of the Gulf Stream at 73°W. *J. Phys. Oceanogr.*, **15**, 1439–1452.
- Hanawa, K. and L. D. Talley (2001). Mode waters. In *Ocean Circulation and Climate: Observing and Modelling the Global Oceans*, ed. G. Siedler, J. Church and J. Gould. San Diego, CA: Academic Press, pp. 373–386.
- Hansell, D. A., N. R. Bates, and D. B. Olson (2004). Excess nitrate and nitrogen fixation in the North Atlantic. *Mar. Chem.*, **284**, 243–265.
- Hiscock, M. R., J. Marra, W. O. Smith Jr., et al. (2003). Primary productivity and its regulation in the Pacific sector of the Southern Ocean. *Deep-Sea Res. II*, **50**, 533–558.
- Ho, T.-Y., A. Quigg, Z. V. Finkel, et al. (2003). The elemental composition of some marine phytoplankton. *J. Phycol.*, **39**(6), 1145–1159, doi:10.1111/j.0022-3646.2003.090.x.
- Hogg, N. G. (1992). On the transport of the Gulf Stream between Cape Hatteras and the Grand Banks. *Deep-Sea Res.*, **39**, 1231–1246.
- Hogg, N. G. (2001). Quantification of the deep circulation. In *Ocean Circulation and Climate: Observing and Modelling the Global Ocean*, ed. G. Siedler, J. Church and J. Gould. San Diego, CA: Academic Press, pp. 259–270.
- Holland, H. D. (2006). The oxygenation of the atmosphere and oceans. *Phil. Trans. R. Soc. B*, **361**, 903–915.
- Holland, W. R. and P. B. Rhines (1980). An example of eddy induced ocean circulation. *J. Phys. Oceanogr.*, **10**, 1010–1031.
- Holling, C. S. (1959). Some characteristics of simple types of predation and parasitism. *Canadian Entomol.*, **91**, 385–398.
- Hoskins, B. J. (1983). Modelling of transient eddies and their feedback on the mean flow. In *Large-Scale Dynamical Processes in the Atmosphere*. ed. B. J. Hoskins and R. P. Pearce. Burlington, MA: Academic Press/Elsevier, pp. 169–199.
- Hoskins, B. J. and P. J. Valdes (1990). On the existence of storm tracks. *J. Atmos. Sci.*, **47**, 1854–1864.
- Hoskins, B. J., I. N. James, and G. H. White (1983). The shape, propagation and mean-flow interaction of large-scale weather systems. *J. Atmos. Sci.*, **40**, 1595–1612.

- Huang, R. X. (2004). Energy flows in the Ocean. In *Encyclopedia of Energy*, ed. C. J. Cleveland. Amsterdam: Elsevier, pp. 497–509.
- Huang, R. X. and W. Wang (2003). Gravitational potential energy sinks in the oceans. Near-Boundary processes and their parameterization. In *Proceedings of 'Aha Huliko'a Hawaiian Winter Workshop*, University of Hawaii, Honolulu, HI, pp. 239–247.
- Hughes, C. W. and B. A. de Cuevas (2001). Why western boundary currents in realistic oceans are inviscid: a link between form stress and bottom pressure torques. *J. Phys. Oceanogr.*, **31**, 2871–2885.
- Hurrell, J. W., Y. Kushnir, G. Ottersen, and M. Visbeck (2003). *The North Atlantic Oscillation: Climate Significance and Environmental Impact*. Geophysical Monograph Series, Vol. 134. Washington, D.C.: American Geophysical Union, 279pp.
- Huthnance, J. M., H. Coelho, C. R. Griffiths, et al. (2001). Physical structures, advection and mixing in the region of Goban Spur. *Deep-Sea Res. II*, **48**(14–15), 2979–3021.
- IPCC (2007). *Climate Change 2007: The Physical Science Basis. Contribution of Working Group I to the Fourth Assessment Report of the Intergovernmental Panel on Climate Change*, ed. S. Solomon, D. Qin, M. Manning, Z. Chen, M. Marquis, K. B. Averyt, M. Tignor and H. L. Miller. Cambridge: Cambridge University Press, 996pp.
- Ito, T. and M. J. Follows (2005). Preformed phosphate, soft tissue pump and atmospheric CO₂. *J. Mar. Res.*, **63**, 813–839. doi:10.1357/0022240054663231.
- Ito, T., M. J. Follows and E. A. Boyle (2004a). Is AOU a good measure of respiration in the oceans? *Geophys. Res. Lett.*, **31**, L17305, doi:10.1029/2004GL020900.
- Ito, T., J. Marshall and M. Follows (2004b). What controls the uptake of transient tracers in the Southern Ocean. *Global Biogeochem. Cycles*, **18**, GB2021, doi:10.1029/2003GB002103.
- Ivanov, V. V., G. I. Shapiro, J. M. Huthnance, D. L. Aleynik, and P. N. Golovin (2004). Cascades of dense water around the world ocean. *Prog. Oceanogr.*, **60**(1), 47–98.
- Jackett, D. R. and T. J. McDougall (1997). A neutral density variable for the world's oceans. *J. Phys. Oceanogr.*, **27**(2), 237–263.
- Jackson, L., C. W. Hughes, and R. G. Williams (2006). Topographic control of basin and channel flows: the role of bottom pressure torques and friction. *J. Phys. Oceanogr.*, **36**, 1786–1805.
- Jähne, B. and H. Haussecker (1998). Air-water gas exchange. *Annu. Rev. Fluid Mech.*, **30**, 443–468.
- Jenkins, W. J. (1988a). The use of anthropogenic tritium and helium-3 to study subtropical gyre ventilation and circulation. *Phil. Trans. Roy. Soc. Lon.*, **A325**, 43–61.
- Jenkins, W. J. (1988b). Nitrate flux into the photic zone near Bermuda. *Nature*, **331**, 521–523.
- Jenkins, W. J. and J. C. Goldman (1985). Seasonal oxygen cycling and primary production in the Sargasso Sea. *J. Mar. Res.*, **43**, 465–491.
- Jenkins, W. J. and D. W. R. Wallace (1992). Tracer based inferences of new primary production in the sea. In *Primary Productivity and Biogeochemical Cycles in the Sea*, ed. P. G. Falkowski and A. D. Woodhead. New York: Plenum Press, pp. 299–316.
- Johnson, K. S., F. P. Chavez, and G. E. Friederich (1999). Continental-shelf sediment as a primary source of iron for coastal phytoplankton. *Nature*, **398**, 697–700, doi:10.1038/19511.
- Johnson, K., R. Gordon, and K. Coale (1997). What controls dissolved iron concentrations in the world ocean? *Mar. Chem.*, **57**, 137–161.
- Josey, S. A., E. C. Kent, and P. K. Taylor (1999). New insights into the ocean heat budget closure problem from analysis of the SOC air-sea flux climatology. *J. Clim.*, **12**, 2856–2880.
- Josey, S. A., E. C. Kent, and P. K. Taylor (2002). On the wind stress forcing of the ocean in the SOC climatology: comparisons with the NCEP/NCAR, ECMWF, UWM/COADS and Hellerman and Rosenstein datasets. *J. Phys. Oceanogr.*, **32**(7), 1993–2019.
- Kanzow, T., S. A. Cunningham, W. E. Johns, et al. (2010). Seasonal variability of the Atlantic meridional overturning circulation at 26.5°N. *J. Clim.*, **23**, doi:10.1175/2010JCLI3389.1.
- Kasting, J. (2010). *How to Find a Habitable Planet*. Princeton, NJ: Princeton University Press, 360pp.
- Kasting, J. F. (2001). The rise of atmospheric oxygen. *Science*, **293**, 819–820.
- Kato, H. and O. M. Phillips (1969). On the penetration of a turbulent layer into a stratified layer. *J. Fluid Mech.*, **37**, 643–655.
- Keeling, C. D., R. B. Bacastow, A. E. Bainbridge, et al. (1976). Atmospheric carbon dioxide variations at Mauna Loa Observatory, Hawaii. *Tellus*, **28**, 538–551.
- Key, R. M., A. Kozyr, C. L. Sabine, et al. (2004). A global ocean carbon climatology: results from Global Data Analysis Project (GLODAP). *Global Biogeochem. Cycles*, **18**, GB4031, doi:10.1029/2004GB002247.
- Kiørboe, T. (2009). *A Mechanistic Approach to Plankton Ecology*. Princeton, NJ: Princeton University Press.
- Knap, A., T. Jickells, A. Pszenny, and J. Galloway (1986). Significance of atmospheric-derived fixed nitrogen on productivity of the Sargasso Sea. *Nature*, **320**, 158–160.

- Körtzinger, A., J. Schimanski, U. Send, and D. Wallace (2004). The ocean takes a deep breath. *Science*, **306**, 1337.
- Kraus, E. B. and J. S. Turner (1967). A one-dimensional model of the seasonal thermocline: II. The general theory and its consequences. *Tellus*, **19**, 19–106.
- Labrador Sea Monitoring Group (2007). Status of the Labrador Sea. *Atlantic Zone Monitoring Program Bull.*, **6**, 11–15.
- Langmuir, D. (1997). *Aqueous Environmental Geochemistry*. Upper Saddle River, NJ: Prentice-Hall.
- Large, W. G. and A. J. G. Nurser (2001). Ocean surface water mass transformation, In *Ocean Circulation and Climate: Observing and Modelling the Global Ocean*, ed. G. Siedler, J. Church and J. Gould. San Diego, CA: Academic Press, pp. 317–336.
- Lavender, K. L., R. E. Davis, and W. B. Owens (2002). Observations of open-ocean deep convection in the Labrador Sea from subsurface floats. *J. Phys. Oceanogr.*, **32**, 511–526.
- Laws, E. A., P. G. Falkowski, W. O. J. Smith, H. Ducklow, and J. J. McCarthy (2000). Temperature effects on export production in the open ocean. *Global Biogeochem. Cycles*, **14**(4), 1231–1246.
- Lazier, J., R. Hendry, A. Clarke, I. Yashayaev, and P. Rhines (2002). Convection and restratification in the Labrador Sea, 1990–2000. *Deep-Sea Res. I*, **49**, 1819–1835.
- Lee, M.-M. and R. G. Williams (2000). The role of eddies in the isopycnic transfer of nutrients and their impact on biological production. *J. Mar. Res.*, **58**, 895–917.
- Lee, M.-M., D. P. Marshall, and R. G. Williams (1997). On the eddy transfer of tracers: advective or diffusive? *J. Mar. Res.*, **55**(3), 483–505.
- Lévy, M. (2008). The modulation of biological production by ocean mesoscale turbulence. *Lect. Notes Phys.*, **744**, 219–261, In *Transport in Geophysical Flow: Ten Years After*, ed. J. B. Weiss and A. Provenzale, Heidelberg: Springer.
- Lévy, M., P. Klein and A. M. Treguier (2001). Impacts of sub-mesoscale physics on phytoplankton production and subduction. *J. Mar. Res.*, **59**, 535–565.
- Lévy, M., D. Shankar, J.-M. André, et al. (2007). Basin-wide seasonal evolution of the Indian Ocean's phytoplankton blooms. *J. Geophys. Res.*, **112**, doi:10.1029/2007JC004090.
- Lewis, M. R., W. G. Harrison, N. S. Oakley, D. Hebert, and T. Platt (1986). Vertical nitrate fluxes in the oligotrophic ocean. *Science*, **234**, 870–873.
- Lilly, J. M., P. B. Rhines, F. Schott, et al. (2003). Observations of the Labrador Sea eddy field. *Prog. Oceanogr.*, **59**, 75–176.
- Lindzen, R. S. and B. Farrell (1980). A simple approximate result for the maximum growth rate of baroclinic instabilities. *J. Atmos. Sci.*, **37**, 1648–1654.
- Liss, P. S. and L. Merlivat (1986). Air-sea gas exchange rates: introduction and synthesis. In *The Role of Air-Sea Exchange in Geochemical Cycling*, ed. P. Buat-Ménard. Boston, MA: D. Reidel Publishing Company, pp. 113–127.
- Litchman, E., C. A. Klausmeier, O. M. Schofield, and P. G. Falkowski (2007). The role of functional traits and trade-offs in structuring phytoplankton communities: scaling from cellular to ecosystem level. *Ecol. Lett.*, **10**, 1170–1181.
- Lozier, M. S. (1997). Evidence for large-scale eddy-driven gyres in the North Atlantic. *Science*, **277**, 361–364.
- Lozier, M. S. (2010). Deconstructing the conveyor belt. *Science*, **328**, 1507, doi:10.1126/science.1189250.
- Lozier, M. S., V. Roussenov, M. S. C. Reed, and R. G. Williams (2010). Opposing decadal changes for the North Atlantic meridional overturning circulation. *Nat. Geosc.*, doi:10.1038/ngeo947.
- Lumpkin, R. and M. Pazos (2006). Measuring surface currents with Surface Velocity Program drifters: the instrument, its data and some recent results. In *Lagrangian Analysis and Prediction of Coastal and Ocean Dynamics*, ed. A. Mariano, T. Rossby and D. Dirwan. Cambridge: Cambridge University Press, pp. 39–67.
- Lumpkin, R. and K. Speer (2007). Global ocean meridional overturning. *J. Phys. Oceanogr.*, **37**, 2550–2562.
- Luyten, J. R., J. Pedlosky, and H. Stommel (1983). The ventilated thermocline. *J. Phys. Oceanogr.*, **13**, 292–309.
- MacArthur, R. H. and E. O. Wilson (1967). *The Theory of Island Biogeography*. Princeton, NJ: Princeton University Press, 203pp.
- Mahaffey, C., A. F. Michaels, and D. G. Capone (2005). The conundrum of marine N₂ fixation. *Am. J. Sci.*, **305**, 546–595.
- Mahowald, N., S. Engelstaedter, C. Luo, et al. (2009). Atmospheric iron deposition: global distribution, variability and human perturbations. *Annu. Rev. Mar. Sci.*, **1**, 245–278, doi:10.1146/annurev/marine.010908.163727.
- Marañón, E., P. M. Holligan, M. Varela, B. Mouríño, and A. J. Bale (2000). Basin-scale variability of phytoplankton biomass, production and growth in the Atlantic Ocean. *Deep-Sea Res. I*, **47**(5), 825–857.
- Marotzke, J. (2000). Abrupt climate change and thermohaline circulation: mechanisms and predictability. *Proc. Natl. Acad. Sci. USA*, **97**(4), 1347–1350.

- Marotzke, J. and J. R. Scott (1999). Convective mixing and the thermohaline circulation. *J. Phys. Oceanogr.*, **29**, 2962–2970.
- Marshall, D. P. (1997). Subduction of water masses in an eddying ocean. *J. Mar. Res.*, **55**, 201–222.
- Marshall, J. and A. R. Plumb (2007). *Atmosphere, Ocean and Climate Dynamics: An Introductory Text*. Burlington, MA: Academic Press/Elsevier, 319pp.
- Marshall, J. and T. Radko (2003). Residual-mean solutions for the Antarctic Circumpolar Current and its associated overturning circulation. *J. Phys. Oceanogr.*, **33**, 2341–2354.
- Marshall, J. and F. Schott (1999). Open-ocean convection: observations, theory and models. *Rev. Geophys.*, **37**(1), 1–64.
- Marshall, J., D. Jamous, and J. Nilsson (1999). Reconciling thermodynamic and dynamic methods of computation of water-mass transformation rates. *Deep-Sea Res. I*, **46**, 545–572.
- Marshall, J. C., A. J. G. Nurser, and R. G. Williams (1993). Inferring the subduction rate and period over the North Atlantic. *J. Phys. Oceanogr.*, **23**, 1315–1329.
- Martin, A. P. (2003). Phytoplankton patchiness: the role of lateral stirring and mixing. *Prog. Oceanogr.*, **57**, 125–174.
- Martin, J. H. and S. E. Fitzwater (1988). Iron deficiency limits phytoplankton growth in the north-east Pacific Subarctic. *Nature*, **331**, 341–343.
- Martin, J. H., G. A. Knauer, D. M. Karl, and W. W. Broenkow (1987). VERTEX: carbon cycling in the northeast Pacific. *Deep-Sea Res. A*, **34**(2), 267–285.
- Mauritzen, C., J. Price, T. Sanford, and D. Torres (2005). Circulation and mixing in the Faroese Channels. *Deep-Sea Res. I*, **52**, 883–913.
- Maximenko, N. A. and P. P. Niiler (2005). Hybrid decade-mean global sea level with mesoscale resolution. In *Recent Advances in Marine Science and Technology 2004*, ed. N. Saxena. Honolulu, HI: PACON International, pp. 55–59.
- McArthur, R. H. and E. O. Wilson (1967). *The Theory of Island Biogeography*. Princeton, NJ: Princeton University Press, 203pp.
- McCartney, M. S. and L. D. Talley (1982). The subpolar mode water of the North Atlantic Ocean. *J. Phys. Oceanogr.*, **12**, 1169–1189.
- McDonagh, E. L., P. McLeod, B. A. King, H. L. Bryden, and S. Torres-Valdes (2010). Circulation, heat and freshwater transport at 36°N in the Atlantic. *J. Phys. Oceanogr.*, **40**, 2661–2678.
- McDougall, T. J., D. R. Jackett, and F. J. Millero (2009). An algorithm for estimating absolute salinity in the global ocean. *Ocean Sci. Discuss.*, **6**, 215–242.
- McDowell, S., P. B. Rhines, and T. Keffer (1982). North Atlantic potential vorticity and its relation to the general circulation. *J. Phys. Oceanogr.*, **12**, 1417–1436.
- McGillicuddy, D. J. and A. R. Robinson (1997). Eddy-induced nutrient supply and new production in the Sargasso Sea. *Deep-Sea Res. I*, **44**, 1427–1449.
- McGillicuddy, D. J., A. R. Robinson, D. A. Siegel, et al. (1998). New evidence for the impact of mesoscale eddies on biogeochemical cycling in the Sargasso Sea. *Nature*, **394**, 263–266.
- Measures, C. I., W. M. Landing, M. T. Brown and C. S. Buck (2008). High resolution Al and Fe data from the Atlantic Ocean CLIVAR-CO₂ Repeat Hydrology transect. *Global Biogeochem. Cycles*, **22**, GB1005, doi:10.1029/2007GB003042.
- Menemenlis, D., C. Hill, A. Adcroft, J. Campin, B. Cheng, B. Ciotti, et al. (2005). NASA super computer improves prospects for ocean climate research. *EOS Trans. AGU*, **86**(9), 89, doi:10.1029/2005EO090002.
- Menzel, D. W. and J. H. Ryther (1961). Annual variations in primary production of the Sargasso Sea off Bermuda. *Deep-Sea Res.*, **7**, 282–288.
- Michaelis, L. and M. Menten (1913). Die Kinetic der Inverinwirkung. *Biochem. Z.*, **49**, 333–369.
- Michaels, A. F., A. H. Knap, R. L. Dow, et al. (1994). Seasonal patterns of ocean biogeochemistry at the U.S. JGOFS Bermuda Atlantic Time-series Study site. *Deep-Sea Res. I*, **41**, 1013–1038.
- Miller, C. B. (2004). *Biological Oceanography*. Malden, MA: Blackwell, 416pp.
- Miller, P. I. (2009). Composite front maps for improved visibility of dynamic sea-surface features on cloudy SeaWiFS and AVHRR data. *J. Mar. Sys.*, **78**(3), 327–336, doi:10.1016/j.jmarsys.2008.11.019.
- Millero, F. J. (1995). Thermodynamics of the carbon dioxide system in the oceans. *Geochim. Cosmochim. Acta*, **59**(4), 661–677.
- Moore, C. M., M. M. Mills, E. P. Achterberg, et al. (2009). Large-scale distribution of Atlantic nitrogen fixation controlled by iron availability. *Nat. Geosc.*, **2**, 867–871.
- Morel, F. M. M. and J. G. Hering (1993). *Principles and Applications of Aquatic Chemistry*. Hoboken, NJ: Wiley-Interscience, 608pp.
- Müller, P. and C. Frankignoul (1981). Direct atmospheric forcing of geostrophic eddies. *J. Phys. Oceanogr.*, **11**, 287–308.
- Munk, W. H. (1950). On the wind driven ocean circulation. *J. Meteor.*, **7**, 79–93.
- Munk, W. and C. Wunsch (1998). Abyssal recipes II: energetics of tidal and wind mixing. *Deep-Sea Res. I*, **45**, 1977–2010.

- Munk, W., L. Armi, K. Fischer, and F. Zachariasen (2000). Spirals on the sea. *Proc. R. Soc. Lon. A.*, **456**, 1217–1280.
- Murgatroyd, R. J. and F. Singleton (1961). Possible meridional circulations in the stratosphere and mesosphere. *Q. J. Roy. Meteorol. Soc.*, **84**, 225–234.
- Murnane, R. J., J. L. Sarmiento, and C. Le Quéré (1999). Spatial distribution of air-sea CO₂ fluxes and the interhemispheric transport of carbon by the oceans. *Global Biogeochem. Cycles*, **13**, 287–305.
- Murray, J. (2004). Ocean carbonate chemistry: the aquatic chemistry fundamentals. In *The Ocean Carbon Cycle and Climate*, ed. M. Follows and T. Oguz, NATO Science Series, IV, Vol. 40. Dordrecht: Kluwer Academic Publishers.
- Murray, A. B., M. LeBars, and C. Guillou (2003). Tests of a new hypothesis for non-bathymetrically driven rip currents. *J. Coastal Res.*, **19**(2), 269–277.
- Naveira Garabato, A. C., K. L. Polzin, B. A. King, K. J. Heywood, and M. Visbeck (2004). Widespread intense turbulent mixing in the Southern Ocean. *Science*, **303**(5655), 210–213.
- Nightingale, P. D., P. S. Liss, and P. Schlosser (2000). Measurements of air-sea gas transfer during an open ocean algal bloom. *Geophys. Res. Lett.*, **27**, 2117–2120.
- Niiler, P. P. and E. B. Kraus (1977). One-dimensional models of the upper ocean. In *Modelling and Prediction of the Upper Layers of the Ocean*, ed. by E. B. Kraus. New York: Pergamon, pp. 143–172.
- Niiler, P. P., N. A. Maximenko, and J. C. McWilliams (2003). Dynamically balanced absolute sea level of the global ocean derived from near-surface velocity observations. *Geophys. Res. Lett.*, **30**, 2164, doi:10.1029/2003GL018628.
- Nurser, A. J. G., R. Marsh, and R. G. Williams (1999). Diagnosing water mass formation from air-sea fluxes and surface mixing. *J. Phys. Oceanogr.*, **29**, 1468–1487.
- Omata, A. W., S. Dutkiewicz, and M. J. Follows (2011). Dependence of the ocean-atmosphere partitioning of carbon on temperature and alkalinity, *Global Biogeochem. Cycles*, **25**, GB1003, doi:10.1029/2010GB003839.
- Oschlies, A. (2002). Can eddies make ocean deserts bloom? *Global Biogeochem. Cycles*, **16**, 1106, doi:10.1029/2001GB001830.
- Oschlies, A., H. Dietze, and P. Kähler (2003). Salt-finger induced enhancement of upper-ocean nutrient supply. *Geophys. Res. Letts.*, **30**(23), doi:10.1029/2003GL018552.
- Parekh, P., S. Dutkiewicz, M. J. Follows, and T. Ito (2006). Atmospheric carbon dioxide in a less dusty world. *Geophys. Res. Lett.*, **33**, L03610, doi:10.1029/2005GL025098.
- Parsons, A. T. (1969). A two-layer model of Gulf Stream separation. *J. Fluid Mech.*, **39**, 511–528.
- Pasciak, W. J. and J. Gavis (1974). Transport limitation of nutrient uptake in phytoplankton. *Limnol. Oceanogr.*, **19**, 881–888.
- Peacock, S., E. Lane, and J. M. Restrepo (2006). A possible sequence of events for the generalized glacial-interglacial cycle. *Global Biogeochem. Cycles*, **20**, GB2010, doi:10.1029/2005GB002448.
- Pedlosky, J. (1987). *Geophysical Fluid Dynamics*. New York: Springer-Verlag, 710pp.
- Pedlosky, J. (1996). *Ocean Circulation Theory*. Berlin: Springer-Verlag, 453pp.
- Pelegrí, J. L. and G. T. Csanady (1991). Nutrient transport and mixing in the Gulf Stream. *J. Geophys. Res.*, **96**, 2577–2583.
- Pelegrí, J. L. and G. T. Csanady (1994). Diapycnal mixing in western boundary currents. *J. Geophys. Res.*, **99**, 18 275–18 304.
- Pelegrí, J. L., G. T. Csanady, and A. Martins (1996). The North Atlantic nutrient stream. *J. Oceanogr.*, **52**, 275–299.
- Petit, J. R., J. Jouzel, D. Raynaud, et al. (1999). Climate and atmospheric history of the past 420,000 years from the Vostok ice core, Antarctica. *Nature*, **399**, 429–436.
- Petit, J. R. et al. (2001). Vostok Ice Core Data for 420,000 Years. IGBP PAGES/World Data Center for Paleoclimatology Data Contribution Series 2001-076. NOAA/NGDC Paleoclimatology Program, Boulder, CO, USA, 293pp.
- Philander, S. G. H. (1990). *El Niño, La Niña and the Southern Oscillation*. San Diego, CA: Academic Press, 293pp.
- Pickart, R. S. and M. A. Spall (2007). Impact of Labrador Sea Convection on the North Atlantic Meridional Overturning Circulation. *J. Phys. Oceanogr.*, **37**, 2207–2227.
- Pilson, M. E. Q. (1998). *An Introduction to the Chemistry of the Sea*. Prentice-Hall, 431pp.
- Pollack, H. N., S. J. Hunter, and J. R. Johnson (1993). Heat flow from the Earth's interior: analysis of the global data set. *Rev. Geophys.*, **31**(3), 267–280.
- Polzin, K. L., K. G. Speer, J. M. Toole, and R. W. Schmitt (1996). Intense mixing of Antarctic Bottom Water in the equatorial Atlantic Ocean. *Nature*, **380**, 54–57.
- Pratt, L. J., M. S. Lozier, and N. Beliakova (1995). Parcel trajectories in quasigeostrophic jets: neutral modes. *J. Phys. Oceanogr.*, **25**, 1451–1466.

- Price, J. F. (1992). Overflows: the source of new abyssal ocean waters. *Oceanus*, **35**, 28–34.
- Price, J. F. (2001). Subduction. In *Ocean Circulation and Climate: Observing and Modelling the Global Ocean*, ed. G. Siedler, J. Church and J. Gould. San Diego, CA: Academic Press, pp. 357–372.
- Price, J. F., M. O'Neil Baringer, R. G. Lueck, et al. (1993). Mediterranean outflow mixing and dynamics. *Science*, **259**, 1277–1282.
- Redfield, A. C. (1934). On the proportions of organic derivatives in seawater and their relation to the composition of the plankton. In *The James Johnstone Memorial Volume*, ed. R. J. Daniel. Liverpool: University Press of Liverpool, pp. 176–192.
- Redfield, A. C., B. H. Ketchum, and F. A. Richards (1963). The influence of organisms on the composition of seawater. In *The Sea*, Vol. 2., ed. M. N. Hill, Hoboken, NJ: Wiley-Interscience, pp. 26–77.
- Reid, J. L. (1979). On the contribution of the Mediterranean Sea outflow to the Norwegian-Greenland Sea. *Deep-Sea Res.*, **26A**, 1199–1223.
- Rhines, P. B. and W. R. Young (1982a). Homogenization of potential vorticity in planetary gyres. *J. Fluid Mech.*, **122**, 347–368.
- Rhines, P. B. and W. R. Young (1982b). A theory of the wind-driven circulation: I. Mid-ocean gyres. *J. Mar. Res.*, **40** (Suppl.), 559–596.
- Rhines, P. B., S. Häkkinen, and S. A. Josey (2008). Is oceanic heat transport significant in the climate system? In *Arctic-Subarctic Ocean Fluxes: Defining the Role of the Northern Seas in Climate*, ed. R. R. Dickson, J. Meincke, and P. B. Rhines. New York: Springer, pp. 265–279.
- Richardson, P. L., R. E. Cheney, and L. V. Worthington (1976). A census of Gulf Stream rings, Spring 1975. *J. Geophys. Res.*, **83**(C12), 6136–6144.
- Ridgwell, A. and J. Hargreaves (2007). Regulation of atmospheric CO₂ by deep-sea sediments in an Earth System Model. *Global Biogeochem. Cycles*, **21**, doi:10.1029/2006GB002764.
- Rintoul, S., C. W. Hughes and D. Olbers (2001). The Antarctic Circumpolar Current System. In *Ocean Circulation and Climate: Observing and Modelling the Global Ocean*, ed. G. Siedler, J. Church and J. Gould. San Diego, CA: Academic Press, pp. 271–302.
- Robertson, J. E., C. Robinson, D. R. Turner, et al. (1994). The impact of a coccolithophore bloom on oceanic carbon uptake in the northeast Atlantic during summer 1991. *Deep-Sea Res. I*, **41**(2), 297–314.
- Rogner, H. H. (1997). An assessment of world hydrocarbon resources. *Annu. Rev. Energy Environ.*, **22**, 217–262.
- Rooth, C. (1982). Hydrology and ocean circulation. *Prog. Oceanogr.*, **11**, 131–149.
- Rossby, H. T. and P. I. Miller (2003). Ocean eddies in the 1539 Carta Marina by Olaus Magnus. *Oceanogr.*, **16**(4), 77–88.
- Roussenov, V., R. G. Williams, M. J. Follows, and R. M. Key (2004). Role of bottom water transport and diapycnic mixing in determining the radiocarbon distribution in the Pacific. *J. Geophys. Res.*, **109**, C06015, doi:10.1029/2003JC002188.
- Roussenov, V., R. G. Williams, C. Mahaffey, and G. A. Wolff (2006). Does the transport of dissolved organic nutrients affect export production in the Atlantic Ocean? *Global Biogeochem. Cycles*, **20**, doi:10.1029/2005GB00210.
- Runge, S. W., B. J. F. Hill, and W. M. Moran (2006). A simple classroom teaching technique to help students understand Michaelis-Menten Kinetics. *CBE-Life Sciences Education*, **5**, 348–352.
- Sabine, C. L., R. A. Feely, N. Gruber, et al. (2004). The oceanic sink for anthropogenic CO₂. *Science*, **305**, 367–371.
- Salmon, R. (1998). *Lectures on Geophysical Fluid Dynamics*. New York: Oxford University Press, 378pp.
- Sarmiento, J. L. and N. Gruber (2002). Sinks for anthropogenic carbon. *Phys. Today*, August, 30–36.
- Sarmiento, J. L. and N. Gruber (2006). *Ocean Biogeochemical Dynamics*. Princeton, NJ: Princeton University Press, 526pp.
- Sarmiento, J. L., N. Gruber, M. A. Brzezinski and J. P. Dunne (2004). High-latitude controls of thermocline nutrients and low latitude biological productivity. *Nature*, **427**, 56–60.
- Schlitzer, R. (2000). Applying the adjoint method for global biogeochemical modeling. In ed. P. Kasibhatla, M. Heimann, D. Hartley, N. Mahowald, R. Prinn, and P. Rayner. *Inverse Methods in Global Biogeochemical Cycles*, Geophysical Monograph Series, Vol. 114. Washington, D.C.: American Geophysical Union, pp. 107–124.
- Schmitz, W. J., Jr. (1996). *On the World Ocean Circulation: Vol. I. Some Global Features/North Atlantic Circulation*. Technical Report WHOL-96-03. Woods Hole, MA: Woods Hole Oceanographic Institution, 140pp.
- Scott, R. B., B. K. Arbic, E. P. Chassignet, et al. (2010). Total kinetic energy in three global eddying ocean circulation models and over 5000 current meter records. *Ocean Model.*, **32**, doi:10.1016/j.ocemod.2010.01.005.
- Seager, R., D. S. Battisti, J. Yin, et al. (2002). Is the Gulf Stream responsible for Europe's mild winters? *Quart. J. Roy. Meteorol. Soc.*, **128**, 2563–2586.

- Sharples, J., C. M. Moore, T. P. Rippeth, *et al.* (2001). Phytoplankton distribution and survival in the thermocline. *Limnol. Oceanogr.*, **46**(3), 486–496.
- Sharples, J., O. N. Ross, B. E. Scott, S. P. R. Greenstreet, and H. Fraser (2006). Inter-annual variability in the timing of the stratification and the spring bloom in the north-western North Sea. *Continental Shelf Res.*, **26**, 733–751.
- Siedler, G., J. Church, and J. Gould (2001). *Ocean Circulation and Climate: Observing and Modelling the Global Ocean*. San Diego, CA: Academic Press, 693pp.
- Sigman, D. M. and E. A. Boyle (2000). Glacial/interglacial variations in atmospheric carbon dioxide. *Nature*, **407**, 859–869.
- Simpson, J. H. and J. Sharples. *An Introduction to the Physical and Biological Oceanography of Shelf Seas*. Cambridge: Cambridge University Press, not yet published.
- Smethie, W. M., Jr. and R. A. Fine (2001). Rates of North Atlantic Deep Water formation calculated from chlorofluorocarbon inventories. *Deep-Sea Res. I*, **48**, 189–215.
- Smith, K. S. (2007). The geography of linear baroclinic instability in Earth's oceans. *J. Mar. Res.*, **65**, 655–683.
- Smyth, T. J., G. F. Moore, S. B. Groom, P. E. Land, and T. Tyrrell (2002). Optical modelling and measurements of a coccolithophore bloom. *Appl. Opt.*, **41**, 7679–7688.
- Speer, K. (1997). A note on average cross-isopycnal mixing in the North Atlantic Ocean. *Deep-Sea Res. I*, **44**(12), 1981–1990.
- Speer, K. G. and M. S. McCartney (1992). Bottom water circulation in the western North Atlantic. *J. Phys. Oceanogr.*, **22**, 83–92.
- Speer, K. and E. Tziperman (1992). Rates of water mass formation in the North Atlantic ocean. *J. Phys. Oceanogr.*, **22**, 93–104.
- Speer, K. G., S. R. Rintoul, and B. M. Sloyan (2000). The diabatic Deacon cell. *J. Phys. Oceanogr.*, **30**, 3212–3221.
- Spitzer, W. S. and W. J. Jenkins (1989). Rates of vertical mixing, gas exchange and new production: estimates from seasonal gas cycles in the upper ocean near Bermuda. *J. Mar. Res.*, **47**, 169–196.
- Stephens, J. C. and D. P. Marshall (2000). Dynamical pathways of Antarctic Bottom Water in the Atlantic. *J. Phys. Oceanogr.*, **30**, 622–640.
- Stewart, F. M. and B. R. Levin (1973). Partitioning of resources and the outcome of interspecific competition: a model and some general considerations. *Am. Nat.*, **107**, 171–198.
- Stommel, H. (1948). The westward intensification of wind-driven ocean currents. *Trans. Am. Geophys. Union*, **29**, 202–206.
- Stommel, H. (1958). The abyssal circulation. *Deep-Sea Res.*, **5**, 80–82.
- Stommel, H. (1961). Thermohaline convection with two stable regimes of flow. *Tellus*, **13**, 224–230.
- Stommel, H. (1979). Determination of watermass properties of water pumped down from the Ekman layer to the geostrophic flow below. *Proc. Nat. Acad. Sci. USA*, **76**, 3051–3055.
- Stommel, H. and A. B. Arons (1960). On the abyssal circulation of the world ocean: I. Stationary planetary flow patterns on a sphere. *Deep-Sea Res.*, **6**, 140–154.
- Stommel, H., A. B. Arons, and A. J. Faller (1960). Some examples of stationary planetary flow patterns in bounded basins. *Tellus*, **10**, 179–187.
- Sverdrup, H. U. (1947). Wind-driven currents in a baroclinic ocean: with applications to the equatorial currents of the eastern Pacific. *Proc. Nat. Acad. Sci. USA*, **33**, 318–326.
- Sverdrup, H. U. (1953). On conditions of the vernal blooming of phytoplankton. *J. du conseil int. pour l'explor. de la mer*, **18**, 287–295.
- Takahashi, T., W. S. Broecker, and S. Langer (1985). Redfield ratio based on chemical data from isopycnal surfaces. *J. Geophys. Res.*, **90**(C4), 6907–6924, doi:10.1029/JC090iC04p06907.
- Takahashi, T., S. C. Sutherland, Sweeney, *et al.* (2002). Global sea-air CO₂ flux based on climatological surface ocean pCO₂, and seasonal biological and temperature effects, *Deep-Sea Res. II*, **49**, 1601–1622.
- Talley, L. D. (1999). Some aspects of ocean heat transport by the shallow, intermediate and deep overturning circulations. In *Mechanisms of Global Climate Change at Millennial Time Scales*, ed. P. U. Clark, R. S. Webb and L. D. Keigwin, *Geophysical Monograph Series*, Vol. 112. Washington, D.C.: American Geophysical Union, pp. 1–22.
- Talley, L. D., G. L. Pickard, W. J. Emery, and J. H. Swift (2011). *Descriptive Physical Oceanography: An Introduction*. 6th edition. Elsevier.
- Thingstad, T. F., H. Havskum, K. Garde, and B. Riemann (1996). On the strategy of 'eating your competitor': a mathematical analysis of algal mixotrophy. *Ecology*, **77**(7), 2108–2118.
- Thomas, H., Y. Bozec, K. Elkalay, and H. J. W de Baar (2004). Enhanced open ocean storage of CO₂ from shelf sea pumping. *Science*, **304**, 1005–1008.
- Tilman, D. (1977). Resource competition between planktonic algae: an experimental and theoretical approach. *Ecology*, **58**, 338–348.
- Toggweiler, J. R., R. Murnane, S. Carson, A. Gnanadesikan, and J. L. Sarmiento (2003). Representation of the carbon cycle in box models

- and GCMs: 2. Organic pump. *Global Biogeochem. Cycles*, **17**(1), 1027, doi:10.1029/2001GB001841.
- Torres-Valdés, S., V. Roussenov, R. Sanders, et al. (2009). Distribution of dissolved organic nutrients and their effect on export production over the Atlantic Ocean. *Global Biogeochem. Cycles*, **23**, GB4019, doi:10.1029/2008GB003389.
- Tyrrell, T. and J. Wright (2001). Calcium carbonate and climate. *Ocean Chall.*, **11**(1), 13–21.
- Vallis, G. K. (2006). *Atmospheric and Oceanic Fluid Dynamics: Fundamentals and Large-Scale Circulation*. Cambridge: Cambridge University Press, 745pp.
- Veronis, G. (1970). Model of world ocean circulation: I. Wind-driven, two-layer. *J. Mar. Res.*, **31**, 228–288.
- Vrede, K., M. Heldal, S. Norland, and G. Bratbak (2002). Elemental composition (C, N, P) and cell volume of exponentially growing and nutrient-limited bacterioplankton. *Appl. Env. Microbiol.*, **68**(6), 2965–2971, doi:10.1128/AEM.68.6.2965–2971.2002.
- Walin, G. (1982). On the relation between sea-surface heat flow and thermal circulation in the ocean. *Tellus*, **34**, 187–195.
- Wanninkhof, R. and W. R. McGillis (1999). A cubic relationship between air-sea CO₂ exchange and windspeed. *Geophys. Res. Lett.*, **26**(13), 1889–1892.
- Warren, B. A. (1981). Deep circulation of the World Ocean. In *Evolution of Physical Oceanography*, ed. B. A. Warren and C. Wunsch. Cambridge, MA: The MIT Press, pp. 6–41.
- Warren, B. A. (1983). Why is no deep water formed in the North Pacific? *J. Mar. Res.*, **41**, 327–347.
- Watson Jr., S. Alexander, G. Craig, et al. (2001). Simultaneous in-line and off-axis subsea holographic recording of plankton and other marine particles. *Meas. Sci. Tech.*, **12**, L9–L15.
- Waugh, D. W. (1993). Subtropical stratospheric mixing linked to disturbances on the polar vortices. *Nature*, **365**, 535–537.
- Weiss, R. F. (1974). Carbon dioxide in water and seawater: the solubility of a non-ideal gas. *Mar. Chem.*, **2**, 203–215.
- Welander, P. (1955). Studies on the general development of motion in a two-dimensional, ideal fluid. *Tellus*, **7**, 141–156.
- Williams, R. G. (1991). The role of the mixed layer in setting the potential vorticity of the main thermocline. *J. Phys. Oceanogr.*, **21**, 1803–1814.
- Williams, R. G. and M. J. Follows (1998). The Ekman transfer of nutrients and maintenance of new production over the North Atlantic. *Deep-Sea Res. I*, **45**, 461–489.
- Williams, R. G. and M. J. Follows (2003). Physical transport of nutrients and the maintenance of biological production. In *Ocean Biogeochemistry: The Role of the Ocean Carbon Cycle in Global Change*, ed. M. Fasham. Berlin: Springer, pp. 19–51.
- Williams, R. G., E. McDonagh, V. M. Roussenov, et al. (2011). Nutrient streams in the North Atlantic: advective pathways of inorganic and organic nutrients. *Global Biogeochem. Cycles*, submitted.
- Williams, R. G., V. Roussenov, and M. J. Follows (2006). Nutrient Streams and their induction into the mixed layer. *Global Biogeochem. Cycles*, **20**, GB1016, doi:10.1029/2005GB002586.
- Williams, R. G., M. A. Spall, and J. C. Marshall (1995). Does Stommel's mixed-layer 'demon' work? *J. Phys. Oceanogr.*, **25**, 3089–3102.
- Williams, R. G., C. Wilson, and C. W. Hughes (2007). Ocean and atmosphere storm tracks: the role of eddy vorticity forcing. *J. Phys. Oceanogr.*, **37**, 2267–2289.
- Wilson, C. and R. G. Williams (2004). Why are eddy fluxes of potential vorticity difficult to parameterise? *J. Phys. Oceanogr.*, **34**, 142–155.
- Woods, J. D. (1985). The physics of thermocline ventilation. In *Coupled Ocean–Atmosphere Models*, ed. J. C. J. Nihoul. Kiel: Elsevier, pp. 543–590.
- Woolings, T. (2010). Dynamical influences on European climate: an uncertain future. *Phil. Trans. R. Soc. A*, **368**, 3733–3756.
- Worthington, L. V. and W. R. Wright (1970). *North Atlantic Ocean Atlas of Potential Temperature and Salinity in the Deep Water, Including Temperature, Salinity and Oxygen Profiles from the Erika Dan Cruise of 1962*. Atlas Series, Vol. 2. Woods Hole, MA: Woods Hole Oceanographic Institution, 24pp.
- Wunsch, C. (1998). The work done by the wind on the oceanic general circulation. *J. Phys. Oceanogr.*, **28**, 2332–2340.
- Wunsch, C. (2005). The total meridional heat flux and its oceanic and atmospheric partition. *J. Clim.*, **18**, 4374–4380.
- Wunsch, C. and R. Ferrari (2004). Vertical mixing, energy, and the general circulation of the oceans. *Annu. Rev. Fluid. Mech.*, **36**, 281–314.
- Wüst, G. (1935). *The stratosphere of the Atlantic Ocean: Scientific Results of the German Atlantic Expedition of the Research Vessel Meteor 1925–27*. English translation edited by W. J. Emerg. et al. New Delhi: Amerind Publishing Co., pp. 109–288.
- Yamaguchi, A., Y. Watanabea, H. Ishidaa, et al. (2002). Structure and size distribution of plankton communities down to the greater depths in the

- western North Pacific Ocean. *Deep-Sea Res. II*, **49**, 5513–5529.
- Yamamoto, T. and K. Tarutani (1999). Growth and phosphate uptake kinetics of the toxic dinoflagellate *Alexandrium tamarense* from Hiroshima Bay in the Seto Inland Sea, Japan. *Phycol. Res.*, **47**(1), 27–32.
- Young, W. R. (1999). Lectures on stirring and mixing, delivered at the 1999 WHO I Summer Program in Geophysical Fluid Dynamics.
- Zeebe, R. E. and D. Wolf-Gladrow (2001). *CO₂ in Seawater: Equilibrium, Kinetics, Isotopes*. Elsevier Oceanography Series, 65. Amsterdam: Elsevier, p. 346.

Index

- Advection
definition, 43
tracer, 50
- Agulhas Current
Agulhas rings, 214
dynamic height, 186
- Air-sea exchange
carbon dioxide, 36–37, 173–174, 177–178
density, 87–89, 300
effect of extreme events, 174
fresh water, 85–87
gases, 145
heat, 28, 82–85, 299
northern basins, 296–298
thermal versus freshwater anomalies, 89
timescale for gases, 151
- Alkalinity
carbonate, 135
charge balance, 133
depth variation, 140–141
effect on buffering, 135
effect on DIC, 134–135, 138
regenerated alkalinity, 282
salinity dependence, 134
total, 133–134
- Antarctic Circumpolar Current
Drake Passage, 90, 204
dynamic height, 19, 185
Eady growth period, 221
eddy variability, 214
fronts, 203–204
momentum balance, 206
potential energy change, 233
sea-surface temperature flux, 225
speed profile, 205
transport, 205
- Arabian Sea
effect of monsoon on phytoplankton, 170
- Arctic
cascading, 301
- Atmosphere
carbon drawdown, 12
carbon reservoir, 7
cloud distributions, 26
composition, 5–6
heat store, 38
- heat transport, 6–7, 28
oxygen formation, 13
- Atmospheric carbon dioxide
anthropogenic emissions, 331–332, 334–338
anthropogenic increase, 8, 14
Earth's early atmosphere, 11
glacial-interglacial cycles, 13, 338–344
seasonality, 8
- Atmospheric circulation
eddy life cycle, 227
effect on precipitation, 86
horizontal eddy scale, 218
jet streams and storm tracks, 222–223
jets and weather systems, 27
moisture transport, 296
monsoon, 170
North Atlantic Oscillation, 175
schematic view, 27
seasonality, 80
Southern Oscillation, 170
wind stress, 80
zonal jets and angular momentum, 40
- Atmospheric ozone
residual circulation, 60
stirring, 48
transport, 60
- Bacteria
cellular composition, 94
respiration, 113
vertical profiles, 30
- Baroclinic instability, 216
Eady growth period, 220–221
velocity scaling, 222
- Brazil Current
dynamic height, 186
eddy variability, 214
- Buffer factor
definition, 143
variation, 143–145, 332
- Buffered carbon inventory
variation, 332–334
- Calcium carbonate cycling, 141–142
calcium carbonate change, 341
carbonate compensation, 334–337
- coccolithophore, 106
coccolithophorids, 149
effect on alkalinity, 142
- Carbon cycling
air-sea exchange, 36–37
anthropogenic emissions, 281
biological pump, 35
biology, 148
calcium carbonate, 141–142, 149
carbonate contribution, 283–284
chemical weathering, 12
deep ocean, 309–310
dilution, 149
disequilibrium carbon, 280
heating and solubility, 147–148, 339–341
preformed carbon, 281
regenerated carbon, 282–283
reorganisation of circulation, 344
residual carbon, 283
residual contribution, 284–287
saturated carbon, 280, 281, 283
soft-tissue contribution, 283
solubility pump, 35
Southern Ocean, 324
upwelling, 148–149
volcanoes, 12
- Carbon dioxide
air-sea exchange, 145–146, 151
buffering, 142–145
dissolved, 125
partial pressure, 125
- Carbon reservoirs, 7–8, 329
deep ocean, 291
ocean, 154, 283–287
organic carbon in the ocean, 122
- Carbonate chemistry
effect of pH, 137–138
reactions, 128–130, 135, 154
surface HCO_3^- and CO_3^{2-} , 135–137
- Centrifugal acceleration
apparent gravity, 365
derivation, 365
merry-go-round, 67–68
- Climate change
last glacial, 308–309
shelf seas, 181

- Convection
cascading, 301
Labrador Sea, 301–303
mechanism, 301
nutrients, 265–266
spreading of dense waters, 302–303
- Coriolis acceleration
derivation, 365
implications for the atmosphere and ocean, 89
merry-go-round, 67–68
- Coriolis parameter
variation with latitude, 192
- Curl
definition, 360
velocity, 91
- Deep circulation
effect of eddies, 306–307, 314
overflows, 303–304
o overturning, 317–319
spreading pathways, 290–294
- Stommel and Arons model, 311–314, 325
topography, 313–314
western boundary current, 306
- Density, 76
depth variation, 76
neutral, 76
potential, 76
surface forcing, 17, 346
- Diffusion
eddy, 54–55
molecular, 45–46, 50
nutrients onto cell walls, 101–102
vertical nutrient flux, 268
- Dispersion, 43–45
Gulf Stream floats, 231
- Dissolved inorganic carbon, 34
alkalinity dependence, 134–135, 138
definition, 130
departure from equilibrium, 149–151
depth variation, 139–140
temperature dependence, 132, 138
vertical profile, 35
- Divergence
definition, 360
velocity, 91
- Dynamic height
geostrophic flow, 70, 72
- East Australian Current
dynamic height, 187
- Ecosystem
convection, 265–266
elemental ratios, 95
gyres and nutrient transfer, 263
ocean deserts, 266–268, 287
seasonality in surface chlorophyll, 164–168, 176
subsurface chlorophyll maximum, 169, 176
- Eddies
direction of eddy fluxes, 235
effect on deep circulation, 314
effect on dense waters, 306–307
effect on phytoplankton bloom, 168
effect on phytoplankton growth, 270–271
formation, 215–218
horizontal nutrient transfer, 273
horizontal scale, 218
parameterisation, 227
potential energy release, 319–320, 325
sea-surface temperature flux, 223
stirring in the thermocline, 225
timescale for growth, 220
tracer transfer, 51–53, 54–55
variability over the globe, 211–214
velocity scaling, 222
- Eddy transport
atmospheric ozone, 60
bolus velocity, 57, 64, 226
model illustration, 226–227
schematic view, 60
Southern Ocean, 62
tracer equation, 227
- Ekman flow, 72–74
basin-scale upwelling, 247, 263
horizontal nutrient transfer, 272
North Atlantic, 74
spiral, 73
transport, 73
upwelling, 74
upwelling velocity, 258
volume flux, 73
- El Niño–Southern Oscillation, 170
- Energetics
potential energy changes, 319–320
work done by the wind, 325
- Enzymes
definition, 96–97
Michaelis–Menten model, 97–98
- Equatorial currents
dynamic height, 187–189
- Eulerian
time average, 56
- Flux
eddy interpretation, 53
properties, 45
tracer, 49
tracer advection, 50
- Forcing
momentum equations, 362–363
- Fossil fuels
anthropogenic emissions, 8, 14, 331–332, 334–337
carbon reservoir, 7, 329, 331–332
greenhouse warming, 15
- Friction
effect, 67
force, 363
surface drag, 17
wind stress, 80
- Fronts, 271
Antarctic Circumpolar Current, 203–204
effect on phytoplankton growth, 271
shelf seas, 175–176
vorticity balance, 194
- Gases
air-sea exchange, 145–151
air-sea flux, 126–128
mixing ratio, 128
partial pressure, 128
solubility, 125–128
- Geostrophic balance, 69
derivation, 367–368
- Geostrophic flow, 70–72
Antarctic Circumpolar Current, 90
dynamic height, 70, 72
Gulf Stream, 78
North Atlantic drifters, 74
Rossby number, 72
variation with depth, 76–77
- Glacial-interglacial cycles
atmospheric carbon dioxide, 338–339
calcium carbonate change, 341

- Glacial-interglacial cycles (*cont.*)
 circulation change, 344
 ecosystem change, 341–344
 temperature change, 339–341
- Gradient
 definition, 360
- Gravity
 effect, 66
 force, 362
 inclusion of centrifugal, 365
 potential energy changes, 319–320
 tides, 17
- Greenhouse warming, 6, 15, 39
- Gulf Stream
 barrier or blender?, 231–232
 dissolved oxygen contrast, 229
 dynamic height, 184
 Eady growth period, 221
 eddy variability, 211
 float exchange, 231
 geostrophic flow, 78
 nutrient transfer, 261–263
 sea-surface temperature, 189
 sea-surface temperature flux, 223
 surface chlorophyll and temperature, 9
 tracer transfer, 228–231
 transport, 189–191
- Gyres
 definition, 183
 dynamic height, 19, 183–184
 ecosystems and nutrient transfer, 263–265
 exchange across gyre boundaries, 254–257
 northern hemisphere, 184–185
 recirculations, 191
 southern hemisphere, 185–187
 Stommel model, 197–199, 208
 transport definition, 79
- Heat transfer
 air-sea exchange, 82–85
 geothermal, 85
- Hydrostatic balance, 69, 76
 derivation, 367
- Iron cycling
 complexation, 119
 glacial fertilization, 343–344
- High Nitrate, Low Chlorophyll regimes (HNLC), 119–121
- nitrogen fixation, 273
- Kuroshio Current
 dynamic height, 184
 Eady growth period, 221
 eddy variability, 211
 sea-surface temperature flux, 223
- Lagrangian
 rate of change, 360–361
 time average, 56
 view of subduction, 245, 251
- Land
 carbon cycling, 11–13
 carbon reservoir, 7, 329
- Latent heat flux
 surface pattern, 83
- Long-wave heat flux
 surface pattern, 82
- Mass conservation equation
 one dimensional, 50
 three dimensional, 52
- Material derivative, 360–361
- Mathematical definitions
 gradient, divergence, curl, 360
 material derivative, 360–361
 Taylor expansion, 361
- Mediterranean
 outflux, 51, 296
 overflow, 304
- Mixed layer, 20
 convection and nutrients, 265–266
 global variation, 164
 one-dimensional model, 161
 physics, 161–163
 seasonal and diurnal cycles, 161
 subtropical North Atlantic, 163
 turbulence, 159–161
 ventilation, 245
 ventilation and potential vorticity, 259
- Mixing
 fracture zones, 304–305
 lightening of dense waters, 316
 overflows, 303–304
 Southern Ocean, 319–320
- Momentum equations, 68
 coordinate transformations, 364–365
 derivation, 361–366
 geostrophic balance, 367–368
 hydrostatic balance, 367
 zonal channel, 206
- North Atlantic
 deep western boundary current, 306
 dense waters, 305–306
 eddy stirring, 306–307
 overflow, 303
- North Atlantic Oscillation, 175
- Nutrient cycling
 chemostat, 123
 dissolved organic matter, 111, 113
 dissolved organic nutrients, 274–276
 iron, 116–119
 mixed-layer budget, 288
 nitrogen, 116–118
 nitrogen fixation, 273–274
 nutrient utilisation, 278–279
 phosphorus, 116–118
 preformed nutrients, 277
 Redfield ratio, 95–96, 115–116
 regenerated nutrients, 277–279, 283
- Southern Ocean, 322–324
- Ocean
 carbon reservoir, 7–8, 34, 309–310, 329–331
 deep properties, 290–291
 heat store, 6, 38
 heat transfer, 298–299, 324
 heat transport, 6–7
 special characteristics of water, 3–5
 vertical structure, 20–22
- Ocean circulation
 dynamic height, 18
- Organic carbon
 dissolved organic carbon, 111
 particulate, 114–115
- Overflows, 303–304
- OVERTURNING
 cascading, 301
 convection, 301–303
 heat transfer, 298–299
 link to pressure contrasts, 325
 multiple equilibria, 309
 northern basins, 294–298
 schematic view, 25
 Southern Ocean, 292–294, 317–319
 transport definition, 79
 variability, 307–309
- Particle exchange
 across a zonal jet, 234
 across the Gulf Stream, 231–232

- pH
distribution, 129
effect on carbonate chemistry, 137–138
- Photosynthesis
chlorophyll, 32
definition, 93, 96
phytoplankton, 9
- Phytoplankton
bloom, 165–168
cellular composition, 94–95
coccolithophore, 106
community structure, 108–109, 113
different types, 106
diversity, 33
effect of upwelling, 269–271
fate, 111
functional groups, 9
Prochlorococcus, 95
seasonal succession, 171–172
sinking, 112
vertical profiles, 30
- Phytoplankton growth
biomass model, 103
export production, 113–114
light regulation, 103–105
nutrient regulation, 98
primary production, 110–111
temperature regulation, 105–106
- Potential energy release
ball rolling down a hill, 215
Drake Passage, 233
slantwise exchange, 216
- Potential vorticity
eddy perturbations, 218
eddy stirring, 225, 254
effect of sloping topography, 199–201
thermocline, 252, 253
ventilation, 253–254, 259
- Pressure contrasts
effect, 66
effect on horizontal flow, 70–72
force, 362
- Radiative heating
anthropogenic emissions, 39
atmospheric composition, 5–6
implied global-mean temperature, 38
latitudinal contrasts, 6–7
surface pattern, 82
- Redfield ratio
elemental ratios, 95–96, 115–116
- Residual circulation, 60–62
Southern Ocean, 317–319
- Respiration
bacteria, 113
ballast, 114–115
definition, 94
- Rossby deformation radius, 218
- Rossby number, 72, 367
- Rossby waves, 209–210
- Rotation
implications for the atmosphere and ocean, 89
merry-go-round, 67–68
momentum equations, 363–364
- Salinity
definition, 76
effect of freshwater exchange, 85–87
- Scale analysis
tracer equation, 50
momentum balance, 91, 366–368
vorticity, 194, 208
- Seasonality
air-sea exchange of carbon dioxide, 173–174
DIC in the subtropical North Atlantic, 172
ecosystem in the shelf seas, 176
effect of the monsoon on chlorophyll, 170
mixed layer, 164
wind stress, 80
- Sensible heat flux
surface pattern, 83
- Shelf seas
air-sea exchange of carbon dioxide, 177–178
cascading, 301
fronts, 175
long-term change, 181
mechanical forcing, 181
phytoplankton bloom, 176
slope current, 313
turbulence, 175–176
- Solar heat flux
surface pattern, 82
- Southern Ocean
carbon, 324
mixing, 319–320
nutrients, 322–324
overturning, 292–294, 317–319
- residual circulation, 62
work done by the wind, 325
- Stirring
atmospheric ozone, 48
cream in coffee, 46
dense water masses, 306–307
phytoplankton, 48, 63
potential vorticity, 254
thermocline, 225
- Stokes' drift
particles moving in water waves, 56
shallow-water waves, 57–60, 64
- Stommel model, 197–199
width of boundary current, 208
- Sverdrup balance, 195–196
- Taylor expansion, 361
- Taylor–Proudman column, 313
- Thermal-wind balance, 76–77, 90–91
thermocline signal, 189
- Thermocline, 20–22
basin-scale variations, 189
Ekman pumping, 248–249
North Atlantic subtropical gyre, 78
- Tides
gravitational forcing, 17, 319–320
mechanical forcing in shelf seas, 181
turbulence, 175
- Topography, 26
effect on gyres, 198–201
effect on western boundary currents, 201–203
mixing in fracture zones, 304–305
sinking of dense waters, 303
slope current, 313
Taylor–Proudman column, 313
vorticity balance, 201–202
- Tracer
variance budget, 235
- Tracer conservation equation
eddy transfer, 53
one dimensional, 49–50
three dimensional, 52
- Tracer transport, 50
eddy transfer, 51–53, 226–227
Mediterranean water, 51
- Transport
advection, 43
bolus velocity, 57
horizontal, 79
rip currents, 56, 59–60

- Transport (*cont.*)
stirring and mixing, 46–49
Stokes' drift, 56–60
vertical overturning, 79
- Tropics
equatorial currents, 19, 187–189
inter-annual variability in ecosystem, 170–171
nitrogen fixation and iron, 273
seasonal variability in ecosystem, 169–170
- Turbulence
shelf seas, 175–176
surface mixed layer, 159–161
- Upwelling
basin scale, 247
coastal, 74
dense waters returned to the surface, 316
effect on phytoplankton, 269–271
- Vector operators
gradient, divergence, curl, 360
- Ventilation
deep and bottom waters, 242–243
idealised view, 236–237
- intermediate waters, 242
Luyten, Pedlosky and Stommel model, 253
nutrient transfer, 263–265
radiocarbon age, 291
rate, 249–252
seasonal mixed layer, 245–247
temperature and salinity classes, 244
thermocline, 252–254
tritium–helium age, 252–253, 258
upper mode waters, 237–241
- Vorticity
equation, 209
ocean response, 194
relative, planetary and absolute, 192
spinning top, 192
Sverdrup balance, 195–196
- Walin framework
diffusive fluxes, 346, 352
isopycnal view, 345
transformation rate, 352
water-mass formation, 345
water-mass transformation, 345–350
- Water masses, 22
deep and bottom waters, 242–243
formation rate, 345–346
intermediate waters, 242
link to the Southern Ocean, 292–294
mode waters, 23–25
temperature and salinity classes, 244
transformation rate, 345–350
upper mode waters, 237–241
- Weather systems
formation, 215–218
- Western boundary currents
deep, 306
effect of topography, 201–203
exchange across gyre boundaries, 254–257, 259
Munk model, 209
nutrient transfer, 261–263, 287
Stommel model, 198, 208
- Wind stress, 80
seasonality, 80
surface pattern, 80
- Zooplankton
feeding, 111
vertical profiles, 31